2019

Development of High-speed Optical Coherence Tomography for Time-lapse Non-destructive Characterization of Samples

Yongyang Huang
Lehigh University

Development of High-speed Optical Coherence Tomography for Time-lapse Non-destructive Characterization of Samples

by

Yongyang Huang

A Dissertation

Presented to the Graduate and Research Committee

of Lehigh University

in

Electrical Engineering

Lehigh University

May 2019

SIGNATURE SHEET

Approved and recommended for acceptance as a dissertation in partial fulfillment of the requirements for the degree of Doctor of Philosophy.

_____
Date

_____
Prof. Chao Zhou

_____
Accepted Date

Committee Members:

_____
Prof. Chao Zhou

_____
Prof. Nelson Tansu

_____
Prof. James Hwang

_____
Prof. Lesley Chow

_____
Prof. Daniel Ou-Yang

ACKNOWLEDGMENTS

I would like to express my sincere appreciations to the following people, including my advisor, my committee members, my labmates, my family and my girlfriend.

- First, I would like to thank my advisor, Prof. Chao Zhou, who provides me the opportunity to continue my pursuit for a higher degree. He has introduced me to the field of biomedical imaging, especially the technology of optical coherence tomography (OCT), which I find the research topic really interesting and potentially impactful on our everday life. During the last six years, he has guided me through the entire training process so that I can grow from a novice to an expert in OCT technology. In my impression, Chao is a passionate principle investigator (PI), who has a lot of novel and really impactful ideas to make full use of our technology for various potential applications. Under his guidance, I am exposed to various projects and have a lot of chances to try out different things and to expand my skill sets. Although many of them don't work out as expected, I'm appreciated for his support and patience for my research work in the meantime. Moreover, he has shared with me a lot of technical skills for the researchers, including oral presentations, preparation of proposals and critical thinking of other researcher's work, which I benefit a lot and can utilize these skills for my future work.
- I would like to thank Prof. Nelson Tansu, Prof. James Hwang, Prof. Daniel Ou-Yang and Prof. Lesley Chow for serving as the committee for my PhD defense. In my first committee presentation and the general exams, they provided a lot of constructive feedbacks for my research work. Especially, one critical comment from them was that, I should concentrate on one research topic of the technical development of OCT, make it work and finish my degree. I'm very grateful when they acknowledge my research work and my contribution to the science during my defense presentation.
- I would like to thank Fengqiang (Neal) Li, my first colleague in the lab, for his guidance during the early years. He was the one who helped me to build the first prototype OCT system, guided me through the entire process of how to characterize the system performance, how to collect OCT data and how to analyze OCT data. He also shared a lot of research experience, which helped a lot during my later years of research.

- I would like to thank my colleagues, Jitendra Solanki, Mudabbir Badar, Zhao Dong and Jason Jerwick for our teamwork to improve the performance of space-division multiplexing OCT (SDM-OCT), the state-of-the-art OCT technology in our lab. During the last few years, we have figured out and solved a lot of technical issues for the SDM-OCT, including hardware configuration, data acquisition and the post-processing procedure, to make the SDM-OCT system more stable and robust. Without the contribution from each of us, we cannot really make good progresses in the SDM-OCT project, including developing the first-generation and second-generation chip-based SDM-OCT, full-range SDM-OCT and phase-stable SDM-OCT for angiography and elastography.
- I would like to thank my advisor Prof. Chao Zhou, Peter Li and Marc Ferrer, who initiated the collaborated work of OCT imaging of tumor spheroids and brought me into this project. This project has become one of my main research projects and my most impactful research work in related fields, which was published in *Cancer Research* and *Journal of Visualized Experiments*. Regarding this project, I would like to thank Dr. Qiongyu Guo, who has brought her expertise in biomedical engineering into this project and contributed a lot to the revision of the *Cancer Research* paper. I would like to thank Jinyun Zou, Keren Luo for their contributions to the follow-up research work of the tumor spheroid project, including collecting new data, analyzing the data and optimizing the performance of the OCT system. I would like to thank Tao Xu and Junchao Liu, visiting students from Wuhan University, for their technical supports to re-configure the OCT acquisition software to perform sequential scanning of tumor spheroids for high-throughput imaging. I would like to thank Shunqiang Wang, Wentao Shi and Yuyuan Zhou from Prof. Yaling Liu's lab located upstairs in the same building, for their assistance and guidance in 2D and 3D cell culturing. Our collaborated work on a new protocol to prepare large-quantity, uniform-shape tumor spheroids has been accepted in *Scientific Reports*. Also, I would like to thank our collaborators from Nexcelom Bioscience, Inc. and National Center for Advancing Translational Sciences (NCATS), including Leo Chan, Sarah Kessel, Steve Titus, Natalia Martinez, Yu-chi Chen and Molly Boutin, for preparing tumor spheroid samples and performing an initial screening of tumor spheroids with bright field imaging for a correlation study.

- I would like to thank my advisor Prof. Chao Zhou, Prof. Arjun Yodh and Prof. Daniel Ou-Yang for initializing the collaborated work on OCT imaging of liquid crystal droplet and latex system, which has significant impacts in both fundamental researches in material science and industrial applications. Regarding these projects, I would like to thank Dr. Zoey S. Davidson, who introduced the liquid crystal droplet model to us, conducted most of the research work in the collaborated project, and introduce our OCT technology to the audience in the field of material science through the published paper in *Nature Communications*. I would like to thank Dr. Hao Huang and Zhiyu Jiang from Prof. Daniel Ou-Yang's lab in physics department, for their comprehensive knowledge of latex systems and their momentum to push the latex imaging project forward. Without their efforts, we cannot wrap out this collaborated work of latex characterization with the integrated OCT-gravimetric-video imaging platform into a published paper in *Scientific Reports*.
- I would like to thank Dr. Sophie Astrof and Dr. Karl. Degenhardt for their interests in employing OCT for developmental biology studies. During the collaborated work, they have provided their expertise in identifying the fundamental questions that could be resolved by OCT in embryonic studies, preparing mouse embryos samples for us to characterize, and guiding us to identify the features of mouse embryonic hearts in the OCT images.
- I would like to thank Dr. Lei Zhang for his knowledge in OCT angiography so that we can get some good skin angiography data from the human subjects. Also I would like to thank Dr. Guoyan Liu, who is a medical expert in skin disease, for the comprehensive discussions about the finger nail anatomy.
- I would also like to thank other colleagues and visiting students in our lab, including Aneesh Alex, Jing Men, Guangming Ni, Zhiwen Yang, Lian Duan, Penghe Wu, Xianxu Zeng, Xiaofang Wang, Jinming Wang, Kan Wu, Ian Rubinoff, Andre Sukernik, Luisa Goepfert for the helpful discussions and participations in different projects.
- At last, I would like to thank my parents, Zhiying Huang and Jingfen Xu, for raising me up and supporting my decision to pursuit my Bachelor's and Ph.D degree outside my hometown and home country. Also, I'm so lucky to meet my girlfriend, Li Jiang, during my graduate studies in Lehigh. She

provides a lot of support when I'm having a hard time finishing my final research work and writing my dissertation. Hopefully, we can start a new life together after my graduation.

TABLE OF CONTENTS

LIST OF TABLES

LIST OF FIGURES

ABSTRACT

Optical coherence tomography (OCT) is an established optical imaging modality which can obtain label-free, non-destructive 3D images of samples with micron-scale resolution and millimeter penetration. OCT has been widely adopted for biomedical researches, especially in the fields of ophthalmology and cardiology. In addition to biomedical applications, OCT has also been employed to characterize various industrial products, including tapes, tablet coatings, thin films, and paints. Given its advantages, OCT, especially high-speed OCT, is suited for time-lapse (or longitudinal) non-destructive imaging of samples to monitor their dynamic changes over time.

In the first part of my dissertation, I have focused on the topic of the advances of high-speed OCT technologies. The OCT technology has been briefly introduced, with the focus on the principles and key performance metrics. A detailed tutorial on how to build a custom spectral domain OCT (SD-OCT) has been described. Next, I have introduced the space-division-multiplexing OCT (SDM-OCT) technology, a parallel imaging OCT technology with a more complex and intricate system setup. The principles of SDM-OCT and step-by-step procedures to build a SDM-OCT and to characterize its performance have been described in details. I have demonstrated the feasibility of both fiber-based and chip-based SDM-OCT to perform *in vivo*, high-speed imaging of human fingers. Furthermore, I have presented my work on improving the performance of SDM-OCT with the implementation of the galvo-based phase-modulation full-range technique, which can facilitate the SDM-OCT acquisition of multi-channel images with reduced hardware requirements. Detailed descriptions of theoretical foundations, experimental designs and post-processing procedures of the galvo-based phase-modulation full-range technique have been shown. The feasibilty of the full-range SDM-OCT (FR-SDM-OCT) has been demonstrated by characterizing its performance in mirror and tape images and acquiring the images from human fingers *in vivo*.

In the second part of my dissertation, I have presented the unique observations using high-speed OCT systems to characterize dynamic processes in biological and non-biological samples. First, a functional OCT, OCT angiography (OCTA), has been shown to visualize the vascular network. Specifically, I have demonstrated the feasibility of SDM-OCT angiography to visualize the capillary network in the human finger nail, showing the advantages of SDM-OCT technology with a parallel imaging scheme to further improve

the imaging speed and the field of view (FOV) with reduce motion artifacts. Second, I have shown my research work of characterization of drying process of droplets and latex systems. With a short time window from a few milliseconds to ~1 second, high-speed OCT systems can be used to capture the fast fluid flows in the drying droplets and the fast packing process in drying latex system. With a multi-modal imaging platform including OCT, gravimetry and video measurements, we have characterized progressions of global and local drying phenomena in polystyrene latex system for ~500 min. Third, I have shown my work on establishing an OCT-based, 3D high-throughput imaging (HTI) platform to perform screening of tumor spheroid assays in 96-well plate. I have developed a program for quantification of tumor spheroid morphology (i.e. diameter, height, volume) to track growth kinetics. I have also developed a strategy to label the 3D distribution of dead-cell regions within the tumor spheroid for viability characterization, based on intrinsic optical attenuation contrast. With the established platform, I have performed the OCT screening of tumor spheroid invasion assays to characterize 3D cell invasion and evaluate inhibition effects of drugs. Fourth, I have described my research work on utilizing OCT to image mouse embryonic hearts at different developmental stages, with the implementation of optical clearing methods to enhance the light penetration in mouse embryos. Representation results of using OCT to phenotype congenital heart defects (CHDs) in mutant mouse embryo models have been shown.

Chapter 1: Optical Coherence Tomography (OCT): an Introduction

1.1 Overview

Optical coherence tomography (OCT) [1] is an established optical imaging modality which can obtain label-free, non-destructive 3D images in biological tissues. As the optical analog of ultrasound, OCT can detect back-scattered signals within the sample from the depths of up to 1-2 mm below the surface. Instead of measuring the echo time from each depth for ultrasound, OCT employs low-coherence interfometry to reconstruct with structural images with high depth resolvability. Serving as "optical biopsy", OCT can provide *in situ*, non-destructive measurements of tissue properties, without the need for sample excision and fixation. By scanning the incident beam on the sample in one lateral direction, tomographic image of the tissue structure in cross-sectional planes (B-scan) can be captured. While the beam is scanning in both lateral directions, 3D OCT data (C-scan, cubic scan) can be obtained to reconstruct the volumetric structure of the sample. The acquisition time for a OCT volume is on the order of seconds, which are suitable for *in vivo* clinical studies. The resolution of the OCT images is approaching that of confocal microscope and histology, which demonstrated the feasibility of OCT as an alternative imaging technique to resolve fine tissue structure. Since OCT does not require any labeling or injection of contrast agents (i.e. inks, dyes, fluorescent dyes, nano particles) to render the signals, it can alleviate the potential damages or side-effects for animals and human subjects. Also, the employment of near-infrared light source with low power level (in mW) ensures that the OCT imaging is safe without radiation and photo-thermal damages. **Table 1.1** summarized the advantages of the OCT imaging technique.

Table 1. 1 Advantages of Optical Coherence Tomography

Advantage of Optical Coherence Tomography	
• 2D and 3D tomography • High depth resolvability • Micron-scale resolution in both axial and lateral direction • High-speed data acquisition	• Non-destructive • Non-contact • No label or contrast agent • Minimal radiation and photothermal damage*
* For retinal imaging, since the threshold damage level is low, the photothermal damage needs to be taken into consideration.	

Table 1. 2 A Chronicle of OCT Development

A Chronicle of OCT Development	
Year	Milestones
1991	First published paper of OCT (TD-OCT)
1993	First retinal images in vivo
1995	First SD-OCT demonstration
1995	Early clinical studies on eye disease
1996	First commercial ophthalmic OCT system
1997	First SS-OCT demonstration
1998	First tomogram of skin
1998	Demonstration of video rate OCT
2003	Theoretical and experimental demonstration of sensitivity advantage of FD-OCT
2003	Speed of SD-OCT reaches 15 kHz
2004	First commercial cardiovascular OCT system
2005	OCT becomes standard of care in ophthalmology
2006	First FDA approved ophthalmic SD-OCT system
2008	Speed of SD-OCT reaches 312.5 kHz
2010	Speed of SS-OCT reaches 20 MHz
2010	First commercial dermatology OCT system
2012	First commercial SS-OCT system
2013	First commercial gastroenterology OCT system
2014	First Commercial OCT angiography system
2018	Speed of SS-OCT reaches 44.5 MHz
* TD-OCT: Time-domain OCT; SD-OCT: Spectral-domain OCT; SS-OCT: Swept-source OCT; FD-OCT: Fourier-domain OCT.	

Table 1.2 shows a chronicle of the development of OCT, adapted from OCT reviews by Fujimoto and Swanson [2], Klein et al. [3] and de Boer et al. [4]. The first OCT paper was published by Huang et al. in 1991 [1]. Two years later, OCT was successfully employed to perform in vivo imaging of the retina [5]. The first spectral domain OCT (SD-OCT) system was demonstrated in 1995 to measure the corneal thickness [6]. In 1997, the first swept source OCT (SS-OCT) system was also demonstrated [7]. Next year, the first tomogram of the skin was captured [8]. In the same year, OCT with a video rate acquisition of 2D images was demonstrated [9]. However, the significance of sensitivity advantages of spectral domain and swept source OCT systems over time-domain OCT system was not clearly stressed in these papers until the

establishment of theoretical foundations in 2003 [10-12]. Since then, Fourier domain OCT was widely adopted for OCT applications. With the rapid development of line-scan cameras and tunable swept lasers, the OCT imaging speed has been improved significantly. In 2003, a SD-OCT system with an imaging speed of 15,000 Hz (axial scans per second, A-scans/s) was demonstrated [13]. The speed reached 312.5 kHz in 2008 [14]. A swept source system with an equivalent imaging speed of 20.8 MHz was demonstrated in 2010, marking a new record of the OCT speed [15]. To date, the record-high speed of the OCT system was 44.5 MHz with the implementation of a mode-locked fiber laser and time stretch technique in a SS-OCT system [16].

OCT was introduced in clinical studies starting from the mid-1990s. In 1995 and 1996, OCT was demonstrated to facilitate the diagnoses of retinal and macular diseases, including glaucoma, macular edema, aged-related macular degeneration and choridal neovascularization [17-20]. With 10-years aggregation of experimental proofs, clinical data and technology advances, OCT finally gained wide clinical adoption and became a standard of care in ophthalmology in 2005 [2]. By 2015, it was estimated that ~15 million ophthalmic OCT procedures was performed in United States in a single year. In worldwide, the number reached ~30 millions per year [2, 21].

The prerequisite for wide adoption of OCT in clinical studies was the commercialization of the OCT technology. The first OCT start-up company was established in 1992 and the first commercial ophthalmic OCT product was released in 1996 [2]. It was until the release of the 3rd generation OCT system in 2002 that the ophthalmic OCT market began to thrive. The introduction of the first FDA-approved SD-OCT further expanded the market with more start-up companies, more OCT systems sold and growing annual revenues. The yearly annual renenue of ophthalmic OCT system reached ~500 million dollars in 2013 and the cumulative revenue reached ~4 billion dollars by 2016 [21]. Other than ophthalmic OCT system, commercial cardiovascular, dermatology, gastroenterology and angiographic OCT systems emerged in the market in 2004, 2010, 2013 and 2014, respectively, further broadened the OCT market [21]. With different types of commercial OCT system available in market, more procedures were performed in clinics. It was estimated that a total number of ~400,000 cardiovascular OCT procedures, ~25,000 dermatology OCT procedures and ~7,000 gastroentterology OCT procedures were performed by 2016 [21]. It is still an ongoing process that

researchers and companies are working together to translate state-of-the-art OCT technology into clinical practice.

1.2 Different Types of OCT

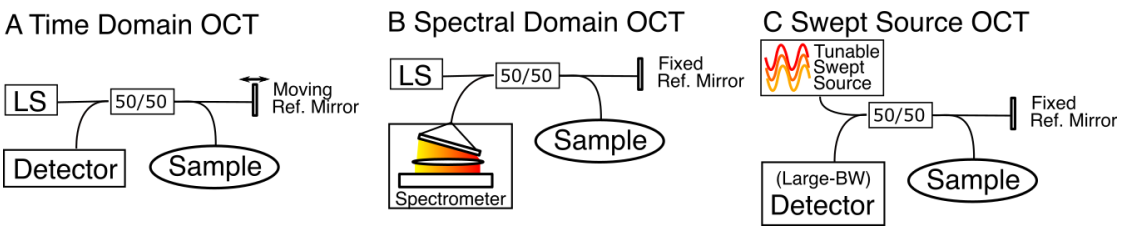

Figure 1. 1 Comparing the configuration of different types of OCTs. (A) Time-domain OCT (B) Spectral domain OCT (C) Swept Source OCT. LS: Light Source; 50/50: 2×2, 50/50 fiber coupler or beam splitter. BW: bandwidth

According to the configuration, OCT can be divided into two categories: Time-domain OCT(Td-OCT) and Fourier domain OCT (FD-OCT). FD-OCT can be further divided into two categories: spectral domain OCT (SD-OCT) and swept source OCT (SS-OCT). **Figure 1.1** shows the schematics diagrams of all three types of OCT. The major parts for all three types of OCT system are the same: the interferometer. All three types of OCT system utilize the Michelson interferometer configuration to generate the interference signals: Emission light from the light source (LS) is first split into two: one portion is transmitted in the reference arm and reflected by the reference mirror, while the rest of the light is transmitted in the sample arm and back-scattered by the sample. The reflected signals from two arms would meet at the splitter and interfere with each other. Finally, the interference signals would arrive at the detector. The Michelson interferometer in the OCT system is usually achieved with a beam splitter in the free space or a 2×2 fiber coupler in fiber-based setup.

Other than the interferometer part, we can find the variations of system configuration in these three types of OCT system. Both TD-OCT and SD-OCT systems utilize broad-band light source to provide incident light. Either a superluminescent diode (SLDs) or a supercontinuum laser (SC) can be used as the broad-band light source. However, the detection parts are quite different: TD-OCT use a single photo-detector to detect the back-scattered interference signals while the SD-OCT uses a spectrometer to detector wavelength-dependent back-scattered interference signals. For the SS-OCT, the detection scheme is the same as TD-OCT system: use a single or balanced detector to detect the back-scattered signals. However, the light source is

quite different for SS-OCT. SS-OCT utilizes a tunable swept laser to provide narrow-band light pulses with continuously-sweeping wavelengths. Thus the detected interference signals are also wavelength-dependent.

Figure 1.2 illustrates the different detected interference signals from three types of OCT systems. The simulated OCT interferogram is presented in **Figure 1.2 A**, which is dependent on both the depth z and the or wavenumber k. For time-domain OCT, the photodetector receives the signals from all the wavelength. The effect is equal to a summation of the 2D inteferogram along the λ direction for a given depth z_1. Due to the partial coherence of the broadband incident light, only the interference signals within a narrow depth range of $z_1 \pm \delta z$ could be detected (**Figure 1.2 B**), which the peak amplitude can indicate the relative tissue reflectivity at the depth z_1 (in arbitrary unit). By moving the reference mirror, the sample reflectivity profile along the depth could be measured sequentially, forming an OCT scan along the axial direction (A-scan, shown in Figure 1.2C). The detected interferometric signals can be expressed as [22]:

$$I(z_n) = 2I_0\sqrt{\alpha_r\alpha_n}|\gamma(z_n)|\cos(\frac{2\pi}{\lambda}z_n + \varphi) \tag{1.1}$$

where $I(z_n)$ is the detected back-scattered intensity at each depth, α_r and α_n are reflectivity of the reference mirror and the n_{th} layer of samples as a function of depth, respectively, $\gamma(z_n)$ is the normalized autocorrelation function, of which the bandwidth determines the axial resolution of the TD-OCT system.

As for FD-OCT, one major difference is that FD-OCT detects wavelength-dependent back-scattered signals. The depth-encoded interference spectrum for a SD-OCT is shown in **Figure 1.2 D**. We should note that, the typical interference signal detected by the SD-OCT contains a DC term, which yields an offset in the fringe. By removing the DC term, we can get the SD-OCT spectra in **Figure 1.2 D**. Then, an inversed Fourier transform is performed to reconstruct the intensity profile along the depth direction, with the result shown in **Figure 1.2 E**.

The detection schemes of depth-encoded interference signals is slightly different between SD-OCT and SS-OCT systems. For SD-OCT, a spectrometer (See Chapter 2.2.4 for the configuration of the spectrometer) is used to collect the wavelength-dependent interference signals at different camera pixels, within the camera integration time (**Figure 1.2 D**). For SS-OCT, the fast photodetector captures the depth-encoded interference signals of a narrow wavelength range (wavenumber range Δk) in a short duration of time (sampling time δt), which is shown in **Figure 1.2 C**. The individual point spread functions (blud lines) indicates the detected

discrete fringe signal within the wavenumber range Δk in a sampling time δt. After one sweep is done, we can gather all spectral data from different wavelength ranges (different wavenumber ranges) to form a depth-encoded wavelength-dependent interferogram that is similar to the SD-OCT spectra [4].

The actual detected signals by FD-OCT (including SD-OCT and SS-OCT) can be expressed as [22]:

$$I(k) \sim S(k) \sum_{n} (\sqrt{\alpha_r \alpha_n} \cos(2z_n k + \varphi)) \tag{1.2}$$

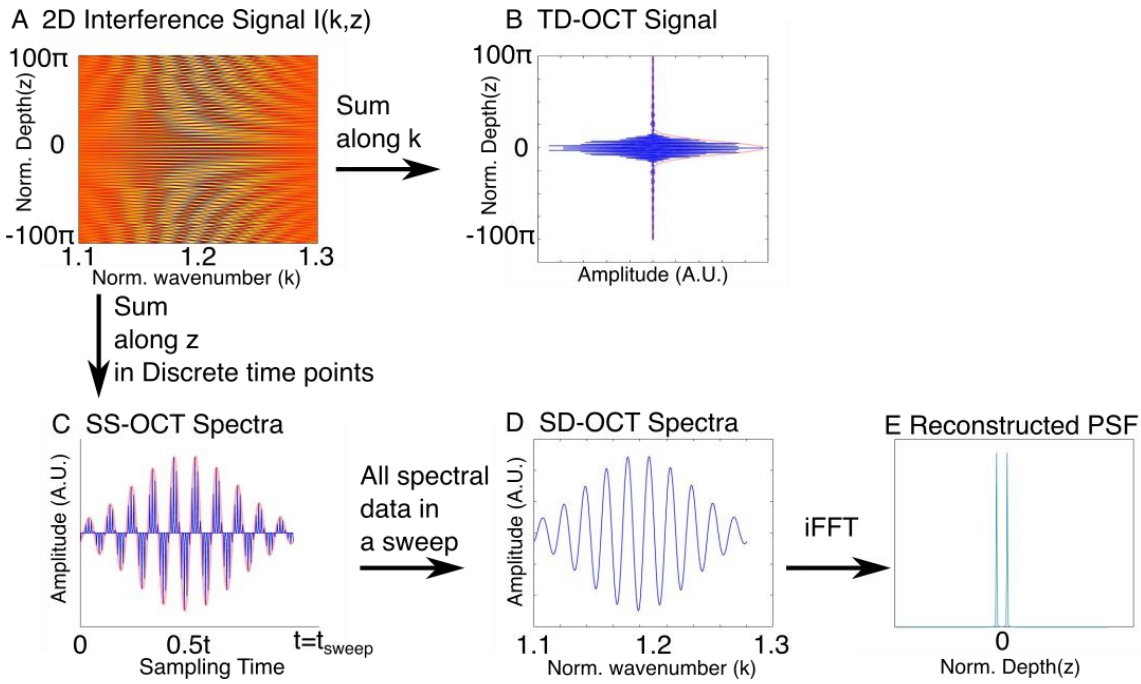

Figure 1. 2 Illustration of detected interference signals (fringe) by different types of OCT. (A) Simulated interference signals as a function of both depth z and wavenumber k. (B) Reprensentative detected TD-OCT intensity profile, with the contour drawn in light red. (C) Representative detected spectral points in SS-OCT spectra, which is shown as discrete blue PSFs. The light red curve shows all spectra data in a sweep, which is equivalent to SD-OCT Spectra in (D). After inverse fast Fourier transform (iFFT), the PSF is reconstructed .

where I(k) is detected back-scattered signals as a function of wavenumber k, S(k) is the power density spectrum as a function of wavenumber, which is correlated with the autocorrelation function via Fourier transform; k is the wavenumber, and z_n is the optical path difference (depth) at n_{th} layer of the sample. After Fourier transform, detected back-scattered signals in spatial domain could be reconstructed as[22]:

$$I(z) \propto S(z) \otimes \sum_{n} \sqrt{\alpha_r \alpha_s(z)} (\delta(z - z_n) + \delta(z + z_n)) \tag{1.3}$$

where $\otimes$ indicates the convolution operator. In the expression 1.3, we can find that there are two mirror terms located in both z_n and $-z_n$, indicating the existence of the mirror image after the Fourier reconstruction (shown in Figure 1.2C). Note that, for TD-OCT, no mirrored image would be detected.

1.3 Key Performance Metrics of OCT

Several key metrics are used to evaluate and compare the performance of OCT systems, including central wavelength and spectral range of the light source, axial resolution, lateral (transverse) resolution, depth of focus, total imaging depth, sensitivity and its roll-off.

1.3.1 Central Wavelength and Spectral Range

We first mention about the central wavelength and the spectral range since it would determine or affect the rest of key performance metrics. For OCT, three wavelength ranges are often used: ~800 nm, ~1060 nm and ~1300 nm, depending on the applications. Recently, a few groups use the visible wavelength range [23] and 1.7 µm range for specific applications like measuring oxygen saturation [24, 25], ultra-high-resolution retinal imaging [26] and probing the deeper region of the brain [27, 28].

1.3.2 Axial Resolution

The axial resolution shows the resolving power of OCT along the depth direction. Assuming a Gaussian-shape optical spectrum of the light source, we can derive the theoretical axial resolution as[22]:

$$\Delta z = \frac{2\ln(2)}{\pi n}\frac{\lambda_c^2}{\Delta\lambda_{fwhm}} \tag{1.4}$$

where λ_c is the central wavelength of the incident light, and $\Delta\lambda_{fwhm}$ is its full-width-at-half-maximum (FWHM) spectral bandwidth of the spectrum of the light source.

Based on the equation, in most of the cases, the theoretical axial resolution can be determined by the central wavelength and the spectral bandwidth of the light source of the OCT system. However, the spectral bandwidth of detected signals will be affected by these following factors: transmission window of the fiber and the optical lenses, the bandwidth of the fiber coupler and the detection range of the detector. Moreover,

since the spectrum shape is usually not Gaussian, it would affect the axial resolution as well [3]. Digital spectral shaping techniques can be employed to convert the non-Gaussian-shaped spectra from the light source to Gaussian-shape spectra to suppress the sidelobes [29-31]. Also, if the detected signals are not linearly sampled in wavenumber, the axial resolution will become poorer as the imaging depth gets deeper. In this cases, spectral resampling would be required in order to maintain the axial resolution in the deeper depth [32].

1.3.3 Lateral/Transverse resolution

One important note about the lateral resolution is that it is independent of the bandwidth of the light source. Assuming a Gaussian distribution of the beam spot, the theoretical lateral resolution follows the Abbe's criteria, which is given by [22]:

$$\Delta x = \frac{0.61\lambda_c}{NA} \tag{1.5}$$

where NA is the numerical aperture of the objective.

Similarly, the lateral resolution is also affective by the beam spot size and light distribution. In most of the time, the beam spot size only occupies a small portion of the aperture of the objective, which affects the effective NA of the objective. As a result, the actual lateral resolution, estimated by replacing the labeled NA of the objective with effective NA, is usually poorer than the theoretical value.

1.3.4 Depth of Focus

The theoretical value of depth of focus (DOF) is given by the following formula [33]:

$$DOF = 2z_R = \frac{2n\lambda_c}{NA^2} \tag{1.6}$$

In which the z_R represents the Raylegh range and NA is the numerical aperture of the objective. In another literature, $DOF = \lambda_c/(2 \cdot NA^2)$ [34]. Similarly, effective NA should be used in the calculation. Since both

DOF and lateral resolution are proportional to the central wavelength, there is a trade-off between the choices of higher lateral resolution and higher DOF [33].

1.3.5 Total Measurement Range

For TD-OCT, since the reference mirror is moved the obtain the sample reflectivity profile along the depth, the measurement range is purely determined by the travel range of the translation stage.

For FD-OCT, the measurement range is inversely proportional to spectral resolution, which is determined by $\Delta\lambda_{FWHM}/N$. Thus, the measurement range is given by [3, 33]:

$$z_{max} = \frac{\lambda_c^2}{4n\Delta\lambda_{full}} N \tag{1.7}$$

Where N is the number of sampling point in an axial scan and $\Delta\lambda_{full}$ is the total bandwidth of the light source. For swept source OCT, N = digitizer sampling rate / laser sweep rate. Also note that, the measurement range would be doubled if the full-range technique is applied (See Chapter 4 for details)

1.3.6 Sensitivity

The theoretical shot-noise-limit sensitivity of the SD-OCT system is defined as [35]:

$$Sensitivity = 10\log(\frac{\rho\eta T_{int}}{e} P_0\kappa_s) \tag{1.8}$$

Where ρ denotes the spectrometer efficiency, which comprises the diffraction grating efficiency and losses due to optical components and spectrometer geometry. η is quantum efficiency (conversion ratio) of the detection unit, T is camera integration time, P_0 is average optical power entering the interferometer, κ_s denotes the coupling coefficient of the coupler. Or we can use the back-coupled sample arm power $P_{backcoupled} = P_0\kappa_s$ (to the detector) to calculate the sensitivity. We should note that, no optical loss is assumed in the theoretical sensitivity calculation. If the losses due to the optical components and back-

coupling are considered, we can use an effective κ_s' to represent the coupling coefficient of the coupler including the optical losses, which can be expressed by $\kappa_s' = P_{backcoupled}/P_0$. Note that the camera integration time is not exactly equal to inverse of the camera line-rate (in Ascan rates) due to the duty cycle of each camera acquisition. For SS-OCT system, T is replaced by 2/sweep rate [22]. The factor of 2 comes from the balanced detection, in which the intensity square is quadrupled while the noise variance is doubled (See Chapter 3.2).

We should mention that the theoretical sensitivity is calculated based on the assumptions of Gaussian spectrum and shot-noise-limit detection, where the shot-noise is far more larger than the rest of the noise. See detail discussion of the sensitivity and the source of the noise in Chapter 3.2.

The sensitivity roll-off is determined by the imaging depth whether the sensitivity decreases by a certain value (usually 3 dB, 6 dB and 10 dB) from the peak value. For the spectral domain system, the sensitivity roll-off is more severe due to the fringe washout occurred at the spectrometer. For swept-source system, the sensitivity roll-off is less a concern and usually determined by the coherence length of the tunable swept laser (for each narrow band of wavelength).

1.4 OCT applications and list of OCT literature

As is mentioned in Chapter 1.1, commercial OCT systems have been widely adopted for clinical studies in the field of ophthalmology, cardiology, dermatology and gastroenterology. Other than these clinical fields, we can also find the application of OCT imaging in oncology [83], pulmolory [52], urology [57], dentistry [56]. **Table 1.3** shows a list of recent OCT literatures, including reviews and book chapters in different aspects.

1.5 Summary

In this chapter, we introduced the basic principles and key performance metrics of optical coherence tomography. Three types of OCT, including time-domain, spectral domain and swept source OCTs, were briefly discussed. A chronicle of the OCT development was reviewed, highlighting the commercial and clinical impacts of OCT. OCT applications in all different aspects were mentioned, with a provided list of

OCT literature. Given the advantages of OCT in speed, resolution, 3D capability, penetration and non-

Table 1. 3 List of OCT Reviews and Book Chapters

Category	Sub-Category	Reviews and Book Chapter
Textbook		Drexler and Fujimoto [36]
General	Principles	Wojtkowski [22], de Boer et al. [4]
	OCT history	Fujimoto and Swanson [2]
	OCT market	Swanson [21]
Clincial	Ophthalmology	Wojtkowski et al. [37], Drexler and Fujimoto [38]
	Cardiology	Ali et al. [39], Yonetsu et al. [40], Kume et al. [41], Tearney [42]
	Dermatology	Olsen et al. [43], Liu and Drexler [44], Deegan and Wang [45]
	Gastroenterology	Leggett et al. [46], Tsai et al. [47]
	Oncology	[48]
	Neurology	Baumann et al [49], Men et al. [50], Calabresi et al. [51]
	Pulmonology	Shaipanich et al. [52]
	Gynecology	Kirillin et al. [53], Wang et al. [54]
	Dentistry	Machoy et al. [55], Hsieh et al. [56]
	Urology	Freund et al. [57]
	Otolaryngology	Hawkshaw et al. [58]
	Surgical Guidance	El-Haddad and Tao [59], Carrasco-Zevallos et al. [60]
Biomedical	Developmental Biology	Men et al. [50], Raghunathan et al. [61]
NDE/NDT	General	Golde et al. [62]
	Artworks	Iwanicka et al. [63], Targowski et al. [64]
Technology Advances: Hardware & Software	Swept Source	Klein et al. [3], Drexler et al. [33]
	Multiplexing	Klein et al. [3]
	Full-range	de Boer et al. [4]
	Multimodality	Drexler et al. [33], Leitgeb and Baumann [65]
	Probe and Endoscope Design	Gora et al. [66], Monroy et al. [67]
	Despeckle	Anoop et al. [68]
	Deep Learning	Ting et al. [69], Grewal et al. [70]
Functional OCT and OCT extensions	Line-field/Full-field	Thouvenin et al. [71], Thouvenin et al. [72], de Boer et al. [4]
	Angiography	Spaide et al. [73], Chen and Wang [74], Zhang et al. [75]
	PS-OCT	Baumann [76], de Boer et al. [77]
	Spectroscopic	Leitgeb and Baumann [65]
	Elastography	Larin and Sampson [78], Wang and Larin [79]
	AO-OCT	Jonnal et al. [80]
	vis-OCT	Shu et al. [81]
	Molecular	Kim et al. [82]

destructiveness, OCT has significant potential in non-destructive evaluation of time-lapse dynamic process.

Chapter 2: Building a Spectral Domain OCT system

2.1 Introduction

To perform imaging using OCT, building a working OCT system is the first and important step. Depending on sample conditions and image quality requirement, the key performance metrics (See Chapter 1.3) need to be taken into consideration. For special handling like OCT system equipped with a stage, the configuration of the optics need to be arranged ahead of time.

In this chapter, I describe the details of building a spectral domain OCT system. Specifically, I describe the design and construction of a SD-OCT system equipped with a 3D translation stage for high-throughput imaging of tumor spheroids. I will discuss the requirements of the key performance metrics for tumor spheroid imaging with OCT and choose the appropriate parts to build the system towards the goal. Results of the tumor spheroid imaging using this custom SD-OCT system would be presented in Chapter 7.

2.2 Building a SD-OCT System

Figure 2.1 shows the schematic diagram of the custom SD-OCT system. It consists of a light source (Superluminescent diode), a 2×2 fiber coupler with 50/50 splitting ratio working as the Michelson interferometer, a spectrometer, the sample and reference arm optics and a 3D motorized translation stage.

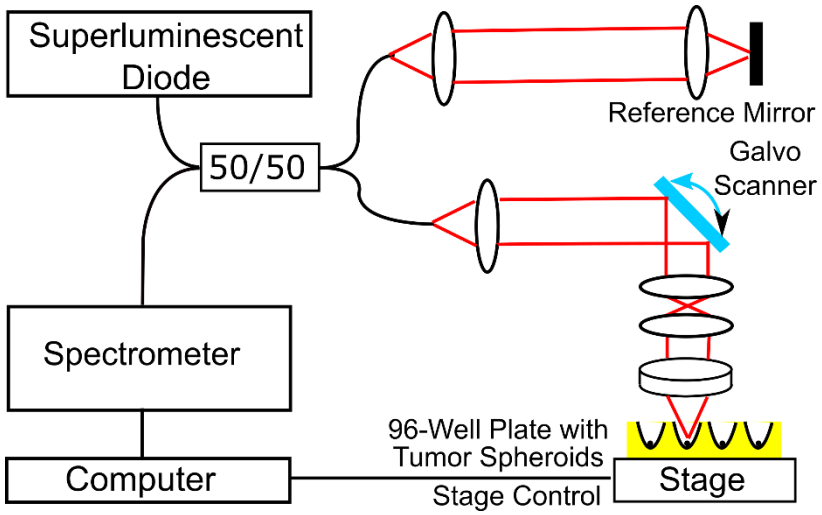

Figure 2. 1 Schematic diagram of a spectral domain optical coherence tomography (SD-OCT) imaging platform for tumor spheroid imaging

Other than the stage, the main part of the SD-OCT is analogous to a standard SD-OCT setup.

Figure 2.2 shows the corresponding actual setup of prototype spectral domain OCT systemfor tumor spheroid imaging. In Figure 2.2A, four main parts of the OCT system are shown, highlighted with different dashed line regions: Light source of the OCT system is shown in yellow dashed line region; Sample arm optics are shown in orange dash line region; Reference arm setup is shown in Magenta L-shape region; Cyan dash line region marks the 3D motorized translational stages.

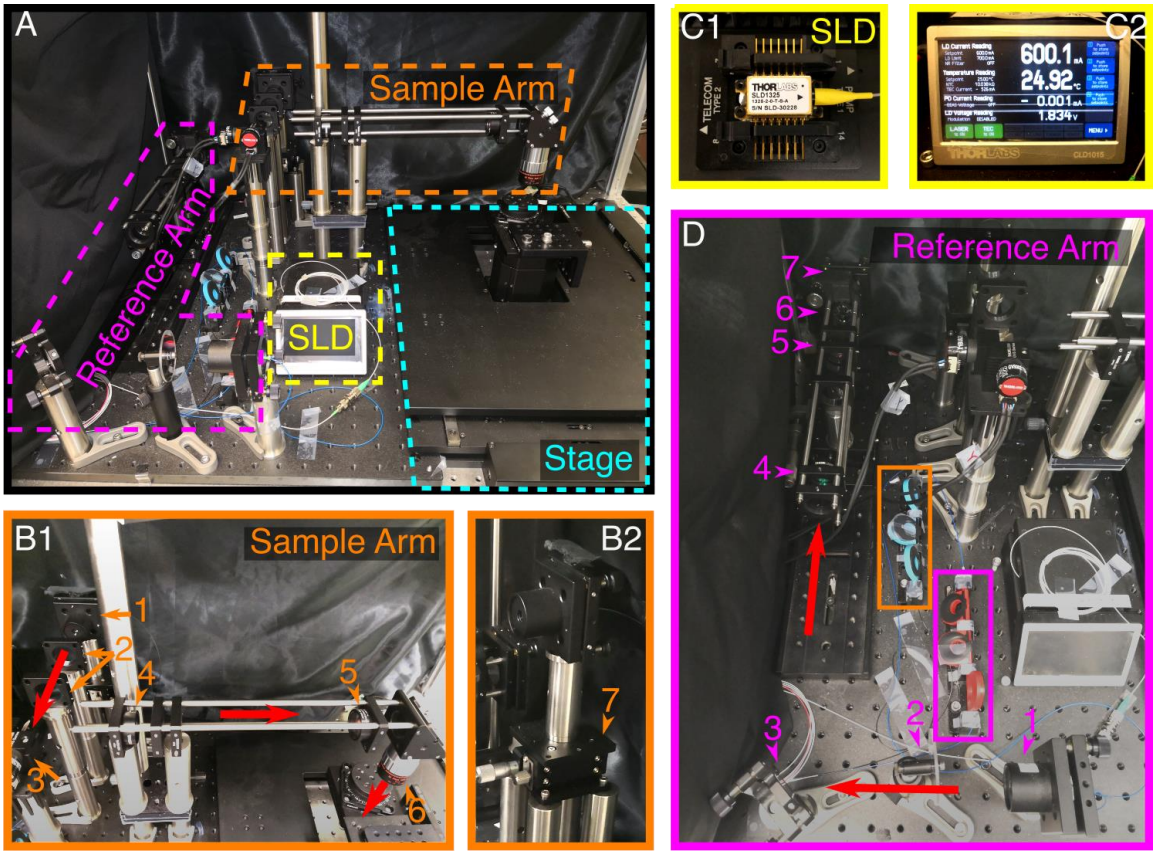

Figure 2. 2 Actual system setup of the prototype spectral domain optical coherence tomography with the motorized translational stage for tumor spheroid imaging. (A) Overall view of the system. Yellow rectangle: laser source, Orange rectangle: Sample arm, Magenta rectangle: Reference arm, Cyan rectangle:3D motorized translational stage. (B1, B2) Sample arm setup. (C1, C2) Light source. (D) Reference arm setup.

2.2.1 Light Source

The light source determines the properties of ouput light for the OCT systems, including the wavelength range, spectral bandwidth and output power. These properties would ultimately affect the resolution and

sensitivity of the OCT system. When choosing the light source for the OCT system, the following aspects need to be taken into consideration.

1) **The output power:** we need to know how much power will be delivered to the sample and reference arms, respectively. The higher power delivered to the sample arm, the higher sensitivity it would be, according to the formula of sensitivity calculation (See Chapter 1.3.6). The reference arm power should be sufficient enough so that the shot-noise-limit detection can be realized to achieve the best sensitivity. However, it should not be too large to saturate the detector. In the sample arm, there is an upper limit for the maximum power exposure for eye and skin imaging, instructed by the ANSI standard. This will ultimately limit the sensitivity of OCT.

2) **Central wavelength:** the choice of wavelength range depends on the sample properties as well as what kind of features we are looking at. Two questions are involved:

1) How deep are we going to probe into the sample?

2) What is the required resolution of the OCT system to resolve the features?

The answers to these two questions are related to three performance metrics: light penetration, axial and transverse resolutions. The light penetration depth is dependent on the scattering and absorption properties of the sample. Generally, 1300 nm-wavelength light has relative deeper penetration in turbid tissues than 800 nm wavelength light due to significant reduction of light scattering with increased wavelength [84]. However, for biological tissues with high water concentration, i.e. eye lens, 800 nm and 1060 nm wavelength-range lights can easily penetrate through it and reach the retinal layer, while 1300 nm wavelength-range light cannot, due to significant increase of water absorption [84-86]. Therefore, 800 nm and 1060 nm wavelength light can reach the retinal layer of the eye while 1300nm wavelength light cannot. Another consideration will be the resolution of the oct system. According to the resolution calcuation (See Chapter 1.3.2 and 1.3.3), the axial resolution is proportional to the square of the central wavelength and the transverse resolution is proportional to the central wavelength. It means that, larger central wavelength, poorer axial and lateral resolution (See **Figure 2.3**). Thus, there would be a trade-off between the choice of penetration depth and resolution. For tumor spheroid imaging, if we target on imaging the whole 3D structure of tumor spheroid, penetration depth is more preferred than the resolution. Thus, we choose the source with 1300 nm central

wavelength. On the other hand, if we focus on imaging the local cellular dynamics of the outer layer of tumor spheroid, i.e. cell migration, resolution would be preferred.

3) **Spectral bandwidth**: Since the spectral bandwidth is inversely related to the axial resolution (See Chapter 1.3.2) , the larger bandwidth is preferred in order to obtain better resolutions.

4) **Spectral shape of the spectrum**: If the spectral shape does not follow a Gaussian profile, the axial resolution might be compromised (See Chapter 1.3.2).

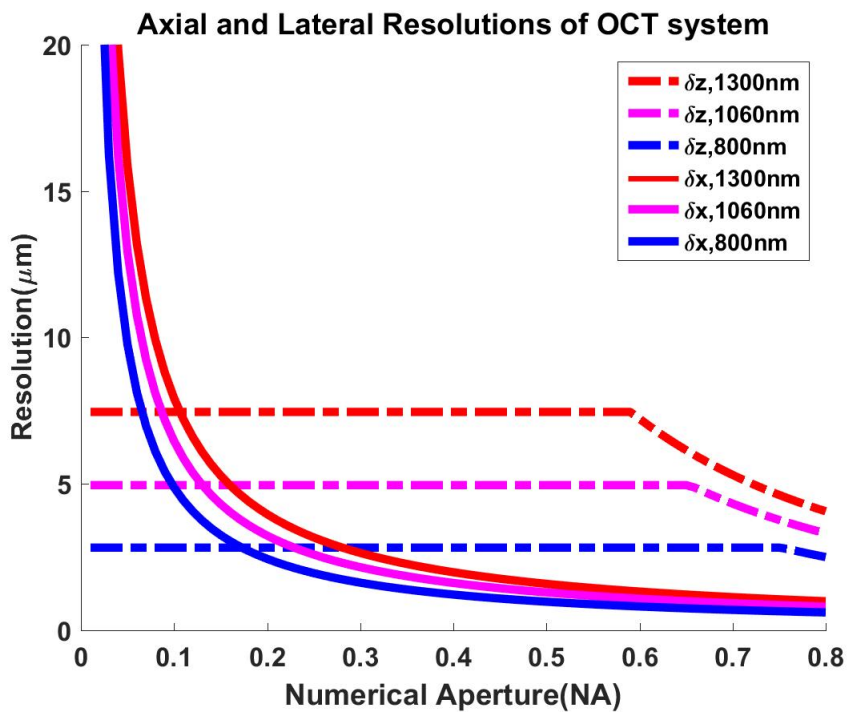

Figure 2. 3 A comparison of simulated axial and lateral resolutions with different central wavelengths. The spectral bandwidth is set to the same value of 100nm for all three wavelength conditions. Refractive index n = 1. Note that, for high NA objective, the depth of focus determines the axial resolution instead of the coherence length of the broadband laser source, yielding a decreasing curve of the axial resolution as the NA further increases.

Taken all factors into consideration, we choose the laser source from Thorlabs: SLD 1325, which is specialized for spectral domain OCT system for the tumor spheroid imaging system. The reasons are:

1) Use 1300 nm wavelength to maintain the large penetration depth.

2) A relative broad spectral bandwidth to maintain axial resolution.

3) The output spectrum is relative uniform.

In **Figure 2.2 C1**, the light source, Thorlabs SLD 1325, is shown. The butterfly packaged superluminescent diode (SLD) is mounted in a temperature controller (CLD1015, Thorlabs, see Figure 2.2 C2).

2.2.2 Sample Arm Optics

Figure 2.2 B1 and B2 show the configuration of the sample arm of the custom SD-OCT system. The orange numbers labeled different optical components (parts) in the sample arm.

Part 1is a collimator, converting output beam from a diverting beam to a collimated beam, where lights are transmitted in parallel. The detailed configuration of the part 1 is shown in **Figure 2.2 B2**. In the middle, a one-dimensional (1D) translation stage is used to precisely control the output location of the collimated beam in vertical direction, which is critical for full-range applications if needed.

Part 2 is a pair of lens mounts, which could be used with a pair of lenses to adjust the beam spot size. In the current system, a paired of f = 30mm/f = 60mm lenses can be mounted on the lens mounts to adjust the beam spot size to be twice (30/60) or half (60/30) of the original spot size. The spacing between the lens mounts are well aligned to ensure the output beam remains collimated.

Part 3 is the galvanometer (Galvo) system, which utilizes a paired of mirrors controlled by the motors to convert light transmitting direction in two dimensions. In such way, point-scanning of the sample is realized. Since FD-OCT acquires the intensity profile along the depth in each axial scan, a 2D cross-sectional image could be captured by scanning the beam in one dimenstion and 3D scan could be realized by scanning the beamin two dimensions.

Part 4 and 5 are another pair of lenses in a telescope setting. The input and output of this pair of lenses are collimated beams. The purposes of using lens pair 4 and 5 are:

1) Convert the diverting collimated beam from the Galvo to a converging beam before the objective;

2) Serve as a relay lens pair to transmit the scanning beam within the cage system for a long distance.

3) Potentially increase the size of the beam incident into the objective to enhance the lateral resolution, with a higher effective numerical aperture (NA) of the objective.

4) Adjust the maximum scan angle by changing the NA.

In the customed SD-OCT systems, we make the choice of the lens pair 4 and 5 with the following considerations:

1) The focal length of the first lens (Part 4, f4) shouldn't be too large. If f4 is too large, the collimated beam from the Galvo could be diverted outside the aperture of the lens. Therefore, the scanning angle at the Galvo would be limited.

2) The focal length of the second lens (Part 5, f5) determines the distance between the second lens and the objective. If we need some freedom to align the second lens in the cage system, f5 could not be too small. In our case, we mount the objective lens on a triangular cage mount with a mirror to divert the beam by 90°. Thus, a minimum f5 of 2" (50.8 mm) is required.

3) The difference of f4 and f5 could not be too large, since the relay lens pair also determines the magnification of the beam spot. If the magnification, M=|f5/f4|, is too big, the radius of the beam spot itself or plus the beam offset due to galvo scanning might be larger than the radius of the 2nd lens, yielding beam cropping.

4) The beam spot at the back aperture of the objective lens should be sufficient to maintain a decent lateral resolution, which is inversely proportional to the magnification M .

5) The total length of the cage system in the sample arm is considered. To accommodate the spectral domain OCT system with the large-size motorized translation stage with long travelling ranges , a long sample arm cage system is required as a rigid cantilever to hold the objective on top of the center of the translation stage with the relay lenses inside the cage system to transmit the beam from the Galvo to the objective.

Taking all considerations, we decide to use a pair of lenses with f4= f5 = 100 mm in the sample arm.

Part 6 is the objective mounted on the distal end of the sample arm cage system. The NA of the objective determines both lateral resolution, maximum field of view (FOV) and depth of focus (DOF). Lower NA of the objective yields larger FOV and DOF, but poorer lateral resolution. Conversely, higher NA value yields better lateral resolution.

2.2.3 Reference ArmOptics

Figure 2.2D shows the configuration of the reference arm of the SD-OCT system. To be simple, the reference arm can use the identical optics as sample arm, with a reference mirror placed at the distal end to reflect the light back. The major advantage of using identical reference and sample arm optics is that chromatic dispersion due to mismatched optics between the reference arm and sample arm could be avoided. However,

building the same referefence arm would be relative expensive, due to the high cost of the objective. To cut down the system cost, a modified reference arm is configured. The modified reference arm consist of a collimator (Part 1 labeled in magenta number), a mirror to divert the beam by 90 degree (Part 3), a pair of relay lens (Part 4 and 5), a focusing lens (Part 6) and the reference mirror (Part 7). In addition, a wheel-shape continuous variable neutral density filter (Part 2) is placed in the reference arm as an optical attenuator. In such way, the power level in the reference arm could be controlled to avoid saturation of the detection unit. Also, we can add glasses in the reference arm to compensate the dispersion between the reference and sample arm. In the case of 1300 nm SD-OCT system, the dispersion effect is minimal and dispersion compensating glasses are not necessary needed. However, for 800 nm and 1060 nm system, hardware dispersion compensation is required in the reference arm.

2.2.4 Spectrometer Design

Figure 2.4 and Figure 2.5A show the actual configuration and the schematic diagram of a spectrometer, the detection unit for SD-OCT system. The lights backcoupled from the reference mirror and the sample interfere at the 2x2 fiber coupler. Then, interference signals would be sent to the spectrometer via the fiber.

The spectrometer consists of 4 different parts: a collimator, a grating, a F-theta lens and a line-scan camera. The line-scan camera (SU1024-LDH2) is purchased from Sensor Unlimited. It has 1024 pixels in a horizontal line. The detection area of each pixel is 1500 µm (Height) × 25 µm(pitch size). The maximum line rate of the line-scan camera is 92 kHz. The total length L of the 1024 pixels would be 25.6 mm.

The design of the spectrometer starts from the choice of the component that can achieve spectral dispersion. In our case, a first order diffraction grating is chosen since they are less bulky as compared to a dispersion prism. One key parameter of the diffraction grating is the groove density (G), which is related to angular dispersion. The larger the groove density, the larger the angular dispersion. In our custom spectrometer, we choose a transmission grating with the groove density G = 1145 lpmm(Wasatch,. HD 1145 lpmm at 1310 nm).

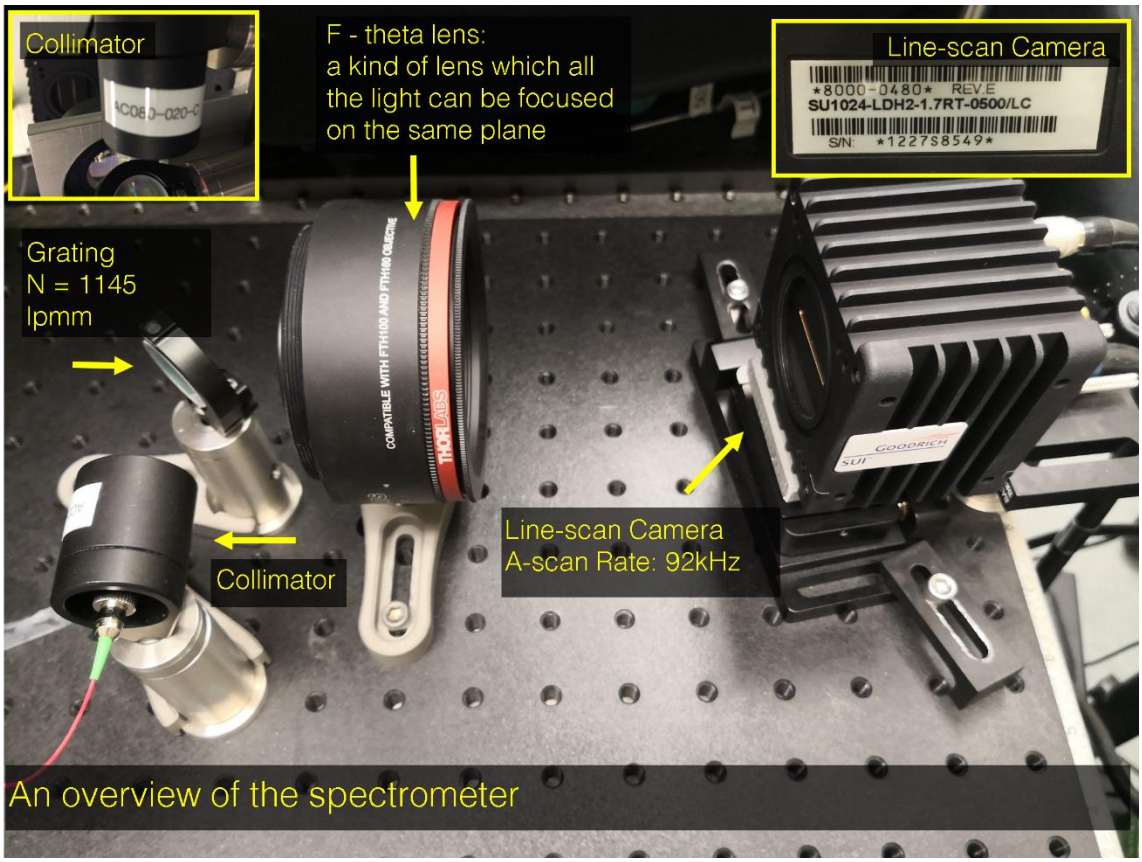

Figure 2. 4 Actual setup of the custom spectrometer for 1300 nm SD-OCT system, which consists of a collimator, a grating, a F-theta lens and a line-scan camera.

Next, we check the wavelength-dependent dispersion angle of the grating. The SLD1325 has a spectral range of ~1240 – 1420 nm with a central wavelength of 1317 nm. According to the dispersion angle chart provided by the manufacturer (**Figure 2.5 Right**), an incident angle of ~49° (49.2°) for the grating yields the optimal diffraction efficiency. Therefore, we can calculate the maximum and minimum dispersion angles with the two boundary wavelengths λ_{min}=1240 nm and λ_{max}=1420 nm based on the grating function[87]:

$$\sin(\theta_{min}) - \sin(\theta_i) = mG\lambda_{min} \tag{2.1}$$

$$\sin(\theta_{max}) - \sin(\theta_i) = mG\lambda_{max} \tag{2.2}$$

Where the θ_i = -49.2° is the incident angle and m = 1(First order). Replacing all the parameters with numbers, we can get:

$$\vartheta_{min} = 41.5°$$

(2.3)

$$\vartheta_{max} = 60.3°$$

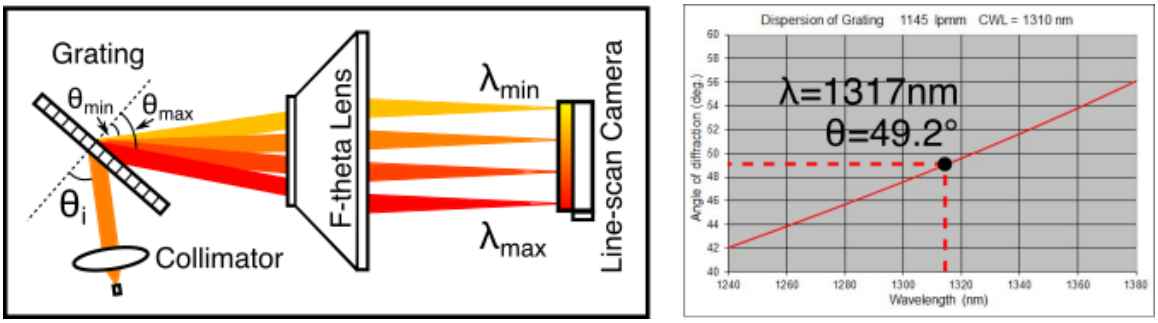

Figure 2. 5 (Left) Schematic diagram of the spectrometer. (Right) Dispersion of grating showing the optimal angle of incidence for different wavelengths. Right figure are referred to the manufacturer specification of the grating.

(2.4)

That means, the maximum diverging angle between the two boundary wav elengths would be $\Delta\theta$ = 18.8°. Using this, we can calculate the optimal focal length of the focusing lens.

$$f_{opt} = \frac{L}{2} \div \tan\left(\frac{\Delta\vartheta}{2}\right) = \frac{25.6}{2} \div \tan\left(\frac{18.8}{2}\right) = 77.3 \text{ mm}$$

(2.5)

In our spectrometer design, we choose the f = 100 mm F-theta lens (FTH100-1064, Thorlabs) as the focusing lens. The reason to choose the F-theta lens is that it is optimized to have a flat field at the focal plane, which ensures that most of the light in various diffraction angles would be all focused on the same focal plane. In such case, we can align the focal plane of the F-theta lens to the detection plane of the line-scan camera to ensure that the beam spot size of each wavelength component of light would be minimized on the corresponding camera pixel. If the budget is limited, regular 2” lenses with a f = 75 mm or f = 100 mm can satisfy the need with slight compromise of performance for the boundary camera pixels, due to the

spherical aberration of the lens that leads to faster fringe washout for these pixels. Moreover, this F-theta lens has a relative large scan angle (±28°) and scan field (70 mm × 70 mm). Also, the diffraction-limit spot size of this F-theta lens is 16 µm, which is smaller than the pitch size of the camera. If the focal length is larger, the spot size on the camera pixel would be enlarged, which may introduce signal cross-talks between adjacent camera pixels.

Finally, the choice of the collimator needs to satisfy the minimum condition of the spot size on the grating, which is 1024/1145 = 0.9 mm. In our case, we choose a collimated lens of f = 20 mm (AC080-020C, Thorlabs). Thus, the output spot size would be:

$$d_{spot} = 2f\tan(\theta_{col}) \tag{2.6}$$

Where θ_{col} = 8° is half of diverging angle of incident light from the fiber. Thus, d_{spot} = 5.6 mm, which would be sufficient to illuminate the grating.

2.2.5 Other Parts of SD-OCT System

A 2x2, 50/50 fiber coupler (AC Photonics) is used, serving as the Michelson interferometer in the system. For SD-OCT system, 50/50 splitting ratio is used for 2x2 fiber coupler since it has the best back-coupling efficiency of 25% if no other loss is considered. However, if the sample has limited power exposure, other splitting ratios could be employed. For example, a 2x2, 20/80 fiber coupler could be used in an ophthalmic OCT system, with 20% power sent to the retina and 80% of the reflected light back-coupled to the detector.

To control the polarization state to optimize the amplitude of interference signals, two polarization controllers (**Figure 2.2D**) can be added in the reference arm and sample arm, respectively.

2.3 Alignment of SD-OCT system

2.3.1 Set Up the Light Source

Place the light source into the temperature controller following the procedure provided by the controller's manual. If the output port of the light source is not a fiber connector (e.g. a free-space laser like a supercontinuum laser), set up a coupling system using two collimator (and additional two mirrors for fine

adjustments). Align the coupling system using weak output power level from the light source to avoid damage of the fiber tip if incident light does not hit at the center of the fiber tip. Using the screws on the two mirror mounts to fine adjust the incident angle to the collimator and use the powermeter to measure the coupling power. Adjust until the coupling power reaches the maximum under the weak light. Then, gradually increase the power to measure the coupling power at different power levels.

After the light source is set up, one port (i.e. Port 1) of 2×2 fiber coupler is connected to the light source. The other ports would connect to sample arm (i.e. Port 3), reference arm (Port 4) and spectrometer (Port 2). Measure the output power from port 3 and port 4 to check the splittin ratio as well as additional internal loss of the coupler.

2.3.2 Alignment of Sample Arm Optics

The alignment steps for the sample arm are described as followed:

1) Based on the need, determine whether the sample arm cage system should be configured in upright or inverted mode. For tumor spheroid imaging, an upright setup has the advantage that image distortion due to light refraction from the round bottom can be avoided. Also, the configuration of the cage system would be easier. However, the incident light needs to pass through both the lid surface of the plate and air-liquid interface, which might lose more power before it reaches the tumor spheroid.

2) Estimate the height of the sample arm cage system. In the case of tumor spheroid imaging system, the height of the 3D translation stage, thickness of the plate holder, length of the objective lens, working distance of the objective add up in the height measurement.

3) Estimate the location of the galvo system. Fix and hold the galvo system with pedestal posts.

4) If the collimator is directly purchased from the manufacturer (e.g. Thorlabs), this step could be neglected. Otherwise, if a lens and a fiber adapter are used together as a custom collimator, adjust the location of the lens (usually by rotating the lens in the tube or moving the lens in the cage system) until the output beam spot size remains constant for a long distance, tested with a laser viewing card (IR-card, VRC2, 400 to 640 nm and 800 to 1700 nm, Thorlabs). If constant beam spot size could not be satisfied, another judgment criterion could be that, the output beam maintains a sharp outer boundary at all cross-sections within a long distance. After adjustment, the output beam should be close to the collimated state.

Since the design and alignment of the lens and objective are not perfect, the beam spot will get distorted and blurry in the far field. Generally, the achromatic lens and objective lens are tested only in the distance between 20 cm to 1 m. The higher the NA, the higher chance the collimated beam gets distorted in a shorter distance. Empirically, for a small NA lens, we can check the collimation state in the "far field" of ~5 – 10 meters, while the collimation state could be checked at a distance of ~1 meter away from a high NA lens.

5) Using a laser viewing card (IR-card, VRC2, 400 to 640 nm and 800 to 1700 nm, Thorlabs) as a tool to indicate the optical path. Align the collimator (Part 1) to the Galvo (Part 3) so that the beam transmitting direction should be perpendicular to the edge of the first galvo mirror and the beam spot should hit the center of both mirrors. If the beam hits the center of the first one but not second one, fine tune the output angle of the collimated beamusing the screws on the collimator mount and the output location of the beam.

6) (Optional) Mount the f = 60 mm/f = 30 mm lens pair between the collimator and the galvo mirror. Use the cage system to facilitate the alignment of these two lens pair. Mount the lens pair on pedestal posts. Place the lens pair in the appropriate positions to maintain the original optical path. Fix the pedestal posts with clamping forks. Then, release one of the clamping forks and move the lens back and forth until the output beam from the lens pair remains collimated. Then, the lens pair is well aligned. Note that the neutral density filter could be mounted on the Part 2 position as well.

7) The rest of the sample arm would be mounted in the 30 mm cage system. A 90° triangle mount (KCB1C, Thorlabs) at the distal end is used to convert the beam transmitting direction to vertical direction and mount the objective. Tighten the cage rods to the triangle mount. Then add the mirror mount into the cage system. Match the height of the cage system to the center of the second galvo mirror.

8) Align the cage system so that the beam is transmitting through the center of the cage system at every horizontal location. Use the alignment plate (Pinhole, CPA1, Thorlabs) to check the beam locations back and forth in the cage system to verify whether the beam is hitting at the center all the time. During the alignment, the galvo systemshould be turned on and both BNC control cables should be connected to the ground, using a BNC terminator with 50 Ohmresistance.

The alignment of the cage system could be aligned iteratively. On one hand, both galvo mirrors can be rotated manually by loosening or fixing the screws to adjust beam transmitting direction in 2D plane. On the

other hand, the 3D manual translation stage supporting the cage system can provide both horizontal and vertical movements.

Since the cage system is heavy, ensure that the cage system is tightened firmly. Once the beam transmission is well aligned in the horizontal directions in the cage system, tune the screws on the triangle mount to adjust the beam direction to hit the center of the objective's back aperture.

9) Mount both the objective and the 2nd relay lens (Part 5). Adjust the location of 2nd relay lens to construct a telescope system. In other words, the output beam from the objective should be collimated. Then, take off the objective and mount the 1st relay lens (part 4). Move the 1st relay lens to construct another telescope system.

Next, adjust the position of the whole cage system towards or away from the galvo system with the 3D translation stage. The back focal point of the 1st relay lens should be at the position in the middle of the 1st and the 2nd galvo mirrors.

There are two ways to check the position of the cage system: 1)Use an auxillary light source to provide collimated light from the other side of the 1st relay lens, so that the back focal point can be checked using the IR-card. Move the cage system until the spot size is minimumat the designated position. 2) Use the IR-card to check the focusing beam after the objective up and down when the galvo mirrors are scanning. The best position of the cage system is achieved while the scanning range remains constant while moving the IR card up and down.

Figure 2.6 illustrates the reason why the back focal point of the 1st relay lens (Part 4) should be placed in between the galvo mirrors. If the distance between the galvo mirror and the 1st relay lens increases, the edge beams may not pass the 1st relay lens with large scanning angles (Red beam). On the other hand, decreasing the distance may lead to the result that the edge beams cannot pass the 2nd relay lens (Yellow beam).

10) Once the sample arm is aligned properly, place a mirror close to focal plane of the objective. Connect the output port (port 2) of the 2×2 fiber coupler to the powermeter. Fine adjust the tilting angle and vertical position of the mirror to ensure the mirror is exactly at the focal plane, which is shown with the highest back-coupled power to the powermeter.

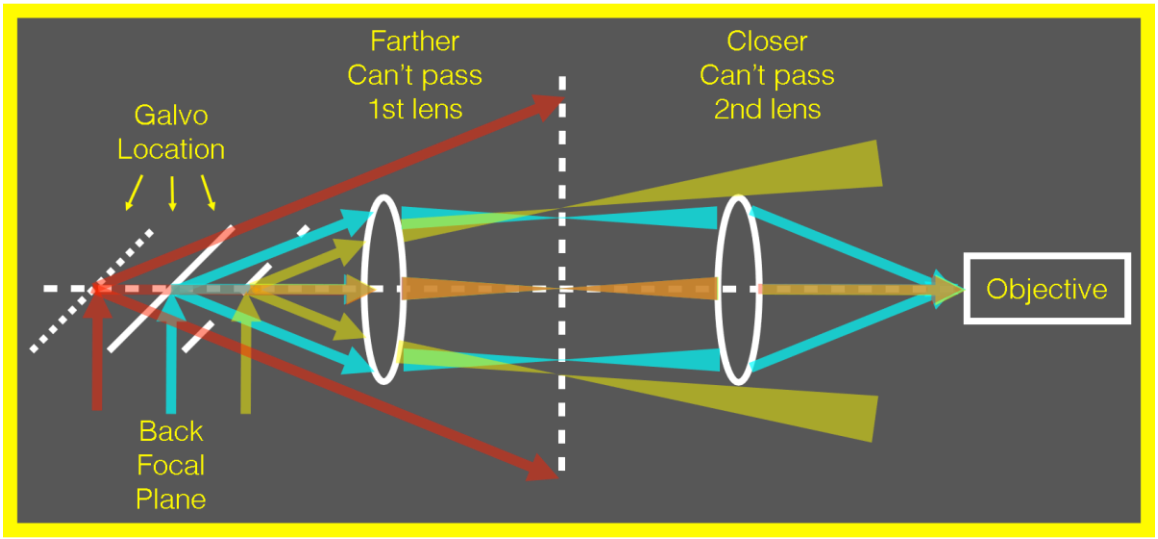

Figure 2. 6 Illustration of the reason to place the back focal point of the 1st relay lens in between galvo mirrors

2.3.3 Alignment of Reference Arm Optics

The procedures to align the reference arm is similar with the alignments of the sample arm. The procedures of reference arm alignments are described as followed:

1) Measure the total length of the sample arm components. The reference arm should have a similar free-space length with the sample arm. Pre-allocate the space for the reference arm with a similar optical path length.

2) Add the collimator to the reference arm, following the same procedure as the step 4 of Chapter 2.3.2.

3) Consider setting up the reference arm cage system including the reference mirror on a 1D translation stage to provide adjustment of the reference arm optical path length.

4) Set up the cage system with rods and mirror mounts. Align the collimator and the reference mirror at the same height.

5) Align the cage systemto ensure that cage rods are in parallel with the moving direction of the 1D translation stage.

6) Place the mirror (Part 3) so that the reflected light roughly goes through the center of the cage system. Then, adjust the screws on both the mirror mount and the collimator mount iteratively to align the beam to pass through the center of the cage system at all locations.

7) Add the reference mirror (Part 7) to the distal end of the reference arm cage system. Mount the focusing lens (Part 6) in the cage system. Move the lens so that the beam is roughly focused on the reference mirror.

8) Connect the output port (port 2) of 2×2 fiber coupler to a powermeter. Block the sample arm with a cloth so that no light is coupled back from the sample arm. Adjust the screws on the kinematic mirror mount of the reference mirror so that the light is reflected back in the same optical path. Use the powermeter reading to guide the back-coupling status. Once the back-coupled power reaches the local maximum, the tilting angle of the reference mirror is well-adjusted.

9) Fine tune the location of the focusing lens (Part 6) to maximize the back-coupled power.

10) Check whether the back-coupled power remains constant when moving the translation stage for the whole traveling range. If the back-coupled power changes a lot, the cage system is not well aligned. In this case, repeat step 6 to 10 to further optimize the alignment of the reference arm.

11) Add the continuous variable neutral density filter (Part 2) into the reference arm.

2.3.4 Spectrometer Alignment

Spectrometer alignment requires that the sample and reference arms are aligned properly and their lengths are closely matched, so that interference signals can be detected by the spectrometer. A weak single reflector (a mirror with a ND filter) is placed at the objective's focal plane in the sample arm and well adjusted to maximize back-coupled power. Alignments steps for the spectrometer are described as followed:

1) Turn on the light source and the galvo system. Connect control cables of the galvo system to the ground (using a BNC 50 Ohm terminator). Connect the output port (Port2) of the 2×2 fiber coupler to the collimator of the spectrometer. If the collimator is a custom collimator, follow the step 4 of Chaper 2.3.2 to construct one.

2) Mount the grating and fix it with appropriate orientation. Use the protractor (angle measurement tool) and IR-card to measure the incident angle of light from collimator to the grating until the incident angle is close to the optimal angle with high diffraction efficiency.

3) Use the IR-card to indicate the diffracted light. Place the small-aperture end of F-theta lens towards the output direction of the diffracted light. Also, place the line-scan camera towards the F-theta lens.

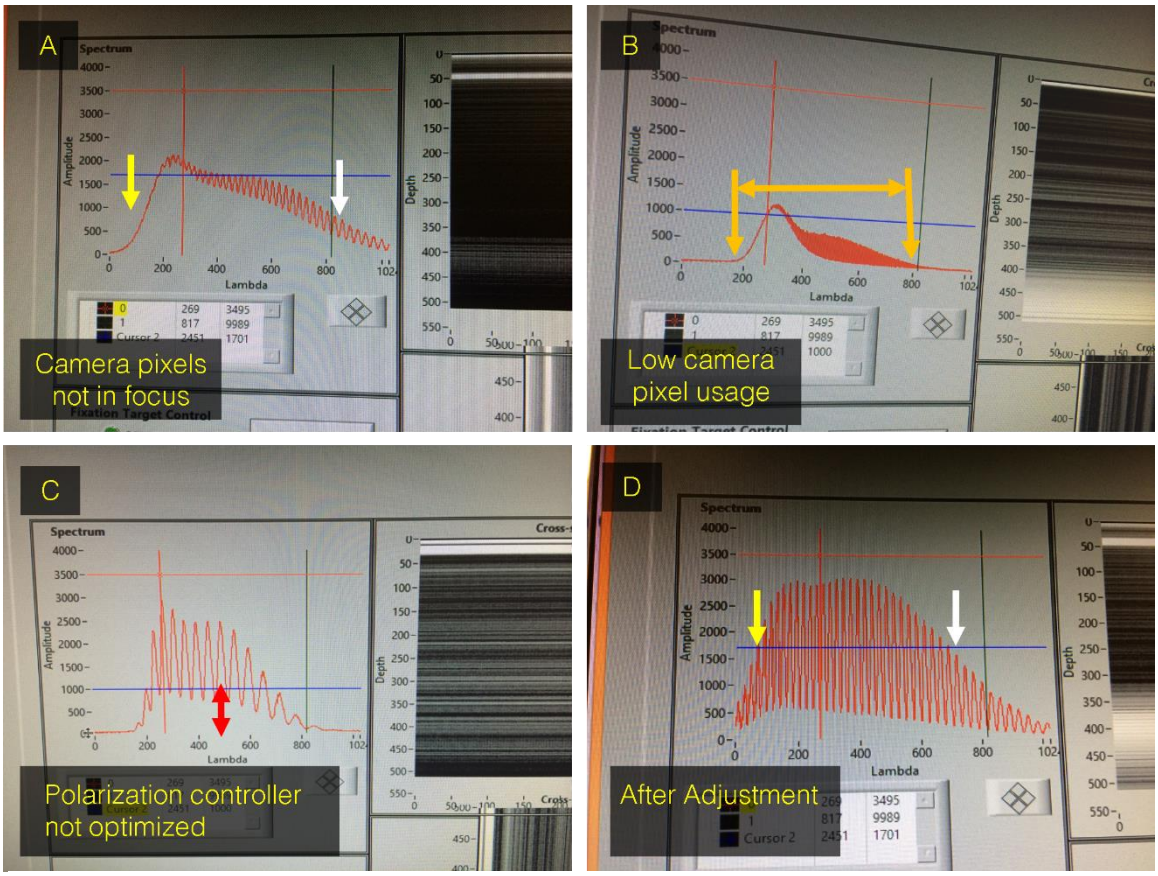

Figure 2. 7 Spectrometer alignment based on the detected interference signals from the line-scan camera. (A - C) Misaligned interference signals due to different issues. (D) Aligned interference signal after the camera and F-theta lens are properly adjusted. Issues: Yellow arrow: Camera pixels are not in focus due to tilting of the camera. White arrow, camera pixels are not in focus because the camera are too close/far away from the F-theta lens. Orange arrows: the detected interference signal doesn't occupy all the camera pixels. (Low camera pixel usage). Red arrow: Polarization controller is not optimized so that the amplitude of the interference signal doesn't reach the maximum.

4) Iterative adjustments of F-theta lens and line-scan camera: Adjust the locations of F-theta lens and line-scan camera one-after-another based on the interference signals detected by the line-scan camera (**Figure 2.7**). First, move the line-scan camera until the fringe pattern can be detected (**Figure 2.7 B**). If the whole fringe spectrum only covers part of the camera pixels (low camera pixel usage, orange arrows in Figure 2.7 B) or if the whole spectrum exceeds the range of the detection window of the camera, move the F-theta lens back and forth to adjust the relative location between grating and the F-theta lens until the fringe spectrum covers all camera pixels (Figure 2.7A). Then, if diffracted lights after F-theta lens are not focused on the camera's CCD, light still can be detected by the camera pixels but interference signals cannot be resolved due to fringe washout (See Figure 2.7 A, yellow arrow). In such case, move the camera until all the pixels

are located in the focal plane of the F-theta lens (Figure 2.7D). Next, if the amplitude of the interference signal is not optimized (Figure 2.7 C, red arrow), adjust the polarization controller to maximized it. Adjust locations of F-theta lens and line-scan camera iteratively until the detected interference signals are optimized. 5) Fine adjustment of the line-scan camera: After we optimize detected interference signal which is obtained with a small optical path difference (OPD) between reference and sample arms , we can further improve the alignment of line-scan camera by adjusting the screws of the 5-axis stage underneath the line-scan camera (**Figure 2.8**).

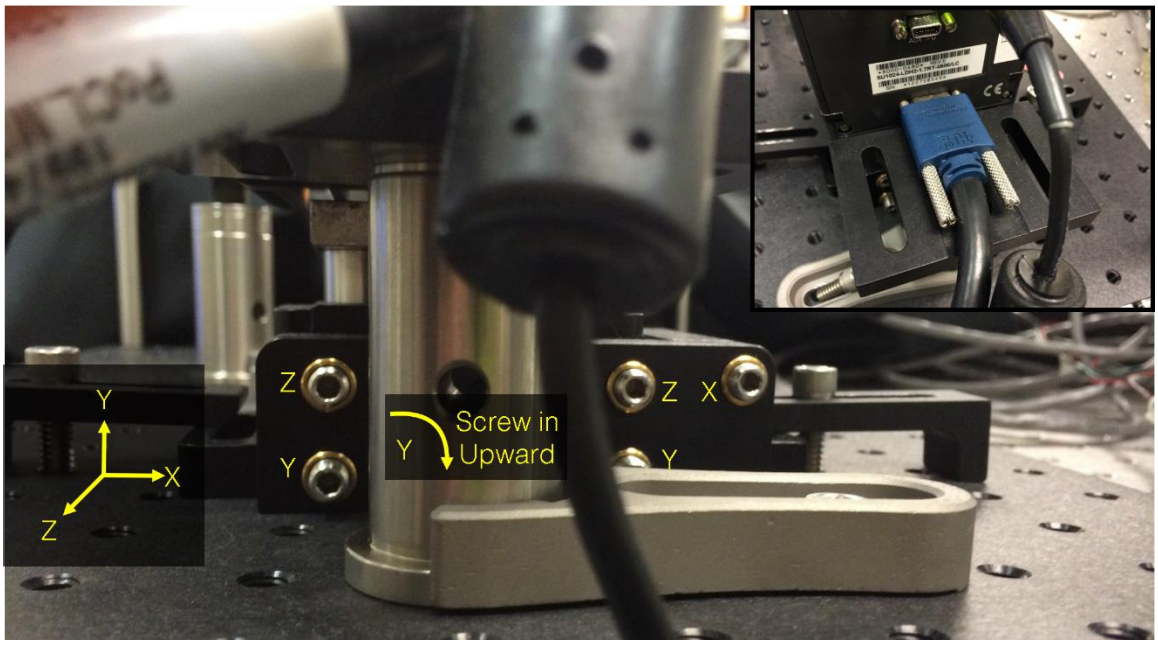

Figure 2. 8 **The back of the line-scan camera and the screws on the 5-axis stage to fine adjust the orientation of line-scan camera to achieve best signal detection.**

There are 3 types of defocusing effects on the camera: 1)The fringe is shifted to one side (See Figure 2.7 A, the spectrum is slightly shifted to right side). By adjusting the X screw, the detected fringe could be shifted back. 2) One side of fringe disappears due to tilting of the camera (Figure 2.7 A. Yellow arrow). By adjusting the Y screws in pairs, the camera can be tilted back. 3) One side of the fringe has faster fringe wash-out. It is shown by comparing amplitudes of the fringe under white arrows between Figure 2.7 A and 2.7 D (the well-adjusted one). The reason for fast fringe wash-out is that light are not focused exactly on the camera's CCD. By adjusting the Z screws of the 5-axis stage to move the camera back and forth, the amplitudes of the fringe could be maximized. After correcting these 3 types of defocusing effects for the detected interference signal

at small OPD (Mirror image in the Preview is close to zero delay), gradually move the mirror image to deeper imaging depths (larger OPDs) by moving the reference arm. Check the fringes and maximize their amplitudes at these depths by fine tuning screws of the 5-axis stage. The fast fringe wash-out should be minimized when the fringe amplitudes are maximized at all imaging depths. **Figure 2.9** shows representative interference signals at different imaging depths (OPDs) from a well-aligned line-scan camera. In **Figure 2.9H**, the fringe is still visible when moving the location of the mirror image at the imaging depth of 3.0mm, which is close to maximum imaging depth.

2.3.5 Hardware Dispersion Correction

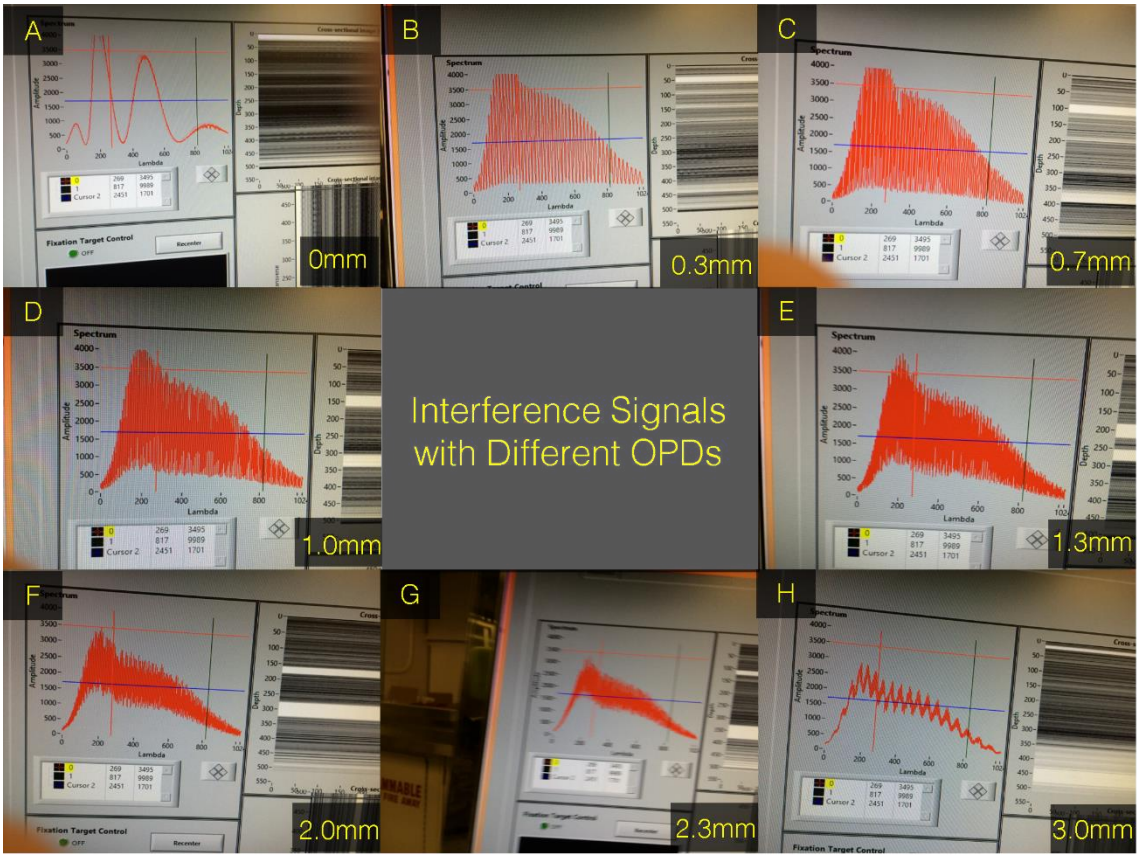

Figure 2. 9 Representative interference signals from different imaging depths (Optical path differences, OPDs) from a well-aligned spectrometer. Numbers at the right-below of each sub-figure indicates the imaging depths measured in air.

Due to the modified reference arm configuration, dispersion mismatch exists between the reference and sample arms, which may lead to the asymmetric point spread function distribution of the mirror image and

deteriorated axial resolution. To resolve the dispersion issue in hardware, additional compensating glasses are added in the reference arm. In order to determine the thickness of glasses to be added in the reference arm, we'll monitor distance changes of the two point spread functions (PSFs), which are obtained by filtering the interference signals with two narrow optical windows and performing the Fourier transform (the approach is similar to short-time Fourier transform, STFT). **Figure 2.10** shows the procedure to characterize the dispersion mismatch. In the top window of software, two Gaussian windows, one with a small central wavelength λmin (in blue) and the other with a large central wavelength λmax (in green), are applied to filter out sections of the fringe. The point spread functions from the filtered fringes would be shown in bottomwindow. First, move the two PSFs to the imaging depth of |D| from the zero delay. These two PSFs

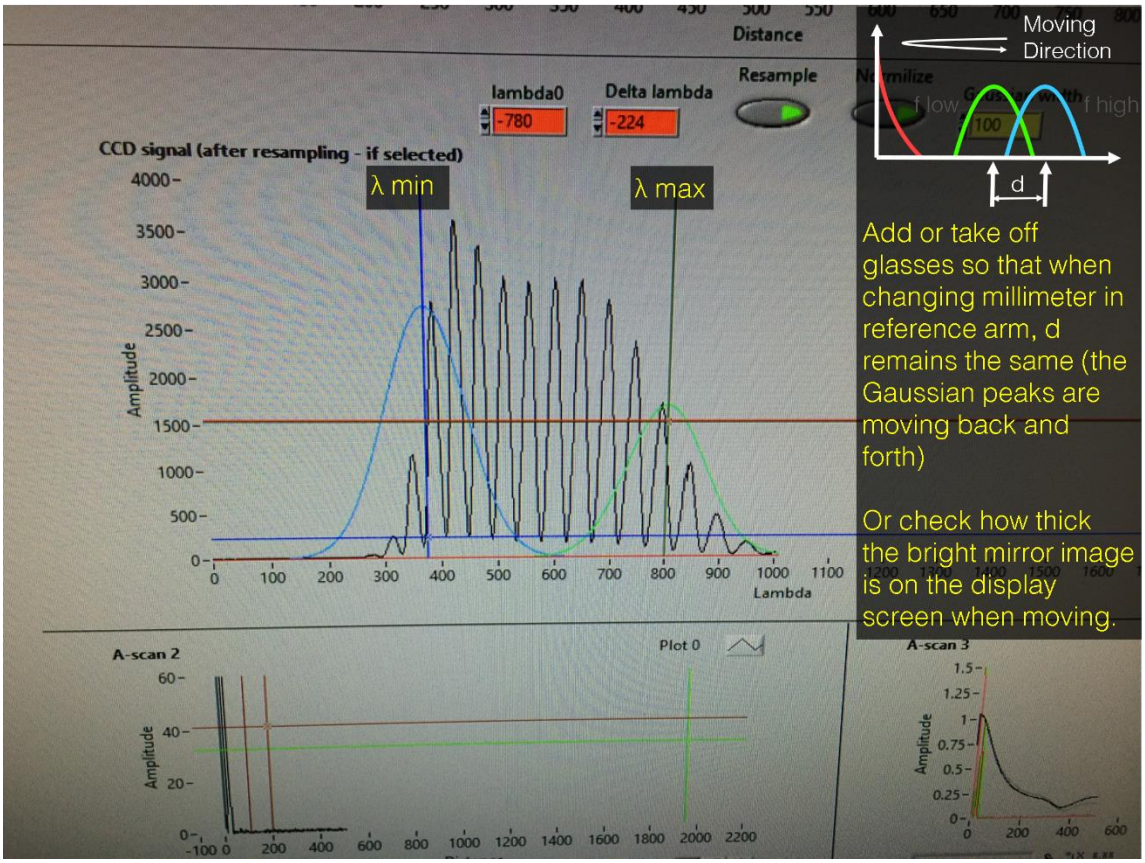

Figure 2. 10 Illustration of hardware dispersion compensation.

would be separated by d_1 due to dispersion. Then, adjust the reference arm to move these two PSFs across the zero delay to the same absolute imaging depth |D| (-D). Calculate the peak-to-peak distance d_2. If $d_1 = d_2$, dispersion is matched between reference and sample arms. However, $d_1 = d_2$ is difficult to achieve due

to limited options of glass thickness. In such case, we can find the glass thickness that minimize $|d1 - d2|$ to correct the dispersion mismatch .

2.4 Characterization of SD-OCT System

2.4.1 Characterization of the Light Source

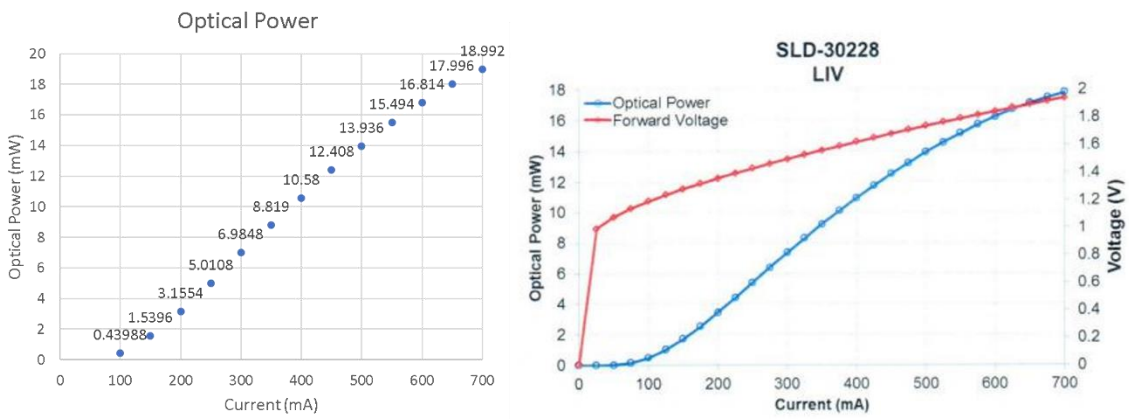

Figure 2. 11 Optical power measurements of Thorlabs SLD1325 superluminescent diode as a function of operating currents of the controller. Left: Lab measurement. Right: Product Specification.

To characterize the light source, we first measure the output spectra and output power levels under different operating current conditions. **Figure 2.11** and **Table 2.1** show the optical power measurements of the Thorlabs SLD1325 superluminescent diode. The output power of the SLD as a function of operating current by the controller is shown in left panel of the **Figure 2.11**. The output power follows a linear increasing trend as the operating current increases. The measured output power curve matches well with the product specification from the manufacturer (Right panel in **Figure 2.11**).

Table 2. 1 Optical Power Measurements of Thorlabs SLD1325 Superluminescent Diode

	1	2	3	4	5	6	7	8	9	10	11	12	13
I (mA)	100	150	200	250	300	350	400	450	500	550	600	650	700
V (V)	1.178	1.268	1.345	1.418	1.485	1.549	1.611	1.671	1.728	1.783	1.836	1.887	1.936
P (mW)	0.440	1.54	3.16	5.01	6.98	8.8	10.6	12.4	13.9	15.5	16.8	18.0	18.99
Std (mW)	0.009	0.01	0.06	0.08	0.09	0.1	0.1	0.1	0.2	0.1	0.2	0.1	0.09

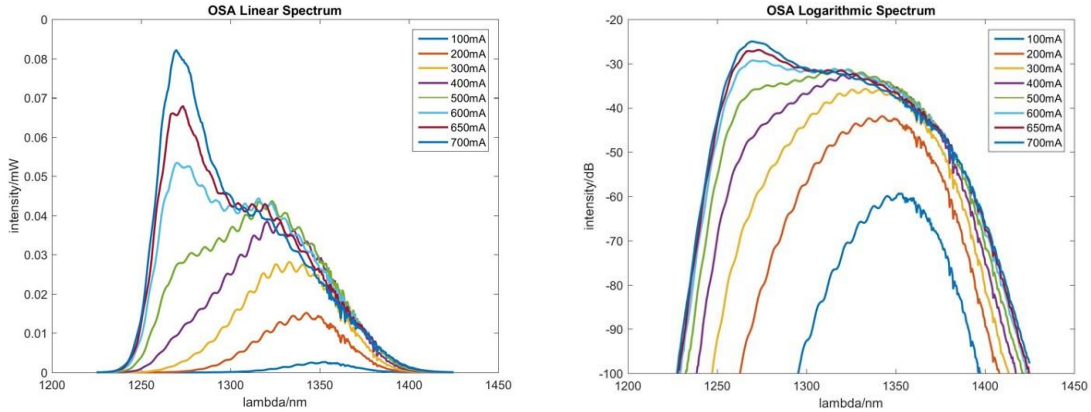

Figure 2. 12. The output spectra of the Thorlabs SLD1325 superluminescent diode in linear (left) and logarithmic (right) scales under different operating currents.

Next, we measure the output spectra of the SLD under different operating currents using optical spectrum analyzer (OSA). Results are shown in **Figure 2.12**. As the operating current increased from 100 mA to 400 mA, the spectral amplitudes between 1300 – 1360 nm increase significantly while optical powers in other wavelength ranges don't change much. When operating currents continue to increase from 400 mA to 700 mA, optical powers in 1250-1300 nm range increase substantially while spectral amplitudes in 1300-1360 nm range remain the same. When the operating current is between 500-600 mA, the SLD output spectrum has relative uniform shape with broad bandwidth. To maintain the broad bandwidth for a better axial resolution, operating currents of 550 mA and 600 mA are used by default. The corresponding output powers under 550 mA and 600 mA currents are 15.5 mW and 16.8 mW, respectively.

We also compare the measured output spectrum of the SLD with the test data from the product specification, running at the same 600 mA operating current. Results are shown in **Figure 2.13**. The characterization results are quite similar, indicating a good performance from the SLD. We can further quantify the output bandwidth from the logarithmic OSA spectrum. The measured full-width half maximum (FWHM, spectral bandwidth) of the output spectrum is 95 nm, which is slightly smaller than the value in the product specification (109.7 nm).

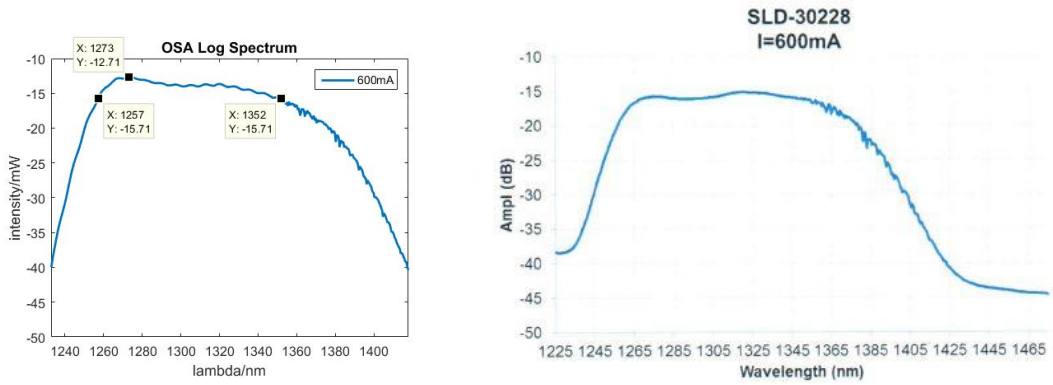

Figure 2. 13 Logarithmic output spectra of the Thorlabs SLD1325 diode The operating current was 600 mA. Left: Measured spectrum by optical spectrum analyzer (OSA); Right: Test data from manufacturer.

2.4.2 Phase Calibration

As is mentioned in Chapter 1.2, the detected coherence fringe of the spectrometer can be expressed by the following equation:

$$I(k) \sim S(k) \sum_{n} (\sqrt{\alpha_r \alpha_n} \cos(2z_n k + \varphi))$$

(1.2)

Where the phase term $\Phi = 2z_n k + \varphi$. However, k is also a function of λ. For the spectrometer, the detected interference signal for each pixel is a function of λ. The relationship between the index of pixel and λ is determined by the diffraction grating, f-theta lens and their alignment. As an approximation, if the wavelength range is not that huge, we can deduct the relationship from the grating function[87]:

$$\sin(|\theta_i| + \Delta\theta) + \sin(|\theta_i|) = mG(\lambda_i + \Delta\lambda)$$

(2.7)

Considering Δθ and Δλ are small, we can get:

$$\cos(|\theta_i|)\,\Delta\theta \approx \mathrm{mG}\Delta\lambda$$

(2.8)

Using the F-theta lens, if properly aligned, θ is proportional to the index of the pixel i. So, we can conclude that in the approximation, λ is linearly related to the index of the pixel i. Therefore, the detected signal I(i) can be written as $I(\lambda)$.

However, in general, we need to perform Fourier transform to reconstruct the depth profile in the time domain. In order to reconstruct the linear depth profile in time-domain, we need to convert the wavelength dependent interference signals to wavenumber dependent interference signal. Especially, it requires that the interference signals are linearly sampled in wavenumber k instead of wavelength λ. This resampling step is called phase calibration, since we would utilize the phase information to resample the fringe to k-space. Without the phase calibration step, the resultant point spread functions would be broadened in the deeper imaging depths, yielding poor axial resolutions [32].

The procedure to perform the phase calibration for the detected fringe spectrum is described as followed [32]. **Figure 2.14 A to I** show the intermediate results for each step of the phase calibration.

1) Background removal : The obtained OCT fringes from the SD-OCT system consist of AC terms of interference signals between reflected lights from reference and sample arms, and DC terms that originate from the self-interference of reference arm or sample arm. In the phase calibration step, we will remove the DC terms of interference signals to enhance image quality, which is called "background removal". There are two ways to perform background removal: (1) Average fringes from multiple A-ascans and subtract the averaged fringe from each original fringes. (2) Take a separate OCT background data with the sample-arm light blocked. This background data will contain most of the DC terms from the self-interference of reference-arm lights. Then, subtract the background data from the original data. We can use a low order polynomial fitting to remove low frequency noise signals and further balance the interference signals. **Figure 2.14 B** shows the results of the background removed fringes.

2) Inverse Fast Fourier Transform (iFFT): Perform the iFFT of the balanced fringes to get the point spread functions (PSFs, peaks) of the mirror images (**Figure 2.14 D**).

3) Window function: Use the window functions as a filter to keep the peak regions and remove the residue speckle noises. Perform separate window functions for different PSFs. Filtered results are shown in **Figure 2.14 E**.

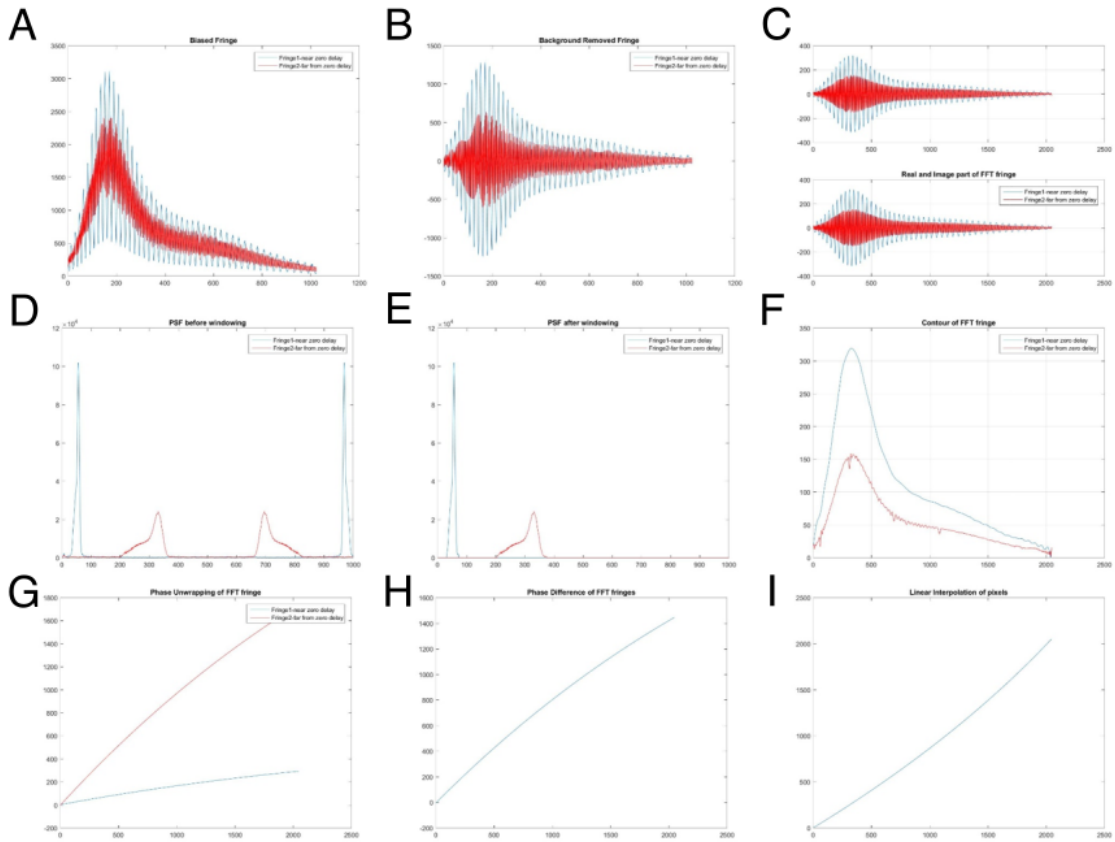

Figure 2. 14 Intermediate results of phase calibration procedure. (A) Original interference signals (fringes) of two mirror images fromdifferent imaging depths (OPDs). (B) Fringes after the background removal. (C) Real part and image part of the fringe. (D) Inverse fast Fourier transform (iFFT) of the fringes. Two point spread functions (PSFs, peaks) are shown. (E) PSFs after window function to remove background speckle noises. (F) Contours of the fringes after filtered PSFs are FFTed back to spectral domain. Complex analytic fringes are constructed. (G) Unwrapped phase curves obtained from complex fringes. (H) Calculated phase difference between these two unwrapped phase curves as a function of pixel indices. (I) The non-linear function of pixel index i as a function of wavenumber k with the fixed Δz, derived from the inverse function of the phase difference curve.

4) Zero padding: Add additional zero pixels afterwards to pad the PSFs. Usually the vector size after the padding will be twice the number of camera pixels. To maintain the original amplitudes of the fringe after the inverse FFT, multiply the amplitude of the PSFs by two.

5) Perform fast Fourier transform (FFT) to convert the PSFs back to the spectral domain. The complex analytic interference signals are constructed after FFT. The contours of the fringes are plotted in **Figure 2.14 F**. The real part and the image part of the fringe are plotted in **Figure 2.14 C**.

6) Phase unwrapping: Obtain the phases of the complex fringes. Unwrap the phases for all the pixels by resolving the 2π phase changes. Unwrapped phase curves are shown in **Figure 2.14 G**.

7) Calculate phase difference: Since the phase term contains the arbitrary term φ, we can calculate the phase difference between the two unwrapped phase curves from fringes of two different depths. Thus, the arbitraty term φ is cancelled out and the phase differences are proportional to wavenumber k. $\Delta\Phi = k\Delta z$. The phase difference curve is plotted in **Figure 2.14 H**. Therefore, the non-linear function between wavenumber and pixel index i can be obtained.

8) Interpolation: Utilize the inverse function of the phase difference curve to derive the correspoinding pixel indices with linearly sampled phase difference (linearly sampled k) as new sampling points, using the interpolation function. The non-uniform pixel curve as a function of linearly sampled phase difference (wavenumber k) is shown in the **Figure 2.14 I**.

9) Calculate the interpolated values of the fringes using updated non-uniform pixel indices. Thus, the updated fringes are linearly sampled in wavenumber k.

Note: the phase calibration step requires that the detected inteference signals from the mirror have large amplitudes. During the calibration, a neutral density filter with an OD value of 1.0 or 1.5 is placed in the sample arm to maintain a proper amplitude of fringes.

2.4.3 Numerical Dispersion Compensation

In the alignment steps, we perform hardware dispersion compensation by using the same optics for both reference and sample arms, or by adding compensating glasses in the reference arm. However, the latter method may not be optimal because the material of glasses may be different from the lenses used in the sample arm, yielding the dispersion not fully compensated. The consequence, in the worse case, may be that, the fringe spectrum may not be a single peak at the zero OPD, i.e. different wavelenths might have constructive or destructive interferences at the zero delay due to dispersion. In order to correct it, a numerical dispersion compensation can be applied.

First, we need to know the source of dispersion. Start with the Taylor expansion of the propagation constant β(ω) near the center frequency of the light source [88]:

$$\beta(\omega) = \beta(\omega_0) + \frac{d\beta}{d\omega}|_{\omega_0}(\omega - \omega_0) + \frac{1}{2}\frac{d^2\beta}{d\omega^2}|_{\omega_0}(\omega - \omega_0)^2$$

$$+ \frac{1}{6}\frac{d^3\beta}{d\omega^3}|_{\omega_0}(\omega - \omega_0)^3 + \cdots$$

(2.9)

In this taylor series of the propagation constant β(ω), the first term describes the propagation constant at the center frequency ω_0. The second term $\frac{d\beta}{d\omega}$ is the inverse group velocity. The first dispersion term, the 3rd term (2nd order term) of the Taylor series, is the group velocity dispersion that yields the broadening of the PSFs in the intensity profiles along the depths. The 4th term of the Taylor series is the 3rd order dispersion, which yields asymmetric shape of the PSFs. Higher-order terms in the Taylor series of the propagation constant are counted as high order dispersion terms.

In the expression of the phase term $\Phi = 2\Delta x_n k + \varphi$ of the OCT interference signal, the second term φ actually contains the phase shift due to the dispersion mismatch, which is frequency and depth-dependent. We can label the related phase-shift as $\Phi_d(\omega, z_n)$. If the OPD is relative small (i.e. 1-2mm), the dispersion variation due to the OPD changes are usually neglectable [88]. Under such approximation, we can assume that Φ_d is only wavenumber (frequency) dependent. Thus, we can numerically compensate the phase by adding the dispersion-related phase term described as [88]:

$$\Phi_d(\omega) = -a_2(\omega - \omega_0)^2 - a_3(\omega - \omega_0)^3$$

(2.10)

which corrects both the 2nd order and 3rd order dispersion. In the post-processing procedure, it is done by multiplying the additional phase term $\exp(\mathrm{i}\Phi_d(\omega))$ to the complex interference signals. If the dispersion mismatch is huge, higher order dispersion term can be introduced in the dispersion-related phase term to further compensate dispersion.

Based on this, we can figure out the a_2 and a_3 values by applying numerical dispersion compensation to optimize the PSFs of the mirror images. We can perform an automatic or manual iterative search for the

optimal a_2 and a_3 values and measure the FWHM of PSFs of the mirror images. If the FWHM is minimized, the dispersion mismatch is compensated, given the above approximation.

A more generalized way to perform the dispersion compensation is to optimize the $\Phi_d(\omega)$ for the mirror images for different depth ranges, using the window function to filter out different sections of the OCT depth profile [89].

2.4.4 Sensitivity Measurement and Roll-off Analysis

After the phase calibration and numerical dispersion compensation are performed, the PSFs of the mirror images from different depths are well optimized. By analyzing these PSFs, we can characterize the performance of the OCT system by measuring the key performance metrics such as sensitivity and its roll-off, as well as axial resolution. This characterization step is called roll-off analysis.

To perform the roll-off analysis, we first collect a set of mirror images at different imaging depths by moving the reference armalong one direction. The reference positions of these mirror images are recorded to calculate the axial pixel size, which is the distance of one pixel along the axial direction. To characterize 1300 nm SD-OCT system, we collect the OCT images by moving the reference arm with a step size of 100 µm. For large imaging depths, we move the reference arm with a step size of 200 µm or 300 µm. In total, we move the reference arm by 2300 µm. After resampling and dispersion compensation, we can plot out the PSFs for all the mirror images from multiple depths.

Table 2.2 shows the operating conditions of 1300 nm SD-OCT system during roll-off analysis. The line-scan camera is running at 47 kHz (OPR16), with the exposure time set at 22.0 µs. The reference arm output power (P_{ref}) from the port 3 of the 2×2 fiber coupler is measured to be ~8.9 mW with 600mA operating current of the controller. The detected backcoupled power from the reference arm ($P_{refback}$) is 1.69 mW, measured from the output port (Port 2) of the 2×2 fiber coupler connecting to the spectrometer. Note that this value is half of the backcoupled power measured before the 2×2 fiber coupler. The power incident to the sample arm (P_{inc}) is 8.97 mW, measure from the port 4 of the 2×2 fiber coupler. The power on the sample arm (P_{samp}) is ~5.4 mW, measured under the objective. We measure the backcoupled powers under three operating current conditions. The backcoupled powers from the sample arm ($P_{backcoupled}$) are measured to be 0.975 mW (550 mA current), 1.053 mW (600 mA current) and 1.131 mW (650 mA current). Transmission

loss in the sample armis estimated. The forward transmission loss, including the collimation and optics, would be:

Table 2. 2 Operating Conditions of 1300nm SD-OCT during Roll-off Analysis

Basic Measurment	P_{inc}	P_{samp}	$P_{backcoupled}$	Opearating Current	PhaseCal OD	RO OD	a2	a3
47kHz, 22µs P_{ref} = 8.9mW (600mA), $P_{refback}$ = 1.69+/- 0.01mW (600mA)			0.975+/- 0.004mW	550mA	1	2	-1.89e-6	3.03e-9
	8.97+/- 0.08mW	~5.4mW	1.053+/- 0.007mW	600mA	1	2	-2.125e-6	-1.12e-9
			1.131+/- 0.007mW	650mA	1	2	-1e-6	-1.95e-9

$$\eta_{forward} = 10\log\left(\frac{5.4}{8.97}\right) = -2.2\text{dB}$$

(2.11)

The backward transmission loss is calculated to be:

$$\eta_{back} = 10\log\left(\frac{1.053}{5.4}\right) = -7.1\text{dB}$$

(2.12)

The loss includes >3 dB additional loss in the 2 × 2 fiber coupler, the transmission loss in the optics, the loss from the reflection of mirrors as well as coupling loss from the air back to the fiber. We can estimate that the coupling loss back to the fiber was no more than

$$\eta_{coupling} < -7.1 - (-2.2) - (-3) = -1.9\text{dB}$$

(2.13)

The quantum efficiency of the line-scan camera is estimated to be ~75-80% for the line-scan camera. Therefore, the theoretical shot-noise-limited sensitivity is calculated using the formula (See Chapter 1.3.6):

$$Sensitivity = 10\log(\frac{\rho\eta T}{e} P_0 \kappa_s')$$

(1.9)

We use ρ=0.75, η = 0.8, T $= 22 \times 10^{-6}$ (s), $P_0\kappa_s' = P_{backcoupled} = 1.053 \times 10^{-3}$ (W), $e = 1.6 \times 10^{-19}$ (Coulomb). Putting these values back into the sensitivity calculations yields the shot-noise-limit sensitivity to be ~109 dB.

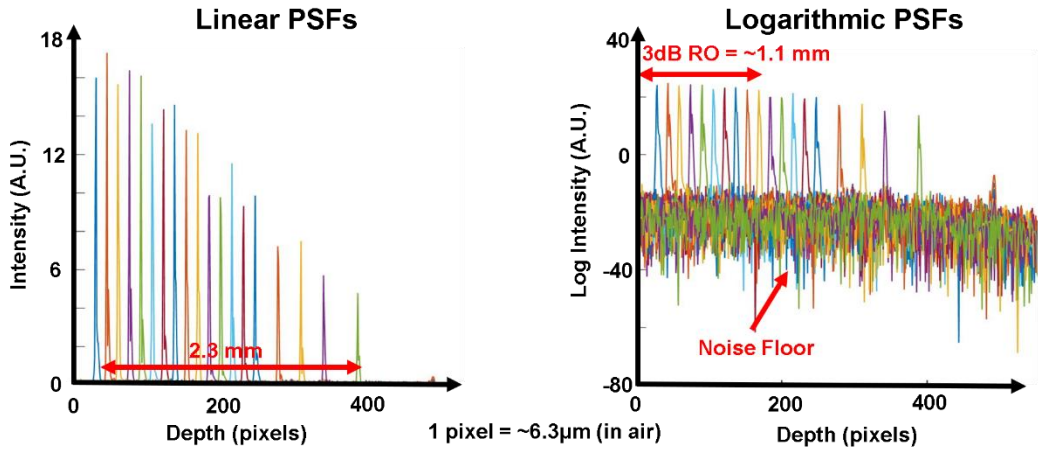

Figure 2. 15 Roll-off analysis: Linear (Left) and Logarithmic (Right) point spread functions (PSFs) of the mirror images from multiple depths. The operating current of the controller is **550 mA**. The 3dB roll-off is measured to be ~1.1 mm.

Figure 2.15 shows the results of the roll-off analysis with the plotted PSFs in both linear (Left panel) and logarithmic (Right panel) scales under the operating current of 550 mA. During the roll-off measurement, a neutral density filter with OD = 2.0 is added to the sample arm. The measured sensitivity is calculated to be the ratio between the peak intensity of each PSF and the standard deviation of the noise signals near the PSF. We can use a small region near the PSF containing only noise signals to calculate the standard deviation of the noise signals. For the custom SD-OCT system, the sensitivity is measured to be 98.3 dB at best. The axial resolution is measured as the full width half maximum (FWHM) of each PSF. The optimal axial resolution is measured to be 6.8 μm in air (See **Table 2.3**, second row). Using the 2.3 mm travel range recorded from the reference arm, we can calculate the axial pixel size to be:

$$\text{Pixel size} = \frac{2.3\ \text{mm}}{365\ \text{pixels}} = \sim 6.3\ \mu\text{m} \tag{2.14}$$

Therefore, the total imaging range is:

$$\text{Imaging Range} = \text{Pixel size } \times \text{Number of Pixels}$$

$$= \sim 6.3\ \mu\text{m } \times \frac{1024}{2} = \sim 3.2\ \text{mm} \tag{2.15}$$

Table 2. 3 Results of Roll-off Analysis under Two Different Operating Current Conditions

Operating Current	**Max sensitivity**	**Min Resolution (in air)**	**Axial Pixel Size (in air)**	**Total Imaging Range**	**3dB Roll-off**
550mA	98.3 dB	6.8 µm	~6.3 µm	~3.2 mm	~1.1mm
600mA	99.6 dB	6.1 µm	~6.3 µm	~3.2 mm	~1.3 mm

The 3dB sensitivity roll-off (RO) is measured by checking the sensitivity values for all the PSFs of the mirror images and find out where the sensitivity drops by 3dB from the maximum value. Based on the plotted PSFs and calculated sensitivities, we obtain the 3dB roll-off value to be ~1.1 mm.

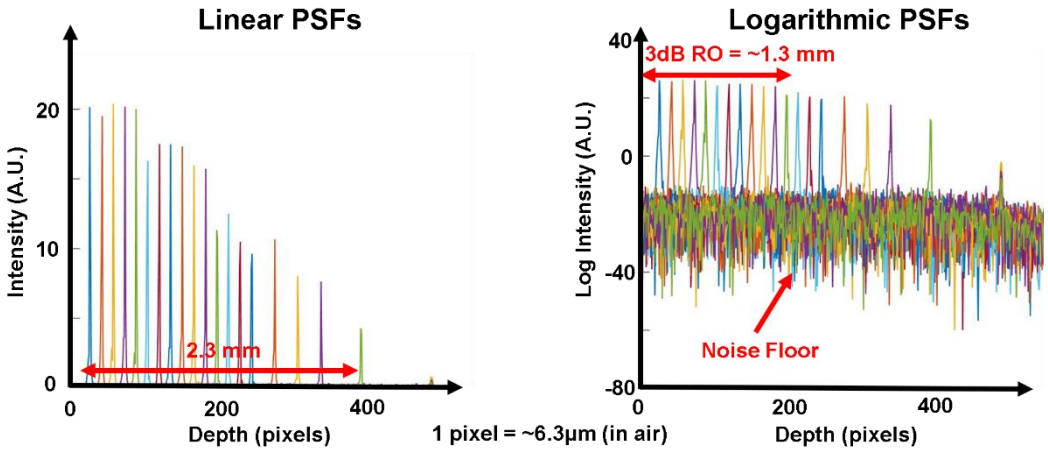

Figure 2. 16 Roll-off analysis: Linear (Left) and Logarithmic (Right) point spread functions (PSFs) of the mirror images from multiple depths. The operating current of the controller is **600 mA**. The 3 dB roll-off is measured to be ~1.3 mm.

Under 600 mA operating current, the characterization results of the roll-off analysis are shown in **Figure 2.16** and **Table 2.3**. The maximum sensitivity is measured to be 99.6 dB and the best axial resolution was measured to be 6.1µm in air (**Table 2.3**, third row). The axial pixel size is measured to be the same ~6.3 µm in air. Total imaging depth is also ~3.2 mm. The 3 dB sensitivity roll-off is measured to be ~1.3 mm. Variation of sensitivity values under different operating currents of the controller may come from the fluctuation of the

SLD outputs and polarization states while moving the reference arms. In addition, since we optimize the PSFs of the mirror image at one location to get the a2 and a3 value and use the same value for the rest of PSFs, variation of measured minimal resolution values under different operating currents may come from measurement errors as well as non-optimal a2 and a3 values for PSFs that are not used during dispersion compensation step. Additional efforts could be made to find the optimal a2 and a3 values for each point spread function.

2.4.5 Transverse Measurements

In the transverse measurements, we will characterize the following parameters: Transverse resolution; Transverse scanning ranges (Field of View, FOV) in X and Y directions with different scanning voltages to derive transverse pixel sizes in X and Y directions with known number of axial scans per frame and known number of frames ; Depth of focus (DOF).

To characterize these parameters, we use a USAF target as the sample, instead of the mirror. First, we need to find out the exact location of the focal plane under the objective. We move the translation stage holding the USAF target up and down and obtain 3D OCT images of USAF targets at multiple sample locations. Since we use a 5× objective in the sample arm for the 1300 nm SD-OCT system, yiedling a large depth of focus, we can set the step size of the movement to be 50 µm. Once the data are processed, we take the average of a stack of enface OCT images (stack size is set to 20) to see which USAF target image is the clearest. The in-focus OCT image of the USAF target should have the sharpest bars and the best lateral resolution. If the step size of 50 µm is too big, we can collect another set of OCT target images with a reduced step size of 10 µm. After we figure out the best vertical location of the USAF target, we move the target to the optimal position in the transverse plane by checking the fundus preview (en face summation) in the acquisition software. Then, we take the OCT image of the USAF target at the optimal position. **Figure 2.17** shows the result of the en face OCT image of the USAF target at the optimal position. In the image, the bars

up to Group 5, Element 3 are distinguishable. Checking the USAF target table (See Appendix 2.1), we conclude that the lateral resolution for the 1300 nm SD-OCT system with the 5× objective is 12.4 µm.

The theoretical lateral resolution could be calculated as (See Chapter 1.3.3):

$$\Delta x = \frac{0.61\lambda_c}{NA} \tag{1.6}$$

Using the effective NA = 0.062 for the 5X objective lens used in our system (the objective aperture is partially filled), we obtain the theoretical value of the lateral resolution to be ~13 µm. Thus, the measured

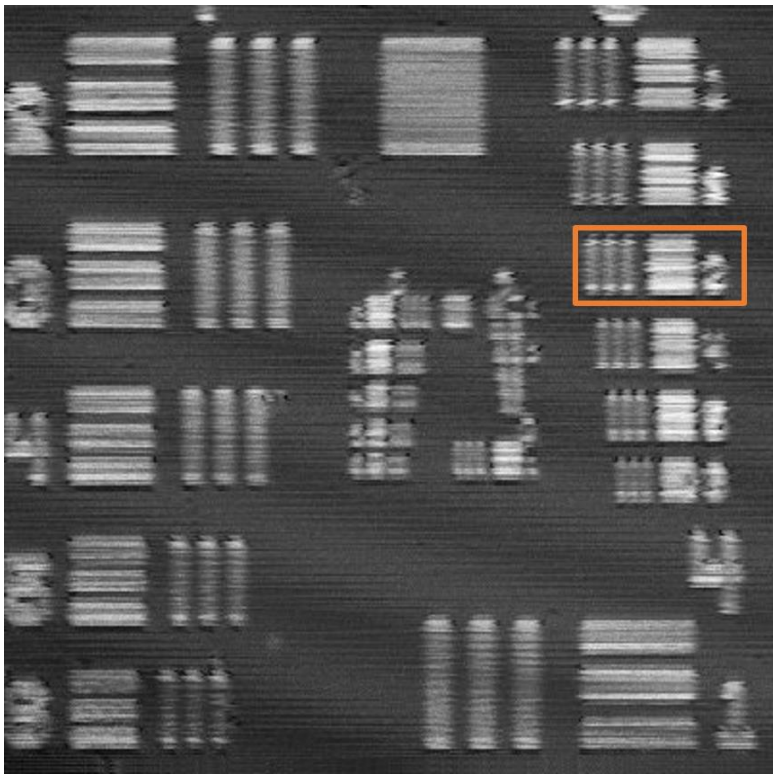

Figure 2. 17 En face OCT image of the USAF target, showing the characterization of lateral resolution. The bars up to group 5, element 3 can be distinguished, yielding the transverse resolution to be 12.4 µm.

lateral resolution matches well with the theoretical value.

Next, we characterize the depth of focus (DOF) of the 1300 nm SD-OCT system. The theoretical value of DOF was given by the following formula (See Chapter 1.3.4):

$$DOF = \frac{2n\lambda_c}{NA^2},$$

(1.7)

Considering λ = 1320 nm and NA = 0.062 for the 5X objective lens, DOF is calculated to be ~680 μm in air. We also measure the DOF of the OCT system by characterizing the image resolution in en face OCT images of the USAF targets at different sample locations collected in the previous step. The upper and lower threshold sample locations are determined by finding the en face OCT target images with the clearest bar width to be $\sqrt{2}$ of the lateral resolution of the OCT system, which is three elements above the clearest elements. That means, if the lateral resolution is measured from Group 5, Element 3 of the USAF target, we should check the USAF target with the clearest bars measured from Group 4, Element 6 of the target. The measured DOF is ~400 μm in air for the 1300nm SD-OCT system.

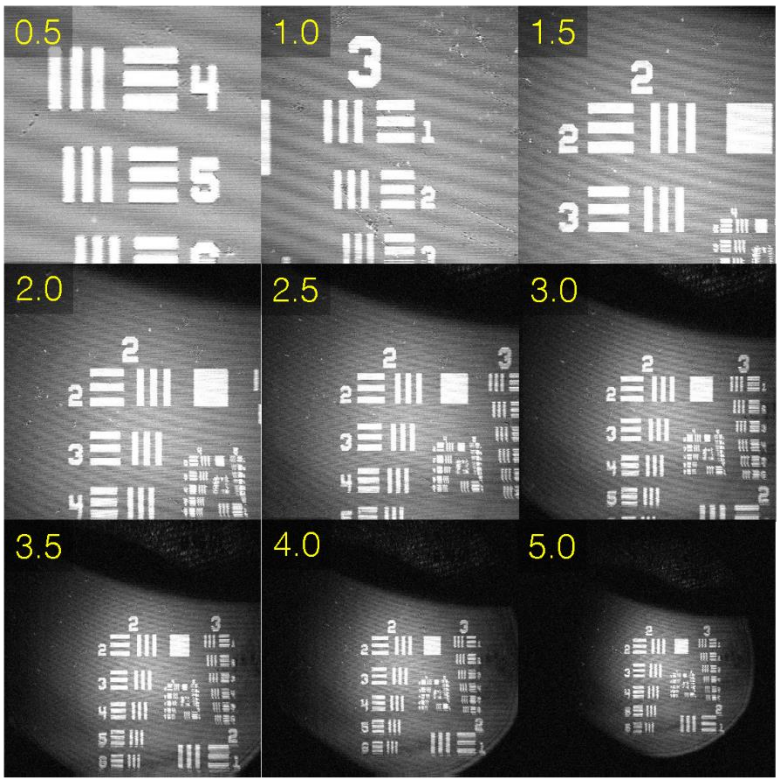

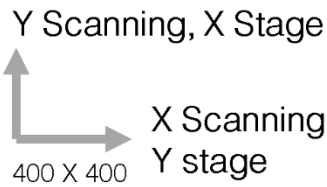

Voltage	X (μm)	Y (μm)
0.5	2.599	2.278
1	5.208	4.735
1.5	7.733	7.048
2	10.51	9.768
2.5	13.26	11.85
3	15.91	14.28
3.5	18.56	16.37
4	21.42	19.20
5	26.51	24.21

Figure 2. 18 En face OCT images of the USAF target with different transverse scanning ranges (Galvo scanning voltages). Each OCT data size is 400 × 400 × 1024 pixels. The numbers on the top left region of each subfigure indicated the galvo scanning voltages used to acquire the OCT images. The corresponding transverse pixel size for each scanning voltage is measured and shown in the table on the bottom right.

Next we measured the actual X and Y transverse scanning range with different galvo scanning voltages. **Figure 2.18** shows the en face OCT images of the USAF target with different transverse scanning ranges, which are controlled by the scanning voltages provided to the galvo system. The galvo scanning voltages are

set from 0.5 V to 5 V with a step size of 0.5 V. Each OCT data size is 400 × 400 × 1024 pixels. Based on these en face OCT images, we could calculate the pixel size for each galvo scanning voltage, which is the ratio of the actual length of a bar from a specific element (e.g. Group 2, element 2) and the number of pixels counted within the bar length. Note that the bar length equals five times the bar width, which can be read from the USAF target table. Results of calculated pixel sizes of different scanning voltages in X and Y directions under the current acquisition scheme (400 × 400) are listed in the table in **Figure 2.18**.

Voltage	X (μm)	Y (μm)
0.5	1039.6	911.2
1	2083.2	1894
1.5	3093.2	2819.2
2	4204	3907.2
2.5	5304	4740
3	6364	5712
3.5	7424	6548
4	8568	7680
5	10604	9684

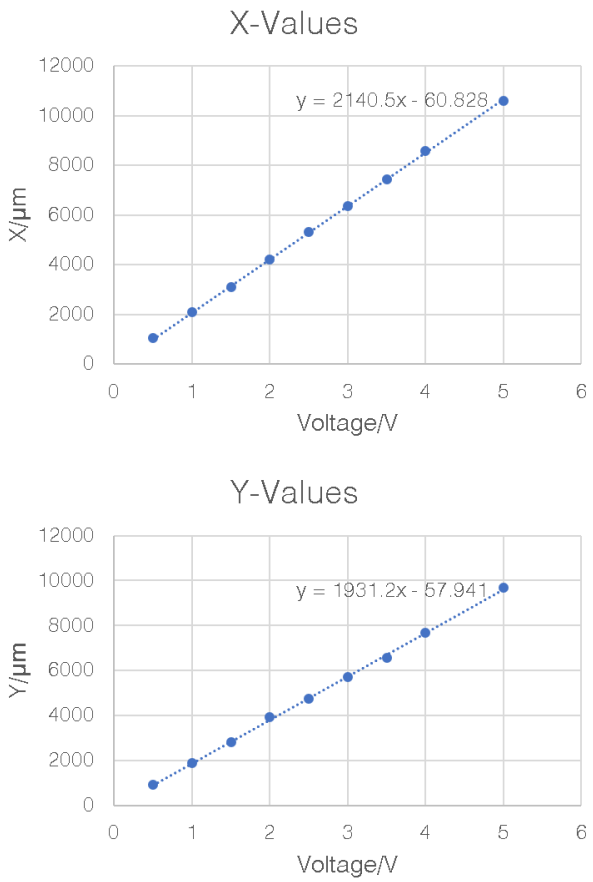

Figure 2. 19 Measurement of actual transverse scanning ranges of the SD-OCT system with different galvo scanning voltages. Left: Tables of Results. Right: Linear fittings between the actual scanning ranges and the galvo scanning voltages. The actual scanning ranges are linearly proportional to the galvo scanning voltages.

After we obtain the transverse pixel sizes for different galvo scanning voltages, we calculate the actual transverse scanning range of the OCT system by multiplying the transverse pixel size to the number of pixels in X or Y directions of the OCT data, which are 400 and 400. The table on the left of **Figure 2.19** lists the actual transverse scanning ranges of the SD-OCT system with different galvo scanning voltages from 0.5 V

to 5 V. A linear fitting is performed between the galvo scanning voltages and the X or Y actual scanning ranges. The fitting results for X and Y scanning ranges are shown in the right panels of **Figure 2.19**. In the fitting results, the actual scanning ranges are linearly proportional to the galvo scanning voltages with high correlation coefficient values in both X and Y directions. Using this fitting functions, we could derive the transverse scanning ranges for arbitrary galvo scanning voltages, which would be used for the rescaling of the OCT images.

2.5 Summary

In this chapter, a custom spectral domain OCT (SD-OCT) system is developed and characterized for the purpose of 3D tumor spheroid imaging. The configuration of the SD-OCT system and its extensions, the alignment and characterization methods are described in details. The key performance metrics of the custom SD-OCT are characterized. A superluminescent diode provides broadband incident light with a central wavelength of 1,320 nm and a spectral range (FWHM) of ~95 nm. Axial resolution of the system is measured to be 6.8 µm (550 mA) and 6.1 µm(600 mA) in air. The total imaging depth of the SD-OCT system is close to 3.4 mm in air. The best sensitivity of the SD-OCT is measured to be ~100 dB (600 mA) with 47 kHz axial scan rate. The 3 dB sensitivity roll-off is measured to be ~1.3 mm. The lateral resolution is measured to be ~12.4 µm using a USAF target. The DOF of the OCT system is measured to be approximately 400 µm in air. The fitting curve of the transverse scanning range as a function of galvo scanning voltage is derived.

The results of using the custom SD-OCT system for 3D tumor spheroid imaging would be presented in Chapter 7. Previous versions of the custom SD-OCT system, with small modifications in the sample arm, are used to image the latex sample and mouse embryos. The results would be presented in Chapter 6 and Chapter 8.

Appendix 2.1 Table of a 1951 USAF Resolution Test Chart (USAF Target)

The bar width of different elements of the USAF targets are listed in the table, which is cited from Wikipedia [90].

Width of 1 line in micrometers in USAF Resolving Power Test Target 1951

	Group Number											
Element	**−2**	**−1**	**0**	**1**	**2**	**3**	**4**	**5**	**6**	**7**	**8**	**9**
1	2000.00	1000.00	500.00	250.00	125.00	62.50	31.25	15.63	7.81	3.91	1.95	0.98
2	1781.80	890.90	445.45	222.72	111.36	55.68	27.84	13.92	6.96	3.48	1.74	0.87
3	1587.40	793.70	396.85	198.43	99.21	49.61	24.80	12.40	6.20	3.10	1.55	0.78
4	1414.21	707.11	353.55	176.78	88.39	44.19	22.10	11.05	5.52	2.76	1.38	0.69
5	1259.92	629.96	314.98	157.49	78.75	39.37	19.69	9.84	4.92	2.46	1.23	0.62
6	1122.46	561.23	280.62	140.31	70.15	35.08	17.54	8.77	4.38	2.19	1.10	0.55

Chapter 3: Development of a High-speed OCT System for Time-lapse Imaging

3.1 The Need for High-speed Imaging

In the past 28 years, one of the major momentum for OCT development is to improve the imaging speed for the OCT system. Introduction of Fourier-domain OCT, including spectral domain OCT (SD-OCT) and swept source OCT (SS-OCT), resulted in a drastic improvement in both imaging speed and sensitivity over the time-domain OCT system [10-12]. Development of new wavelength-tunable laser further pushed the imaging speed from 100,000 axial scans per second (A-scans/s) level to millions of A-scans/s [91].

High imaging speed benefits various *in vivo* OCT applications, including ophthalmic[92], endoscopic[93] and intravascular imaging[94]. For these applications, motion artifacts are the key concerns that significantly affected OCT image quality. If the total acquisition time of *in vivo* imaging of animal or human subjects, i.e. mouse ear or human eye, is longer than ~1 second, motion artifacts due to involuntary movements of animal or human subjects, respiration or cardiac motion[95], seemed unavoidable. Furthermore, voluntary subject movements may occur if the animal or human subject motions are not prevented via breath-holding, sedation or immobilization [95]. Although a series of complex numerical correction of motion artifacts can be employed to mitigate or correct for motion artifacts, they require additional time and hardware resources for data processing [22].

High imaging speed is desirable for functional OCT imaging like angiography. The red blood cells (RBC) in the capillary blood vessels have a speed of ~0.1 – 0.9 mm/s. To render the contrast of moving RBCs in the OCT angiographic (OCTA) images, it is recommended that the frame rate of the 3D OCT imaging to be >100Hz for a stable sample (i.e. sleeping mouse eye) and >400 Hz for a moving sample (i.e. human eye). Also, since the OCTA relies on either the Doppler effect or speckles, repeated-frame imaging is required. Five to eight repeats are recommended in acquisition of OCTA data. In order to acquire a high-frame-rate, multi-repeat, 3D OCTA data with sufficient lateral sampling density, a high speed OCT system is imperative.

For time-lapse imaging, a high frame rate is required to monitor the motions of individual particles. In the case of the moving particles in a droplet (See Chapter 6), a frame rate of ~40 Hz is required to track the circular movement of polystyrene particles to show the convectional flows during the dynamic process of

evaporation. In another case, to observe the vertical packing process in the polystyrene latex system, time-lapse imaging with a frame rate of ~85 Hz is employed to distinguish the packed layer with low particles' mobility from the suspension layer with freely moving particles. In these cases, high imaging speed of the OCT system can help maintaining a high frame rate and a sufficient lateral sampling density for time-lapse, M-mode or 3D OCT imaging.

3.2 Trade-offs of Imaging Speed Improvement

Although speed improvement benefits various OCT applications, several factors need to be taken into consideration. The key factor is the sensitivity of the system, which is also an important performance metric of OCT. In the shot-noise-limit sensitivity calculation in expression (1.8) for SD-OCT system[96]:

$$Sensitivity = 10\log(\frac{\rho\eta T_{int}}{e} P_0 \kappa_s')$$

or

$$Sensitivity = 10\log10\left(\frac{\rho\eta}{2ef_{ss}} P_0 \kappa_s'\right)$$

(1.8)

for the SS-OCT system, the imaging speed, which is either expressed as the camera line rate $f_{sd}=1/T_{line}$ (camera integration time T_{int} = Duty cycle × T_{line}), or laser swept rate f_{ss} would be inversely related to the shot-noise-limit sensitivity. If the imaging speed is doubled, i.e.

$$f_{new} = 2f$$

(3.1)

The shot-noise-limit sensitivity would change by:

$$\Delta Sensitivity = 10\log\left(\frac{1}{2}\right) \approx -3\ \mathrm{dB}$$

(3.2)

Thus, there is a trade-off between the imaging speed and the sensitivity. While improving the OCT imaging speed, we have to maintain sufficient sensitivity level so that the image quality is decent.

Further more, increasing the imaging speed may further reduce the sensitivity, if the shot-noise-limit cannot be satisfied. According to the sensitivity calculation [96]:

$$Sensitivity = 10\log(1/R_{min})$$

(3.3)

Where R_{min} indicated the the minimum sample reflectivity that the amplitude of the interference signal can be just differentiated from the noise floor, which means the signal to noise ratio, SNR, is close or equal to 1.

$$SNR \approx 1$$

(3.4)

According to the definition of signal to noise ratio for OCT system [4, 96]:

$$SNR = \frac{|AC|^2}{\sigma^2}$$

(3.5)

Where $|AC|^2$ denotes the square of the amplitude of interference signal and $\boldsymbol{\sigma^2}$ is the total noise variance. The total noise variance terms in detected photo-electrons squared per sampling time for SD-OCT and SS-OCT are given by [4]:

$$\sigma_{SD}^2 = \sigma_{r+d}^2 + \sigma_{shot,SD}^2 + \sigma_{RIN,SD}^2$$

(3.6)

$$\sigma_{SS}^2 = \sigma_{th}^2 + \sigma_{shot,SS}^2 + \sigma_{RIN,SS}^2$$

(3.7)

In the expression (3.6) and (3.7), the second term, σ_{shot}^2 is shot-noise variance in detected photo-electrons squared per sampling time, which is originated when the photodetector randomly detects the individual photons, and inherent in OCT detection [4, 96]. Shot noise per detector element can be expressed as [4]:

$$\sigma_{shot,SD}^2 = \frac{\rho\eta e^2 T_{int}}{E_v}\frac{P_{ref}}{N} \ [e^2]$$

(3.8)

$$\sigma_{shot,SS}^2 = \frac{\rho\eta e^2 T_{samp}}{E_v} P_{ref} \ [e^2]$$

(3.9)

In the expression (3.8) and (3.9), $\boldsymbol{P_{ref}}$ is the effective reference arm power, $\boldsymbol{P_{ref} = P_0 \kappa_r'}$, where $\boldsymbol{\kappa_r'}$ is the effective unidirectional coupling efficiency including the square root of optical and coupling losses. Also, in the expression (3.8) and (3.9), the assumption

$$P_{ref} \gg P_{samp}$$

(3.10)

is applied, yielding only the reference power term shown in the expression. Otherwise, $P_{total} = P_{ref} + P_{samp}$ should be used instead of P_{ref} in the expression.

From the expression (3.8) and (3.9), shot noise is proportional to the camera integration time and inversely proportional to the number of camera pixels for SD-OCT, and proportional to the sampling time for SS-OCT. We should note that, if the A-scan rate is equal for both SD-OCT and SS-OCT, the following equation can be satisfied [4]:

$$T_{samp} = \frac{T_{int}}{N}$$

(3.11)

assuming a 100% duty cycle for camera integration time and the same total spectral bandwidth for both SD-OCT and SS-OCT, yielding the identical expression of shot noise variance.

The final expressions of signal to noise ratio (SNR) of SD-OCT and SS-OCT are given by:

$$SNR_{SD} = \frac{|AC|^2}{\sigma_{SD}^2} = \frac{(\frac{\rho\eta T_{int}}{E_v})^2 P_{ref} P_{samp} \frac{e^2}{N}}{\sigma_{r+d}^2 + \frac{\rho\eta T_{int}}{E_v} \frac{P_{ref}}{N} e^2 + \sigma_{RIN,SD}^2}$$

(3.12)

$$SNR_{SS} = \frac{|AC|^2}{\sigma_{SS}^2} = \frac{(\frac{\rho\eta T_{samp}}{E_v})^2 P_{ref} P_{samp} N e^2}{\sigma_{r+d}^2 + \frac{\rho\eta T_{samp}}{E_v} P_{ref} e^2 + \sigma_{RIN,SS}^2}$$

(3.13)

OCT systems have the best performance when the shot-noise-limit detection is achieved, with the shot-noise dominates the source of the noise. Under the shot-noise-limit assumptions:

$$\sigma_{shot,SD}^2 \gg \sigma_{r+d}^2 + \sigma_{RIN,SD}^2$$

(3.14)

$$\sigma_{shot,SS}^2 \gg \sigma_{th}^2 + \sigma_{RIN,SS}^2$$

(3.15)

We can derive the expressions of shot-noise-limit sensitivity for SD-OCT and SS-OCT in expression (1.8).

However, from the SNR calculation, other noise sources, including the read-out and dark noise term σ_{r+d}^2 or thermal noise σ_{th}^2 for SS-OCT (the first term of noise in expression (3.6) and (3.7)), and relative intensity noise (RIN) term (the 3rd term in the expression (3.6) and (3.7)), may also dominate, yielding a decreased absolute value of sensitivity. Read-out noise, dark noise and thermal noise are attributed to the detection unit itself, the photon detection process or the analog to digital conversion process [96]. They do not depend on the incident optical power [4] and can be treated as a constant value in the SNR calculation. Another source of noise, the RIN noise, originates from the intensity fluctuation of the OCT light source. The RIN noise variance for SD-OCT (in e^2 per read-out cycle and per spectral detector element) and SS-OCT (in e^2 per sampling time) are given by:

$$\sigma_{RIN,SD}^2 = (\frac{\rho\eta e T_{int}}{E_v}\frac{P_{ref}}{N})^{\,2} \cdot \frac{T_{coh}}{T_{int}}\ [e^2]$$

(3.16)

$$\sigma_{RIN,SS}^2 = (\frac{\rho\eta e T_{samp} P_{ref}}{E_v})^{\,2} \cdot \frac{T_{coh}}{T_{samp}}\ [e^2]$$

(3.17)

where the inverse optical bandwidth per detection element is expressed by the coherence time T_{coh}, given by [4]:

$$T_{coh} = \frac{1}{\delta f} = \sqrt{\frac{2\ln(2)}{\pi}}\frac{\lambda_c^2}{c\delta\lambda}$$

(3.18)

Where $\boldsymbol{\delta\lambda}$ is the spectral bandwidth per detector element for SD-OCT or the spectral bandwidth for each pulse of the swept laser for SS-OCT. In the expression (3.16) and (3.17), the reference and sample arm power approximation (expression (3.10)) is also applied.

Note that, if the expression (3.11) holds and assuming the rest of the parameters ($P_{ref}, \rho, \eta, E_v, T_{coh}$) are the same, we can get:

$$\frac{\sigma_{RIN,SS}^2}{\sigma_{RIN,SD}^2} = \frac{T_{int}}{T_{samp}} = N$$

(3.19)

Thus, the RIN noise could be several order of magnitude higher for SS-OCT than the SD-OCT. In a previous study, a ~7 dB higher RIN noise was measured from the swept source system as compared to the one from the SD-OCT system, with the same input power [97]. To reduce the RIN noise for the SS-OCT system, a dual-balanced (heterodyne) detection scheme can be employed, which was first introduced in OCT in 1999 by Rollins and Izatt [98] and further conveyed in Podoleanu [99] and Yun et al. [100]. In the unbalanced

detection scheme, the RIN noise, using the total power instead of reference arm power, is expressed [4, 98, 99]:

$$\sigma_{RIN,SS}^2 = \left(\frac{\rho\eta e T_{samp} P_{total}}{E_v}\right)^2 \cdot \frac{T_{coh}}{T_{samp}} \ [e^2]$$

(3.20)

where

$$P_{total} = P_{ref} + P_{samp} + P_{inc}$$

(3.21)

Here, we mentioned an additional term P_{inc}, which represents the part of reflected optical power from the sample arm that is *incoherent* with the reference light [77]. If the balanced detection is employed, the common noise, which is proportional to the P_{ref}^2, P_{Samp}^2, and P_{inc}^2, will be rejected. If both P_{samp} and P_{inc} are negligible, the RIN noise term will be largely cancelled. However, if P_{inc} is not negligible, there will be a residue noise term, beat noise, which is proportional to $P_{ref} \cdot P_{inc}$ [98]:

$$\sigma_{be,SS}^2 = \left(\frac{\rho\eta e T_{samp}}{E_v}\right)^2 \cdot \frac{T_{coh}}{T_{samp}} \cdot \ 2P_{ref}P_{inc} \ [e^2]$$

(3.22)

We should note that, with the dual balanced detection, the detected intensity square would be quadrupled and the total noise variance would be doubled, yielding the SNR expression as [98]:

$$SNR_{bal} = \frac{4|AC|^2}{2\sigma^2} = \frac{4|AC|^2}{2(\sigma_{th}^2 + \sigma_{shot,SS}^2 + \sigma_{be,SS}^2)}$$

(3.23)

In the paper from Yun et al., a common-noise rejection ratio of ~25 dB in the range between DC and 5 MHz was reported for their balanced detector [100].

Let's revisit the SNR definition in the expression (3.12), (3.13) and (3.23). If the imaging speed is increased by n times, the line rate or the swept rate will be reduced to 1/n of the original value. Also, the averaged number of detected photons is reduced to 1/n of the original value. In such a case, the assumption

of the shot-noise-limit detection might not hold, since the shot-noise variance $\sigma_{shot,SD}^2$ or $\sigma_{shot,SS}^2$ would reduce to 1/n while the read/dark noise σ_{r+d}^2 (for SD-OCT) or the thermal noise σ_{th}^2 remains the same. Thus, read/dark noise or thermal noise will contribute to additional sensitivity reduction. A derivation of additional sensitivity reduction is given in the following expressions:

$$SNR_{SD,-} \sim \frac{C_1 T_{int}^2/n^2}{C_2 + C_3 T_{int}/n} \tag{3.24}$$

$$\Delta SNR_{SD,-} \sim SNR_{SD,Shot,-} - SNR_{SD,-} \sim \frac{C_1 T_{int}}{C_3 n} - \frac{\frac{C_1 T_{int}^2}{n^2}}{C_2 + \frac{C_3 T_{int}}{n}} = \frac{C_1 C_2}{\frac{C_2 C_3}{T_{int}/n} + C_3^2} \tag{3.25}$$

Where C_1, C_2 C_3 represents the constants that are not changed if the integration time is reduced to 1/n. A larger n yields a larger denominator term is the expression (3.25), yielding a larger additional sensitivity reduction.

Besides the sensitivity, another factor would be the availability of the high-speed light source or detectors. For spectral domain OCT system, imaging speed is limited by the line-scan camera. For example, the Sensor-Unlimited line-scan camera used in our lab (Sensor Unlimited, SU1024LDH2), has a maximum line-rate of ~92 kHz. Another model of the line-scan camera from the same company has a maximum line-rate of 147 kHz (GL2048R, Sensor Unlimited). Options of higher-speed line-scan cameras beyond ~147 kHz are limited.

For swept source system, the imaging speed is determined by the swept rate of the light source. The record-high swept source laser for OCT imaging has a swept rate of 44.5 MHz [16]. Since the total imaging range is also inversely proportional to the laser swept rate (See Chapter 1.3.5), increasing the imaging speed will reduce the total imaging range, if the sampling rate remains the same. Or, if we want to maintain a long imaging range, the required sampling rate of the digitizer as well as the required frequency bandwidth of the

balanced detector will increase proportionally, yielding limited availability of these two hardware (See Chapter 4.1).

3.3 Multiplexing in OCT Systems

In previous section, I have described the trade-offs between the incentive to pushing the imaging speed up and factors that limit the performance of the OCT system, especially for the swept source system. However, there are approaches that can circumvent such situations. Instead of solely pushing the speed limit of either the wavelength-tunable lasers of a swept source OCT system or the line-scan camera of the spectral domain OCT system, a feasible approach is multiplexing, which means using multiple light beams (parallel imaging) or/and multiple detectors (parallel detection) to achieve equivalent speed improvement.

Table 3. 1 Multiplexing in OCT Systems

Ref.	Year	OCT type	λ_c (nm)	f_{eff} (kHz)	Sensi-tivity(dB)	# beams	Key component or key technique	Categories
Zotter et al. [101]	2011	SD	840	20	95	2	2 SLD, 2 Camera	Doppler OCT
Blatter et al. [102]	2013	SS	1050	100	94	2	2 DBD, dove prism	
Trasischker et al. [103]	2013	SD	840	20	98	3	3 SLD, 3 Camera	
Wartak et al. [104]	2017	SS	1060	100	92	1	1 active and 2 passive channels, path length encoding	
Eugui et al. [105]	2018	SS	1310	100	91	1	Few Mode Fiber: 3 Major modes	Angular dependence. Contrast enhancement
Leung et al. [106]	2009	SS	1329	258	NA	6	Fan Out, 6 BD, 3 DAQ	Parallel imaging (w multiple detectors)
Potsaid et al. [107]	2010	SS	1050	400	94	2	2 BD, 2 DAQ	
Wieser et al. [15]	2010	SS	1310	20,800	98	4	4 BD, 4 Channel Oscilloscope	
Choi et al. [108]	2008	SD	1559	60,000	88	1	Optical demultiplexer, 256 BD, 32 DAQs	Multiplexed Detection
Kocaoglu et al. [109]	2014	SD	790	1,000	71.2	1	2 layer optical switch, 4 camera	
Wieser et al. [110]	2014	SS	1310	3216	102	1	RF splitter, 2DAQ	
Lee et al. [111] [112]	2013, 2014	SS	1310	3200	89.1	16	Virtually-imagesd phased array	Parallel imaging w a single detector
Nankivil et al. [113]	2014	SS	1040	400	98	2	2x with sweep buffering, 2 beam, path length encoding	
Zhou et al. [114], Huang et al. [115]	2013	SS	1310	800	94.6	8	Space Division Multiplexing: Fiber Array + path-length encoding	
Song et al. [116]	2018	SS	1410	200		2		

Table 3.1 lists the different techniques to realize multiplexing for both SD-OCT and SS-OCT system reported in the literature. The simplest way to realize multiplexing is to use multiple beams to illuminate the sample. To achieve multi-beam illumination, one can use multiple light source (i.e. SLD) or splitting the output of the laser source using the polarization beam splitter or fiber coupler. Multi-beam illumination has

been employed for Doppler OCT [101-104]. Using Doppler OCT to measure the total vascular blood flows is sensitive to the orientation of the vessels (See Chapter 5.2). Since Doppler OCT can only detect axial flow components in parallel with the beam illumination, the transverse components of blood flows perpendicular to the beam illumination, i.e. retinal blood flows containing mostly transverse components[101], cannot be directly detected. Using multiple beams from different orientations to illuminate the blood vessels, we can get several velocity components of blood flows in different orientations to reconstruct the actual blood flow velocity vector. In one study, Zotter et al. utilize 2 SLDs in the SD-OCT system to realize 2 beam Doppler imaging of retinal blood flows [101]. In their system, two separate spectrometers were used to detect the interference signal collected from each beam. Later, 2 beam illumination was also realized in a swept source OCT system, using a 1 × 2 fiber coupler to split the light into two and use the dove prism to orient the beam in different incident angles [102]. In these two cases, transverse retinal blood flows have been measured, assuming the retinal blood vessels are perpendicular to the optics axis of the objective [101, 102]. In order to reconstruct the velocity vector in 3D space, 3 velocity components need to be measured. Trasischker et al. demonstrated a three-beam Doppler SD-OCT using 3 SLDs and 3 separate spectrometers [103]. In 2016, Wartak proposed a prototype Doppler OCT-system, using one beam to illuminate the sample (retina), but using 3 separate channels (1 active channel in original optical path and 2 passive channels in oblique angles) to detect the back-scattered lights in different orientations [104]. Velocity components measured from the active and passive channels can be used to reconstruct the blood flow vector precisely. In 2017, Eugui et al. proposed a SS-OCT system, using the few mode fiber in the detection part to observe the angular-dependence of the back-scattered signal from the sample [105]. In his setup, not only the fundamental mode (LP01) of the interference signal was allowed to transmit back to the detector, but also the second mode and the third mode that had relative high back-scattered intensities could be coupled into the few mode fiber and transmitted to the detector. Since the allowed coupling angles of these three modes are different, the detected interference signals from these three modes could be used to show the angular-dependent scattering contrast of the sample. In their paper, they demonstrated the OCT imaging of the amyloid-beta (Aβ) plaque, which was believed to be one critical hallmark of Alzheimer's Disease (AD), with a high angular-dependent contrast in the second and the third mode OCT images [105]. However, we should note that, these abovementioned multiplexing approaches were employed to explore the angular-dependent back-scattered properties of the

sample.In either case, using multiple beams or multiple modes of lights with multiple detecting angles helps to determine the actual flow vectors or enhance the scattering contrast. However, since all these beams are illuminating the same spot, the abovementioned multiplexing methods are not intended for speed improvement.

Multi-beam illumination (parallel imaging) and detection (parallel detection) techniques have been reported to increase the effective imaging speed of the system, if these beams are illuminating on different parts of the sample. Especially for SS-OCT, since the imaging speed of SS-OCT system is determined by the swept laser, the effective imaging speed can easily scale up when employing parallel imaging and appropriate detection schemes, which is equal to the swept frequency multiply by the number of the illuminating beams. Leung et al reported a 6-beam SS-OCT system with an effective imagng speed of 258 kHz [106]. They used a fan-out cable, with each of the 2-output swept laser powering 3 channels to achieve multiplexing. Six balanced detectors and three two-channel DAQ cards were employed to detect the interference signals from 6 beams. Potsaid et al. reported a multiplexed VCSEL SS-OCT system with two channels and effective speed of 400 kHz [107]. Wieser et al. reported a 4-beam multiplexed FDML SS-OCT system with a record-high effective imaging speed of 20.8 MHz [15]. In these cases, the same number of balanced detectors need to be employed to detect interference signals from each beam. Also the number of DAQs also needs to scale up accordingly.

Another category of multiplexing techniques focuses on the detection part. These multiplexing techniques increase the imaging speed by modifying the OCT detection system. In 2008, Choi et al. reported a modified SD-OCT system which can achieve an effective imaging speed of 60 MHz [108]. Instead of using a grating in the spectrometer of the SD-OCT to separate the spectrum and detect the interference signals as a function of wavelength, they used optical demultiplexers (OD) to separate the interference signal at different frequencies in equal frequency intervals. After the OD, 256 photodetectors with balanced detection setups were employed to detect the interference signals and a DAQ system consisting of 32 DAQ boards were used to receive the outputs from these 256 photodetectors. Thus the imaging speed is limited by the speed of the DAQ system instead of the line-scan camera. Another study by Kocaoglu et al. utilized the 4 line-scan cameras to detect the interference signal from the SD-OCT signals and successfully scale up the imaging speed to 1MHz [109]. A two-layer optical switches with 3 1x2 optical switches at each layer were employed

to switch the outputs towards the 4 cameras. Careful design and synchronization of triggers of the cameras and optical switches needed to be taken into consideration. However, the sensitivity is traded in for the imaging speed for this approach. Wieser et al. also reported a SS-OCT system with a high data-throughput [110]. Although the effective imaging speed was not improved due to single beam illumination, they utilized a RF splitter to split the output of the balanced detector into two channels and transmitted interference signals into two DAQ boards to enhance the data throughput for consecutive volume imaging.

One scaling factor while employing multiplexing in OCT systems is the cost. For the SD-OCT system, both the light source and the spectrometer (the line-scan camera) can be the major source of the cost of the system. The cost easily scales up using multiple light source to illuminate the sample and multiple spectrometers to detect the backscattered interference signals from each beam. For the 3-beam multiplexed OCT system by Transischker et al., the cost was tripled. For the modified SD-OCT system reported by Choi et al, the 256 photodetectors and the DAQ system consisting of 32 DAQ boards was a huge cost. For the SS-OCT system, the cost of the balanced detector is cheaper as compared to the swept laser source, which easily costs tens of thousands dollars. Thus, using multiple BDs to detect the signals in the multiplexed SS-OCT system won't be a big concern. However, the cost of the digitizer scales up quickly as the sampling rate further increases. If the multiplexing technique requires multiple pieces of digitizers, the cost will be huge.

Another scaling factor is the complexity of OCT systems. For multiplexed OCT systems with parallel imaging, multiple incident beams can share the same sample arm setup. A key consideration is that whether they can share the same reference setup. If the optical path lengths are not the same for different channels, separate reference arms have to be built, which significantly add up the system complexity. Also, different beam spots on the sample need to be perfectly positioned in the sample arm. For example, the three-beam Doppler OCT required that the 3 beam spots are in equilateral triangle positions incident on the Galvo mirror [103]. Aligning all these beams to focus at the same positions required a lot of efforts and patience.

Under such considerations, multiplexing techniques with a single light source, a single detector and a single digitizer, shared optical paths of multiple beam in both sample and reference arm, would be more preferred. Up to now, there were two multiplexing techniques which could satisfy all these requirements: interleaved OCT (iOCT) [111, 112] and the space-division multiplexing OCT (SDM-OCT) [114, 115]. The idea of the interleaved OCT is similar to a frequency comb swept laser [112]. The key component of the

interleaved OCT (iOCT) is the multi-beam demultiplexer (MBDX), which, in the case of the iOCT, is the virtually imaged phase array (VIPA) [111]. The VIPA performs multiplexing of multiple lateral points in the spectral domain. To be specific, for example, in a sweep of 1000 pulses to two lateral sample positions in the imaging plane, the odd index of the pulses with corresponding swept wavelengths will be sent to the first lateral positions while the even index of the pulses with corresponding swept wavelengths will be sent to the second lateral positions. Therefore, interference signals from the first position of the imaging plane are sampled with odd indices of points in a sweep and interference signals from the second lateral position are sampled with even indices of points. These signals from different wavelength ("frequency comb") are detected by the detectors sequentially within a sweep. Next, the signals are demultiplexed by putting the odd indices of points together and even indices of points together. Thus, images from two lateral positions are reconstructed separately. An interleaved OCT system with 16 channels were demonstrated with an effective imaging speed of 3.2 MHz [112]. However, the short separation between the beams in iOCT could lead to cross-talk between the channels [115]. A trade-off between sensitivity and number of lateral points is also observed due to the choise of different key parameters of VIPA, including the free spectral range (FSR, the minimum spacing between two wavelengths that belongs to the same frequency comb, or the same lateral spot), and the "finesse", which is related to reflectivity of the VIPA [115].

Space-division multiplexing OCT (SDM-OCT) [114, 115] shares the same advantages as VIPA regarding system cost and complexity. It utilizes a single source and a detector, and shared reference arm and sample arm. The details of the space-division multiplexing are described in the next session.

3.4 Introduction of Space-division Multiplexing OCT (SDM-OCT)

In this session, I will describe the principles of space-division multiplexing OCT (SDM-OCT), which utilizes a parallel imaging scheme to achieve speed improvement over an order of magnitude [114]. **Figure 3.1 A** shows a schematic diagram of a first-generation, fiber-based SDM-OCT system (prototype SDM-OCT). The key difference between interleaved OCT and SDM-OCT is that, interleaved OCT performs multiplexing in the spectral domain (i.e. like frequency comb), while SDM-OCT performs multiplexing in the spatial domain,

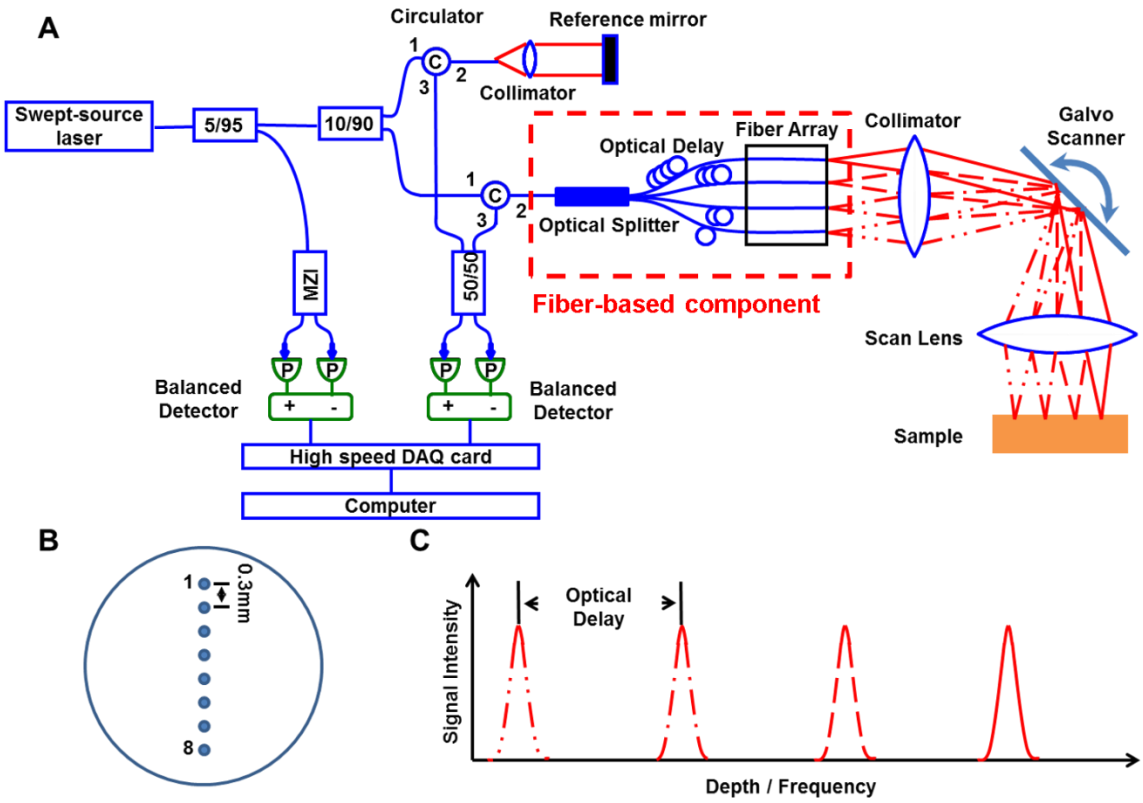

Figure 3. 1 Prototype SDM-OCT system. (A) Schematic diagram of the prototype SDM-OCT system. Fiber-based components, including the optical splitter, fibers with different optical delays, and the fiber array, were shown within red rectangle. (B) A 1×8 fiber array at the output port was used to achieve 8× speed improvement. (C) Each beam was optically delayed. Signals from different beams, corresponding to different sample locations, were presented at different frequency ranges (i.e. depths). For simplicity, only 4 beams are shown in the figure. Adapted from Zhou et al., 2013.

which is later converted to the time domain with encoded path length. The key space-division multiplexing (SDM) component is shown in the red-dashed rectangle in **Figure 3.1A**, including three main parts: a splitter, a path-length-encoding component, and a fiber array. In the first part, splitting of incident lights is realized either with a PLC splitter or cascaded 1x2 fiber couplers. For example, in the prototype 1310 nm SDM-OCT, the incident beam is split into 8 channels with a PLC splitter [114]. Light splitting with a fiber coupler is a common approach in multiplexed SS-OCT system. In both multiplexed SS-OCT system reported by Potsaid et al. [107] and Wieser et al. [15], 50/50 fiber couplers were utilized to split the incident light into two separate channels to illuminate two different regions of the sample. Note that the PLC splitter is widely available in the telecom wavelength ranges of 1300 nm and 1550 nm , with a relative low cost. However, for 1060 nm range, since the PLC splitter is not common in the market, fiber couplers will be an alternative option.

The second part of SDM component is the path-length-encoding component. In the SDM-OCT, the path length encoding is realized by adding patch fibers with different lengths for each split channel. Thus, signals from different channels (different scanned regions) will be detected by the balanced detector with a small optical delay between neighbouring channels. In the reconstructed OCT intensity profile (A-scan), the images from different sample locations (different channels) will be rendered in different frequency ranges (i.e. depth ranges, optical pathlength differences). An illustration of path-length-encoding of images from different channels is shown in **Figure 3.1 C**. With the path-length-encoding method, images from multiple sample locations can be captured simultaneously in the same sweep, detected by the same balanced detector, and demultiplexed in the post-processing. The path-length-encoding method was first introduced by Iftimia et al. to reduce the speckles of OCT images [117]. Wang et al. utilized the path-length-encoding method to detect the angular-dependent contrast of scattering properties of the retinal layer [118]. Wartak et al. also utilized the path-length-encoding method to facilitate the detection of back-scattered signals from 3 different orientations to determine the blood flow vector [104].

After the path-length-encoding component, different split channels are arranged in a fiber array as the output part of the SDM component. The V-groove fiber array can position different fiber channels with a fixed spacing (pitch size) between neighbouring channels. Thus, we can ensure that the orientation and the spacing of fiber channels are uniform. With the fiber array as the output part of the SDM component, all the fiber channels can share the sample arm setup, which reduces system complexity. Parallel imaging with a fiber array as the output port was also introduced by Wieser et al. [15]. A uniform angle polish for all fiber channels are realized by directly polishing the whole fiber array, which ensures that output beam directions for all fiber channels are the same. A similar fiber array setup with different polished angles were reported, enabling the angular compounding for speckle reduction [119]. With their fiber array setup, all the 3 output beams focused at the same final spot.

We should mention that total optical path lengths have to be carefully measured for each channel in all parts of the SDM components, including the internal part of the PLC splitter or cascaded fiber couplers, patch fibers with different lengths in the middle, and the fibers within the fiber array. Otherwise, the path-length-encoded images with be separated by different optical path differences in the reconstructed OCT images. In the worst case, the encoded images will be out of the total imaging range.

One key aspect of the SDM-OCT is that, the total imaging range is traded for a high imaging speed, which is the same as the interleaved OCT. However, one advantage of the SDM-OCT is that optical delays between neighbouring channels are separated from other OCT parameters and can be manually determined to ensure sufficient separation between images from neighbouring channels to avoid overlap. However, a large total imaging range is required for SDM-OCT, which adds burden to the data acquisition part (See Chapter 4.1).

In the prototype SDM-OCT described in Zhou et al. [114], the incident light was split into 8 channels in a fiber-based SDM component, with ~2.5 mm optical delays between neighbouring channels to generate multiplexed interference signals that was detected simultaneously. The spacing between neighbouring output channel at the fiber array was ~0.3 mm and the final spacing on the sample was ~0.37 mm. The effective imaging speed of the prototype SDM-OCT system was increased by a factor of 8, with an ultrahigh imaging speed of 800,000 A-scans/s demonstrated using a long-coherence-length VCSEL laser operating at 100 kHz (Thorlabs, SL131090).

3.5 Building up a 1×4 Fiber-based SDM-OCT System

3.5.1 Configuration of the 1×4 Fiber-based SDM-OCT System

Figure 3.2 shows the configuration of a fiber-based SDM-OCT system. Three major free-space optical sub-systems are presented: a sample arm, a reference arm and a Mach-Zehnder interferometer (MZI). In the following sections, I'll describe the procedures to build each optical sub-systems.

3.5.2 Light Source

In this SDM-OCT prototype, we utilize a vertical-cavity surface-emitting laser (VCSEL) as the swept laser source. **Figure 3.3** shows the front panel and the back anel of a VCSEL. In the back panel, there are five output ports with SMA connectors and the laser output with a FC/APC connector. Five SMA output ports are laser monitor output, DAQ trigger, cavity monitor, λ sweept trigger and optical clock output. The laser monitor output and cavity monitor output are used to monitor the laser working status for the diagnosis purpose. The DAQ trigger output is connected to the digitizer to provide triggers for each sweep. The optional optical clock (k-clock) can provide external clock signals to the digitizer to perform the data acquisition in the external mode.

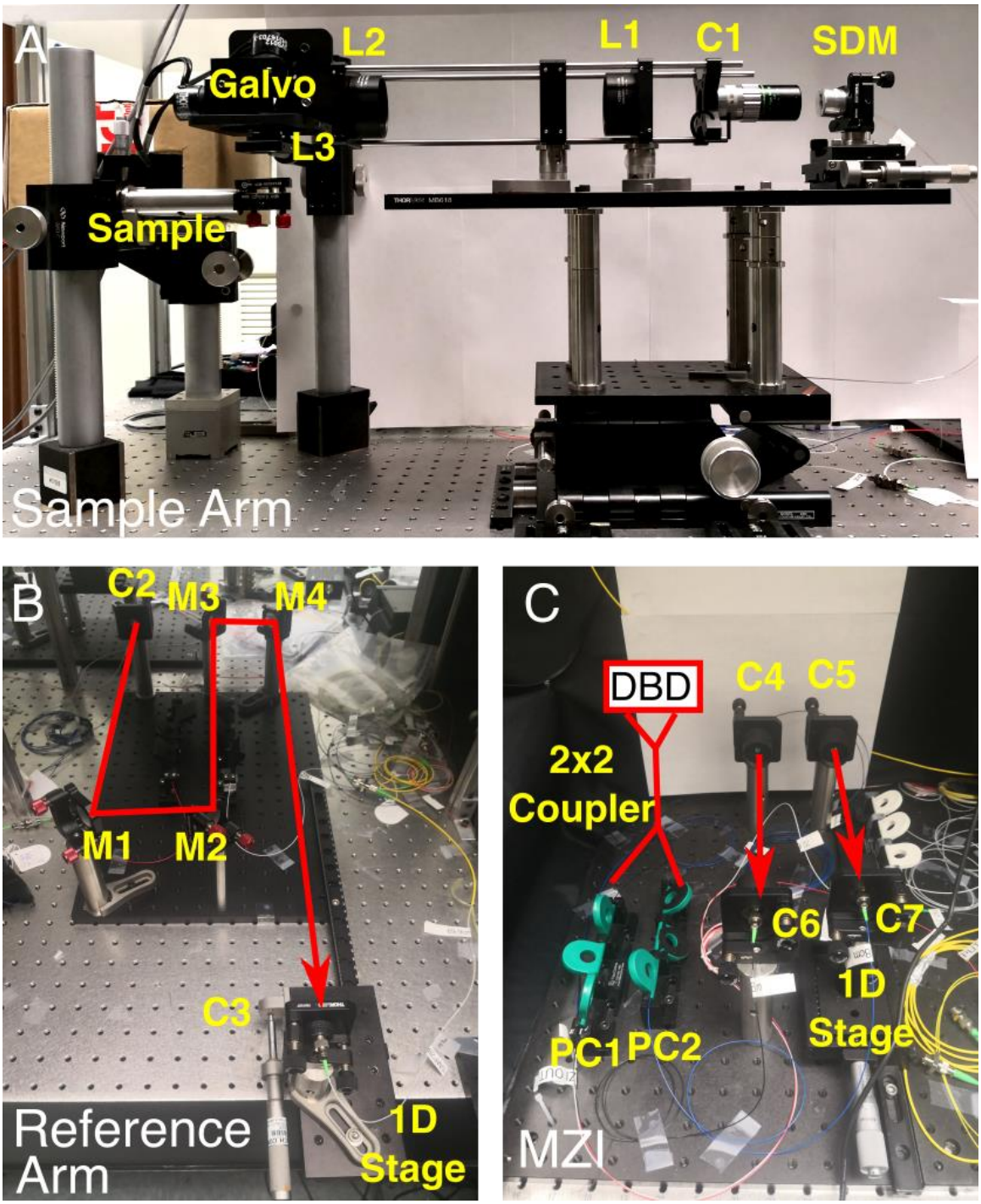

Figure 3. 2 System configuration of the SDM-OCT, including all the free-space optics. (A) Sample arm free-space optics. (B) Single-path reference arm. (C) Mach-Zehnder interferometer (MZI) setup. Abbreviations: C1-C7: Collimators; M1-M4: mirrors; L1-L3: Lenses. DBD: dual balanced detector.

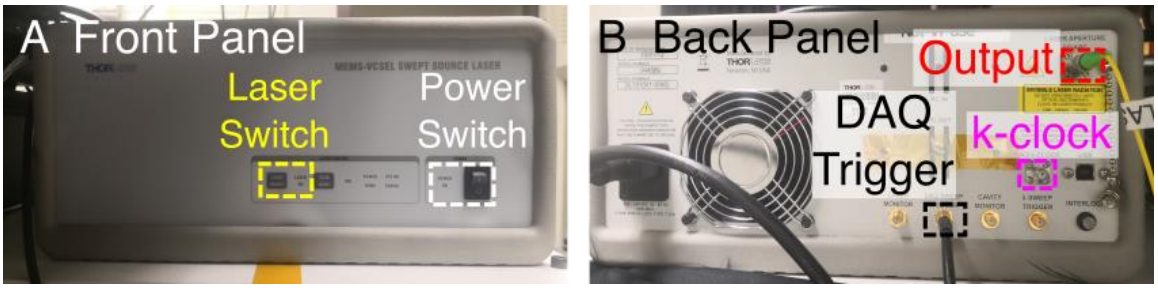

Figure 3. 3 Front panel (A) and back panel (B) of a vertical-cavity surface-emitting laser (VCSEL).

The laser output is first connected to a 97/3 2×2 fiber coupler (AC Photonics). 97% of the power will be sent to the OCT system and 3% of the power will supply the Mach-Zehnder interferometer (MZI). Since the laser output power is ~26 mW. 3% of the light (~750 µW) for the MZI setup can provide MZI fringes with sufficient amplitudes. Next, the 97% output port of the fiber coupler is connected to an O-band booster optical amplifier (BOA, BOA1130S, Thorlabs) to further boost the optical power to the OCT system to ~90 mW (maximum). Then, a 95/5 2×2 fiber coupler (AC Photonics) is used to split the power, with 95% of the power provided to the sample arm and 5% to the reference arm. With a boosted power of ~90 mW, 5% of the power to reference arm is sufficient to achieve the shot-noise-limited detection with a low sample arm back-coupling power (See Chapter 3.2).

3.5.3 Design and alignment of the sample arm

After the 95/5 fiber coupler, the 95% output port is routed to the sample arm. First, it is connected to the port 1 of the polarization insensitive optical circulator (AC Photonics). The port 2 of the optical circulator will connect to the sample arm free-space optical sub-system (**Figure 3.2 A**). The sample arm consists of the fiber-based space-division multiplexing (SDM) component, which is the key component for SDM-OCT technology. **Figure 3.4** shows the different setups of the fiber-based SDM components, with different number of split channels. The SDM component in **Figure 3.4 A** has 4 output channels from 1D V-groove fiber array; **Figure 3.4 B** shows an 8-channel SDM component; **Figure 3.4 C** shows the SDM component with 16 output channels configured in a 4×4 grid with a 2D fiber array. In this session, the 1×4 SDM component is used in the SDM-OCT system to split the beam in 4 channels with a 1mm output spacing and ~4 mm physical path length delays between neighbouring channels.

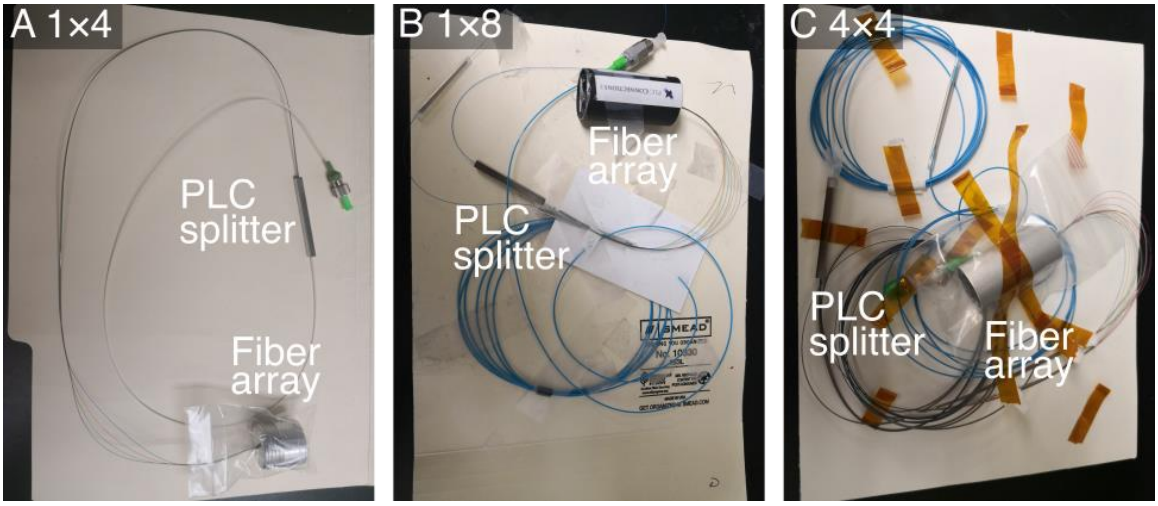

Figure 3. 4 Actual setups of the fiber-based space-division multiplexing (SDM) components with different split ratio. (A) 1×4; (B) 1×8; (C) 4×4.

After the SDM components, diverging output beams from each channel are converted to collimated beams with a collimator. The choice of the collimator depends on many factors: the spot size of the output collimated beam, which is determined by the beam diverging angle and the focal length of the collimator; the initial beam spacing between neighbouring channels; the aperture of the collimator. When choosing the focal length of the collimator to control the spot size, ensure that the aperture of the collimator doesn't block any diverging output lights from SDM component. In some cases when both a small focal length and a large aperture are required for the collimator, a pair of doublets can be employed, with the curved surface facing each other. The effective focal length of a pair of doublets can be reduced by half as compared to each single doublet, while the aperture is maintained.

For this 1×4 fiber-based SDM-OCT, we choose to use a 20× objective with an effective focal length f = 10mm as a collimator. Note that the objective is inverted placed (See **Figure 3.2A**). The output collimated beams from different channels will first converge at the back-focal point and diverge. We measure the diverging angle θ of edge collimated beams, which is shown in **Figure 3.5**. At the output aperture of the 20× objective, the 4 collmated beams are almost at the same spot. Thus, We can consider that the 4 collimated beams start to diverge from the output aperture. The measured total spacing between edge collimated beams is 23 mm at a distance of 132 mm. Thus, the diverging angle θ can be calculated as:

$$\theta = 2\arctan\left(\frac{23\text{ mm}}{2 \times 132\text{mm}}\right) = 10°$$

In **Figure 3.5**, we can roughly measure the spot size of the beam after the 20× objective with a ruler. The spot size for each collimated beam is measured to be ~2 mm,.

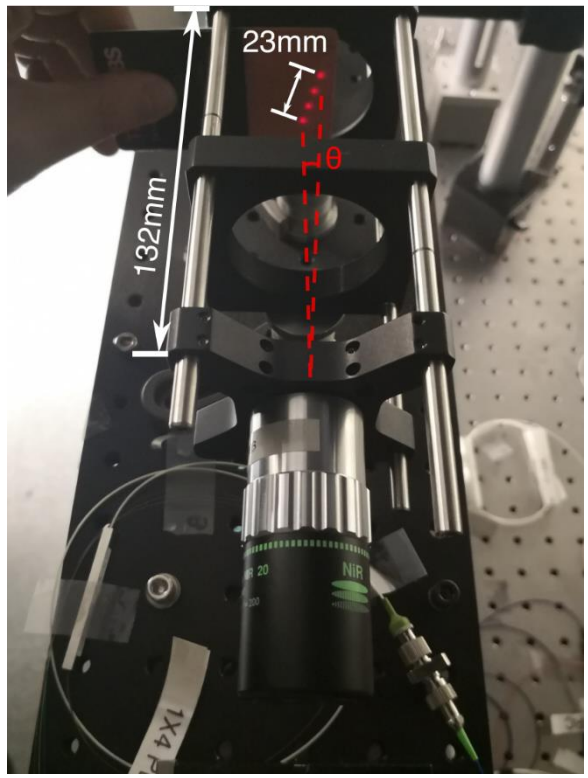

Figure 3. 5 Measurement of the diverging angle between edge collimated beams.

After the collimator, a 100mm/100mm lens pair is placed as a telescope system to relay multi-channel collimated beams and converge the collimated beams on the galvo mirror.

To align the optics before the galvanometer system, a cage system is set up and the relay lens are mounted and aligned in a telescope setting, with the aid of a single-channel collimated beam or a laser pointer. Next, the 1st relay lens and the collimator are aligned to be a telescope system. For the SDM component, since the fiber array is fixed in a 1" lens tube, we can fix the lens tube in a kinematic mirror mount. Then, we further mount the kinematic mount on a rotation stage. In this way, we can use the kinematic mirror mount and the rotation stage to control the directions of output beams from the SDM component. A 1D translation stage is added underneath the rotation stage to adjust the distance between the collimator and the SDM component.

Once the SDM component is fixed on the aluminum optical breadboard (Thorlabs, MB618), the cage system is aligned to the SDM component using an iterative approach. A short dovetail rail (Thorlabs) and spacers can facilitate the alignment of the cage system. The iterative steps are:

1. Place the cage system on the breadboard along with the fiber-based SDM component.
2. Adjust the height of the cage system so that the center of the cage system is at the same height as the output of the SDM component.
3. Move the 1D translation stage of the SDM component to adjust the output beam from the collimator to be collimated.
4. Attach the cage system to a fixed rail so that the cage system is in parallel with the edge of the breadboard.
5. Horizontal alignment: If the distribution of the beams is off the center in horizontal direction in the far field, adjust the tilting screw and the rotation stage to correct the direction of output beams from the SDM component. If the beams are off the center in the near field (close to the collimator), move the cage system horizontally by adding or removing spacers in between the rail and the cage system. An alignment plate (pinhole, Thorlabs, LCPA1) can be placed at different cage positions to check the adjustment. Repeat the adjustments until multi-beams are symmetrically distributed in the horizontal direction in the cage system (See **Figure 3.5**).
6. Vertical alignment: If the distribution of the beams is off the center in vertical direction in the far field, adjust the tilting screw to correct the direction of output beams from the SDM component. Then, if the beams are off the center in the near field, increase or decrease the height of the cage system by adding or removing spacers to the pedestral posts. Repeat the adjustments until multi-beams are symmetrically distributed in the vertical direction in the cage system.
7. Repeat step 3, 6, 7 until the cage system is well aligned to the SDM component.

Next, we align the cage system to a galvanometer system (galvo). The galvo system is mounted on a thick pedestral posts (Newport, 70) with the rod clamps (Newport, 370-RC) on the hand switch magnetic base (Newport, M-MB-2). The cage system on the breadboard is lifted with a lab jack (Newport, 281) and supporting pedestral posts to match the height of the galvo system. The galvo system is manually moved until the multi-chanel collimated beams are incident at the centers of both galvo mirrors, with their converging spot in between two galvo mirrors. A NIR detection card (Thorlabs, VRC2) is used to check the

the collimated beams at the galvo mirrors. Note that the axis of four channels are in a rotated orientation incident on the first galvo mirror to ensure the axis after the galvo system is either perpendicular or parallel to the scanning direction to maintain a rectangular scan area (See **Figure 3.6**).

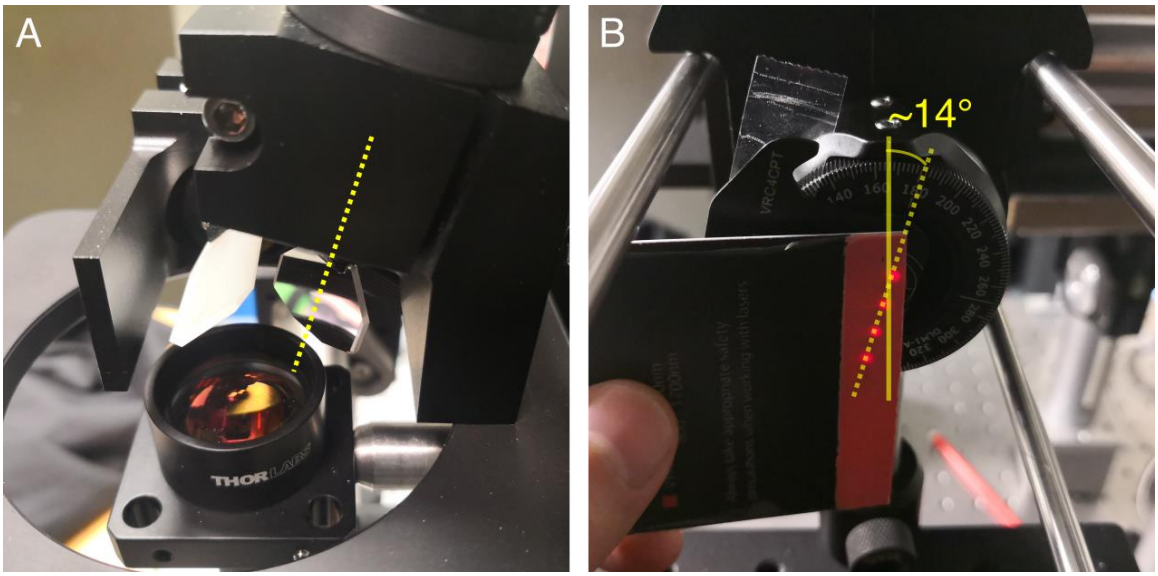

Figure 3. 6 Four beams before the galvanometer. Due to the tilting of the first galvo mirror, the axis of the four beams needed to be rotated by a few degrees to ensure the axis after the 2D galvo system is either perpendicular or parallel to the scanning direction to maintain a rectangular scan area.

Last, an objective or a lens is aligned after the galvo system. We can use either of the two following protocols to align the objective.

Protocol 1:

1. Take off the 1st relay lens right after the collimator.

2. Move the objective vertically until the output beams of the objective are collimated beams.

Protocol 2:

1. Use the IR card to check the beam spacing between neighbouring channels after the objective. If the objective is well aligned, the beam spacing should be the same at all vertical locations.

One thing we should mention is that, both the final beam spacing and the lateral resolution is proportional to the total magnification (M) of the sample arm optics. Considering the beam spacing at the output port of the fiber array to be d and the size of the fiber for 1300nm to be d_{fiber} = ~9 µm (SMF-28), we can estimate the final beam spacing d_{final} and the lateral resolution Δx as:

$$d_{final} = |M|d$$

(3.26)

$$\Delta x = |M|d_{fiber}$$

(3.27)

3.5.4 Design and alignment of the reference arm

Considerations for the reference arm of the SDM-OCT is similar to the one in the SD-OCT: Match both the fiber lengths and free-space optical paths of the sample arm and reference arm.

For swept-source OCT systems, since a second 2×2 coupler (a 50/50 2×2 fiber coupler) other than the 95/5 2×2 fiber coupler is used to generate interference of the sample and the reference arm signals, the reference arm signals are not required to reflect back in the same optical path to the 95/5 coupler. There are two methods to build the reference arm here. The first method is similar to the sample arm setup: Use a circulator to direct the incident lights to the reference arm; Use a double-optical-path setup with a reference mirror to reflect the light back to the circulator; Use the third port of the circulator to transmit the lights to the second 50/50 coupler. This method has the advantage that the total translation range of the stage can be smaller. However, the optical circulator will introduce an additional transmission loss of ~3 dB. The second method is to build a one-way free-space light transmission system, with one collimator to output the collimated beam into the free space and another collimator to couple the collimated beam back into the fiber to the second 50/50 coupler. One of the collimator is mounted on the 1D translation stage to adjust the reference optical path. The dispersion is compensated by adding glasses in the middle of the reference arm or compensated numerically. The second method has a higher coupling power from the reference arm, at a cost of doubled free-space optical path length.

In the 1×4 SDM-OCT system, the second method of the reference arm configuration is chosen, shown in **Figure 3.2 B**. The maximum coupling power from the reference arm is measured to be ~3 - 3.5 mW prior to 50/50 2×2 fiber coupler. By carefully adjust the reference arm coupling power, we can achieve shot-noise-

limit detection (See Chapter 3.7). Note that, to fit the long optical path of the reference arm in the breadboard, the light is reflected 4 times with additional 4 mirrors in the reference arm (See **Figure 3.2 B**).

3.5.5 Design and alignment of the Mach-Zehnder interferometer

For SS-OCT, the detected spectral fringes may not be linearly sampled in the wavenumber (k) domain, since the tunable swept laser may not be linearly swept across all the wavenumber (wavelength) ranges. Two approaches can be employed to resolve the issue. One approach is to use an external clock (k-clock) to trigger the acquisition of each spectral data of the spectral fringes, so that the detected spectral fringes are linearly sampled in wavenumber [107]. With external k-clock sampling, the sampling rate is approximately the (central) frequency of the external k-clock and the detection bandwidth is half of the k-clock frequency. With a k-clock frequency of ~485 MHz provided by the VCSEL laser, the maximum detection bandwidth is ~240 MHz, corresponding to a ~12mm total imaging range. However, sampling of spectral fringes may suffer from a poor k-clock signals with missing clock signals in the middle. Also, ~12 mm total imaging range is not sufficient to render all four images from the 1×4 SDM-OCT system with a physical delay of ~4 mm between neightbouring channels.

The second approach, similar to SD-OCT, is to perform the phase calibration step to resample the spectral fringes to be linear in wavenumber. Although the OCT spectral fringes can be used for phase calibration, phase reconstruction from the low-magnitude OCT fringes may suffer from the fluctuating noises. Similar to SD-OCT, a calibrated phase curve (index-wavenumber relationship) can be generated *in priori* to calibrate all other spectral fringes. However, trigger jitters during the wavelength sweeping of the tunable swept laser may lead to inconsistent phase calibration results for different spectral fringes. Thus, to perform a proper phase calibration for each spectral fringe, we collect two copies of spectral fringes from two channels, one from OCT and the other from the Mach-Zehnder interferometer (MZI). Then, we utilize the MZI fringe to construct a phase curve to perform linear resampling for each OCT fringe. Since the OCT and MZI fringes are collected simultaneously within each laser sweep, we can ensure that the sweeping ranges are the same for both OCT and MZI fringes, yielding the right phase calibration curve for each OCT fringe.

The actual MZI setup was presented in **Figure 3.2 C**. To align it, first we set up the four collimator and connect the 3% of the laser output to a 2×2 50/50 fiber coupler, with the two output ports of the coupler

connected to two collimator. Lights are coupled back to the fiber from the other two collimators. Coupled lights from the two MZI arms are interfered in a second 2×2 50/50 fiber coupler. Output MZI interference signals from the coupler are detected by a balanced detector. By adjusting the optical pathlength difference between two MZI arms, we can generate the MZI interference signals with different frequency ranges

3.5.6 Detection and control system for SDM-OCT

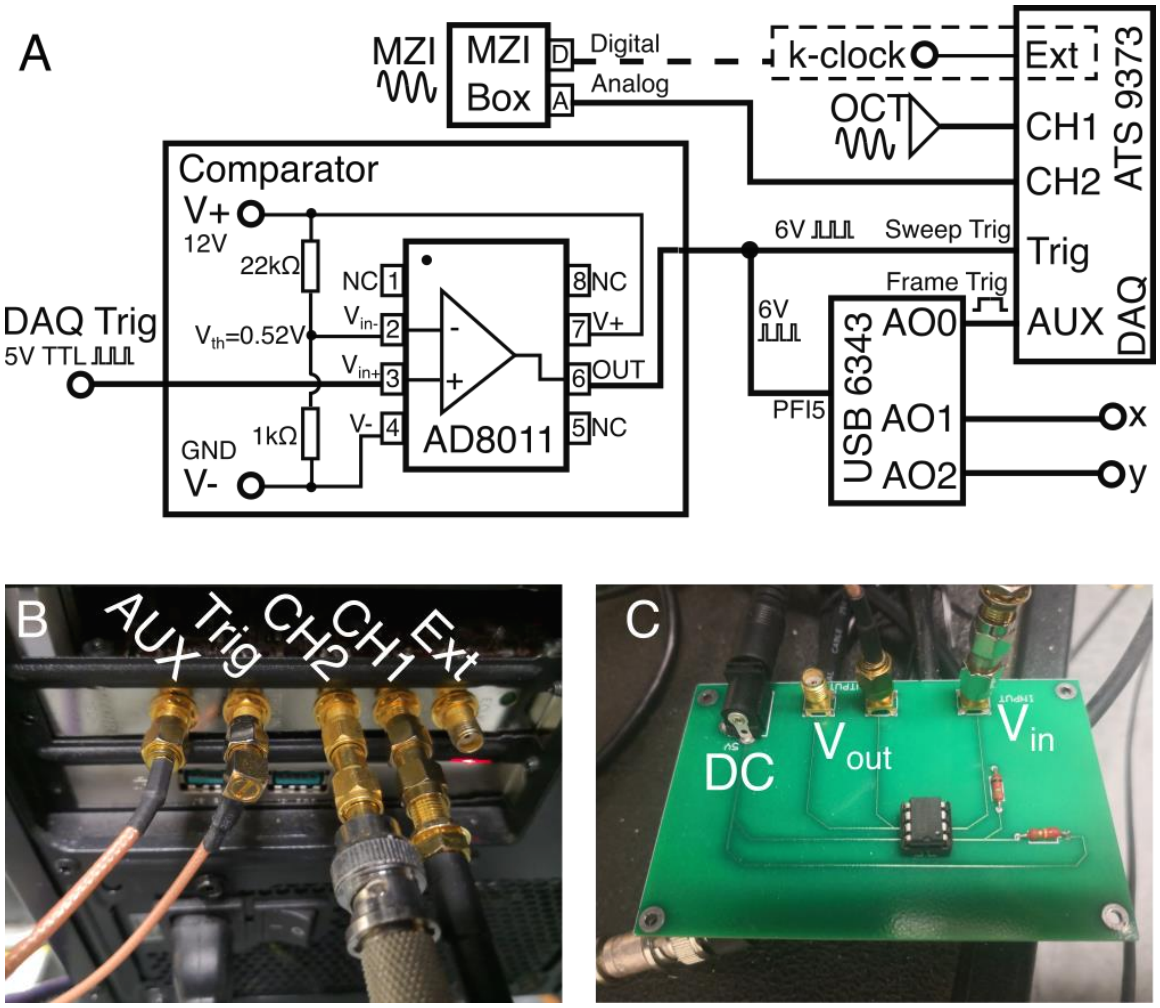

Figure 3. 7 Detection and control system for the SDM-OCT. (A) Block diagram of the detection and control system. (B) Actual cable connection of the data acquisition card (DAQ, or digitizer). (C) Photo of the comparator circuit.

Figure 3.7 shows the design of the detection and control system of the SDM-OCT. **Figure 3.7 A** shows the block diagram of the system. The main part is a high-speed data acquisition board (DAQ) or a digitizer, which can digitize the signals with a high sampling rate and a high bandwidth. We use an Alazar digitizer

(Alazar, ATS9373) for the 1×4 SDM-OCT system. It can operate in dual-channel mode with a maximum sampling rate of 2 GS/s for each channel. With dual edge sampling (DES), the digitizer can achieve 4 GS/s sampling rate with single channel acquisition. The bandwidth of the digitizer is 1.0 GHz, which is sufficient to detect interference signals from SDM-OCT. See a detail discussion of hardware requirements for the SDM-OCT in Chapter 4.1.

OCT interfernce signals after the 50/50 2×2 fiber coupler are detected by the dual balanced detector (DBD, Thorlabs, PDB480C-AC). The dual balanced detector has a bandwidth of 30 kHz – 1.6 GHz. The saturated power of the DBD is ~1.5 mW for each input and the damage threshold of the DBD is ~10 mW. The output RF signals are transmitted to Channel 1 (CH1) of the digitizer.

In the internal mode, the additional MZI signals are collected by a custom or a commercial dual balanced detector. If the custom DBD is used, the analog output of the MZI interference signals are sent to Channel 2 (CH2) of DAQ. Note that, a high-pass filter is contained in the custom DBD to filter out low-frequency components of the interference signals. The custom DBD also converts the analog MZI signals to digital external clock signals. We can use the digital output of the custom DBD to provide external k-clock signals.

Trigger signals are required to initiate acquisition of OCT and MZI spectral fringes. In SDM-OCT system, the laser source provides a 5 V TTL DAQ sweep trigger signal to the trigger port (Trig) of the digitizer. However, an auxillary trigger signal is required to initiate the acquisition for each frame. To generate the frame trigger, we split the laser sweep trigger into two channels. One channel is connected to the Trig port and the other channel is connected to the PFI channel of a multifunction I/O device (National Instruments, USB 6343). Received laser sweep trigger signals are used to generate the frame trigger signals in the acquisition software, which are transmitted from the analog output channel 0 (AO0) to the AUX port. The X and Y trajectory signals to the galvo system are also generated from the acquisition software and sent out from AO1 and AO2 to control the galvo scanning.

Due to the splitting of the laser sweep trigger signals, the peak amplitude drops by half for each split channel, which may not be enough for either Trig port or PFI inputs. A minimum 3.3V TTL is required for the Trig port and the PFI port requires a minimum input high voltage of 2.2V. To resolve the issue, our group designs a comparator cicuit to amplify the amplitudes of laser sweep trigger signals. The block diagram of the comparator circuit is presented in **Figure 3.7 A**. **Figure 3.7 C** shows the printed circuit board (PCB) of

the comparator circuit. In the block diagram, an operation amplifier (Analog Devices, AD8011) is used as a voltage comparator with single 12V power supplied to the circuit. The reference voltage is set by choosing the combination of the two resistors. In our design, a 22 kΩ and a 1kΩ resistors are chosen, yielding a reference voltage of:

$$V_{ref} = 12V \times \frac{1k\Omega}{1k\Omega + 22k\Omega} = 0.52\ V \tag{3.28}$$

The reference voltage is connected to the V_{in-} and the laser sweep trigger is sent to the V_{in+}. The output of the comparator (V_{out}) are the amplified trigger signals with the amplitude of the higher voltage at the positive saturation level, which is 12 V from the power supply. Thus, after the splitting, each channel has a 6 V TTL trigger signal, which are sufficient for both Trig port and PFI input.

3.6 Post-processing for SDM-OCT

Figure 3.8 shows the flow chart of the post-processing procedure for SDM-OCT. The procedure is mostly the same as the post-processing for SD-OCT, which includes the steps of zero-padding, linear resampling, dispersion compensation, Gaussian window and the final inverse FFT along the depth direction. In the following section, I will describe the steps in the post-processing procedure for SDM-OCT that are different from the steps in the SD-OCT.

3.6.1 Separation of OCT and MZI Signals

Since OCT and MZI spectral fringes are recorded in an interleaved mode (ABAB…AB) from both CHA and CHB by the digitizer, we need to separate the interleaved OCT and MZI signals as the first step of the post-processing.

3.6.2 Phase Calibration

As is mentioned in Chapter 3.5.5, we perform simultaneous acquisitions of both OCT and MZI spectral fringes and utilize the MZI fringe to construct a phase curve to perform linear resampling for each OCT fringe. The detailed phase calibration steps are described in the left-bottom dashed rectangle in **Figure 3.8**.

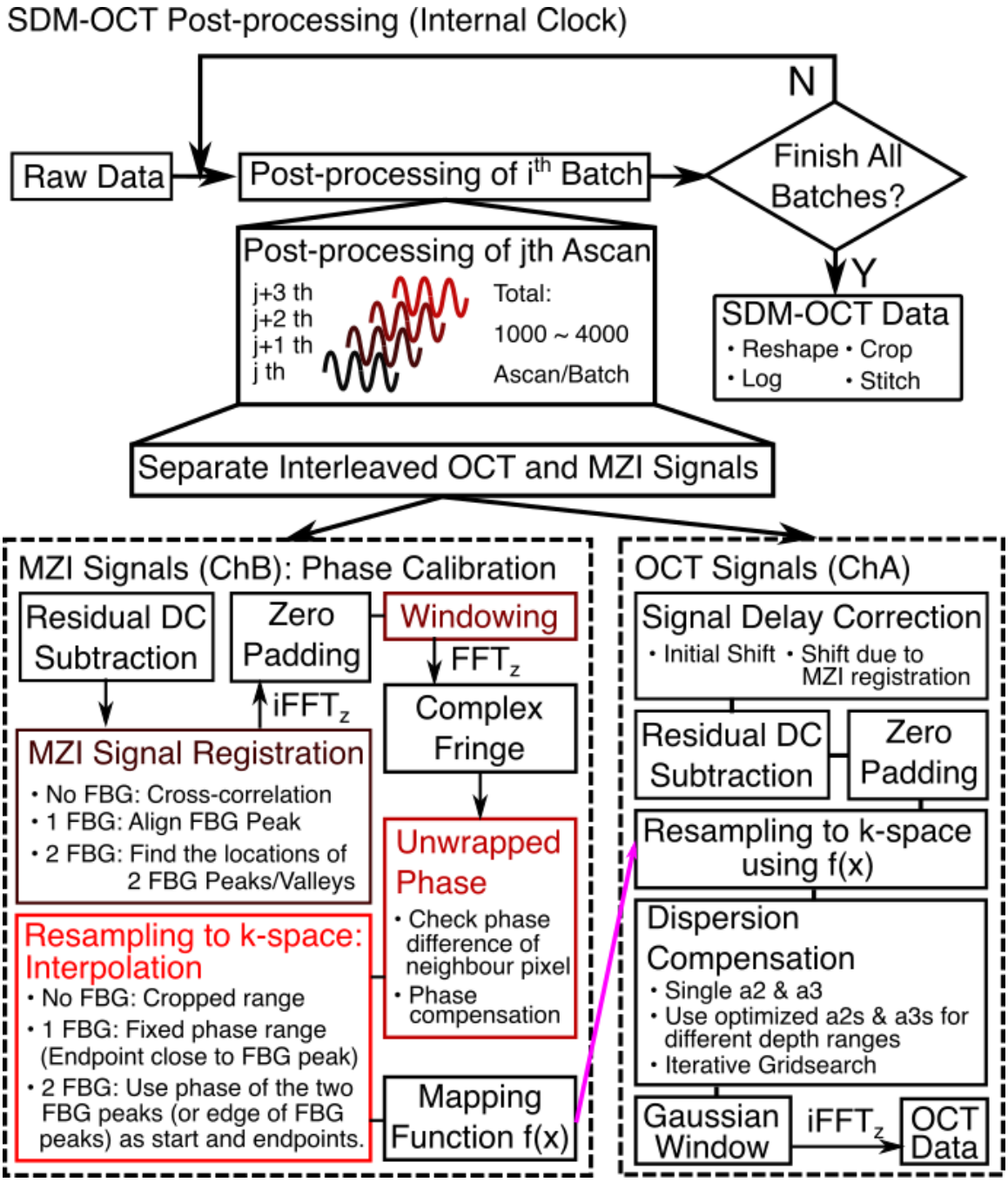

Figure 3. 8 Post-processing for SDM-OCT.

One key issue for the SS-OCT is the trigger jitter, in which the data acquisitions of OCT spectral fringes start from different wavelengths (wavenumbers) for different laser sweeps (A-scans), yielding the irregular movements of detected spectral fringes. The phenomenon of trigger jitter is illustrated in **Figure 3.9**, in which a fiber Bragg grating (FBG) is used in the MZI channel as the indicator of the trigger jitter. The FBG is placed in between one output port of the 50/50 coupler and the dual balanced detector. A patch fiber with the same

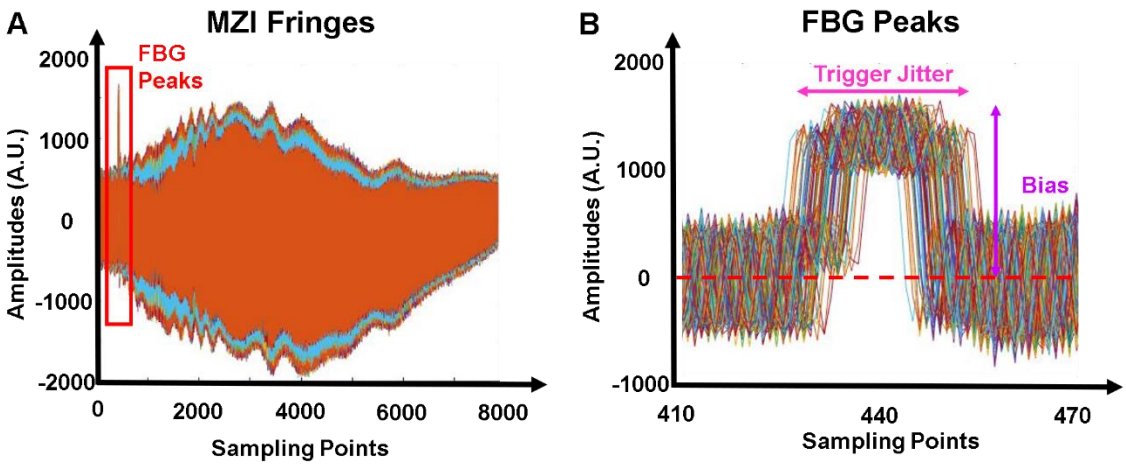

Figure 3. 9 Illustration of trigger jitter in MZI signals from different laser sweeps (A-scans). (A) MZI fringes from different sweeps. FBG peaks are highlighted. (B) Zoomed MZI fringes within the red rectangle regions in (A). MZI fringes are biased (purple arrow) within the filtered wavelength range of the FBG. Trigger jitter is shown as the FBG peaks are moved irregularly for different laser sweeps.

length as the FBG is added to the other output port of the 50/50 coupler. The FBG serves as an optical filter to filter out the signals in a particular wavelength range, with the central filtered wavelength and the filtered bandwidth indicated in their specification. As a result, the detected interference signals from the balanced detector will be biased at the filtered wavelength range of the FBG. In **Figure 3.9A**, MZI fringes from different laser sweeps are shown, with the FBG peaks indicated in the red rectangular regions. **Figure 3.9B** shows the zoomed views of the red rectangular region in **Figure 3.9 A**, showing the biased fringes in FBG peaks (Purple arrow in **Figure 3.9 B**). The trigger jitter (Pink arrow in **Figure 3.9 B**) is clearly visible since the FBG peaks are moving back and forth for different laser sweeps. To correct for the trigger jitter, we can perform a MZI signal registration to align the FBG peaks for different laser sweeps so that the wavelength ranges of the spectral fringes from different sweeps can be aligned.

However, using one FBG to align different spectral fringes does not ensure that the wavelength ranges are the same for different sweeps, due to the missing trigger signals in the middle. This phenomenon can be

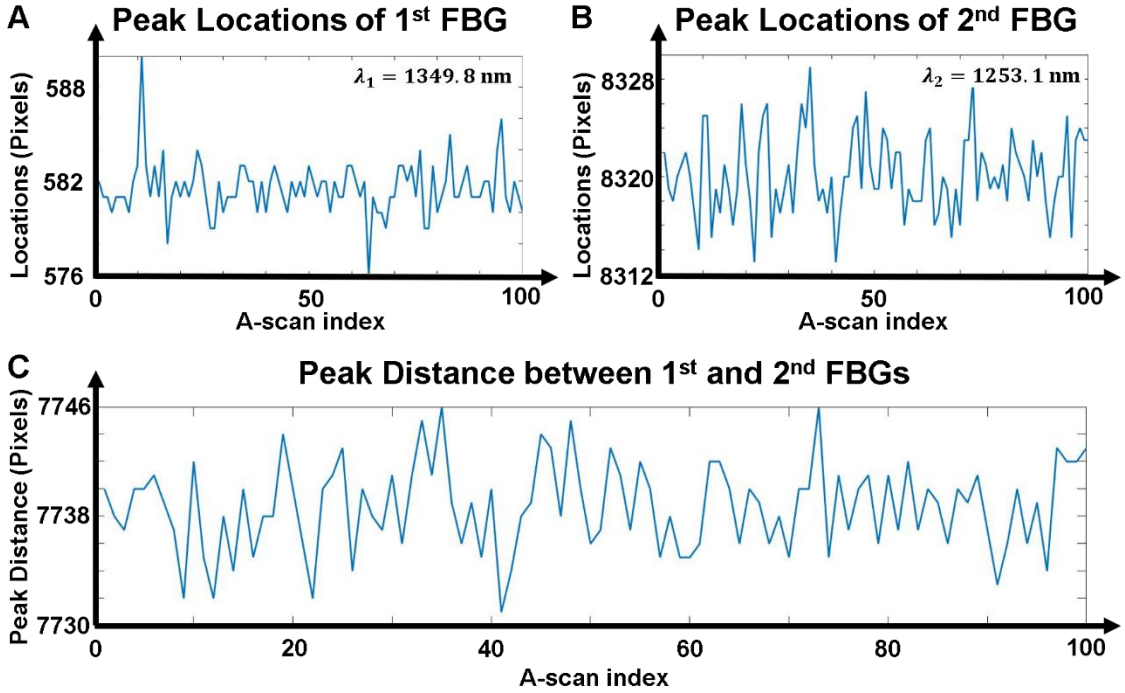

Figure 3. 10 Characterization of locations of 1st and 2nd FBG peaks and their peak distance for consecutive 100 A-scans.

characterized with two FBGs with their central filtered wavelengths on either side of the MZI fringes. **Figure 3.10** shows a software screenshot of representative OCT and MZI fringes with two FBG peaks in the MZI channels. Note that, two FBGs are connected separately to the two output ports of the 50/50 coupler. **Figure 3.11** shows the characterization results of locations of 1st and 2nd FBG peaks and their peak distance for consecutive 100 A-scans. **Figure 3.11 A and B** show the peak locations of 1st and 2nd FBG, with their central filtered wavelength to be $\lambda_1 = 1349.8$ nm and $\lambda_2 = 1253.1$ nm. If the wavelength ranges are all the same for these 100 A-scans, the peak distance in pixels between the two FBGs should be the same. However, in **Figure 3.11 C**, fluctuation of the peak distance for different A-scans is clearly observed, indicating that registering the first FBG peaks for trigger jitter correction is not sufficient to ensure the same wavelength ranges for different sweeps, which can lead to jittering of mirror images in the deep depth ranges.

With the known central filtered wavelengths (wavenumber) for these two FBG peaks, we can use the MZI fringe between these two FBG peaks to derive the phase calibration curve and generate the mapping function f(x) for the linear resampling of OCT fringes (**Figure 3.8**). In this way, we can ensure that the

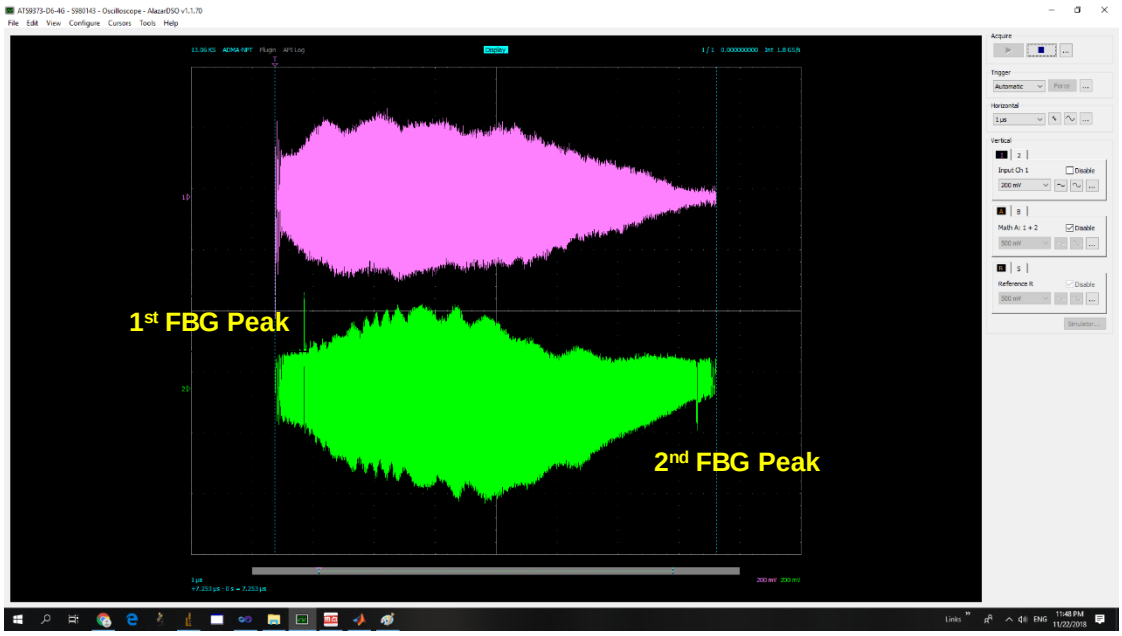

Figure 3. 11 A screenshot of representative OCT (pink) and MZI (green) fringes, with the two FBG peaks shown in the MZI fringe.

wavelength ranges of the cropped MZI fringes are the same for all the sweeps, yielding an accurate reconstruction of the mirror image without any jitter.

We should note that, when adding FBGs in the MZI, the fiber Bragg grating peak is considered as low frequency component of the MZI fringe. Thus, we should avoid employing high-pass filters after the balanced detector of the MZI channel to preserve the FBG peaks.

In **Figure 3.8**, we also mention two other approaches to resolve the trigger jitter issue, if one or both FBGs are not available. With one FBG in the MZI setup, we can first register the FBG peaks for different sweeps. Then, we use a fixed phase range. starting from the unwrapped phase of the FBG peak, to generate the mapping function f(x) for the linear resampling of OCT fringes. If no FBG is available, the only option to mitigate the trigger jitter is to use cross-correlation to align MZI fringes from different sweeps.

3.6.3 Signal Delay Correction

In the previous alignment, the OCT arm and MZI arm may have different total optical path lengths from the two output ports of the 97/3 fiber coupler. Also, the cable lengths after the DBDs in OCT and MZI sub-systems may be different. As a results, the OCT and MZI fringes may not be detected at the same time by

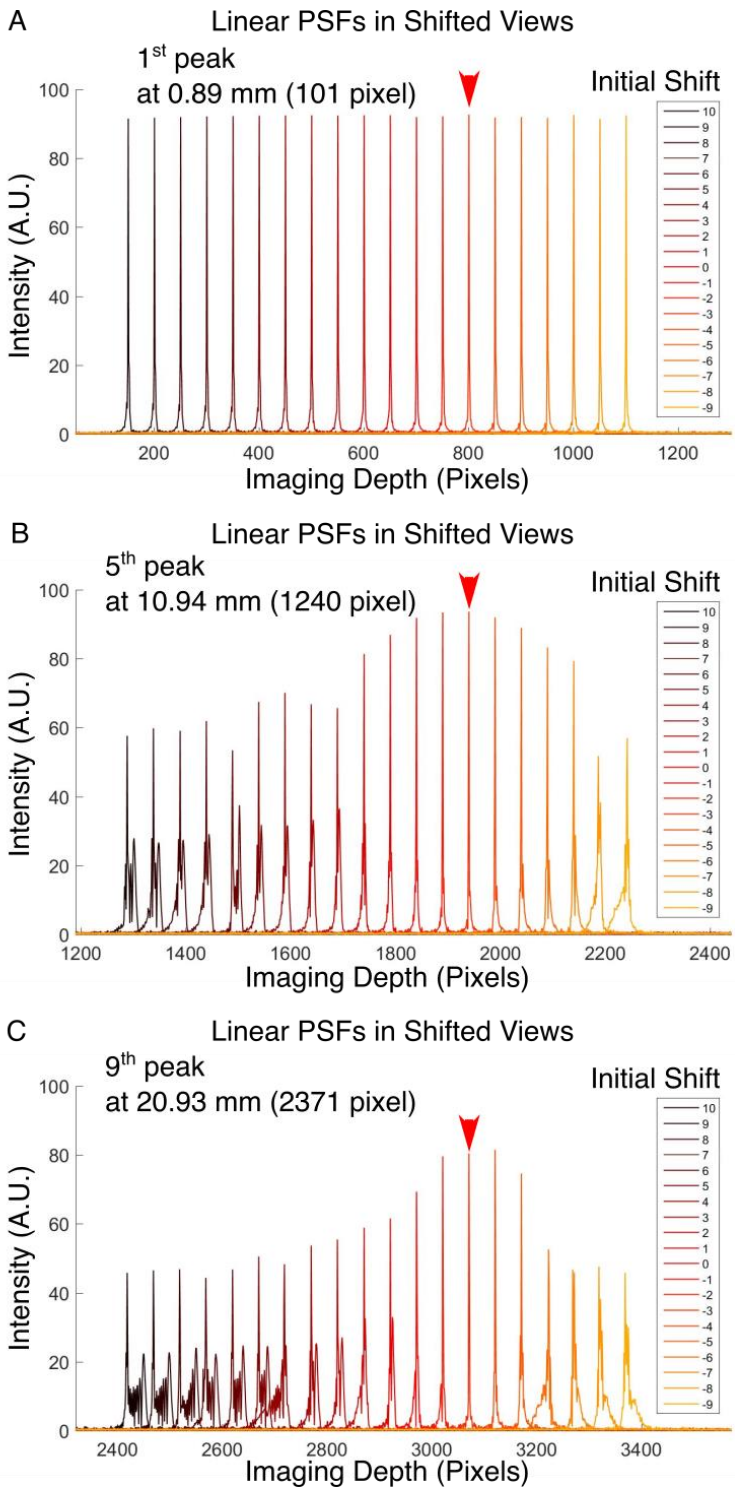

Figure 3. 12 The influence of the signal delay between OCT and MZI channels on the final shape of the point spread functions of a single reflector at different imaging depths. The signal delay between OCT and MZI channels is called Initial Shift in the post-processing code. Red Arrow indicates the optimal initial shift value for the SDM-OCT system by choosing the PSF with a sharp peak, symmetric profile and low-side lobes. (A) to (C) showed the influence of signal delay for mirror images at different depth ranges.

the digitizer, yielding the signal delay between these two channels. In the detected fringes, the signal delay is measured as the relative shift (initial shift) of the MZI fringe from the OCT fringe. If a digitizer sampling rate of 1.2GS/s is used, one pixel shift between MZI and OCT fringes corresponds to 1/(1.2 GS/s) = 0.8 ns signal delay.

Figure 3.12 shows the influence of the signal delay on the final shape of the point spread function of the mirror at different imagng depths. If a signal delay exists, linear sampling of OCT fringes using the mapping function f(x) generated from MZI fringes may not be perfect, since the wavelength ranges of OCT and MZI fringes do not match. As a result, the point spread functions (PSFs) of the mirror in a deeper imaging depth will be affected, yielding a poorer shape of the mirror PSF as well as poorer axial resolution. In **Figure 3.12**, a signal delay of 2.4 ns (3 pixels) exists between OCT and MZI channels. To perform signal delay correction, the MZI fringes will be numerically shifted by the amount of initial shift. Different numbers of initial shifts are used to test the performance of signal delay correction. If the signal delay is perfectly corrected, the point spread function of the mirror will maintain a sharp peak with a symmetric profile and low side-lobes in all the depth ranges. In **Figure 3.12 A**, no significant amplitude drop of the PSFs are observed with an initial shift of ~10 pixels, when the peak is at a depth of 0.89 mm. However, in **Figure 3.12 C**, the PSF of the mirror is located at the depth of ~20.93 mm, the influence of the signal delay is significant. With a proper correction of the signal delay, the PSF of the mirror remains sharp with a large amplitude, indicated by the red arrow. Otherwise, asymmetric PSFs with clear sidelobes and reduced amplitudes are clearly observed, indicated by the other PSFs in **Figure 3.12 C**. In this way, we can measure the relative signal delay between OCT and MZI channels. The signal delay can be corrected in the hardware by adding or removing SMA cables after the DBDs in OCT and MZI sub-systems and evaluating the value of the initial shift. An initial shift value of 0 indicates that the signal delay between OCT and MZI channels are minimized (< 0.8 ns).

3.7 Characterization of fiber-based SDM-OCT system

3.7.1 Laser spectrum

Figure 3.13 shows the output spectrum from the VCSEL, measured with the optical spectrum analyzer (OSA). The central wavelength of the output spectrum is ~1300 nm and the wavelength range is from ~1250 nm to ~1355 nm. The 3dB bandwidth of the VCSEL is ~80 nm.

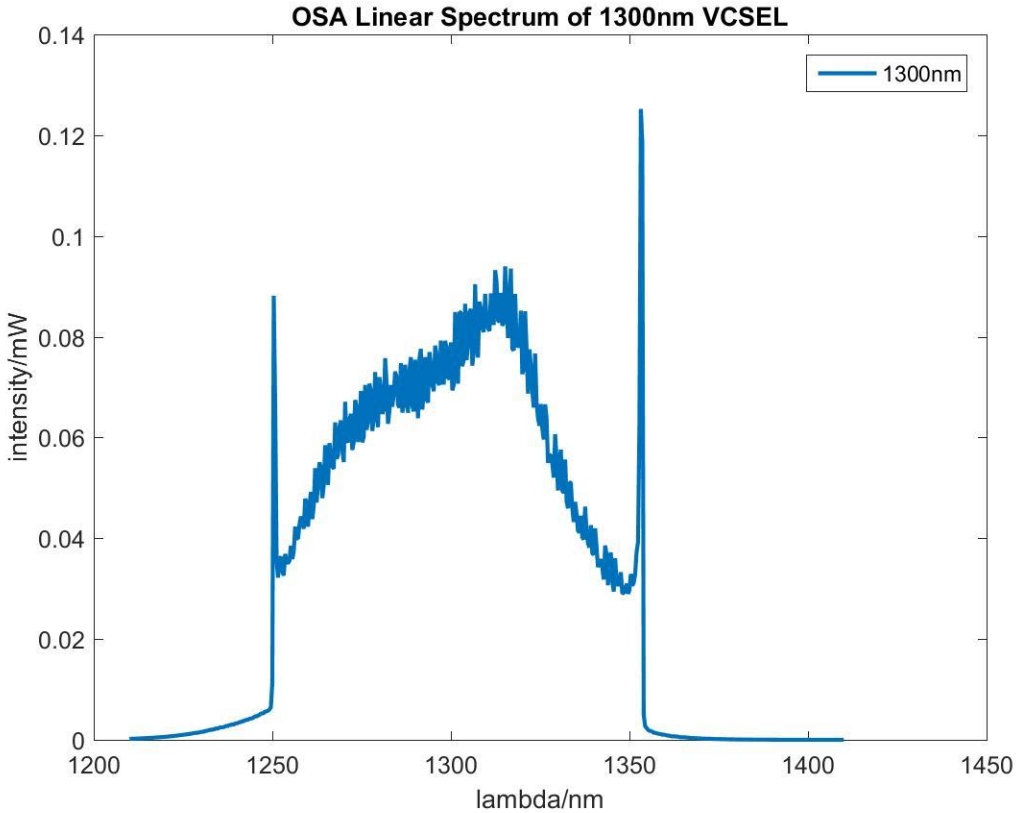

Figure 3. 13 Output spectrum of the VCSEL measured with optical spectrum analyzer (OSA).

3.7.2 Roll-off Analysis

Figure 3.14 shows the results of roll-off analysis with the plotted PSFs in both linear and logarithmic scales. Only the central beam (3rd beam from the top) is used for the roll-off analysis. A neutral density filter with OD = 2.0 and a measured attenuation of -47.2 dB is applied in the sample arm, mounted after the collimator. The PSFs of mirror images are measured by moving the reference arm with a step size of ~5 mm. Since the reference arm is a single-path setup, the actual spacing of the neighbouring PSFs will be half of the step size, which is ~2.5 mm. The reference arm power incident into the 50/50 fiber coupler is measured to be ~1.0 mW. A sampling rate of 1.2 GS/s is used for the acquisition of roll-off data. The measured pixel size after post-processing is 8.826 µm (in air). Note that the pixel size should be the same when employing different sampling rates for data acquisition, if the OCT fringes are cropped using the peak locations of two FBGs in

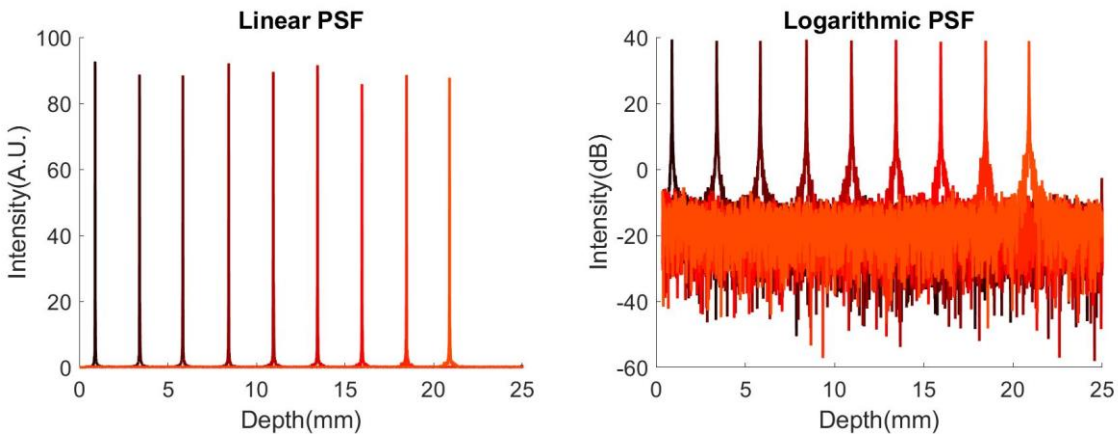

Figure 3. 14 Roll-off measurement results showing point spread functions (PSFs) of a single reflector (mirror) from multiple imaging depths, which are controlled by the movement of the reference arm. Left: PSFs in linear scale. Right: PSFs in logarithmic scale. A neutral density filter with OD = 2.0 and an attenuation of -47.2 dB is applied in the sample arm.

the MZI fringe as the start and the end points. From the roll-off measurement, we clearly observe that the amplitude of the mirror PSF is well maintained when moving the PSF from the zero delay to a depth of ~20 mm, yielding a long 3dB roll-off.

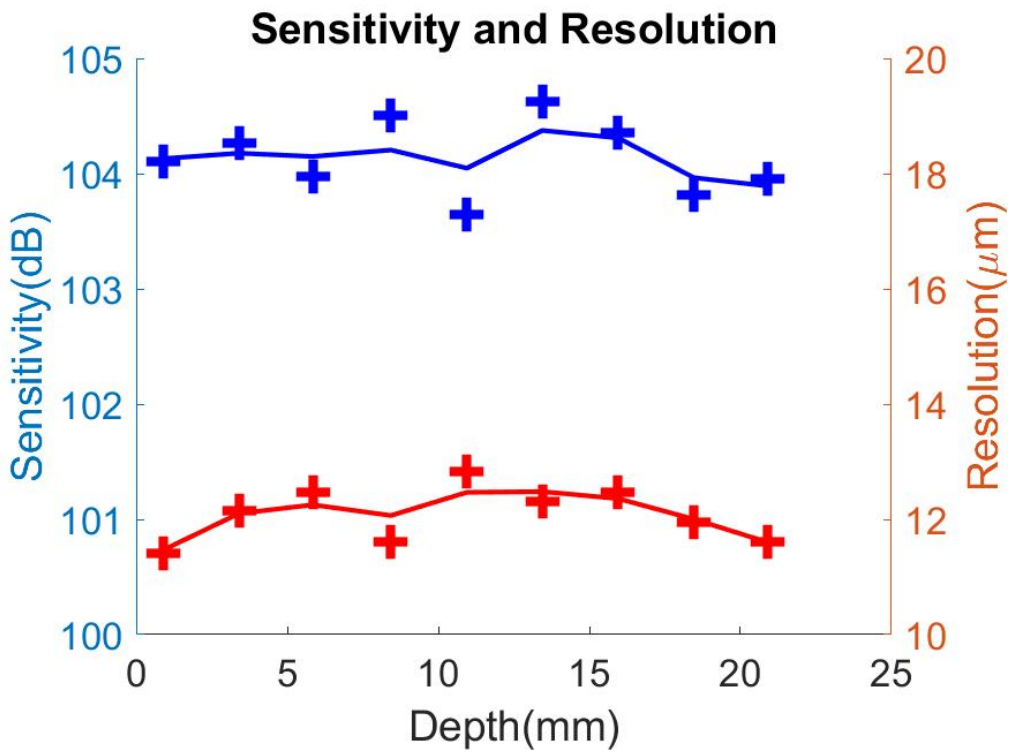

Figure 3. 15 Sensitivity and Resolution of 1×4 the fiber-based SDM-OCT system, measured from one of the central beams (3rd beam from top).

Figure 3.15 shows the characterized results of the sensitivity and the axial resolution (in air) of the SDM-OCT, measured from the PSFs in **Figure 3.14**. The sensitivity of the SDM-OCT, measured with the 3rd channel, is ~104 dB. The sensitivity is well maintained around ~104 dB within a total measurement range of ~20 mm, indicating the 3 dB sensitivity roll-off is >20 mm. The axial resolution of the SDM-OCT is ~12 µm in air or ~9 µm in tissue. We also observe that the axial resolution is well preserved for all the PSFs in our roll-off measurements.

3.7.3 Optical Delay

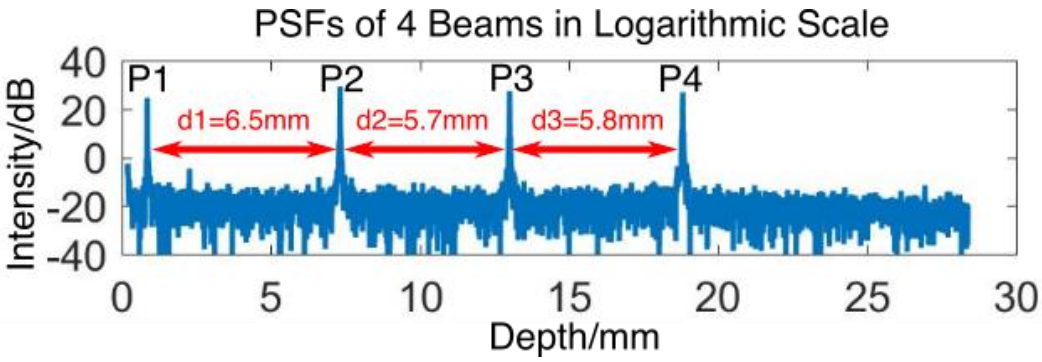

Figure 3. 16 Point spread functions (PSFs) of mirror images from four beams showing the actual optical delays between neighbor channels.

Actual optical delay between neighbouring channels are measured for the 1×4 SDM-OCT system. F**igure 3.16** shows a SDM-OCT image of a mirror with a neutral density filter. Point spread functions (P1 – P4) of the mirror images from four channels are clearly observed to be separated at different depth ranges. The actual optical delays between neighboring channels are characterized to be d1 = 6.5 mm, d2 = 5.7 mm and d3 = 5.8 mm in air, respectively. Variation of the optical delay between neighbouring channels is reasonable since the achievable accuracy of the fiber-length in the fiber-based SDM component is +/- 1.5 mm during the fabrication process.

3.7.4 Lateral characterization with a USAF target

In order to characterize the key performance metrics of the SDM-OCT system in transverse scanning direction, we take images of a 1951 USAF resolution test chart (USAF target) with the 1×4 SDM-OCT system. A neutral density filter of OD=1.0 is added to the sample arm to suppress the strong surface reflection. **Figure 3.17** shows the lateral characterization results in *en face* SDM-OCT images of the USAF

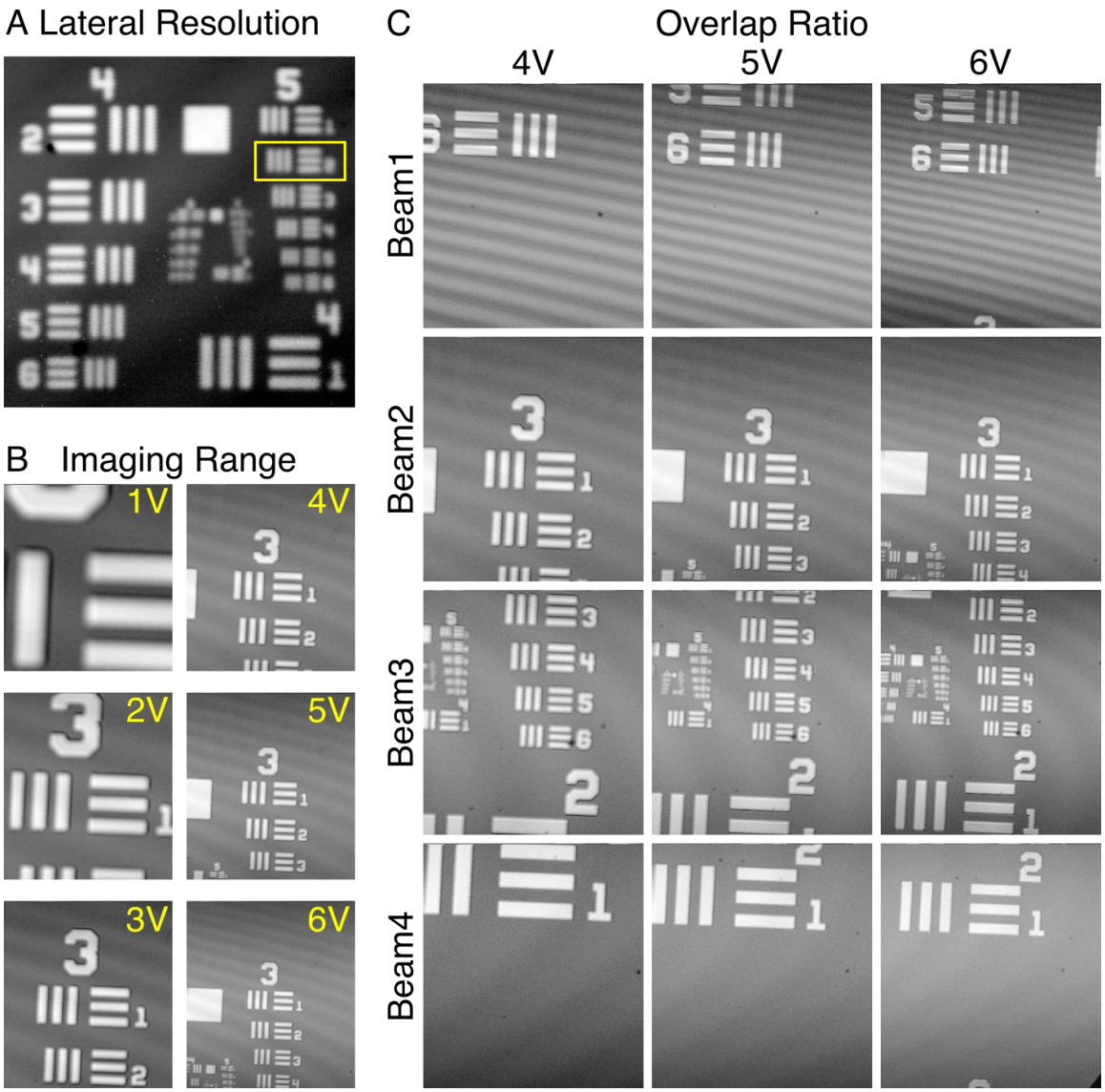

Figure 3. 17 Lateral characterization of the 1×4 SDM-OCT system with a 1951 USAF resolution test chart (USAF target). (A) Measurement of lateral resolution. Bars of group 5, element 2 are differentiable, indicating the resolution to be ~14 µm. (B) Determination of actual imaging ranges with different scanning voltages. (C) Determination of overlap ratio with larger imaging ranges.

target, taken with one central beam (3rd beam from top). **Figure 3.17 A** shows a measurement of lateral resolution. The lateral scan voltages are set to be 4V × 4V, corresponding to a scan area of 1.9 mm × 1.9 mm. Number of A-scans per B-scan is 800 and number of B-scans is also 800. In **Figure 3.17 A**, the smallest resolvable bars are group 5, element 2, indicated by yellow rectangle region, which corresponds to a lateral resolution of 13.92 µm (See Appendix 2.1).

Figure 3.17 B shows the characterization results of the imaging range with different scanning voltages. The targeted element of the USAF target is group 3, element 1, and its bars have a length of 312.5 µm and a width of 62.5 µm. *En face* SDM-OCT images of the group 3, element 1 bars with scanning voltages from 1V to 6 V are presented. Both A-scan and B-scan numbers are set to 400. Characterization results of actual imaging ranges as a function of the scan voltage are shown in the second column of **Table 3.2**. Based on these data, we perform a linear fitting between actual imaging range and the scan voltage. The fitted linear function is shown in the **Figure 3.18**, with a slope of 0.4892 (mm/V), an intercept of 0.0062 (mm), and a R-square value of 0.9996. Using this fitted linear function, we can estimate the actual imaging ranges with other scan voltages.

Table 3. 2 USAF Target Characterization Results

Scan Voltage (V)	Actual Imaging Range (µm) / 400 px	Horizontal X shift (px, µm, %)*		Vertical Y overlap (px, µm, %)**		Final Spacing Center/Edge (µm)
		Center	Edge	Center	Edge	
1	503	No overlap				
2	989					
3	1477					
4	1941	-13/63/3.2	-14/68/3.5	30/146/7.6	26/126/6.5	1795/1815
5	2432	-10/61/2.5	-11/67/2.8	103/626/25.9	101/614/25.4	1806/1818
6	2969	-8/59/2.0	-9/67/2.2	152/1128/38.3	150/1113/37.8	1841/1856

* Percentage is calculated with 400 px

** Overlap pixels and percentage is calculated with 397 pixels. First 3 frames are discarded.

One lateral characterization for SDM-OCT is to measure the final beam spacing between neighbouring channels and potential overlap ratio along slow axis (Y-axis) direction with different scan voltages. **Figure 3.17 C** shows the *en face* SDM-OCT images of the USAF target from all four beams with different scan voltages. With scan voltages from 1 V to 3 V, no overlapping regions are observed in USAF target images from neighbouring beams. Starting from 4 V, we can find the overlap region in USAF target images from neighbouring beams. The number of overlap pixels along Y-axis is characterized by comparing images from 2nd and 3rd beams (Center, column 5 of **Table 3.2**), and from 3rd and 4th beam (Edge, column 6 of **Table 3.2**). A manual pairwise stitching is performed to stitch the two *en face* OCT images of the USAF target from neighbouring beams. Then, the number of over pixels is equal to (2 × the width in Y-axis of the *en face* OCT image from a single beam) minus (the width of stitched image). Characterization results are shown in **Table 3.2**, column 5 and 6. The overlap ratios between neighbouring beams are measured to be ~7% at a scan

voltage of 4 V, 25% at 5 V and 38% at 6 V. Note that a small variation of the overlap width in Y-axis between 2nd / 3rd beam (Center, column 5) and 3rd/4th beams (Edge, column 6) is observed, which is ~2-4 pixels or

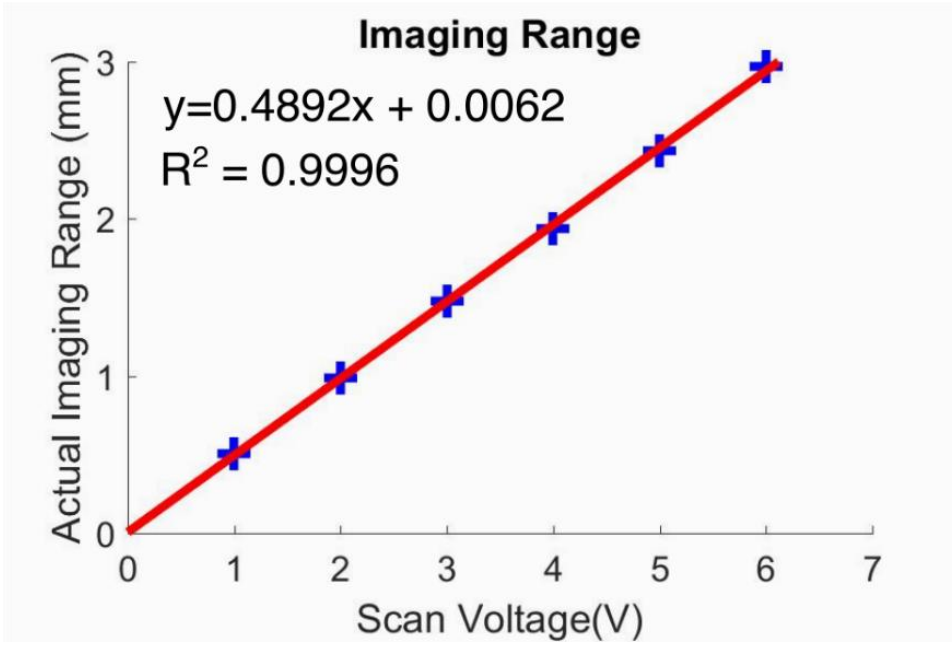

Figure 3. 18 Linear fitting of the actual imaging range as a function of the scan voltage.

~12 - 20 µm in an actual distance. This can be attributed to spherical aberration in sample arm optics. The final spacing between neighbouring channels is measured to be ~1.8 mm (**Table 3.2**, column 7).

In **Figure 3.17 C**, some small horizontal shifts between SDM-OCT images from neighbouring beams are also observed, which is due to imperfect alignment of four channels (See Chapter 3.5.3 and **Figure 3.6**). Based on the *en face* USAF target images, the horizontal pixel shift between neighbouring beams can be characterized. The results are shown in the 3rd and 4th columns of **Table 3.2**. The actual horizontal shifts between neighbouring channels are ~60 µm between 2nd/3rd beams (Center, column 3, **Table 3.2**) and 67 µm between 3rd/4th beams (Edge, column 4, **Table 3.2**). Using these information, we can better align images from different beams to generate the final stitched SDM-OCT image.

3.8 Images of the fiber-based SDM-OCT systems

3.8.1 SDM-OCT image of a Scotch tape

To test the performance of the 1×4 SDM-OCT system, we first use it to take an image of a Scotch tape. **Figure 3.19 A** showed the 1×4 SDM-OCT image of a Scotch tape. The SDM-OCT image was acquired with

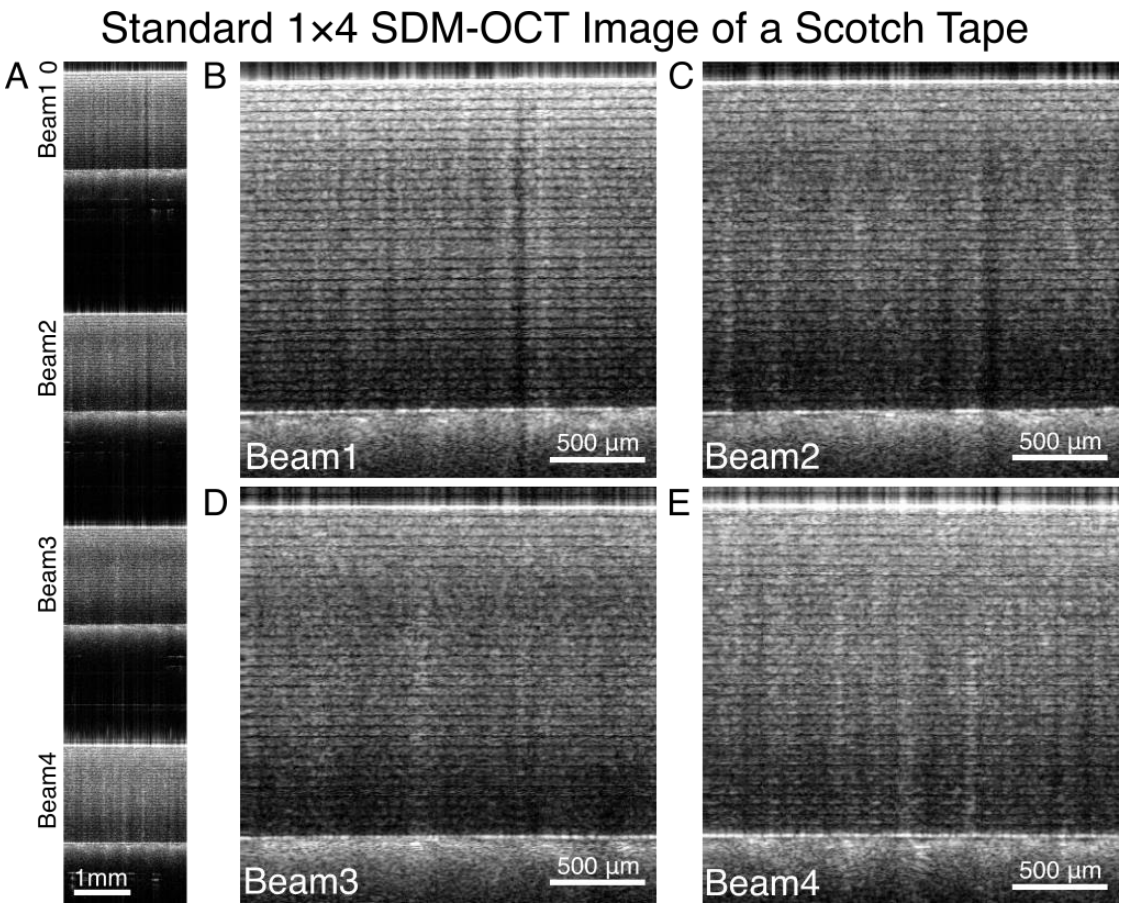

Figure 3. 19 1×4 SDM-OCT image of a Scotch tape. (A) SDM-OCT images with different beams displayed at different depth ranges. (B -E) Zoomed images of the Scotch tape from Beam 1 to Beam 4.

a digitizer sampling rate of 1.0 GS/s. The SDM-OCT dataset consists of 7168 pixels in an A-scan and 400 A-scans per B-scan. The processed SDM-OCT images were further rescaled and cropped. An average of 10 images was employed to generate the tape image with reduced speckles. In **Figure 3.19 A**, tape images from four different beams were well separated at different depth ranges. The tape image from Beam 1 was displayed at a depth range close to the zero delay on the top while the tape image from Beam 4 was the farthest one away from the zero delay. The total imaging range was calculated to be ~14.9 mm, using a refractive index n = 1.5 for the Scotch tape. **Figure 3.19 B to E** showed the zoomed tape images from Beam 1 to Beam 4. The tape layers in all the four zoomed images were clearly resolved, indicating the axial resolution was well preserved within the total imaging range.

3.8.2 SDM-OCT Image of the Finger Nailfold

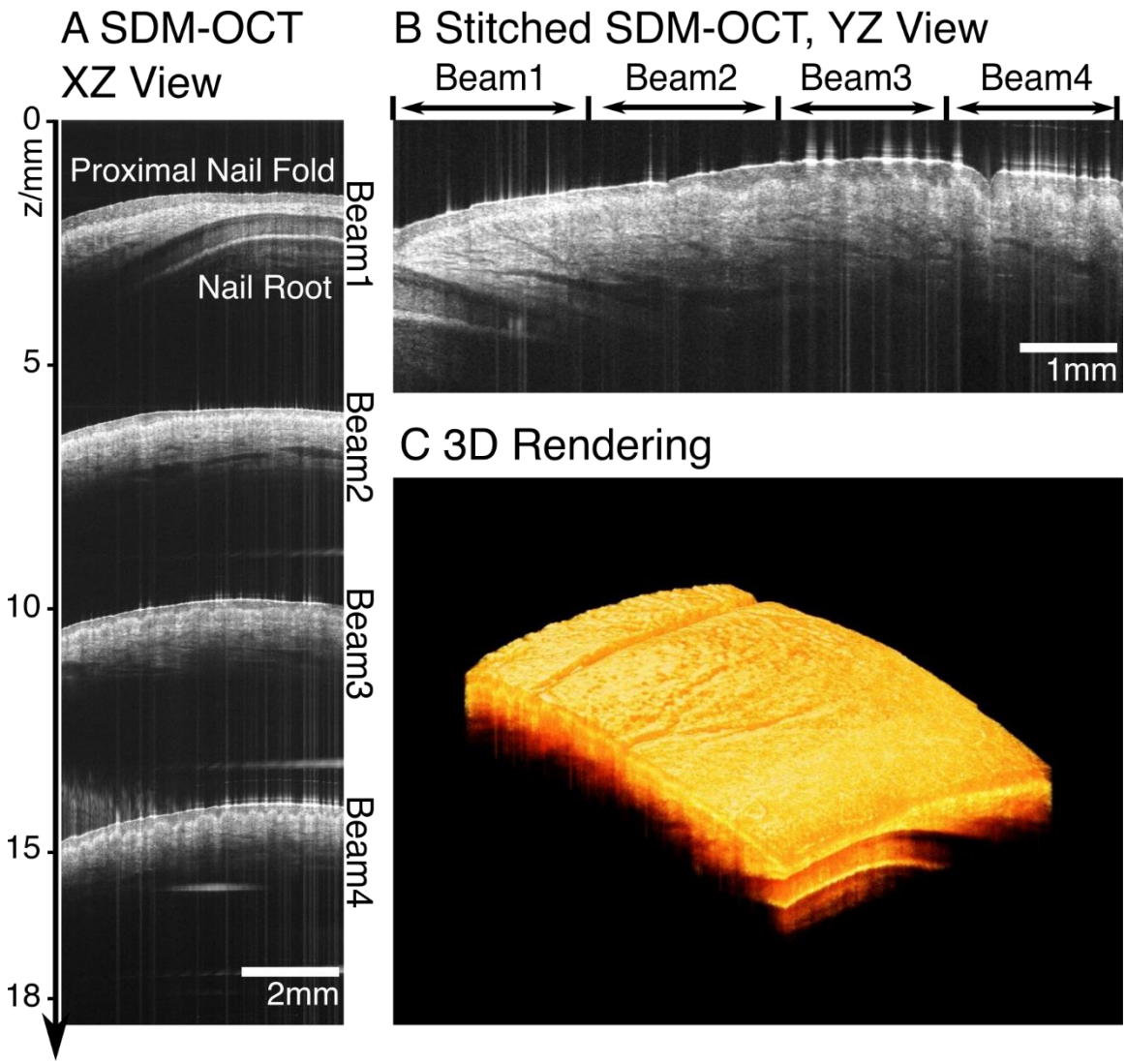

Figure 3. 20 1×4 SDM-OCT image of a human finger nail fold. (A) SDM-OCT image with finger image from different beams displayed at different depth ranges, in XZ cross-sectional view. Total measurement range in (A) is ~18.6 mm (in tissue). Nail junction between proximal nail fold and nail root was clearly seen. (B) Stitched SDM-OCT image of the proximal nail fold. (C) 3D rendered SDM-OCT image of the finger nail fold.

Figure 3.20 showed a representative result of OCT imaging of a human finger nail fold with the 1×4 SDM-OCT system. The total scan area was ~5.9 mm × ~7.5 mm, with each beam covering an area of ~5.9 mm × ~2.2 mm. Each OCT acquisition consisted of 850 A-scans per B-scan and 162 B-scans, yielding a pixel spacing of ~7 µm and ~14 µm in fast and slow axes. In **Figure 3.20 A**, finger nail fold images from four different locations were displayed at different depth ranges due to the optical delays between neighbouring channels. The total measurement range in **Figure 3.20 A** was ~18.6 mm in tissue. In the finger nail fold

image from Beam 1, the nail junction between proximal nail fold and nail root were clearly visible, with the nail root underneath the proximal nail fold. After we registered the 3D data from the four beams, we generated a stitched SDM-OCT data of the nail fold, with a representative YZ cross-sectional view shown in **Figure 3.20 B**. The sources of each part of the stitched SDM-OCT image from each beam were labeled on top. In the left of the stitched image, the nail root was observed to be extended to the regions under the proximal nail fold. The separation of epidermal and dermal layer in the proximal nail fold was also visible. A 3D rendered image of the finger nail fold was shown in Figure 3.20 C. Thus, we demonstrated the feasibility of the 1×4 fiber-based SDM-OCT to perform parallel OCT imaging on live subjects.

3.9 Discussion of the Fiber-based OCT System

In the previous sections, I describe the step-by-step procedure to build a fiber-based SDM-OCT system and demonstrate the feasibility of this SDM-OCT system to obtain multi-channel high-quality images from human subjects. Here, we further discuss about losses in the SDM-OCT system, the tuning of the reference arm power to achieve shot-noise detection, the effect of the sampling rate on the sensitivity, and the limitation of the fiber-based SDM component.

3.9.1 Loss Characterization of 1×4 SDM-OCT System

To characterize the sources of optical losses in the 1×4 SDM-OCT system, we measured the optical powers after different optical components. **Table 3.3** shows the results of the optical power measurements. P_{BOA}, $P_{circulator}$, $P_{1stlens}$, P_{samp}, $P_{backcoupled}$ (from port 3 of the circulator), $P_{backcoupled}$ (before the detector) reprented the optical power after the BOA, the optical power after port 2 of the circulator incident to the SDM component, the optical power after 1st relay lens, the optical powers on the sample from each channel, the back-coupled power from each channel measured from the port 3 of the circulator, and the back-coupled power incident into the balanced detector, respectively. With an output power of 91.4 mW provided to the OCT system, the maximum detected back-coupled power from the sample arm was ~312 μW. Based on the power measurement, we characterized the losses for each step, shown in the 6th row of **Table 3.3**. The transmission loss from port 1 to port 2 of the circulator was ~0.77 dB. The forward transmission loss (for all the beams) in the sample arm was ~3.58 dB, calculated as sum(P_{samp})/ $P_{circulator}$. We should note that, within this ~3.58

dB loss, ~2 dB was attributed to the SDM component, including the insertion, transmission and coupling loss from the fiber to the free space; ~1.5 dB was attributed to the 20× objective (results not shown); and the residue losses due to the rest of the sample arm optics. The high transmission loss in the 20× objective could be attributed to the mismatched wavelength ranges. The backward losses from the sample to the port 3 of the circulator was -10.99 dB, measured from the 3rd beam. The -10.99 dB losses could be further split into several parts: 6 dB loss due to 50% loss at each layer of 1 × 2 splitter; ~3.6 dB losses with the same contribution as the forward transmission loss; the rest of ~1.4 dB loss attributed to additional back-coupling loss from the free-space to the fiber. After the loss characterization, we can potentially figure out the way to mitigate the optical losses and further improve the performance of the SDM-OCT system.

Table 3. 3 Loss Characterization of 1×4 SDM-OCT System

Beam #	P_{BOA}	$P_{circulator}$	$P_{1stlens}$	P_{samp}	$P_{backcoupled}$, at port 3 of the circulator	$P_{backcoupled}$ before the detector
1	91.4 mW	76.6 mW	N.A.	8.43 mW	455.8 µW	N.A.
2				8.35 mW	655.7 µW	
3			8.66 mW	8.52 mW	678.3 µW	310 µW, 313 µW**
4			N.A.	8.28 mW	487.4 µW	N.A.
Losses		-0.77 dB	-3.58 dB*		-10.99 dB (3rd beam)	-3.38 dB

* A total loss from the circulator output to the powers on the sample is measured, calculated as sum(P_{samp})/ $P_{circulator}$, The sources of the losses include the SDM component, the collimator and optics in the sample arm.
** Measure from each output port of the 50/50 fiber coupler.

3.9.2 Shot-noise-limit detection with Tuning of Reference Arm Power

The shot-noise-limit detection for the SDM-OCT is achieved when the shot-noise variance is significant larger than other types of noise variance, yielding the highest sensitivity value. In the experiment, we need to adjust the reference arm power to maximize the sensitivity value to achieve the optimal system performance. **Figure 3.21** shows the effect of the reference arm power adjustments on the sensitivity. The measured reference arm power is the back-coupled power before the final 50/50 coupler. The PSFs in the linear (**Figure 3.21 A**) or logarithmic-scale (**Figure 3.21 B**) shows a trend of increasing peak values as the reference arm power increases from ~0.1 mW to ~1.0 mW. The sensitivity as a function of reference arm power is shown in **Figure 3.21 C**. The sensitivity follows the linear-increase line of the read-noise sensitivity

as the reference arm power increased from ~0.1 mW to ~0.6 mW. The sensitivity reachesthe maximum at ~0.6 mW and then reduces when the reference arm power further increased from ~0.6 mW to ~1.0 mW. We should note that the change of the sensitivity value from the reference arm power of ~0.6 mW to ~1.0 mW is small. Thus, we figure out the optimal reference arm power is ~0.6 mW. However, we should note that shot-noise-limit detection may not be achieved if the shot noise cannot dominate over the read noise before RIN noise (or beat noise in balanced detection mode) becomes significant.

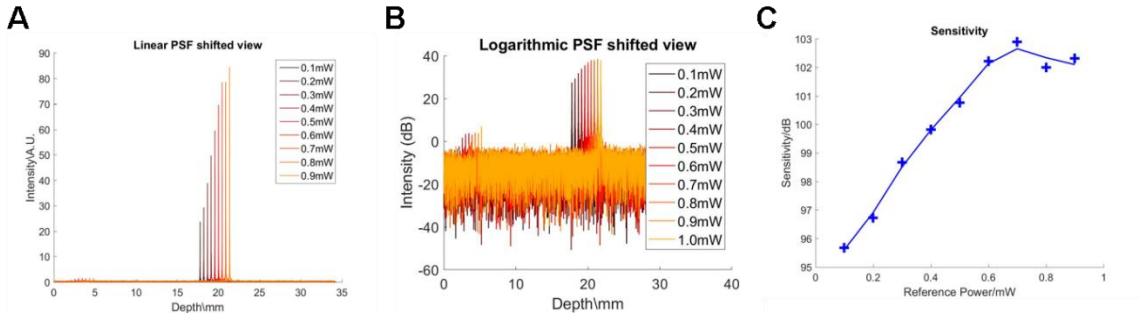

Figure 3. 21 Effect of reference arm power on sensitivity. (A) Linear point spread functions (PSFs) in shifted view, with the reference arm power increased from ~0.1 mW to ~1.0 mW. (B) Logarithmic-scale PSFs in shifted view. (C) Sensitivity as a function of reference arm power.

3.9.3 Effect of the Sampling Rate on the Sensitivity

An experiment was performed to test the effect of the sampling rate on the sensitivity value of the SDM-OCT. **Figure 3.22 A and B** show the characterization results of PSFs in linear and logarithmic scales from a mirror with a OD=2.0 neutral density filter, with different sampling rates. The sampling rate is set to be 500 MS/s, 800 MS/s, 1000 MS/s and 1200 MS/s. Note that the PSFs are manually shifted for the display purpose. The actual location of the mirror PSFs remained the same while the sampling rate is modified. The amplitude of the PSFs in the linear (**Figure 3.22 A**) and logarithmic-scale (**Figure 3.22 B**) increases a little bit as the sampling rate is increased. **Figure 3.22 C** showed the characterization results of the sensitivity and resolution as a function of the sampling rate, measured from the PSFs in **Figure 3.22 A**. A steady increasing sensitivity value is observed as the sampling rate is increased. The axial resolution is not affected if the sampling rate was changed.

The increase of the sensitivity value with an increasing sampling rate was mostly attributed to the change of the noise floor. **Figure 3.23** shows the characterization results of the noise floor as a function of the sampling rate. In the first row, different noise floors in the linear (first column) and logarithmic (second column) scales are shown. The standard deviation of the noise with different sampling rate is measured from a large number of A-scans of the background data. A significant drop of the standard deviation of the noise

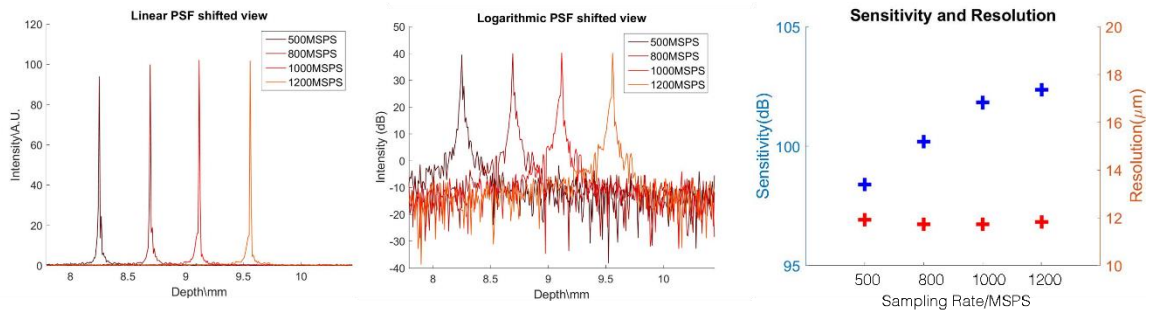

Figure 3. 22 Effect of the sampling rate on sensitivity. PSFs of a mirror with a neutral density filter (OD = 2.0) in linear (A) or logarithmic scale as a function of the sampling rate were shown. Characterized sensitivity and axial resolution was shown in (C). An increase of the sensitivity with increased sampling rate was observed, while the axial resolution was not affected.

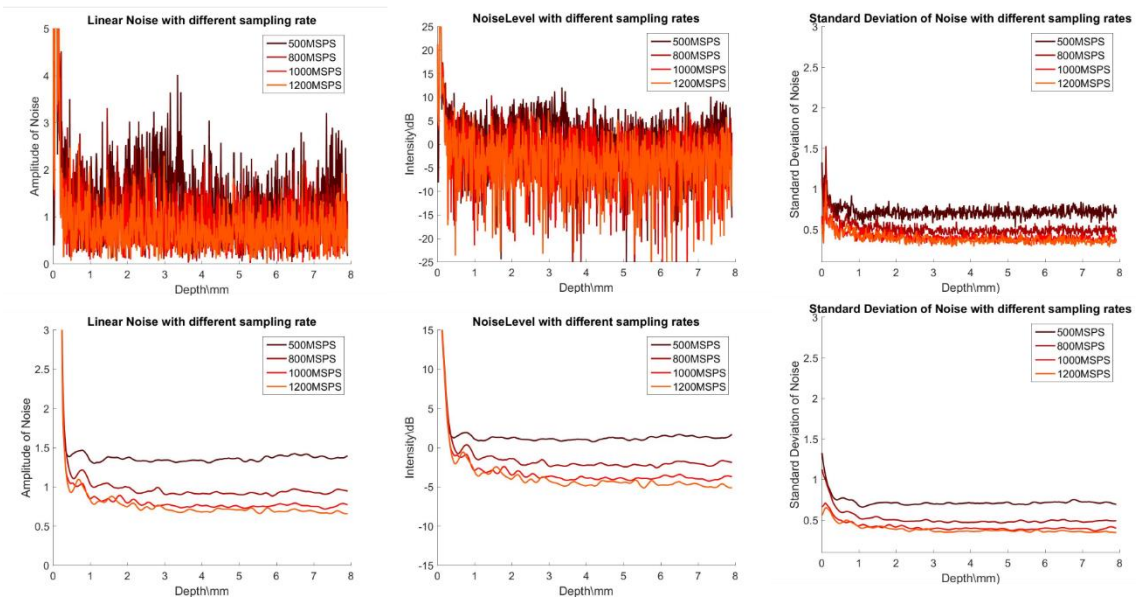

Figure 3. 23 Characterization of the noise level with different sampling rates. The first row showed the linear and logarithmic noise term, as well as standard deviation of the noise term, without any filtering. The second row showed the corresponding moving-average-filtered images to show different level of noise as a function of sampling rate.

(for each depth) is observed as the sampling rate increased from 500 MS/s to 1200 MS/s. We further smoothen the images in the first row with a moving average filter. The corresponding filtered image is shown

in the second row. The filtered noise floors in the linear or logarithmic scale and the filtered standard deviation of the noise clearly show the decreasing level of the noise as the sampling rate increased, which explain the increase of the sensitivity. Note that the amount of the noise floor drop or the amount of the sensitivity increase from a sampling rate of 1000 MS/s to 1200 MS/s is small.

3.9.4 Limitation of Fiber-based SDM Component

Although the first lab prototype SDM-OCT system offered scalable speed improvement with a simple system configuration, several factors may limit the broad dissemination of the SDM-OCT technology. First, it requires extensive time and manual efforts to assemble custom fiber-based space-division-multiplexing components. The key part will be the precision of the optical path delay between neighbouring channels. The commercial fiber-length meter has a resolution of ~2 mm and an accuracy of +/- (0.1%L + 1.5 mm). Thus, it is difficult to measure the fiber length would the total length of several meters with a sub-millimiter resolution. However, the required patch fiber length difference between neighbouring channel (~4 mm) is on the same order as the resolution of the fiber length meter. Thus, if we utilize the fiber length meter to control the patch fiber length difference, it can be only controlled to ~4 mm +/- 2 mm. Thus, it will be difficult to guarantee that the fiber-based SDM component has the required patch fiber length difference with high precision.

The second limitation is the output spacing between neighbouring channels. Since the standard V-groove fiber-array has a pitch size of 125 µm or 250 µm, options of the output spacing are limited to a multiple of 125 µm.

3.10 Development of Chip-based SDM-OCT System

In the last section we mention about the difficulty to build a SDM component with high-precision optical delays between neighbouring channels, which is a major limiting factor for the translation of the prototype SDM-OCT to a commercial system. To build SDM components with high repeatability and reliability, we seek to assemble these components into one compact product.

One tangible solution would be the integrated photonic chip. Integration of components onto a single photonic chip has advantages of size, cost and stability of the overall system[4]. As a growing market valued

~500 million in 2017, it is estimated that the photonic integrated circuit industry would reach ~$1.7 billion by 2022, with an annual growth rate of ~28% [120]. Benefiting from the extensive knowlege of mass production in semiconductor industry as well as the latest advances in the Si-based processing capability, the cost of nano/micro-fabrication of photonic integrated circuits (PICs) could potentially decrease significantly, ultimately bringing in significant cost reduction with large scale manufacturing for SDM-OCT technology. The PICs also provide the ability to achieve new functionalities with increased yield and reduced errors in packaging.

In the case of SDM-OCT technology, using a PIC to replace fiber-based SDM component could bring in significant benefits [115]. The major benefit is that the optical delays between neighbouring channels can be precised controlled during the nano/micro-fabrication process. Using lithography, high precision of the designed optical delays can be achieved with a tolerance of sub-microns, yielding the reliable performance of the SDM component without concerning the overlapping (short OPD) or missing (long OPD) images. Moreover, the spacing and height of the output channels could be defined lithographically with sub-micron resolution, yielding the accurate output light from different channels. Also, the PIC is compact, with all components integrated in a single chip and properly shielded with the thick substrates. Thus, we don't need to concern about damaging the components, i.e. breaking a fiber in the middle.

Given these advantages, we design a PIC to realize the same function as the prototype fiber-based SDM component and integrate it into the SDM-OCT system, considering that the chip-based SDM component has has advantages of smaller-size, cost-effectiveness, ease of manufacture and precise control of optical delays over fiber-based SDM-OCT [115]. In the following sections, I will describe the configuration of the chip-based system and test its performance.

3.11 Building up a chip-based SDM-OCT System

Figure 3.24 A showed the schematics of the chip-based SDM-OCT system [115]. The major difference of the chip-based SDM-OCT system as compared to the prototype fiber-based system was the replacement of fiber-based SDM-component with the integrated photonic chip. The layout of the silicon-based photonic chip (PC) was shown in **Figure 3.24 B**. The incident beam, with a central wavelength of 1310nm, was coupled into the chip from the optical fiber (SMF-28). In the chip, the incident beam was first split into eight channels

through a three-layer cascade of 1×2 waveguide splitters (**Figure 3.24 B**). Each layer of the waveguide splitters was indicated by red dash lines. All the waveguide channels had the same optical path lengths in the cascaded splitters. Next, optical path length delays werer introduced after the cascaded splitters by arranging different waveguide lengths for each channel. A physical length difference (ΔL) of ~2.5 mm in the waveguide or ~3.7 mm optical delay in air was introduced between adjacent channels. Last, The waveguide spacing (d) between neighbouring channels at the output port was set to be 250 μm in order to reduce cross-talks between neighbouring channels (**Figure 3.24 C**). The output surface of the whole PIC chip was 8° angle polished to reduce direct back-reflections (return loss) from the surface. By polishing the whole chip, we guaranteed that directions of all the output beams were the same. **Figure 3.24 D** shows a size comparison of the integrated photonic chip with a US quarter coin. The overall size of the chip was ~2.5×2.0 cm^2.

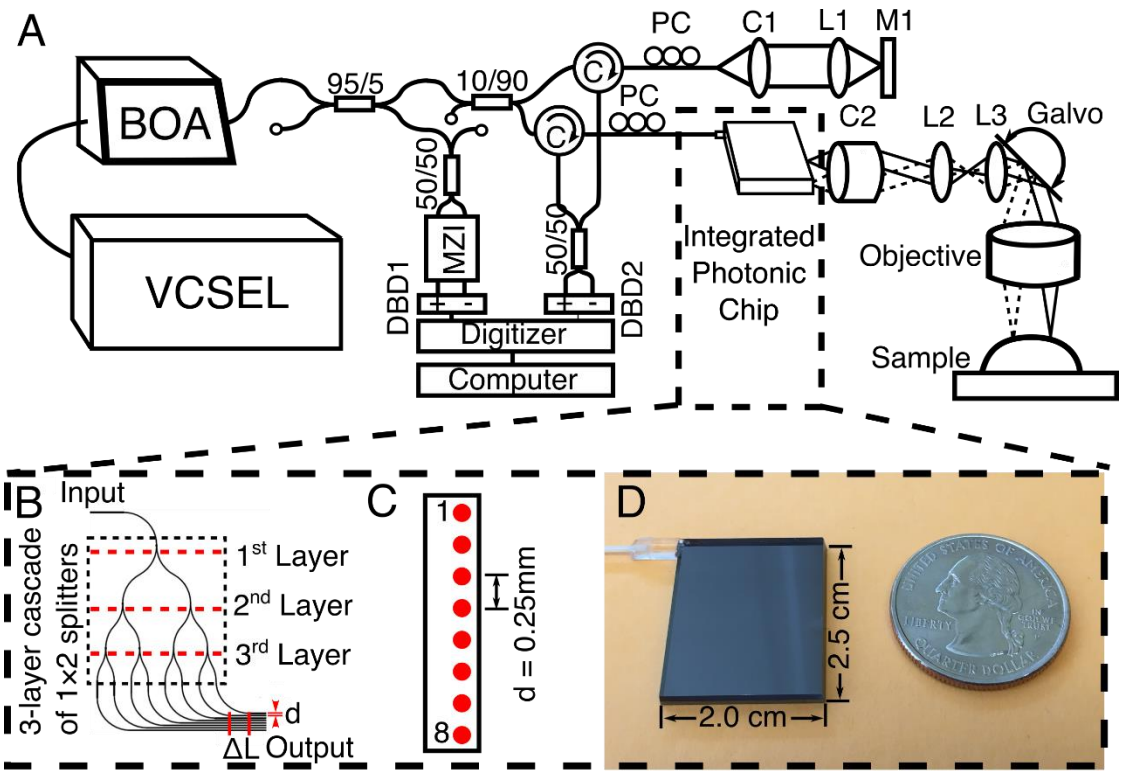

Figure 3. 24 Chip-based SDM-OCT system. (A) Schematic diagram of the chip-based SDM-OCT. (B) Layout of the PIC-based SDM component. Input and output of the chip was labeled. A three-layer cascade of 1×2 splitters were shown. The cascaded splitters, with each layer indicated by red dash lines, were used to split the incident beam evenly from 1 to 8. Optical delay (ΔL) was ~2.5 mm between neighbouring channels. (C) Zoom-in view of output ports of the chip-based SDM component showing eight waveguide channels with a d = 0.25 mm spacing between them. Output channels were 8° angle polished to reduce back reflections. (D) Photograph of the chip with its size measured to be 2.5 × 2.0 cm^2, close to the size of a US quarter coin. C: Circulator; C1, C2: collimator; DBD1, DBD2: dual balanced detectors; L1, L2, L3: lenses; M1: mirror; PC: polarization controller.

3.12 Characterization of the Chip-based SDM-OCT System

The output power from the BOA to the OCT system and the incident power to the integrated photonic chip in the sample arm were the same as the 1×4 SDM-OCT system since we used the same laser source, the same coupler (97/3) to split the lights into the MZI setup and OCT system, and the same coupler (95/5) to split the incident light into the reference and sample arms of the OCT system. The only difference was that we use a double-path reference arm setup with a circulator instead of the single-path setup to reduce the travel range of 1D translation stage during reference arm path-length adjustments.

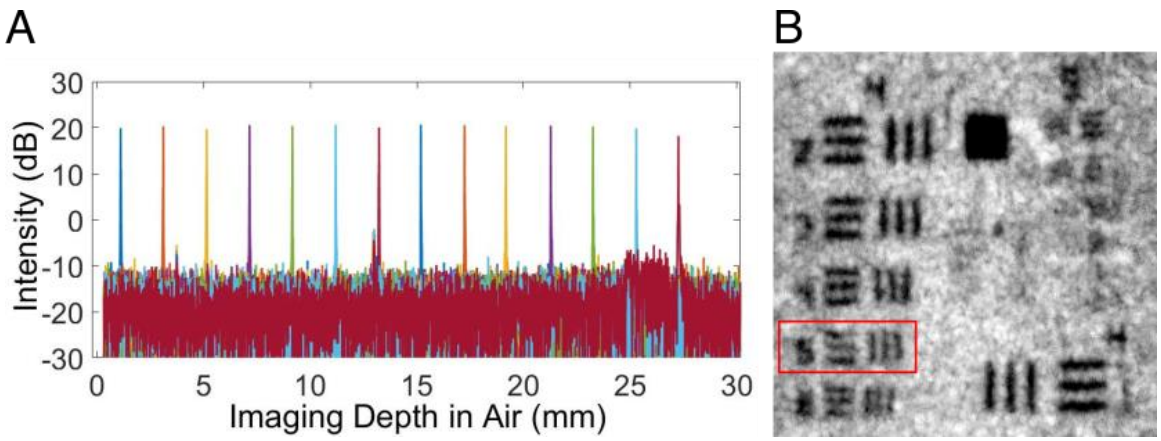

Figure 3. 25 Performance characterization of the chip-based SDM-OCT system. (A) Roll-off measurement of the central beam of the chip-based SDM-OCT in logarithmic scale. A roll-off of ~2dB was measured over ~27 mm depth range in air. (F) Lateral resolution was measured to be ~20 μm in *en face* SDM-OCT image of a USAF target from the central beam (Group 4, element 5).

After we integrated the photonic chip into the system, we characterized the key performance metrics of the chip-based SDM-OCT, including the depth-dependent sensitivity, sensitivity roll-off, axial resolution and lateral resolution. Since the maximum travel range for the 1D translation stage used in the reference arm of the chip-based SDM-OCT system was 25 mm, we needed to move the 1D translation stage along the rail to get the full roll-off measurement along all the depth ranges. During the roll-off analysis, we measured the point spread function of the central beam (4th beam) and maximized the back-coupling power by optimizing the mirror position. **Figure 3.25 A** showed the result of the roll-off analysis from chip-based SDM-OCT. The sensitivity was measured to be ~91 dB, with a mirror and a neutral density filter (OD = 2.0) with a calibrated attenuation value of -47.2 dB in the sample arm. The sensitivity was well preserved, with only a small roll-off of ~2 dB over ~27 mm imaging range. The axial resolution of the chip-based SDM-OCT system was

measured to be ~11 μm in air for all the depth ranges. **Figure 3.25 B** showed the *en face* OCT image of a USAF target with a small scan area. The minimum resolvable bars in the *en face* OCT image were from group 4, element 5 of the USDA target, yielding a measured value of the lateral resolution to be ~20 μm. The large value of the lateral resolution was due to the use of a low-magnification scan lens for wide-field imaging.

3.13 Wide-field, Chip-based SDM-OCT Imaging of a Porcine Eye

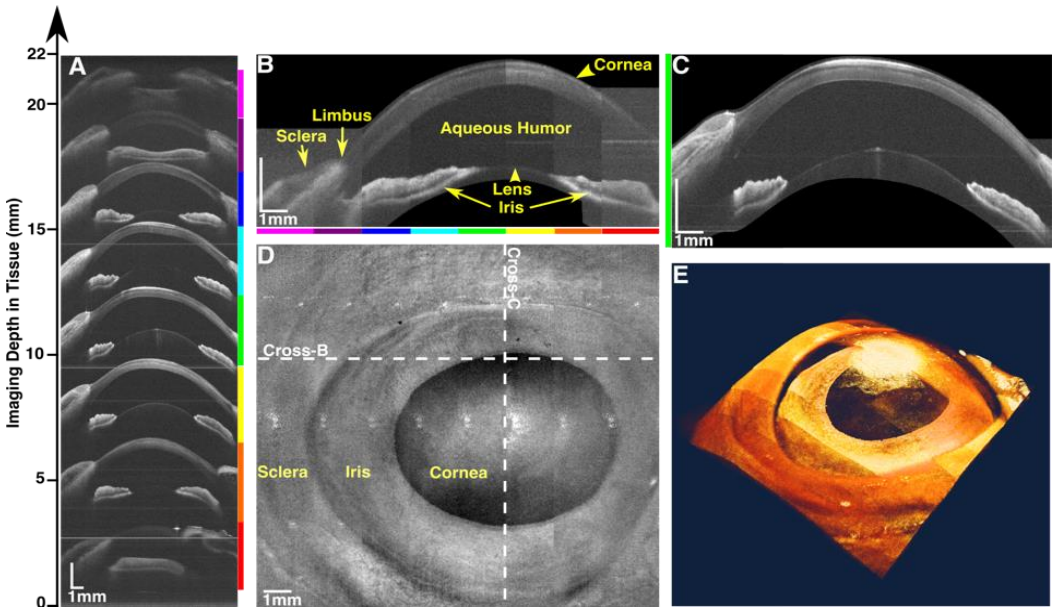

Figure 3. 26. **Chip based SDM-OCT image of *ex vivo* porcine eyeball**. The scan area was ~13.5 × 14.3 mm^2. (A) A single 2D cross-sectional B-scan (average of 10 frames) showed 8 images corresponding to 8 beams appearing at separate depth ranges. Eight images covered a depth range of ~22 mm in tissue. Different color bands at the left of the B-scan represented imaging area covered by each beam. (B) 2D cross-section of final stitched image of 8 beams, color bands on the bottom show area of the image acquired by each beam. (C) Cross sectional image of the single beam cropped out of a single B-scan. (D) *En face* image of the final stitched image, horizontal and vertical dashed lines show the directions of 2D cross sectional images shown in (B) and (C) respectively. (E) 3D volumetric reconstruction of anterior segment of the eyeball using final stitched image.

The feasibility of high-speed, chip-based SDM-OCT was demonstrated with wide-field imaging capabilities. We employed the chip-based SDM-OCT to image the anterior segment of a piglet eye *ex vivo*, of which the results were shown in **Figure 3.26** [115]. To image the entire anterior segment of the piglet eye, each beam was scanned ~13.5 mm and ~2.4 mm in the fast and slow axis directions, respectively. The total scan area covered by eight beams was ~13.5×14.3 mm^2, considering a 29% overlap between scan areas from

neighbouring beams. The total acquisition time for a 3D data was ~1s, with 700 A-scans in one B-scan and 150 B-scans in a 3D data. **Figure 3.26 A** showed a single cross-sectional (B-scan) SDM-OCT image of the anterior segment of the piglet eyeball. Acquired depth-resolved SDM-OCT images of the piglet eye from eight beams appeared simultaneously at eight separated depth ranges within the 22 mm total imaging range. The depth range of each image was indicated by the rainbow color bands at the lef t side of the **Figure 3.26 A**. The ~2.8 mm optical delay in tissue between neighbouring channels were sufficient to avoid the overlap between neighboring images in the axial direction. Note that the anterior segment images from edge beams (1st beam and 8th beam) were not as clear as those images from central beams, which was attributed to the steep curvature of the eyeball surface, yielding the edge regions out of focus. Next, images from 8 beams in **Figure 3.26 A** were segmented and stitched together to generate a 3D volumetric image of the whole anterior segment. **Figure 3.26 B-E** showed the cross-sectional views along the slow and fast-scanning axes, top-view and 3D rendering of the final stitched image of the anterior segment of piglet eye, respectively. Cornea, iris, top surface of the lens, sclera and limbus surrounding the anterior chamber of the piglet eye were clearly visualized in two cross-sectional images. The *en face* averaged image of the final stitched data clearly showed cornea, iris and sclera parts of the eyeball.

3.14 Chip-based SDM-OCT Images of the Human Fingerprint

We also used the chip-based SDM-OCT system to perform *in vivo* scanning of human fingerprints [115]. The results were shown in **Figure 3.27**. SDM-OCT images of human fingerprints wer acquired from the ventral side of the middle finger of a healthy volunteer. **Figure 3.27 A** showed eight parallel-imaging beams scanning at different finger regions. Each beam covered an area of ~18 × ~2.4 mm^2 and the total scan area covered by all 8 beams was ~18 ×14.3 mm^2 with a ~29% overlap along the slow axis. The whole 3D data set was acquired in ~1 second, using the same acquisition protocol as the one for piglet eye imaging (with a larger X scan range). **Figure 3.27 B** showed a single cross-sectional (B-scan) SDM-OCT image with eight different segments of the finger from eight channels. Images from all the 8 beams were of similar quality because of the relatively flat surface of the finger along the slow axis direction. A zoomed view of the finger image from the cyan band of SDM-OCT image was shown in **Figure 3.27 C**. Epidermis and dermis layers

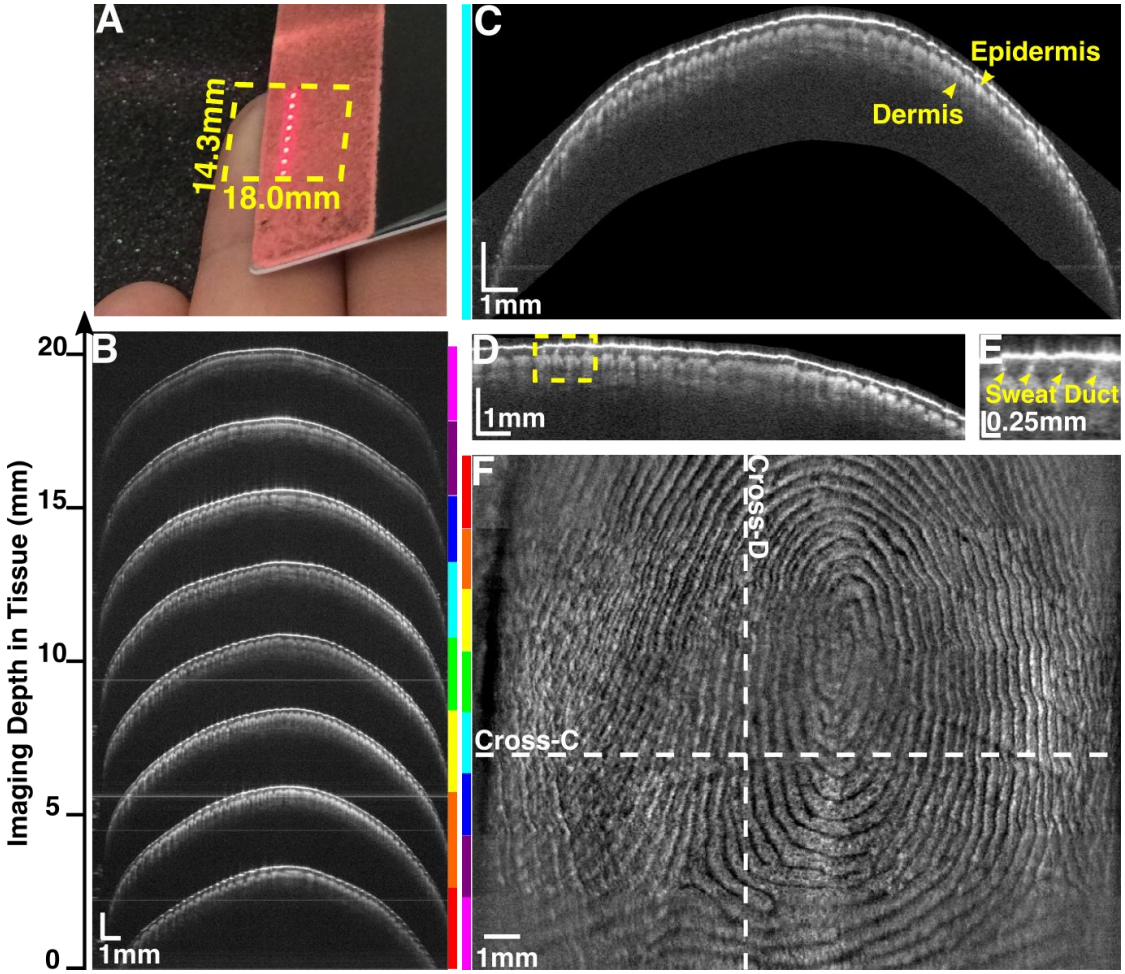

Figure 3. 27 Wide-field, chip-based SDM-OCT imaging of the ventral side of a human finger, showing fingerprints. The total scan area was ~18.0×14.3 mm^2. (A) Photograph of a human middle finger showing 8 beams illumination with the yellow rectangular box defining the total scan area. (B) A single 2-D cross sectional B-scan (average of 10 frames) showing 8 images corresponding to 8 beams appearing at different depth ranges. Different color bands at the left of the B-scan indicated the finger images covered by each beam. (C) Zoomed 2D cross sectional image of the finger from the central beam. (D) Stitched cross-sectional image of the finger. (E) Enlarged area of the yellow rectangle region in (D) showing sweat ducts. (F) En face projection of the final stitched image of the ventral side of the middle finger, showing fingerprints. Horizontal and vertical dashed lines show the directions of 2D cross sectional images shown in (C) and (D), respectively.

of the skin were clearly differentiated in the ventral side of the middle finger. Connected friction ridges across the finger were also clearly visible. The cross-sectional view of the final stitched image of the ventral side of the middle finger along the slow axis was shown in **Figure 3.27 D**, with a enlarged view of the yellow rectangle region in **Figure 3.27 E** showing sweat ducts. **Figure 3.27 F** showed the *en face* projection of the ventral side of the middle finger. A whorl pattern of the fingerprint was clearly observed. Thus, we demonstrated the feasibility of the chip-based SDM-OCT for *in vivo* studies.

3.15 Chip-based SDM-OCT Images of the Human Nail Fold

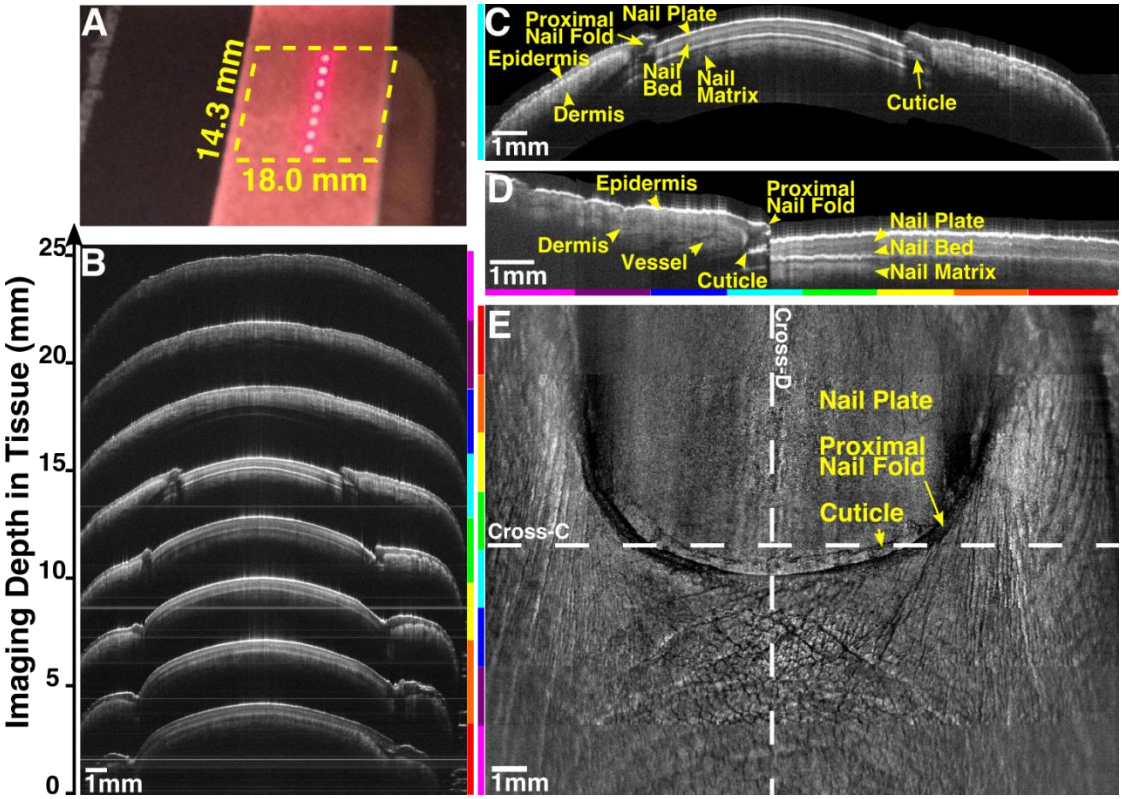

Figure 3. 28 Chip-based SDM-OCT imaging of the human finger nail and nail fold region. The total scan area was 18.0×14.3 mm^2. Each data consisted of 1500×200 A-scans/s. (A) Photograph of dorsal side of the middle finger showing 8 beams illumination. (B) 2D cross sectional SDM-OCT image (average of 10 frames) showing 8 images at different depth ranges. Color bands on the left indicated imaging region covered by each beam. (C) Zoomed 2D cross-sectional image from the central beam. (D) YZ cross-section view of the nail junction from the final stitched image. (E) En face projection of the final stitched image of the human nail and nail fold region. Horizontal and vertical dashed lines showed the directions of 2D cross-sectional images in (C) and (D), respectively.

We also demonstrated wide-field, *in vivo* imaging of the human finger nail and nail fold with the chip-based SDM-OCT system [115]. A high-definition acquisition protocol was employed to scan the nail fold region of a volunteer's middle finger. The high-definition SDM-OCT data consisted of 1500 A-scans per B-scan and 200 B-scan per volume, yielding a total data acquisition time of ~3 seconds. The total scan area was ~18 ×14.3 mm^2. Hence, lateral pixel sizes in both X and Y directions were ~12 µm. Results were shown in **Figure 3.28**. A photograph showing 8 beams illumination on the dorsal side of the middle finger was shown in **Figure 3.28 A**. Among eight different segments of the cross-sectional SDM-OCT image of the finger nail fold region shown in **Figure 3.28 B**, five of them covered the nail structure and three of them covered the

proximal nail fold structure. Similarly to **Figure 3.26 and 3.27**, color bands were drawn on the left side of the cross-sectional SDM-OCT image to indicate the sources of different segments. A zoomed view of the cyan band of cross-sectional SDM-OCT image was shown in **Figure 3.28 C**, showing the nail junction region. Nail structure was observed at the central region of **Figure 3.28 C**, with a layered structure of the nail plate, the nail bed and the nail matrix from top to bottom. In the connected nail fold region in **Figure 3.28 C**, a clear separation of epidermal and dermal layers was observed. **Figure 3.28 D** showed the YZ cross-sectional view of the final stitched image of the human finger nail and nail fold structure. Nail junction was clearly visible, with the proximal nail fold region on the left, a small cuticle region in the middle and the nail region on the right. The *en face* projection of final stitched SDM-OCT image was shown in **Figure 3.28 E**. Curve stripes of the cuticle were discernible along the nail junction. The skin pattern of the dorsal side of the finger was also visible.

3.16 Discussion of the Chip-based SDM-OCT

3.16.1 Potential Improvement of Imaging Speed of SDM-OCT

In the previou sections, we demonstrated a prototype SDM-OCT system with an integrated photonic device. An equivalent imaging speed of 800,000 A-scans/s was achieved by the chip-based SDM-OCT system, with eight parallel channels. Imaging speed of SDM-OCT can be further improved if the number of parallel channels are further increased. To realize it, a swept laser with a larger coherence length is required to render the images from these channels at different depth ranges, if the optical delay between neighbouring channels remains the same. State-of-the-art tunable swept lasers with long coherence lengths, e.g. akinetic programmable swept sources [89], meter-range VCSEL [121] and tunable-range FDML [122], can potentially be employed for this purpose.

3.16.2 Loss Characterization of the Chip-based SDM-OCT System

We have demonstrated the sensitivity advantage of the SDM-OCT in Chapter 3.4. SDM-OCT preserves the dwell time at each imaging spot while increases OCT imaging speed through parallel imaging with multiple sample beams [115]. For example, the dwell time of an 8 channel SDM-OCT system using a 100 kHz swept source laser is 10 µs, which is 8 times longer compared to a single beam OCT system operating at 800 kHz

(dwell time at each imaging spot is 1.25 us). Eight times more back-scattered photons may be collected from each imaging spot using SDM-OCT compared to a single beam OCT system running at the same A-scan rate, leading to a significant sensitivity advantage for SDM-OCT. However, the sensitivity of the chip-based SDM-OCT system is greatly affected by backward transmission loss in the sample arm, especially the coupling loss at the input and output ports of the photonic chip, and the splitting loss within the chip. **Table 3.4** showed the loss characterization results for chip-based SDM-OCT system, which was discussed in our published paper [115]. In the forward direction, input power from the port 2 of the circulator to the chip was ~ 70 mW. The sample arm power for each beam was ~ 3 mW (total ~24 mW for 8 beams). This translated to ~4.5 dB light loss for all eight channels, including coupling loss and transmission loss in the chip, as well as transmission loss of the rest of the optical components. In the backward direction, the measured back-coupling power was ~90 µW, resulting in a total back-coupling loss of ~15 dB. The source of the back-coupling loss was analyzed: the three-layer cascade of 1×2 splitters inside the photonic chip contributed to a ~9 dB loss in the backward transmission, with 3 dB loss at each layer of the splitter; A 4.5 dB coupling and transmission losses in the chip and sample arm optics were expected in the backward transmission; The rest of backward loss (~1.7 dB) was attributed to the additional coupling loss at the output port of the chip, where the back-scattered light was coupled into the chip from free space. A low-loss design using circulators or couplers to bypass two layers of cascaded splitters in the return path may be used to significantly improve the sensitivity of SDM-OCT [123].

Table 3. 4 Loss Characterization for Chip-based SDM-OCT system

Beam #	$P_{circulator}$	P_{samp}	$P_{backcoupled}$
1 - 4	~70 mW	~3 mW	~90 µW
Losses		-4.5 dB	-15.2 dB

3.17 Summary and Outlook

In this chapter, I described the principles and applications of space division multiplexing OCT (SDM-OCT) technology, a state-of-the-art parallel imaging OCT. Employing multi-channel illumination and path-length-encoding, SDM-OCT can achieve multi-fold speed improvement (proportional to the number of parallel

channels), with a single source and a detector, and shared reference arm and sample arm. I described the step-by-step procedure to build a four-channel fiber-based SDM-OCT system, characterize its performance, and demonstrated its feasibility of in vivo imaging of a human finger nail. We also demonstrated an eight-channel SDM-OCT system using an integrated photonic chip to achieve the same function as the fiber-based SDM component, which brought in potential advantages of smaller-size, cost-effectiveness, ease of manufacture and precise control of optical delays over fiber-based SDM-OCT. Eight times increase in imaging speed was achieved with the chip-based SDM-OCT system with eight parallel channels. The chip-based SDM-OCT system was then used to demonstrate the feasibility for high-speed and wide-field imaging applications. Three-dimensional (3D) imaging of porcine eye, human fingerprint and human finger nail were demonstrated, with a maximum scan area of 18.0×14.3 mm^2 covered by eight beams.

In the next Chapter, I will introduce an improvement of SDM-OCT technology with the implementation of full-range techniques. In Chapter 5, I will show the demonstration of one functional application of SDM-OCT, SDM-OCT angiography, to provide additional contrast of the moving red blood cells to visualize vascular network in the human nail fold regions. In Chapter 7, I'll describe the potential applications of SDM-OCT for tumor spheroid imaging in the discussion section.

Chapter 4: Full-range OCT

4.1 Burden on Data Acquisition with SDM-OCT

In Chapter 3, we mentioned that, one key consideration of SDM-OCT is that the imaging range of the SDM-OCT is traded for the speed improvement. To accommodate images from multiple channels separated at different depth range, a large total imaging range is required. In Chapter 1.3.6, we mentioned that, the total imaging range z_{max} is proportional to number of spectral data points, which is the ratio between the digitizer sampling rate and the laser swept rate. z_{max} can be expressed as [33]:

$$z_{max} = \frac{1}{2} N\Delta z = \frac{1}{2}\frac{f_s}{f_{sweep}}\Delta z = \frac{1}{2}\frac{f_s}{f_{sweep}}\frac{\lambda_c^2}{2n\Delta\lambda_{full}} \tag{4.1}$$

Since Δz is determined once the swept-source OCT system is set up and f_{sweep} is a fixed value determined by the swept laser, the required sampling rate of the digitizer will increase proportionally as the z_{max} is increased to cover more channels.

For the prototype 8-channel chip-based SDM-OCT system, a minimum total imaging range of 29 mm in the air is required to cover images from all eight channels. With a 100kHz swept rate, the theoretical minimum sampling rate is calculated to be ~690 MS/s. Considering the cropping of the spectrum due to the usages of two FBG in the MZI signals for phase calibration (See Chapter 3.6), a sampling rate of 1.0 GS/s would be preferred.

Next, a signal at a depth of ~29 mm in air corresponds to a ~345 MHz signal in the spectrum analyzer. In order to detect such a high-frequency signal, a balanced detector with the bandwidth that covers the frequencies from near DC value to > 345 MHz is required. Considering that detected OCT and MZI signals are non-linear in wavenumber, a balanced detector with a cut-off frequency of ~500 MHz is recommended.

To continuous record the signals with the digitizer and tranfer the signals to the memory, a data stream rate of 2 GS/s is required to obtain signals from both OCT and MZI channels with a sampling rate of 1GS/s. Also, the size of the memory would set a limit on how many sweeps we can acquire in a 3D data.

Table 4.1 also showed the protocol of data acquisition for the prototype four-channel fiber-based SDM-OCT system described in Chapter 3.

Table 4. 1 Data Acquisition Protocol for the prototype 1×4 SDM-OCT system

Parameter	Value	Related Hardware
Data Size	7168 (pixels) ×850 (Ascans) × 350 (B-scans) × 2 (Bytes) × 2 Channels = ~8 GB	Memory
Total Imaging Range	>20 mm	Laser Source
Signal Bandwidth	~500 MHz	Detector
Sampling Rate	1 GS/s	Digitizer
Data Transfer Rate	2 GS/s	Digitizer PCI-e channel
# Beams	4	SDM component

One key consideration to facilitate the broad dissemination of SDM-OCT is hardware availability and cost. Based on the abovementioned calculation, the minimum bandwidth of the balanced detector and the minimum sampling rate of the data acquisition unit are shown. **Appendix 4.1** and **Appendix 4.2** show the lists of the commercially available high-speed data-acquisition units and large-bandwidth balanced detectors for NIR applications. Note that the listed products are the high-end products from each company.

Several considerations should be noted. First, if we double the laser swept rate to 200 kHz, which is commercially available (Thorlabs, SL132120), the sampling rate also needs to double in order to maintain the same total imaging range. In such a case, a sampling rate of 2 GS/s would be required if we use the 200 kHz VCSEL for our prototype SDM-OCT system. Also, the minimum bandwidth of the detector will increase to ~690 MHz. If we further increase the laser swept rate to 1 MHz, which was reported by Tsai et al. [91], and employed the laser in our prototype SDM-OCT system, a digitizer with a 10 GS/s sampling rate and a balanced detector with a minimum bandwidth of 3450 MHz are required to cover the same total imaging range, yielding limited or no options of balanced detectors and digitizers. Second, the high sampling rate of commercial digitizers is achieved by interleaving multiple channels. For example, the ATS9373 digitizer can obtain signals with a 4 GS/s sampling rate from a single channel utilizing interleaving. For dual-channel

acquisition, the maximum sampling rate is limited to 2 GS/s. Third, the swept laser in the SDM-OCT system is working in the 1300 nm wavelength range. If we utilize a swept laser with a central wavelength of ~1060 nm and a spectral bandwidth of ~90 nm (Thorlabs OEM VCSEL) in the prototype SDM-OCT system, $\Delta z \approx 6\ \mu m$ in air. To maintain a total imaging range of ~29 mm in air, the sampling rate has to be further increased by 40% to 1.4 GS/s, yielding higher requirements for the digitizers and balanced detectors.

Next, we would like to mention the data streaming rate of the digitizers in the computer. For OCT imaging, 10 bit or 12 bit resolution would be preferred for each spectral data. Although 8 bit A/D resolution would be ok for OCT imaging [15], the effect number of bits (ENOB) might be 1-2 bits lower than the resolution if the sampling rate is high, yielding a poorer capability to resolve small intensity differences. With a sampling rate of 4 GS/s, and a 12 bit resolution, the data streaming rate has to be at least 6 Gbps in order to ensure a sustainable data readout and transfer from the digitizer. Especially, if each 12-bit data would be written in a 2-byte format, a 8 Gbps data streaming rate is required. This would be quite demanding for the high-end digitizers to ensure a high-efficient data transfer from digitizer to computer. Our current digitizer (Alazar, ATS 9373) utilized 8-lane PCI Express (PCIe 3.0 x8) port for data transfer with a highest data streaming rate of ~6.8 Gbps. Thus, the data streaming rate would set the upper limit of the maximum sampling rate for continuous OCT data acquisition. Further enhancement of data streaming rate requires the digitizer to make full use of all the 16-lane of the PCIe 3.0 slot to enable a faster data transfer rate of ~15.8 Gbps [124]. The next generation PCIe 4.0 protocol has been released in 2017, which would be expected to have a doubled data transfer rate of ~31.5 Gbps [124].

In summary, data acquisition with SDM-OCT system requires a lot of source from the hardwares, yielding limited availability of the hardwares as well as significantly increasing system costs. In the following sections, we are looking for a solution to alleviate the burden on the hardwares and facilitate the wide adoption of SDM-OCT technology.

4.2 Full-range Techniques

For both SD-OCT and SS-OCT systems, interferometric signals (fringes) are obtained in the spectral domain as a function of wavelength. After phase calibration, spectral fringes will be linearly resampled in wavenumber along the axial scan direction (k_z). Then, the final intensity profile of the sample along the axial

scan direction will be reconstructed by an inverse Fourier transform (IFT). Note that each interference signal recorded by the detector is a real-value function, which can be expressed as:

$$I(k_z) \sim Re\left(S(k_z)\sum_n\left(\sqrt{\alpha_r\alpha_n}\exp(i\cdot 2z_n k_z)\right)\right)$$

(4.2)

Since

$$\exp(i\cdot 2z_n k_z) = \cos(2z_n k_z) + i\cdot sin(2z_n k_z)$$

(4.3)

We can get

$$I(k_z) \sim S(k_z)\sum_n\left(\sqrt{\alpha_r\alpha_n}Re(\exp(i\cdot 2z_n k_z))\right)$$

$$\sim S(k_z)\sum_n\left(\sqrt{\alpha_r\alpha_n}\cos(2z_n k_z)\right)$$

(4.4)

which is a summation of multiple cosine functions from different imaging depths (z_n). S(k) represent the laser spectral profile in spectral domain and α_n is the sample reflectivity at n^{th} imaging depth z_n.

Inverse Fourier tranform of the spectral fringe is a Hermitian function [4]. **Figure 4.1 A** shows an illustration of IFT of the real-value FD-OCT spectral fringes. Given that:

$$\cos(2z_n k_z) = \frac{1}{2}\ (e^{i\cdot 2z_n k_z} + e^{-i\cdot 2z_n k_z})$$

(4.5)

We can derive the sample scattering profile (intensity profile) along the axial scan direction after IFT to be:

$$I(z) \sim S(z) \otimes \sum_n \sqrt{\alpha_r\alpha_s(z)}(\delta(z - z_n) + \ \delta(z + z_n))$$

(4.6)

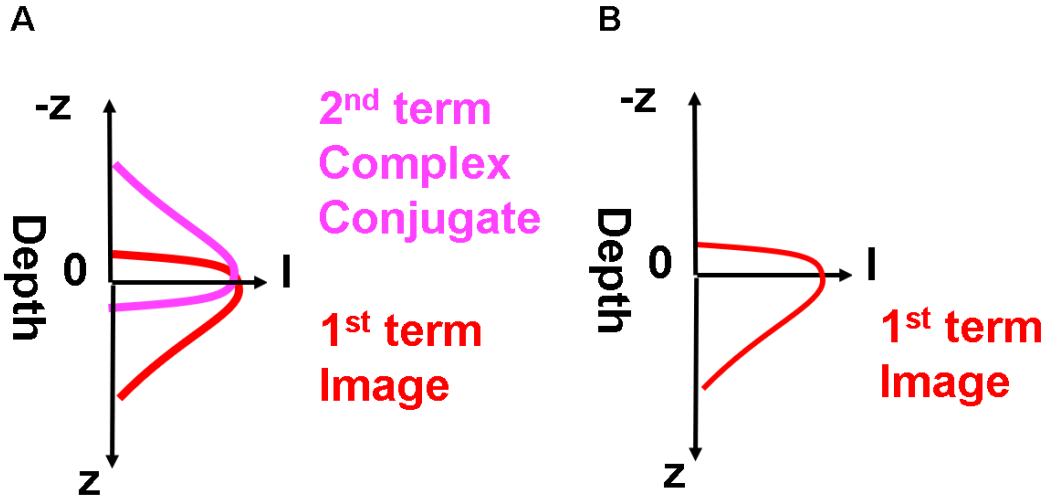

Figure 4. 1 Illustrations of IFT of real-value FD-OCT spectral fringes (A) and complex-value FD-OCT spectral fringes (B).

The first term $S(z)\otimes\sum\sqrt{\alpha_r\alpha_s(z)}\delta(z-z_n)$ is the discrete representation of the sample scattering profile, which we denote it as image term. In **Figure 4.1 A**, the red curve represents the image term of the sample scattering profile. The second term, $S(z)\otimes\sum\sqrt{\alpha_r\alpha_s(z)}\delta(z+z_n)$, is a mirrored term of 1st term. In **Figure 4.1 A**, it is represented by the magenta curve. We denote the second term as complex conjugate (c.c.) term. In the illustration (**Figure 4.1 A**), the mirrored c.c. term is overlapped with the image term, yielding inaccurate representation of the sample scattering profile in the overlap region. This phenomenon is called complex conjugate ambiguity. As a result, less than half of full imaging range can be used to show the intensity profile.

If we can reconstruct the complex representation of the fringe signals in the spectral domain as a function of wavenumber k_z, which can be derived from (4.2):

$$\hat{I}(k_z)\sim S(k_z)\sum_n(\sqrt{\alpha_r\alpha_n}\exp(i\cdot 2z_nk_z))$$

(4.7)

The sample scattering profile after inverse Fourier transform will be:

$$I(z) \sim S(z) \otimes \sum_{n} \sqrt{\alpha_r \alpha_s(z)} (\delta(z - z_n))$$

(4.8)

In the expression of (4.8), only the image term (the first term of expression (4.6)) is remained. The complex conjugate term (the second term of expression (4.6)) no longer exists. **Figure 4.1 B** shows the illustration of IFT of the complex-value FD-OCT spectral fringe, with only the image term shown in the reconstructed OCT image. Since the complex conjugate term is removed, we can make full use of all the imaging range to show the sample scattering profile, which would be more than doubled as compared to the usable imaging range illustrated in **Figure 4.1 A**.

The procedure to reconstruct the complex representation of the interference signals is called full-range (detection) technique [4].

4.3 List of Full-range Techniques

Table 4.2 shows a list of different techniques to realize full range detection in SD-OCT and SS-OCT.

The first method introduced to reconstruct the phase term is introduced by Wojtkowski et al. [125]. By consecutively acquired five cross-sectional OCT frames taken with a phase shift in increments of π/2, (i.e. fringe spectra S_1, S_2, S_3, S_4, S_5 have phase differences of π/2 between two consecutive acquisition) with the phase term and the amplitude of the complex interference signal can be retrieved by the following formula [126]:

$$\phi = \arctan\left[\frac{2(S_2 - S_4)}{2S_3 - S_1 - S_5}\right]$$

(4.9)

$$|S| = \frac{1}{4}\sqrt{[2(S_2 - S_4)]^2 + (2S_3 - S_1 - S_5)^2}$$

(4.10)

Table 4. 2 List of Full-range Techniques

Categories	References	Year	System	Key component or step
Phase shifting with piezo translator	Wojtkowski et al. [125]	2002	SD	Five frame method: 5 acquisition with phase shifts in increments of π/2, piezo translator in reference arm
	Leitgeb et al. [127]	2003	SD	Piezo translator in reference arm
Reference Tilting	Yasuno et al. [128]	2004	SD	Reference tilting
	Fechtig. [129]	2015	SS	Line-field SS-OCT
	Hillman et al. [130]	2017	SS	Full-field SS-OCT
Phase modulator	Yun et al. [131]	2004	SS	Acousto-optic frequency shifter (AOFS)
	Zhang et al. [132]	2005	SS	Electro-optic phase modulator (EOM)
	Maheshwari et al. [133]	2005	SS	Acoustic-optic modulator (AOM), k-clock
	Gotzinger et al. [134]	2005	SD	Electro-optic phase modulator, 2 frame method
	Bachmann et al. [135]	2006	SD	AOFS with 4 frame method (similar to quadrature detection)
Dual Channel Quadrature detection	Lee et al. [136]	2010	SS	Free space, rotating PBS, 1300nm
	Wang et al. [137]	2015	SS	Silicon PIC, 1550nm
	Choma et al. [138]	2003	TD	2x2 followed by 3x3 coupler
	Sarunic et al. [139]	2005	SD,SS	One 3x3 coupler only, 2 detectors.
	Bo et al. [140]	2017	SD	3x3 coupler
	Vakoc et al. [141]	2006	SS	Fiber-based, 1300nm, spectrum calibration
	Siddiqui et al. [142]	2015	SS	Fiber-based, spectrum calibration, RF error calibration
Dispersion Encoding	Hofer et al. [143]	2009	SD	Add SF-11 prism with different thickness
	Wang et al. [144]	2012	SS	GPU processing
	Kottig et al. [145]	2012	SD	ZnSe
Coherence revival	Dhalla et al. [146]	2012	SS	External cavity tunable laer (ECTL)
Time-dependent Phase Modulation in B-scan, carrier frequency	Yasuno et al. [147]	2006	SD	BM-scan, Piezotranslator, f = 1/32 camera speed, small translation, Hilbert Transform
	Wang et al. [148]	2007	SD	Piezotranslator, f = frame rate, large translation, Hilbert Transform
	Makita et al. [149]	2008	SD	EOM, increment π/2, f=1/4 camera speed, Hilbert Transform
	Yamanari et al. [150]	2010	SS	EOM
Phase modulation with galvo	Baumann et al. [151]	2007	SD	
	Leitgeb et al. [152]	2007	SD	
	An et al. [153]	2007	SD	
	Kawagoe et al. [154]	2016	SD	1700 nm

To collect the five consecutive OCT frames with certain phase shift, a piezo translator is employed in the reference arm to provide minor shift of optical path length. An optical path length shift with as small as λ/4 doesn't change the actual depth of the OCT image but change the phase of the fringe spectra by π/2. By moving the reference arm reflective mirror 4 times with a optical path shift of λ/4 at each time, five consecutive acquisitions of the OCT frames could be done. Although this full-range technique is straightforward, it requires five consecutive acquisition, which increases the data acquisition time and size by 5 times. Also, it is not suitable to detect the sample dynamics with five consecutive acquisition with a manual control of the piezo translator (i.e. Doppler OCT). The main drawback of this approach is that any motion of either the reference mirror or sample by as little as λ/10 would totally mess up the phase reconstruction. Thus, it couldn't work for any *in vivo* OCT applications.

Instead of using a piezotranslator to provide a minor optical path delay, the manual phase shift could also be achieved by small tilting of the reference mirror off the axis, similar to a holographic setting [128-130]. The sample and off-axis reference beam would merge at the CCD camera with a small tilting angle. This approach avoids the mechanical scanning of the piezotranslator for phase shifting. However, the whole system, including the detection unit, has to be set up in the free space to allow the small tilting angle at the detection unit, yielding the complex alignment of the system.

The next category of full-range detection relies on the phase modulation, utilizing acousto-optic frequency shifter (AOFS) or electro-optic frequency shifter. AOFS was first introduced by Yun et al. to resolve the ambiguity of OCT images and their complex conjugates [131]. Two AOFSs were placed in the sample arm and reference arm, respectively, to balance the achromatic dispersion. A frequency shift difference between reference and sample arm was introduced by operating the two AOFSs with slightly different frequency shifts, which yielded the shifting of the images to either positive plane or negative plane (See **Figure 4.2**). By carefully calibrate the frequency shift, the whole image could be rendered without the conjugate ambiguity. This method worked pretty well for the swept source system since the detected frequencies of the fringe is on the order of MHz, which could be easily controlled by tunable AOFSs (Brimrose) that usually operated at MHz frequencies. Similar approach had been applied in the study by Zhang et al. [132],where electro-optic modulator was used to provide the carrier frequency. Maheshwari et al. also demonstrated a similar complex conjugate removal SS-OCT setup running with external k-clock [133]. However, we should mention that, although the complex conjugate ambiguity, which meant the overlap between the image and its complex conjugate, had been resolved, the total imaging range did not increase. The carrier frequency had to be set that after shifting, OCT image and its complex conjugate were fully separated. After that, the plane including the complex conjugate signals would be discarded by either heavyside function [132]or band pass filters [133] Second, if the total imaging range or coherence length was not long enough, part of the OCT image would be shifted out of the imaging depth after the frequency

shifting. Also, the image quality would be affected when employing this method in SD-OCT, due to sensitivity roll-offs.

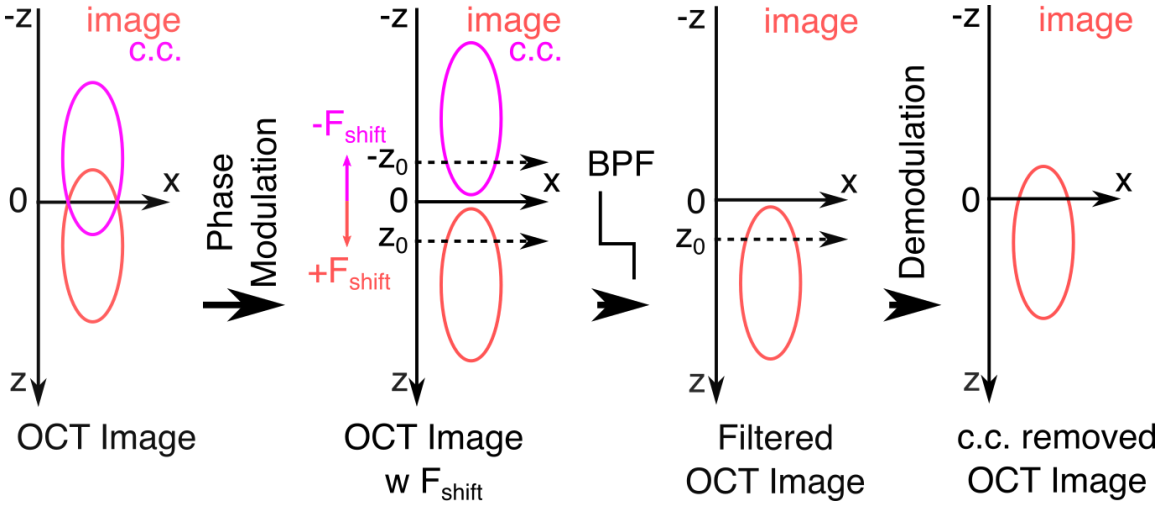

Figure 4. 2 Illustration of phase modulation on complex conjugate removal for FD-OCT.

Efforts were made to combine the phase modulation method with the acquisition method from the phase-shifting approaches to implement the full range detection for SD-OCT. Gotzinger et al. utilized the electro optic phase modulator in the reference arm and applied a two-frame method to collect consecutive two A-scans with 90° phase shift [134]. The phase modulator was synchronized with a frequency set to be half of the camera speed. Bachmann et al. combined the AOFS approach with the 4 frame method to collect the consecutive four A-scans with a phase increment of $\pi/2$, which was similar to quadrature detection [135].The camera speed needed to be 4 times of the beating frequency, which was the frequency shift difference between the sample arm and reference arm. Regarding to these approaches, as long as the camera speed was fast enough and sample motion was stable enough ($<\lambda/4$ in twice the camera exposure time), the full-range image quality could maintain.

Another feasible full-range technique to reconstruct the phase term of the complex signal was to directly detect the in-phase and quadrature signals in different channels. This technique had the advantage that no additional synchronized phase modulation was required in the reference and sample arm, which required a careful calibration of the modulation frequency. Also the in-phase and quadrature signals were collected simultaneously, which removed the chance of phase fluctuation due to different axial line acquisitions, i.e. 2, 4, 5 frame methods. Also, the reconstruction of the complex interference signals was straightforward. After

the in-phase and quadrature components of spectral fringe signal were digitized and retrieved, the complex spectral fringe could be reconstructed by [121, 137]:

$$\hat{I}(k) = I_I(k) + iI_Q(k) \tag{4.11}$$

Thus, the reconstructed complex conjugate removed OCT image after IFT could be expressed in the same way as formula (4.8). Dual detection was first realized in SD and SS-OCT system with a 3×3 coupler, instead of 2×2 coupler in regular FD-OCT system [139]. Two of the output ports were connected to the reference arm and sample arm, respectively. The two ports other than the incident port were connected to the two detectors. Interference signals received from these two detectors were used to reconstruct the signals. The only concern for this method was that, the phase difference between the two received signals was, most likely, not 90°. Calibration was required to determined the phase difference between these two channels. Also, the amplitudes of the in-phase and quadrature signals (corrected from the second channel signal), might not be the same, which would result in small residual complex conjugate signals in the image. A free space dual detection setup in 1300 nm wavelength range was demonstrated by Lee et al., using a polarization beam splitter (PBS) to split the interference signal in two orthogonal states into two channels [136]. By carefully shifting and rotating the PBS, a phase difference of π/2 between these two channels were created, yielding both in-phase and quadrature detection of the signal. The only concern was that the manual alignment of the PBS had to be pretty accurate. A silicon photonic integrated circuit based detection unit for SS-OCT was also demonstrated to receive both in-phase and quadrature signals for a fiber-based system in the 1550nm wavelength range [137]. The key component in this detection unit was the 90° optical hybrid. The sample and reference signals were first split by the PBSs into two orthogonal states, respectively. The signals of the same orthogonal states from both sample and reference arm would enter the 90° optical hybrid and interfere. Output of the 90° optical hybrid had two in-phase channels going into one balanced receiver and two quadrature channels going into the second balanced receiver. In such case, the simultaneously balanced detection of both in-phase and quadrature signals could be easily achieved. Although the method to use of the 90° optical hybrid to reconstruct the complex interference signal was pretty straightforward, the option

for a commercial 90° optical hybrid other than the telecom band (1550 nm), i.e. 1300 nm, 1060 nm, was not readily available. Custom 90° optical hybrid in free space could be built, similar to the setup described in Lee et al., with a proper polarization control. Any conversion of the light transmission in the fiber and the free space would introduce coupling loss. Building a custom 90° optical hybrid with the fiber-based components, including polarization maintaining (PM) fibers, polarization controllers and PM fiber couplers, would be also difficult. Several concerns were involved in the construction. First, the optics axis of the 2×2 PM fiber-based coupler mixing the reference and sample arm signals was unknown, which made it hard to control the incident polarization state of the reference and sample signals in regard to the optics axis. Second, the current PANDA PM fiber has a better performance to maintain one linear polarized state. However, the option for the PM fiber to maintain transmission of the circularly polarization state with low loss was limited, let alone the corresponding fiber-based component. In order to accurate calibrate the input and output amplitude and phase of the fiber-based 90° optical hybrid, polarimeter was required, which was expensive. To resolve this, Vakoc et al. provided a calibration method to calculate corrected in-phase and quadrature signals based on a statistical approach [141]. In his setup, the 2×2 PM fiber-based coupler was replaced by a polarization beam combiner plus a 50/50 fiber coupler (not PM). The detected dual channel would have an amplitude ratio α and phase difference ε, which could be expressed as[141]:

$$\alpha = \frac{\sigma_2}{\sigma_1} \tag{4.12}$$

$$\sin(\varepsilon) = \frac{\sigma_2^2 + \sigma_1^2 - \sigma_{(2)-(1)}^2}{2\sigma_2} \tag{4.13}$$

Where σ_1 represented the standard deviation of the signal from in-phase channel $S_1 = I\sin(\phi)$ and σ_2 represented the standard deviation of the signal from off-phase channel $S_2 = \alpha I\cos(\phi-\varepsilon)$.

$$\sigma_1 = \mathrm{std}(S_1) = \mathrm{std}(I\sin(\phi))$$

$$\sigma_2 = \mathrm{std}(\mathrm{S}_2) = \mathrm{std}(\alpha \mathrm{I}\cos(\phi - \varepsilon))$$

(4.14)

$\sigma^2_{(2)-(1)}$ was the variance of the subtracted signals between these two channels:

$$\sigma^2_{(2)-(1)} = \mathrm{var}(S_1 - S_2) = var(\mathrm{I}\sin(\phi) - \alpha \mathrm{I}\cos(\phi - \varepsilon))$$

(4.15)

To retrieve the α and ε, a mirror was placed at the focal plane while the reference arm was displaced with a certain optical path difference. Next, a piezo translator was used to move the reference arm mirror slowly over a few micrometers with a slow triangular waveform (i.e. 30 Hz). Signals from both channels were recorded for a few seconds to collect enough data for statistical analysis. After the α and ε were calibrated, quadrature representation could be expressed as[141]:

$$S_Q = \frac{S_2}{\alpha \cos(\varepsilon)} - \tan(\varepsilon)\, S_1$$

(4.16)

$$S_I = S_1$$

(4.17)

With the calculated quadrature signal, the complex representation of the signal could be retrieved. Note that the fiber-based polarization part was sensitive to the surrounding environment, i.e. temperature fluctuation. Proper shielding was required to guarantee the calibrated α and ε at each time would be valid for the following measurement for over 60 min. In another study, they proposed the second source of the error, RF errors, which originated by the path length mismatches and non-flat electronic RF filtering, and became significant with multi-hundred MHz signal ranges and high sampling rate [142]. A detail calibration step was provided to correct the RF errors.

Several interesting approaches have been introduced to resolve the complex conjugate ambiguity as well. One approach utilized coherence revival to resolve the complex conjugate ambiguity, where the interference signal could be detected again in other imaging depths with an optical path difference of an integer multiple

of the laser cavity length [146].The coherence revival was inherent to the type of the tunable laser. Another approach, called dispersion encoded full range (DEFR) approach, deliberately introduced a dispersion mismatch between the sample arm and the reference arm to broaden the complex conjugate image [143]. After iterative numerical correction, the complex conjugate could be suppressed while maintaining a sharp OCT images. This approach worked best in 800 nm and 1060 nm OCT systems since large dispersion mismatch could be achieved. The main concern would be the computational complexity due to the iterative optimization scheme, which could be accelerated with the graphic processing units (GPU) [144, 145].

The last category of full range detection techniques introduced in the session would be the time-dependent phase-modulation approach (along the B-scan). Instead of phase modulation for each single axial scan, a periodic phase modulation of the reference beam was performed while the beam was scanning along the transverse direction. No repeated A-scans were performed in this case. Since the phase modulation and the intensity fluctuation due to the scanning were mixed together, the frequency of the intensity fluctuation (speckle changes) would be shifted by a carrier frequency introduced by the phase modulation. The signals would be demodulated by analyzing the whole B-scan of the OCT image and applying a Hilbert transform along the transverse direction for each wavenumber.The modulated signal containing the object image would be shifted away from the zero spatial frequency. With a high-pass or band-pass filter, the complex representation of the interference signal could be reliably reconstructed. The time-dependent phase modulation method was first introduced by Yasuno et al., called BM scan [147]. The phase modulation was introduced by using a piezotranslator in the reference arm and its frequency was set to be 1/32 of the camera speed. The moving distance was set so that for neighbouring A-scans, the phase shift was $\pi/2$, which was similar with the 4-frame acquisition approach [135]. The key difference was that a continuous scanning pattern and continuous phase modulation were employed instead of a step-wise scanning and phase modulation pattern. Wang et al. also utilized the piezo translator that synchronized with the OCT frame acquisition to introduce a carrier frequency in the OCT B-scan interferogram [148]. Makita et al. and Yamanari et al. also demonstrated the full range detection for SD and SS-OCT systems with this technique, using the EOM as the phase modulator [149, 150]. Similar with the conventional phase modulation approach, the phase modulation frequency and amplitude had to be designed properly so that the Hilbert transformed interference signals with a carrier frequency would be sufficiently shifted away from the zero frequency.

Instead of phase modulator, the time-dependent phase modulation could be also introduced via the galvanometer [151-153]. This approach, named galvo-based phase modulation technique in this chapter, was selected to employ in our OCT system. Details of this full range technique would be described in the next section.

4.4 Principles of Galvo-based Phase Modulation Full-range Technique

In this section, we would describe the principles of galvo-based phase modulation full-range technique. The idea originated from the work of Wojtkowski et al., utilizing the modulation of the optical paths between reference and sample arm to realize phase modulation[125]. The time-dependent phase modulation and digital reconstruction of complex signals utilized the similar idea introduced by Yasuno et al and Wang et al. [147, 148]. Instead of modulating the phase in the reference arm with the periodic movement of the piezo translator [147]or periodic control of the electro-optic modulator [149], the phase was modulated in the sample arm. By shifting the incident beam off the pivot axis of the fast mirror of the galvanometer, changes of the optical path length could be created during the transverse scanning, yielding constant phase shifts between neighboring axial scan. In the post processing, a Hilbert transform or equivalent method would be applied to digitally reconstruct the analytic complex signals that could resolve the complex conjugate ambiguity. The modulation frequency would be the same as the frame rate since both transverse scanning and phase modulation were realized by the Galvo simultaneously. The major advantage of this full-range technique was that no additional hardware was employed in the system, yielding a simpler system configuration and alignment. The same full range technique was introduced by Baumann et al, Leitgeb et al and An et al at almost the same time with the SD-OCT system [151-153]. To sum up, we listed two key points of galvo-based phase modulation technique:

1) Phase modulation is applied during the B-scan by offsetting the beam on the galvo mirror to introduce a changing phase term $\boldsymbol{\Phi}(\boldsymbol{x})$.

2) Digital reconstruction of complex interference signals is performed along the transverse direction, via Hilbert Transform or equivalent methods.

4.4.1 Phase Modulation introduced by the Galvanometer

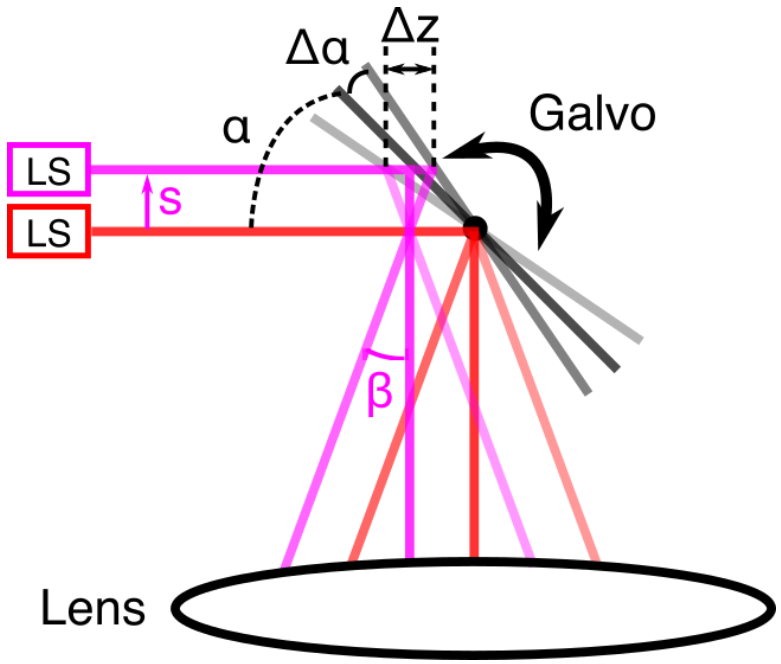

Figure 4. 3 Illustration of the galvo-based phase modulation. Three mirror positions were presented in different transparency level. Red light indicated the original light beam without shifting. Reflection beams in three transparency level indicated the reflection direction corresponding to different mirror position. Magenta light indicated the shifting incident beam off the pivoting point by s (distance), with different transparency level indicating the reflected beams in different orientation. As a consequence, the sample arm optical path length would change by Δz when the galvo is scanning from one side to the other. α, Δα and β indicate the mirror reflection angle, rotating angle and beam scanning angle, respectively.

Figure 4.3 showed the illustration of the effect of the beam shifting off the pivoting point of the galvanometer. Three mirror positions were presented in different transparency level, with mirror rotation angles of 0 (dark), +Δα (normal) and -Δα (light). Red lines showed original light path with the beam incident on the pivoting axis. Reflection beams in three transparency level indicated the reflection direction corresponding to different mirror position, with a scanning angle from -β to β. From the reflection law we can get:

$$\beta = 2\Delta\alpha \tag{4.18}$$

The unmodulated spectral fringes could be expressed as:

$$I(k_z, x) \sim S(k_z, x) \sum_n (\sqrt{\alpha_r \alpha_n}\, cos(2z_n k_z))$$

(4.19)

Magenta light indicated the offset light path, of which the incident beam was offset from the pivoting axis by s (distance), with different transparency level indicating the reflected beams in different orientations. As a result, the sample arm optical path length (OPL) would change by Δz when the galvo-mirror is scanning from one side to the other.

The OPL change would be expressed as, at the first order, with a small angle approximation:

$$\Delta z \approx 2\frac{s}{\sin\alpha}\cdot\Delta\alpha\cdot\frac{1}{\sin\alpha} = \frac{s\beta}{\sin^2\alpha}$$

(4.20)

In a general galvo setting, α = 45°. $\sin^2\alpha = 1/2$. Thus

$$\Delta z \approx 2\beta s$$

(4.21)

The offset of the light path on the galvo mirror will introduce a phase modulation term $\Phi(x)$, which is related to the transverse scanning parameter (we expressed it as x to indicate that this parameter is related to the scanning direction x):

$$I(k) \sim S(k)\sum_n (\sqrt{\alpha_r\alpha_n}\cos(2z_n k_z + \Phi(x)))$$

(4.22)

Note that we can use the index of the A-scan in the B-scan to represent the transverse scanning parameter, which is denoted as m. Thus, $\Phi(x)$ can be expressed as $\Phi(m)$. The total number of A-scans in a B-scan is denoted as M.

The total phase change in a B-scan could be derived as:

$$\Phi(M) = 2k_z\Delta z = \frac{4\pi\cdot s\cdot 2\beta}{\lambda} \sim \frac{4\pi\cdot s\cdot x_M}{\lambda\cdot F}$$

(4.23)

Where x_M represented the transverse (lateral) scan range and F is the back-focal length of the objective.

We could also define a equivalent carrier frequency k_x, which was the phase change between neighbouring axial scans. Since:

$$\Phi(M) = k_x M \tag{4.24}$$

We could get:

$$k_x = \frac{\Phi(M)}{M} \sim \frac{4\pi \cdot s \cdot x_M}{\lambda \cdot F \cdot M} \tag{4.25}$$

We can see that the equivalent carrier frequency k_x is proportional to the offset distance s and transverse scan range x_M (which is determined by the input voltage to the galvo mirror), and inversely proportional to the number of axial scans (M) in a B-scan. With a properly value set of s, x_M and M, the amount of the phase modulation could be controlled.

4.4.2 Digital Reconstruction of the Complex Representation of OCT Interference Signals

Figure 4.4 illustrates the flow chart of the post-processing procedure for the galvo-based phase-modulation technique. **Figure 4.4 A** shows the post-processing procedure for the standard OCT system. To reconstruct complex interference signals, additional steps re performed, which are included in the magenta rectangular box (**Figure 4.4 B**). In the first step, a FFT is performed on the B-frame raw data along the transverse scanning direction (X direction) for each wavenumber k_z. Next, a filter is applied on each row to filter out half of the spectra in the k_z – k_x domain. The filter can be a high-pass filter, band-pass filter or a Heaviside function. After this step, an inverse FFT is performed along the transverse direction to convert the OCT B-frame from k_z-k_x domain back to k_z-x domain to reconstruct the analytic complex representation of the OCT interference signal. Afterwards, the rest of the standard OCT processing procedure can be performed. Digital reconstruction of complex signals could be performed either right after the DC subtraction [151] or after dispersion compensation for the SD-OCT setup. However, since the digital reconstruction can only be applied to the AC term of the interference signals [151], DC subtraction is required prior to digital reconstruction of

complex signals. We should note that, If a Heaviside function is applied as a filter, the whole procedure in the magenta box is equivalent to reconstruction of complex signals via the Hilbert transform, which is mentioned by Yasuno et al. and Wang et al. [147, 148].

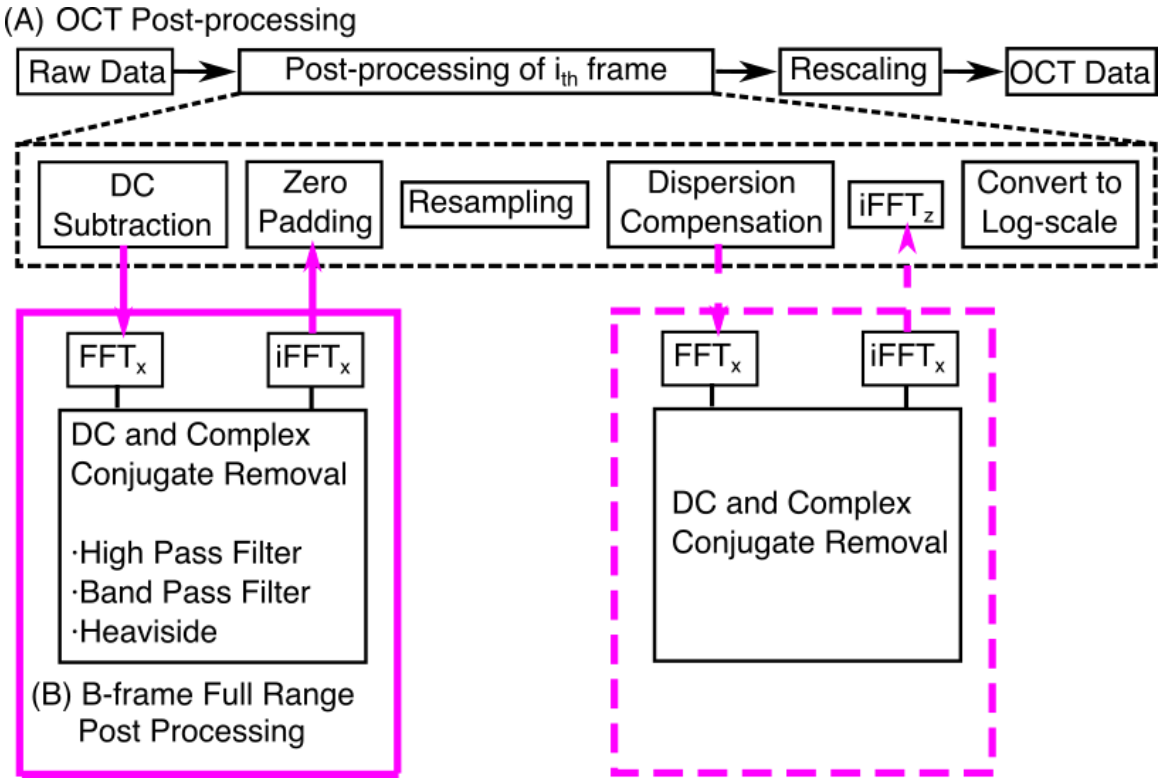

Figure 4. 4 Flow chart of the post-processing procedure of galvo-based phase modulation. (A) shows the standard post-processing procedure for OCT image. To digitally reconstruct analytic complex representation of interference signals, additional steps, included in the magenta rectangular box, are performed (B). These additional steps could be processed either right after the DC subtraction (in most literature) or after dispersion compensation for the SD-OCT system. If a Heaviside function is applied as a filter, the whole procedure in the magenta box is equivalent to reconstruction of complex signals via the Hilbert transform.

4.5 Simulation of the Full-range Technique

We performed a simulation to illustrate the procedure of the digital reconstruction of complex representation of interference signals. To begin with, we designed the simulated function of interference signal along each axial scan as:

$$S(k_z) = real(I \cdot \exp(-\alpha k_z^2) \cdot \exp(-ik_z z));$$

(4.26)

Where I was the amplitude, $\exp(-\alpha k_z^2)$ simulated the Gaussian profile of the interference signal and the last term $\exp(-ik_z z)$ simulated the phase change along the axial direction. In the simulation, I was set to a constant number, 10,000, α was set to 2 to control the shape of the Gaussian profile interference signal and z was set to be 8π. k_z was set as a normalized vector starting from -1 to 1. Since the camera only detected the intensity signals, we obtain the real part of the function to be the simulated interference signal. The number of pixels along the z and x direction were set to 401 and 400, respectively. This function could simulated the case of a single reflector, i.e. a mirror, without phase modulation. To simulated interference signals from a single reflector with phase modulation along the transverse direction, an additional term $\exp(-ik_x x)$ was added to the formula (4.26), yielding the simulated function expressed as:

$$S = real(I \cdot \exp(-\alpha k_z^2) \cdot \exp(-ik_z z) \cdot \exp(-ik_x x));$$

(4.27)

In the simulation, k_x was set to be 0.25π and the x value ranged from -199 to 200.

Figure 4.5 was the simulation result showing the effect of phase modulation during the digital reconstruction of complex signals. With no phase modulation (**Figure 4.5 A**), FFT result along the x direction (FFT_x) showed a single peak at the zero spatial frequency ($k_x = 0$) in **Figure 4.5 B**. This could be explained in expresssions by deriving Fourier transform (FT) of expression (4.19), yielding the result to be:

$$I(k_z, k_x) \propto S(k_z, k_x) \otimes \sum_n \sqrt{\alpha_r \alpha_n} \delta(k_x - 0)$$

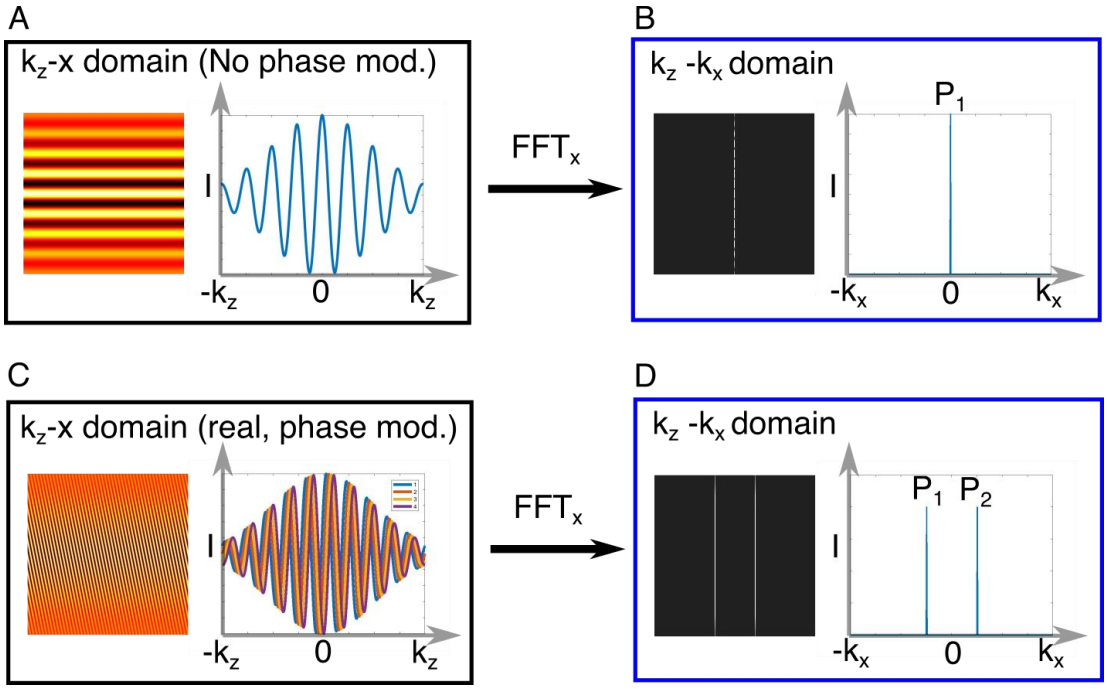

Figure 4. 5. Simulating the effect of phase modulation during digital reconstruction.The color of the surrounding rectangle indicated different domains. Without phase modulation, FFT result along the x direction (FFT$_x$) showed a single peak at the zero spatial frequency (k_x = 0), while the FFT$_x$ of the phase modulated signals showed two peaks shifted away from the zero spatial frequency.

(4.28)

The delta function $\delta(k_x - 0)$ indicated the existence of the single peak at k_x = 0. In comparison, FFT result of phase modulated interference signals showed two peaks shifted away from the zero spatial frequency in **Figure 4.5 D**. In expressions, FT of expression (4.18) along the x direction, with $\Phi(x) \sim x \cdot k_{x,n}$, yielded:

$$I(k_z, k_x) \propto S(k_z, k_x) \otimes \sum_n \sqrt{\alpha_r \alpha_n} (\delta(k_x + k_{x,n}) e^{-2iz_n k_z}$$

$$+ \delta(k_x - k_{x,n}) e^{+2iz_n k_z})$$

(4.29)

The first convolution term $S(k_z, k_x) \otimes \sum_n \sqrt{\alpha_r \alpha_n} \delta(k_x + k_{x,n})\, e^{-2iz_n k_z}$ and second convolution term $S(k_z, k_x) \otimes \sum_n \sqrt{\alpha_r \alpha_n} \delta(k_x - k_{x,n}) e^{+2iz_n k_z}$ indicated the complex conjugate and image terms, which was shown as two mirrored peaks (P_1 and P_2) in **Figure 4.5 D**. In the simulation, k_x was set to be 0.25π, yielding

the shifted distances of these two peaks to be 1/8 of the full bandwidth of spatial frequency away from zero spatial frequency.

Figure 4.6 showed the simulation result of the post-processing of phase-modulated interference signals. Since two phase terms as a function of z and x coexisted, the interference signals in k_z - x domain appeared as tilting stripes (left panel of **Figure 4.6 A**), with the continuously shifting fringe pattern for different axial scans. Interference signals of four consecutive A-scans with π/4, π/2, 3π/4 and π phase changes were shown in the right panel of **Figure 4.6 A**, showing the shifting fringe pattern. A direct inverse FFT of the phase-modulated signals along the z direction ($iFFT_z$), without digital reconstruction of complex interference signals, yielded the mirrored images, with the image term located at 8 pixels away from the zero delay and complex conjugate term. at -8 pixels (**Figure 4.6 B**). In expressions, IFT of expression (4.18) along the z direction, with $\Phi(x) \sim M \cdot k_{x,n}$, yielded:

$$I(z,x) \propto S(z,x) \otimes \sum_n \sqrt{\alpha_r \alpha_s(z,x)} \left(\delta(z - z_n) \exp\left(-iMk_{x,n}\right) + \delta(z + z_n) \exp\left(iMk_{x,n}\right)\right) \tag{4.30}$$

In the expression (4.30), the additional exponential terms $\exp\left(-iMk_{x,n}\right)$ and $\exp\left(+iMk_{x,n}\right)$ were multiplied to the image and complex conjugate terms, respectively, which lead to the modulated fringe pattern for different A-scans.

To realize the digital reconstruction of complex interference signals, first, a FFT along the x direction was performed, leading to two shifted lines in the 2D image in the k_z – k_x domain (**Figure 4.6 C**). **Figure 4.6 C** was the same result as **Figure 4.5 D**. After band pass filter (BPF), the complex conjugate term in the left half of the plane and the DC term at the zero spatial frequency would be digitally removed (**Figure 4.6 D**), while the amplitude of the image term would be doubled. In the expression, the first convolution term $(k_z, k_x) \otimes \sum_n \sqrt{\alpha_r \alpha_n} \delta\left(k_x + k_{x,n}\right) e^{-2iz_n k_z}$ of expression (4.29) was removed, yielding:

$$I(k_z, k_x) \propto S(k_z, k_x) \otimes \sum_n \sqrt{\alpha_r \alpha_n} (\delta\left(k_x - k_{x,n}\right) \exp(2iz_n k_z))$$

(4.31)

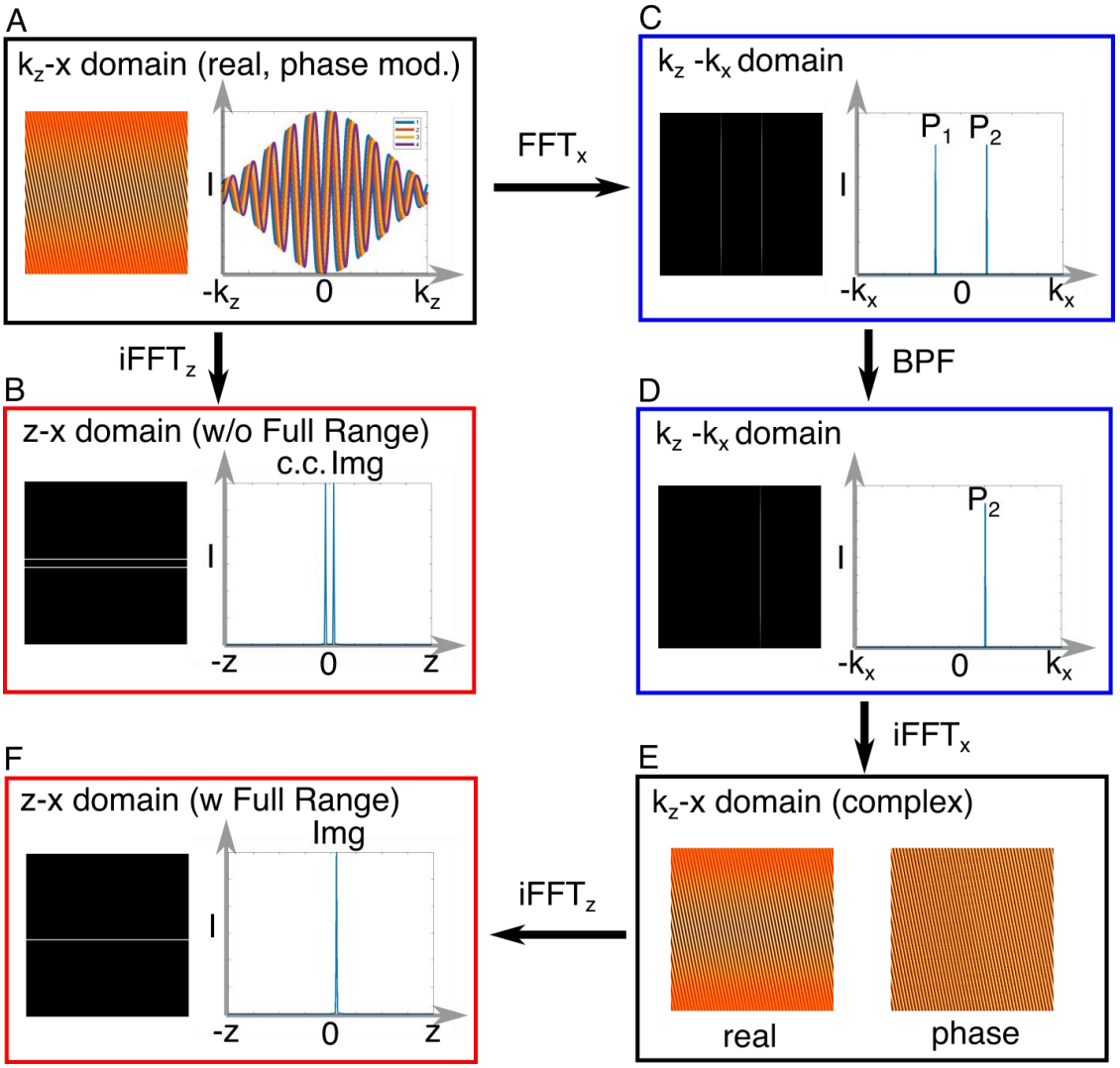

Figure 4. 6 Simulation of the post-processing of phase-modulated interference signals. The color of the surrounding rectangle indicated different domains. Since the phase modulation existed in both z and x direction, the original interference signals in 2D frames looked like tilting stripes. Interference signals of four consecutive A-scans with $\pi/4$, $\pi/2$, $3\pi/4$ and π phase changes were shown. A direct iFFTz yielded a Hermitian representation, with both image and complex conjugate terms. Direct FFT_x lead to two peaks along the x direction. After band pass filter (BPF) and iFFTx, a complex representation of the interference signal was reconstructed, yielding a complex-conjugate-free image after the $iFFT_z$.

Then, the inverse FFT was performed for each wavenumber k_z along the x direction, yielding the reconstructed complex representation of 2D interference signals, with the real part of the complex interference signal the same as the original image (**Figure 4.6 E**). The simulated function of complex representation of 2D interference signals could be expressed as:

$$I(k_z,x) \sim S(k_z,x) \sum_n \left(\sqrt{\alpha_r \alpha_n} \exp\left(2iz_n k_z + iMk_{x,n}\right)\right)$$

(4.32)

After the inverse FFT along the z direction, the complex-conjugate-free 2D image of the single reflector could be reconstructed (**Figure 4.6 F**). The simulated function of this sub-figure was expressed as:

$$I(z,x) \propto S(z,x) \otimes \sum_n \sqrt{\alpha_r \alpha_s(z,x)} \delta(z - z_n) \exp\left(-iMk_{x,n}\right)$$

(4.33)

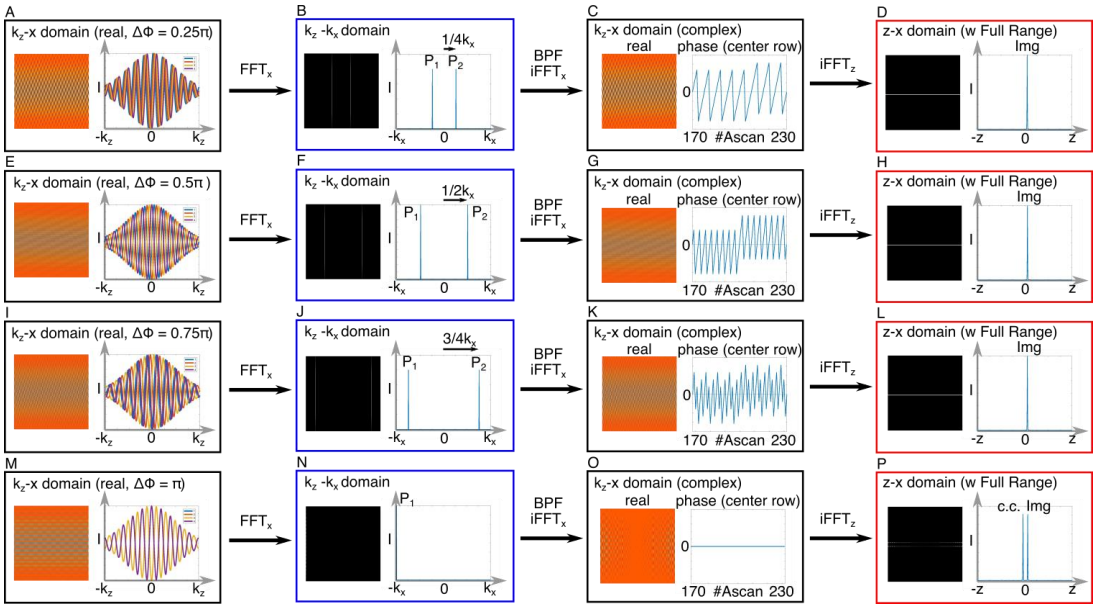

Figure 4. 7 Simulation of the post-processing of phase-modulated interference signals with different amounts of phase modulation along the transverse direction. The color of the surrounding rectangle indicated different domains. Phase modulated interference signals with the phase change of π/4, π/2, 3π/4 and π between neighbouring A-scans were simulated and shown in different rows. The interference signals next to original images showed the interference signals from 1st to 4th A-scans. The Doppler shifts in the kz - kx domain were indicated with black arrows in the 2nd column. After the digital reconstruction, the phase curves along the center horizontal line, from 168th to 232nd pixels (32 pixels from each side of the center column) was plotted. The final results were shown in the 4th column in the x-z domain, with the 1st A-scan plotted.

We further simulated the post-processing of phase-modulated interference signals with different amounts of phase modulation along the transverse direction. Simulation results were shown in **Figure 4.7**. With the abovementioned simulation function, we could set the phase change between the neighbouring axial scans to

be $\pi/4$, $\pi/2$, $3\pi/4$ and π, with the comparison of post-processing results shown in different rows in **Figure 4.7**. Intermediate results after each processing step were shown in different columns in **Figure 4.7**. The plots of interference signals of the first four axial scans (1st to 4th) could show the different shifting pattern of interference signal correspoinding to different amounts of phase modulation (**Figure 4.7 A, E, I, M**). After the FFT along the x direction, various Doppler shifts could be clearly observed in the 2D images and 1D plots in the $k_z - k_x$ domain (**Figure 4.7 B, F J, N**). We could easily link the amount of horizontal shift in the 2D images in the $k_z - k_x$ domain with the phase change between neighbouring axial scans. A horizontal shift of ¼ k_x corresponded to a phase shift of $\pi/4$; 1/2 k_x corresponded to $\pi/2$; 3/4 k_x corresponded to $3\pi/4$. A π phase shift indicated a horizontal shift of k_x, which moved the peak to the edge of the 2D image. In such case, there would be ambiguity which side of the edge the shifted interference signal located, yielding a failed reconstruction of the complex signal. After the band pass filter and inverse FFT along the x direction, the complex representations of the interference signals with different phase modulations were presented in **Figure 4.7 C, G, K, O**. The phase curves of the pixels in the center row from 168th to 232nd pixels (65 pixels in total) were plotted in the right panel of **Figure 4.7 C, G, K, O**. Phase wrapping was more frequently observed as the phase shift increased from 0.25π to $0.75\ \pi$. In the case of π phase shift, a failed reconstruction was clearly observed with no phase changes along the center row. After the inverse FFT along the z direction, successful removals of complex conjugate terms were clearly observed in **Figure 4.7 D, H, L** except the case with a phase shift of π in **Figure 4.7 P**. The simulation results indicated that, to achieve a successful reconstruction of the complex representation of interference signals for full range imaging, the phase shift must avoid the number of integer multiplication of π.

4.6 Modification of the SD-OCT System for Galvo-based Full-range Applications

The detailed configuration of the SD-OCT was described in Chapter 2. **Figure 4.8** showed the modification of a standard SD-OCT system to a galvo-based full range SD-OCT system. The collimator part of the sample arm was mounted on a 1D translation stage (**Figure 4.8 B**), which could move in the vertical direction and control the beam offset on the galvo mirror. Also, we could place a lens pair in between the collimator and the galvo to reduce the beam size to be ~2.5 mm.

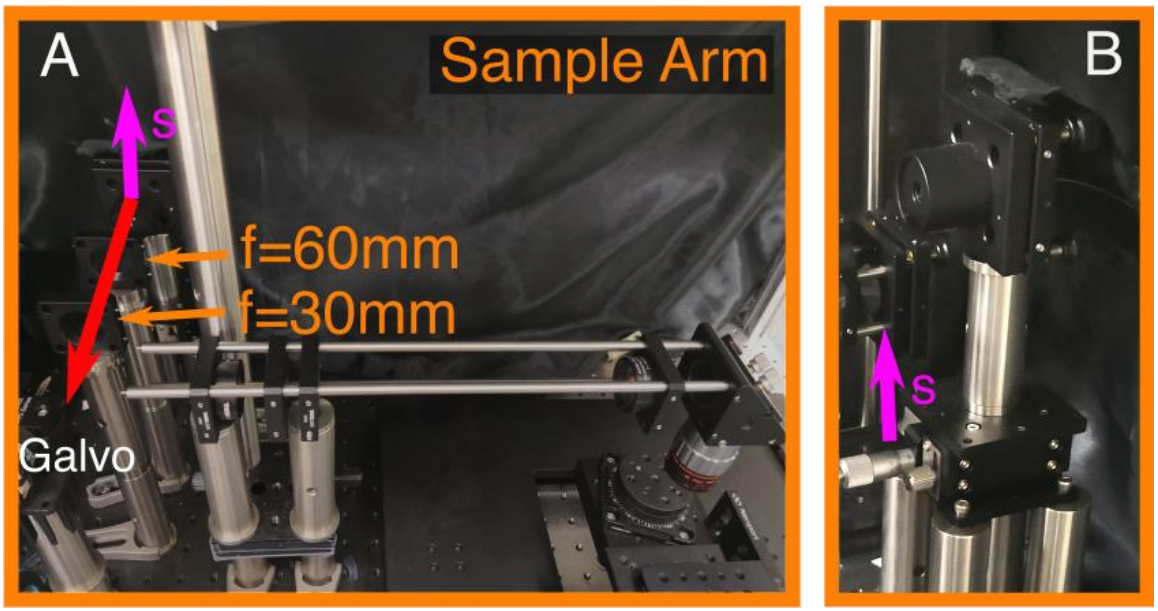

Figure 4. 8 Modification of a custom SD-OCT system to realize full-range imaging.

4.7 Results of Full-range Imaging with the SD-OCT System

To demonstrate the feasibility of the galvo-based phase modulation full-range technique, we utilized the modified SD-OCT system to obtain OCT images of a Scotch tape. Results of the demonstration of full-range technique with SD-OCT system was shown in **Figure 4.9**. The line-scan camera was operating at ~92 kHz mode, with the actual A-scan rate of ~88.8 kHz. Each B-scan consisted of 600 A-scans (M = 600). The scan voltage was set to 1V, corresponding to an actual scan range of ~1.67 mm (x_M = 1.67). To test the effect of different phase modulations, we changed the beam offset s and set it as ~0 mm, ~1 mm, ~2 mm and ~3 mm from the pivoting axis. Effects of phase modulation was evaluated in the 1D plots of the FFT_x spectra of the B-scan raw data across the central row, which were shown in **Figure 4.9 A-D.** The corresponding full-range OCT images of the Scotch tape with varied beam offsets were shown in **Figure 4.9 E-H**. The Doppler shift was not observed in **Figure 4.9A**, yielding the co-existence of both tape image and its complex conjugate term, with some overlap close to zero delay (**Figure 4.9E**). With a small Doppler shift (**Figure 4.9B**), the complex conjugate term was suppressed. However, since the image and complex conjugate term in FFT_x spectra were not fully separated with a small Doppler shift, we could observe some residue complex

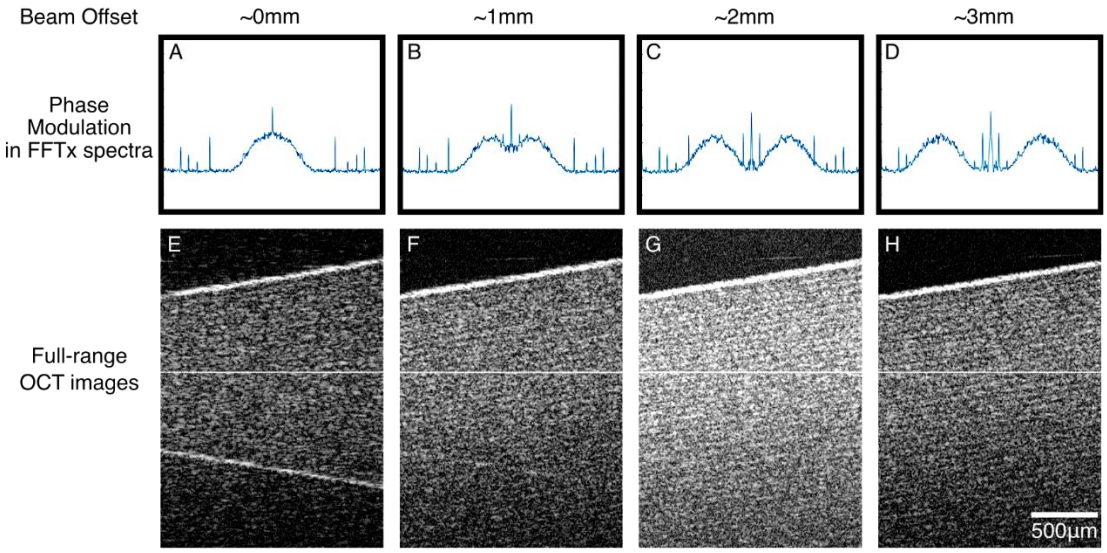

Figure 4. 9 Demonstration of full-range technique with SD-OCT system. (A-D) showed the amount of phase modulation in Fourier transformed fringes along the central row, with ~0mm (A), ~1 mm (B), ~2 mm (C) and ~3 mm (D) beam offset on the galvo-mirror. (E-H)Corresponding full-range OCT images showed the effectiveness of complex conjugate removal.

conjugate signals of the bright tape surface at the mirrored location (**Figure 4.9 F**). With a large Doppler shift with increased beam offsets to fully separate the image and complex conjugate terms in FFT_x spectra (**Figure 4.9 C-D**), the complex conjugate term in the full-range OCT images could be completely removed, yielding an increasing imaging range to render multiple layers of the tape up to a depth of ~2 mm below the tape surface (**Figure 4.9 G-H**). Thus, we demonstrated that the galvo-based phase modulation full-range technique was working well with SD-OCT setups.

4.8 Modification of the Fiber-based SDM-OCT System for Full-range Imaging

The galvo-based phase modulation full-range technique could be adopted in SDM-OCT system. To achieve phase modulation, we just need to offset the incident beam on the first galvo mirror in the sample arm of the SDM-OCT system. Since the SDM component/relay lens system and the galvanometer were separated in the sample arm of the SDM-OCT, we could just move the SDM component/relay lens system off the axis of the galvo mirror to create the beam offset. **Figure 4.10** illustrates the modification of SDM-OCT system. The red dash line indicates beam incident on the pivoting axis of the x galvo mirror. The beam offset could be created by simply moving the jack that supported the cage system with SDM component and relay lens in the direction perpendicular to the x galvo mirror axis in the horizontal plane (magenta arrow in **Figure 4.10**).

Since we attached the jack to a rail during the system alignment, we could simply add the spacers in between the jack and the rail to control the beam offset s. Note that the minimum spacer thickness was 1 mm, we could control the beam offsets from ~ 1mm to ~5 mm with an increment of 1 mm.

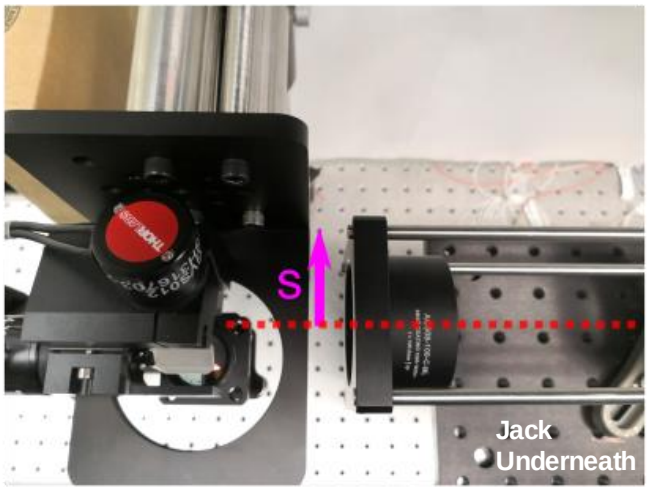

Figure 4. 10 A photograph of the galvanometer of the SDM-OCT system to illustrate how to create the beam offset in the SDM-OCT system.

For single-channel OCT system, only one parallel beam was incident on the galvo mirrors, with its beam size barely changed during the transmission in the galvo system. Thus, the back-focal spot of the 1st relay lens after the galvanometer system was not strictly required to be placed on the x galvo mirror. However, in the SDM-OCT system, the location of the 2nd relay lens (shown in **Figure 4.10**) was critical. After the 2nd relay lens, four collimated beams from different channels would converge on the front focal point of the 2nd relay lens and diverge afterwards. Considering four beams together as an extended source, it had the minimum spot size on the front focal point of the 2nd relay lens and diverged when the four beams move away from the front focal point. Since the beam spot size on the galvo mirror was highly relevant to the performance of galvo-based full-range technique (will be discussed in the following section, or see the reference of Baumann et al. [151]), the front focus point of the 2nd relay lens had to be placed exactly on the first galvo mirror to allow all the collimated beams to converge at the first galvo mirror, yielding optimal full-range imaging quality. Due to the abovementioned consideration of the alignment of the 2nd relay lens, we should be cautious if we intended to swap the fast-axis of the galvanometer. If the fast-axes of the galvo mirrors were swapped, the relative distance between the swapped fast-axis mirror and the 2nd relay lens

needed to be re-adjusted to ensure the converging point of the 4 channels was located at the fast-axis mirror to ensure the minimum beam size.

4.9 Modification of the Post-processing Procedure for the Full-range SDM-OCT System

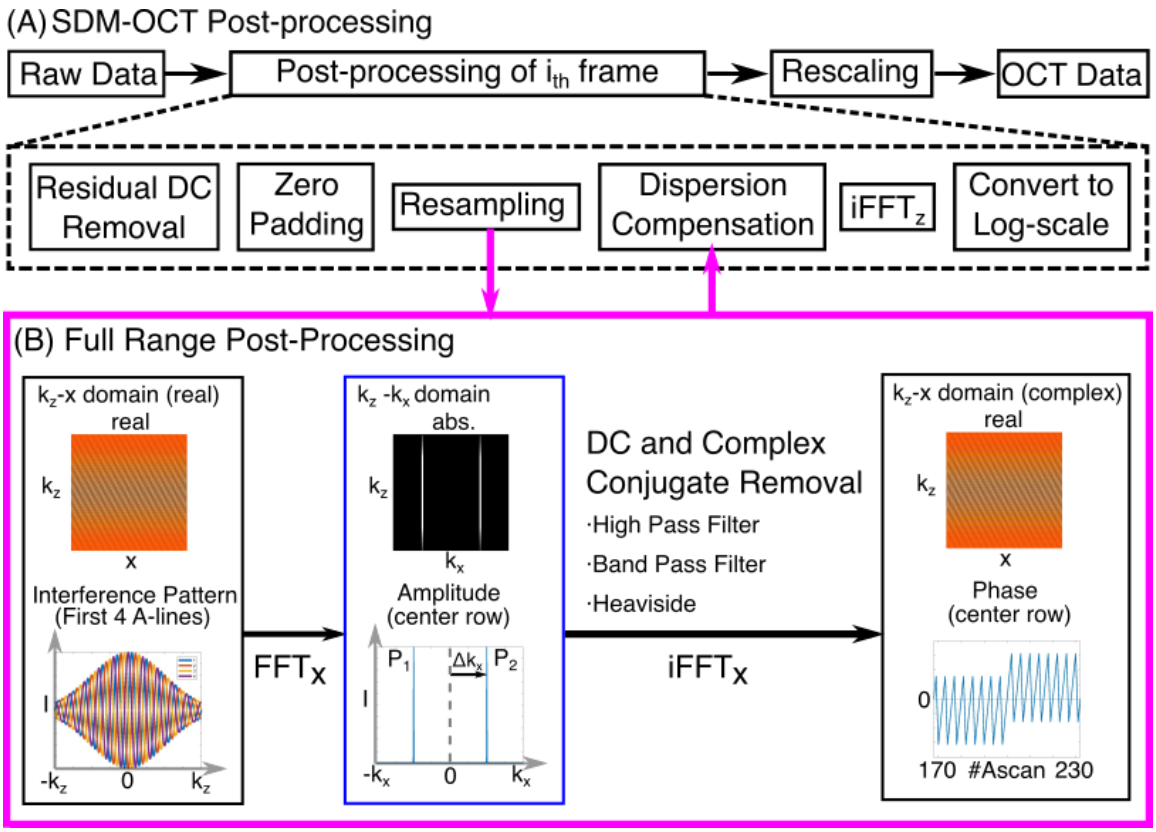

Figure 4. 11 Flow chart of post-processing procedure of full-range SDM-OCT. (A) Standard SDM-OCT post-processing procedure. (B) Additional full-range post-processing procedure.

Figure 4.11 shows the flow chart for the post-processing procedure for the full-range SDM-OCT. As compared to the post-processing procedure for full-range SD-OCT, the digital reconstruction of the complex interference signal requires that the trigger jitter issue was resolved before any digital reconstruction steps, which was rarely observed for SD-OCT systems. So, a proper phase calibration procedure (resampling) was performed prior to the full-range post-processing steps to ensure that the spectral fringes were linear in wavenumber k_z, as well as the wavenumber ranges of the cropped spectral fringes, defined by the two FBG peaks (See Chapter 3), were the same for all the sweeps (A-scans).

4.10 Results of Full-range Imaging with SDM-OCT

4.10.1 Full-range 1x4 SDM-OCT Images of a Mirror

The effect of complex conjugate suppression with the full-range SDM-OCT system was first characterized with a weak single reflector. A mirror was placed at the focal plane of the objective in the sample arm. A neutral density filter with the OD = 2.0 was used to attenuate the back-scattered light from the mirror to ensure the interference signals were not saturated at the detector. A 10 dB SMA fixed attenuator (VAT10+, Mini Circuit) was used after the balanced detector to further attenuate the signal to avoid satuation at the digitizer. The knots of the mirror mounts were tuned to maximize the backcoupling power of all the four beams. In this demonstration, the sampling rate of the digitizer was set to 1.0 GS/s to ensure a total imaging range of >20 mm in air to cover all the 4 images with unnoticable aliasing effects. To realize full-range

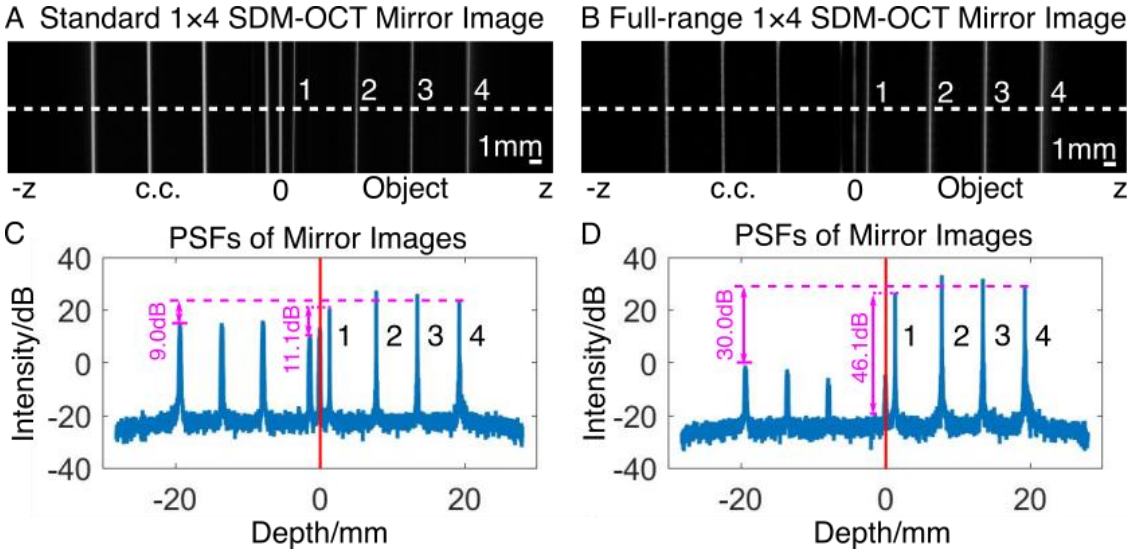

Figure 4. 12: A comparison of SDM-OCT images of a weak single reflector (mirror) with standard and full-range setups. (A) was the four-beam mirror image from a standard 1×4 SDM-OCT system and (B) is the corresponding image from the full-range 1×4 SDM-OCT system. The mirror images from 4 channels and their complex conjugates were indicated. (C) and (D) were intensity profiles across the center rows of Figure (A) and (B). Complex conjugate rejection ratio (in dB) of the 1st and the 4th beams with standard and full-range approaches were indicated, showing the two-step complex conjugate suppression process.

imaging, we set the beam offset to be ~3 mm, transverse scan range to be 1.5 mm (with 3 V input voltage to the fast axis of the galvo mirror), and the number of effective A-scans to be 750 (by cropping the first 50 A-scans due to galvo fly back from a total number of 800 A-scans).

Figure 4.12 showed the results of the mirror image acquired with standard SDM-OCT and full-range SDM-OCT system. **Figure 4.12 A** showed the mirror images from 4 different channels, separated at different

depth ranges. Their complex conjugate terms were also shown in the same image in the negative depth ranges. Due to the dispersion encoding effect [143], the four-beam mirror images became sharp and bright while their complex conjugate terms became broadened and blurry, which yielded a visually brighter peak in the log-scale standard SDM-OCT image. The intensity profile across the central row of **Figure 4.12 A** was plotted in **Figure 4.12 C**, showing a small intensity drop of complex conjugate peaks due to dispersion encoding effect. We employed the parameter, complex conjugate rejection ratio (CCRR) to evaluate the effectiveness of suppression of complex conjugate terms, which was defined as the ratio between the peak intensity of mirror image and the peak intensity of complex conjugate term, calculated as the distance between the mirror peak and the corresponding complex conjugate term in the log-scale intensity profile, and expressed in a unit of dB. CCRR for each beam due to dispersion encoding were characterized from the standard SDM-OCT intensity profile (**Figure 4.12 C**) and shown in the third row of **Table 4.3**. The average CCRR value due to dispersion encoding effect was ~11.2 dB. The center two beams had relative higher suppression ratio of ~12 dB while the 4th beam (farthest one) had ~9.0 dB suppression ratio. Although ~10 dB suppression was achieved, the complex conjugate terms of the mirror in the negative depth ranges remained visible in the intensity profile of the mirror from the standard SDM-OCT.

Table 4. 3 Complex Conjugate Rejection Ratio (CCRR) for Standard and Full-range SDM-OCT

	1st beam	2nd beam	3rd beam	4th beam
Actual depth from zero delay (in air)	1.4 mm	7.9 mm	13.6 mm	19.4 mm
CCRR (standard)	11.1 dB	12.3 dB	12.3 dB	9.0 dB
CCRR (full range)	46.1 dB	39.1 dB	34.7 dB	30.0 dB
Additional CCRR due to Galvo offset	35.0 dB	26.8 dB	22.4 dB	21.0 dB

With the galvo-based phase modulation, the effect of the complex conjugate suppression was significantly enhanced. **Figure 4.12 B** showed the 4-channel mirror images taken with the full-range SDM-OCT system at the same mirror position. The complex conjugate term had been significantly suppressed. Especially, the complex conjugate term of the 1st beam, which was 1.4 mm away from the zero delay, had been completely suppressed. **Figure 4.12 D** showed the intensity profile across the central row of **Figure 4.12 B**. Although the 2nd, 3rd and 4th complex conjugate peaks remained in the image, a significant drop of the peak intensity was observed for these peaks. Characterization results of CCRR for full-range SDM-OCT were shown in the

fourth row of **Table 4.3**. A total rejection ratio of 46.1 dB was achieved for the 1st beam while the total rejection ratio was 30.0 dB for the 4th beam, which was 19.4 mm away from the zero delay. Subtracting the CCRR of each beam due to dispersion encoding effect from the total CCRR measured with the full-range SDM-OCT system, we could get the additional CCRR values due to the galvo-based phase modulation. The CCRR due to galvo-based phase modulation was 35.0 dB, 26.8 dB, 22.4 dB and 21.0 dB for the 1st, 2nd, 3rd, and 4th beams, respectively. Therefore, the effect of complex conjugate suppresion from the galvo-based phase modulation was more significant than that from the dispersion encoding effect. Combining these two effect, we were able to suppress the complex conjugate terms and potentially utilized the negative depth ranges to accommodate images from one or two channels of the SDM-OCT system.

4.10.2 Full-range SDM-OCT images of a Scotch tape

Figure 4.13 showed the results of the standard and full-range SDM-OCT images of a Scotch tape. The sampling rate of the DAQ card is set to 1.0 GS/s, so that the number of pixel in an axial scan is set to 7168. To realize galvo-based phase modulation, 3 mm beam offset was applied in the sample. The scan range was set to be ~1.5 mm and the number of effective Ascans per Bscan were set to be 750. Images from all four channels were placed in the positive depth ranges. Once the dataset was collected, the same dataset was processed with both standard and full-range SDM-OCT post-processing procedures. In **Figure 4.13 B** and zoomed images of the tape in **Figure 4.13 G-J**, a clearly suppression of the complex conjugates terms of the tape images was observed for all the four beams. In the zoomed tape image, most of the tape layers in the complex conjugate term of the first beam was completely suppressed in the full-range SDM-OCT images, with some residue signals from high-scattered surficial taper layer (**Figure 4.13 G**). Significant signal suppression were also observed in the zoomed complex conjugate images in **Figure 4.13 I and J** from the 2nd and 3rd beams. We could potentially employ an intensity threshold to further suppress the low intensity signals in the complex conjugate term of the tape layer.

4.10.3 Characterizing Phase Modulation Effects with Varied Control Parameters

In the expression of (4.25):

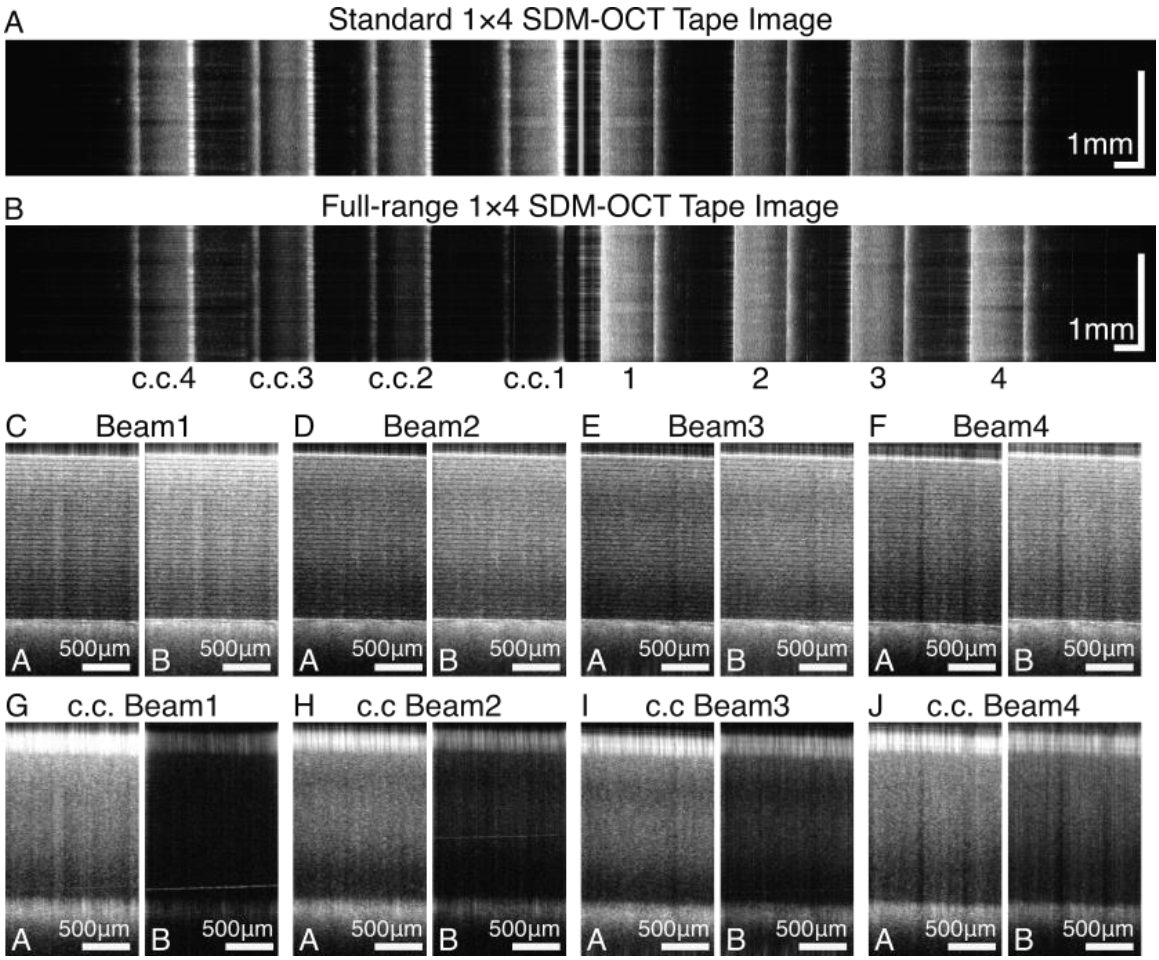

Figure 4. 13 Standard (A) and full-range (B) 1×4 SDM-OCT images of a Scotch tape. (C – J) Zoomed tape images from each beam as well as its complex conjugate term from the standard and full-range SDM-OCT images.

$$k_x = \frac{\Phi(m)}{M} \sim \frac{4\pi \cdot s \cdot x_M}{\lambda \cdot F \cdot M}$$

(4.25)

we showed that, the amount of equivalent carrier frequency k_x was proportional to beam offset s, transverse scan range x_M and number of A-scans per B-scan M. Thus, we could potential control these phase modulation parameters to achieve the optimal suppression of complex conjugate terms. In the full-range SD-OCT images of the tape in **Figure 4.9**, we showed that we could increase the beam offsets to increase the Doppler shift to fully separate the image term from the complex conjugate term in the FFT_x spectra of the spectral fringe. As a result, we could obtain the complex-conjugate-free full-range images. In this section, we characterized

phase modulation effect by measuring the normalized carrier frequencies $k_{x,n}$ in the FFT_x spectra of the interference signals, which were obtained during full-range SDM-OCT images of a Scotch tape. Then, we evaluated the relationships between $k_{x,n}$ and different phase modulation parameters, i.e. the beam offset, the transverse scan range and the number of effective A-scans per B-scan, to see whether the relationships followed the expression of (4.25).

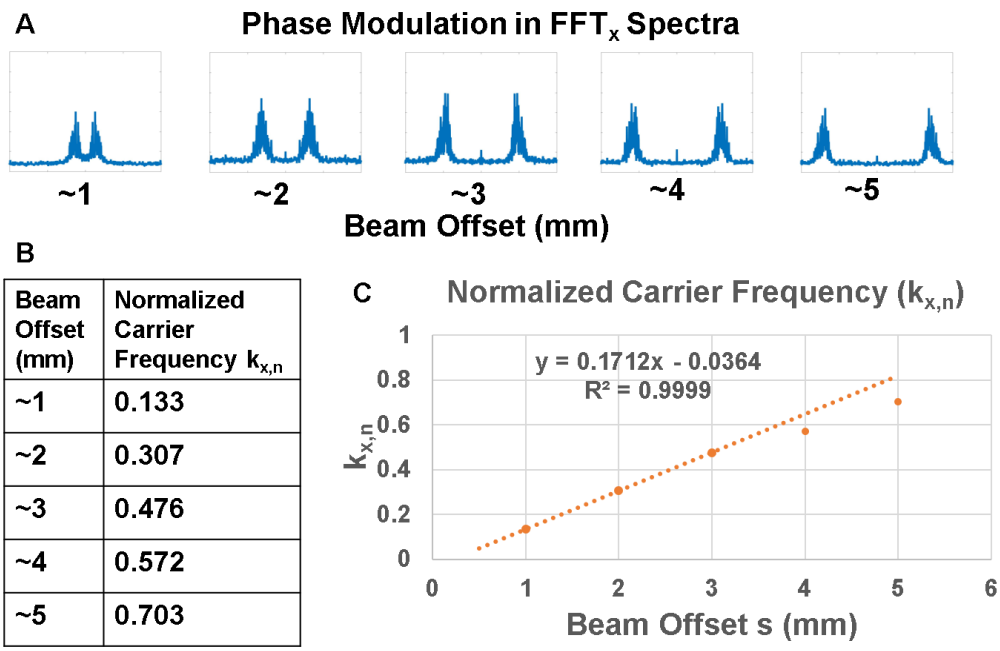

Beam Offset (mm)	Normalized Carrier Frequency $k_{x,n}$
~1	0.133
~2	0.307
~3	0.476
~4	0.572
~5	0.703

Figure 4. 14 Phase modulation with variable beam offsets. Transverse scan range (x_M) was ~1.5 mm. Number of effective A-scans (M) was 750. (A) Effects of phase modulation were shown in FFTx spectra of the fringes. Normalized carrier frequency, measured as half of the separation distance between image and complex conjugate terms changes with varied beam offsets. We could characterize the normalized carrier frequency as a function of the beam offset (B). (C)A high correlation between normalized carrier frequency and the beam offset was found by linearly fitting the first three rows of data. With large beam offsets, normalized carrier frequency continued to increase but did not follow the linear relationship.

Figure 4.14 showed the characterized results of phase modulation with variable beam offsets. All the SDM-OCT B-scans were obtained using a Scotch tape as the sample. Varied phase modulation effects were observed in **Figure 4.14 A**, as the beam offsets (s) were tuned from ~1 mm to ~5 mm. Separation between image and complex conjugate terms in 1D plot of FFT_x spectra in **Figure 4.14 A**, enlarged as the beam offsets increased. By smoothing the 1D plot of FFT_x spectra with a moving average filter with a filter size of (0.04 × Number of effective A-scans) , and finding the peak locations of image and complex conjugate terms, we could derive the normalized carrier frequency $k_{x,n}$ as half of the peak distance between image and complex

conjugate term, if the spatial frequency range along the k_x direction was normalized to (-1, 1). Characterized results of normalized carrier frequencies for different beam offsets were shown in **Figure 4.14 B**. Then, we performed a linear fitting between normalized carrier frequencies and beam offsets, indicated by expression (4.25). A high correlation was found between $k_{x,n}$ and s for the first three beam offsets from ~1 mm to ~3 mm, with the R^2 value to be ~0.9999. However, as the beam offset (s) further increased, $k_{x,n}$ continued to increase but did not follow the linear relationship, with a slow-down increasing rate. Since the minimum beam radius (~1.2 mm) plus beam offset was larger than half of the galvo mirror size, the deviation of $k_{x,n}$ from the linear fitting curve might be attributed to the cropping of the beam on the galvo mirror.

Next, we characterized the relationship between $k_{x,n}$ and transverse scan range x_M. **Figure 4.15** showed the characterized results of phase modulation with variable transverse scan ranges. Separation of image and

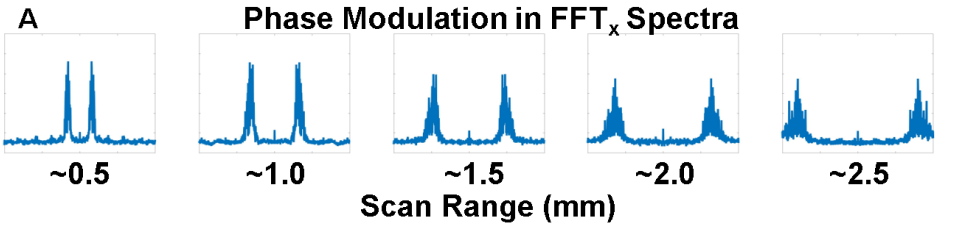

B

Scan Range (mm)	Normalized Carrier Frequency $k_{x,n}$
~0.5	0.156
~1.0	0.321
~1.5	0.476
~2.0	0.637
~2.5	0.794

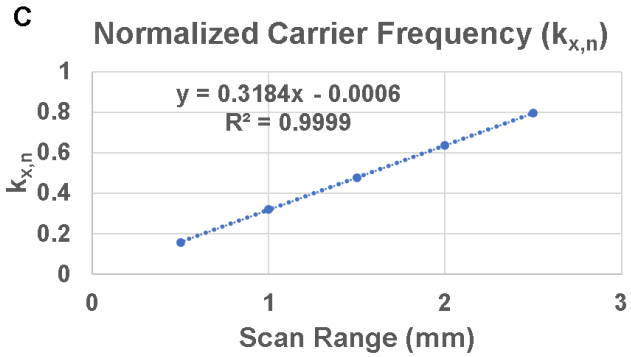

Figure 4. 15 Phase modulation with variable transverse scan ranges. Beam offset s was set to be ~3 mm. Number of effective A-scans (M) was 750. (A) Varied phase modulation effects were shown in FFT_x spectra of the fringes as the transverse scan range was tuned from ~0.5 mm to ~2.5 mm. (B) Chacterized normalized carrier frequencies for different values of the scan range. (C) Linear fitting between normalized carrier frequency and the transverse scan range was performed, showing a high correlation between these two parameters.

complex conjugate terms in 1D plot of FFT_x spectra also enlarged with an increasing transverse scan range from ~0.5 mm to ~2.5 mm. Normalized carrier frequencies for different scan ranges were characterized and

shown in **Figure 4.15 B**. **Figure 4.15 C** showed the result of the linear fitting between $k_{x,n}$ and x_M, indicating a high correlation between this two parameters.

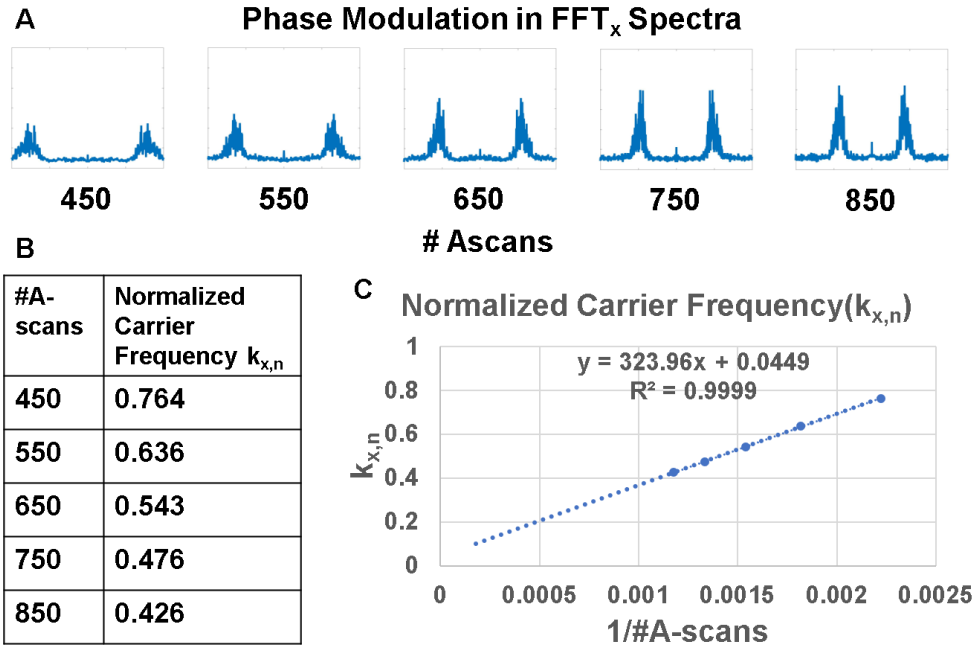

#A-scans	Normalized Carrier Frequency $k_{x,n}$
450	0.764
550	0.636
650	0.543
750	0.476
850	0.426

Figure 4. 16 Phase modulation with varied number of A-scans per B-scan. Beam offset s was set to be ~3 mm. Transverse scan range was ~1.5 mm. (A) Varied phase modulation effects were shown in FFT_x spectra of the fringes as the number of A-scans (M) was tuned from 450 to 850. Peak separation decreased as the M increased. (B) Chacterized normalized carrier frequencies $k_{x,n}$ for different values of the number of A-scans. (C) Linear fitting results showed that the normalized carrier frequencies were inversely proportional to the number of A-scans.

Characterization results of the relationship between $k_{x,n}$ and number of Ascans M were presented in **Figure 4.16**. **Figure 4.16 A** showed the varied phase modulation effects in FFT_x spectra of the interference signals. Different from the cases of variable beam offsets and transverse scan ranges, separation between image and complex conjugate terms decreased as the number of A-scans increased. The calculated normalized carrier frequencies $k_{x,n}$ for different numbers of A-scans were shown in **Figure 4.16 B**. Following the expression of (4.21), we performed a linear fitting between $k_{x,n}$ and the reciprocal of the number of A-scans (1/M). Results in **Figure 4.16 C** demonstrated that $k_{x,n}$ was inversely proportional to the number of A-scans.

Based on characterization results of normalized carrier frequencies, we demonstrated that we could reliably modify the beam offset, the transverse scan range and the number of A-scans per B-scan to control

the amount of phase modulation to fully separate image and complex conjugate terms in the FFTx spectra of the interference signals to optimize the performance of full-range imaging.

4.10.4 Full-range SDM-OCT Images of a Scotch Tape with Half Sampling Rate

In order to show the advantage of full-range technique on reducing the requirement of the hardware, we tested the performance of the SDM-OCT with a lower sampling rate. According to the principle of the full-range technique in Chapter 4.4, we could cut down the sampling rate by half with the same total imaging range, if the total imaging range could be fully utilized with the full-range technique. In the following experiment, we successfully demonstrated the full-range SDM-OCT imaging of a Scotch tape, with all the four beams covered within the total imaging range using only a half sampling rate. The results were shown in **Figure 4.17**. **Figure 4.17 A** showed the SDM-OCT image of all the four beams of a Scotch tape with the standard SDM-OCT system, with a sampling rate of 0.5 GS/s. In the standard SDM-OCT image, the complex conjugate (c.c.) term of the 4th beam was overlapped with the image of the 1st beam; the c.c. term of the 3rd beam was overlapped on the image of the 2nd beam; and the same for the c.c terms of the 2nd and 1st beams. The overlapping made the original four-beam images of the Scotch tape blurry, with the layer structure of the Scotch tape unresolvable. We also acquired the tape images by blocking either upper two beams (1st and 2nd) or lower two beams (3rd and 4th). The results were shown in the **Figure 4.17 B and C**. In these two images, the layered structures of the Scotch tape from both beams were distinguishable, indicating we could only obtain standard SDM-OCT image of two beams without complex conjugate ambiguity under such sampling rate. However, with the employment of the full-range technique, the complex conjugate ambiguity could be minimized. **Figure 4.17 D** showed the result of the four-beam image of the Scotch tape acquired with the full-range SDM-OCT. Most of the complex conjugate images was suppressed significantly and the tape structure of all the 4 beams could be resolvely clearly in most regions, as compared to image of the Scotch tape from standard SDM-OCT (**Figure 4.17 A**). A zoomed viewed of the tape images of the 3rd beam from the full-range SDM-OCT clearly showed that the complex conjugate term was fully suppressed in this depth range (**Figure 4.17 F**), as compared to the same cropping regions from the standard SDM-OCT image (**Figure 4.17E**). Based on the experimental results above, we could claim that we could reliably get clear images of all the 4 channels with a half sampling rate using the full-range SDM-OCT. We should note that,

due to the strong mismatch of the refractive index of air and the Scotch tape as well as the smooth surface of the Scotch tape, the surface of the Scotch tape would have strong scattering in OCT signals. The 30 dB

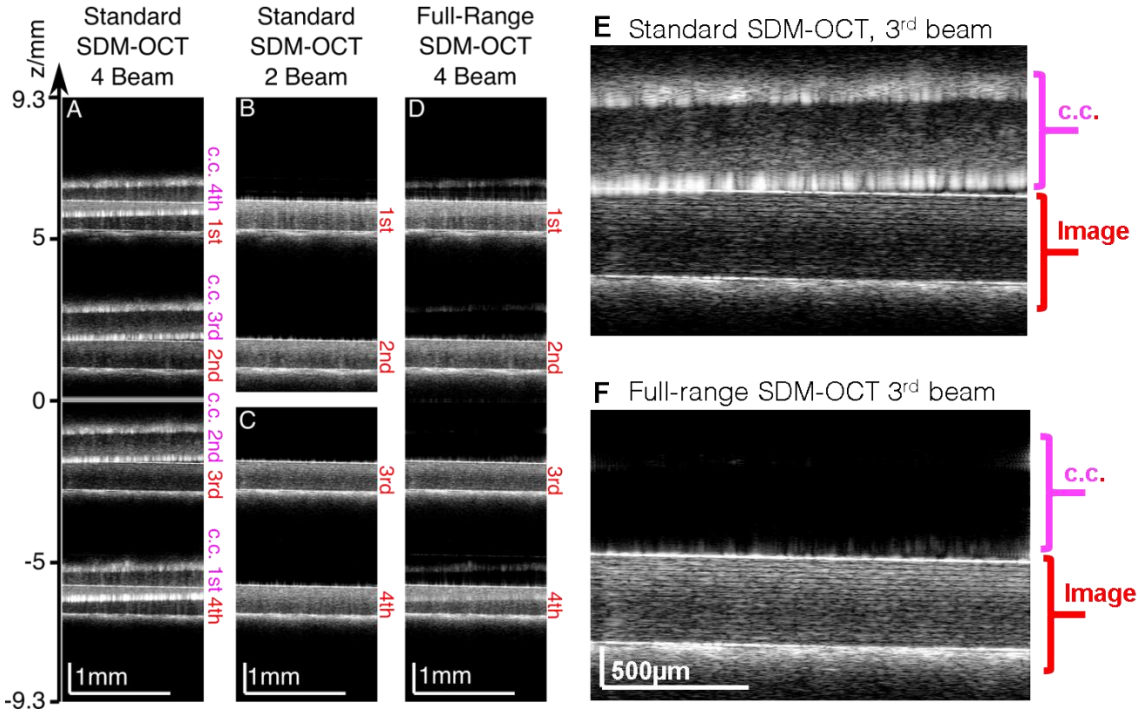

Figure 4. 17 Demonstartion of full-range SDM-OCT with a half sampling rate. Sampling rate was 0.5 GS/s. Standard SDM-OCT image of a scotch tape was shown in (A). Images from the 3rd and the 4th beams are overlapping with the complex conjugates images of the 1st and 2nd beams, indicated by the red and magenta labels of image and complex conjugate terms from different beams. (B) and (C) are the SDM-OCT images of 1st and 2nd beams, 3rd and 4th beams, respectively, by blocking two channels, showing that only images of two beams could be properly rendered with current sampling rate with the standard SDM-OCT post-processing procedure. (D) With the full-range technique, images from all channels could be rendered at the same time, with significant suppression of complex conjugate terms. Zoomed views of tape images from the 3rd beam in (A) and (D) were shown in (E) and (F).

suppression ratio measured from the full-range technique could not help to completely remove the surface of the tape in complex conjugate term, yielding some weak but noticeable bright lines in the tape images of 1st, 2nd and 4th beams in full-range SDM-OCT images.

4.10.5 Full-range SDM-OCT Images of the Finger Nail

At last, we would like to demonstrate the capability of full-range SDM-OCT (FR-SDM-OCT) to image the biological sample. **Figure 4.18** showed the FR-SDM-OCT images of the human finger nail fold *in vivo*. A sampling rate of 0.5 GS/s was applied. With the full-range technique, we could render all the images from four different beams within the doubled imaging range of ~21 mm in tissue (**Figure 4.18 A**). **Figure 4.18 B-E** showed the 3× zoomed views of finger nail fold imaged by the 1st to 4th beams. Since the direction of the

four beams was in parallel to the boundary of the nail junction, we could clearly observe the structure of nail junction connecting the proximal nail fold and the nail plate in the images from all the channels. In addition, the dermal/epidermal junction (DEJ) was clearly visible in **Figure 4.18 B-E**. In **Figure 4.18 C and D**, we could see the cuticle structure that extended from the epidermis of the proximal nail fold. A clearly separation of nail plate and nail bed was observed, indicated by the high-scattering interface between these two regions. In the FR-SDM-OCT image of the nail fold, most of the complex conjugate terms were suppressed by the full-range techniques, although some residue complex conjugate terms from the high-scattering regions remained in the FR-SDM-OCT image. However, we should note that, the artifacts on top of the 1st beam in **Figure 4.18 B** were not the residue complex conjugate term. They were caused by the aliasing effect, where a sub-band of the high-frequency signals from the 4th beam in the raw data was higher than the spectral bandwidth of ~250 MHz.

4.11 Discussion of full-range technique on SDM-OCT

In Chapter 4.3, we have shown that, various types of full-range techniques has been adopted in spectral domain OCT systems to resolve the complex conjugate ambiguity of the image and expand the total imaging range. However, for swept-source OCT system, full-range technique is less appreciated since the imaging range of the swept source OCT system is usually sufficient to render the sample image with a penetration depth of ~1-2 mm. However, the SDM-OCT technology, which requires a long imaging range to render the images from multiple channels with optical delays between neighbouring channels, poses new challenge for the requirements of the hardware, including the detector, digitizer, the laser source and the memory. In this chapter, we successfully modify the SDM-OCT system to enable full-range imaging. Compared to the standard SDM-OCT system, the full-range SDM-OCT can utilize only a half sampling rate to cover the same total imagng range to render images from all different beams at different depth ranges. We also showed that, with the half sampling rate, the standard SDM-OCT can only render images from half number of beams with no complex conjugate ambiguity. Thus, the full-range technique can effectively lower the minimum requirements of the hardware for the SDM-OCT technology. Specifically, we can reduce the requirement of the maximum bandwidth of the dual balanced detector by half; reduce the requirement of the maximum

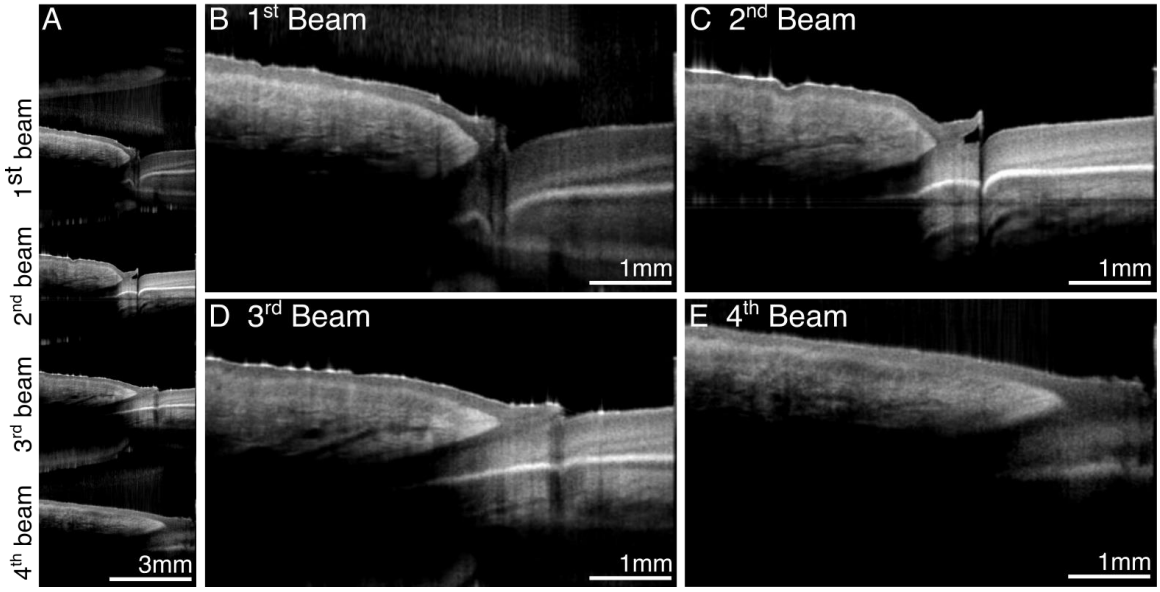

Figure 4. 18 Full-range SDM-OCT images of the human finger nail *in vivo*. Sampling rate was 0.5 GS/s. Images from four beams were shown in (A), with a total imaging depth of ~21 mm. (B)-(D) were 3× zoomed images of each beam, showing clear structure of the nail junction, dermal/epidermal junction (DEJ) in proximal nail fold region, the cuticle, as well as separation of nail plate and nail bed.

sampling rate of the digitizer by half; reduce the requirement of the maximum data transfer rate of the PCI/PCIe bus by half; reduced the data size of the single A-scan by half. Furthermore, the first and second generation of the standard SDM-OCT system requires the laser source to have a minimum (half) coherence length of >30 mm, yielding limited choices of commercially available laser source (VCSEL from Thorlabs and Santec, akinetic swept laser from Insight). With the full-range technique, the requirement of the minimum coherence length could also be reduced by half, yielding increased availability of the swept laser (i.e. Axsun swept laser with 10mm (half) coherence length) for SDM-OCT technology.

In another aspect, if we are using the maximum performance of all the hardware, the full-range technique can further expand the total imaging range. In **Figure 4.13**, we showed the we could use 1 GS/s sampling rate to cover 4 beams with the standard SDM-OCT system in a total imaging depth of ~18.6 mm in the tape. If use the maximum sampling rate of 2 GS/s in the full-range SDM-OCT system, the total imaging range could be potentially extended to ~74.4 mm in the tape, yielding the capability to render 16 beams within the total imaging range, if other settings, including the laser swept rate and the optical delay between neighbouring channels, remain the same. In such case, we can expand the potential of SDM-OCT to achieve extra speed improvement with full-range technique.

To evaluate the effectiveness of the full-range techniques, one important metric is the complex conjugate rejection ratio (CCRR). **Table 4.4** showed the values of complex conjugate suppression ratio reported in the literature with different full-range techniques. The tilted rows in the tables indicated a comparison of CCRR values from different groups employing the same galvo-based phase modulation as our group to realize full-range imaging. In our results, we reported a total CCRR value of ~46 dB at the imaging depth of 1.4mm. Excluding the contribution of the CCRR from the dispersion encoding, an additional 35 dB suppression was observed with the galvo-based phase modulation technique with a phase shift close to $\pi/2$ between adjacent Ascans, which was comparable with previous studies[151, 152]. We should note that, most of the CCRR values from SD-OCT or SS-OCT system were measured close to zero delay. Little was reported on the CCRR value of full-range techniques in deeper depth ranges. For our SDM-OCT system, we observed that the CCRR values from galvo-based phase modulation decreased gradually as the imaging depth increased. In our measurement, the CCRR values were 35.0 dB at 1.4 mm, 26.8 dB at 7.9 mm, 22.4 dB at 13.6 mm and 21.0 dB at 19.0 mm. Although the decreasing CCRR was not reported in any study employing the galvo-based full-range technique, it was reported in other full-range studies. Sarunic et al. observed that the CCRR value was 25 db near zero delay but dropped to 18 dB at ~4 mm depth[139]. Wang et al. measured the CCRR in his cubic-meter SS-OCT system with quadrature detection. A >40 dB CCRR was measured at ~100mm depth but it slightly decreased to <20 dB at the depth of ~700 mm [121]. Since our measured fringe signals have a frequency range of hundreds of MHz, the high-frequency RF dependent noise started to play a role and might distort the phase for the high frequency fringes. With a proper phase correction [121, 142] to suppression high-frequency RF noise, a gain of CCRR in the deeper imaging depth might be achieved. Also, dispersion encoding further contributed to a gain of CCRR in our FR-SDM-OCT system. Since the configuration of the reference and sample arms are only slightly different in the free space, the dispersion is slightly mismatched between these two arms, yielding a relative constant ~9-1 2dB CCRR gain for our system. A ~14 dB additional gain was reported in Makita et al. [149] at 1040 nm range and a ~10-25 dB additional gain was reported in Wang's study [121] with a 1310 nm VCSEL laser. Although dispersion encoding technique doesn't improve the CCRR that much in the 1310 nm wavelength range since the optics are less dispersive, it may significantly enhance the CCRR for 800 nm and 1060 nm OCT systems to >50 dB with larger dispersion mismatches [143, 145].

Table 4. 4 Reported Complex Conjugate Suppression Ratio of Full-range Techniques

Reference	Year	System	Complex Conjugate Suppression Ratio
Maheshwari et al. [133]	2005	SS	25 dB
Bachmann et al. [135]	2006	SD	~30 – 40 dB
Lee et al. [136]	2010	SS	35 dB (at 0.4 mm)
Wang et al. [137]	2015	SS	~28 dB
Wang et al. [121]	2016	SS	~30 dB (close), >40 dB (total at 100 mm), 29 dB (average)
Sarunic et al. [139]	2005	SD,SS	25 dB (near DC), 18 dB (at 4 mm)
Bo et al. [140]	2017	SD	25 dB
Vakoc et al. [141]	2006	SS	>50 dB (at 2 mm)
Siddiqui et al. [142]	2015	SS	~60 dB
Hofer et al. [143]	2009	SD	>55 dB
Kottig et al. [145]	2012	SD	>50 dB
Makita et al. [149]	2008	SD	~41.2 dB (total), ~26.8 dB
Yamanari et al. [150]	2010	SS	~40.5 dB (at 0.6 mm)
Baumann et al. [151]	*2007*	*SD*	*~30 dB*
Leitgeb et al. [152]	*2007*	*SD*	*~30 dB*
Kawagoe et al. [154]	*2016*	*SD*	*~40 dB (<1.2 mm)*
Li et al. [155]	*2017*	*SS*	*~40 dB*
This paper	*2019*	*SS*	*46 dB (total, at 1.4 mm), 30dB (total at 19.4 mm)*

Although a decent value of CCRR was reported in our study, the complex conjugate ambiguity is not fully resolved in our system. In **Figure 4.12**, although the weak mirror image was fully suppressed with ~46 dB CCRR, residues were observed for the rest of the 3 beam. In the full-range images of the tapes and skins, residues of complex conjugate images were observed for the images located in the deeper depth ranges with the intensity of complex conjugate images suppressed significantly. Most of the residues could be removed or suppressed by thresholding the image. However, the residue complex conjugates signals from the strong reflection/scattering of the superficial layers with a SNR of >50 dB above noise floor would be difficult to be fully removed. Further enhancement of the CCRR for all depths would be critical to fully resolve the complex conjugate ambiguity in full-range SDM-OCT images.

Baumann et al. listed several major factors that would affect the CCRR of the galvo-based full-range SD-OCT system [151]. Similarly, these factors must be taken into consideration when employing galvo-based phase-modulation full-range technique in SDM-OCT system. First, the beam spot size significantly affects the CCRR value of the full-range SDM-OCT, due to the fact that different part of the beam will have different beam offsets, yielding a distribution of carrier frequencies in the FFT_x spectra. The larger the beam spot size,

the broader the distribution of carrier frequencies in the FFT_x spectra. Also, the cross-section of the collimated beam on the galvo scanner followed the Gaussian distribution, which indicates that, the larger ratio of beam offset versus FWHM beam diameter, the larger portion of beam shifted to one side of the pivoting axis than the other side, the better CCRR[151]. Thus, smaller FWHM beam diameter would make it easier to achieve better suppression of complex conjugate signals. In our setup, the diameter of the single beam was measured to be ~2 mm, which indicated that an offset of >1 mm would be sufficient to get a relative decent CCRR value. Since four collimated beams are converging at the back focus of the 2nd relay lens, any offset between the back focus of the 2nd relay lens and the fast-axis galvo mirror would yield the expansion of the beams and inferior suppression of complex conjugate signals. However, the smaller beam spot size results in a smaller effective NA after the objective and poorer lateral resolution, as compared to larger beam spot size incident on the same objective. Second, the CCRR would be affected by the amount of phase shift between adjacent A-scans. Theoretically, a phase shift of $\pi/2$ yields the best CCRR value and other phase shift values would yield inferior performance of the complex conjugate suppression [151]. Thus, to achieve the best CCRR, one parameter among the beam offsets, lateral scanning range and number of Ascans per Bscan, would be determined by the rest of two. In our study, the sampling density has to be set oversampled in order to achieve a phase shift close to $\pi/2$, yielding a larger overall size and longer acquisition time for FR-SDM-OCT data as compared to Nyquist sampled data collected by standard SDM-OCT. In principle, phase shifts close to $(2n+1)\pi/2$ can also yield the optimal CCRR. However, the distribution of carrier frequencies in the FFT_x spectra of the interference signals, would also be (2n+1) times broader. The broader distribution of carrier frequencies in the k_z - k_x domain would lead to a higher chance that the edge of spatial frequency bands crossing either zero spatial frequency or cut-off spatial frequency, both of which significantly reduced CCRR value. Third, the surface structure of the sample as well as multi-scattering in the sample would affect the shape and the bandwidth of the distribution of carrier frequencies in the FFT_x spectra. When imaging a mirror with full-range OCT system, the distribution of carrier frequencies in the FFT_x spectra would be a delta function. For tape or fingers, the distribution of the carrier frequencies in the FFT_x spectra would be significantly broadened and the shape would be distorted. The curvature of the finger would make the spatial distribution even worse. Thus, it is highly recommended that a few imaging tests be performed prior to final data acquisition to find out the optimal number of Ascans to achieve the full-range with best CCRR, given

the fixed scanning range and beam offset. Chromatic aberration could also cause the broadening of the distribution of the carrier frequencies in the FFT_x spectra, which would be considered as a constant effect given the system configuration is fixed.

To ensure the proper complex signal reconstruction when employing Hilbert transform along the fast-axis scan direction, the phase calibration step is of great importance. SD-OCT has a fixed relationship between the camera pixels and the wavelength for all the Ascans, yielding a high phase stability. Thus, the Hilbert transform can be performed as the first step of the post-processing, as described in Ref. [151] [148]. However, the phase stability of SS-OCT systems suffers from the triggering jitters, yielding fluctuating relations between indices of pixels and wavelengths for different Ascans. Thus, phase calibration is necessary for SS-OCT system to retrieve the proper phase relation for different Ascans. Wang et al. has introduced a method, using a fixed phase range to crop the phase curve of each Ascan to resolve the trigger jitter [137]. A drawback was that it doesn't not guarantee that the one to one relationship between pixel index and the wavenumber is the same for different Ascans. In our approach, we add two FBG after the interference of the MZI arm to indicate the location of pixel indices with known wavelengths values (See Chapter 3). Using these two FBG peaks as indicators, we can ensure that the pixel-wavenumber relationship is fixed for all the Ascans, yielding the digital reconstruction of 2D complex signals along the horizontal direction to be valid.

For our FR-SDM-OCT system, we use internal clock mode to collect the fringe signals. In this mode, additional MZI signals are collected along with the OCT system to obtain the proper phase calibration curve, which doubles the total data size. To further reduce the pressure of data size and transfer rate, we can perform the data acquisition in the external mode, using a k-clock [156]. However, the phase jitter in the external mode needs to be addressed. It could be resolved by either using the FBG peak as the trigger of fringe acquisition for the external clock signals [157, 158] or adding the FBG before the detector in OCT channel [156]. Furthermore, with the dual-edge sampling to trigger the data acquisition in external clock mode, the effective sampling rate could be doubled and the total imaging depth could be further doubled [116].

During the SDM-OCT imaging, we notice the whole imaging range could not be fully utilized if the swept laser source is not perfectly linearly sampled in wavenumber. The frequency range of the last beam in the oscilloscope will be broadened as it moves further away from the zero delay, exceeding the cut-off frequency and causing aliasing. During our measurement, about 2/3 of the whole imaging depth could be reliably used

without aliasing effect, which may further increase the requirement for the sampling rate and detector bandwidth. A laser with perfect linearized phase (Insight, akinetic source) would help resolve such issue.

4.12 Summary

In this chapter, we demonstrated another modification of the SDM-OCT system by adding the full-range imaging capability. Based on the galvo-based phase modulation full-range technique, we successfully demonstrated full-range SDM-OCT imaging of tapes and human finger nails with a half sampling rate of 0.5 GS/s to render images from all four channels. In comparison, the standard SDM-OCT has to utilize a sampling rate of 1 GS/s to reliably render images from all four channels. In such case, the full-range technique can effectively cut down the requirements of the hardware for the SDM-OCT technology, yielding an increased availability of parts to build a SDM-OCT system. Potentially, if we make full use of the hardware capability, we can significantly extend the total imaging range to ~80mm range to render images from more parallel channels from SDM-OCT.

Appendix 4.1 Commercial High-speed Data Acquisition Units (DAQ)

Table 4. 5 Commercial High-speed Data Acquisition Units*

Company	Type	Model	Reso-lution	Chs	Sampling Rate (GS/s)	Data Stream Rate (Gbps)	BW (GHz)	On board RAM (GB)	Input range	Other specifi-cation
AlazarTech	PCIe Digitizer	ATS9373	12 bit	2	4 (1ch), 2 (2ch)	6.8	1.0	8	+/- 400 mV	Ext Clock
Teledyne SP Device	PCIe Digitizer	ADQ412	12 bit	4	4 (2 ch), 2 (4 ch)	3.2	2.0 (4ch), 1.3 (2ch)	0.7	800 mV_{pp}	Ext Clock 2Vpp
		ADQ7DC	14 bit	2	10 (1ch), 5 (2ch)	5	2.5	4	1 Vpp	
Acqiris (formerly part of Keysight)	PCIe Digitizer	U5303A	12 bit	4	4 (1ch), 1 (4ch)	NA	1.3	4	1 V or 2 V	Ext Clock
		U5310A	10 bit	2	10 (1ch), 5 (2ch)	NA	2.5	4	1 V	Ext Clock
Gage Applied	PCIe Digitizer	EON Express	12 bit	2	6 (1ch), 3 (2ch)	4	1.75	4	NA	
Signatec	PCIe Digitizer	PX1500-4	8 bit	2	3 (2ch) 1.5 (4ch)	1.4	2	2	0.5 Vpp	Ext Clock
Pico Technology	USB Digitizer	PicoScope 6407	8 or 12 bit	4	0.97	NA	1	NA	+/- 100 mV	
UltraView	PCIe Digitizer	AD12-2000	12 bit	2	4 (1ch), 2 (2ch)	7	1.6	8	+/-375 mV	Ext Clock
Tektronix	Oscilloscope	MSO5204B	8 bit (11 bit w HiRes)	4	10 (2ch) 5 (4ch)	Up to 0.125 GB	2	NA	5 Vrms	

* Only the products with the best performance for OCT imaging were listed.

Appendix 4.2 Commercial large-bandwidth balanced detectors for NIR applications

Table 4. 6 Commercial Large-bandwidth Balanced Detectors for NIR Applications

Company	Model	Detector Type	λ (nm)	BW (GHz)	RF Output Transimpedence Gain (V/A), Conversion Gain (V/W)	Noise Equivalent Power(pW/Hz$^{1/2}$)
Thorlabs	PDB480C-AC	InGaAs	1200-1700	0.03-1.6	16×10^3 V/A 14.4×10^3 V/W	9.3
Wieser	WL-BPD1GA	InGaAs	1000-1700	0.3-1.0	3.3×10^3 V/W	20
NewPort	1617-AC-FC	InGaAs	900-1799	0.04-0.8	0.7×10^3 V/A	20
Insight	BPD-1	InGaAs	950-1650	DC – 0.4	5 V/W	5
Exalos		InGaAs	1200-1700	0.03 – 0.35	5×10^3 V/A	NA
Hamamatsu	C12668-04	InGaAs	1300	DC - 0.4	10×10^3 V/A	NA
General Photonics	BPD-002	InGaAs	1310+/-50	DC - 0.2	30×10^3 V/A	10

Chapter 5: Optical Coherence Tomography Angiography

5.1 Introduction

Optical coherence tomography can reliably provide the 3D structural image of the tissue structure based on the scattering properties of the tissue. However, the 3D structural OCT data lack the capability to provide any information about the dynamic process that occurred in the tissue. In such case, optical coherence tomography angiography (OCTA), a functional extension of OCT, is employed to image the dynamic process of blood flows. OCT can utilize time-lapse measurement to detect the dynamic processes occurred in the sample, which is contained in intensity changes, phase or speckles of OCT signals. Especially, utilizing moving red blood cells as the source of contrast, OCT can track their movement in the vessels and map out the 3D vascular networks of the tissue, which is called angiography.

Other than OCTA, a list of methods, including the fluorescence imaging, CT, MRI and photoacoustic imaging can be used to image the vascular network inside the tissues and organs. Similar with the comparison of different microscopy methods, CT and MR angiography share the advanges of deep imaging depths but suffer from the poor resolution. Fluorescein angiography was the gold standard for retinal angiography [33]. However, the adminstration of fluorescent dyes might lead to adverse effects for the patients, e.g. nausea and vomiting [33, 159]. On the other hand, OCTA can provide the 3D angiograms of the superficial vascular networks inside the tissue with sufficient resolution to resolve the capillaries, without injecting any contrast agents. Photoacoustic imaging is another popular method to visualize the vascular network up to a few millimeter depths, which would be sufficient to visualize the cutaneous vascular layers[160-163]. However, the tracking of dynamic process of blood flows was not as fast as OCTA. Thus, multimodal-imaging with OCTA and photoacoustic imaging can be employed together to show the vascular network with complimentary optical imaging contrasts from scattering and absorption and red blood cells [33].

OCTA has been successfully applied to visualize microvasculature in the retina and choroid, monitoring blood flow supplies in these layers [73, 164-166]. Other than that, OCTA can be utilize to visualize the superficical vascular network in the sub-dermal and dermal layer of the skin, facilitate the diagnoses of skin disease [44]. OCTA can also be used to quantify the cerebral blood flows to evaluate the traumatic brain injury and monitor dynamic process of vascular occlusion and reperfusion in the brain [167-170].

Since OCTA monitors the fast dynamics of red blood cells, repeated scans are usually needed, which poses new challenge to the acquisition speed of OCT system. In such case, OCT systems with faster imaging speed, i.e. SDM-OCT system, can improve the performance of the OCTA. In this chapter, we would demonstrate the angiography with standard and SDM-OCT system, showing the dynamic contrast of blood flows in the tissue.

5.2 OCTA techniques

Table 5. 1 List of OCTA Techniques

Phase-signal-based OCTA	**Intensity-signal-based OCTA**	**Complex-signal-based OCTA**
• Doppler OCT • Phase variance	• Speckle Variance (SV, LOGIV, DLOGIV) • Correlation Mapping (cmOCT) • Split-spectrum Amplitude Decorrelation Angiography (SSADA)	• Optical microangiography (OMAG) • Eigen-decomposition-based OMAG • Doppler Variance and Complex differential variance • Imaginary-part-based cmOCT • Phase gradient angiography (PGA)

Table 5.1 shows a list of OCTA techniques reviewed by the Chen et al and other literatures [33, 74]. Since the dynamic information of the red blood cells movements are contained in changes of complex OCT signals, we can utilize changes of amplitude, phase, or complex signals to extract these information and generate the angiogram to show the vascular network. Based on the source of OCT signals, we can divide the OCTA techniques into three categories, i.e. phase-signal-based OCTA; intensity-signal-based OCTA and complex-signal-based OCTA.

5.2.1 Phase-signal-based OCTA

Among all the OCTA techniques, Doppler OCT, one of the phase-signal-based OCTA techniques, was the first to be proposed to measure the blood flow velocity, using time-domain OCT system [171]. Based on Doppler effect, the moving particles (in the angiography, moving red blood cells) along the beam transmitting direction (axial direction) would generate a frequency shift, which would ultimately affect the phase of back-

scattered OCT signals. The phase shift and the velocity of the particles could be related with the formula[171]:

$$\Delta\Phi(z,T) = 2k \cdot \Delta z = \frac{4\pi}{\lambda} \cdot (v_s \cdot T \cdot n)$$

(5.1)

Rearranging the formula, we can get the velocity of the particle (red blood cell), denoted as v_s, as[74]:

$$v_s = \frac{\Delta\Phi(z,T)\lambda}{4\pi nT}$$

(5.2)

Once the phase difference $\Delta\Phi(z, T)$ and the time interval τ is known, the blood velocity could be quantified. We should note that, v_s is the axial component of the blood velocity.

Doppler OCT can provides direct measurement of the axial component of the blood velocity since it is linearly related to phase changes of OCT signals. However, one main limitation of Doppler OCT is that this method is not sensitive to any blood flows or blood flow components that are moving perpendicular to light transmitting direction (axial direction). To retrieve the blood velocity in any directions, one has to obtain the angle between the incident beam and the vessels in priori from the 3D OCT structural image. Or, we can detect the different component of the blood velocity with multi-beams to reconstruct the vectorial blood velocity (See Chapter 3.3 for a list of two-beam, three-beam OCT system for Doppler OCT) [101-103]. With such multi-beam OCT system, we can monitor the blood flows moving in any direction.

Since the dynamic range of the phase is limited to $(-\pi, \pi)$, the measured flow velocity range would be also limited. Hendargo et al. deducted the dynamic range of detectable velocity [157]. The phase wrapping threshold velocity (only consider the axial direction) was determined by the following formula:

$$v_{wrap} = \frac{\lambda}{4nT}$$

(5.3)

which is valid when $\Delta\Phi(z, \tau)$ is equal to π in the formula:

Also, the dynamic range of the detectable velocity is also related to other factors. The minimum detectable velocity was expressed as [157]:

$$v_{min} = \frac{\lambda}{4\pi nT}\delta\phi_{sens}$$

(5.4)

In which $\delta\phi_{sens}$ is the smallest detectable phase change between two A-scans, which can be used to derive the phase stability. $\delta\phi_{sens}$ depends on shot-noise-limit sensitivity of the OCT system and can be expressed as [172]:

$$\delta\phi_{sens} = \frac{2}{\pi}\int_0^{\pi/2} \tan^{-1}\left(\frac{|I_{noise}|}{|I_{signal}|}\sin(\phi_{rand})\right) d\phi_{rand}$$

$$= \frac{2}{\pi}\frac{1}{(SNR)^{0.5}}$$

(5.5)

Combining (5.4) and (5.5), we can get the expression of vmin as a function of shot-noise-limit sensitivity [157]:

$$v_{min} = \frac{\lambda}{2\pi^2 nT}\frac{1}{(SNR)^{0.5}}$$

(5.6)

The maximum detectable axial velocity is also limited by the fringe wash-out, which is expressed as [157]:

Spectral domain system: $v_{wash} = \frac{\lambda}{4nDT}$

(5.7)

Swept source system: $v_{wash} = \frac{N\lambda}{4nDT}$

(5.8)

where D is the duty cycle of the detector, which could be estimated as exposure time divided by the line rate. N is number of sampling points in a sweep for swept source system, T is the time interval between A-scan acquisitions, which is the reciprocal of camera imaging speed in SD-OCT system or laser swept rate for SS-OCT. In most of the case, v_{wash} is larger than v_{wrap}. Thus, the dynamic range of the detectable axial velocity is determined by the SNR and the time interval between axial scans. To visualize the blood flows in either arterioles or capillaries, the time interval needs to be carefully set. For faster blood flows, the phase difference could be calculated between consequent A-scans. For capillary blood flows, larger time intervals between consequent frames or consequent volumes could be employed.

Other than standard Doppler OCT angiography technique, phase variance technique, first proposed by Fingler et al. [173, 174] also utilized the phase information to retrieve the angiography information. The variance of the phase signals were calculated to extract the flow signals. Compared with Doppler OCT, phase variance OCTA is more sensitive to the phase changes and it can detect the lateral blood flows. However, variance of the phase signals doesn't directly link to flow information, making it hard to quantify blood velocity.

5.2.2 Intensity-signal-based OCTA

Dynamic information from the blood flows is not only contained in the phase term, but also lead to intensity changes, which was expressed as speckle changes. Speckles are inherent in OCT images due to laser properties. Speckles outside the tissue region is usually the noise. However, speckles inside the tissue regions might contain the dynamic information. Similar with laser speckle imaging [175], we could utilize the speckle changes from OCT data with certain time interval to evaluate the dynamic process of blood flows.

The first method is speckle variance OCT (SV-OCT), which was first employed in SD-OCT by Mariampillai et al. [176, 177]. The variance of OCT intensity signals along the repeated scan direction was calculated. The static regions would have smaller intensity variance while the dynamic regions of blood flows would have larger intensity variation. In such case, the dynamic blood flows could be distinguished from the static region within the tissue. Similar with phase variance, speckle variance is insensitive to the flow directions and doesn't directly provide any quantification of blood velocity. An improved SV-OCT method,

named differential logarithmic intensity variance (DLOGIV) OCTA technique is proposed by Motaghiannezam et al. to show the slightly enhanced contrast of flow signals [178].

Another method, correlation mapping OCT (cmOCT), utilize the correlation of the intensity signals between neighbouring frames to enhance the flow contrast [179, 180]. In this technique, the flow regions with faster dynamics would have smaller correlation value while the static regions without any particle movements would have higher correlation. Correlation value of each pixel in the 2D angiograms was calculated within a small 2D moving window, usually 3 × 3 or 5 × 5, to smoothen the image. More repeated frames could be employed to calculate the averaged correlation value to enhance the contrast.

Speckle decorrelation between adjacent frames could be also utilized to analyze the flow dynamics. Actually, speckle decorrelation value is equal to one minus the speckle correlation value. To further enhance the contrast, we can split the full OCT fringes into several narrow bands and using short-time Fourier transform (STFT) to generate batches of 2D cross-sectional images. The OCT image from each narrow band is processed separately to generate the correlation map. The correlation map from all narrow bands were averaged then subtracted from 1. The abovementioned OCTA technique, denoted as split-spectrum amplitude-decorrelation angiography (SSADA), translated the axial resolution into enhanced flow contrast with increased averaging [181, 182].

5.2.3 Complex-signal-based OCTA

Similar with the Doppler OCT, the dynamic information could be also extracted by calculating the change of the complex OCT signals. This OCTA technique, first proposed by Wang et al. [183], was denoted as optical microangiography (OMAG). As compared to Doppler OCT, OMAG is more sensitive to the blood flows due to the use of complex signals [74, 184]. Similarly, increasing the number of repeats could help enhance the flow contrast due to averaging effect.

Similarly, variance of complex OCT signals were utilized to extract the flow signals, which was first proposed by Zhao et al[185] and later denoted as Doppler variance OCT [186]. An improved version was developed by Nam et al., named complex differential variance OCT, to further take the average of variance signals along the depth direction to enhance the flow contrast [187, 188].

Also, the correlation mapping OCTA technique could be extended to be employed on complex signals, which is called imaginary part-based correlation mapping OCTA [189]. This technique was demonstrated *in vivo* to visualize the vascular network of the mouse ear.

5.3 Consideration of the choice of OCTA techniques

In this study, we chose differential logarithmic intensity variance (DLOGIV) technique[178], an extension of speckle variance technique, to process our OCTA data obtained from SDM-OCT and FR-SDM-OCT. The reasons were listed as followed:

1) Speckle variance technique is simpler and easier to implement as compared to phase- and complex-based angiography techniques.

2) It doesn't require the phase information, which reduces the required memory size by half for data processing

3) Phase compensation is also not required.

4) As compared to standard speckle variance OCT[177], the DLOGIV has slightly improved SNR of blood vessel detection [178] with only one additional step in the post-processing.

5.4 Details of OCTA post-processing steps

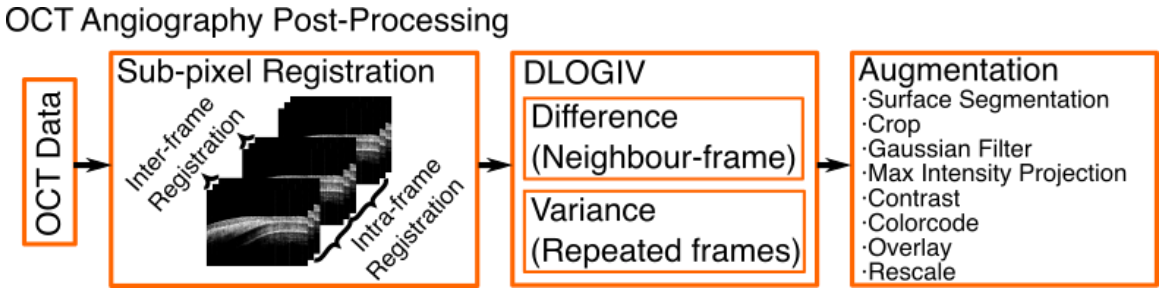

Figure 5. 1 Post-processing procedure for DLOGIV OCTA technique.

The post-processing procedure of OCTA is described in **Figure 5.1**. After OCT data are generated following standard or full-range SDM-OCT post-processing procedures, a two-step subpixel registration[190], involving an inter-frame registration on repeated frames and an intra-frame registration on frames from different locations, is performed to align all the B-scans. This step facilitates the suppression of dynamic

signals from the micron-scale translational sample motion, yielding a better contrast of flow signals. Next, DLOGIV is employed from each stack of repeated frames to extract the vascular information for each frame. After all the frames were processed, en face OCT angiograms could be generated and optimized with additional augmentation steps listed in **Figure 5.1**.

5.5 OCTA Results of Human Finger with SD-OCT System

To characterize the performance of that the DLOGIV method, we first tested it with the SD-OCT system. **Figure 5.2** showed a demonstration of SD-OCTA on human finger *in vivo*. SD-OCT system used in the experiment was the 1300 nm system described in Chapter 2. The line-scan camera was running at a speed of 92 kHz (Actual speed was 88.8 kHz). The dorsal side of the volunteer's thumb was placed under the objective. 400 A-scans was obtained in each frame, yielding the frame rate to be 189 frams per second (fps). At each B-scan location in the slow axis, 8 repeated scans were obtained to generate the angiographic data. Repeated scans were obtained at 400 B-scan locations, yielding the total OCT scan time of ~17s. The actual OCT scan area was 3.3 × 2.8 mm^2. **Figure 5.2 A** showed the cross-sectional OCT structural images of the finger, showing a boundary between the epidermis and dermis. **Figure 5.2 B** showed the angiogram provided by SV-OCT. Large vessels stood out from the static regions in the SV-OCT image (yellow arrows), with slightly higher signal intensities. However, small vessels were not visible in the cross-sectional SV-OCT image. In **Figure 5.2 C**, angiogram provided by DLOGIV showed a higher contrast between the vessels and the static regions. As a result, not only the large vessels were clearly resolved with high contrast (yellow arrows), small papillary vessels were also visible in cross-sectional OCT angiogram, indicated by white arrows.

En face OCT angiograms by DLOGIV were presented in **Figure 5.3,** showing different vascular network pattern at different depths. The *en face* OCT angiograms were encoded in different colors according to the depth range. The en face OCT angiograms were generated by a list of augmentation steps, including surface flatterning, 3D Gaussian filter, contrast adjustment and maximum intensity projection in each depth range. **Figure 5.3 A** showed the color-coded *en face* OCT angiograms from a large depth range of 200 – 500 µm.

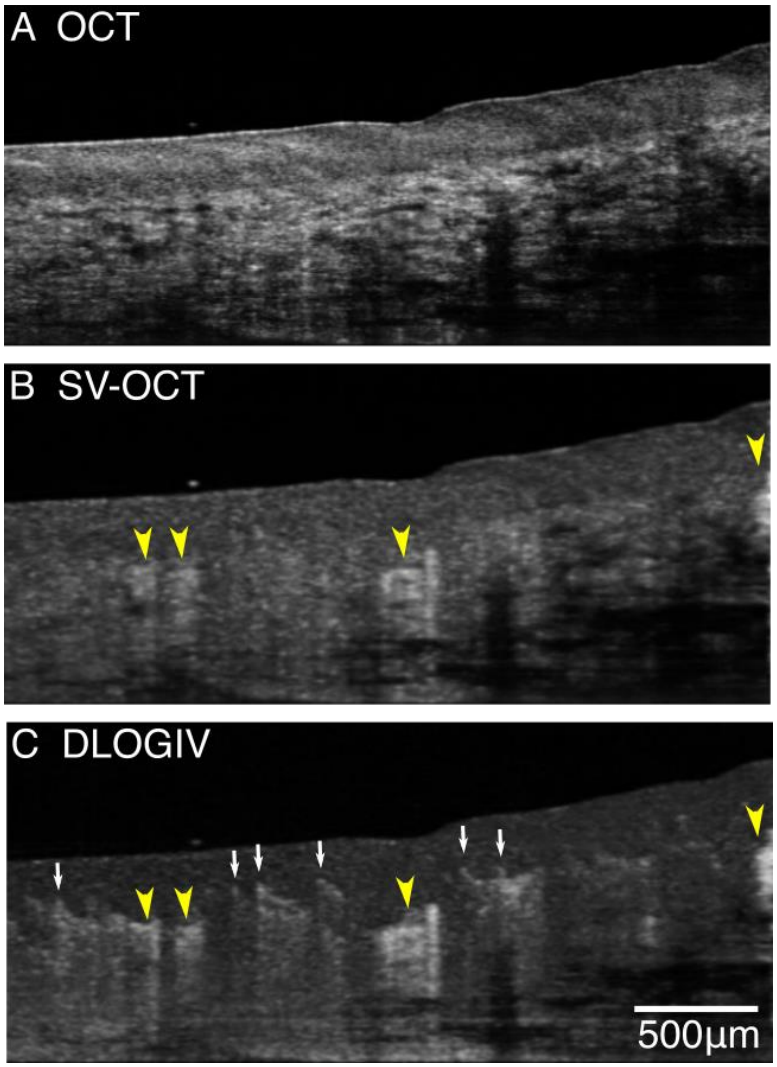

Figure 5. 2 Demonstration of SD-OCT angiography on human finger *in vivo*. (A) Cross-sectional OCT structural image of the dorsal side of the thumb. (B) Angiogram provided by SV-OCT. (C) Angiogram provided by DLOGIV. While SV-OCT image could show some large vessels (yellow arrows), DLOGIV was able to resolve small vessels (white arrows) with higher contrast. Scale bar: 500 µm

Vascular network with a high density could be clearly seen. **Figure 5.3 B-D** showed the vascular network at the depth range of 200 – 300 µm, 300 – 400 µm and 400 – 500 µm, respectively. We could clearly found a vessel emerging from the deeper layer (yellow arrow in **Figure 5.3 D**), bifurcating in the middle layer (yellow arrow in **Figure 5.3 C**) and ended with small branches (yellow arrows in **Figure 5.3 B**). Note that the two horizontal bright lines in all the en face OCT angiograms were due to involuntary motion of the volunteer, which was not fully corrected in post-processing.

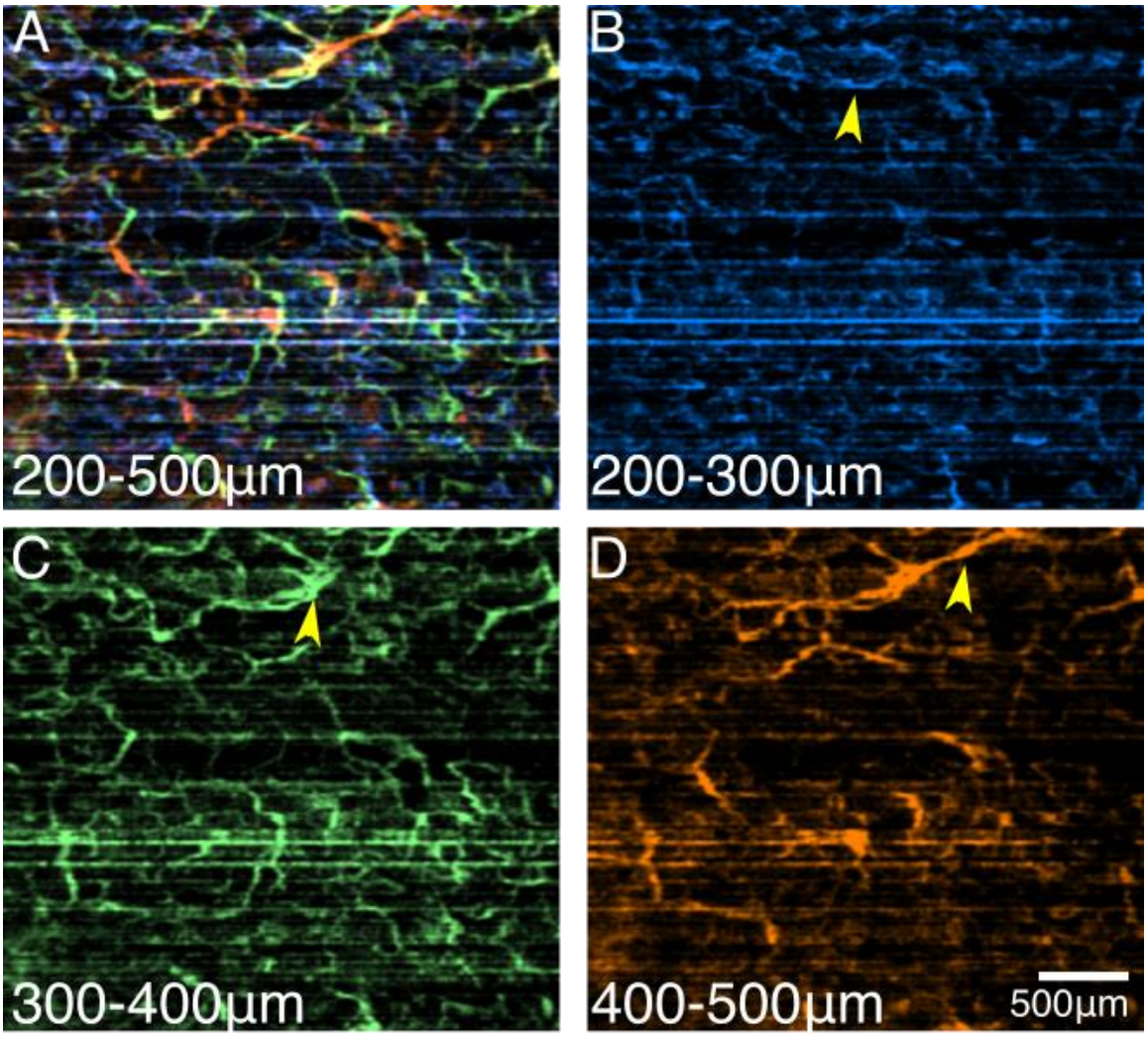

Figure 5. 3 En face OCT angiograms of human finger processed by DLOGIV. Vascular network was colorcoded based on the depth range (B – D) showed the vascular network at the depth range of 200 – 300 µm, 300 – 400 µm and 400 – 500 µm. (A) was the colorcoded vascular network generated from maximum intensity projection of (B) to (D).

5.6 Results of SDM-OCT angiography

5.6.1 SDM-OCT Angiography on human finger nail

From the SD-OCT results, we have demonstrated the feasibility of DLOGIV method to provide the high-contrast OCT angiograms to render capillary network. In this section, we demonstrated the feasibility of angiography with SDM-OCT system. In vivo imaging of human finger nail fold was performed with standard 1×4 SDM-OCT system. Angiographic results of the finger nail fold were shown in **Figure 5.4**. **Figure 5.4A** showed a photograph of the volunteer's middle finger, with a caliper on top to show its size. A dashed white

rectangle box was drawn to indicate the scan area of four parallel beams. Each beam covered an area of 5.9mm× 2.2 mm. The total scan area was 5.9 mm × 7.5 mm, which covered about half of the nail fold. Each OCT acquisition consists of 850 A-scans per B-scan and 162 B-scans, yielding a pixel spacing of ~7 µm and 14 µm in fast and slow axes. With 5 repeats applied for angiographic data acquisition, the equivalent total number A-scans for all the four beams would be 2.754 million. With the equivalent A-scan rate of 400,000 kHz, the total scan time for the whole data was 8.1s, with 85% duty cycle in the fast axis. The frame rate was set to 100 Hz in this acquisition. **Figure 5.4 B - D** showed the SDM-OCT angiographic result of the nail fold. The generated OCT angiogram showing the microvascular network, labeled in red channels, is overlaid on top of corresponding OCT structural image in gray scale, with maximum intensity projection. **Figure 5.4 B** showed the en face view of the overlaid microvascular map at a depth of 1mm from the upmost surface of the nail fold. Meshed structure of arterioles and venules in the vascular network was observed in the deeper region of the nail fold, indicated in the white dashed rectangle box in the left bottom panel. Due to the maximum intensity projection, not all the capillaries stood out from the bright OCT structure image in the epidermal layers. For the rest of the visible capillaries, they appeared small and scattered in the en face image, indicated by the two yellow dashed rectangles in the top panel. **Figure 5.4 C and D** were the XZ and YZ cross-section views of overlaid OCT structural images and angiograms at the corresponding locations indicated by the white dash lines in **Figure 5.4 B**. The vascular map was cropped from 250 µm to 1050 µm below the surface of the nail fold for each axial scan. The upper layer was cropped to remove the speckles and artifacts close to surface region. Also, most of the region in the first 250 µm depth belonged to stratum corneum layer, with minimal vessels inside this region. The region below the depth of ~1050 µm was cropped due to low contrast of angiographic signals. Below these regions, the logarithmic-scale intensity of structural images of the nail fold also dropped a lot, which would significantly affect the SNR of the angiographic signals. In these two images, individual vessels were clearly visible in both images, with most of visible vessels located at the bottom of epidermal layers and subdermal layers. The larger vessels (white arrows) located slightly deeper than the smaller vessels (yellow arrows). Note that projection artifacts, where the blood vessel signal extended from superficial layers to deeper layer and formed a vertical line in the cross-sectional image, were also visible in **Figure 5.4 C and D**. It was well explained in the literature that they were caused by both multiple scatterings inside the tissue passing through the red blood cells (RBCs) in

different directions, as well as fluctuation of intensity underneath the moving red blood cells[74, 191]. Stitching of images from four parallel beams were denoted in **Figure 5.4 D**. **Figure 5.4 E** showed the corresponding 3D rendered image of finger nail fold vasculature. With the noise bed removed from top and bottom layers, microvasculature of the nail fold could be clearly rendered.

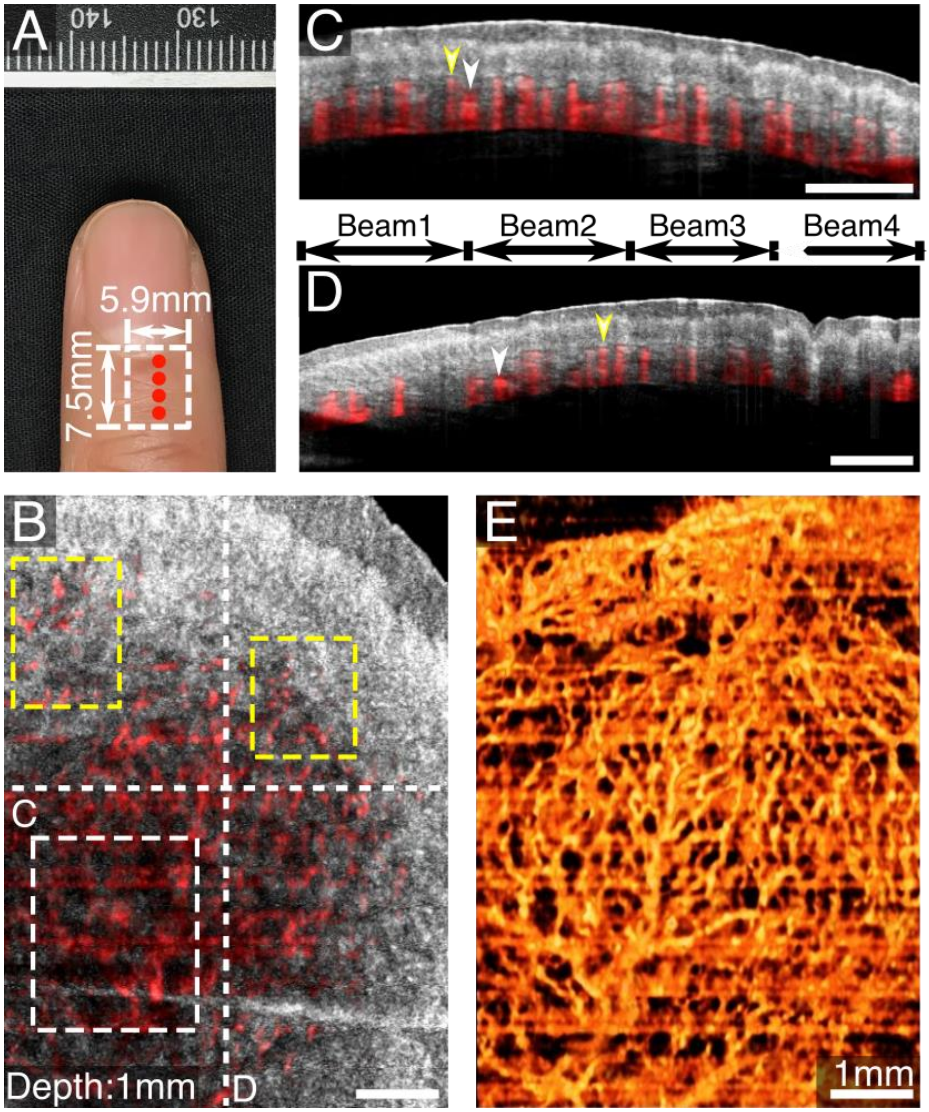

Figure 5. 4 Angiography with the standard 1×4 SDM-OCT system. (A) Photograph of volunteer's middle finger. Four beams were scanning simultaneously, covering a total imaging area of 5.9mm × 7.5 mm. (B-D) SDM-OCT angiographic results showing vascular network of the finger nail in *en face*, XZ cross-section and YZ cross-section views. The blood vascular network, labeled in red, overlaid on top of corresponding OCT structural image. White rectangle: meshed vasculature in the deeper skin layer. Yellow rectangles: scattered small vessels in the superficial skin layer. White arrows: large vessels; Yellow arrows: smaller vessels. Stitching of both structural images and angiograms from 4 different beams were indicated in (D). (E) 3D rendering of vascular network from all depths, viewed from the top. Scale bar: 1 mm for all the images.

In order to visualize different patterns of the microvascular network, the generated angiograms of the finger nail fold from the previous obtained SDM-OCT data were further color-coded in depth. To generate the color-coded SDM-OCT angiograms, the surface of the nail fold region was first mapped out based on 3D OCT structural data. A mean filter was applied to the mapped surface to remove discrepancies of the nail fold surface and smoothen it due to saturated reflections of the baby oil layer applied onto the skin. Then, the 3D OCT angiograms were flattened according to the mapped surface to ensure that the microvasculature at the same depth range was coded with the same color. Results of color-coded SDM-OCT angiograms were presented in **Figure 5.5**. **Figure 5.5 A** showed the merged color-coded SDM-OCT angiograms with a depth range from 250 µm to 1050 µm below the nail fold surface, using maximum intensity projection (MIP) for each color channel. **Figure 5.5 B – Q** showed the individual color-coded angiograms from 250 µm to 1050 µm. Each en face OCT angiogram represented the MIP result within a skin layer of 50 µm thickness in the nail fold region, from epidermal layers below the stratum corneum to deeper sub-dermal layer. In the

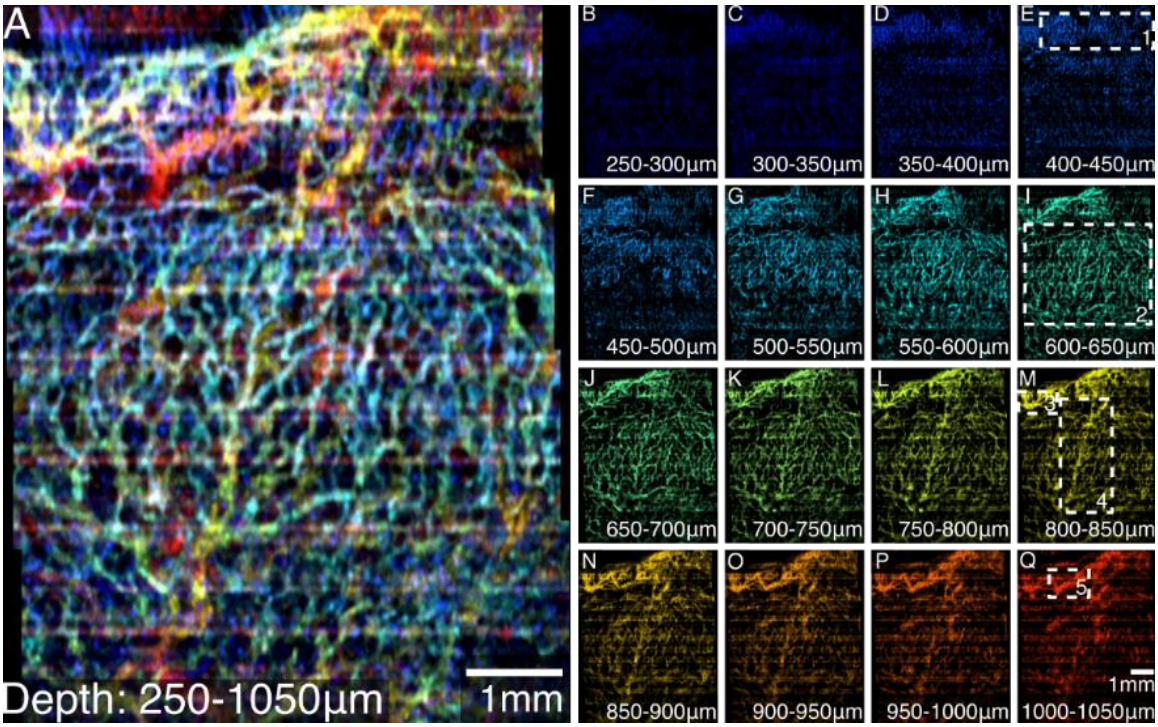

Figure 5. 5 Color-coded SDM-OCT angiograms of the finger nail fold. (A) Merged color-coded SDM-OCT angiograms from a depth range of 250 µm to 1050 µm. Vessels from different depths could be differentiated from the colors. (B – Q) 16 SDM-OCT angiograms showing the vascular network at different skin layers, with a 50 µm increment in depth. Different pattern of vasculature, i.e. thin line and dots in rectangle 1; mesh structure in rectangle 2; main vessels in rectangle 3 to 5, could be easily identified. Scale bar: 1mm for all images.

superficial layer (**Figure 5.5 B to E**, 250 µm -450 µm, first row), the capillaries appeared as thin lines close to the end of the nail fold (rectangle 1 in **Figure 5.5 E**) and scattered points in the angiograms, indicating they were growing close to normal direction of the surface. In the middle layer (**Figure 5.5 F to I**, 450 µm - 650 µm, 2nd row), right below the dermo-epidermal junction (DEJ) of a depth of ~430 µm measured from the cross-sectional OCT structural image, the vessels were observed to have medium sizes and mesh-like network structure (rectangle 2 in **Figure 5.5 I**). In the deeper, sub-dermal layers, large vessels started to appear (rectangle 3 and 4 in the **Figure 5.5 M**), forming main circulatory system for the proximal nail fold. Another larger vessel appeared at ~900 - 1050 µm depth (rectangle 5 in **the Figure 5.5Q**). With the color-coding onto the different layers of the SDM-OCT angiograms, we could easily identify the vessels from different depths and observe different patterns of microvasculature in different skin layers.

5.6.2 Full-range SDM-OCT Angiography

With the same approach to modify the SDM-OCT system for full-range application, we demonstrated the full-range SDM-OCT angiography (FR-SDM-OCTA) on human finger nail. **Figure 5.6** showed the results of a full-range SDM-OCT angiogram of human finger nail. A photograph of the volunteer's index finger was shown in **Figure 5.6 A**. Due to dense sampling to achieve proper angular speed for full-range application, the imaging range was set smaller in the fast axis to maintain the appropriate frame rate for angiography. In this data, 600 axial scans were captured in each frame, yielding a frame rate of ~140 Hz with 85% duty cycle for each frame. The scan range in the fast axis was set to be ~1.95 mm, yielding a pixel spacing of 3.25 µm and a sampling density of ~2.2 times of Nyquist sampling density. In the slow axis direction, each volume consisted of 300 frames, covering a range of ~1.95 mm. The sampling density in the slow axis direction was close to Nyquist sampling. A number of 8 repeat was employed for each frame acquisition to generate angiography data. Thus, the equivalent total number of Ascans was 5.76 million (600 × 300 × 8 repeats × 4 beams). The total acquisition time for this data was ~17 s. After registration, the frame jitters and overlap regions were removed, yielding a final scan area of 1.7 mm × 7.5 mm. The four-beam stitched cross-sectional FR-SDM-OCT structural image and corresponding angiogram along the slow axis direction were presented in **Figure 5.6 B**. The angiogram was overlaid on top of the structural images using maximum intensity

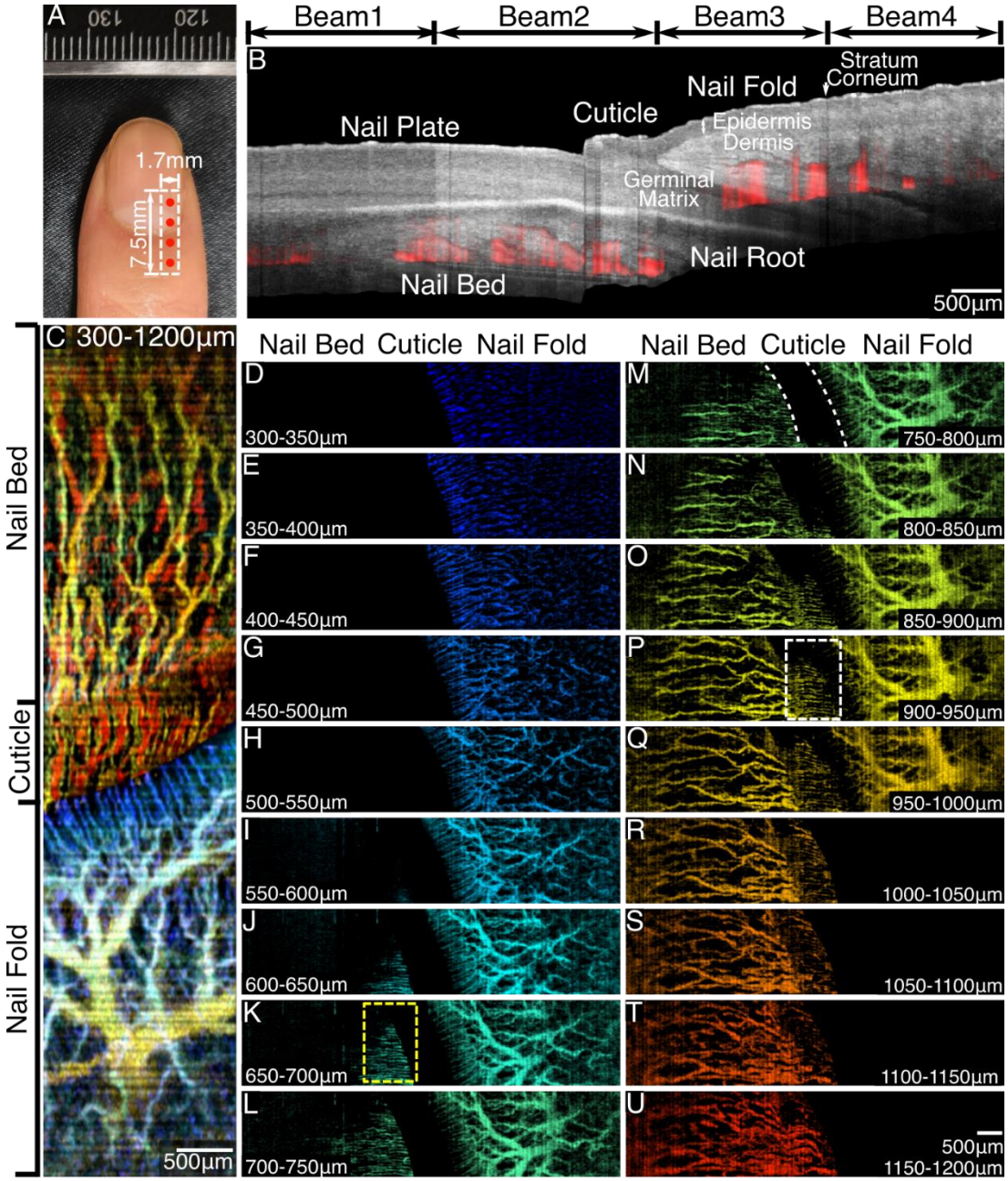

Figure 5. 6 Angiograms of the finger nail junction obtained with the full-range SDM-OCT. (A) Photograph of volunteer's index finger. The scan range of four parallel beams was 1.7mm and 7.5mm in fast and slow axis, indicated by the white rectangle box. (B) Stitched YZ cross-sectional FR-SDM-OCT image of the nail junction. The corresponding angiograms were overlaid on top of the structural image in the red channel. (C) Color-coded FR-SDM-OCTA image of the nail junction, merged from the depth range of 300-1200 µm below the surface. (D – U) 18 FR-SDM-OCT angiograms showing the vascular network at different skin layers, with a 50 µm increment in depth. Representative features of vascular network in nail fold, nail bed and cuticle regions were labeled in white, yellow and orange rectangular boxes, respectively. White dashed line in (M) indicate the separation between nail bed, cuticle and nail fold regions. Scale bars: 500 µm for all the images.

projection in the red channel. Large vessels were observed mostly in the sub-dermal region and part of the

spinous layer in the nail fold. In the nail part, most of large vessels were situated in the nail bed regions. Due to the projection effect, some angiography signals fell into the nail plate region that extending underneath the proximal nail fold, which caused projection shadows in the angiograms. **Figure 5.6 C** showed the depth-coded FR-SDM-OCT angiograms of the corresponding finger nail junction. Both the vasculature in the nail fold and nail bed regions were clearly visible. **Figure 5.6 D - U** showed 18 depth-color-coded angiograms with an increment thickness of 50 µm. Specifically, the depth range of the vasculature in the nail fold and nail bed region were quite different in OCT images. The vascular networks were located at the depth range of 250-1000 µm below the surface in the nail fold region and 600 - 1200 µm in the nail bed region. Below these regions, the angiographic signals of the vascular network could not be distinguished from the noise bed. Above these regions, artifacts were observed, which were attributed to the fluctuation of strong back-reflected signals from the nail surface and the refractive-index-matching oil on top of nail surface, and residue speckle variance signals from imperfect registration of repeated frames. Thus, we manually cropped them off to improve the quality of the OCT angiograms, which were generated by en face maximum intensity projection. In both OCT structural image and angiograms, the cuticle, the ~1mm extension of the proximal nail fold to the nail plate, was visible (Dashed curves in **Figure 5.6 M** showed the boundary of cuticles), yielding discrepancy of the depth range of angiographic signals in these regions. The depth range of vasculature in the cuticle regions were ~200-250 µm deeper than the nail bed region, which started to be seen at the depth of ~850-900 µm below the cuticle surface. Since the vasculatures in the nail bed and the cuticle regions were located at the same depth, they were actually connected. For example, the nail-bed vasculature in the yellow rectangle box in **Figure 5.6 K** could match with the vasculature in the cuticle region in the white rectangle box in **Figure 5.6 P**.

Features of vasculature in different skin layers were extracted from the FR-SDM-OCT images, which were presented in **Figure 5.7**. These features were compared and identified based on Sangiorgi et al. [192], which were realized by corrosion casting technique and imaged under scanning electron microscopy. **Figure 5.7 A** showed the papillary vascular pattern, which located in the depth range of ~200 - 400 µm below the surface. These capillary vessels were located within the dermal papillae extending into the epidermis. In the nail fold region, they were shown as dots in the angiograms (See **Figure 5.6 D**), which were cross-sections

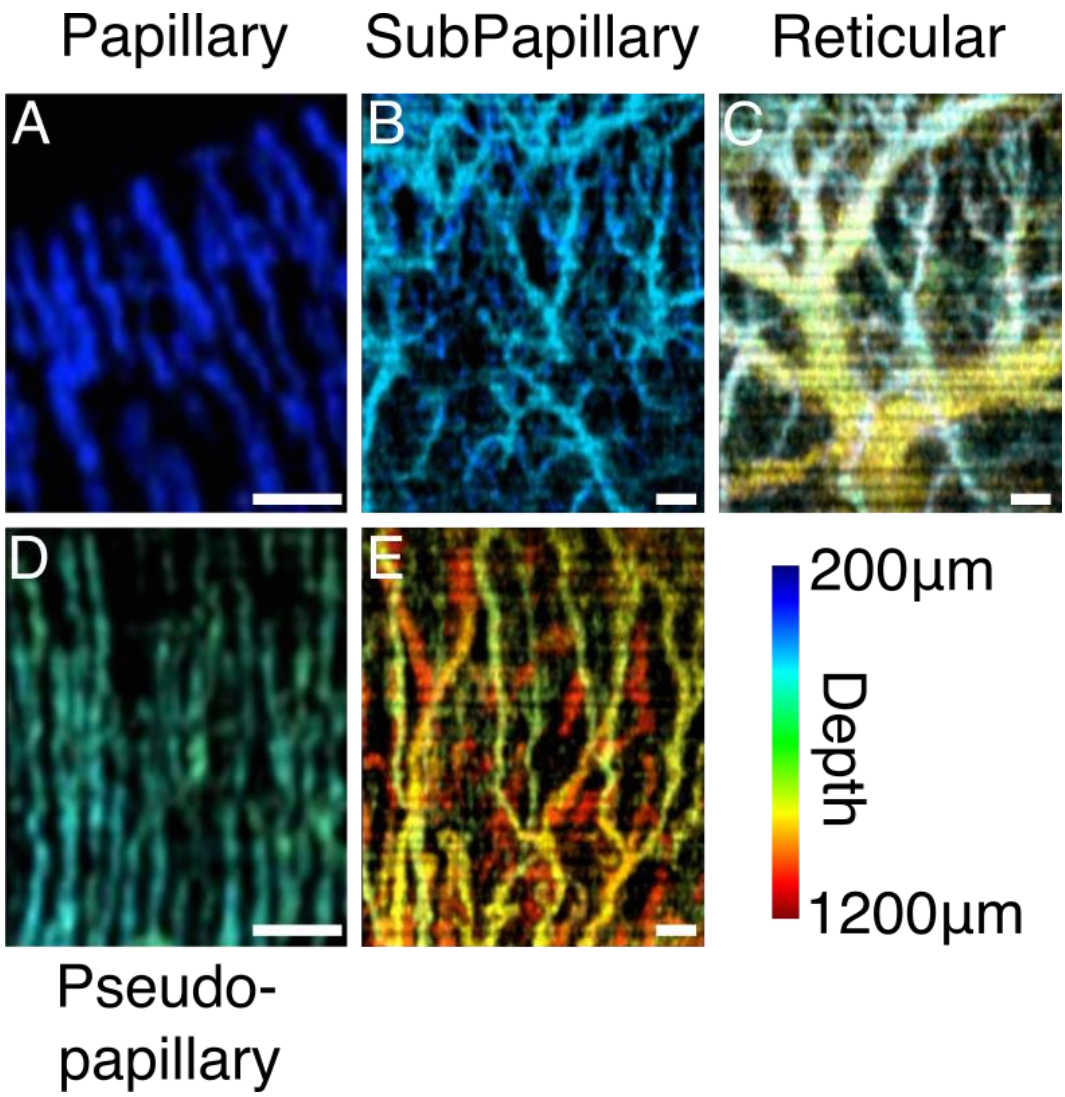

Figure 5. 7 Vascular feature of the nail extracted from FR-SDM-OCTA images. (A) Papillary vascular layers in nail fold. (B) Sub-papillary layer in nail fold (C) Reticular layer in nail fold (D) Pseudo-papillary layer in nail root/nail matrix (E) Sub-papillary layer in nail bed. Scale bar: 200µm

of tilted capillaries. Close to nail junction, at the distal end of the proximal nail fold, the capillaries formed elongated, long loops. An example capillary loop was observed in the top-right side of **Figure 5.7 A.** They were also oriented perpendicular to the nail border and the tilting angle was becoming smaller and smaller. Thus, in the en face projection, in a small field of view, they were shown as parallel, long lines in the image. These features were also well examined by Baran et al. [193] under the OCT. Due to the resolution of the system, not all loop connections between pairs of capillaries at the distal end were visible. **Figure 5.7 B** showed the sub-papillary vascular network in the nail fold, which were located right below the dermal-

epidermal junction (DEJ), located at a depth range of 400-600 μm. The medium-size arterioles and venules formed a meshed network orienting in the same plane. **Figure 5.7 C** showed the reticular vascular layer in the sub-dermal region of the nail fold. A large vessel was originated from the deeper layer and its distal branches were connected to the sub-papillary vascular network. **Figure 5.7 D** showed the pseudo-papillary vascular layer located close to nail junction. The vessels in the pseudo-papillary vascular layer were observed as parallel lines within a thin depth range. The orientations of these vessels were along the major axis of the finger. These capillaries were believed to be straightened longitudinal vessels, originated from the nail root located at the passage from nail root to the nail bed [192]. **Figure 5.7 E** showed the sub-papillary vascular network of the nail bed regions. These vessels were connected to the pseudo-papillary network (**Figure 5.6 M**) in the superficial layer. They were all oriented close to the direction of the major axis of the nail in the nail bed (yellow vessels) in the same plane in a thin layer, and cross linked (orange vessels) to the vascular network in the deeper layer (red vessels).

5.7 Discussions

5.7.1 Multiplexed OCT System for Angiography

In the last two sessions, we successfully demonstrated OCT angiography of the human finger *in vivo* with the SDM-OCT system. Previously, several multiplexed OCT systems have been demonstrated to have the capability of angiography detection. Two-beam or three-beam approached have been established, with multiple detectors, to detect the blood flows of the same spots from different angles and reconstruct directional velocity map with Doppler OCT (See Chapter 3.3). Song et al. also reported a Fourier domain multiplexed dual-beam SS-OCTA system [116]. The detection scheme was similar with our system, with the images from the two beams separated at different imaging depths. However, the major difference was that the two beams were transmitted in different sample arms with one flexible arm to adjust the focus of the beam, which made the system more complex and difficult to align. SDM-OCTA utilizes only one sample arm to accommodate all the four split channels and utilizes a single detector to detect the OCT angiography signals from all channels, which proved it to be a practical and cost-efficient multiplexed system for functional OCT imaging. With the multi-beam illumination provided by SDM-OCT technology, the acquisition speed of the angiography data could be enhanced by several folds. Since the angiography data

was also sensitive to the SNR of the system [158, 194-196], SDM-OCT technology also maintain the image quality of angiography data without sacrificing the system sensitivity.

5.7.2 Phase Stability of SDM-OCT System

One concern of successful detection of angiography signals with SDM-OCT were the depth-dependent phase stability. The triggering jitter may induce large phase variation between A-scans, yielding poor phase stability and performance of angiography in the deeper depth range[158]. With the proper phase calibration described in Chapter 3, our system has a minimum detectable phase change of ~0.3 rad at the imaging depth of ~20 mm, which was still ok to resolve the blood flows for the farthest beam. We should note that, the minimum detectable phase change in the SDM-OCT system was observed to be proportional to the imaging depth. Within the imaging depth of first ~1 mm from zero delay, the minimum detectable phase change could be as small as a few mrad, which was comparable with the performance of SD-OCT (0.4 mrad at ~170 μm [172]). Further improvement can be performed to optimize the sub-pixel FBG peak locations by fitting the smoothed FBG peak regions with a Gaussian function, ensuring that the phase differences between these two FBG peaks have small variance among all the A-scans.

5.7.3 Imaging Protocols for SDM-OCT Angiography

Two key parameters would be considered during the acquisition of angiography data. First, the time interval, the inverse of frame rate, determines the dynamic range of detectable velocity of blood flows in Doppler or speckle signals [33, 157] (See Chapter 5.2.1). To obtain a good angiogram, the frame rate between 100 to 400 was recommended in practice. For standard SDM-OCT angiography, we can control the pixel spacing to maintain the appropriate frame rate. Sometimes, it might lead to reduced lateral resolution due to insufficient sampling density. However, for FR-SDM-OCTA, the scan range was proportional to the frame rate once the offset was predetermined. Thus, additional limitation would be posed to the scan range once the frame rate and beam offsets are determined. In our study, a maximum scan range of ~6 mm could be achieved with 850 Ascans per Bscan with standard SDM-OCT (Nyquist sampled) while the scan range was limited to ~2 mm with 600 Ascans per Bscan with full-range SDM-OCTA (twice oversampling density), with ~2 mm beam offset. Second, the number of repeats, determines the contrast of blood flow signals. In

our study, a repeat number of 5 and 8 is tested, with a good contrast of vasculature of human finger nail fold. A repeat number of 4 was also tested with visible vasculature. Futher investigation would be made to find out the optimal imaging protocol that balance the need betweeen the contrast of angiograms and acquisition time to mitigate the motion artifacts.

5.7.4 Improving OCTA Performance

The SV-OCT and DLOGIV were implemented in our study due to their simplicity, yielding a fast output from the post-processing. To further optimize the performance of angiography with a higher vascular contrast to detect smaller vessels, other complex OCTA methods, described in Chapter 5.2, could be applied to our OCT angiographic data. In a preliminary test, we compared the performance of DLOGIV method with the eigen-decomposition method by processing the same data [197]. The angiography data processed by eigen-decomposition has better contrast for the papillary vascular network as compared to DLOGIV method. Also, the noise bed was naturally removed during the processing, enhancing the projection contrast of angiograms. However, one noticeable difference was that the large vessels in the reticular layer, right above the noise bed of the angiograms, were picked up by the DLOGIV method but not clearly differentiable by the eigen-decomposition method.

Additional post-processing augmentation steps could be employed to further enhance the quality of the SDM-OCT angiograms. First, projection artifacts could be potential removed to remove the false-positive vessels in the deeper layer, which has been validated in retinal OCTA images [198-200]. Second, residues of static signals could be further removed by Hessian-filter based methods to enhance the contrast of blood vessels [201-204]. Third, images from the four different beams could be registered separately to address the issue of finger rotation that yields different translational movements for different parts of the finger.

5.8 Summary

In this chapter, we demonstrated the feasibility of the OCT angiography (OCTA) with SD-OCT and SDM-OCT to visualize blood flows and vascular network in human fingers *in vivo*. With the repeated scanning pattern at each B-scan location, we can detect the moving red blood cells based on the speckle changes in OCT images, showing the capability of OCT to perform functional monitoring of the skin microvasculature.

SDM-OCT, with multi-fold speed improvement, can significantly reduce the acquisition time of OCTA to cover the same area, yielding reduced motion artifacts as well as improved patient comfort during OCTA imaging. In the future, SDM-OCTA could be potentially employed to visualize retinal microvasculature to facilite the diagnosis of retinal diseases.

Chapter 6: OCT Application on Non-destructive Characterization of Drying Droplets and Latex Systems

6.1 OCT in Non-destructive Testing and Evaluation

Most of OCT applications are dedicated to characterize biological samples and study the disease-related problems. However, impact of OCT is less recognized outside the biomedical field. Given the OCT advantages of fast 2D cross-sectional or 3D, high-resolution, non-contact and non-destructive imaging, OCT can be a valuable tool in the field of non-destructive evaluation (NDE) and non-destructive testing (NDT), to answer scientific questions in fundamental researches and in industry [205].

Table 6. 1 Representative OCT Applications in Non-destructive Testing and Evaluation

Representative OCT Applications in Non-destructive Testing and Evaluation

Applications	**References**
Multilayered Foils	Nemeth et al. [206]
Tablet Coating	Zhong et al. [207], Koller et al. [208], Lin et al. [209]
Micromachining	Wiesner et al. [210]
Solar Cells	Thrane et al. [211], Tsai et al. [212]
Paper	Prykari et al. [213], Alarousu et al. [214]
Circuits	Shao et al. [215]. Serrels et al. [216], Anna et al. [217]
Plant & Food	Meglinski et al. [218], Goclawski et al. [219], Verboven et al. [220]
Jade & Pearl	Lee et al. [221], Zhou et al. [222], Yang et al. [223], Chang et al. [224]
Artwork conservation	Cheung et al. [225], Cheung et al. [226], Targowski et al. [227]
Contact lens metrology	Davidson et al. [228], Coldrick et al. [229]
Ceramics	Su et al. [230], Su et al. [231]
Ferroelectrics	Haussmann et al. [232]
Coating	Lenz et al. [233], Veilleux et al. [234]
Automotive Paint	Zhang et al. [235], Dong et al. [236], Zhang et al. [237]
Glass	Chen et al. [238], Chen et al. [239],Kunicki-Goldfinger et al. [240]
Biofilm	Xi et al. [241], Dreszer et al. [242], Blauert et al. [243], Wagner et al. [244]
Adhesive, Dental Adhesive	Ford et al. [245], Makishi et al. [246], Bista et al. [247]
Polymer composites	Dunkers et al. [248], Stifter et al. [249], Liu et al. [250], Shirazi et al. [251]

Table 6.1 lists a few representative OCT applications in NDE and NDT, which has been mostly reviewed by Nemeth et al. [205] and Golde et al. [62]. With micron-scale resolution, OCT can be utilized to detect surface defects of glass, solar cells, polymer composites and pearls. With the superior depth-resolvability provided in cross-sectional measurement, OCT has the advantage to characterize layered structures, i.e. foils, paintings, automotive and tablet coatings, biofilms, ceramic and paper, and conduct thickness measurement with high-precision.

In this chapter, I will describe the OCT application on non-destructive characterization of drying dynamics of soft matter system. Specifically, we will use OCT in combination with other imaging modalities to characterize three drying models: 1)Evaporating water droplets with low initial concentration of additions; 2)Drying colloidal droplets with a high initial concentration of particles; 3)Drying latex film. The drying process of these systems can last for as short as a few minutes for droplets to as long as a few days for latex. Given the fast acquisition time for OCT cross-sections, we can use OCT to detect fast-dynamics of flows or particle mobility. Given the non-destructive nature of OCT, we can use time-lapse OCT for long-term monitoring of the drying process of droplets and latex.

6.2 Drying Progression of Evaporating Water Droplets

6.2.1 Introduction

Drying droplet models have gained widespread interest since 1980s [252]. Studies of drying droplet, including changes of drying rate and contact angle, progression of its shape, and final deposition pattern help us to understand many interesting phenomena, e.g. coffee ring effects [253], electro-wetting effects [254], and Marangoni flows [255]. Mechanisms behind these phenomena may involve a complex interplay of convection and evaporation, surface tension and capillary interactions, membrane stretching and bending, contact line pinning and depinning, hydrophobicity, and Marangoni forces [254, 256]. During drying, other than the pure water droplet, the composition of droplets, including various concentration of particles [257], polymers [258-260], surfactants [261], solvents [262] and salts [263] would alter the interactions among these transport mechanisms, thus affect the drying behaviors. Additionally, the environmental condition and the substrate properties would also affect the drying progression and final deposition [264, 265]. The insight gained from these studies of evaporating droplets ultimately transform to applications in polymer science, biomedicine, food control and nanotechnology [265], which involves inkjet printing [266], , DNA chip [267], biosensor [268, 269] and disease diagnosis (based of deposition pattern of biologicalfluid) [270-273], food quality analysis [274], particle separation [275], production of nanoparticles for drug delivery [276, 277], to name a few.

6.2.2 OCT Studies on Evaporating Water Droplets

To date, four studies have been conducted using OCT to monitor the drying progression of evaporating droplets with low initial concentration of components in water. **Table 6.2** summarize the details of experimental designs for these studies. Also, **Figure 6.1** illustrated the schematics of drying progression and final deposition of these four droplets models.

Table 6. 2 Experimental Designs of OCT Studies on Evaporating Water Droplets

Experimental Designs of OCT Studies on Evaporating Water Droplets

Reference	**Trantum et al.**	**Trantum et al.**	**Davidson et al.**	**Edwards et al.**
Year	2013	2014	2017	2018
Components	Polystyrene (PS) Melamine Formaldehyde (MF) Silica (Si) Dia: 1 µm	Particles surface functionalized with anti-M13 monoclonal antibodies Glycerol Dia: 1 µm	Lyotropic chormonic liquid crystal (LCLC): Sunset Yellow FCF (SSF) Tracer: Polystyrene Dia: 1 µm	Binary Drops: Ethanol; n-butanol Tracer: 2% polystyrene Dia: 2 µm
Initial concentration	vol%:0.005% (10^5/uL)	vol%:0.05% (10^6/ul) Glycerol: 8%	wt%: 5-20%	wt%: 2-20% Tracer: 0.01%
Substrate	Plain glass slide	PDMS	Glass slide Coverslip	Glass Glass coated with Flutech LE15
Environment	Ambient	Ambient	Chambered	Chambered
Droplet Model	Sessile	Sessile	Sessile	Sessile Pendant
λ_{OCT}	860 nm		800 nm	1300 nm
Axial & Lateral Resolutions (in air)	6.4 µm 8 µm		1.9 µm 3.5 µm	5.5µm 13 µm
Acquisition Mode	Cross-section 5 fps or 0.5 fps 200 frames		Cross-section Early stage: 33 fps Time-lapse: 50 fps, 30 frame step: ~3-4 s	Cross-section 50 fps

Trantum et al has demonstrated the first study to utilize the OCT to visualize the cross-section of drying water droplets with particles (See **Figure 6.1 A**) [278]. Low concentration of polystyrene, melamine formaldehyde or silica particles with a diameter of 1 µm and a volume fraction of 0.005% were diluted in distilled water. The water droplet was deposited on a cleaned, plained glass slide. The drying experiment was conducted in the ambient condition with relative humidity (RH) controlled to 30% or 40%. Their results showed that both sedimentation rate and evaporate rate would affect the drying dynamics of particle-

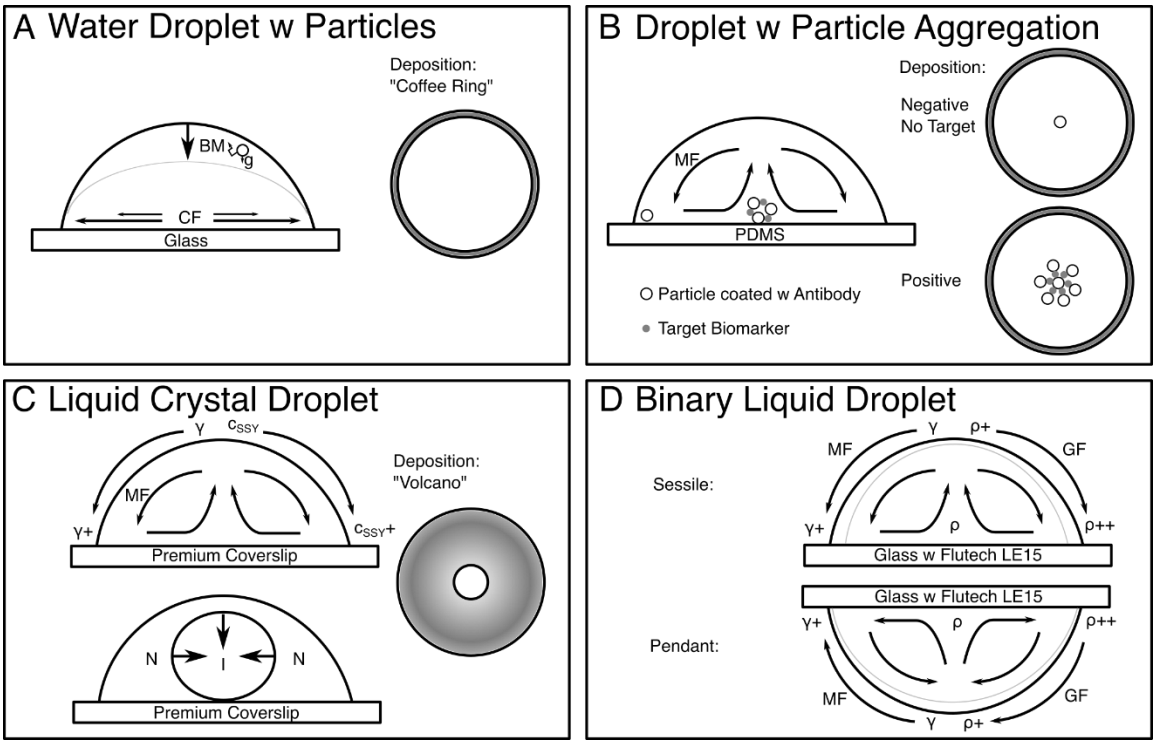

Figure 6. 1 Illustrations of Drying Progression and Final Deposition of Four Droplet Models. (A) Water droplets with particles, i.e. polystyrene, melamine formaldehyde, silica. (B) Water droplet with antibody coated particles to detect biomarkers. (C) Liquid crystal droplet (D) Binary liquid droplet.

contained water droplets. In fast evaporating mode, the decreasing rate of droplet height might be faster than the particle sedimentation rate, yielding the particles trapped at the air-water interface (top surface) of the water droplet. Close to the water-substrate interface, the capillary flows (CF, "coffee ring" flows) played a main role to transport the particles to the pinned contact line, yielding a "coffee ring" final deposition pattern. Increased particle densities, i.e. silica (2.00 g/cm^3) as compared to polystyrene (1.04 g/cm^3) lead to early sediment of particles and early transportation of particles to the edge by capillary flows. Their results suggested a way to control the final deposition of coffee ring structure based on particles' density.

Based on the water droplet model, the same group has proposed a design of biosensor utilizing the drying behaviors and final deposition pattern to track the existence and concentration of target biomarkers (**Figure 6.1 B**) [268]. In the experiment, the tracer particles were coated with antibodies. These particles would aggregate in the presence of targeted biomarker (M13 bacteriophage in the study). Also, the PDMS with a low thermal conductivity (0.15 W/mK) was used as the subtrate to promote Marangoni flows.

During the drying process, the particle aggregates in the presence of biomarkers showed a thicker convective flow pattern in the cross-sectional OCT images, while the dispersed particles showed a uniformly-distributed convective flow pattern in the absence of biomarkers [268]. Under the influence of Marangoni flows, increase of viscosity by glycerol and gravitation, the particle aggregates would concentrate and deposit at the droplet center, forming a concentric final deposition pattern. Note that, with the glass substrate, the particle aggregates won't concentrate at the droplet center.

Davidson et al., collaborating with our group, have investigated the drying progression of water droplets containing lyotropic chromonic liquid crystals (LCLCs), using polarized optical microscopy (POM) and OCT (**Figure 6.1C**) [279, 280]. LCLCs were composed of organic, charged, and plank-like molecules. During the drying process of LCLC containing droplets, changes of local temperature and concentration of LCLCs induced multiple phases of the LCLCs, including isotropic, nematic, columnar and crystalline phases. In the experiment, sunset yellow FCF (SSY), a dye that belonged to LCLC family, was deposited on the premium coverslip as the substrate. Low concentration polystyrene particles were added in the droplets as tracers. The experiment was conducted in semi-enclosed PDMS chamber, which was sealed right after the droplet was deposited. The total drying time under OCT experiment was ~10 – 15 min. OCT results showed that the convective flows were initiated right after the liquid crystal droplet was deposited. A substantial Marangoni-like flows was visualized in the OCT image, which was opposite to the phenomena observed in the typical water-surfactant droplets. The convective flows were attributed to the increased concentration of SSY near the pinned contact line during the evaporation, yielding a local increase of surface tension gradient along the air-water interface of the droplet. In the next stage, the formation of nematic phase (N) pushed the isotropic (I) liquid boundary to the center, like a shrinking bubble. Finally, the liquid phase diminished at the droplet center. The final deposition pattern of the liquid crystal droplet was like a volcano shape, depending on the initial concentration of SSY particles.

Recently, Edwards et al has utilized OCT to investigate the flow patterns of the drying binary liquid droplets (**Figure 6.1 D**) [281]. Low concentration of solvents, i.e. ethanol or n-butanol, were diluted in the water solution to form binary liquid droplets. Different from the previous three studies, they investigated the flow pattern under different tilting conditions, including the sessile droplet mode with 0° tilting and pendant

droplet mode with 180° tilting. In their OCT results, axisymmetric toroidal flow patterns were observed in the middle of drying processes of tilted binary liquid droplets. In the sessile droplet, a convective flow pattern in the same direction as expected Marangoni driven flow was observed. However, in the pendant droplet, the flow direction was opposite to the Marangoni flow direction, suggesting that Marangoni flows might not dominate in the evaporating binary liquid droplets. They suggested that, the convective flows were driven by the density of the liquid and gravity. In the case of water-ethanol droplet with the preferential evaporation of ethanol, the binary liquid was denser close to the air-water interface than the bulk. Thus, surficial binary liquids would fall along the air-water interface from top to edge in sessile droplets and from edge to bottom in the pendant droplets, driving convective flows in different patterns. Also, they monitored the full drying process of the binary liquid droplets with OCT, showing a three-stage drying process, including first stage of chaotic flows, second stage of convective flows and third stage of outward capillary flows.

6.2.3 OCT Configuration for Droplet Imaging

In the following section, we will describe the experimental details for OCT imaging of water droplets containing polystyrene particles and lyotropic chromonic liquid crystals.

Figure 6.2 shows the configuration of the ultra-high resolution spectral domain optical coherence microscopy (UHR-OCM) for water and LCLC droplet imaging. The schematic diagram of the UHR-OCM is shown in **Figure 6.2 A**. A supercontinuum laser (SC) is employed as the light source with a central wavelength of 800 nm and a spectral bandwidth of ~220 nm, yielding an axial resolution of ~1.5 μm in water. Lateral resolution is measured to be ~3.5μm with a 10× objective. To image the sub-micron crystallized structure, we use a 63× objective instead of 10× objective to further improve the lateral resolution.

Different from other OCT setups employed for droplet imaging, an inverted sample arm setup is employed to illuminate the droplet from the bottom so as to minimize distortion from light refraction from the surface. Also, since the OCT measured the optical path length instead of actual distance, the inverted illumination will avoid the distortion of water-substrate interface of the droplet **(Figure 6.2 B**).

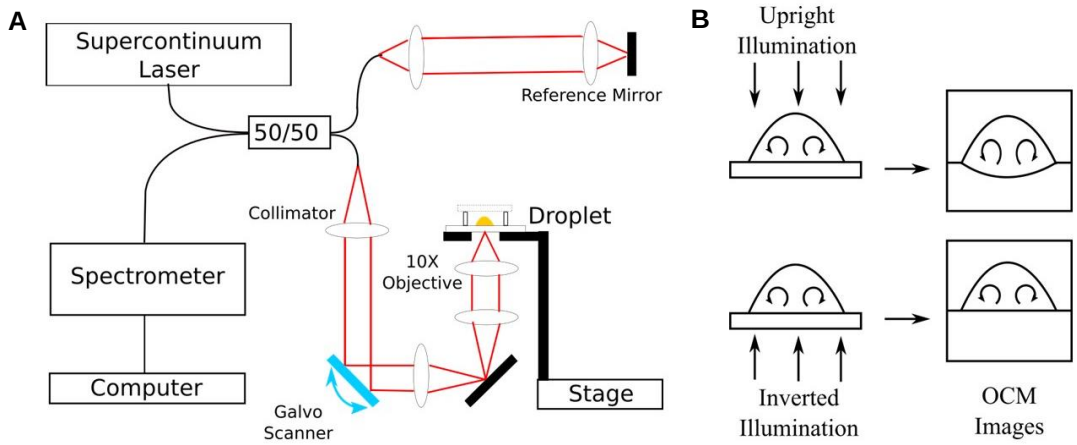

Figure 6. 2 (A) A schematic diagram of the inverted ultra-high resolution optical coherence microscopy system (UHR-OCM). (B) Illustration of the effect of illumination direction on final OCM images. Inverted illumination minimized distortion from light refraction.

6.2.4 Protocols of OCT Imaging of Droplets

Table 6.3 summarized the OCT imaging protoocls for water and LCLC droplets. For the water droplets containing low-concentration polystyrene particles as tracers, we would explore the drying progression of these water droplets with particles under three controlled environments: Ambient condition with fast evaporation rate; Loosely Sealed PDMS chamber with slow evaporation rate; Tightly Sealed PDMS chamber with slowest evaporation rate. In all three conditions, we employed M-mode, time-lapse OCT to monitor the drying progression with OCT imaging initiated prior to droplet pipetting. In the open environment and slow drying condition, the entire drying progression was monitored by OCT. The total drying duration of the water droplets was ~5-6 min in ambient condition and 15 – 20 min in loosely sealed PDMS chamber, respectively. The step time for time-lapse imaging was set to ~3 s, including the acquisition and saving time of individual OCT dataset into the hard drive. The step time was sufficient to catch the motion of polystyrene particles in the drying water droplets. For long-term drying progression of water droplets in tightly-sealed PDMS chamber with extremely slow evaporation rate, we only monitored the drying progression for 30-40 min. After 40min drying, the height of the apex of the droplet only dropped by ~25%.

For LCLC droplets, we employed two separate protocols to monitor their drying phenomena. First, we employed a M-mode, continuous OCT acquisition to detect the initiation of convective flows. In such case,

OCT acquisition started prior to the pipetting of the LCLC droplet. Right after the droplet was pipetted, the PDMS chamber was loosely sealed to reduce the evaporation rate. The frame rate was set to 33 fps. The total OCT acquisition time was 24 s, including 800 repeated cross-sectional droplet images. In another mode, we focused on the entire drying progression of LCLC droplets to monitor the convective flows and phase changes of the LCLC droplets. Time-lapse, M-mode OCT acquisition was employed in this protocol. After the LCLC droplet was pipetted on the premium coverslip, the PDMS chambered was first loosely sealed. Then, OCT previews and position of the droplet cross-section was optimized. It took about 0.5 to 1 min for these procedures before the initiation of time-lapse OCT imaging. The step time was set to 3.8 s and the total drying duration of the LCLC droplet in the slow drying mode was ~15-20 min.

In all the experiments, the droplet volume was maintained at 0.2 – 0.5 µL, deposited using a pipette with a volume range of 0.2 – 2.0 µL.

Table 6. 3 Summary of OCT imaging Protocols for Water and LCLC Droplets

Summary of OCT imaging Protocols for Water and LCLC Droplets

Target Sample	**Phenomena**	**OCT Acquisition Mode**	**Frame Rate, Step Time and Duration**
Water Droplet: Entire Drying Progression	Capillary Flow; Brownian Motion; Contact Line Pinning and Depinning	M-Mode, Time-lapse, Acquire before droplet pipetting, **Ambient Condition (Open)**	43 fps, 2.9 s, 5-6 min
		M-Mode, Time-lapse, Acquire before droplet pipetting, **Loosely Sealed in the PDMS chamber**	43 fps, 3.0 s, 15-20 min
Water Droplet: Early and Intermediate Drying Progression		M-Mode, Time-lapse, Acquire before droplet pipetting, **Tightly Sealed in the PDMS chamber**	43 fps, 15 s, 30-40 min
LCLC Droplet: Initial stage	Initiation of Convective flows	M-Mode; Continuous; Acquire before drop pipetting; **Loosely Sealed** right after drop pipetting	33 fps, Single-shot, 24 s
LCLC Droplet: Entire drying progression	Convective flows, LC phase formation and progression, final shape	M-Mode Time-Lapse; Acquire after optimization of cross-sectional OCT previews (~1min after initiation), **Loosely Sealed** before imaging.	43 fps, 3.8 s (Depend on computer saving time), 15-20 min

6.2.5 OCT Images of Drying Water Droplets Containing Polystyrene Particles

Figure 6.3 showed the drying progression of the water droplet containing polystyrene particles in ambient environment with fast evaporation rate. In the earliest stage (**Figure 6.3 A**), in the bottom layer of the water

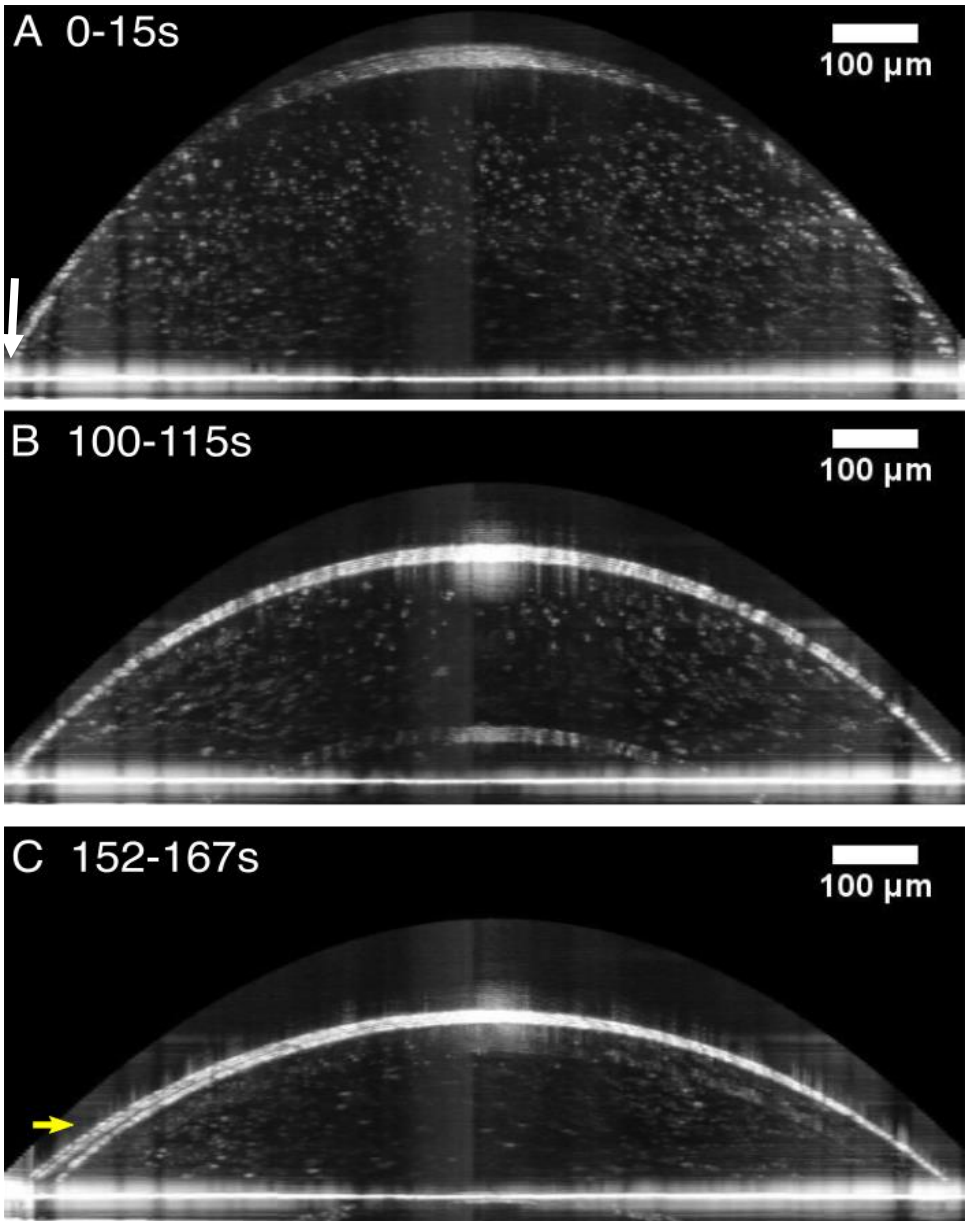

Figure 6. 3 Drying progression of water droplets containing polystyrene particles in ambient environment with fast evaporation rate. Yellow arrow: Contact line depinning.

droplet close to water-substrate interface, particle motions were driven by the capillary flows that compensate the lost water at the contact pinned line (white arrow in **Figure 6.3 A**), where the droplet had the greatest evaporation flux. In the top layer, the particles remained mostly stationary. According to Trantum et al. these

particles were "trapped" with a slow sedimentation rate [278]. In the first 15 second, the initial droplet height of ~400 µm was decreased by 29 µm (7%), yielding an averaging decreasing rate of 116 µm/min. After 100 seconds, the droplet height was reduced to 277 µm (69%) with an averaging decreasing rate of 83 µm/min. In this stage, most of the particles were transported to the contacted pinned line by capillary flows (**Figure 6.3B**). In the middle of the drying process, we noticed that one side of the contact line was depinned (Yellow arrow in **Figure 6.3C**) and moved inward. The moving distance was small compared to the droplet diameter. The droplet was fully dried at ~340 seconds. The observed drying phenomena were comparable with the results in Trantum's study[278].

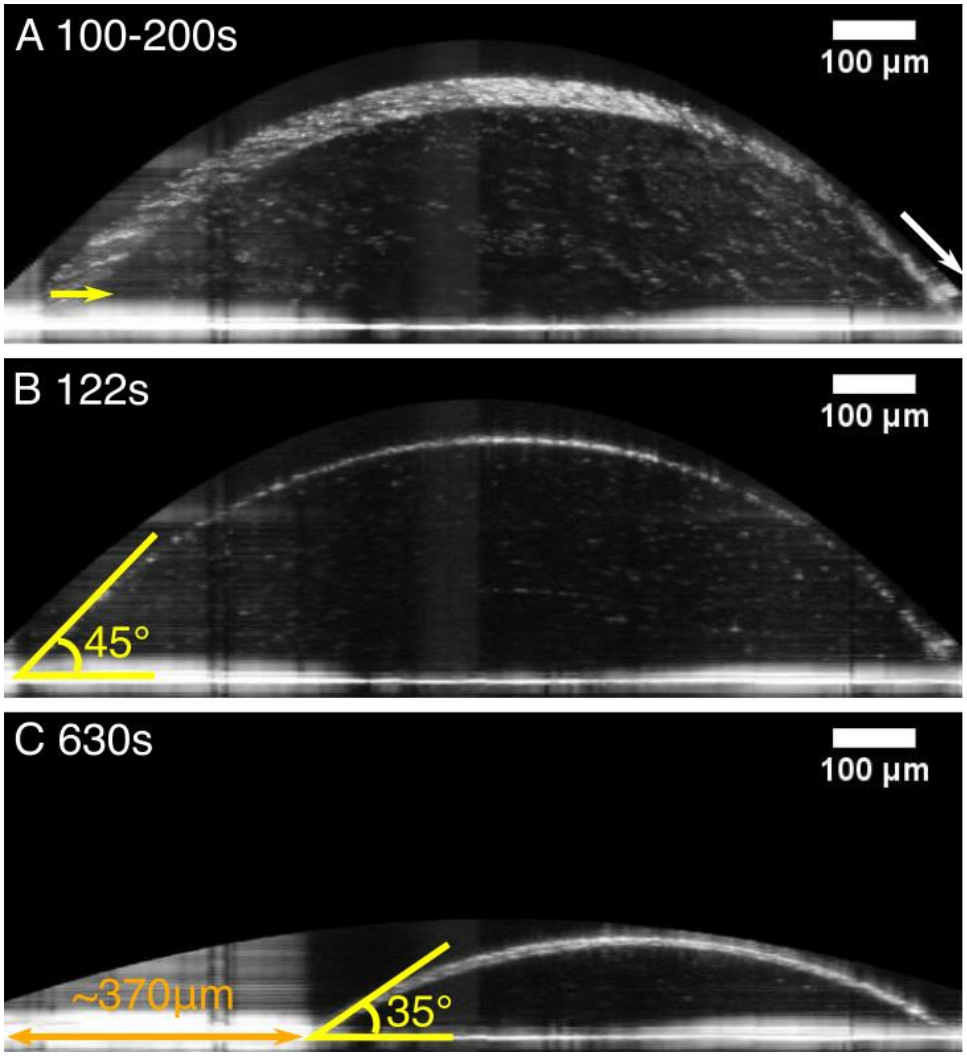

Figure 6. 4 Drying progression of water droplets containing polystyrene particles in loosely sealed PDMS chamber with intermediate evaporation rate. White Arrow: Capillary Flows. Yellow Arrow: Contact line depinning. Contact angles were measured at ~122 s (B) and 630 s (C). The contact line was moved by ~370 µm.

Figure 6.4 showed the drying process of the same droplet in loosely sealed PDMS chamber. The observed phenomena was similar: The particle motions were driven by the capillary flows, with a slower speed. It took ~100 seconds to move the particles in a similar distance (illustrated by the tail length of the tracer particles) as the one in Figure 6.3 B, which took ~15 seconds. However, the contact line depinning was more significant in this case. The contact line kept moving from ~120 seconds ($0.15t_{full}$) to 630 seconds ($0.77t_{full}$). And its total moving distance was ~370 µm, which accounted for 1/3 of its initial diameter. During the depinning process, the contact angle at the depinning line reduced slowly from ~45° to 35°, measured at the time point of 122 s and ~630 s. The total drying time for this droplet was ~815 seconds.

Figure 6.5 showed the drying progression of water droplet in a tightly sealed PDMS chamber. In this drying condition, the overall evaporation rate was extremely slow. Right after the droplet was deposited on the coverslip and the chamber was sealed, in the earliest stage of a few seconds, the capillary flow dominated, driving the particles to the edge (White arrow in **Figure 6.5A**). The particles looked stretched due to the averaging effect of fast particle motion. However, since the droplet was tightly sealed in the chamber, the uneven evaporation flux at the air-water interface of the droplet in the earliest stage caused the relative humidity (RH) outside the the droplet edge reached the saturation level first. In such case, the vertical gradient of the relative humidity was formed, reversing the evaporation rate along the surface. During this time, the apex of the droplet had the highest evaporation rate, inducing the flow to move towards the apex in a form of Marangoni flows to compensate for the water loss (**Figure 6.5B**).The convective flows only lasted for ~3 min (~180 s) until RH inside the sealed PDMS chamber reached the saturation level everywhere, yielding a balanced evaporation rate along the surface. In the next drying stage, the particles inside the droplet underwent two process: Brownian motion and sedimentation. In a short duration, the particles moved randomly in a local region (See **Figure 6.5 C**). In the long term, the polystyrene particles are dropping slowly, which could be observed in Figure 6.5C with a 105 second duration. After ~30 min drying, most of the particles were dropped to the water-substrate interface, with reduced particle concentration (reduced OCT particle intensities in **Figure 6.5D**) the middle of the droplet. In 30min, the droplet height reduced from ~380 µm to ~337 µm, with a total decrease percentage of only 11.3%.

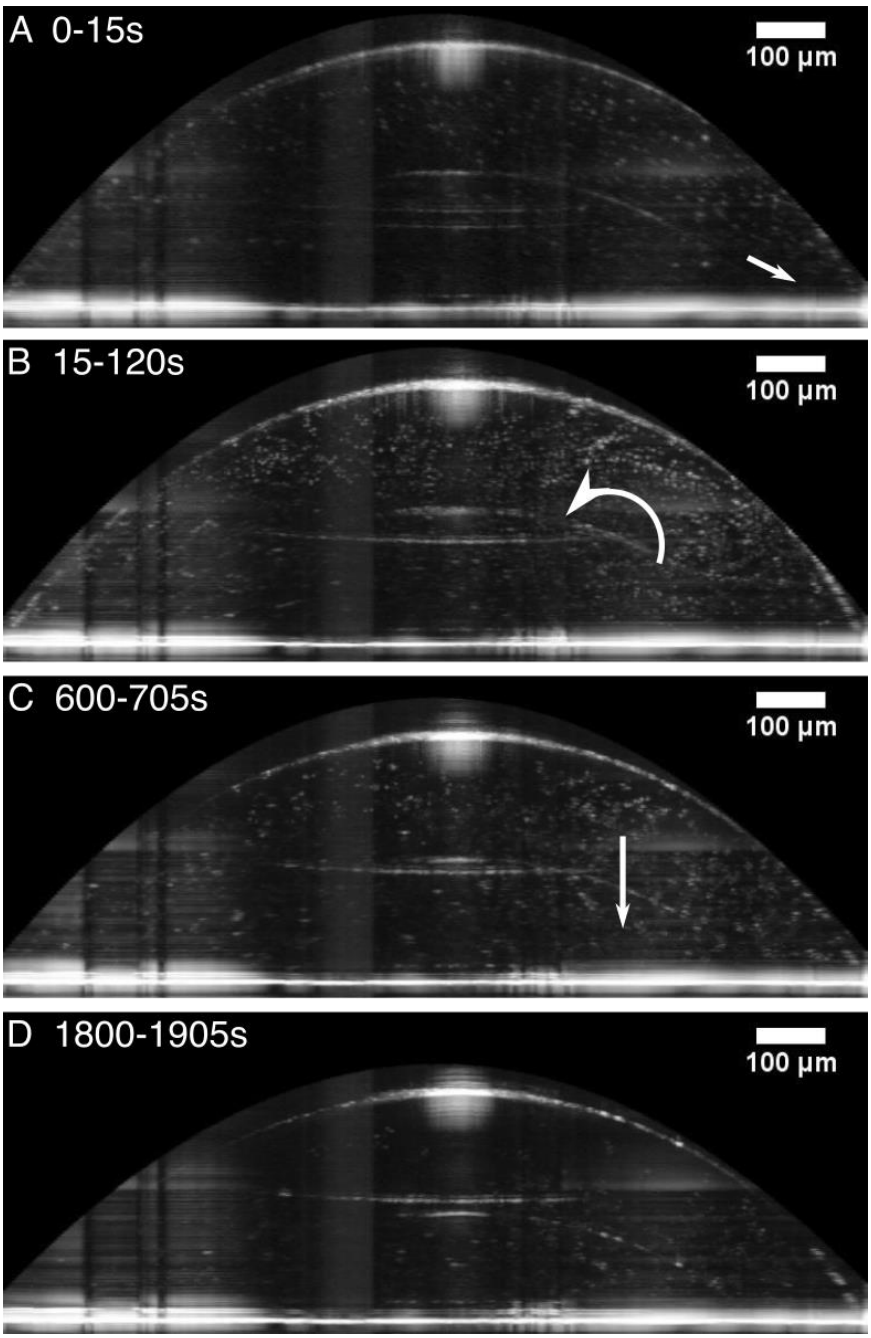

Figure 6. 5 Drying progression of water droplets containing polystyrene particles in the tightly sealed PDMS chamber. White Arrows: (A) Capillary Flows (B) Marangoni Flows (C) Sedimentation.

These three studies showed how we can control the drying rate to alter the drying behaviors of water droplets with low concentration of tracers. With 3D imaging capability, OCT can easily identify the existence of the fluid flows, especially the convective flows, in drying water droplets.

6.2.6 Drying Progression of LCLC Droplets by OCT

Figure 6.6 and **Figure 6.7** showed the results of drying progression of LCLC droplets using time-lapse OCM imaging.The results were included in the published paper by Davidson et al.[282].

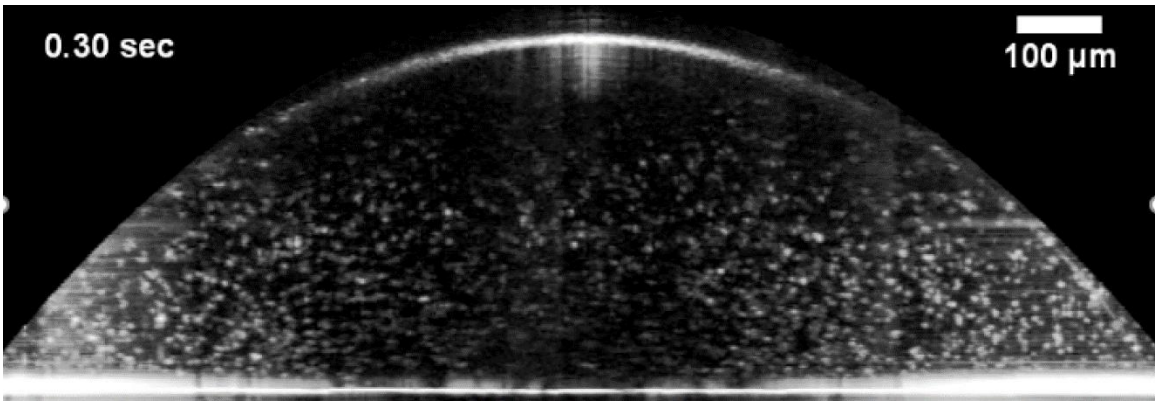

Figure 6. 6 Time-lapse UHR-OCM imaging on initiation of convective flows in SSY solution droplets.

Figure 6.6 showed the cross-sectional UHR-OCM images of the SSY solution droplet at ~0.3s, one frame after the droplet pipetting. From the time-lapse imaging, initiation of convective flows was clearly observed as indicated by movements of tracers, confirming that convective flows were initiated within 0.3s after pipetting.

Figure 6.7 illustrated time-lapse OCM imaging of the entire drying process of a SSY solution droplet imaged by UHR-OCM. **Figure 6.7A** showed the schematic illustration of the phase behaviors of SSY solution droplets at different drying stages. **Figure 6.7B-G** showed the UHR-OCM images of the SSY solution droplet at corresponding drying stages. At the initial drying stage, convective flows were observed, with the flows near the droplet-air interface moving along the surface toward the pinned contact line (white arrows, Figure 6.7B), which was opposite to Marangoni flows observed in water-surfactant droplets (See explanation in Section 6.2.2). After 475s, polystyrene tracers were swept toward the center, forming a shell around the shrinking isotropic fluid region (**Figure 6.7C** and **6.7E**). Outside the isotropic fluid region in the droplet, the SSY molecules were aligned and assembled, forming the nematic phase, which was one of the liquid crystal phase. White arrows in **Figure 6.7C** indicated the phase boundary between isotropic phase and the nematic phase of the SSY solution droplet. Thus, the polystyrene tracers were rejected by the nematic phase of the SSY and irreversibly clustered and deposited at the droplet center by 737 s (**Figure 6.7F**). In the next stage, columnar phase, another liquid crystal phase of the SSY solution droplet, was formed from the

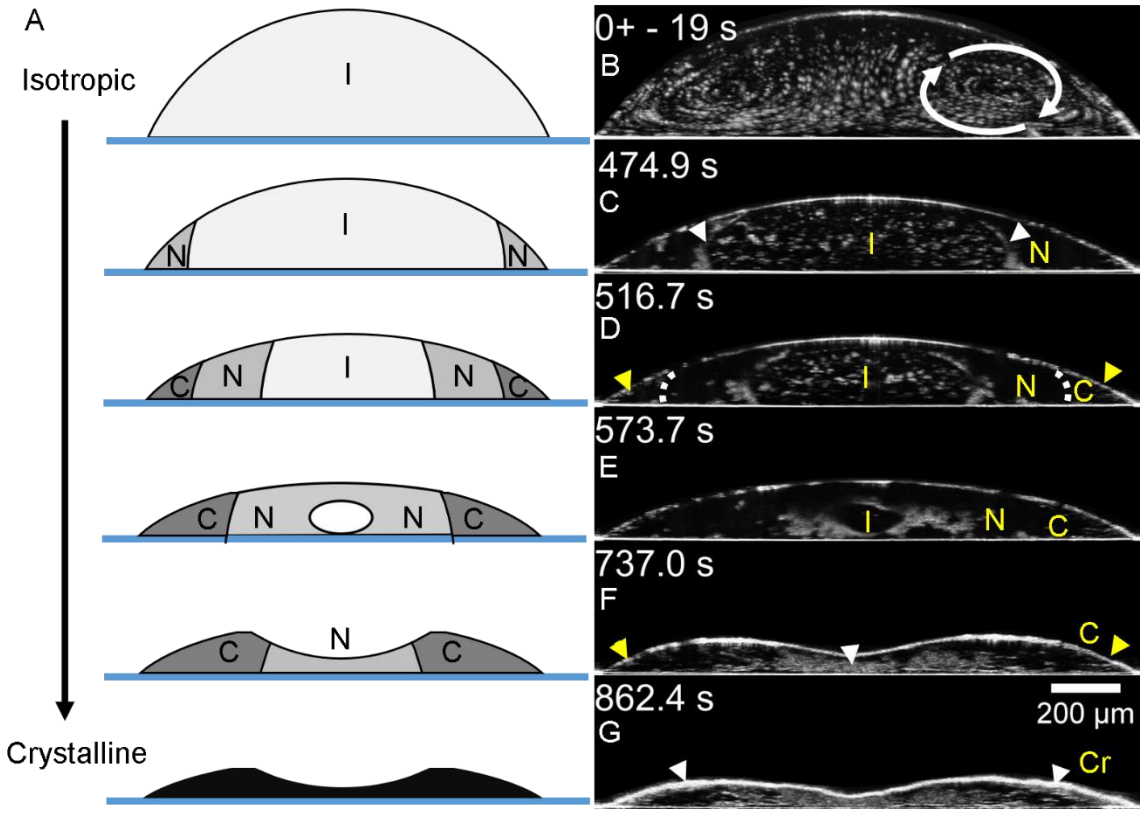

Figure 6. 7 Drying progression of SSY solution droplet imaged by UHR-OCM. Schematic illustration of phase behaviors of SSY droplet at different drying stages was shown in (A). (B-G) UHR-OCM images of the SSY solution droplet at different drying time points. White spots: polystyrene particles as tracers. Cr: crystalline, C: columnar, N: nematic, I: isotropic. White dashed line in (D): Columnar-nematic boundary. White arrows in (C): Nematic-isotropic boundary. Yelow arrows: columnar line structures. White arrow in (G). Crystallized state.

pinned contact line and moved inward. Columnar-nematic phase boundary was not directly observable. However, it could be detected by the end of line structures within the columnar phase (Yellow arrows in **Figure 6.7 D and F**). An illustration of the columnar-nematic phase boundary was shown in **Figure 6.7 D**, indicated by the dotted curve. After 862s, SSY molecules were crystallized (**Figure 6.7 G**). A volcano shape final deposition pattern was observed in **Figure 6.7 G**.

With a high magnification objective lens, we could observe the columnar line structures close to the droplet edge in the en face OCT images. **Figure 6.8** showed the preliminary results of line structures in the en face OCT images, taken with the aid of 63× objective. **Figure 6.8 A** showed the columnar structure under the POM in cross-polarization mode. The columns were mostly aligned in tangential orientation to the droplet edge. Columnar structures with slightly different orientations would be separated by the boundary walls

[282]. **Figure 6.8 B** showed the columnar line structures in the cross-sectional UHR-OCM images and **Figure 6.8 C** showed the columnar structure in the en face OCM image with the maximum intensity projection of ~40 µm. From the cross-sectional UHR-OCM image, a few layers of columnar structures with slightly varying orientation were observed. The observed pattern of the columnar structure in en face UHR-OCM image (**Figure 6.8 C**) was comparable with POM image in **Figure 6.8 A**. However, it was yet to be investigated what is the exact correlation between the columnar structures in POM and OCT images. One potential explanation was that the boundary walls, caused by the discontinuous alignment of the columnar structures, might consist of tiny cracks. These tiny cracks might induce abrupt changes of refractive indices, which could be detected by the UHR-OCM. In our preliminary observation, the columnar structures were not uniformly formed and distributed around the droplet edge in the ambient condition and loosely sealed PDMS chamber, making it difficult for repeated characterization. Further OCT characterization could be conducted on SSY solution droplet in tightly sealed PDMS chamber with optimized OCT monitoring protocols (i.e. time-lapse 3D OCT imaging for a few days).

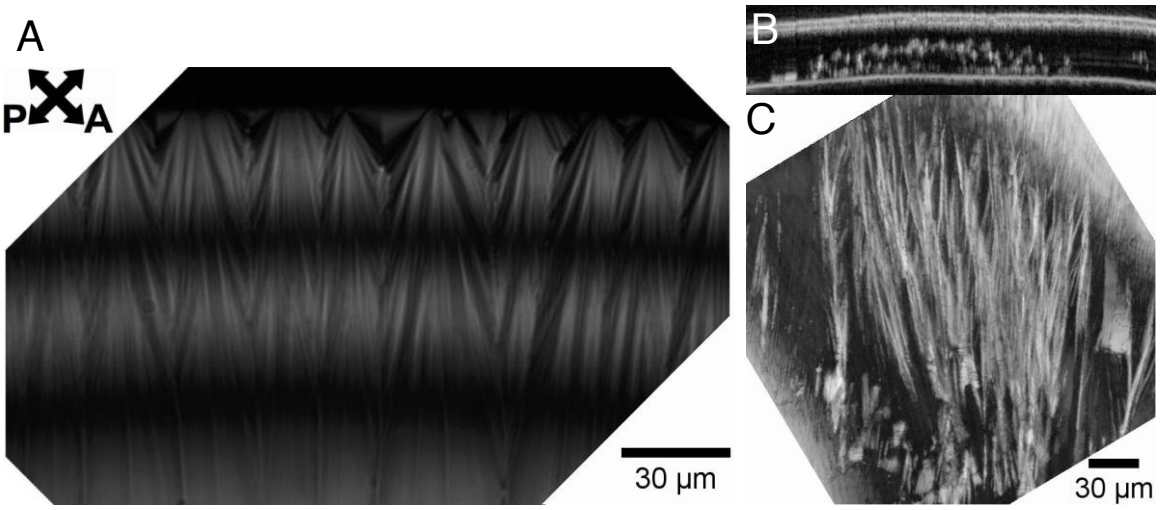

Figure 6. 8 An drying SSY solution droplet in the columnar phase under high-magnification POM and UHR-OCM. (A) POM with cross-polarizer. (B, C) OCM XZ and transverse views.

6.2.7 Summary of OCT imaging of Evaporating Water Droplets

We employed ultrahigh-resolution OCM (UHR-OCM) with the M-mode, time-lapse acquisition protocol to characterize the drying progression of water droplets containing polystyrene particles and LCLC droplets.

Time-lapse UHR-OCM cross-sectional images could directly reveal the dynamic process of these droplets, including capillary flows, convective flows, particle sedimentation, formation and progression of multiple liquid crystal phases and their boundaries. Also, the contact angle and the droplet heights could be easily retrieved from cross-sectional OCM images. These studies have proved the exceptional capability of OCT as a non-destructive testing tool to characterize various droplet models with 3D imaging views.

6.3 Drying Progression of Colloidal Droplets

6.3.1 Introduction

In the last section, we have discussed the water-based droplets with low initial concentration of particles or solvents to monitor the influence of additions on altering the drying behaviors of the water droplets. The particles or tracers are sparsely dispersed in the water droplets. When the OCT light is incident on the particles, it can be directly back-reflected or back-scattered, with only a small probability to meet other particles in the droplet. Thus, individual particles or tracers can be resolved in the OCT image of the droplet. The larger the particle or tracer size (>1 μm), the higher scattered signals from the individual particles or tracers. The stable distribution of the particles with high concentration may not occur or won't last long inside the droplet as the particles are driven by the capillary flows and brought to the droplet edge due to "coffee ring" effect.

In this section, we will discuss the drying progression of colloidal droplets. The definition of colloidal system and latex are described in Section 6.4.1. Generally, the polymer particles are uniformly dispersed in the colloidal droplet with a relatively high initial concentration (>10%). When the OCT light is incident on the droplet, the light will undergo multiple scattering, due to short distance between particles, before it goes back to the detector. As a result, the droplet appears uniformly scattered [283], without the capability to resolve individual particles with smaller particle size in the colloidal drops. However, since the light is uniformly scattered in the droplet, the top surface of the colloidal droplet can be clearly distinguished, which can be used to track the dynamic changes of droplet morphology and final deposition pattern of the colloidal droplets.

6.3.2 Previous Studies on OCT imaging of Colloidal Droplets

Up to now, only one study was reported using OCT to observe the drying progression of colloidal droplet. Manukyan et al. reported using OCT to characterize the internal flows during the drying progression of a colloidal droplet [283]. In their study, a commercial model paint droplet was examined, with an initial volume fraction of the model paint to be 10%, 30% and 50%. Two substrates, a hydrophilic glass slide and a hydrophobic coated glass slide, were tested to hold the sessile droplet. The model paints were mixed with copolymer microspheres as tracer particles, with large sizes of 4.3 µm or 7.9 µm. Paint droplets with a initial volume of 5 – 8 µL were deposited on different substrates to monitor the drying progression. The total drying time for the droplets lasted from 10 min to 25 min.

In their results, since the back-scattering dominated, individual tracer particles could be differentiated in the colloidal droplet. On hydrophilic surface, the moving tracer particles in the cross-sectional OCT images showed the outward radial flows close to the substrate under the influence of the coffee ring effect. The final deposition of a donut shape structure could be partially attributed to the coffee ring effect. However, on the hydrophobic surface, a reversed Marangoni flow was established, shown as a convective flow moving down along the surface and then moving inward along the droplet-substrate interface. As the paint droplet further dried, they observed the skin formation inside the droplet, yielding the suppression of convective flows. In the final deposition pattern, a cavity was observed beneath the outer skin layer in OCT cross-sectional images, containing water inside the cavity.

6.3.3 OCT Imaging of Drying Latex Droplets

In this section, we utilized OCT to characterize the drying progression of the latex droplets. The polystyrene latices with different particles sizes (L latex, S latex) were prepared, which was described in Chapter 6.4.4. The same OCT system was utilized to characterize both latex droplets and latex films, which was described in Chapter 6.4.3. In the experiment, a latex droplet with a volume of ~5 µL was pipetted on the regular glass slide. The drying process of the droplet was monitored in ambient condition. Thus, the total drying time for both L and S latex droplets were ~13 – 15 min. Time-lapse, M-mode OCT imaging was initiated after ~80 s from the pipetting of latex droplet, with a time step of 10 s.

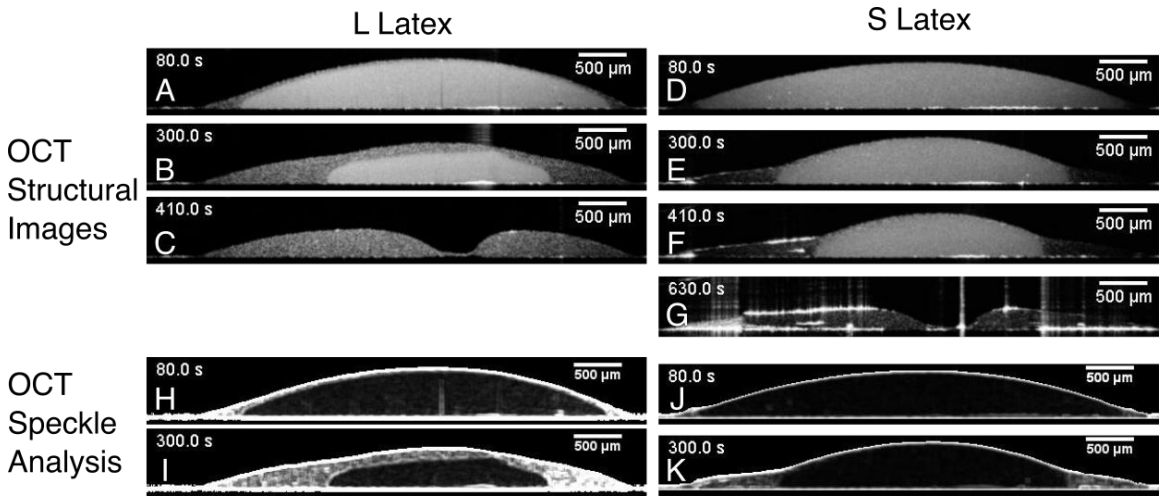

Figure 6. 9 Drying progression of latex droplets showing the horizontal and vertical drying inhomogeneities. ~5 µL latex droplets containing large (L Latex, Dia: ~125 nm) and small (S Latex, Dia: ~53 nm) polystyrene particles were deposited on the glass slide, with initial solid contents of 40.11wt% and 33.43 wt%, respectively. OCT structural images of L (A-C) and S (D-G) latex droplets clearly showed domain boundaries between surficial packed region close to air-latex interface and inner suspension regions with different scattering properties. OCT speckle contrast analysis (H-K) further confirmed the inhomogeneous particles' packing process for L and S latex droplets, with different particles' mobility in the packed and suspension regions.

Figure 6.9 showed the time-lapse OCT characterization of drying L and S latex droplets. In the **Figure 6.9 A and B**, a domain boundary was clearly observed inside the L latex droplet with distinct scattering properties. The outer layer had lower scattering intensity and the inner layer had higher scattering intensity. We further characterize it by performing the OCT speckle contrast analysis (See Chapter 6.4.5 for detail procedures) on the same data. In the outer layer, the higher speckle contrast indicated that particles in these regions were restricted. The dark hollow inside the L latex droplet inferred that the particles were still freely moved inside the hollow. With these analysis, we confirmed our observation that particles' packing also occurred in the latex droplet, similar with the drying latex film in the Petri dish. Packing process was also observed in S latex droplet, in both OCT structural images (**Figure 6.9 D-G**) and speckle images (**Figure 6.9 J, K**). However, different from the 1D packing process occurred in the large latex film, the drying inhomogeneities of the packing process occurred in both horizontal and vertical directions in the latex droplets. In the **Figure 6.9 I**, we can see that, the horizontal packing process was much faster than the vertical packing process in L latex, which was attributed to faster evaporation rate at the pinned contact line at droplet edge than the apex of the droplet. In S latex droplet, the vertical packing process was delayed as compared to horizontal packing process. At ~410 s, we could barely see a very thin layer in the **Figure 6.9 F**, indicating

the existence of vertical packed layer. The vertical layer would be clearly visible until ~500 s. As a comparison, the vertical packed layer was clearly visible in the L latex droplet at ~300 s. The particle droplets were fully packed at ~410 s for L latex droplet and ~630 s for S latex droplet.

Figure 6.10 further showed the drying progression of L and S latex droplets after the particles were packed in the droplet. The latex droplets had became a donut shape before the particles were fully packed. Later on, the apparent shear band structure was observed in the L latex droplet (**Figure 6.10 A**). Then, the particles underwent rearrangement (**Figure 6.10 B**) and finally formed a uniform scattered final deposition pattern (**Figure 6.10 C**). Similarly, the apparent shear band structure was likely observed in S latex droplet in **Figure 6.10 D.** However, due to the short time window and long acquisition time step of 10 s, **in Figure 6.10 D**, we could only see the particle rearrangement process with the shear band lines barely diffentiated. In the previous frame and next frame, apparent shear band structures was not observed. Interestingly, a crack was formed in the S latex droplet, which was clearly visualized in Figure 6.10 D – F. The observed drying phenomena in the latex droplets could be correlated to the OCT results of drying latex films in the Petri dish, which were described in Section 6.4.5 – 6.4.9.

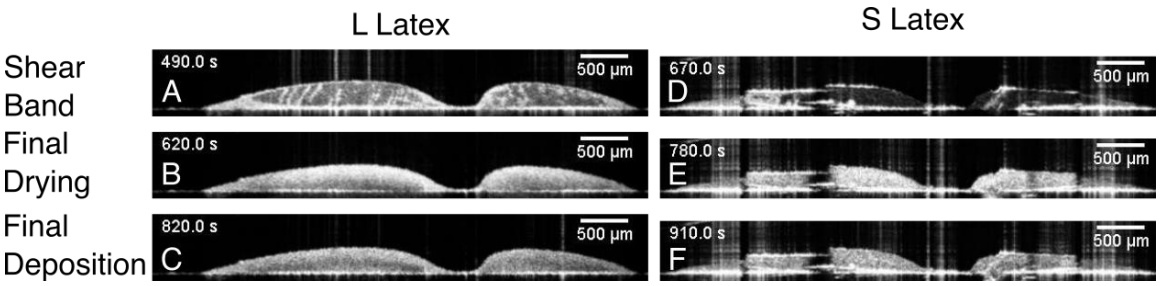

Figure 6. 10 Late-stage drying progression of latex drolets with undetected particle motions. Shear band formation, cracks, final drying process and final deposition pattern were examined.

6.4 Drying Progression of Latex

6.4.1 Introduction of Latex

A latex (or polymer colloids), is a stable colloidal system with polymer particles dispersed and suspended in an aqueous solution. Size of polymer particles in the latex is usually smaller than 500 nm, which is small enough to suspend or move in Brownian motion [284]. A latex is usually synthesized by the emulsion polymerization procedure [285]. Latex has been widely used in the field of paints, coatings and adhesive products [284, 286, 287], including the binder in waterborne paints [288], waterborne pressure-senstivie

adhesives [289], inkjet printing [290, 291], sun screen [292], paper coating [293, 294], tablet coating [295, 296], carpet backing [297] and evaporative lithography [298-300].

Drying progression of latex might be inhomogeneous. That is, latex particles distribute non-uniformly in space. As the latex continues drying, the inhomogeneous distribution would lead to formation of drying defects. The drying inhomogeneity can occur in both horizontal and vertical directions. In the horizontal direction, the evaporation rate is faster near the circumferential edge, leading to faster drying on the edge. Further, the capillary flows would bring the particles from the center to the edge, resulting in "coffee ring" deposition, which means uneven coating surface [301-303]. In the vertical direction, particles sometimes may aggregates near the top surface, forming a "skin layer" that causes the drying process to slow down [284, 304-307]. Furthermore, cracks may form in the latex containing particles with high polymer's glass-transition temperature (T_g), due to the development of capillary pressures inside the latex as the water further evaporates [308-311]. To deal with these drying defects, it is important to understand and characterize the drying process for different latex. A complete review of horizontal and vertical drying processes, drying inhomogeneities and crack formation in the latex (as well as colloidal droplets) can be found in Routh et al. [284].

6.4.2 Experimental Methods to Characterize Drying Latex

Routh et al. [284] and Huang et al. [286] have summarized different experimental methods to characterize drying process of latex. **Table 6.4** shows the list of different experimental methods for drying latex characterization. The simplest way to observe the drying latex is to look at it by eye or camera (videography) [284]. Global appearance of the latex, such as color, drying fronts and cracks can be easily observed and described qualitatively. To see the tiny features and further the particle distribution, microscopes with the micron or even nanometer level resolution would be highly preferred. Note that the higher resolution of the microscope, the smaller field of view and penetration depth, yielding the observation region limited to a local spot at the top surface of the latex film. Since latex contains a lot of water (if the solvent is water), experimental techniques using water as contrast, i.e. NMR and Raman Spectroscopy, would be highly preferred to monitor dynamic change of water contents inside the latex at different regions. In this case, the gravimetry approach, which utilizes a high-precision digital scale to measure the water loss, could also provide information of global water content. To understand the stress changes during the drying process, a

list of methods including the beam bending, membrane bending and traction force microscopy could be utilized. Further, various special techniques are employed to study the scattering properties and surficial composition of the latex to gain insights from an alternative view. Recently, some novel techniques have been proposed to detect the particles' kinetics in the latex, most notably diffusing-wave spectroscopy (DWS) [312], laser speckle imaging (LSI) [313] and optical coherence tomography (OCT) [286]. Specifically, LSI can map the drying inhomogeneity in the horizontal imaging plane and observe the delamination of coating from the substrate, but lacks the depth resolvability to distinguish the vertical drying phenomena. On the other hand, OCT, with the exceptional depth resolvability, can monitor the vertical drying phenomena, including the thickness changes and dynamic packing process of particles in vertical direction that potentially results in the vertical drying homogeneity.

Table 6. 4 Experimental Methods to Characterize Drying Latex

Cate-gory	Experimental Methods	Contrast/Key Features/Procedure	Pros	Cons	Ref.
Global Appearance	Eye	Color, Drying fronts, Cracks (Features occurred over cm scale)	Straight-forward	Lacks quantification	
	Videography	Macroscopic appearance. Long term recording		Mostly top-down views	Divry et al. [303]
Microscopy	Optical Microscopy	Microscopic features, tracer particle tracking (Diameter in µm)	Simple		Weon and Je [314]
	Confocal Microscopy	Depth resolved microscopic features	µm resolution	Depth depend on light penetration	Birk-Braun et al. [310]
	Cryogenic scanning electron microscopy (Cryo-SEM)	Particle arrangement (packing) in vertical direction	nm resolution	Sample damage	Luo et al. [315-317]
	Environmental SEM (ESEM)	Wet sample. Crack propagation		Top surface only or with limited height of a few microns. Limited FOV.	Keddie et al. [318], Dragnevski et al. [319], Donald et al. [320]
	Atomic force microscopy (AFM)	Individual particles, cracks, surface topology (in tapping mode)			Wang et al. [321] Goehring et al. [322], Mallegol et al. [323]
	Ellipsometry	RI, extinction coefficients			Keddie et al. [318]

Table 6.4, Continued.

Cate-gory	Experimental Methods	Contrast/Key Features/Procedure	Pros	Cons	Ref.
Water Characterization	Gravimetry (Balance or Scale)	Global water loss	Can derive global water content and drying rate	Limited to global measurement, cannot provide spatial mapping	Huang et al. [286], Divry et al. [303]
	Magnetic resonance imaging (MRI) or nuclear magnetic resonance (NMR)	Water contents, evaporation pathway	Track water concentration	Resolution: a few hundread µm	Salamanca et al. [324], Mantle and Sederman [325]
	Garfield NMR	Water contents, evaporation pathway, film thickness	Track water concentration , Resolution 5 µm	Shape of permanent magnet is required to produce well-defined magnetic field strength gradient in vertical direction	Mallegol et al. [326]
	Laser scanning coherent anti-Stokes Raman spectroscopy (CARS)	Crack formation, compaction fronts	Microscopic features, resolution can reach 2-3 µm	Limited penetration depth	Dufresne et al. [327], Dufresne et al. [328]
	(confocal) Raman spectroscopy	Horizontal drying front, vertical drying profiles, local concentration of surfactant			Ludwig et al. [329], Ludwig et al. [330]
Stress Characterization	Beam Bending	Deflection of beams can be related to compressive stress	Simple	Single-value	Tirumkudulu and Russel [309], Yow et al. [331]
	Membrane Bending	Membrane as substrate with dot array to predict deformation	Spatially resolved stress field	Limitation on substrate property	von der Ehe and Johannsmann [332], Koenig et al. [333]

Table 6.4, Continued.

Cate-gory	Experimental Methods	Contrast/Key Features/Procedure	Pros	Cons	Ref.
Stress Characterization	Traction Force Microscopy	Stress around the crack			Xu et al. [334], Jerison et al. [335]
	Newton's Ring	Stress through the compaction front of a drying film			Rossnagel et al. [336]
Height Monitoring	(Contact) Profilometry	Needle protruding into the film	Absolute thickness data	Potential Film damage or height change	Gundabala and Routh [337]
	Laser profilometry	Light reflection	Long-term, Simple	Height change instead of absolute film thickness	Martinez and Lewis [338]
	(Vertical) Laser scanning	Laser scan vertically until topest surface of the film is detected			Holmes et al. [339]
Scattering	Small angle X-ray scattering (SAXS)	Structure factor as a function of scattering vector			Li et al. [340]
	Neuron Scattering	Crystallinity, Formation of lumps of hydrophililic material		Limited use. On dried film	Rieger et al. [341]
Composition	Rutherford back scattering	Energy of $^{4}He^{+}$ ion		Limited to surficial layers (<1 µm)	Mallegol et al.[342]
	Atternuated total reflection Fourier transform infrared spectroscopy (ATR-FTIR	Measure amount of exuded surfactants near the film surface.			Gundabala et al.[343], Kunkel and Urban [344]
	X-ray photoelectron spectroscopy (XPS)	Exudation of surfactants			Zhao et al. [345]
Kinetics	Diffusing wave spectroscopy (DWS)	Dyanmics of complex fluids, film formation			Zhakarov and Scheffold[346], Brun et al.[312]

Table 6.4, Continued.

Cate-gory	Experimental Methods	Contrast/Key Features/Procedure	Pros	Cons	Ref.
Kinetics	Laser Speckle Imaging	Delamination of coating from the substrate	Map horizontal drying inhomogeneity	Limited depth resolvability	Van der Kooij et al.[313], Balamurugan and Rajarajan[347]
	Optical Coherence Tomography	Vertical drying, particle packing	Can also detect microscopic features and perform film thickness measurement	Limited FOV. Detect local features	Huang et al.[286]

6.4.3 OCT-Gravimetry-Video Method for Characterization of the drying process of latex

Combining different experimental methods, we can characterize the drying process of latex and show the dynamic changes of both macroscopic and microscopic features. A non-destructive platform integrating OCT, gravimetric measurement and video camera, which we called the "OCT-Gravimetry-Video" method, has been developed to longitudinally and systematically characterize the drying progression of polystyrene lattices with high T_g [286].

Figure 6.11 showed the schematic diagram of integrated OCT-Gravimetry-Video system. The OCT system was modified from the custom OCT system described in Chapter 2. Instead of 5× objective with f = 40 mm, a f = 50 mm achromatic lens was employed to further increase the depth of focus (DOF) to ~500µm. Above the objective, a wedge (PS814-C, Thorlabs) was added to slightly distort the incident beam to avoid the strong, direct surface reflection from the latex. Note that, since the initial drying of the latex is in liquid state, tilting the Petri dish would not help to tilt the latex surface to reduce the reflection. The camera was running at 20.7 kHz, yielding the final sensitivity to be ~101 dB. The axial and lateral resolution were measured to be 4.3µm (RI = 1.57) and 14 µm, respectively. OCT system can be used to monitor the thickness changes of the latex up to millimeter scale. Also, OCT showed the microscopic changes of the latex film, e.g. debonding of coating, formation of apparent shear band structure. In addition, packing of particles was detected via speckle analysis of OCT images.

Other than OCT system, the gravimetry method with a digital balance could measure the global drying curve and drying rate of the latex. The video camera can record macroscopic appearances of the latex like color, cracks and drying fronts.

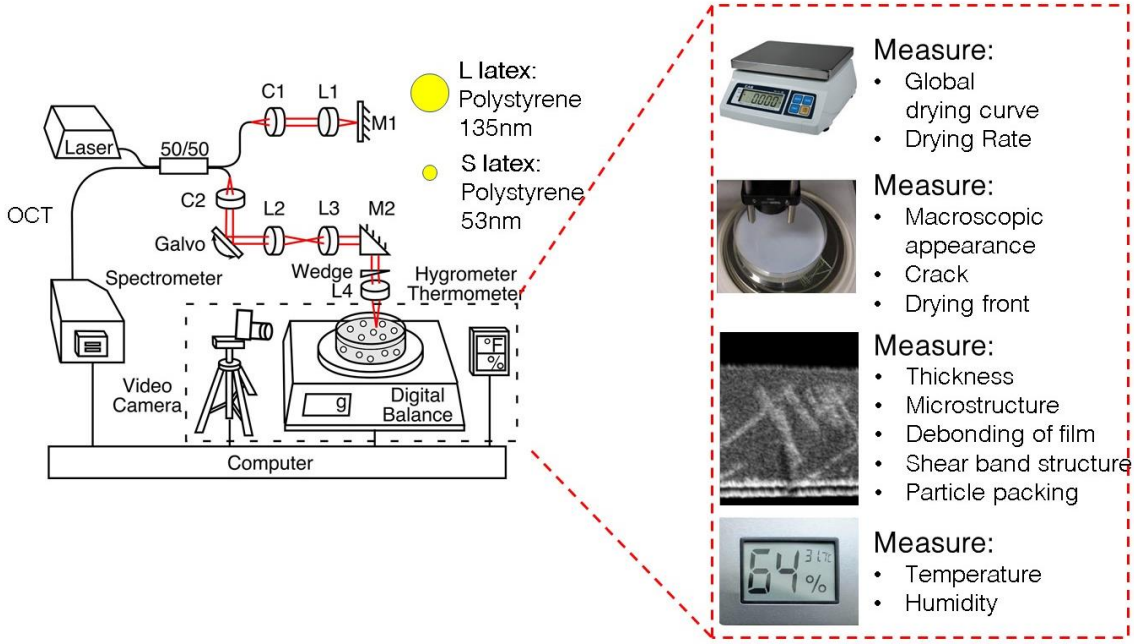

Figure 6. 11: Schematic diagram for integrated OCT-Gravimetry-Video system for latex imaging. The OCT system was a modified version of the custom 1300 nm SD-OCT system in Chapter 2**.**

6.4.4 Latex Preparation and Protocol of Data Acquisition

Polystyrene (PS) latices were synthesized by semi-batch emulsion polymerization. The polymer composition of PS particles is 99 wt% PS with 1 wt% polymethacrylic acid. Details of the preparation step could be referred to Hao Huang's thesis[348]. Two types of polystyrene latexes, "L latex" and "S latex", were tested in our experiments to monitor their drying progression. The "L latex" contained polystyrene particles with larger particles' sizes of ~125 nm ± 23 nm. The polystyrene particles in "S latex" has a smaller particle size of ~53 nm ± 7 nm. Initial solid content (weight percentage of polystyrene particles) of L latex and S latex were measured to be 40.11 wt% and 33.43 wt%, respectively. Since the polystyrene particles had a similar density (1.04 g/cm^3) as the water (1.00 g/cm^3), the value of the volume fraction of particles was similar to the solid content. The glass transition temperature (T_g) of both L and S latex polymers were measured to be 107°C and 106°C, respectively. Since both T_g values were way higher than the room temperature, these polystyrene particles were considered as "hard particles", which would not deform during the drying process.

In the experiment, ~5.7 g latex was weighed and deposited uniformly in a large Petri dish with a size of ~8.5 cm in diameter. Initial thickness of both L latex and S latex was controlled at ~1 mm. Acquisitions of gravimetric data and video camera were initiated prior to latex deposition. After the latex was spread uniformly in the Petri dish, M-mode, time-lapse OCT acquisition would be initiated. Each OCT dataset had a size of 512 pixels × 200 pixels × 100 repeats. The actual size of the cross-section OCT frame was ~2.2 mm × ~1.0 mm. The scanning time for the M-mode OCT data was ~1.1 s. The time step for the time-lapse OCT acquisition was set to 2 min, which was fast enough to cover the dynamic changes occurred in the latex. Note that the initiation of the OCT acquisition was synchronized with gravimetric data acquisition and time-lapse video recording. Time-lapse acquisitions from OCT, gravimetry and video camera continued for ~500 min for both L and S latices. For slow drying condition with a cap on the Petri dish, the long-term drying process of the L latex could last for >2 days (2880 min). In this case, we just used the integrated system to monitor the drying process up to 2 days.

6.4.5 Post Processing Procedure for Time-lapse OCT data of Drying Latices

OCT Structural Images and Time-lapse Intensity Profile

Once the time-lapse acquisitions were done, stacks of OCT data were processed frame by frame following the standard protocol for spectral domain OCT (See Chapter 2). A 2D OCT structural image of the latex was generated by averaging all M-mode frames in each OCT dataset. Then, latex images were flattened according to the Petri dish surface to correct the image tilting due to the use of the wedge. Regions above the top surface of the latex and below the top surface of the Petri dish were manually removed. Then, time-lapse OCT intensity profile was generated by averaging each 2D OCT structural image along the horizontal direction and arranging them together in the time sequence. Obtained time-lapse OCT intensity profile could be used to show the 1D vertical drying process of the latex.

Speckle Contrast Analysis for M-mode OCT data

The speckle contrast (K_s) analysis could be conducted on each 2D M-mode OCT dataset to detect particles' kinetics in the latex [175]. **Figure 6.12** illustrated the procedure of OCT speckle contrast analysis, taking an OCT data from L latex as an example. Following the previous step in Chapter 6.4.5.1, we obtained 2D OCT

structural image of the L latex (**Figure 6.12 B**). Then, we performed a moving average filter on the 2D OCT structural image. For 2D OCT speckle analysis (**Figure 6.12 D**), the moving window size was set to be 11 × 11 pixels. For time-lapse OCT speckle analysis (**Figure 6.12 C**), the moving window was set to be the entire row of pixels from the 2D OCT structural image (200 × 1 pixels), which was equal to taking the average of all the pixel values in a row of 2D OCT image. Then, the average intensity $\langle I \rangle$ and the average intensity square $\langle I^2 \rangle$ for each pixel in the filtered OCT image were calculated as:

$$\langle I \rangle = \sum_{k=1}^{N} \frac{I_k}{N} \tag{6.1}$$

and

$$\langle I^2 \rangle = \sum_{k=1}^{N} \frac{{I_k}^2}{N} \tag{6.2}$$

Where N equal to the total pixel number of the moving window. Then, the standard deviation σ_s of OCT intensities for each pixel (in each moving window) was calculated as:

$$\sigma_s = \{\langle I^2 \rangle - \langle I \rangle^2\}^{1/2} \tag{6.3}$$

The speckle contrast (K_s) for each pixel could be derived as:

$$K_s = \frac{\sigma_s}{\langle I \rangle} \tag{6.4}$$

Representative results of speckle contrast analysis on OCT data of L latex were shown in **Figure 6.12 C and D**.

Characterizing Particles' Packing Process with OCT Structural and Speckle Images

Since the results of OCT speckle contrast analysis could be used to map particles' mobility in different regions of latex cross-section, we could use this method to characterize the particles' vertical packing process in the latex.

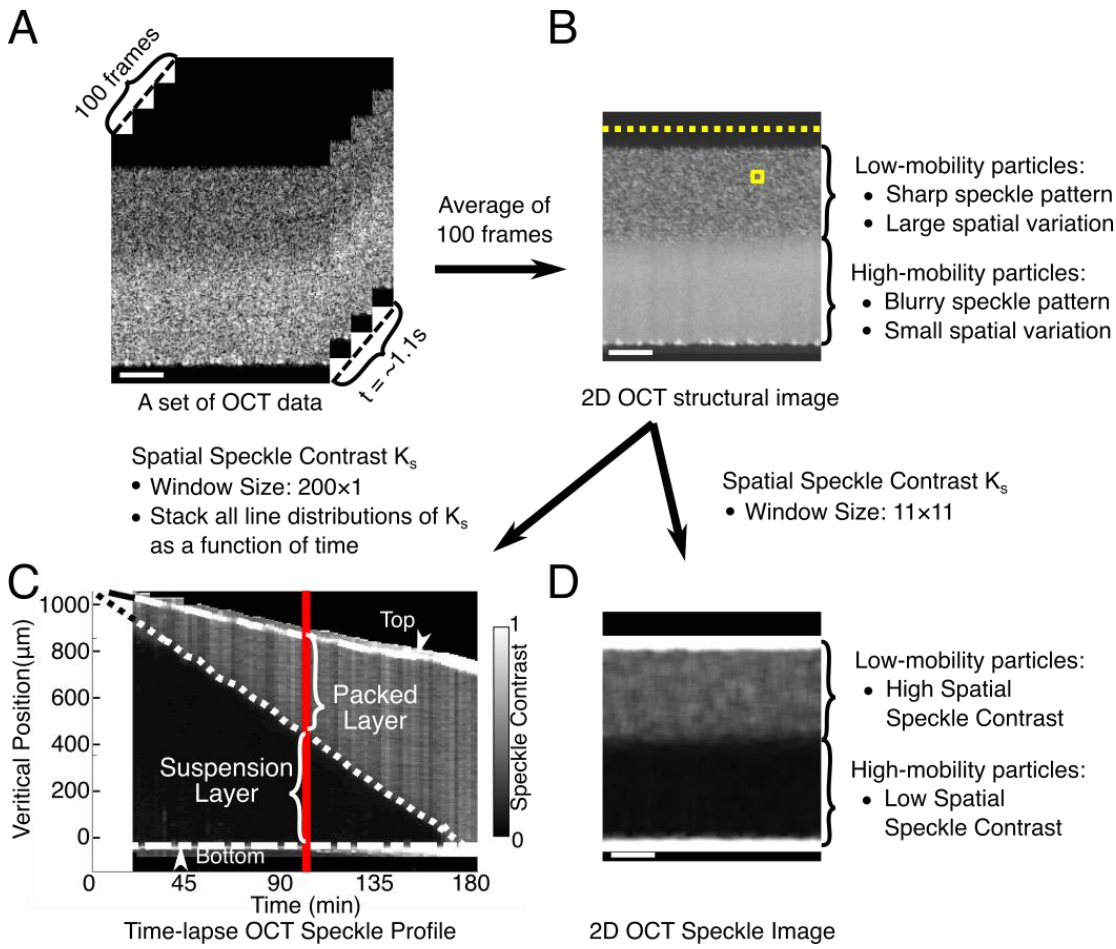

Figure 6. 12 Speckle contrast (K_s) analysis of the packing process for droplets and latex systems. A single M-mode OCT dataset from L latex was used to illustrate the processing procedure. M-mode OCT B-scan images (A) were first averaged to get the 2D OCT structural image (B). Then, speckle contrasts with the moving window size of a row (200 pixel in the example) or 11 × 11 pixels were derived for each M-mode OCT dataset to generate the OCT speckle profile (Red line in C) or 2D OCT speckle Image (D). Time-lapse OCT speckle profile (C) was plotted by arrranging the OCT speckle profiles from multiple time points in an ascending time sequence.

In either 2D or time-lapse OCT speckle images (**Figure 6.12 C and D**), a high speckle contrast K_s indicated low mobility of particles. In this case, the motions of particles were restricted, indicating they were trapped and packed. On the other hand, a low K_s value meant high mobility of particles, indicating that particles maintained a suspension state and moved freely in the water. Based on the differences of speckle contrast, we could further derive the domain boundary between the high K_s region ("packed layer") and the low K_s region ("suspension layer"), which was shown as the middle, white dotted line in **Figure 6.12 C**. The domain boundary curve in the time-lapse OCT speckle image could be determined following the method as described:

1) Calculate the average K_s values for both packed and suspension layers.

2) Set the threshold K_s value as the mean of both K_s values from the packed and suspension layers.

3) The pixels with the equal value as the threshold K_s were defined as the packing/suspension domain boundary curve, which should be a continuous curve.

Once the domain boundary was determined, the thickness change of the packed layer could be measured from the time-lapse OCT speckle image (**Figure 6.12 C**) to track its change.

Note that OCT speckle contrast analysis could be used to characterize both horizontal and vertical packing process in the drying colloidal droplet (See Chapter 6.3.2).

The other way to define domain boundary relied on the differences of scattered light intensities in time-lapse OCT intensity profile. We observed that the packed layer had lower scattering intensities than the suspension layer during the initial drying stage. Setting the threshold value as the mean of intensities of packed and suspension layers in the time-lapse OCT intensity profile, the packed/suspension domain boundary curve could be determined and used to track thickness changes of packed layer.

6.4.6 Time-lapse OCT Imaging of Drying L latex

Figure 6.13 showed the results of time-lapse OCT characterization of they drying progression of large latex (L latex). In **Figure 6.13 B**, a timeline was plotted, showing the drying states defined by gravimetry and video methods above the timeline and listing OCT observations of drying phenomena below the timeline. Between ~0 to ~168 min, thickness of the L latex decreased linearly from ~1100 µm to ~720 µm in time-lapse OCT intensity profile (**Figure 6.13 A**). Inside the L latex, two-layer structure with distinguishable scattering intensities was observed (**Figure 6.13 C**), which was identified as packed and suspension layer during the particles' packing process (See Chapter 6.4.8). After 190 min, the latex bottom was observed to start detaching from the Petri dish and moved upward (**Figure 6.13 F,** Detachment). At ~212 min, we observed the apparent "shear bands" structure in 2D OCT structural image, as indicated by the bright crosses inside the film (**Figure 6.13 F**, See Chapter 6.4.9). The apparent shear band structure lasted for ~68 min and disappeared at ~280min (**Figure 6.13 G**). Between ~190 min to ~314 min, we could observe that the bottom of L latex bottom kept moving up and down (**Figure 6.13 A**). During this time, the interfacial tension and capillary pressure in the L latex due to loss of water and air infiltration built up, yielding the tendency of the

latex to shrink. As a result, detachment of the latex occurred. Later on, cracks were formed (See Chapter 6.4.9). And the particles underwent rearrangement to further release the internal stress, which was partially indicated by gradual change of the scattering intensities over time. From ~314 min to the final imaging time of ~500 min, no significant changes of scattering intensities or thickness were observed in the L latex (**Figure 6.13 A**). The scattering intensities inside the L latex were mostly uniformly distributed (**Figure 6.13 H**). Thus, we defined the time period from ~190 min to ~314 min as "stress relaxation" state and the time period after ~314 min as "final drying" state in **Figure 6.13 B**.

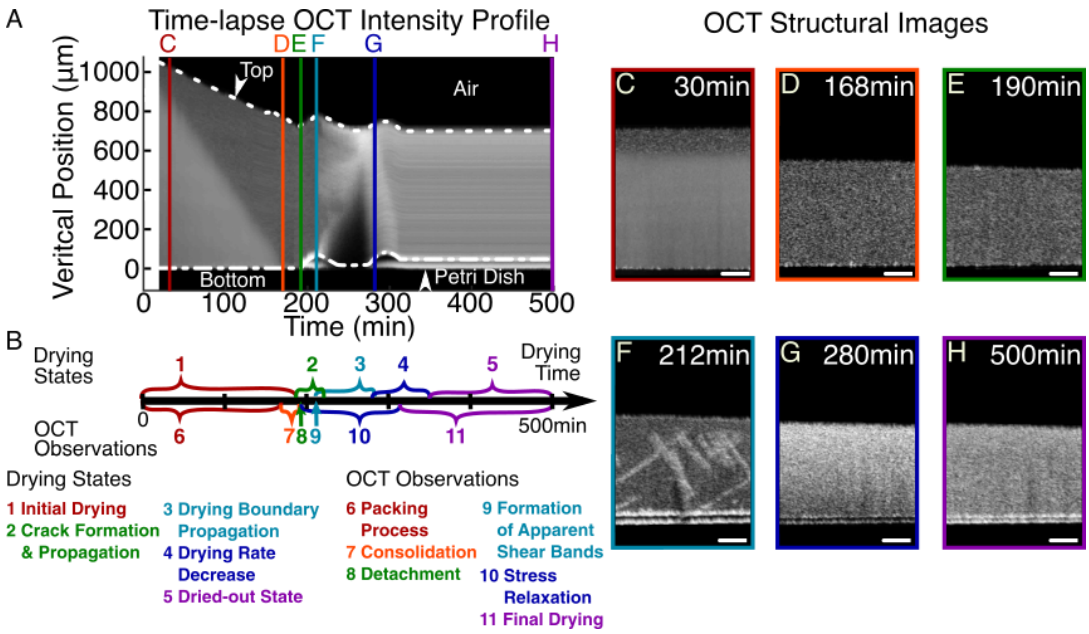

Figure 6. 13 OCT characterization of the drying progression of L latex. (A) Time-lapse OCT intensity profile. (B) Timeline of drying progression of L latex. Drying states (1-5) were defined by the gravimetry and video methods. OCT observations (6-11) of drying phenomena were listed below the timeline. (C - F) 2D OCT structural images at 30, 168, 190, 212, 280 and 500 min, showing OCT observations of different drying behaviors described in (B). White dashed lines: top and bottom of the latex in the time-lapse OCT intensity profile. Color lines in (A), color texts in (B) and color rectangular boxes in (C – H) were matched. Note that observation #8 indicated the initiation of the detachment of L latex, which could be observed in (F).

6.4.7 Time-lapse OCT Imaging of Drying S Latex

Figure 6.14 showed the results of time-lapse OCT characterizations of the drying progression of S latex. Similar observations of drying phenomena as L latex could be found in time-lapse OCT intensity profile of S latex (**Figure 6.14A**), but with a different time window. Two-layer packed/suspension structure was observed in S latex (**Figure 6.14 C**), with the packing process finished at ~162 min (**Figure 6.14D**). The

apparent shear-band structure appeared at a later time of ~292 min (**Figure 6.14F**). Compared to the L latex, the shear-band structure in the S latex lasted for a shorter duration of ~34 min and disappeared at 326 min (**Figure 6.14 E**). At ~220 min, the detachment of S latex away from the substrate was initiated and clearly observed at ~292 min (**Figure 6.14F**). The "stress relaxation" state lasted for ~106 min, from ~220 min to ~326 min. After ~326 min, the S latex entered the "final drying" state, with its scattering properties and film thickness remaining unchanged.

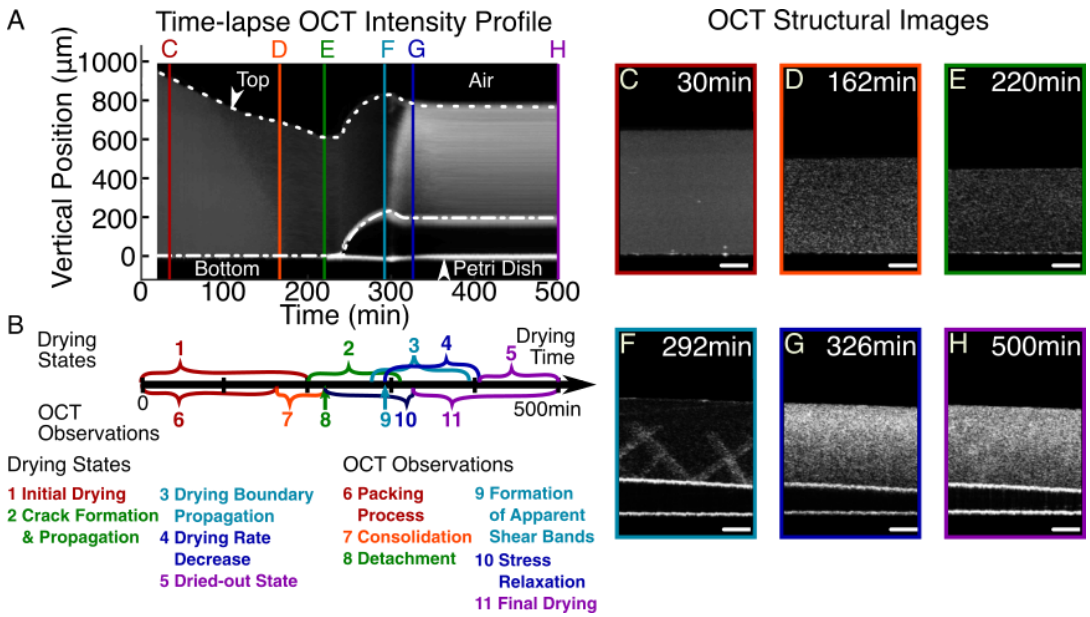

Figure 6. 14 OCT characterization of the drying progression of S latex. (A) Time-lapse OCT intensity profile. (B) Timeline of drying progression of S latex. Drying states (1-5) were defined by the gravimetry and video methods. OCT observations (6-11) of drying phenomena were listed below the timeline. (C - F) 2D OCT structural images at 30, 162, 220, 292, 326 and 500 min, showing OCT observations of different drying behaviors described in (B). White dashed lines: top and bottom of the latex in the time-lapse OCT intensity profile.Color lines in (A), color texts in (B) and color rectanglular boxes in (C – H) were matched. Note that observation #8 indicated the initiation of the detachment of S latex, which could be observed in (F).

6.4.8 OCT Characterization of Particles' Packing Process of Latex

In this section, we described the details about characterization of the particles' packing process occurred in the latex using OCT system. In both L and S latices, particles' packing processes were observed during the early drying stages before ~180 min (See **Figure 6.13** and **Figure 6.14**).

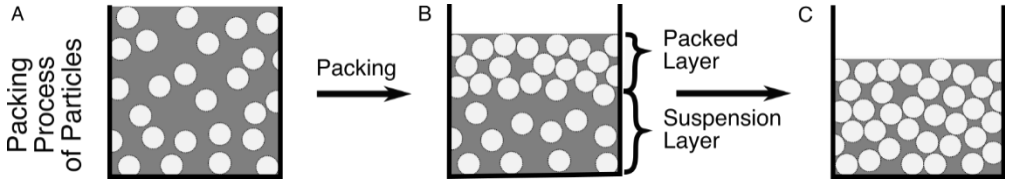

Figure 6. 15 An illustration of the packing process of particles in the latex.

Figure 6.15 illustrates the packing process of particles in the vertical direction in the latex, which is known as the "snow plow" effect[304, 306]. In the initial drying stage (**Figure 6.15A**), particles in latex are well dispersed in the solution and move freely in space. The water contents are relative uniform throughout the latex. As water continues to evaporate away from the top surface, the latex is separated into two domains in the vertical direction (**Figure 6.15 B**). In the upper domain, particles are packed in contact with each other. Interstices between the particles are small and particle motions are restricted with low mobility. In the lower domain, particles remain separately suspended and freely move in water. The distance between particles' surfaces remained large. According to the particle arrangement, the upper domain is named "packed layer" and the lower domain is named "suspension layer". At the end of the packing process, all particles are packed with low mobility (**Figure 6.15 C**).

As is mentioned in Chapter 6.4.5, the dynamic process of particles' packing could be characterized in time-lapse OCT structural and speckle images. **Figure 6.16** and **Figure 6.17** showed the visualization of particles' packing process in L latex. Within the first 180 min, the packed/suspension domain boundary curve was observed, which was plotted as a dotted curve in time-lapse OCT intensity profile (**Figure 6.16 A)**. The domain boundary curve separated the packed layer with lower scattered light intensity and the suspension layer with higher scattered light intensity. The intensity variation suggested that these two layers might have different particle concentration and distributions in water. To demonstrate the domain separation, we performed speckle contrast analysis on 2D OCT structural images and time-lapse OCT intensity profile to identify particles' mobility. Results were shown in **Figure 6.16 B-E**. In the time-lapse OCT speckle image of L latex (Figure 6.16 B), the particles' mobility in these two domains was clearly distinguished. In the upper domain, the high speckle contrast K_s indicated that particle mobility was low in this domain, which confirmed that these particles were packed. In the lower domain, the low K_s value, inversely, indicated high particle

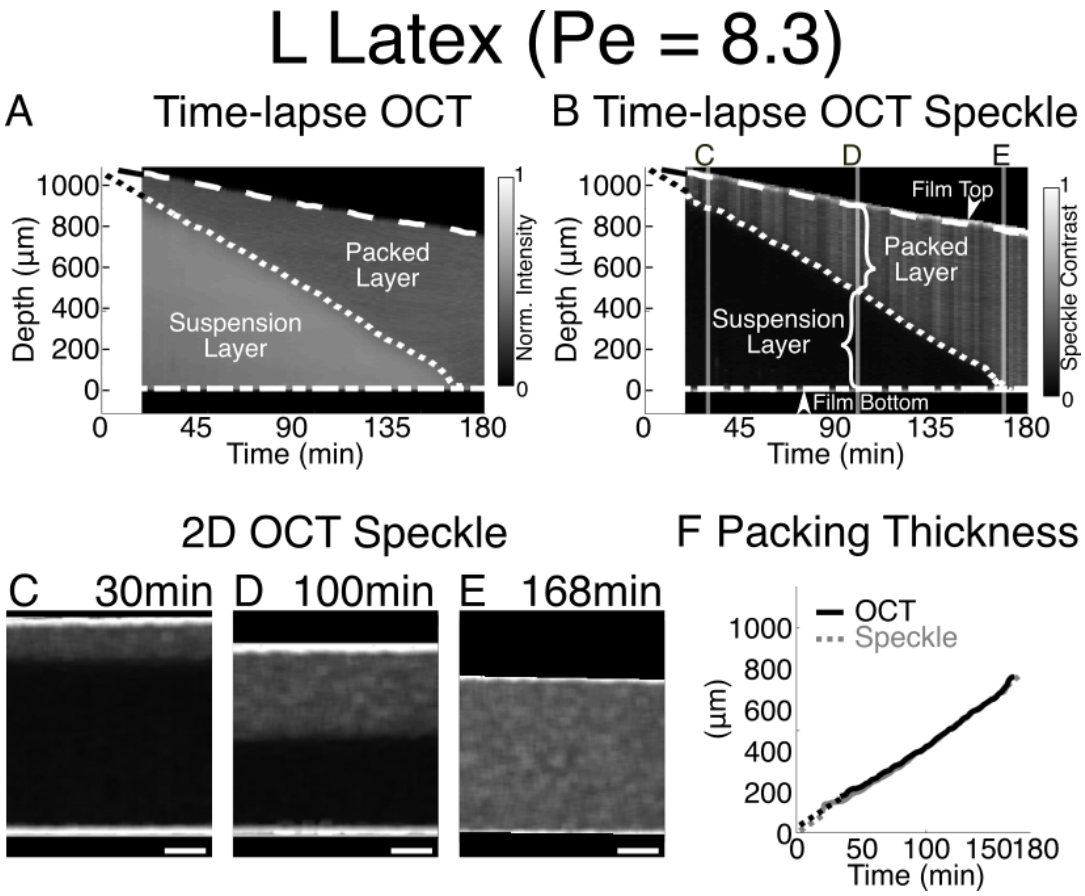

Figure 6. 16 Visualization of entire particles' packing process in L latex with OCT. (A) Time-lapse OCT intensity profile showed the domain boundary between upper packed layer and lower suspension layer with light intensity difference. (B) Time-lapse OCT speckle contrast analysis further differentiated particles' mobility in these two domains. (C – E) 2D OCT speckle contrast image at ~30 min, ~100 min and ~168 min showing the progression of particles' packing process in L latex. (F)Packed layer thickness change as a function of time, derived from time-lapse OCT intensity or speckle contrast images. Scale bar: 200 μm

mobility. High particle mobility meant that these particles were freely moving in the lower domain, inferring that the lower domain was the suspension layer. Such domain separation with different particles' mobility could be also clearly observed in 2D OCT speckle images (**Figure 6.16 C-E**), with the continuously increasing packed layer as the time evolved. The packed/suspension domain boundary could be easily identified in the time-lapse speckle contrast image, shown as dotted curves in **Figure 6.16 B**. The packing process ended at ~168 min, according to the speckle analysis. In **Figure 6.16 F,** time-lapse thickness curves of the packed layer in L latex were shown as black solid and grey dashed lines. The packed layer thickness was derived from time-lapse OCT structural and speckle images, measured as the distance between the top surface and the domain boundary curve. A linear increasing trend was observed from the packed layer

thickness curves of L latex throughout the packing process. A good overlapping was observed between these two derived thickness curves.

It should be noted that, due to the preparation time for latex weighing and spreading onto Petri dish, adjustment of OCT system, and synchronization among OCT, gravimetric and video acquisition, time-lapse OCT imaging was initiated after ~20 min from the first casting of latex. Thus, the domain boundary and the top surface was extrapolated to the ~0 min in time-lapse OCT intensity profile and speckle contrast image (**Figure 6.16 A and B**, dashed lines), assuming a linear decreasing trend for both of them. Thickness curve from ~0 min to ~20 min was also calculated based on the extrapolated lines. The extrapolation results from the thickness curves of L latex showed that the packing process started from the beginning (~0 min), right after the latex was cast on the Petri dish. To further confirm it, we conducted an additional OCT experiment of the packing process of L latex during the initial 30 min, by quickly pouring the latex in Petri dish and placing it under the OCT objective. The results were shown in **Figure 6.17**. The domain boundaries were

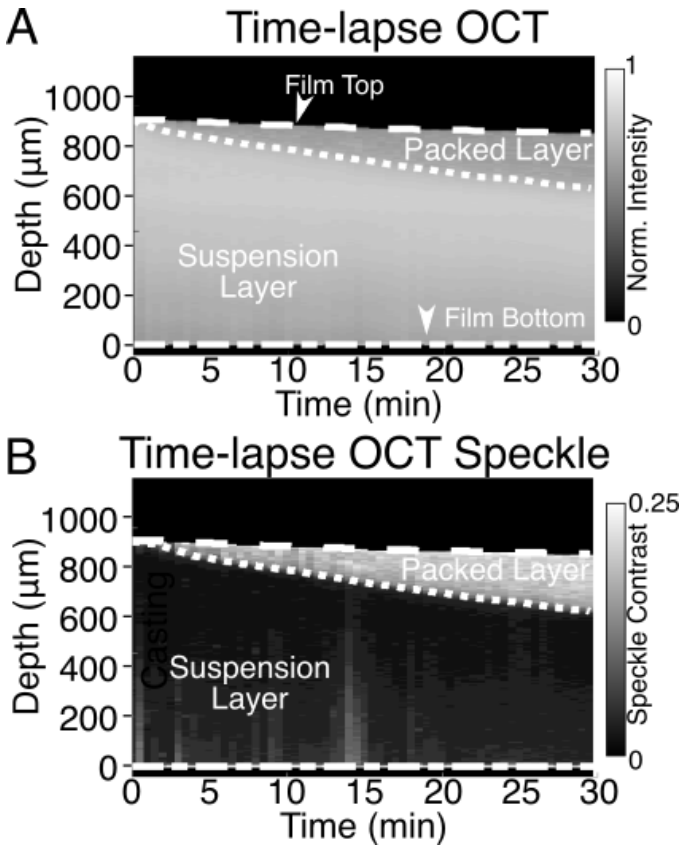

Figure 6. 17 Visualization of initial packing process in L latex by OCT. (A) Time-lapse OCT. (B) Speckle contrast analysis.

characterized in both time-lapse OCT intensity profile and speckle contrast images. From both intensity profile and speckle contrast analysis, we could conclude that the initiation of particles' packing process occurred within the first minute after the casting of the latex.

For S latex, the OCT characterization results of the packing process (**Figure 6.18**) showed several variations from the observations in L latex. First, the packed layer in S latex was not evident during the initial ~48 min, where the packed layer might be too thin to be resolved by OCT. After ~48 min, the packed layer thickness began to increase. Second, the increasing rate of packed layer thickness was faster for S latex than L latex during the later stage of packing process, yielding a slightly earlier finish of the packing process at ~162 min. Third, although the two packing thickness curves derived from OCT intensity profile and speckle

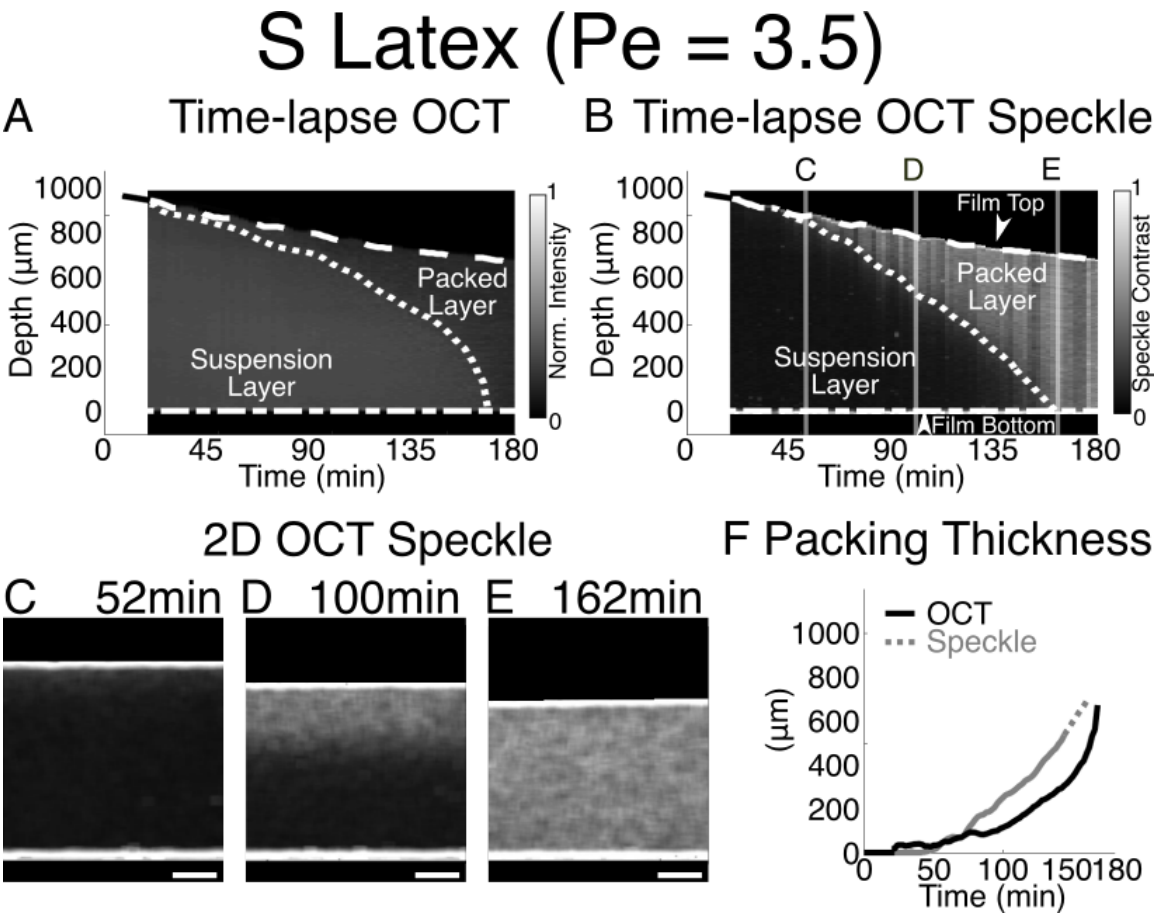

Figure 6. 18 Visualization of entire particles' packing process in S latex with OCT. (A) Time-lapse OCT intensity profile showed the domain boundary between upper packed layer and lower suspension layer with light intensity difference. (B) Time-lapse OCT speckle contrast analysis further differentiated particles' mobility in these two domains. (C – E) 2D OCT speckle contrast image at ~52 min, ~100 min and ~162 min showing the progression of particles' packing process in S latex. (F)Packed layer thickness change as a function of time. Scale bar: 200 μm

contrast images had the similar growing trend after ~48 min, they did not completely overlap with each other for S latex (**Figure 6.18 F**). For time-lapse OCT intensity profile of S latex, the intensity variation between packed and suspension layers was so small that the domain boundary could not be clearly identified (**Figure 6.18 A**). On the other hand, OCT speckle contrast analysis could provide higher contrast between packed and suspension layers due to the high sensitivity of the particles' motions, making the identification of the domain boundary more accurate (**Figure 6.18 B**).

Comparing both time-lapse OCT intensity profiles and speckle contrast images, we clearly observed that L latex has a clearer domain boundary than S latex, which also meant that the domain transition along the vertical direction was faster for L latex than that for S latex. The difference of the boundary sharpness could be partially explained by a simplified model proposed by Routh and Zimmerman [304]. By deriving the diffusion equation for particles, they predicted that the particles' packing process could be determined by a dimensionless group called the Peclet number (Pe), which was the rate of water evaporation divided by the rate of particles' diffusion [284, 304]. In the dilute limit, where Stokes-Einstein equation determines the diffusion coefficient of particles, Pe is given as [284, 307]:

$$Pe = \frac{6\pi\mu R_0 H\dot{E}}{k_B T} \tag{6.5}$$

where μ is the water viscosity, R_0 is the particle radius, H is the latex thickness, $\dot{E}$ is the water level receding velocity (the ratio of drying rate over water density), k_B is the Boltzmann constant and T is the temperature. According to their model, for large Pe value, the vertical gradient of volume fraction was proportional to $Pe^{0,5}$, although an experimental result showed that it was proportional to $Pe^{0,8}$ [349]. For L and S latices, Pe values were calculated to be 8.3 and 3.5, respectively. Thus, the larger Pe value for L latex indicated that the veritical gradient of volume fraction was higher, yielding a faster transition between the two domains.

We also conducted an experiment on L latex with a slow drying rate. By placing the cap on top of the Petri dish during the drying process, the drying rate of L latex could be reduced to 1/20 of the drying rate in ambient condition. In this case, the Pe value was calculated to be 0.4. OCT characterization results were shown in **Figure 6.19**. With a low Pe value smaller than 1, the packed layer of the L latex in slow drying condition was not visible initially until ~2108 min. It was yet to be confirmed that whether the packed layer

was too thin to be observed or the packing process was delayed. Then, the packing process started and finished within ~154 min, from ~2108 min to ~2262 min. Further experiment with a better control of the drying rate could be conducted to explore the relationship between Pe values and the starting time of the packing process.

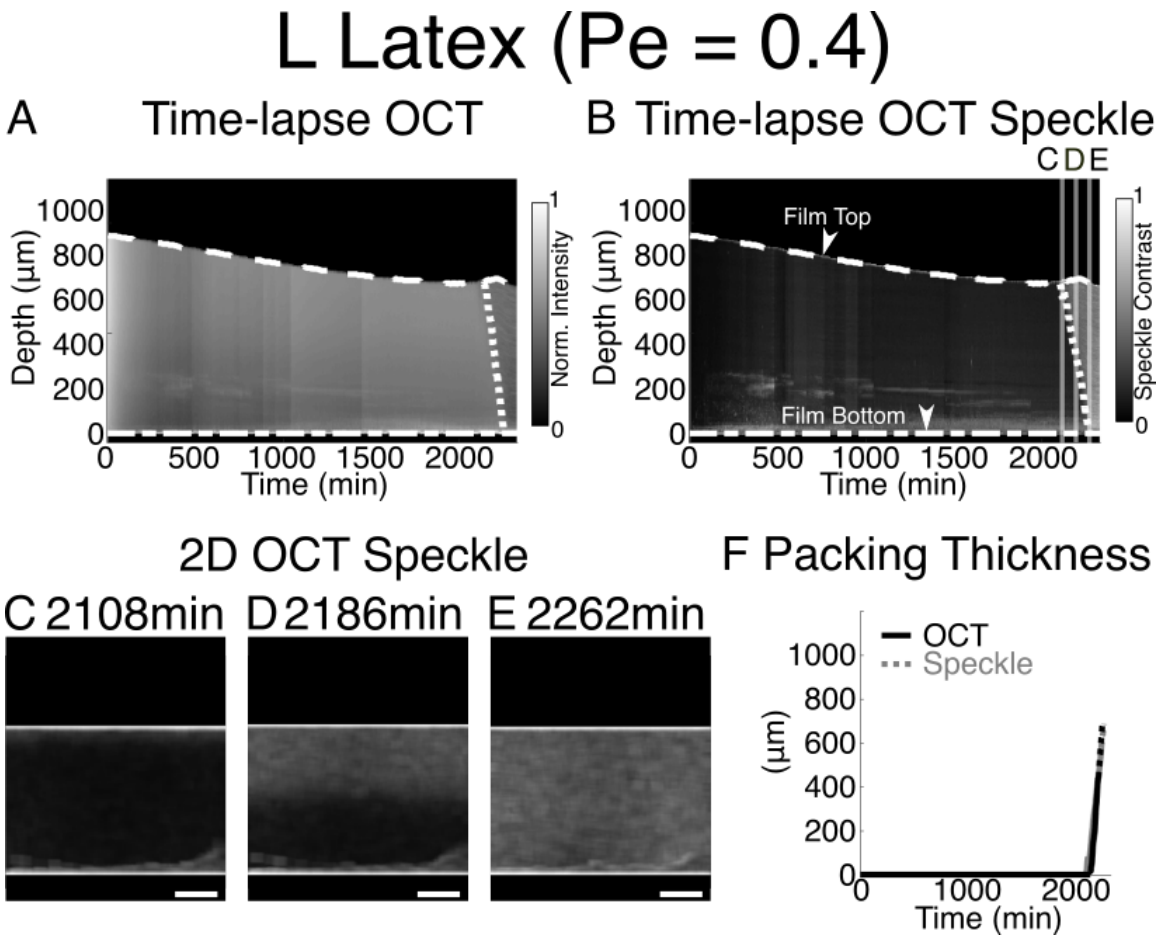

Figure 6. 19 Visualization of entire particles' packing process in L latex with OCT, with a slow drying rate. The cap of the Petri dish was covered to achieve slow drying. Thus, the packing process was significantly delayed as compared to ambient drying condition in **Figure 6.17**. (A) Time-lapse OCT intensity profile showed the domain boundary between upper packed layer and lower suspension layer with light intensity difference. (B) Time-lapse OCT speckle contrast analysis further differentiated particles' mobility in these two domains. (C – E) 2D OCT speckle contrast image at ~2108 min, ~2186 min and ~2262 min showing the progression of particles' packing process in L latex with slow drying rate. (F) Packed layer thickness change as a function of time. Scale bar: 200 μm

6.4.9 Cracking, Detachment and Apparent Shear-band Structures in Time-lapse 3D OCT Images

To further explore the drying phenomena of cracking, detachment and apparent shear band structures in polystyrene latex, we performed the time-lapse 3D OCT imaging of both L latex and S latex. Each 3D OCT

dataset consisted of 800 A-scan per B-scan and 800 B-scans, covering a large FOV of 5.9 × 5.0 mm^2. Time-lapse video captures were conducted at the same time. The time step for time-lapse imaging was set to 2 min.

Figure 6.20 showed the characterization results of the L latex with time-lapse 3D OCT imaging. **Figure 6.20 A1-A6** showed the corresponding video images at ~219 min, ~221 min, ~227 min, ~233 min, ~243 min, ~269 min. The red rectangle box in **Figure 6.20 A1** indicated the local region covered by 3D OCT imaging. Time-lapse OCT en face images of the L latex at two different imaging depths were shown in B1-B6 and C1-C6. In **Figure 6.20 B1**, the L latex was separated by cracks in four regions, labeled as 1-4 in the image. As the time evolved, the crack between region #2 and region #3 became larger, inferring the shrinkage of the latex due to internal compressive stress. In **Figure 6.20 B1-B6**, the progression of apparent shear band structure was observed in region #1 of the latex, indicated by the bright lines in the image. They first appeared at ~219 min and immediately became clearly observed 2min later, indicating the fast progression. Starting from ~233 min, we could observe that part of the region #1 latex became whitened, indicating the particles underwent rearrangement. In the whitened, the apparent shear band structures disappeared due to the altered arrangement. The rearrangement process propagates to other areas (**Figure 6.20 2B**) and at ~269 min, all the region #1 of the L latex became whitened with a uniform look, indicating the end of the shear-band phenomena. The total duration of apparent shear band structure was ~50 min for this L latex sample, which was smaller than ~68 min reported in another sample. This might be attributed to variations of environmental conditions and imaging spots. In **Figure 6.20 C1-C6**, the apparent shear band structures in piece #2 and #3 of the L latex were shown. We clearly observed that the apparent shear band phenomena were initiated at different time points for these three adjacent regions of L latex. Apparent shear band structure was first initiated in region #3, then in region #1 and next in region #2. The sequence corresponded well with the propagation of the drying fronts, which was observed in the video images of **Figure 6.20 A1-A6. Figure 6.20 D1-D6, E1-E6 and F1-F6** showed the time-lapse OCT cross-sectional images of progression of apparent shear band structures in drying L latex, along the corresponding dashed dark orange (D1 - D6), light orange (E1 - E6) and yellow (F1 - F6) lines in **Figure 6.20 B1**. Corrspondingly, the imaging plane for B1 – B6 and C1 – C6 were indicated by the light pink and dark pink dashed lines in **Figure 6.20 D1 and E3**. In **Figure 6.20 D1**, the region #1 of L latex was already detached from the substrate, indicating the detachment and cracking occurred earlier than the initiation of the apparent shear band structure. After the ~227 min

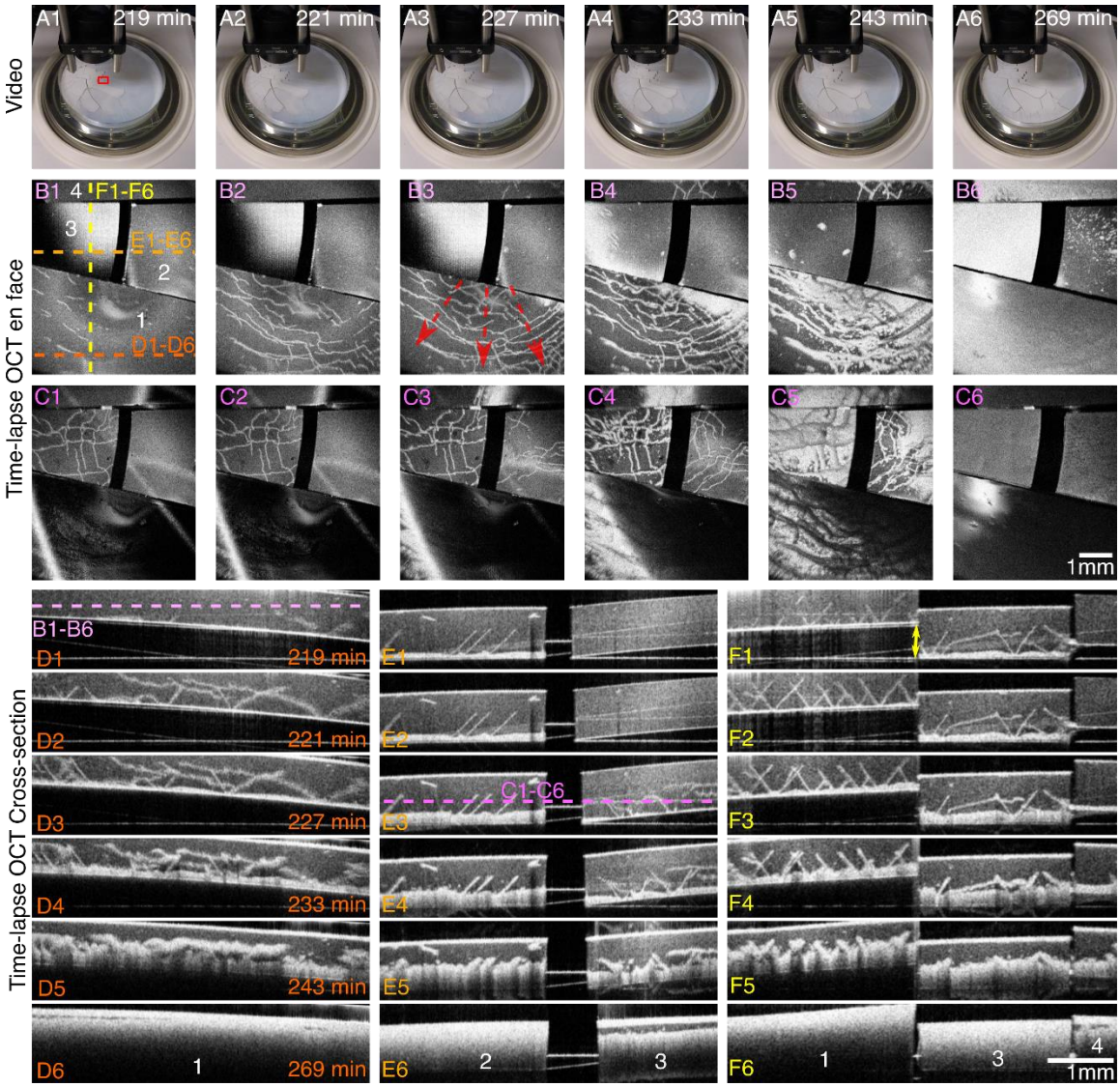

Figure 6. 20 Visualization of cracks, detachments and apparent shear band structures in L latex with time-lapse 3D OCT. (A1-A6) Video images of the drying L latex. The red rectangle box indicated scanning area covered by OCT. (B1-B6) Progression of cracks and apparent shear bands of region 1 in time-lapse en face OCT images at corresponding time points of A1- A6(~219min, ~221min, ~227min, ~233min, ~243min and ~269min). (C1-C6) Progression of apparent shear bands of region 2 and 3 in en face OCT images. (D1-D6, E1-E6, F1-F6) Time-lapse OCT cross-section images of the apparent shear bands structures along dashed dark orange line, light orange line and yellow line in B1, respectively. B1-C6, had the same scale bar as C6. D1-F6 had the same scale bar as F6.

(**Figure 6.20 D3 and F3**), we could observe that the bottom of region #1 latex started to fall down, by comparing the gap size in D3/F3 with D5/F5. At ~269 min, the bottom of the region #1 L latex could not be distinguished due to significant increasing scattering in the upper layer of the L latex. Along the yellow dashed line, we could observe the cross-sections of region #1, #3 and #4 at the same time. In **Figure 6.20 F1**,

we could see that the tiny cracks between region #1 and #3 and between region #3 and #4. Large dislocation between region #1 and region #3 was found, with region #1 latex detached and moved up while the region #3 remained attached to the substrate. The dislocation could be as large as ~500 µm, measured from the dislocation point (yellow arrow in **Figure 6.20 F1**). As time evolved, the dislocation reduced to ~370 µm at ~243 min (**Figure 6.20 F5**). The development of the latex detachment was in agreement with our observation in the time-lapse OCT intensity profile of L latex in Chapter 6.4.6.

In **Figure 6.20 E2 – E4**, the apparent shear band structure in region #2 of the L latex appeared to be bright straight lines tilting in an angle of ~30 - 40°. And, they were arranged in parallel, growing from the latex bottom towards the cracking boundary. As time evolved, they became brighter and thicker (**Figure 6.20 E4**). In **Figure 6.20 F2**, we could see V shaped apparent shear band structures, which grew from the bottom and bifurcated towards the top. However, the bifurcated lines did not reach the top surface, growing to ~1/2 to ~2/3 of the latex height. The V shape structures were separated roughly in equal distances, with the bifurcated lines crossing in the middle of the latex. The observed structures in cross-sectional OCT images resembled the shear band structure investigated by Yang et al.[350] and Kiatkirakajorn et al[351], who used the drying colloids containing polystyrene and silica particles as the tested sample. In our suspection, successful visualization of these shear band structures under OCT was due to dislocation of packed latex particles, where the internal compressive stress built up along both horizontal and vertical directions. These dislocations allowed the air to infiltrate, resulting in a high refractive index mismatch between the air and polystyrene latex in the shear-band structure. Thus, these regions were shown as bright lines in OCT images. As time evolved, we could see that the particles started to undergo rearrangment from the bottom of L latex, shown as the high-scattering regions near the latex bottom in **Figure 6.20 D4, E3 and F4**. The progression of the rearrangement moved upward, gradually covering the shear-band structures (**Figure 6.20 E4 – E6**). A tentative explanation was that, the dislocation would be the first step to release the internal stress inside the latex. In the next step, particle underwent rearrangement to further relax the stress, especially internal capillary stress occurred in the dislocation region. Thus, these shear-band structure would be disrupted and ultimately disappear in the latex. In the en face OCT image of **Figure 6.20 B3 and C3**, the apparent shear bands were observed in a network pattern in region #1 and #2 of the L latex. However, the network pattern was slightly different for these two regions. In region #1, the bright lines of the apparent shear band structrues

resembled arcs from the multiple concentric circles. The distances between the concentric circles at different arc sections were roughly the same. The arc pattern of the apparent shear band might be an indication of the direction of the horizontal compressive stresses, where should be in the normal directions to the shear band structures. The red dashed arrows in **Figure 6.20 B3** labeled the directions of the horizontal compressive stress based on the apparent shear band structures, inferring that they were originated from the crack location. The large stress might lead to formation of cracks and the smaller stress may lead to apparent shear band structure. In **Figure 6.20 C3**, the region #2 was surrounded by three cracking boundaries. Thus, the shear band structures appeared as multiple crossings, with the crossing lines roughly parallel to the cracking boundaries. In **Figure 6.20 D3 and F3**, we could also observe the horizontal shear band lines located in the cross-sections of L latex, with only a small angle between the cross-section plane and cracking boundaries, inferring the orientation of these lines.

Cracking, detachment and formation of apparent shear band structures were also examined in the S latex by time-lapse 3D OCT imaging. Results were shown in **Figure 6.21**. Time-lapse, en face OCT images showed a large crack near the bottom of the image as well as the network like shear band structures. Most of the lines were parallel to the cracking boundary, inferring the direction of horizontal compressive stress. Similar V shape shear band structures were also observed in the cross-sectional OCT images. Several differences were observed between the apparent shear bands in L and S latices. First, initiation of formation of apparent shear band was later in S latex, starting from ~304 min. However, the delay of the initiation might be attributed to different factors, including the longer time for consolidation stage, propagation of the drying front and its propagation speed, as well as the variation of OCT imaging spots between L and S latices. Second, the duration of apparent shear band was shorter for S latex, which lasted for ~30 min. However, we should note that, the time window between the initiation of the apparent shear bands and the initiation of particle rearrangement was similar for both L latex and S latex. Both latices had a short time window with clear visualization of apparent shear band structure for ~10 min. It meant that, the progression of particle rearrangement was faster in S latex than the L latex. Third, the density of apparent shear band structures were higher in the S latex, by compared **Figure 6.21 A2** (S latex) to **Figure 6.20 B3** (L latex). Similar with crack formation, such density difference could be attributed to different compressive stresses that were

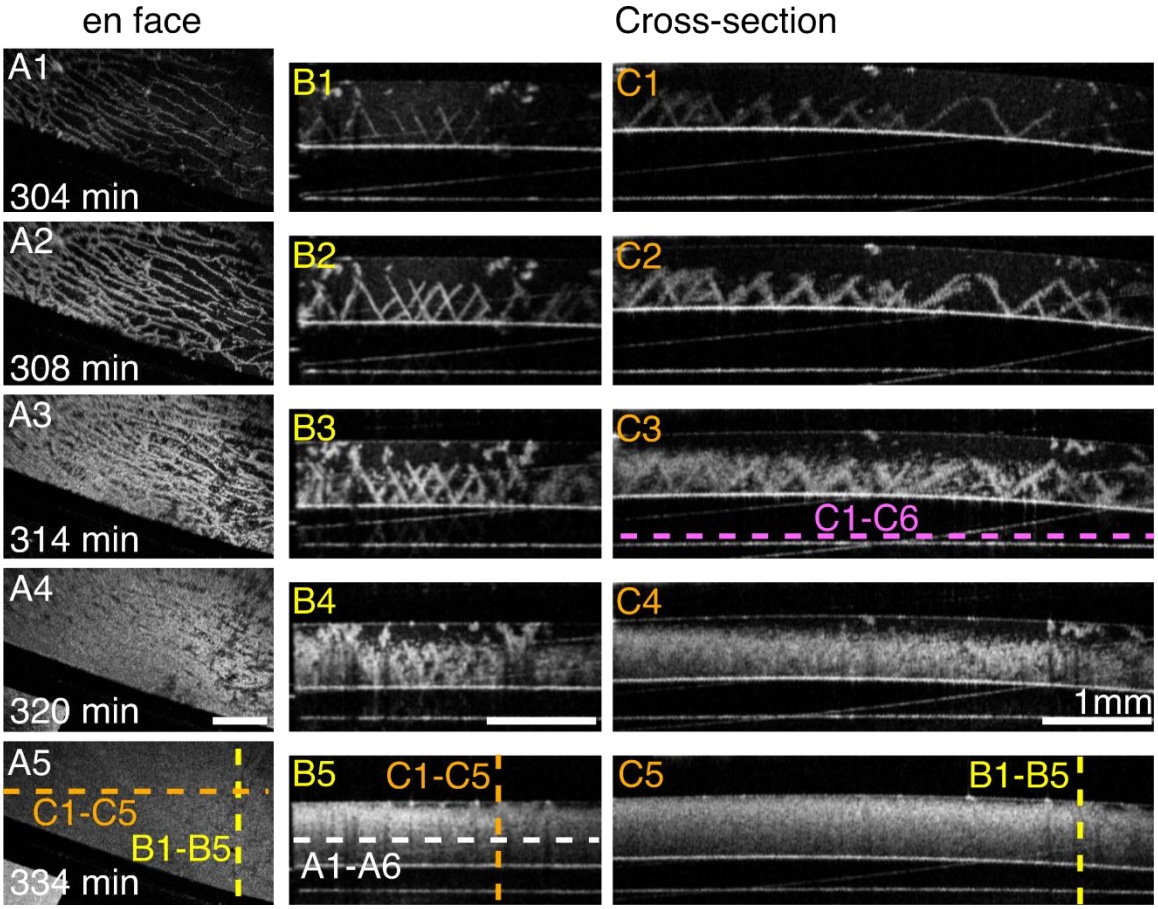

Figure 6. 21 Visualization of cracks, detachments and apparent shear band structures in S latex with time-lapse 3D OCT. (A1-A5) Progression of apparent shear bands in time-lapse en face OCT images at ~304 min, ~308 min, ~314 min, ~320 min and ~334 min. (B1-C5) Time-lapse OCT cross-section images of the apparent shear bands structures along dashed light orange line and yellow line in A5, respectively. A1-A5, had the same scale bar as A4. B1-C5 had the same scale bar as C4. All scale bars were 1 mm.

inversely proportional to the particle size [286, 308]. Since S latex tended to build up higher internal stresses, more cracks as well as more shear bands were needed to release the stress energy step by step.

Given the abovementioned OCT observations of apparent shear band structures, it was yet to be confirmed whether these structures were shear band structures or tiny cracks with sub-micron gaps. The current OCT system didn't have enough resolution to resolve the individual particles and observe their arrangement. One possible solution to further confirm the apparent shear band structure is to combine the real-time OCT monitoring with cryo-SEM. The real-time preview of the OCT could predict the occurrence of the apparent shear-band structure in the latex. Then, the latex with the observed shear band structures was

immediately freezed and sectioned across the cross-sectional plane to observe particle arrangement of the apparent shear-band structure to determine whether it was a dislocation or a crack.

6.4.10 Correlation of OCT Images with Gravimetry and Video Measurement

In the integrated OCT-Gravimetry-Video studies of latices, we tried to correlate the different drying states and observations between OCT, gravimetric and video measurements.

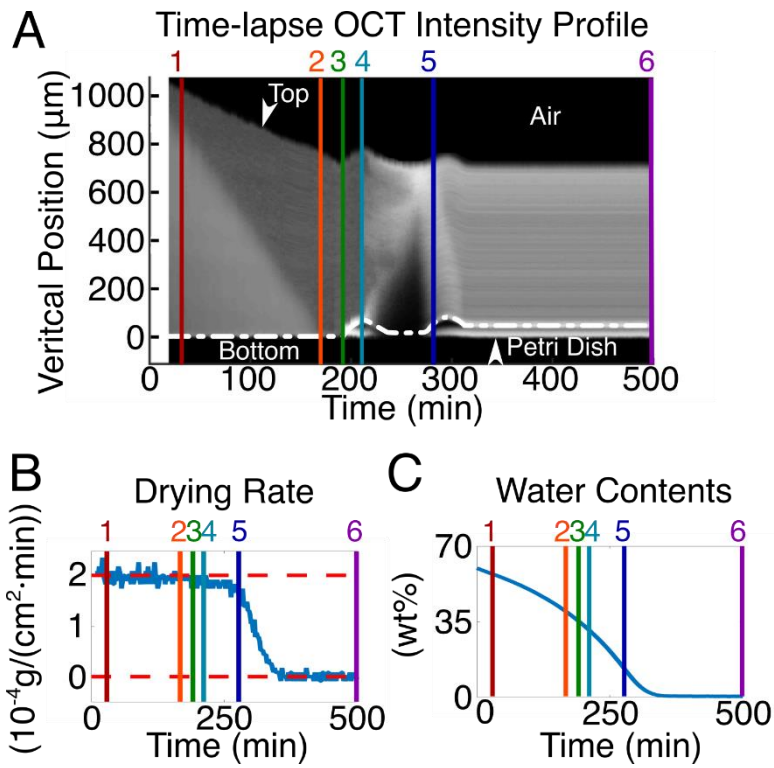

Figure 6. 22 Correlation of OCT and gravimetric measurements of drying progression of L latex. (A) Time-lapse OCT intensity profile. (B, C) Drying rate and water content curves from gravimetry measurement. Line 1-6 in different colors indicated critical time points of different OCT observations in **Figure 6.13**.

Figure 6.22 showed the correlation of OCT and gravimetric measurements of the drying L latex. In the initial drying stage, the latex thickness decreased linearly tilled ~190 min (#3 in the time-lapse OCT intensity profile). The linear decreasing trend matched the observation of constant drying rate and linearly decreased water content in **Figure 6.22 B and C**. Then, the drying rate started to decrease. No direct correlation was found between the stress relaxation state and the decreasing drying rate.

Figure 6.23 showed the correlation of OCT and video measurements of drying S latex. Figure 6.23 A-F showed the video recording of S latex, showing surfical color change and progression of drying fronts (drying boundaries). **Figure 6.23 G-L** showed the corresponding OCT images acquired at a local spot indicated by the dark cross in **Figure 6.23 A**. Two coincident events were correlated between the OCT and video measurement. First, as the cracking front reached the local OCT scanning spot at ~220 min in video images, time-lapse OCT observed the initiation of the detachment of the S latex away from the Petri dish. Second, as the dewetting drying front reached the OCT scanning spot at ~292 min in the video image, formation of apparent shear band structure was found in time-lapse OCT images. In this way, the observation results from the two modalities could be correlated, linking macroscopic drying features of appearance, cracking and drying fronts propagations observed by videography with the microscopic features of detachment and apparent shear band structures observed by OCT to gain an overall understanding of the drying progression of latex.

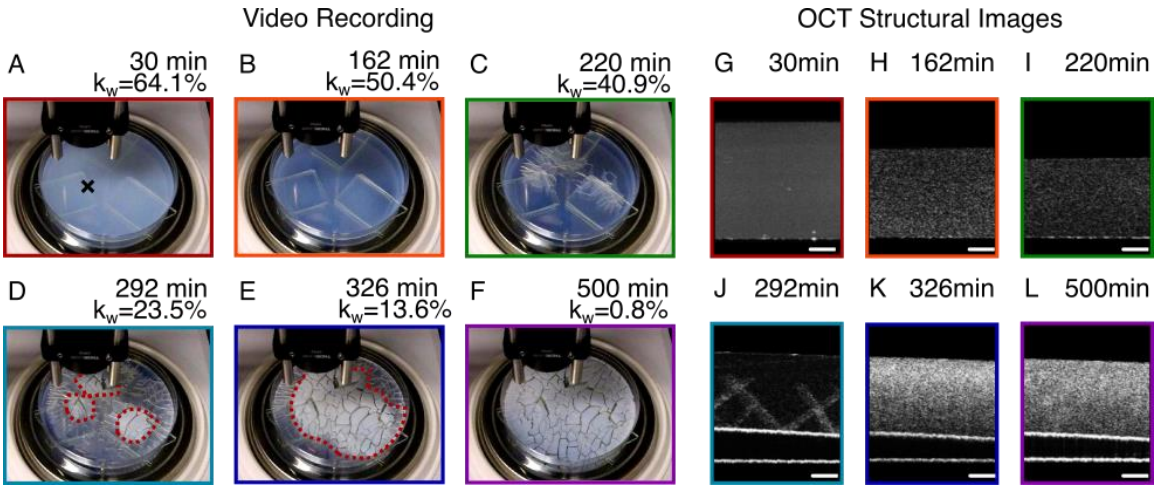

Figure 6. 23 Correlation of OCT and video measurements of drying progression of S latex. (A-F) Time-lapse video recording of S latex, showing surficial color change and progression of drying fronts. (G-L) Corresponding OCT structural images showing the cross-section of the S latex at the local position, indicated by the black cross in (A).

6.4.11 Summary

An integrated system combining OCT with gravimetric measurement and video captures were developed to provide both global and local characterization of polystyrene latices. Time-lapse OCT showed the local dynamic changes from cross-sectional view of the drying latex, i.e. the thickness changes, detachment of

latex bottom and apparent shear-banding phenomena. Moreover, speckle contrast analysis was applied on time-lapse OCT images to characterize packing process of particles over time, based on the distinct particles' mobility in packed and suspension layers. OCT observations could be combined with global observation of gravimetric and video measurements to provide novel insight to the study of different drying latex models. This multimodal system could be further generalized for quality control of latex sytems in the industry.

6.5 Discussions

6.5.1 Water Droplet Imaging

During the OCT imaging of the evaporation water droplet containing particles, the flows are visualized by tracking the motion of the tracer particles, which has a distinct scattering property from the water. Thus, the first prerequisite for visualizing the flows in the water droplet would be: look for a tracer particle with significant mismatched refractive index (RI). Thus, polystyrene particle with a RI = 1.57 could serve as the tracer particle in the water droplet. Other particles with high scattering, such as gold particles and TiO_2 particles, could also be used as the indicator of flows in the droplet.

Second, the tracer particles can not be too small. The tracer particle should be at the same order as the OCT system resolution in order to be resolved in the image. For example, tracer particles with a size of 1 µm were not visible in the water droplets under the 1300 nm OCT system with an axial resolution of ~5 µm.

To visualize the drying progression of the entire water droplet, on one hand, the OCT system resolution should be high enough (at the same order as the size of tracer particles) in both axial and lateral directions. On the other hand, a lower NA objective should be used in order to cover the whole droplet within its FOV. Generally, the water droplet with a volume of ~0.2 µL on a glass plate could spread out with a diameter larger than 1mm. Thus, OCT system with a shorter central wavelength would be recommended for water droplet imaging. In this case, visible light OCT [81], with a central wavelength of ~570 nm, can potential provide superior resolutions to track tracer particle motions and visualize the flows in the water droplet.

6.5.2 Colloidal Droplet Imaging

The consideration for OCT imaging of colloidal droplet is similar to water droplet. If we use the tracer to track the flows, the prerequisite for RI mismatch is still the same. For example, the polystyrene particle cannot

serve as the tracer particles in polystyrene dispersed colloidal droplet. Different from water droplet imaging, light penetration needs to be taken into consideration since the incident light is highly scattered in the colloidal droplet. OCT system with a longer wavelength would be recommended for larger colloidal droplet with a size of ~5 μL (close to the volume of the latex droplet used in our study), if flows are not under investigation. If we want to visualize the flows in the large colloidal droplets, larger tracer particles are required, i.e. microspheres [283].

6.5.3 Latex Film Imaging

For OCT imaging of latex film, the key focus would be 1D vertical drying process, assuming the evaporation rate is uniform in most region of the latex film. Thus, the lateral resolution was not critical as compared to axial resolution. Furthermore, acquired 2D or 3D OCT data are often averaged across the FOV to generate the intensity profile along the depth direction to monitor the 1D vertical drying process.

Compared to video recording, the FOV for OCT is relative small (See **Figure 6.20** A). However, if we want to observe horitonal drying inhomogeneity under OCT, i.e. cracking fronts, propagation of apparent shear band structure, or quality control of the latex film, a wider FOV would be highly preferred. In our study, a 3D OCT imaging of the latex film with a FOV of 5.8 mm × 5.0 mm has been demonstrated. To further expand the FOV, one approach is to use a low NA objective or a camera lens to expand the FOV. In this way, a FOV of a few cm^2 could be potentially achieved. A second approach is to utilize parallel beams to image the latex at different spots. We have previously demonstrated a SDM-OCT system to perform wide field imaging with simultaneous 8 channel illumination, covering an area of 18.0 mm × 14.3 mm (See Chapter 3).

We should note that, OCT measured the optical path length instead of absolute distance. To derive the latex thickness, the measured optical path length value would be divided by the predetermined refractive index values. Thus, the quantification error may occur when the RI is changing dynamically or RI varies at different local positions and different depths.

To monitor the particles' mobility, the time duration for the speckle contrast analysis is of critical importance. Currently we employed the M-mode 2D OCT acquisition pattern to detect the particles' mobility, with a time window of ~1.1 s for each M-mode data. The OCT system was running at 20.7 kHz.

Further improvement of OCT scan rate to MHz level [352] may enable the capability of 3D M-mode OCT imaging, which can be used for the speckle analysis to monitor 3D drying inhomogeneity in drying colloidal droplets or 3D flows in water droplets (using larger size tracer particles).

At last, to facilitate the broad dissemination of OCT technology for non-destructive evaluation and testing (NDE/NDT), a compact OCT system would be highly preferred. A recent study reported that the whole OCT system could be packed in a briefcase [353, 354]. This compact system could be potentially used for the on-site investigation of the coating or painting quality.

6.5.4 Application on Other Drying Models

In the previous sections, we summarize the OCT applications in characterizing the drying progression of droplets and latex films. Besides this, we can also utilize OCT to characterize the drying process of other drying models. For droplet models, 3D OCT can potentially characterize levitated droplets to monitor the flows or particle motions inside the droplet. Also, we have conducted a preliminary study to image a 1D confined droplet to see the formation of apparent shear bands inside the droplet (Results not shown). Also, our collaborator, Hao Huang and his colleagues, has utilized our OCT system to characterize the drying process of commercial latex to see the skin formation and explore the effect of surfactants on skin formation. Details can be found in Hao Huang's thesis [348]. With the micron-scale depth resolvability, OCT could be potentially utilized to see the stratification process in the latex containing multiple types of particles [287].

6.6 Summary

In this chapter, we have demonstrated the feasibility of OCT to characterize the drying progression of the water droplets, latex droplet and latex films, using time-lapse acquisition mode. With fast M-mode scanning, we can track the motion of tracers in the evaporating water droplets to indicate different types of flows, involving the radial capillary flows, convective flows due to Marangoni force. Also, speckle contrast analysis was employed on the M-mode OCT data to distinguish particles' mobility. Time-lapse, long-term OCT imaging ensure the monitoring of the entire drying process of the droplets and the latex films, including the phase changes in the LCLC droplets, packing process in latex droplets and latex films, crack formation, detachment and apparent shear band structures in the latex films. In these studies, we have demonstrated the

advantages of OCT to provide the cross-sectional views with exceptional depth-resolvability. In the future, OCT can be utilized to facilitate the fundamental studies of the soft matter to characterize different drying models. Also, it can be established as a tool for in-line quality control of coatings and paintings.

Chapter 7: OCT Applications in Longitudinal Imaging of Tumor Spheroids

7.1 Introduction of Three-dimensional Tumor Spheroids

Cancer is the second leading cause of death in the world [355]. Developing anti-cancer drugs is of crucial importance for patients. However, more than 90% of new anti-cancer drugs fail in the development phase because of lack of efficacy or unexpected toxicity in clinical trials [356]. Part of the reasons can be attributed to the use of simple two-dimensional (2D) cell culture models for compound screening, which provide results with limited predictive values of compound efficacy and toxicity for the following phases of drug discovery [356-358]. Three-dimensional (3D) tumor spheroids have gained increased recognition as important models in cancer research and anti-cancer drug discovery [359, 360]. These spheroids can simulate important in vivo tumor features, such as oxygen and nutrient gradient, hypoxic core and drug resistance. Thus, they become more reliable models for drug discovery, with greater capacity to predict clinical efficacies for anti-cancer therapy, compared to 2D cultures.

7.2 Imaging Modalities to Characterize 3D Tumor Spheroids

Currently available imaging modalities e.g. bright field [361], fluorescence and confocal imaging [362], and light-sheet fluorescent microscopy [12], can obtain high-quality images of 2D cultures easily. With proper designs and implementations, these microscopes can be well adapted for high-throughput screening (HTS) of drugs tested in 2D cultures. A 96-well plate of 2D cell cultures can be screened in less than 5 minutes , with the commercial high-throughput screening devices in bright field scanning mode. With fast data processing equipped with graphic processing units (GPUs), and advanced machine learning (ML), data mining and artificial intelligence (AI) algorithms, rich details of features can be extracted from the 2D cell cultures images, which yields a better predictions of drug outcomes. The fully integrated system combining different imaging modalities and automatic image processing for screening is called a “high-content screening” system. However, when these systems are employed in 3D tumor spheroid imaging, they have their inherent drawbacks: they are unable to resolve 3D structures deep inside (>50 μm) tumor spheroids. Many factors contribute to these limitations, including penetration of the probing light in the spheroid;

diffusion of the fluorescent dyes into the spheroid; emitting fluorescent signals from excited fluorescent dyes inside or on the opposite surface of the spheroid due to strong absorption and scattering; and depth-resolvability of these imaging modalities [363].

To resolve the geometric shape of a 3D tumor spheroid, a 3D imaging modality is still imperative. First, not all the tumor spheroids are geometrically symmetric, i.e. the shape of the spheroid is not guaranteed as a sphere or ellipsoid. For example, if the shape of the tumor spheroid is purely spherical or ellipsoid, or close to it, we can still use 2D imaging modality to characterize its diameter or sphericity in 2D images, then calculate their volumes. However, if the height is different, or the shape of the spheroid becomes disrupted due to natural cell death or drug treatment, these approaches would become invalid. In this case, a 3D imaging modality would be well suited and robust for characterization of 3D structures of tumor spheroids and get a more valuable characterization results.

7.3 OCT as the 3D Imaging Tool for Tumor Spheroid Characterization

OCT has recently been explored as an alternative candidate for characterization of tumor spheroids. Given its advantages of label-free, non-destructive, fast, 3D imaging capability with high resolution and deep penetration, OCT was well suited for this purpose.

Table 7.1 summarizes the recent studies on using OCT for tumor spheroid characterization. As a 3D imaging modality, OCT has been employed to observe the 3D structure of the tumor spheroids [364, 365]. Specifically, OCT can detect 3D heterogeneous structures of tumor spheroids. In Sharma's study, the spheroid appeared to be oblate at Day 7 [364].. Evans et al. observed a hollow core structure inside the ovarian tumor spheroid, as the spheroid grew larger than ~300 µm, which was after Day 13 in their experiment [366]. Huang et al. observed that the HCT 116 spheroid became flattened and disrupted after Day 11. The obtained 3D OCT data of tumor spheroid can be further analyzed to quantify the sizes, volumes and sphericity [364, 365], which can be used to evaluate the effectiveness of 3D culture methods [367, 368]. Given the non-destructive imaging, OCT has been used for longitudinal or time-lapse monitoring of tumor spheroid to characterize grow kinetics [364, 365] or tumor morphological changes after photo-dynamic therapy (PDT) [369-373].

Table 7. 1 Studies on OCT Imaging of Tumor Spheroids

Reference	Cell line	Grow Method	Characterizations
Sharma et al. [364]	Colo-205 (Colon)	Hanging Drop	Grow Kinetics (Dia :~1mm) Volume; Necrotic core (high scattering, Dia: 200µm)
Evans et al. [366], Celli et al. [369], Evans et al. [370] Jung et al. [371], Klein et al. [372], Jung et al. [373]	OVCAR-5 (ovarian)	Liquid Overlay (in Petri dish, on Matrigel, or 24 wells flat bottom)	Hollow core simulating metastasis (>Day 13, Dia:~300 µm) Merging tumor spheroid PDT response (BPD-PDT, EtNBS-PDT): rupture, with apoptotic cell leaking out. Live/Dead after PDT based on surface/volume ratio and apoptotic density.
Yu et al. [374], Yu et al. [375], Nolte et al. [376]	UMR-106 (bone)	Bioreactor	Dynamic light scattering for necrotic core detection
Huang et al. [365], Huang et al. [363] (Our group)	HCT-116 (colon), U87-MG (brain)	Liquid Overlay with ULA round bottom plate	Grow kinetics Volume (based on voxel counting) Necrotic core (based on attenuation)
Shi et al. [367]	HCT-116 (colon), Hela (cervix), A-431 (skin), U87-MG (brain)	Cell-sheets in dispase-dope media, shaker	3D morphology
Kingsley et al. [368]	MDA-MB-231(breast)	Laser direct write (LDW) bioprinting	Volume and sphericity of microcapsule containing cell aggregates

Other than 3D structure of tumor spheroids, OCT can also provide pathological features of tumor spheroids. Specifically, OCT can be used to identify the dead cell regions inside the tumor spheroids, which could be potentially served as the alternative of live/dead viability test. Currently, three methods have been proposed to characterize the dead cells regions inside the tumor spheroids. Evans et al. observed that, in ovarian tumor spheroid, several high-scattering bodies were found inside the hollow core, which they confirmed to be apoptotic cell aggregates that were broken off from the inner wall of the core in response to a lack of survival signals [366, 371]. They also observed that, after PDT response, the surface structure of the tumor spheroids was disrupted, with the leakage of apoptotic bodies into the outside environment [370]. Based on these observations, they derived two parameters, the surface/volume ratio and apoptotic density, to evaluate the treatment effect of PDT in ovarian tumor spheroid models [373]. In another method, Nolte et al. combined the dynamic light scattering with holographi optical coherenece imaging, a varient of full-field OCT, to detect the motions in different regions of the tumor spheroid [377]. Distinct fluctuating speckle

patterns and fluctuation power spectra were found between the outer profilerating shell and inner quiescent necrotic core in their results. Our group has proposed utilizing the optical intrinsic attenuation contrast to identify the necrotic core regions [363, 365]. Based on distinct optical attenuation values between the outer profilerating layer and inner dead cell regions, we could quantitatively evaluate the distribution of dead cell regions and monitor their growth over time.

7.4 OCT Characterization of Tumor Spheroid

In the following section, we reported the establishment of the high-throughput OCT imaging platform to systematically characterize 3D tumor spheroids in multi-well plates. Specifically, details of how the OCT imaging platform was employed to obtain high-resolution 3D images of tumor spheroids would be described. Next, the step-by-step quantitative analyses of the growth kinetics of 3D tumor spheroids, including accurate measurements of spheroid diameter and volumes, would be shown. Furthermore, the method of the non-destructive detection of dead cell regions using OCT based on the intrinsic optical attenuation contrast would be presented.

7.5 Sample Preparation, OCT Configuration and Imaging Protocol

7.5.1 Preparation of 2D Tumor Cell Culture

Two tumor cell lines, glioblastoma (U-87 MG) and colorectal carcinoma (HCT116), were purchased from the American Type Culture Collection (ATCC, Rockville, MD). Both cell lines were cultured following recommended protocols by suppliers. U-87 MG cells were maintained in EMEM (Lonza, Walkersville, MD) supplemented with 10% FBS (ThermoFisher Scientific, Atlanta, GA), 1% penicillin-streptomycin (Pen-Strep, Lonza), and additionally, 1× non-essential amino acid (NEAA, ThermoFisher Scientific) and 1% sodium pyruvate (ThermoFisher Scientific). HCT116 cells were maintained in McCoy's 5A medium (ThermoFisher Scientific) supplemented with 10% FBS, 1% Pen-Strep, 1× NEAA and 1% sodium pyruvate.

The protocol of preparation of 2D tumor cell cultures were described as followed [363]:

1) Obtain cell lines from a qualified supplier. Verify that cells from the cell lines of interest can form spheroid in the culture media or with the help of a substrate (basement membrane matrix like Matrigel). Look into the literature [360] or perform one-round of a pre-experiment for a check.

2) Thaw the frozen cells following the specific procedure provided by the cell-line supplier. A general procedure can be found from the suppliers' recommended protocols.

3) Culture the cells for 1-2 passages in 25 cm^2 culture flasks. The cells are then ready to use for 3D cell culture.

4) Monitor the health status of the cells every day and maintain them in an incubator under standard condition (37 °C, 5% CO2, 95% humidity). Refresh the media as needed.

7.5.2 Preparation of 3D Tumor Spheroid

Our protocol for preparation of 3D Tumor Spheroid in multi-well plates were adapted from the standard liquid-overlay method for 3D tumor spheroid preparation [360]. The detail steps were described as followed [363]:

1) Remove the culture media from the culture flask and wash it with sterilized phosphate-buffered saline (PBS, heated to 37 °C).

2) Resuspend the cells by adding 1 mL trypsin-ethylenediaminetetraacetic acid (EDTA, 0.5%) into the flask for 3 min. Then, add culture media to dilute the trypsin.

3) Transfer the cell suspension into a 15 mL centrifuge tube and centrifuge for 5 minutes at room temperature, with the speed of 500 × g .

4) Remove the supernatant and resuspend cells with 4 mL, pre-warmed, culture medium. Pipette one drop of sample on the hemocytometer for cell counting to determine cell concentration. Dilute the cells to appropriate concentration for seeding (3000 cells/mL). Make sure that the initial cell concentration of the spheroid was optimized for each cell-line and each type of multi-well plate (96-well, 384-well or 1536-well).

5) Seed cells into the ultra-low attachment (ULA) round-bottomed multi-well plate. For 96-well plate, add 200 µL of cells suspension in each well with the concentration of 3000 cells/mL.

6) At room temperature, centrifuge the whole plate for 7 minutes right after seeding, using a plate adapter, at a speed of 350 x g or the lowest speed available. The centrifugation step could help gather cells to the center of the well to facilitate forming a single, uniform spheroid. The centrifugation step is performed only once at the beginning to form the tumor spheroids. It will not be repeated when the tumor spheroids start growing.

7) Maintain the multi-well plate at 37 °C and 5% CO2 in a culture incubator and refresh the culture media every 3 days.

7.5.3 OCT System Configuration

The configuration of custom OCT system has been described in Chapter 2. The characterization results of key performance metrics of this system has been presented in the same chapter.

In order to utilize the SD-OCT system for high-throughput tumor spheroid imaging, a 2D or 3D motorized translation stage is added into the OCT system to hold and move the multi-well plate so that tumor spheroids in these wells will be imaged sequentially. Since the plate has a size of 128 mm × 84 mm and the well spacing would be (9.00 ± 0.05) mmfor a 96-well plate and (4.50 ± 0.05) mm for a 384-well plate, the stage is required to have long travel ranges in both X and Y directions to cover the whole plate. Requirements of minimum travel range in X and Y directions for the 3D stage are listed in **Table 7.2**.

Table 7. 2 Minimum Travel Range in X and Y Directions Required for the Translational Stage

	96-well (Corning 7007)	384-well (Corning 3830)
X travel range	9 mm × 11 + 6.86 mm (Dia.) = 105.86 mm	4.5 mm × 23 + 3.63 (Dia.) = 107.13 mm
Y travel range	9 mm × 7 + 6.86 mm (Dia.) = 69.86 mm	4.5 mm × 15 + 3.63 (Dia.) = 71.13 mm

In our SD-OCT system, a 3D motorized translation stage (JTH360XY, Beijing Mao Feng Optoelectronics Technology Co., Ltd.) with a travel range of 150 × 250× 20 mm is chosen.

In order to fix the position of the multi-well plate on the motorized stage, a plate adapter (plate holder) is required. Generally, for commercial microscopes for biological studies, the multi-well plate adapter is common. Or, we can choose to customize the plate holder to fit the motorized stage with 3D printing technology.

Figure 7.1 shows a design of the custom plate holder. The design of the plate holder can be fulfilled in Solidworks or edited in STL editor. On the edge of the plate holder, a staircase structure is designed to fit the multi-well plates with slightly varied sizes fromdifferent manufacturers. At the bottom of the plate, multiple holes are drilled. The hole locations are matched to the holes on the top surface of the motorized stage so that we can use screws to fix the plate holder. The plate holder has a size of 138 mm × 94 mm × 11 mm. The height of the plate holder matters, for the following two reasons: 1) It is used to raise the vertical location of

the multi-well plate so that light can focus on the top surface of the tumor spheroid. 2) The plate bottom

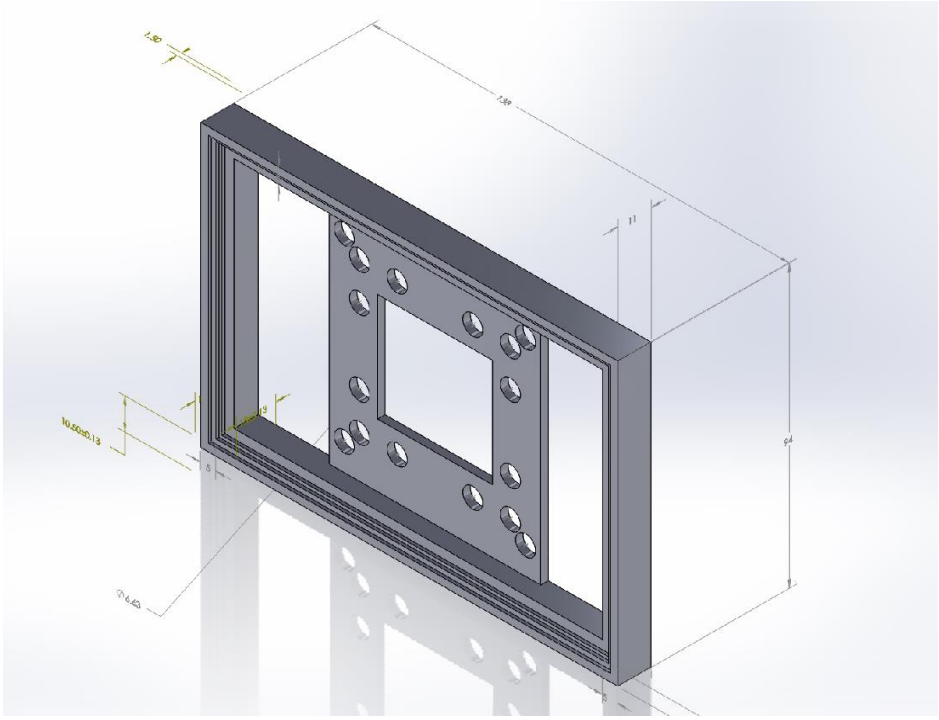

Figure 7. 1 Design of a plate holder for multi-well plate.

should be far away from the top surface of the stage to avoid the strong surface reflection from the stage and the screws. Note that we cannot print the threads in the holes due to insufficient accuracy of 3D printing and insufficient strength of plastic materials.

During the high-throughput imaging, image qualities from multiple wells may not be consistent due to de-focusing effect and sample offsets. One main cause is that the plate position is not fully optimized, with small tilting and rotation angles. In order to correct the plate position, an additional rotation stage and a 2D tilting stage are mounted on top of the motorized stage to provide rotational adjustments with three more degrees of freedom.

Figure 7.2 shows the stage setup for the fine adjustment of the position of the plate holder. In **Figure 7.2A**, a 2D tilting stage, a rotation stage and the plate holder are mounted on top of each other on the 3D motorized stage. **Figure 7.2C** shows how the rotation of the plate will affect the sequential acquisition of the OCT images. If the rotaion exists, locations of the boundary wells (D11 in **Figure 7.2C**) in OCT images will shift horizontally as compared to center one (D6 in **Figure 7.2C**), causing offseted spheroid images. **Figure**

7.2D shows the effect of plate tilting on OCT images. If the plate is tilted, locations of boundary wells will shift vertically (B6 in Figure **7.2D**), causing both offsetting and de-focusing effects in OCT images.

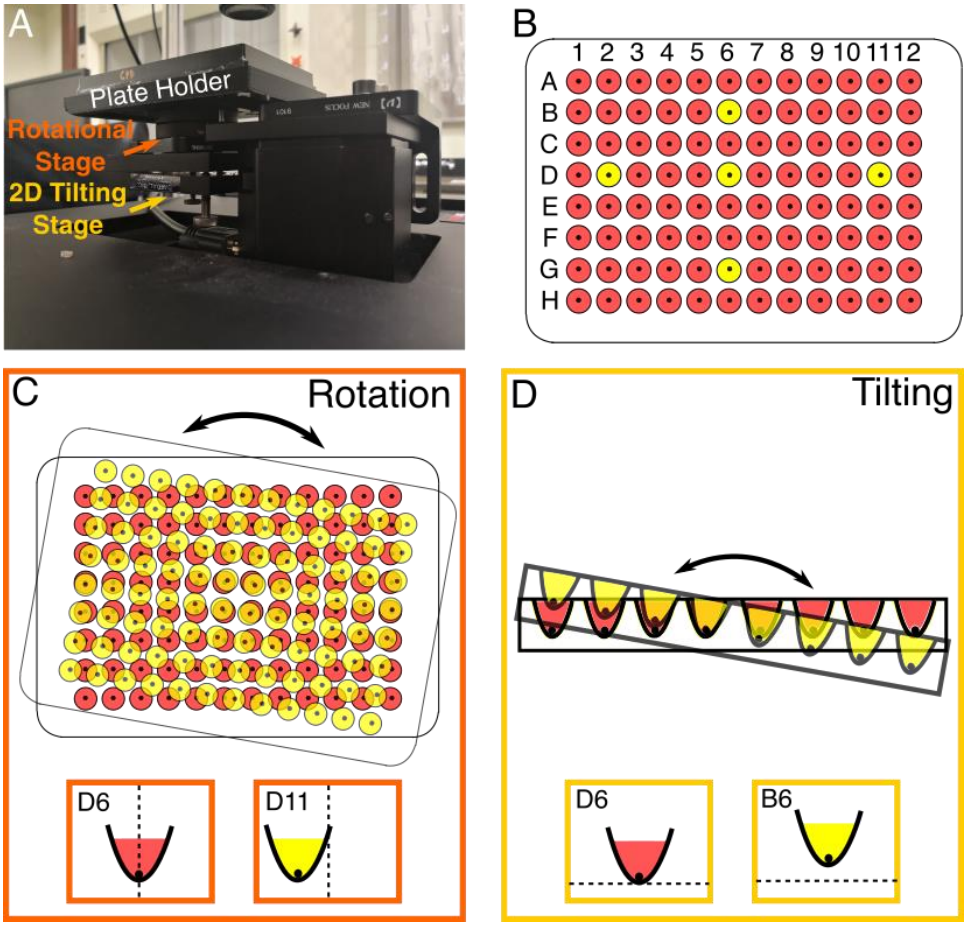

Figure 7. 2 Fine adjustment of the stage system. (A) Illustration of the stage setup with additional rotation and 2D tilting stages. (B) Locations of the wells (Marked in yellow) for fine adjustments. (C) The effect of rotation on OCT images. The plate with wells in yellow is rotated. The location of boundary well (D11) shifts horizontally as compared to center well (D6), causing image offsets. (D) The effect of tilting on well location. The location of boundary well (B6) shifts vertically as compared to center well (D6), causing both image offset and de-focusing effect.

Adjustment of the tilting and rotation of the plate holder can be performed iteratively. **Figure 7.2B** indicates the locations of wells (D6; B6 and G6; D2 and D11) used for fine adjustments. The procedures are described as followed:

1) OCT image of D6 well is used as the reference image and its location is optimized at the center of both XZ and YZ OCT image previews.

2) Move the stage to the boundary wells in the same row (D2, D11) or column (B6, G6) by integer times of the well spacing. Check the XZ and YZ OCT image preview. If the image of the boundary well is shiftd horizontally, adjust the rotation stage. If the image of the boundary well is shifted vertically, adjust the 2D tilting stage. Once it is well adjusted, move the stage back to D6 well.

3) Repeat step 1 and 2 and perform the adjustment of tilting and rotation stages iteratively until the well locations are exactly the same for all wells in both XZ and YZ OCT image previews.

After the fine adjustment, the plate position should be well-aligned for the high-throughput imaging.

7.5.4 OCT Imaging Protocol for Tumor Spheroid

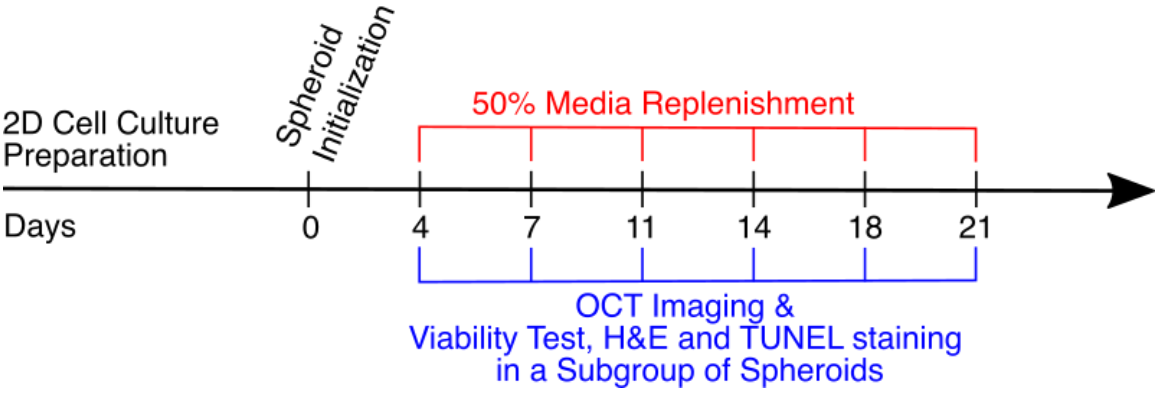

Figure 7. 3 Timeline for spheroid preparation and imaging.

Figure 7.3 shows the timeline for tumor spheroid preparation and imaging. OCT images of tumor spheroids are acquired at 4, 7, 11, 14, 18 and 21 days after spheroid initiation for both cell lines. The protocol for high-throughput OCT imaging of tumor spheroids are described as followed [363]:

1) On the day of the OCT imaging of tumor spheroids, take the multi-well plate from the incubator. Transfer the multi-well plate under the OCT imaging system. Place it on top of the plate adapter (See **Figure 7.4**).

2) OCT imaging of tumor spheroids may be performed with the polystyrene plate lid on for longitudinal imaging or lid off for endpoint study or short term imaging. However, the water condensations on the lid due to evaporation of culture media may affect light transmission and distort the light path, yielding less optimal OCT images from the spheroids. To reduce the water condensation for longitudinal imaging, we can first remove part of the culture media, i.e. 50% of the culture media, from the well to reduce water evaporation.

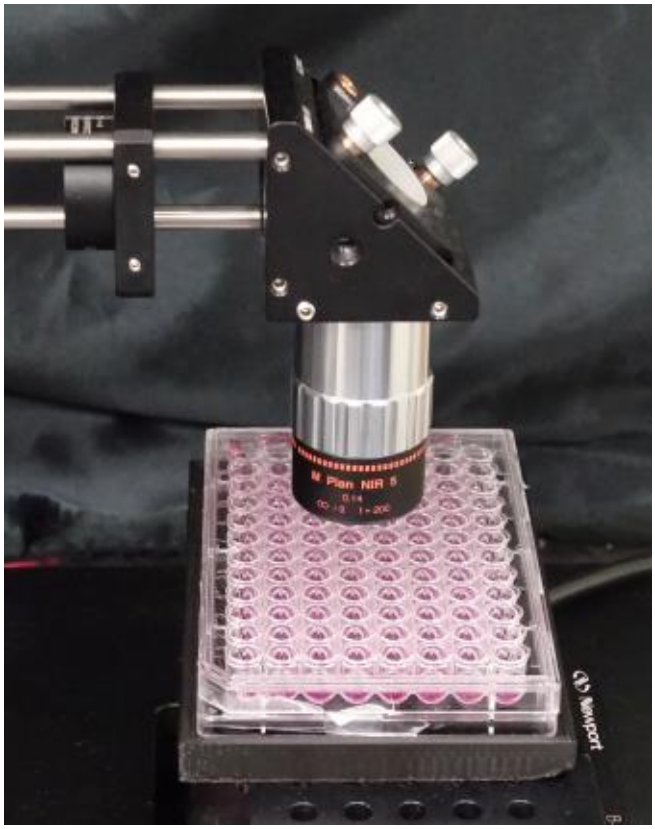

Figure 7. 4 96-well plate placed inder the OCT imaging system

Wipe the lid with tissue paper in the biosafety cabinet to avoid contamination, prior to OCT imaging. After OCT imaging, each well could be replenished with the culture media to original level.

3) Adjust the height of the plate by moving along the z-direction of the translation stage. Maintain the focal plane position at ~100–200 μm below the top surface of each spheroid, to minimize the effect of the non-uniform depth-wise focal profile.

4) Set a proper OCT scanning range (e.g., 1 mm x 1 mm) in the custom software to cover the whole tumor spheroid according to its development stages. Actual scanning range varied from 0.46×0.42 mm^2 to 2.0×1.7 mm^2.

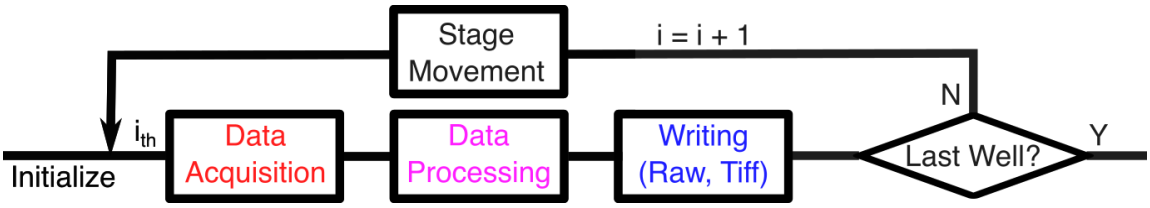

Figure 7. 5 Flow chart of the software implementation of the High-throughput OCT (HT-OCT) system

5) Use the custom software to acquire 3D OCT images of tumor spheroids one by one for all the wells of the plate containing spheroids. During the acquisition, ensure that the OCT spheroid data are collected without any motion. The spheroid is usually located at the center of the U-bottom well. However, the spheroid may be shifted in the culture media when the stage is accelerating or decelerating due to the inertia of the spheroid in the culture media.

A flow chart of software implementation of the high-throughput OCT (HT-OCT) system is shown in **Figure 7.5**, including the data acquisition, data processing, data writing and stage movement steps. After one spheroid data is collected, processed and written, the plate will automatically move to next well, wait for ~2 s to allow the spheroid to rest, and collect the next spheroid data.

7.5.5 Post-processing Procedure for OCT Images of Tumor Spheroids

Figure 7.6 shows a overall flow chart for the post-processing procedure for OCT images of tumor spheroids. The obtained 3D OCT dataset of tumor spheroids were processed with custom C++ processing code to generate OCT structural images, following the steps in **Figure 7.6A**. Details of these steps are described in Chapter 2, Chapter 5 of Drexler and Fujimoto [36] and Jian et al. [378]. Note that, we use n = 1.37 as the refractive index of the tumor spheroid to derive the axial pixel size [365].

Next, the collage of spheroid images can be generated using 2D OCT images in three cross-sectional XY, XZ, and YZ planes across the centroid of the spheroid. Image registration, using the MATLAB function dftregistration[190], is performed for all the spheroids during the collage generation step to ensure that the centroids of all the spheroid are located approximately at the same location.

Then, 3D rendering of the spheroid could be generated using the software Amira or Imaris. **Figure 7.7** showed the orthogonal views, 3D rendering and surface rendering of a tumor spheroid using Imaris software.

7.5.6 Morphological Quantification of 3D Tumor Spheroid

Figure 7.6 B showed the flow chart of the morphological quantification of 3D tumor spheroid. To calculate the tumor volume based on measured diameter of the tumor spheroid, three cross-sectional images in the XY, XZ, and YZ imaging planes across the centroid of the spheroid were selected. Diameter of the spheroid was

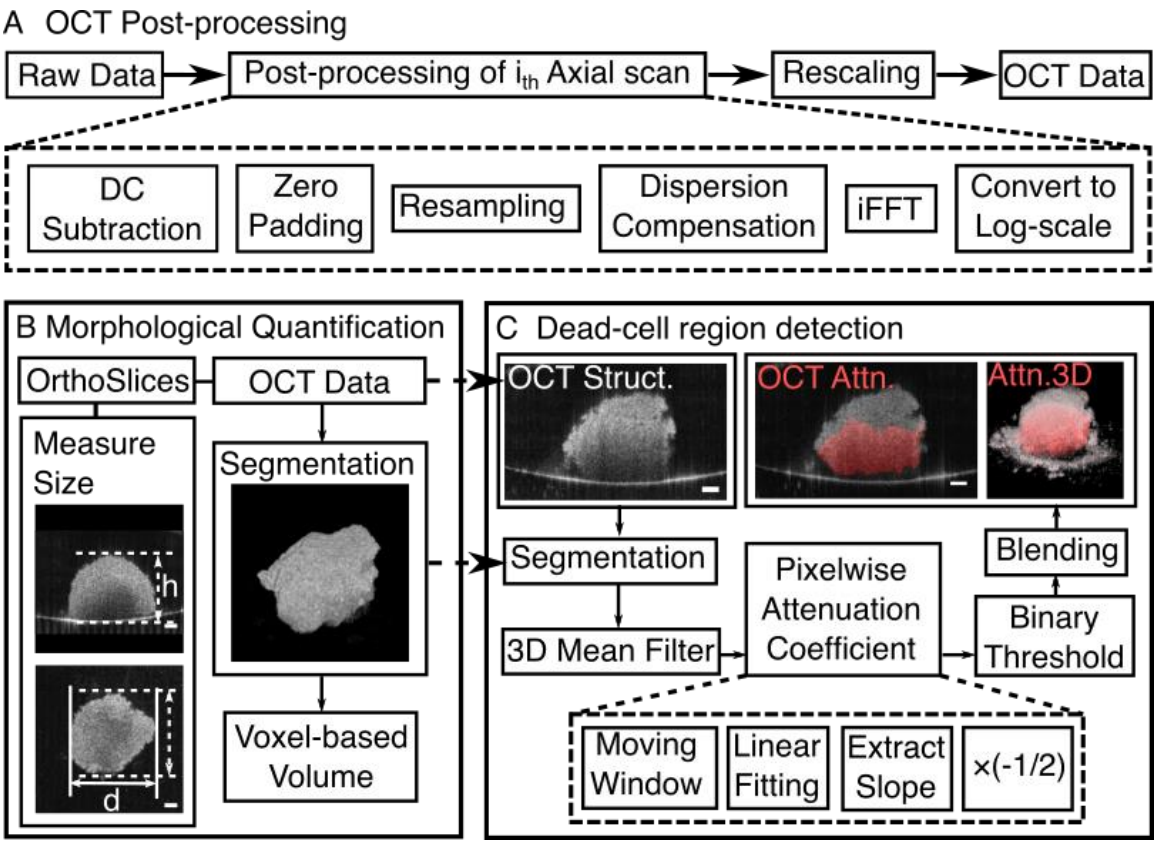

Figure 7. 6 Data Processing for OCT images of tumor spheroids. (A) Flowchart of general post-processing steps for OCT data. (B) Flowchart of morphological quantification of the tumor spheroid. (C) Flowchart of dead cell region detection of the tumor spheroid. Scale bar: 100 μm for all the subfigures.

measured in XY plane and its height was measured in XZ plane. Diameter-based tumor volume was calculated as:

$$V = \frac{1}{6}\pi d^3 \tag{7.1}$$

where d was the average diameter of the spheroid measured in the X and Y directions.

Next, we employed a voxel-based method to quantify the volume of each tumor spheroid, described as followed:

1) Apply a 3D averaging filter on the OCT structural data of spheroid to remove speckles.

2) Segment tumor spheroids using the Canny edge detection[379] filter, frame by frame, with a proper threshold separating the tumor spheroid region from the well bottom.

3) Group connective voxels for 3D data using built-in Matlab function: bwconncomp.

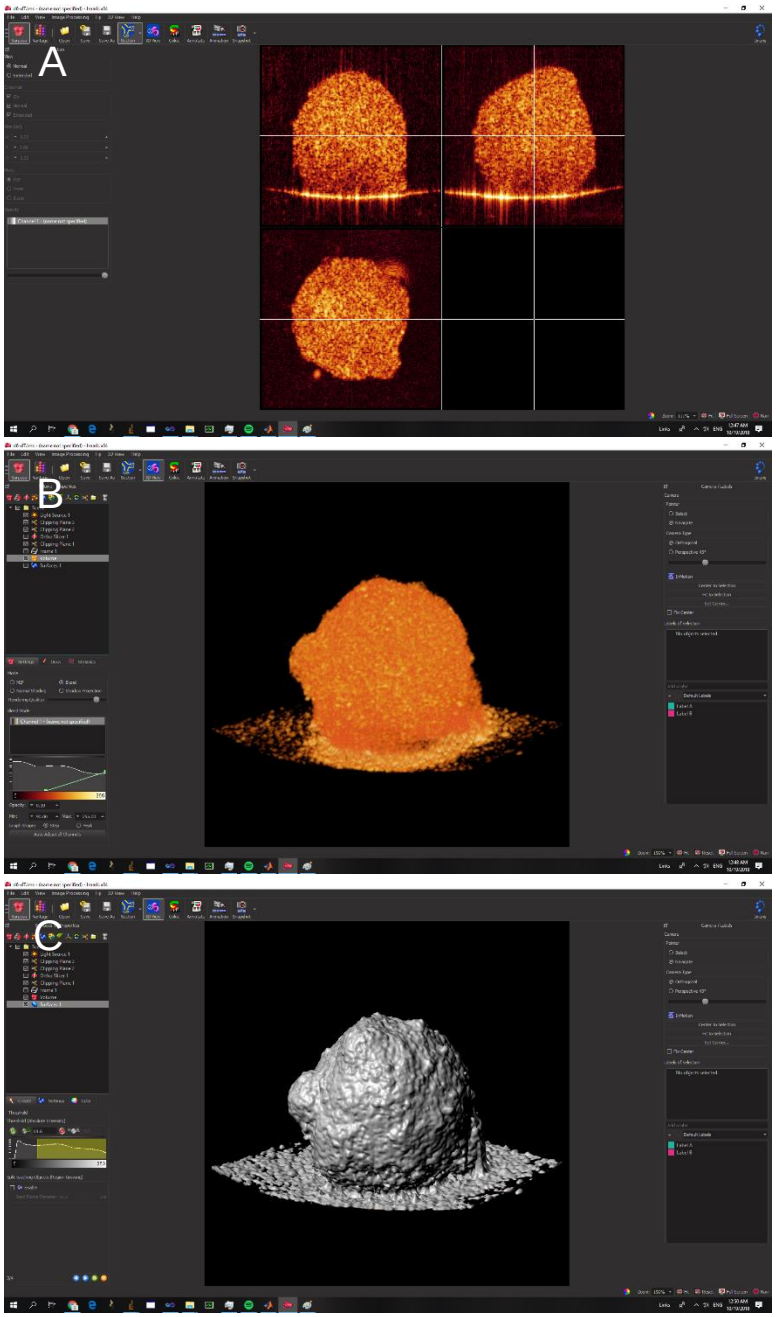

Figure 7. 7 (A) Orthogonal View (B) 3D rendering (C) 3D surface rendering of tumor spheroids generated by Imaris.

4) Calculate the mean distance between each connective voxel in the group and the manually chosen spheroid centroid for each group. Identify the spheroid region as the group with the minimum mean distance and label this group of voxels as true or 1. As a result, a volumetric mask of spheroid region is generated, which can be further used in dead-cell region detection.

5) Count the number of voxels within the spheroid region and then multiply by the actual volume of an individual voxel (volume/voxel), yielding the total volume of the spheroid. The counting step could be done by summing up all the labeled voxels in the volumetric mask.

7.5.7 Dead-cell Region Detection of 3D Tumor Spheroids

Dead cell region in 3D tumor spheroids can be identified with intrinsic optical attenuation measurement. Since OCT signals originate from back-scattering at different depths, OCT intensity detected as a function of depth in a homogeneous medium can be described by the Beer-Lambert Law [380]:

$$I(z) = I_0 e^{-2\mu z} \tag{7.2}$$

where z represents the depth and μ is optical attenuation coefficient, I_0 is a constant representing the source intensity.

As OCT structural images are usually normalized and converted to logarithmic scale to increase the image contrast, the (relative) optical attenuation coefficient can be obtained by finding the derivative of the logarithmic-scale OCT intensity:

$$\hat{\mu} = -\frac{1}{2}\frac{d \log I(z)}{dz} \tag{7.3}$$

where $\hat{\mu}$ represents the estimated value of optical attenuation.

Figure 7.6 C showed the flow chart of the post-process procedure of dead-cell region detection in tumor spheroids to generate the optical attenuation map. The detail steps are described as followed:

1) Perform segmentation to remove unwanted regions outside the spheroid, using the volumetric mask generated above.

2) Perform 3D average filter to suppress the speckle noise that is inherent in OCT images.

3) Obtain voxel-wise optical attenuation coefficients by linear fitting the logarithmic-scale OCT intensity profile over a certain depth range (moving window), extract its slope, and multiply the slope by -1/2. In our

study, we use a 10-voxel moving window, which corresponds to ~40 μm in depth, with the voxel located in the middle of the window, to derive the attenuation coefficient for each voxel.

4) Apply step 3 to each axial scan in a frame and each frame in a 3D dataset containing the segmented spheroid region until optical attenuation coefficients for all voxels of the segmented spheroid region are calculated.

5) Perform the binary thresholding to highlight the high-attenuation region as the final optical attenuation map.

6) Highlight the binarized optical attenuation map on the original image to label the dead-cell region using a blending mode.

7) Generate the 3D-rendering image of the blended attenuation map to visualize the 3D distribution of the dead-cell region.

7.5.8 Histology and Immunohistochemistry Examinations

Histology and immunohistochemistry (IHC) stained images of tumor spheroids are obtained to correlate with the corresponding OCT results. The detail steps are described as followed:

1) At each time points (See **Figure 7.3** for the timeline), select 1–2 tumor spheroids from the multi-well plate for histology and IHC staining. Use a pipette with the 1 mL pipette tips to transfer the spheroid from the well to a 1.5 mL centrifuge tube. Prior to the transfer of spheroids, cut the 1 mL pipette tip to ensure that the opening of the tip is large enough to avoid damaging the spheroid.

2) Fill the centrifuge tube with 10% formaldehyde or 4% paraformaldehyde (PFA) for sample fixation, following the standard procedure.

3) Perform the histology and IHC processes for each spheroid, using standard paraffin embedding techniques.

4) Stain 5 μm thick sections of tumor spheroids for hematoxylin and eosin (H&E) and terminal deoxynucleotidyl transferase dUTP nick end labeling (TUNEL) apoptosis detection. A counterstaining of hematoxylin is applied to TUNEL.

5) A digital slide scanner was used to scan the stained sample and obtain high-resolution histological and IHC images.

7.5.9 Statistical Analysis

Student's paired t-tests are performed to evaluate the significance of differences between diameter and height measurements, and between diameter-based and voxel-based volumes at each time point. A p value of <0.05 indicates statistically significant differences between the paired measurements.

7.6 High-throughput OCT Imaging of Tumor Spheroids

7.6.1 Collages of OCT Spheroid Images

In this section, we showed the demonstration of using high-throughput OCT (HT-OCT) to perform sequential scans of the multi-well plate containing tumor spheroids. HCT 116 tumor spheroids in 96-well plate were scanned by the HT-OCT system at Day 7. Each OCT data consisted of 400 × 400 × 1024 voxels, which corresponded to an actual volume of 1.67 × 1.40 × 2.3 mm^3. These HT-OCT data were processed following the procedure. **Figure 7.8 – 7.11** showed the collages of HT-OCT images of HCT 116 spheroids generated from the processed OCT structural images. **Figure 7.8** showed the collage of en face OCT images of tumor spheroids, which was comparable with images obtained from other 2D high-throughput imaging

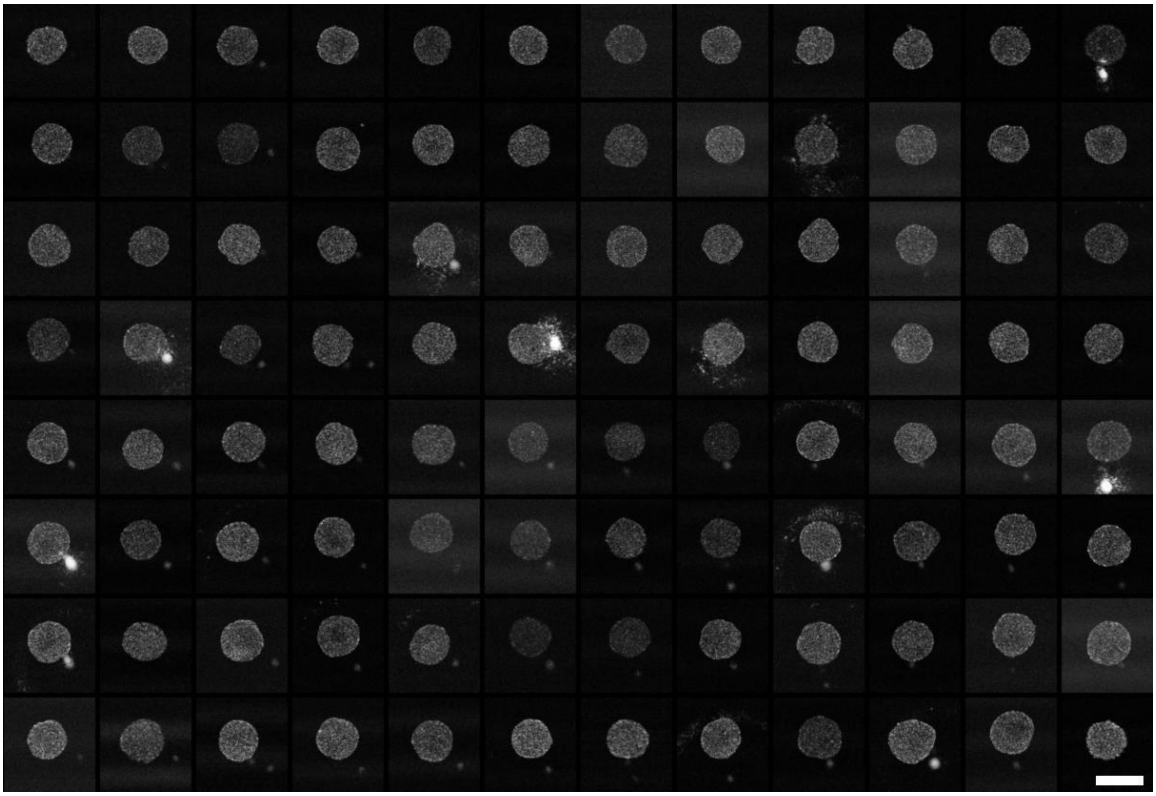

Figure 7. 8 Collage of en-face (XY) OCT images of HCT 116 spheroids. Scale bar: 500μm

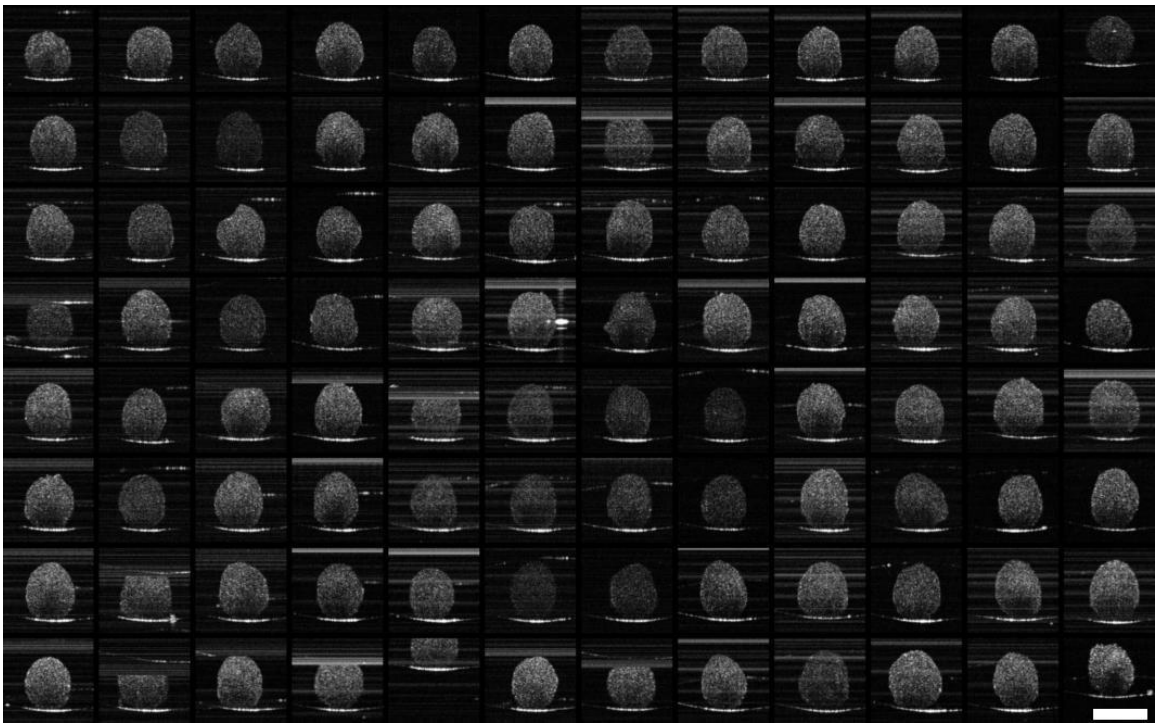

Figure 7. 9 Collage of cross-sectional (XZ) OCT images of HCT 116 spheroids. Scale bar: 500µm

system[381]. From the image, we could estimate that these tumor spheroids had a size of ~400 - 500 µm, close to the size of the scale bar. Given 3D imaging capability of the OCT, we could also generate the collage of 2D cross-sectional spheroid images from 96 wells from the XZ (**Figure 7.9**) and YZ (**Figure 7.10**) orthogonal planes to monitor spheroid heights and visualize spheroid inhomogeneity in the vertical direction. A collage of 3D-rendered spheroid images (**Figure 7.11**) was also feasible from any predefined angle to visualize the overall 3D shape and evaluate the sphericity of the spheroid.

We should note that, various factors might affect the final image quality of tumor spheroids from different wells. First, the fluctuation of OCT intensity among tumor spheroids may be attributed to either water condensation on the lid that absorbing incident light, or fluctuation of polarization states between the reference and sample arm. Second, the direct reflection from the well bottom may lead to saturated signals detected by the camera, yield a vertical saturated line from top to bottom in the cross-sectional images and a bright dot in the *en face* OCT images. Third, since the well bottom had a thickness of a few hundread micrometers, the top of the well bottom would be attached to the spheroid while the bottom of the well bottom might be folded back and overlapped with the tumor spheroid image, due to the complex conjugate ambiguity. Employing full-range technique (See Chapter 4) could alleviate the situation. Fourth, since the

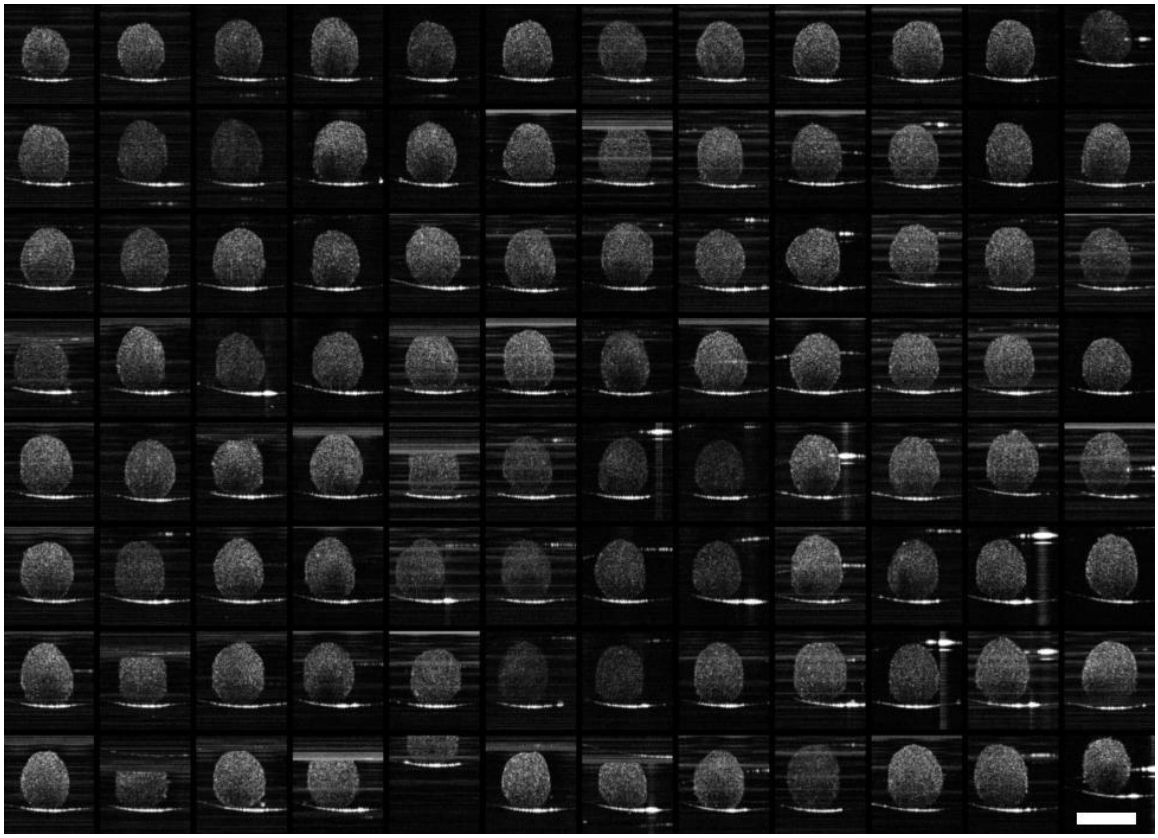

Figure 7. 10 Collage of cross-sectional (YZ) OCT images of HCT 116 spheroids. Scale bar: 500μm

tumor spheroid image was registered based on the spheroid location, the horizontal line artifacts in the image might be the residue DC term if the tumor spheroid was located too close to zero delay in the image. Fifth, the strong reflection from the media surface may contribute to the other horizontal line artifacts, either in a form of self-interference or aliasing effect in the cross-sectional OCT images.

7.6.2 Time Characterization for HT-OCT Screening of a Plate of Tumor Spheroids

In order to characterize the total time for HT-OCT to screen a plate, we performed multiple OCT screening on the same 96-well plate, with different camera line rate. For 2D scan mode, each OCT data consisted of 400 pixels ×1024 pixels × 2 frames. For 3D scan mode, each 3D data consisted of 400×400×1024 voxels. Four different camera line rates, including 10.8 kHz (Sensor Unlimited, SU1024LDH2, OPR20), 20.6 kHz (OPR18), 45.6 kHz (OPR 16) and 88.8 kHz (OPR 12), were tested. **Table 7.3** showed the results of time characterization of HT-OCT screening time in different camera operation modes. The time duration for each step of OCT screening was listed in details. In 2D scan mode, the total screening time for a 96-well plate was

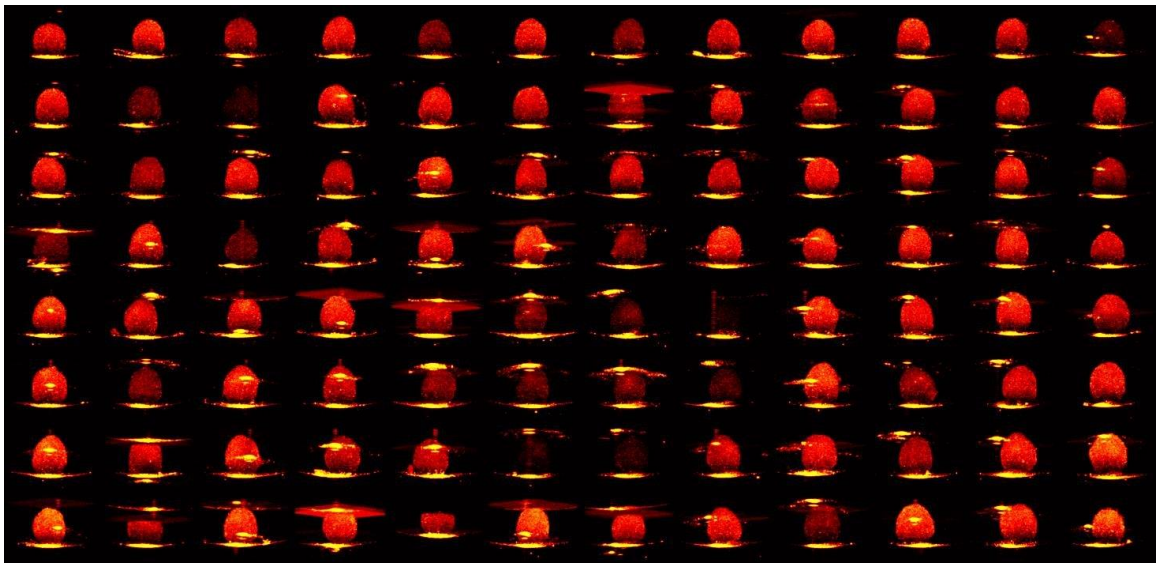

Figure 7. 11 Collage of 3D rendered OCT images of HCT 116 spheroids. Scale bar: 500µm

~6 min, which was comparable with commercial bright field high-throughput imaging system (Celigo, Nexcelom; < 5 min for a 96-well plate). For 3D scan mode, the pure OCT acquisition time for a 96-well plate could be as low as ~3.2 min, with the line-scan camera running at 92 kHz mode (actual line rate 88.8kHz). In this mode, the total screening time for a 96-well plate, including all steps, would be ~23 min. The additional ~20 min was utilized to the process, save the OCT data from all the wells and control the stage movements, which was ~12 s for each data. Within the ~12 s, it took ~4 s to process the data with abovementioned size and took another ~4s to write the data to the solid state drive in raw data mode (320 MB) and TIFF data mode (75MB). For the rest, ~2 s was allocated to the stage movement and the last ~2 s was the gap time to allow spheroid to stop the movement due to inertia and fall to the well bottom.

Table 7. 3 Time Characterization for HT-OCT system

Scan Mode	Camera Line Rate	Acquisition Time	Processing Time	Writing Time	Stage Movement[4]	Average time/well	Total Acquisition Time (96-well)	Total time (96-well)
2D[1]	20.6 kHz	~0.05 s	~0.02 s	~0.02 s	~4 s	~4 s	-	~6 min
3D[2]	88.8 kHz	~2 s	~4 s	~4 s[3]	~4 s	~14 s	**~3.2 min**	~23 min
	45.6 kHz	~4 s				~16 s	**~6.4 min**	~26 min
	20.6 kHz	~9 s				~22 s	**~14.4 min**	~35 min
	10.8 kHz	~18 s				~31 s	**~28.8 min**	~50 min

[1]2 frames with a size of 400×1024 pixels; [2]3D data with a size of 400 × 400 × 1024 pixels; [3]Both raw data and process Tiff data are saved. Average writing time of the 3D raw data is 3.2 s (320 MB). Average writing time of the Tiff data is 0.8 s (75 MB); [4]Including ~2 s of stage movement and 2 s gap time to allow spheroids to stop movement.

Sometimes, we would like to slow down the camera line rate to improve the image quality, since the sensitivity would increase by ~3 dB if the camera line rate slowed down by half. As the camera line rate was reduced, the OCT acquisition time for individual tumor spheroid (the 3rd column of Table 7.2) or the whole plate (the 8th column of Table 7.2) would be increased, yielding a longer total OCT screening time, shown in the last column of **Table 7.2**. For the future practice of OCT screening, we can find a balance between the desired image quality and the imaging time depending on the purpose.

7.7 Longitudinal OCT Imaging of Tumor Spheroids

Given the non-destructiveness of OCT imaging, we could utilize OCT to monitor tumor spheroids over time. **Figure 7.12** showed the development of a U-87 MG tumor spheroid over 21 days. *En face* (first row of Figure 7.10), cross-sectional (second row of Figure 7.19), and 3D rendered images (third row of Figure 7.10) were presented to show the growth of tumor spheroid. In the OCT images, U-87 MG cells were observed to gather and form a spheroid by Day 4. The diameter of the spheroid was estimated to be ~250 μm. Then, the spheroid continued to grow and reached ~550 μm in diameter on Day 14. The spheroid growth slowed down

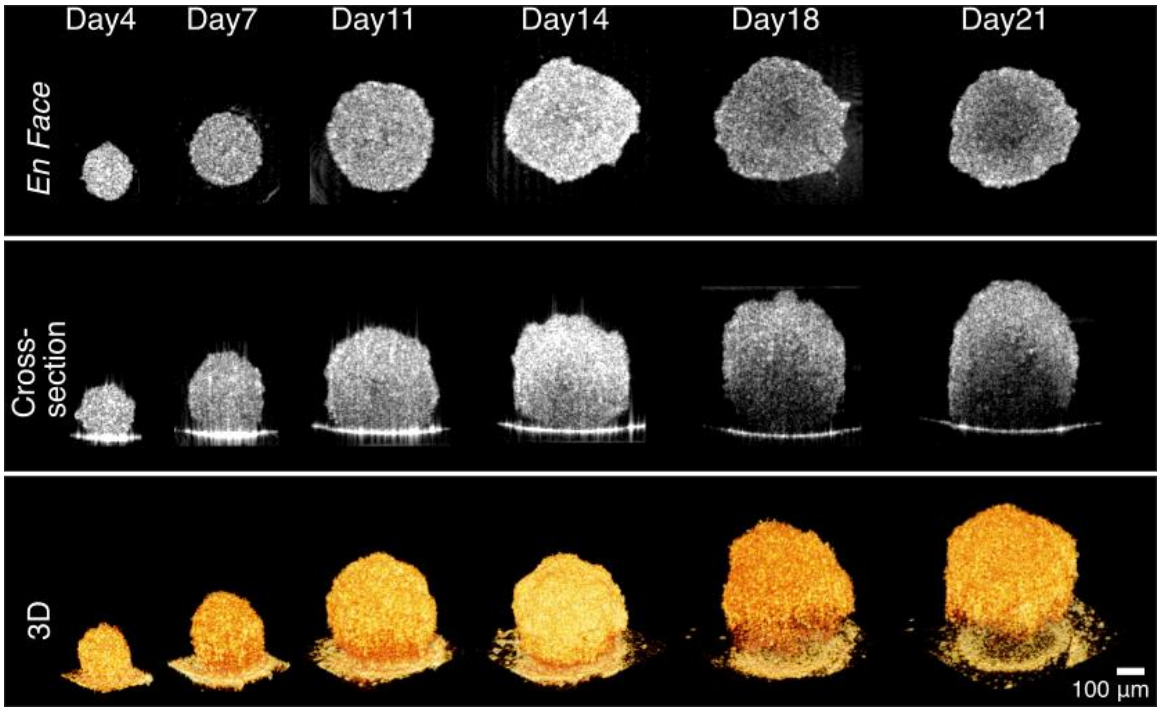

Figure 7. 12 Sequential en face, cross-section and 3D rendered OCT images of a U-87 MG tumor spheroid. Scale bar: 100 μm

afterwards. Throughout the 21-day development, the U-87 MG spheroid maintained a tightly-packed and spherical shape.

Figure 7.13 showed the development of the HCT 116 tumor spheroid over the same duration. Similarly, the spheroid in *en face*, cross-section and 3D rendered OCT views were displayed in different rows. For HCT116 cells, the spheroid grew faster, with a size of ~350 μm on Day 4, and reached ~500 μm on Day 7. After day 7, a heterogeneous growth pattern was observed for the HCT 116 tumor spheroid, In *en face* images, the cell cluster maintained a smooth and near-spherical shape by Day 18. However, an irregular "two-peak" shape of the HCT 116 cluster was seen from the cross-sectional view on Day 11. In addition, tumor height was observed to reach its maximum on day 11 and reduced afterward. 3D rendered images of the HCT 116 spheroid further confirmed that its shape became disrupted and flattened after Day 11. Thus, HCT 116 spheroid may undergo distinctive evolution of the geometric shape at late growth stage, as compared with U-87 MG tumor spheroids.

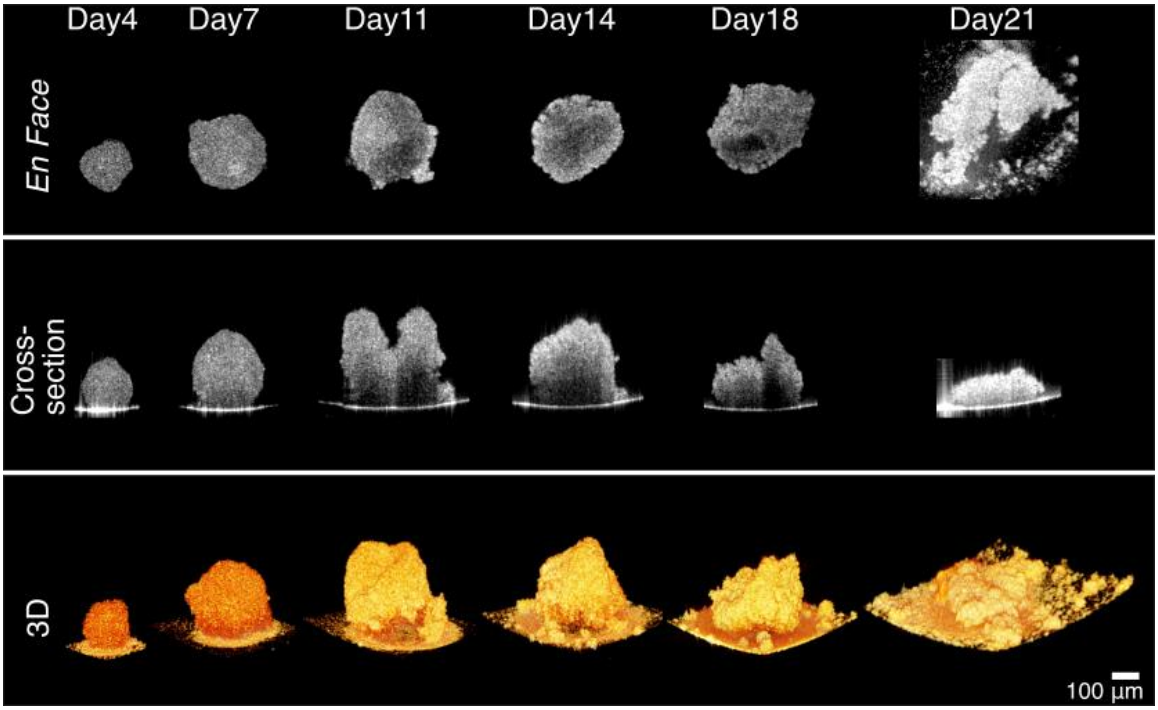

Figure 7. 13 Sequential en face, cross-section and 3D rendered OCT images of a HCT116 tumor spheroid. Scale bar: 100 μm

7.8 Morphological Quantification of Tumor Spheroids

Based on the 3D OCT data, we can further quantify diameter, height and volume of U-87 MG and HCT 116 tumor spheroids to chacterize their grow kinetics. **Figure 7.14** showed the results of quantitative analyses of the growth dynamics of 3D tumor spheroids in terms of its size and volume, based on the longitudinal OCT measurements. **Table 7.4** showed the number of tumor spheroids for each cell line that were quantitatively analyzed at each time point. Two tumor spheroids of U87MG (**Figure 7.14 A-C**) and HCT 116 **(Figure 7.14 D-F**) at Day 18 were shown as examples to illustrate how average diameter and height were measured from *en face* and cross-sectional OCT images The growth kinetics of U-87MG tumor spheroid was shown in **Figure 7.14G**, where U-87 MG tumor spheroids exhibited a linearly increasing trend for both the average diameter from Day 4 (Dia. 220 ± 20 μm) to Day 14 (Dia. 530 ± 30 μm) and the height from Day 4 (Ht. 230 ± 10 μm) to Day 14 (Ht. 550 ± 40 μm). This growth trend for spheroid diameter was consistent with previous studies [360, 382]. No statistically significant difference ($p>0.05$) between growth kinetics of diameter and height of U87-MG was observed before Day 14. Also, we compared the spheroid volume derived from both voxel-based and diameter-based measurements. The U-87 MG volumes derived from the diameter-based measurements were similar but slightly smaller than the voxel-based volume (**Figure 7.14 H**).

Table 7. 4 Numbers of U-87 MG and HCT 116 Tumor Spheroids for Morpholoigcal Quantification

Day	**4**	**7**	**11**	**14**	**18**	**21**
U-87 MG	12	11	9	6	5	4
HCT 116	24	21	18	15	6	3

For HCT 116 spheroids, the average diameter exhibited a fast increase from Day 4 (Dia. 350 ± 30 μm) to Day 11 (Dia. 670 ± 90 μm), but then only increased slowly from Day 11 to Day 21 (**Figure 7.14 I**). However, the spheroid height reached the maximum value on Day 11 (Ht. 560 ± 70 μm) and then rapidly dropped until Day 21 (Ht. 270 ± 100 μm). A large discrepancy between height and diameter were observed at all other measured time points ($p<0.001$ on Days 11, 14; $p<0.01$ on Day 18, and $p<0.05$ on Day 21; **Figure 7.14 I**). For the volume measurement, the average voxel-based volume of HCT 116 tumor spheroids increased from Day 4 to Day 11, but gradually decreased at later time points. In contrast, the growth kinetics for diameter-based volumes of HCT 116 tumor spheroids displayed a steadily increasing trend throughout the entire period. As a result, the diameter-based volumes of HCT 116 tumor spheroids were significantly over-estimated compared to the voxel-based volume after Day 11 (**Figure 7.14 J**). This discrepancy could reach

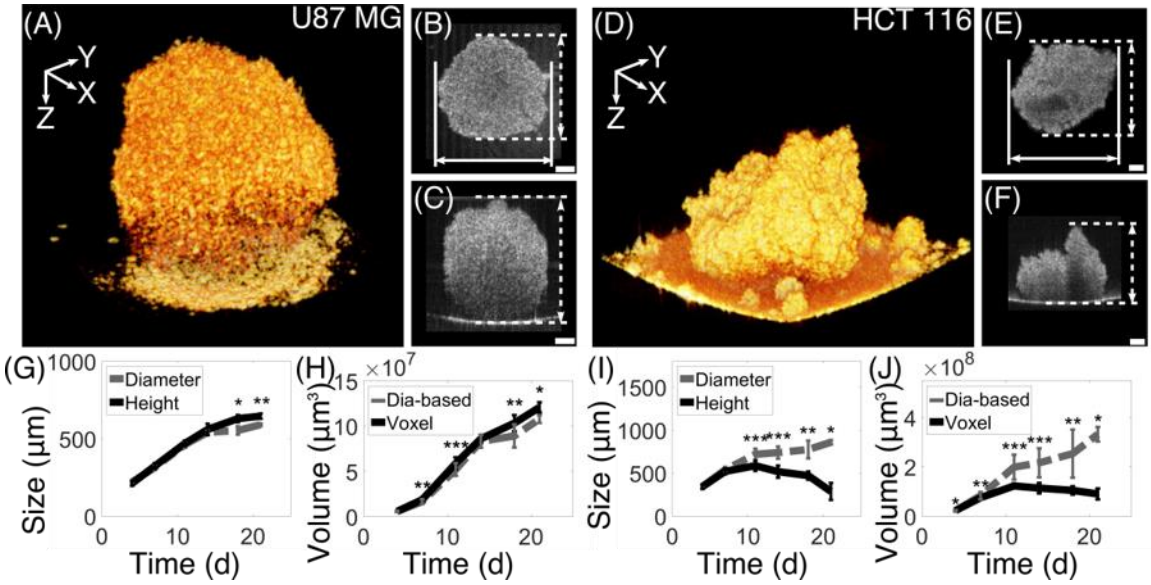

Figure 7. 14 Quantitative analyses of the growth kinetics of 3D tumor spheroids in terms of size (diameter and height) and volume. Two tumor spheroids from U87MG (A-C) and HCT 116 (D-F) cell lines at day 18 were shown as examples to illustrate how average diameter and height were measured from *en face* and cross-sectional OCT images. Quantification of diameter and height, diameter-based and voxel-based volumes for these two cell lines were shown in (G-J) Scale bar: 100 μm.

as high as ~276% on Day 21. The discrepancy of the size and volume measurements could be attributed to the heterogeneous shapes of the HCT 116 spheroid at late stages.

The morphological quantification results of tumor spheroids strongly suggested that, complimentary depth information provided by the OCT could lead to a more robust and accurate characterization of growth kinetics of the 3D tumor spheroids, especially for the volume measurement.

7.9 Identification of Dead Cell Regions Based on Optical Intrinsic Attenuation Contrast

7.9.1 Generation of Optical Attenuation Map

Besides monitoring the growth kinetics of the tumor spheroids, we also demonstrated label-free necrotic region detections of tumor spheroids based on intrinsic optical attenuation contrast. **Figure 7.15** showed an example of dead-cell region detection for Day 4, 14 and 18 HCT 116 tumor spheroids based on the optical attenuation. First, we extracted intensity profiles along each axial scan line based on OCT structural images (**Figure 7.15A, E, I**), which were shown in **Figure 7.15B, F, J**. Two distinct slopes were observed in the intensity profile on day 14 and day 18, fitted in gray and red dashed lines, while no significant intensity drop was observed in Day 4 spheroid. The gray dashed line marked the slow decay region at the top portion of the

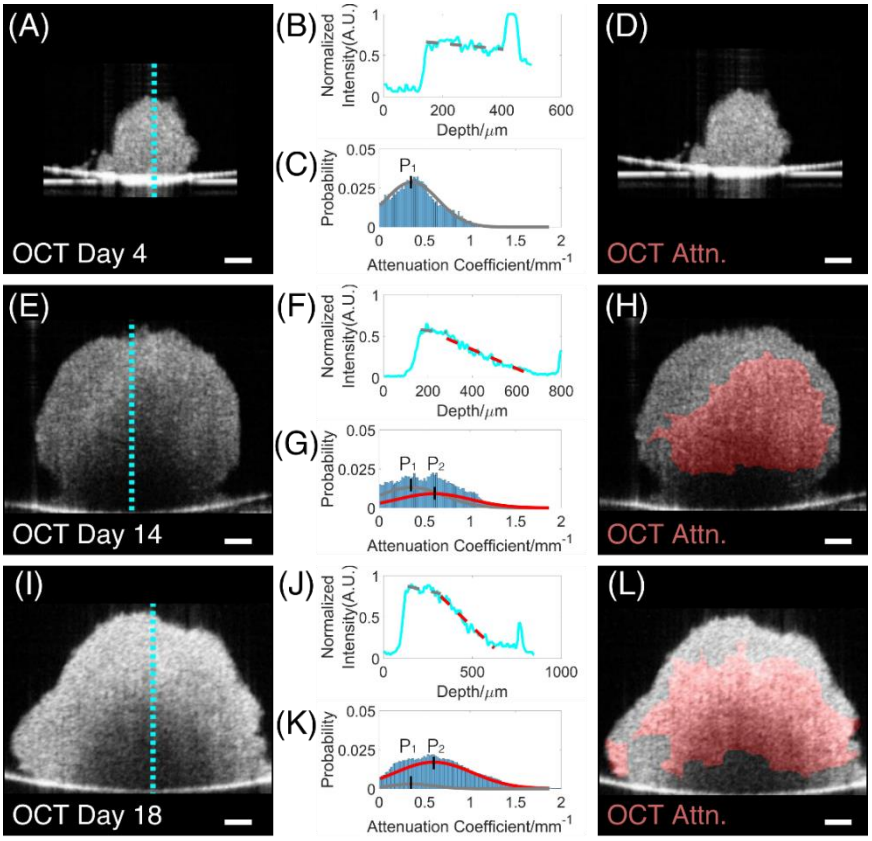

Figure 7. 15. Determination of dead-cell regions of HCT 116 tumor spheroids on Days 4, 14, and 18 based on optical attenuation contrast. The backscattered signals in cross-sectional OCT images (A, E, I) were used to derive intensity profiles along each axial scan line (B, F, J). High attenuation regions (indicated in red lines in F, J) could be clearly observed in the intensity profiles of the tumor spheroids on Days 14 and 18 (F, J), but not on the tumor spheroid on Day 4 (B). Further analyses of optical attenuation coefficient histograms (C, G, K) were performed to determine the threshold to separate low and high attenuation regions (i.e. 0.48 mm^{-1}), which is calculated as the median of the two peak values (P1=0.36 mm^{-1}, P2=0.60 mm^{-1}). High-attenuation regions above the threshold highlighted in red (H, L) were detected as the necrotic cores in the tumor spheroids. The region of necrotic tissue clearly increased as the spheroid developed. Scale bars: 100μm.

spheroid and the red line marked the fast decay region. Based on our observation, we analyzed the optical attenuation coefficients for each voxel within the tumor spheroid. Histograms of optical attenuation coefficients from spheroids of different time points were shown in **Figure 7.15C, G, K**. We observed two distinct peak locations for live and dead-cell tissue on day 14, as indicated by P_1 (P_1 = 0.36 mm^{-1}) and P_2 (P_2 = 0.60 mm^{-1}) in **Figure 7.15 G**. After fitting with two Gaussian curves, we found out the peak locations and set the threshold of high attenuation region as the mean of the two peak values (i.e. 0.48 mm^{-1}). We should note that, the threshold value was an empirical value, which might vary depending on the imaging condition and tumor spheroid conditions. In this way, 3D binary maps highlighting high attenuation regions above the

threshold in red was generated. The blended optical attenuation maps for Day 14 and 18 tumor spheroids were presented in **Figure 7.15 H and L**.

7.9.2 Progression of Dead-cell Regions in Tumor Spheroid

Since the attenuation detection approach was completely non-destructive, we further monitored the progression of dead-cell regions from the same tumor spheroid throughout the growing period. **Figure 7.16** showed a representative result of longitudinal tracking of 3D distribution of the dead-cell regions in the HCT116 tumor spheroid during14-day development, shown in 3D rendered optical attenuation maps. The dead-cell regions were highlighted in red with high optical attenuation coefficients. In the 3D rendered optical attenuation maps, the red regions were expanding, indicating the longitudinal growth of the dead cell regionse as the spheroid developed.

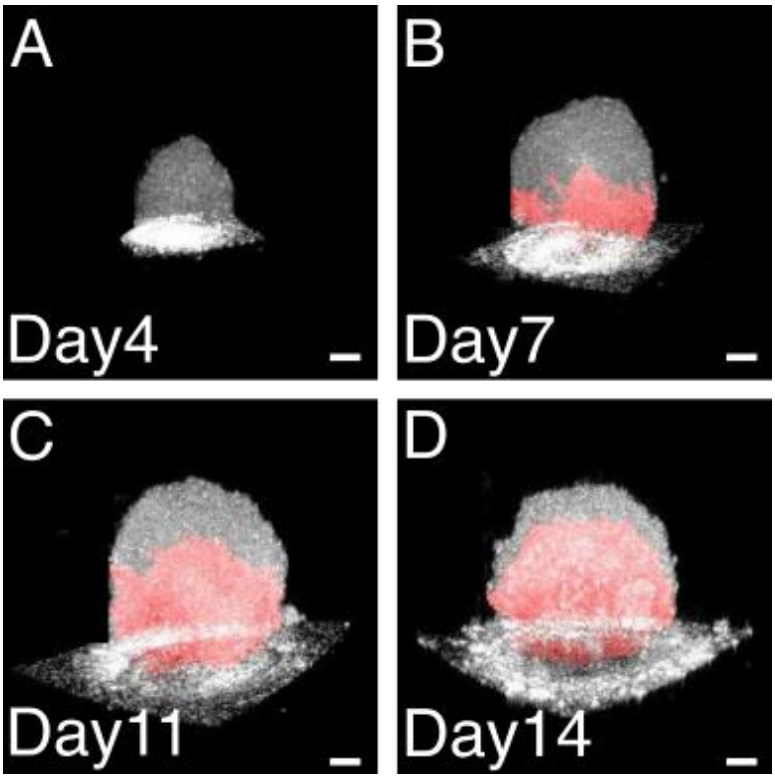

Figure 7. 16 Progression of dead-cell regions in the tumor spheroid over 14 days, shown in 3D rendered optical attenuation maps. Dead-cell regions were highlighted in red.

7.9.3 Correlation of Optical Attenuation Map with Histological and IHC results

The proposed non-destructive dead-cell region detection technique was verified by comparing by comparing OCT optical attenuation map of HCT 116 tumor spheroid with corresponding spheroid images obtained by histology and IHC. **Figure 7.17** showed the correlation between optical attenuation maps of two HCT 116 tumor spheroids at Days 4 and 14 and the corresponding histology and IHC spheroid slices, which were stained with H&E and TUNEL, respectively. On Day 4, no necrotic region was observed in optical attenuation map, H&E and TUNEL stained slices (**Figure 7.17 A-C**). On Day 14, optical attenuation map (**Figure 7.17D**) showed a good correlation with H&E and TUNEL slices (**Figure 7.17 E, F**), as indicated by analyzing the features within the dashed-line surrounded regions in H&E and TUNEL slices. The dashed lines were derived from the contour of highlighted dead-cell regions in optical attenuation map. In H&E slices, the necrotic regions as indicated by less dense and aggregated structure located within the dashed line region (**Figure 7.17E**). In TUNEL slices, a good match was observed between high-attenuation region and TUNEL labeled apoptotic cellular region (**Figure 7.17 F**). Especially, in the region near the dashed lines (zoomed image in **Figure 7.17 F**), high density of apoptotic cells were found, while this region were accurately labeled as dead-cell region in the optical attenuation map. In this way, we demonstrated the feasibility of OCT to detect the dead-cell distributions and monitor their progression, which potentially provide more valuable information of spheroids' growth pattern.

7.10 HT-OCT imaging on Tumor Spheroid Invasion Assay

7.10.1 Introduction of Tumor Spheroid Invasion Assay

Cancer metastasis accounts for ~90% of the death among all the cancer patients, rather than primary tumors [383-388]. In cancer metastasis, cancer cells will undergo a multi-step process, known as the invasion-metastasis cascade [387, 389, 390], to reach distant tissues and form new tumor colonies. During invasion-metastasis cascade, one early critical step to enable cancer cell dissemination is cell invasion, in which cancer cells invade through extracellular matrices (ECMs), the barriers, and intravasate into the vasculature network so that they can travel a long distance to other parts of the body. Therefore, it remains a key topic in cancer research to understand the principles and mechanism of cell behaviors during invasion.

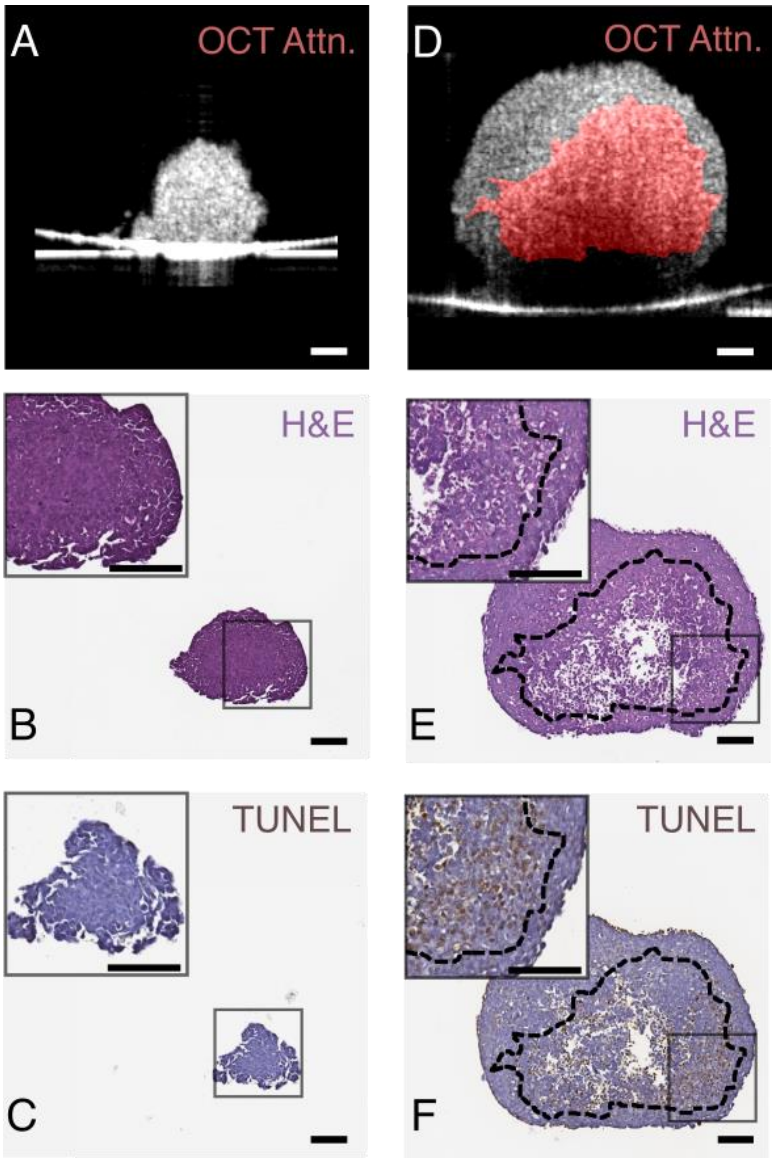

Figure 7. 17 Comparison of necrotic regions identified based on optical attenuation contrast with histology and immunohistochemistry (IHC) results. High attenuation region-labeled OCT images of two HCT 116 tumor spheroids on Day 4 (A) and Day 14 (D) were compared with corresponding H&E (B, E) and TUNEL stained (C, F) slices, respectively. The highlighted region in blended optical attenuation map (D) matched well with the combination of the necrotic (E) and apoptotic regions (F) identified by H&E and TUNEL stainings, respectively. Zoom-in views of gray square-highlighted areas were shown at the left-top panel of H&E and TUNEL images. The contour of high attenuation region in OCT image was indicated in black dash lines in H&E and TUNEL images. Scale bar: 100 μm.

In another aspect, scientists are striving to develop drugs targeting on a single molecule to inhibit growth and proliferation of primary tumors. However, it remains a rare success in finding the effective anti-tumor candidate during drug discovery, which is less than 10% [356]. One key reason is that cancer cells undergo multiple rounds of mutations during tumor progression. Some of the cancer cells will circumvent these

inhibitory compounds, yielding these single-targeted compounds ineffective [391]. Thus, there is a paradigm shift in drug discovery to find potential leads that inhibiting tumor cell migration and invasion rather than killing the cancer cells [391, 392].

During the initial compound finding process, two-dimensional (2D) tumor cell culture models are routinely used to simulate cell migrations and invasions and served as the drug test targets, given their low cost and fast readout. The standard 2D culture model is the Boyden chamber assay [393-395]. First introduced in 1961, the Boyden chamber assay utilized a Transwell with a cell permeable membrane to test whether individual cells can migrate through the membrane. Coating with a layer of extracellular matrix (ECM) on top of the membrane in Transwell, this model can be used to study the invasion of individual cells. However, this model does not truly mimic the cell invasion process in a three-dimensional ECM [396], in which the tumor cells will invade in all directions from the bulk [397]. Also, relevant cell-cell and cell-ECM interactions are lacking in 2D Transwell models [397, 398], in which the ECM actually regulate several cellular activities, i.e. cell differentiation, proliferation, adhesion and migration [398, 399]. Therefore, this model is not suitable to analyze the group activity of cell clusters during invasion process.

Given this, 3D spheroid invasion model have been established, by embedding tumor spheroids in the ECM [392, 400]. In spheroid invasion model, individual or clustered cells can invade out of the spheroid in all directions into the surrounding matrix. This spheroid invasion model been used to test the invasiveness and invasive pattern of different tumor cell lines [392, 396, 397]. Important cell line specific features such as individual vs collective cell movements can be visualized [396, 401]. A previous study is reported to utilize the 3D invasion assay to test the effects of additives, e.g. EGF, to induce cell invasion of tumor spheroids for CALs and CALr cell lines, a human squamous head and neck cancer [392]. A recent study utilized the 3D invasion assay as a test model to facilitate the study of the subclonal diversity and interactions between distinct tumor subpopulations [402]. Drug effect on the cell invasion model is also tested [403, 404].

7.10.2 Current Quantitative Analyses of Tumor Spheroid Invasion Assay

Current quantitative analyses of 3D invasion assay rely on the images taken with 2D imaging modalities, i.e. bright field or fluorescent microscopes. Invasion process would be monitored at sequential time points, i.e. every 24 hours. To quantify invasiveness, invasion fronts and core regions would be segmented separately

[392, 397]. Then, invasion areas could be counted at different time points. Also, individual cells could be tracked at different time point to monitor their movements to evaluate whether they are moving individually or collectively [401]. However, all these analyses and results rely on the assumption that the tumor spheroid and the surrounding tumor microenvironments are homogeneous, i.e. the tumor spheroid is close to a perfect sphere and tumor microenvironments (TMEs) are identical in all directions. However, if the shape of the tumor spheroid is heterogeneous, the invasion distance and density from the core might be different in different directions. If the spheroid is embedded in a complex ECM scaffold [405] or if the ECM is not homogeneous in all directions, tumor cells might interact with TME differently at different sites. Solely taking 2D images may introduce bias on the analysis results. Thus, 3D imaging modalities with the ability to capture the whole tumor spheroids with invadopodia in the 3D ECM are imperative.

7.10.3 HT-OCT Imaging on Tumor Spheroid Invasion Assay

In the following section, I would show the demonstration of using HT-OCT system to characterize tumor spheroid invasion assays. Morphological informations of selected tumor spheroids, including total area and volume, invasion area and volume, have been quantified. Based on 3D morphological characterization provided by OCT, we can evaluate the compound effects on inhibition of cell invasion on these spheroid invasion assays.

7.10.4 Preparation of In vitro tumor spheroid invasion assay for drug screening

The protocol to prepare tumor spheroid invasion assay for drug screening is adapted from the standard liquid overlay method[392]. U87-MG cells are used to form the spheroids in our study. Tumor spheroids are formed following the protocol described in Chapter 7.5.2. The only difference is that, volume of cell-containing culture media added to each well was 140 µL, instead of 200 µL. After 3 days of growth, 10 µL of 1:10 dilution of compounds in media is added to each well. After that, the 96-well plate is placed on top of ice and 150 µL of 50% Matrigel were added to each well. The whole plate is incubated for 24hr to allow cell invasion to proceed and compounds to take effect. After that, the whole plate is first imaged with a high-throughput imaging system (GE, Perkin Elmer or Celigo). Then the plate is transferred to our lab for OCT imaging, which would be 1-2 days after bright field imaging.

Figure 7.18 shows the protocol of compound treatments on each tumor spheroid invasion assay. A total number of five plates of spheroid invasion assays are tested. The first invasion assay #1 is fixed and optical-cleared at Day 4, following the protocol described in Boutin et al. [406]. For the invasion assay #2 and #2, two duplicate plates are prepared and screened. Thus, for each compound and each concentration, a total of six tumor spheroids is screened.

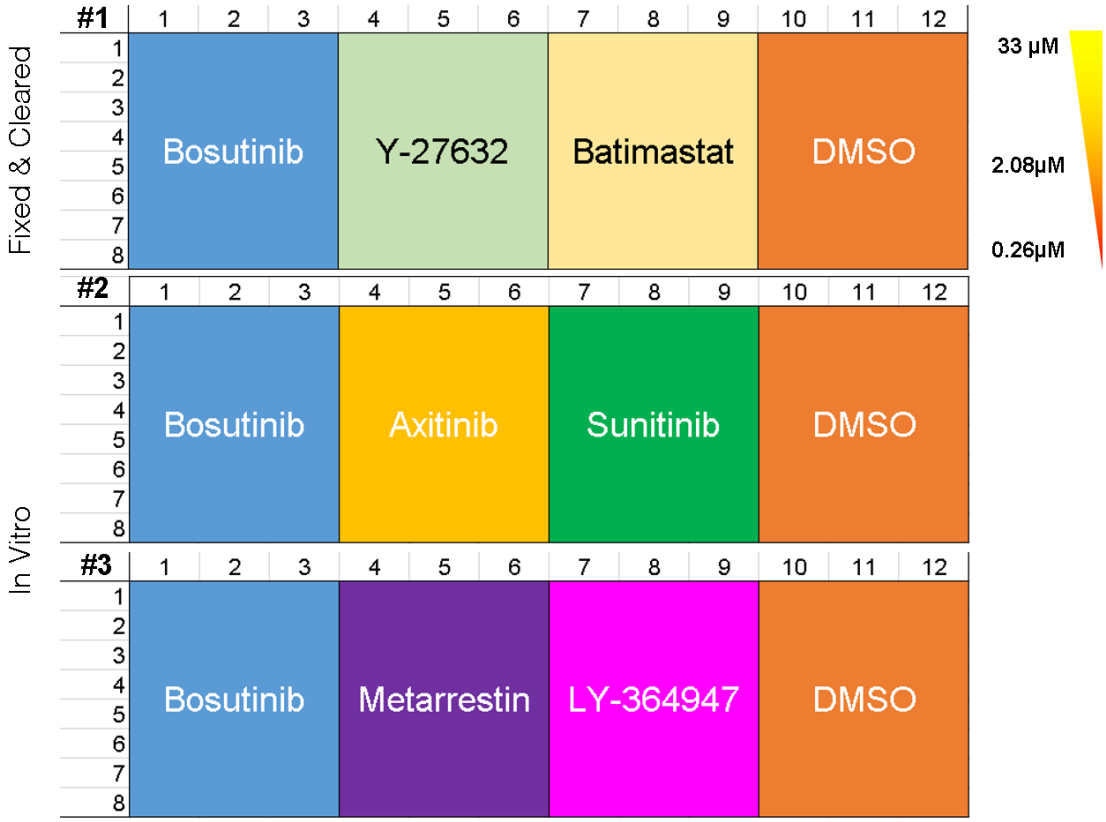

Figure 7. 18 List of Compounds that added to each well. The wells labeled with DMSO were control groups. The final concentration of the compound decreased from 33μM to 0.26 μM from first row to 8th row.

7.10.5 Results of OCT Imaging of Tumor Spheroid Invasion Assays

Figure 7.19 showed results of OCT imaging of U87-MG tumor spheroids modeling cell invasions. In this study, the tumor spheroid invasion assay was fixed and cleared prior to OCT and bright field imaging. Spheroids treated with DMSO (control), Batimastat, Y27632 and Bosutinib were shown in **Figure 7.19 A-D** respectively. For compound treated groups, the spheroids from row B of the plate (B8, B6, B2) were chosen, with the final compound concentration of 16.7 μM. In each subfigure, cross-sectional OCT (OCT XZ), en

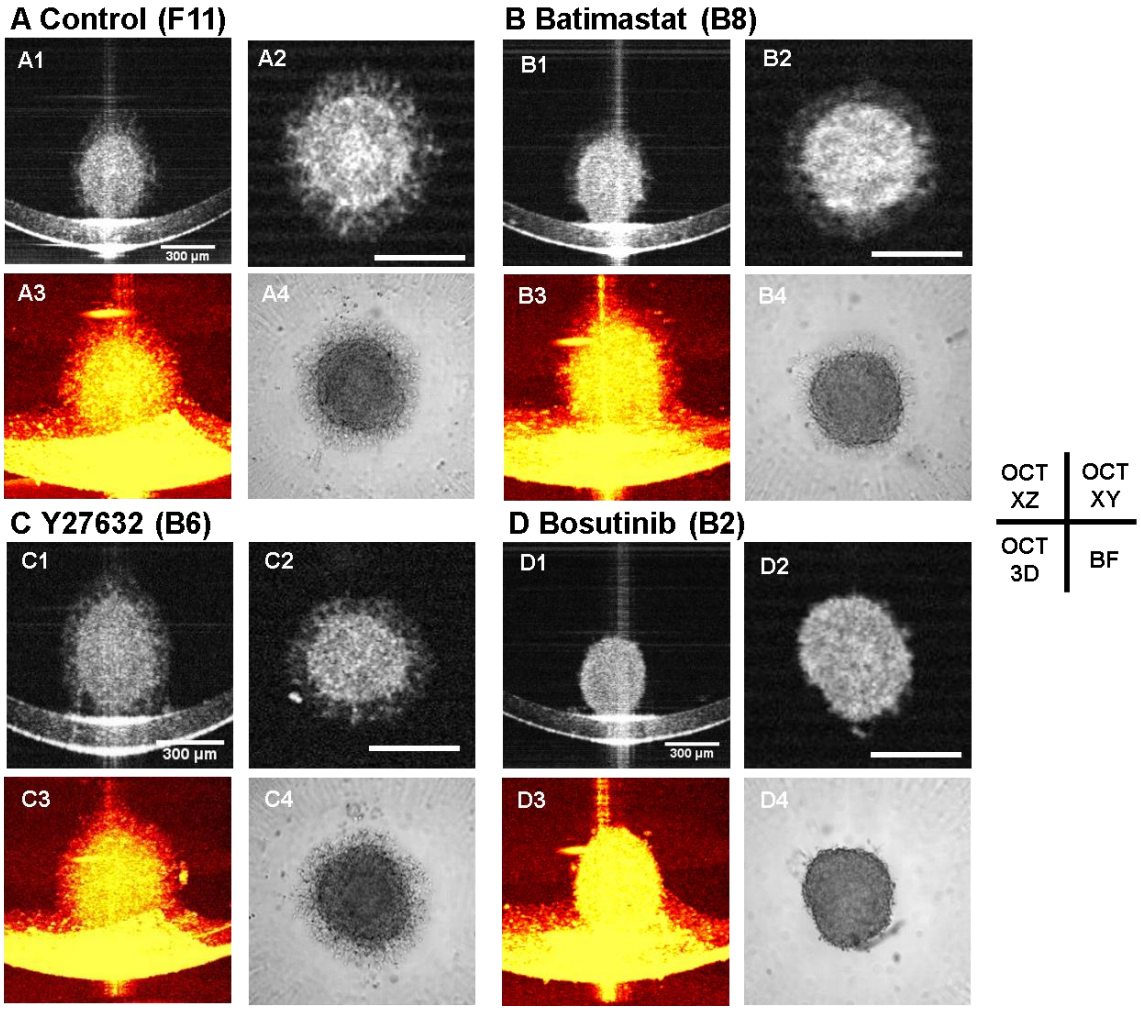

Figure 7. 19 Characterization of compound effects on tumor spheroid invasion assay by HT-OCT. Tumor spheroids were fixed and optical-cleared prior to imaging. Subpanels 1-4 corresponded to cross-sectional OCT (OCT XZ), en face OCT (OCT XY), 3D rendered OCT (OCT 3D) and bright field (BF) images. Scale bar: 300 µm

face OCT (OCT XY), 3D rendered OCT (OCT 3D) were presented to show the spheroid in different views. The bright field (BF) image was also presented for a comparison. In the control group, extensive cellular invasion (fluffy surrounding) was clearly visible in OCT images, with its diameter measured to be ~525 µm. In three compound-treated groups, the surface of the spheroid treated with Bosutinib (**Figure 7.19D**) was uniform and smooth, indicating cell invasion was completely inhibited. The diameter of the Bosutinib-treated spheroid was measured to be ~370 µm. For Batimastat and Y27632 treated spheroids, the invasion features remained on their surface (Figure 7.17 B, C), indicating the compound effect was not significant. In all four

groups, our observations in OCT images matched well with the observations in bright field images (**Figure 7.19 A4 – D4**).

Figure 7.20 showed the characterization results of *in vitro* tumor spheroid invasion assays for compound effects assessments. The bright field images of spheroids, obtained by bright-field, high-throughput screening (HTS) device (InCell 2200, 4×, GE HealthCare) were shown in the **first row of Figure 7.20**. The corresponding *en face* OCT images were shown in the **second rows**. The intensity of invasive cells outside was comparable to the intensity of the core in the en face OCT images of in vitro spheroids. In comparison,

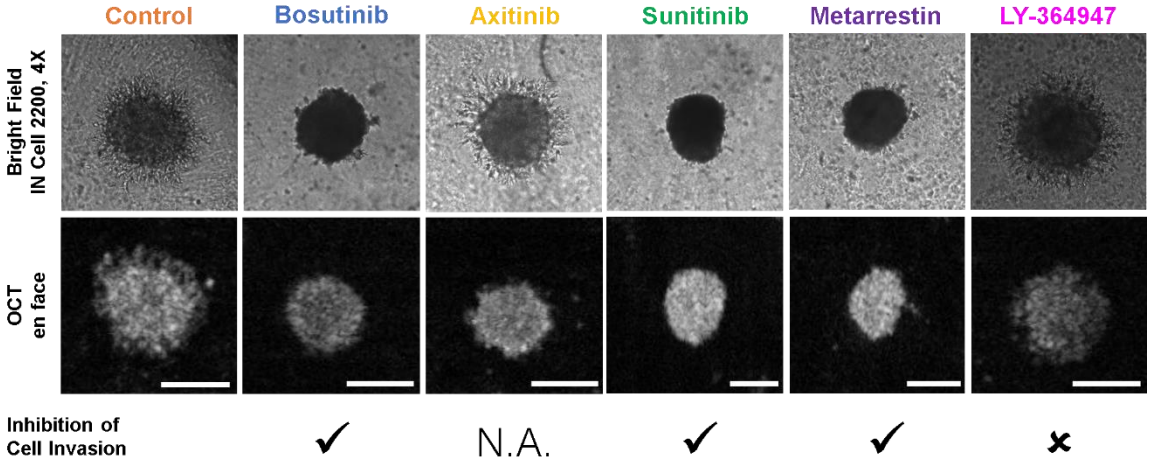

Figure 7. 20 Characterization of compound effects on in vitro tumor spheroid invasion assay. First row showed the bright field images of tumor spheroids treated with DMSO (control), Bosutinib, Axitinib, Sunitinib, Metarrestin and LY-364947. Second row showed the corresponding en face OCT images. Compound concentration: 16.7 µM. Scale bar: 250µm.

the intensity of invasive cells in fixed and cleared plates were much lower than the core region and slightly higher than the background. The intensity difference might be attributed to the optical clearing, while invasive cells outside the core were easier to be cleared than the densely packed core regions with much stronger barriers to resist the diffusion of the clearing agent. Similar to the fixed spheroids, we could easily observe cell invasion outside the spheroid core in the control group (**Figure 7.20, first column**). In the compound treated groups with the compound concentration of 16.7 µM, the response to the compound treatment were different, which were shown in both bright field and OCT images. Spheroids under the treatment of Bosutinib, Sunitinib and Metarrestin showed clear boundaries of the core regions in both bright field and *en face* OCT images, without any observation of invasive cells outside the core, inferring the compounds successfully inhibit cell invasion. For LY-364947 treated spheroids, invasive cells were clearly observed in

both bright field and OCT images, inferring no inhibitory effect of cell invasion. For Axitinib treated group, invasive cells could be observed in the bright field image. However, we didn't see much cells outside the spheroid core in OCT image, which disagreed with the bright field results. We also checked the tumor spheroid under the bright field microscope after OCT imaging and found no signs of cell invasion. Since the OCT images were obtained one day after the bright field imaging, and in the meantime, the plate was shipped from one site to another, the discrepancy of the results might be attributed to either the slow effect of the compound or potential damage during the shipment. Further experiment could be conducted on the same day to confirm the compound effect of Axitinib on cell invasion.

Next, we evaluated the significance of inhibitory effects of cell invasion on tumor spheroids as a function of compound concentrations. **Figure 7.21** showed the characterization results by bright field and OCT imaging. From left to right in the image, the tumor spheroids were treated with increased concentration of compounds from 0.26 μM to 33.3 μM. For Bosutinib group, the compound effect became signficant at a dose higher than 2.08 μM, with minimum amount of invasive cells observed outside the tumor spheroids in bright field and OCT images. For Metarrestin treated spheroids, the compound started to inhibit cell invasion significantly at the compound concentration of 16.7 μM. LY-364947 treated spheroids didn't show any inhibitory effects of cell invasion on the tested spheroid at the highest dose of 33.3 μM. As a result, we demonstrated the use of HT-OCT to perform qualitative assessment of compound effects on tumor spheroid invasion assays.

7.10.6 Quantitative Assessment of Compound Effects on Tumor Spheroid Invasion Assays by HT-OCT

To further evaluate the compound effects quantitatively, we further performed quantitative analyses on spheroids' morphology under different compound treatments. Morphological parameters such as total area, total volume were quantified from the OCT data.

Figure 7.22 showed the quantification results of spheroid areas for different compounds, as a function of concentration. In *en face* OCT images, the representative spheroid was automatically segmented by the built-in function in ImageJ (**Figure 7.22 A**). Then, spheroid area was measured to be the area of the contoured region. **Figure 7.22 B** showed the barplots of spheroid areas measured from the en face OCT images. Orange,

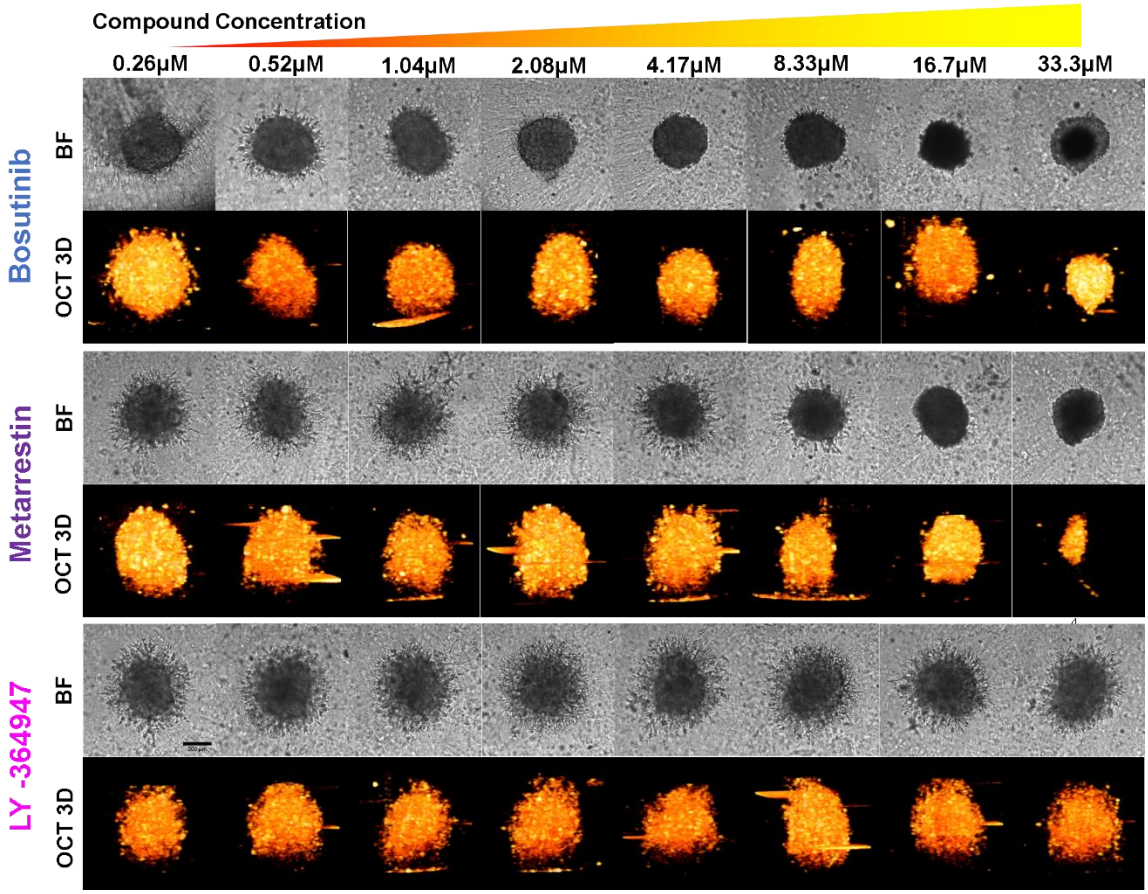

Figure 7. 21 Compound effects of inhibition of cell invasion on tumor spheroids at different concentrations, characterized by bright field and 3D OCT imaging. Compound concentration increased from 0.26 µM to 33.3 µM. Bosutinib, Metarrestin and LY-364947 treated spheroids were shown. Bosutinib started to take effect at a concentration of 2.08 µM; Metarrestin started to take effect at a concentration of 16.7 µM, while LY-364947 didn't show any inhibitory effects on tumor spheroid invasion models. Scale bar: 200 µm.

blue, yellow, green, purple and magenta colors corresponded to control, Bosutinib, Axitinib, Sunitinib, Metarrestin and LY-364947 compound groups, respectively. And the bars in each group were arranged in an ascending order based on compound concentration. In the OCT total area analysis, the Bosutinib group and Metarrestin group showed a clear decreasing trend of spheroid areas as the compound concentration increased, inferring the compound took effect to inhibit cell invasion. We also conducted the statistical analyses to assess the significance of the compound effects for each compound and each dose, using the results of paired t-test between compound treated group and the control group. The statistical significances were labeled as number of stars on top of each bar (*: $p<0.05$; **: $p<0.01$; ***: $p<0.001$). The areas of Bosutinib treated spheroid were significantly different from the control group at a concentration higher than 2.08 µM, which was consistent with our qualitative observation in **Figure 7.21**. The spheroid areas for

Metarrestin treated spheroids were significantly different as the dose went beyond 4.17 µM, which was smaller than the 16.7 µM observed in **Figure 7.21**. However, we observed that, invasion region was reduced in the Metarrestin treated spheroids from 4.17 µM to 16.7 µM in **Figure 7.21**. With the doses in between, the Metarrestin had minor effect to inhibit the cell invasion on tumor spheroid. For Sunitinib treated spheroids, we observed that only spheroids treated with 16.7 µM Sunitinib showed a significant difference of spheroid

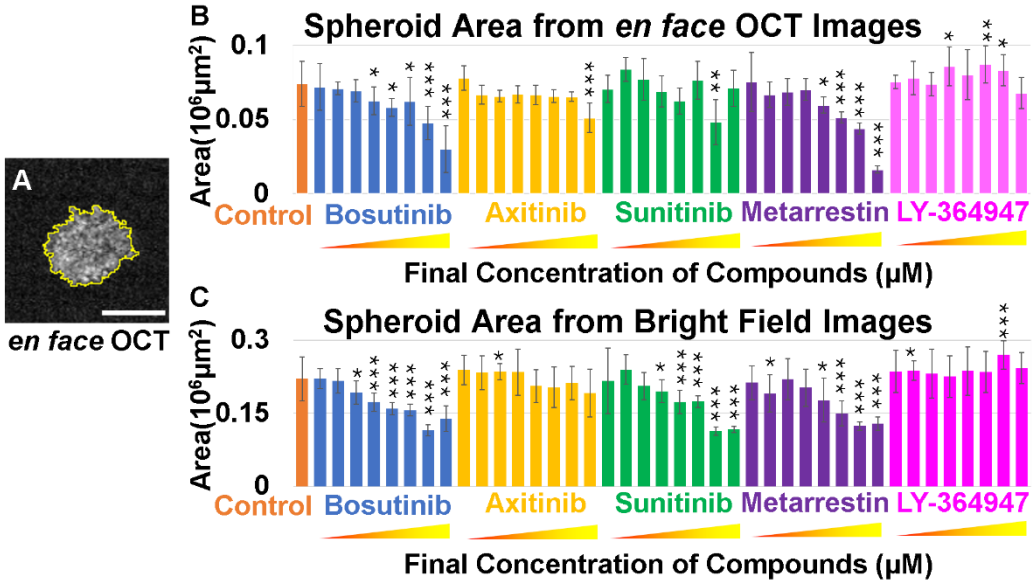

Figure 7. 22 Total area analysis of tumor spheroid invasion assay. The spheroid area was measured for each spheroid in *en face* OCT images (A) and bright field images. Spheroid areas for different compounds as a function of concentration quantified from en face OCT images (B) or bright field images (C) were shown.

area to the control group. For a comparison, we also showed the quantification result of spheroid areas from the bright field images in **Figure 7.22 C**. Quantification results of Bosutinib and Metarrestin groups from OCT and bright field images were quite consistent, with the same decreasing trends and significance. However, for Sunitinib group, the bright field images showed a significant decreasing trend of spheroid area, inferring the compound was effective to stop cell invasion. For Axitinib treated spheroids, spheroid areas didn't show any trend. Lastly, for LY-364947 treated spheroids, the spheroid areas were comparable with the control group and sometimes larger than the control group, inducing the false positive statistical significance. The quantification results of this group were consistent with our observation of no significant compound effect.

Figure 7.23 showed the preliminary result of the volume quantification for one plate of tumor spheroids, measured from the OCT data. Overall, the trend shown in volume analysis was similar with the spheroid area analysis.

We should note that, in the barplots of spheroid area and volume, we observed that some bars were higher than the neighbouring bars (i.e. Bosutinib group with a concentration of 8.33 µM, Sunitinib group with a concentration of 8.33 µM and 33.3 µM). Since the size of the sample in each sub-group was small (3 – 6), there might be chances that the results were affected by the shipment or the poor imaging quality. Future experiments would involve conducting more dupliate screens by HT-OCT with optimized image quality to claim the significance of the compound effects.

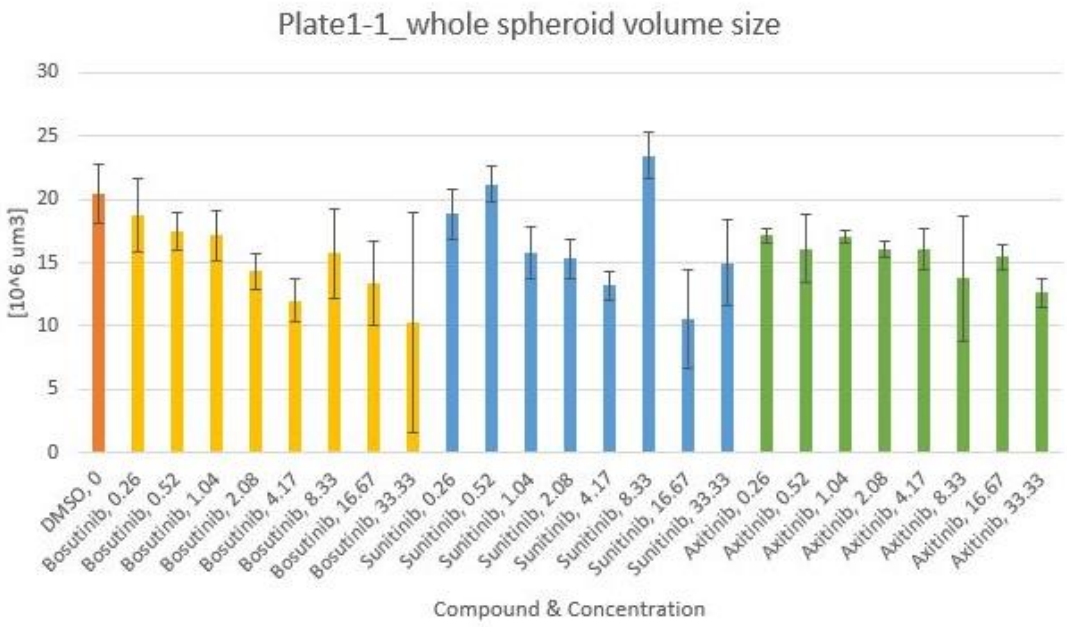

Figure 7. 23 Total volume analysis of tumor spheroid invasion assay with different compound treatment.

7.10.7 Preliminary Analysis of 3D Cell Invasion on Tumor Spheroids

To better evaluate the compound effect, we characterized the cell invasion area and volume for the compound-treated tumor spheroids. **Figure 7.24** showed the preliminary analysis of invasion area for selected compound-treated tumor spheroids in the assay. **Left panels of Figure 7.24 A-F** showed the *en face* OCT images of selected tumor spheroids with different compound treatments (Control spheroid was treated

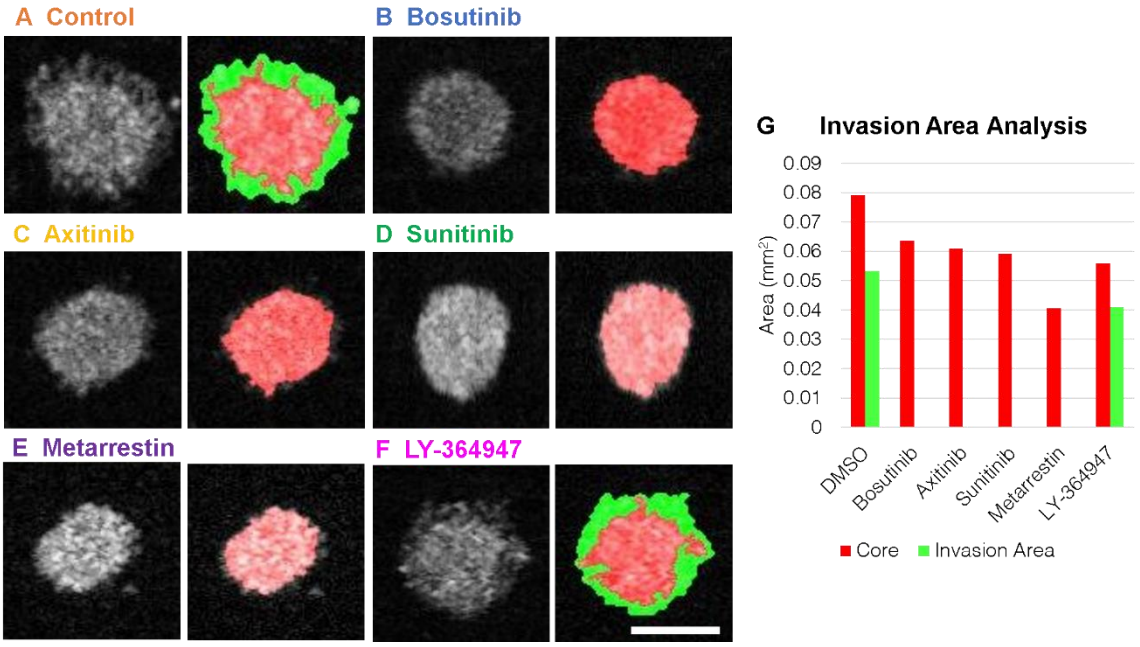

Figure 7. 24 Invasion area analysis on tumor spheroid invasion assay. Left panels of (A-F) showed the en face OCT images of selected tumor spheroids with different compound treatments (Control spheroid was treated with DMSO). The compound concentration was 16.7 µM for all compound-treated spheroids. Right panels showed the segmentation results of spheroid, with the red colored region indicating the core and the green colored regions indicating the invasion area. The corresponding quantification results were shown in (G), with the areas of the core and invasion areas plotted separately in the bar plot.

with DMSO). The compound concentration was 16.7 µM for all compound-treated spheroids. Although the intensity of invasive cells were comparable with the intensity of the core, which made it difficult to separate them apart, the invasive cells were loosely distributed outside the core as compared to the densely packed cells in the core. In such case, we could apply a 2D average filter with a small moving window size to smoothen the spheroid image. Density packed regions would have a higher averaged intensity, while the intensity of the invasion region would be lower down due to the averaging of intensities of invasive cells and the empty background. Then, we could use two thresholds to segment the invasion region, with a higher threshold to mark out the core region and lower threshold to remove background. After segmentation, we further optimized the results, by filling the holes in the core due to the OCT speckle, as well as rejecting the false positive of the thin ring outside the core due to the average filter. The segmentation results for each compound-treated spheroid were shown in the **right panels of Figure 7.24 A-F**. For the control spheroids and LY-364947 treated spheroids, invasion areas were clearly observed and labeled in green color, while, for

the other four groups, only core regions were labeled in red. Based on the segmentaion results, areas of invasion and core regions could be further quantified, which were shown in **Figure 7.24 G**.

Similarly, we could employ the segmentation method on the 3D OCT data to highlight the invasion volume, which was shown in **Figure 7.25**. This method could be further applied to other 3D OCT data of tumor spheroids to characterize the invasion areas and volumes for accurate evaluation of compound effects.

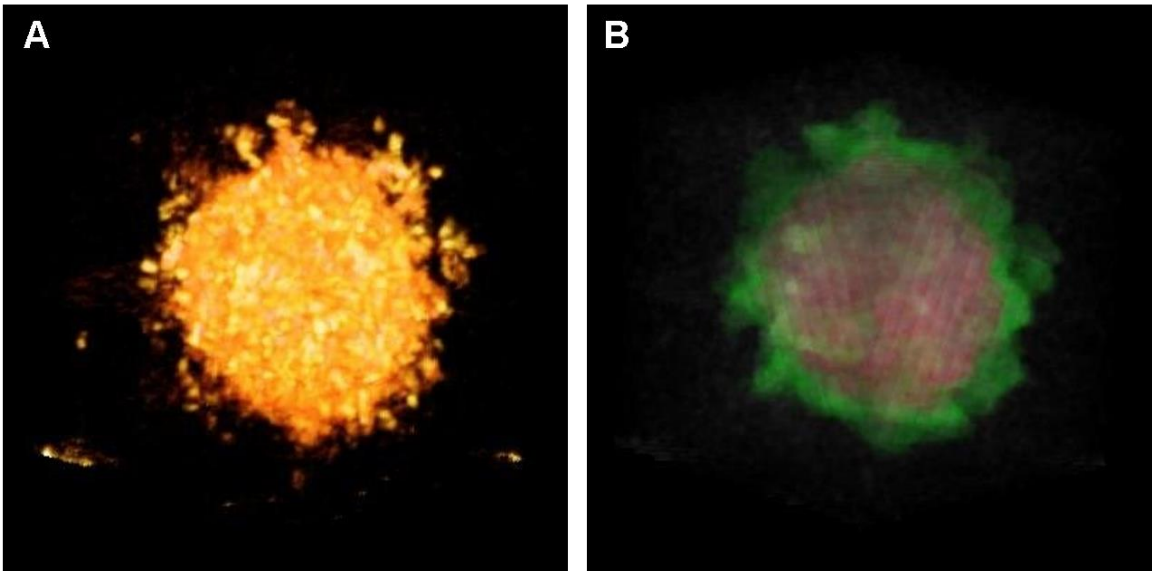

Figure 7. 25 3D rendered OCT image of a tumor spheroid invasion model (A) and corresponding segmented spheroid with green-colored invasion region an red-colored core (B).

7.11 Discussions

7.11.1 Significance of OCT in Tumor Spheroid Characterization

Tumor activity is highly relevant to its morphological structure. Similar to monitoring characteristic growth curve for 2D cell cultures, tracking the growth curve for 3D tumor spheroids is also a conventional approach to characterize the long-term spheroid growth behavior for different cell lines. Notably, we can characterize the drug response by analyzing tumor degradation or tumor regrowth directly reflected in the growth curve. Therefore, quantitative assessment of 3D tumor spheroids, including the size and volume, to derive the growth curve, is of great importance for the characterization of tumor spheroids and the evaluation of compound effect. Currently, imaging platform based on bright field, phase contrast or fluorescent imaging have been established for routine imaging and analysis of morphology or functions of the 3D tumor spheroids [360, 381, 407, 408]. However, they are unable to resolve the entire, large tumor structure due to limited

depth penetration as well as low-resolution depth-resolvability. In the representative results, we have demonstrated the feasibility of OCT to visualize the entire 3D structure of the tumor spheroid developing over time. 3D OCT imaging could provide the view of the spheroid in any orientation and any cross-section with high-resolvability, which was not available in conventional imaging modalities that lack the resolution along the depth. Voxel-based volume quantification based on 3D OCT data yielded an accurate quantification of spheroid volumes without assuming their original shapes. Furthermore, our prelimary results showed that we could potentially quantify the total area, total volume, invasion area and invasion volume of the spheroids to evaluate the inhibitory effects of cell invasion in tumor spheroid invasion assays with compound treatments. Therefore, we have demonstrated that OCT is a robust imaging modality for 3D morphology characterization of tumor spheroids, which ensures accurate measurements of characteristic growth patterns for different cell lines and serves as an alternative for drug response evaluation.

7.11.2 Alternative of Viability Tests Using OCT

Viability tests using fluorescent staining remain a popular approach for functional analyses of tumor spheroids, especially for drug screening [408]. However, the limitation of both light penetration and dye diffusion hindered its potential to probe into the inner core of the spheroid. Although optical clearing could be combined with confocal fluorescence imaging or light-sheet imaging to detect the fluorescent signals from the whole spheroid [406], it remained a challenge to employ optical clearing on the live tumor spheroid, making it less suitable for viability test. In our representative results, we demonstrated an alternative method that can characterize cell viability within the entire spheroid. Our results have shown that OCT could distinguish the dead-cell region from the viable region in the spheroid based on intrinsic optical attenuation contrast. In addition, with 3D imaging capability and non-destructive nature of the OCT system, quantitative evaluation of the dead-cell distributions and in situ monitoring of the progression of dead-cell regions within the spheroid are feasible, which potentially provide more valuable information of the spheroid growth pattern. However, we should note that, in our representative results, we are not able to differentiate different types of cell death modes, such as apoptosis and necrosis, in the binary OCT attenuation map. Future work could involve comparing the performance of three different dead-cell detection methods (See Chapter 7.3) for tumor spheroids with different sizes and from different cell lines.

7.11.3 Potential of 3D High-throughput OCT System

Since a drug compound library can be extensive (>10,000), a high-throughput and robust system to characterize tumor spheroids in multi-well plates during drug screening is imperative. The current high-throughput imaging system can achieve a screening of the whole 96-well plate in <5 min in 2D scan mode [381]. OCT can be adapted for high-throughput screening purpose, with the aid of a motorized stage. One can also obtain a commercially available OCT system with a similar performance to our custom OCT system, and incorporate a motorized stage into the system. However, efforts must be taken to modify the commercial OCT system to integrate the motorized stage. Also, custom software implementation to realize the synchronization between the OCT acquisition trigger and stage movement trigger is required. For our prototype HT-OCT system, the pure OCT acquisition time can be as short as ~3.2 min for all 96 wells. However, the intermediate steps for the current HT-OCT system, including data processing, reading and writing data on hard drives, and stage movements cost additional ~18 min. The total imaging time can be further reduced in several aspects: use state-of-the-art OCT systems equipped with a high-speed tunable laser source [3, 409]; optimized the workflow by arranging intermediate steps (data acquisition, data processing, writing, stage movement) working in parallel; employ a parallel OCT imaging with a space-division multiplexing setup [410]. With system optimization, the high-throughput OCT system can be a powerful screening tool in cancer drug discovery.

7.11.4 800nm OCT System and its Potential Challenges

In the OCT images of tumor spheroid invasion models, one issue is that the outer invasion layer was not clearly presented. Specifically, the individual invasive cells or invadopodia, could not be resolved due to lack of both axial and lateral resolutions. An OCT system with 800 nm or shorter central wavelength could potentially provide better characterization of these features with improved resolutions. However, as the central wavelength moves to 800 nm range, several factors need to be taken into consideration. First, the depth of focus would be reduced proportionally. As the numerical aperture of the objective was further increased to maintain the lateral resolution, the DOF would be further reduced. Thus, 800nm system was best used to characterize small tumor spheroids with a size of 150-300 μm. Also, normalization of light intensity

along the depth direction might be required due to small DOF. Second, as the NA of the objective further increases, the working distance of the objective becomes important. An inverted setup may allow the OCT to detect the spheroid from the well bottom, with a smaller working distance. However, since our multi-well plate was U-shape, correction of light distortion would be required. Third, the light penetration depth would also reduced, which might not be sufficient to penetration through the spheroid. Thus, before OCT imaging, it should be clarified whether we need a higher resolution or deeper penetration.

7.11.5 Potential OCT Application on Other 3D Culture Models

With the established HT-OCT system, we can potentially characterize other 3D culture models, involving organoids, 3D microvascular models and skin equivalents. Recent studies have reported using OCT to characterize viability state of liver spheroid [411] under drug treatment, to monitor morphological changes, cellular motility and the effect of toxicants in mammary epithelial cell (MEC) organoids [412-414], to monitor cellular viability in neurospheroid using dynamic light scattering [415], and monitor the dynamic growth of retinal organoids [416-418].Other than that, OCT has been employed to characterize the angiogenic sprouting in 3D microvascular models [419-421]. OCT can also serve as as the non-destructive evaluation tool for skin equivalents [414, 422-424].

7.12 Summary

In this chapter, we demonstrated the feasibility of OCT to characterize 3D tumor spheroids in a 96 well-plate. By measuring size, volume and growth kinetics of each spheroid in a 3D manner, we have demonstrated the advantage of this 3D imaging modality on characterization of spheroids with heterogeneous structures. In this work, we showed the feasibility of a high-throughput OCT (HT-OCT) system to perform automatic, sequential, 3D imaging and data analysis of tumor spheroids from the whole plate. With an optimized system performance, the total scanning time for a 96-well plate can be as low as ~23 min, including a total OCT acquisition time of only ~3.2 min. Using this HT-OCT system, we successfully screened plates of 3D tumor spheroid invasion assays. Compound treatments on inhibition of cell invasion were assessed on these spheroid invasion assays, based on the 3D morphological characterization provided by OCT. The high-throughput OCT system can potentially serve as a powerful investigation tool for robust 3D morphological

characterization of different 3D *in vitro* models including co-culture tumor spheroids, paper-based 3D cultures, organoids, 3D microvascular models and skin equivalents.

Chapter 8: Visualization of Developing Mouse Embryonic Hearts with OCT

8.1 Introduction

The cardiovascular system is the earliest forming organ system during embryonic development in vertebrates [50, 425]. Although recent studies show that early embryonic heart doesn't provide functions of bulk transport of nutrients, air, wastes and heat that occurs in fetal and adult veterbrates, the beating heart in the early developmental stage are linked to the formation of new peripheral blood vessels (angiogenesis) [425, 426]. During its development, structures of embryonic hearts change dramatically on an hourly basis for small embryos, daily basis for mouse embryos and human fetuses [427]. Abnormal development of heart might results in congenital heart defects (CHD), one of the congenital defects with highest incidence [427]. It is estimated that ~2.4 millions people have CHDs in the United States in 2010 and 1/8 of the cases are critical [428]. More than 24% of the infant deaths due to congenital defects are linked to heart malfunction [427]. To date, the cause of congenital heart defects in most cases remains unknown [429], although genetic [430-432] or non-genetic [433, 434] risk factors are associated with different types of CHDs.

Animal models have often been used to study embryonic heart development and find out the potential causes of CHD, which may help to develop the appropriate therapies for prevention and treatments of CHD [50, 435]. Especially, the rapid development of transgenic technologies has enabled the potential of phenotyping cardiac birth defects with animal models [436, 437]. For mouse, thousands of mouse models have been created by gene knock-out and knock-in to study the relationship between the genes and a variety of diseases [437]. Since the pipeline of gene modification and gene sequencing have been established, it is also imperative to establish a pipeline to screen (image) the gene modified mice to study the genetic causes of CHDs in high-throughput mode [437].

8.2 Animal Models

Various animal models have been employed to evaluate the embryonic heart development, involving the African clawed frog (*Xenopus laevis*), zebrafish (*Danio rerio*), the avian model (chicken *Gallus gallus*; quail,

Coturnix coturnix) and mouse (*Mus musculus*). **Table 8.1** summarizes the advantages of these research animal models, modified from Men et al. and Tobita et al. [50, 435].

Among these models, mouse models have the closest anatomical similarity with humans [50, 435, 436]. Embryonic mouse heart has four-chambered structure, and it undergoes atrial and ventricle septation and progression of cardiac valves. And it has a relative smaller size for observation under microscope. It has a shorter gestational period, which is good for long-term studies. Since transgenic technologies are most advanced in mouse models [435], genetically modified mice are more readily served as the animal model to study the genetic cause of CHDs.

Table 8. 1 Advantages of Different Animal Models in Researches

Models	Pros
Frog	• Easy Handling • Partially Transparent
Zebrafish	• Transparent in the embryonic and larval stage • Survive without functional cardiovascular system
Fly	• Easily access to heart tube (0.2mm below surface) • Partial transparent • Lowest cost
Avian	• Septated, four-chambered heart • Easy access by removing the eggshell at specific developmental stages
Mouse	• High resemblance in genomes • Four-chambered structure • Similar developmental events • Similar developmental pathways that regulate the patterning and morphogenesis • Mature transgenic techniques

8.3 Development of Mouse Embryonic Hearts

Table 8.2 shows a list of developmental events of mouse embryonic hearts, modified from Kowalski et al. and Savolainen et al. [427, 436].

Abnormal heart morphology in mice could be developed at any stage of the embryonic heart development. **Appendix 8.1** lists the common abnormalies occurred in transgenic mice, cited from Savolainen et al. [436].

8.4 Imaging Modalities for Murine Embryonic Heart Development

Various approaches have been utilized to characterize embryonic heart images, involving ex vivo and in vivo approaches. **Table 8.3** summarized a list of approaches to characterize embryos and embryonic hearts[435, 437-439]. Since mouse embryos have a size of only a few millimeters, imaging modalities for whole-body

Table 8. 2 Developmental Events of Mouse Embryonic Hearts in days post fertilization (dpf)
Developmental Events of Mouse Embryonic Hearts in days post fertilization (dpf)

Days(dpf)	Events
8	Linear heart tube
8	Onset of heart beat
8.5	Onset of blood flow
8.5-10.5	Cardiac looping
8.5-10.5	Formation of pharyngeal arch arteries
9	Regular heart beat established
9-14	Ventricular septation
9.5 -11	Ventricular trabeculation
10	Formation of atrioventricular cushions (AVC)
10-13.5	Septation of outflow tract (OFT)
10-14.5	Atrial septation
10.5	Identification of four chambered heart structure
11	Primary pulmonary vein
11	Formation of epicardium
11.5-14	Thickening of ventricular walls
12.5-15.5	Formation of valve leaflets
13.5	Formation of aortic arch system
13.5	Formation of pericardium
15.5-18.5	Modification of valve leaflets
15.5-18.5	Modification of coronary arteries

animal studies, i.e. positron emission tomography with a resolution of >1mm, may not be suitable to resolve the anatomic structure of the embryos.

Necropsy is the standard procedure to understand the cause of death or effects of diseases for small animals. Histology (images provided by standard bright field microscope) remains the gold standard to provide anatomic images of the whole embryos and its organs with high resolution and contrast. Scanning electron microscopy (SEM) can provide images with a higher resolution approaching 1-20 nm. Episcopic fluorescent image capture (EFIC) can provide images of embryonic structures with fluorescence labeling. Combining these approaches with serial tissue sectioning or cryo-sectioning, stacked images from different sections of the embryo could be obtained to reconstruct the 3D structure of the embryos. However, these imaging modalities require similar preparation procedures as histology, which is time-consuming [438]. Also, since the procedure is performed ex vivo, we cannot obtain any dynamic information from the specimen and need to gather multiples samples at different stages to understand the developmental changes occurred in the embryos.

For in vivo imaging, video microscopy can provide images that are limited to tissue surface. Clinical ultrasound can provide 2D images of the fetal mice to explore the features of embryonic growth *in utero*.

Table 8. 3 Various Approaches to Characterize Embryos and Embryonic Hearts

Approaches	Resolution	Imaging depth	Contrast Agent	3D/Stack Imaging time
Necropsy	N.A.	N.A.	N.A.	N.A.
Histopathology	Same as Standard Microscopy	N.A.	Dyes (i.e. H&E)	Combined with series tissue section or cryo-section. Long
Scanning Electron Microscopy (SEM)	1 – 20 nm	N.A.	Gold	
Episcopic Fluorescent Image Capture (EFIC)	Same as Standard Microscopy	N.A.	Dyes	
Video Microscopy	Same as Standard Microscopy	N.A.	No	No.
Confocal	~1 µm	<200 µm	Dyes or N.A.	Yes, can combine with sectioning. Minutes
Multiphoton	~1 µm	<2 mm	Dyes	Yes. Seconds to hours.
Clinical Ultrasound	300 µm axial 500 µm lateral	Whole specimen	Most of time, No. Microbubbles	Yes, in low resolution mode.
Ultrahigh Frequency Ultrasound	30 µm axial 68 µm lateral	35 mm		
Photoacoustic Tomography (PAT)	27 µm axial 115 µm lateral	~20 mm	No.	~8 min
Micro-CT	1 - 25 µm; Typically conducted at 15 µm and 45 µm	80 mm	Iodine-based contrast agent	Yes. ~1 hr (for several specimens)
Micro-MRI	~20-100 µm	100 mm	Most of time, No.Gadolinium-loaded gelatin for vasculature	Yes. ~10 min to several hrs.
Optical Projection Tomography (OPT)	1-15 µm	<3 mm	Optical Clearing Required	~30 min
Optical Coherence Tomography (OCT)	1-15 µm	1-2mm	Most of time, No. Optical clearing or nanoparticles.	Seconds

With the Doppler imaging, cardiac functions such as heart rates and flow velocities can be quantified [437]. Using the dynamic information, we can infer the existence of CHDs. However, the 300 µm axial resolution and 500 µm lateral resolution make it challenging to resolve any finer morphological structures inside the fetal mouse hearts to confirm the diagnosis. Ultrahigh frequency ultrasound are now commonly used in research labs for small animal studies [437]. With higher-grade resolutions (30 µm axial and 90 µm lateral [440]), *in utero* imaging of mouse embryonic hearts at different developmental stages are available in 2D ultrasonic images [440, 441]. In vivo diagnosis from E12.5 are also available, including abnormal

developments of outflow tract (OFT), heart septa, cardiac valves and aorta [437]. Currently, real-time 3D ultrasound imaging are available in low tranducer-frequency and low resolution mode [442, 443]. Although 3D in vivo imaging of rat hearts with high frequency ultrasound has been reported [444], it remains a fast growing field for 3D high-frequency ultrasound imaging. Photoacoustic tomography (PAT), an imaging technology combining absorption of nanosecond laser pulses and detection of generated ultrasound waves, is able to visualize the 3D structure of E15.5 mouse embryos *in vivo* and *in utero* [160, 445]. The resolution of the PAT system is close to ultrahigh frequency ultrasound. And the total imaging time for a 3D data is ~8 min.

To better diagnosis the CHD with high accuracy, imaging modalities that provide cellular-level resolution are needed. Confocal microscopy and multi-photon microscopy have been routinely used in labs to image cellular structures with the resolution of ~1µm. CHDs can be clearly observed in confocal images of dissected and sectioned mouse embryonic hearts [437]. Live imaging of cardiac contractile activity and heart tube development in early stage of embryonic heart development (from E7.5) have been demonstrated under confocal microscopy and multi-photon microscopy, with special handling of mouse embryos in culture media to maintain their life [446, 447]. However, the trade-off between the imaging volume and the acquisition time makes it difficult for *in vitro*, high-resolution imaging of mouse embryos in the later developmental stages. Micro-CT and micro-MRI are adapted from computed tomography (CT) and magnetic resonance imaging (MRI), which are designed for small animal imaging in research labs. Both of these modalities can simultaneously provide 3D morphological images of several mouse embryos or newborn mouse pups with a resolution of 30-70 µm in ~1hr [435, 437]. To achieve better resolution, the acquisition time can increase exponentially with higher density sampling, making it impossible for live imaging [435]. Also, the use of iodide solution to increase the contrast of micro-CT images is only available for fixed samples [437, 448]. Optical projection tomography (OPT) and optical coherence tomography (OCT) are optical analog of CT and ultrasound. The resolution of both modalities ranges from 1 µm to 15 µm, filling the gap between confocal/multiphoton microscopy and micro-CT/micro-MRI. Similar with CT, OPT utilize back-projection to reconstruct the 3D rendered image of embryonic samples, which requires extensive computation [449]. OPT has been successfully employed to provide live imaging of small and transparent specimen like zebrafish [450]. Live OPT 4D imaging of growth of hindlimb bud was demonstrated in E10.5 cultured mouse

embryo at a time interval of 15-20 min [451]. With the point scanning procedure and simpler image reconstruction, OCT can obtain 3D imaging of specimen in seconds, enabling 4D imaging of cardiovascular dynamics in early stage mouse embryos [352, 452]. However, the use of optical light for both modalities hinder their imaging depth to 1-2 mm due to limited light penetration [449, 451].

8.5 Optical Coherence Tomography in Embryonic Cardiac Development Imaging

OCT has been demonstrated to visualize embryonic hear development in different animal models, including African clog frog, zebrafish, avian, fly and mouse[50]. **Table 8.4** summarized the embryonic structures, developmental events, cardiac defects and dynamic processes in frog, zebrafish, avian and fly models that are visualized by OCT[50]. Detail discussions can be referred to Men et al.[50].

Table 8. 4 Morphological and Functional Observation of Animal Models with OCT

Animal Model	**Structures/Events**	**Dynamic Process**
African clawed frog	• Three-chambered structure • Myocardial walls, lumens, trabeculae carneae • Atrium septation[453]	• Heart beat • Heart wall motion • Blood flow[454]
Zebrafish	• Two-chambered structure • Cardiac defects[455]	• Filling and contraction of atrium and ventricle • Pulsatile flow[456]
Avian	• Cardiac defects under alcohol exposure: VSD, DORV, etc. [457, 458] • Microvascular organization under alcohol exposure[459]	• Heart beat[460, 461] • Stroke volume, cardiac output, ejection fraction, wall thickness[462-465] • Conduction velocity[464, 466] • Radial strain and strain rate of heart wall[465]
Fly	• Heart wall thickness[467] • Cardiac developmental diastasis[468] • Enlarged and irregular heart tube[469]	• Heart beat: Heart rate, end systolic and diastolic diameters, fraction shorterning[470, 471] • Retrograde and anterograde heart beats[472] • Velocity[473] • Cardiac activity period (CAP)[468]

A few groups have been working on using OCT to see mouse embryonic heart development. **Table 8.5** summarizes the research work involving using OCT to characterize the mouse embryonic heart development, excluding the OCT imaging of other organs of the mouse embryos. OCT have been utilized to visualize the

cardiac structures, including the heart tube at E8.5 [474], formation of four chambered structure from E9.5 to E13.5 [79, 475, 476], ventricular trabeculae, cushions and great vessels [475, 476]. With fast scan rate, 4D OCT (3D + time) has been employed to monitor dynamic cardiac activities [79, 478, 479]. With OCT angiography, cardiac blood flows can be visualized and monitored [79, 452, 480, 481, 483, 485]. Cardiac defects in mutant mice are also characterized by OCT [477, 479]. However, most of the these studies are focusing on imaging early-stage mouse embryonic hearts (E7.5-E10.5), since the embryonic heart during this stage is relative small and close to embryo surface. As the embryonic heart grows larger and its pericardial walls start to form and enclose itself, it becomes more difficult for the near-infrared red light to penetrate to the heart region, yielding it hard to visualize the intact, whole embryonic heart inside the mouse embryos after E10 [449].

Table 8. 5 OCT Imaging of Mouse Embryonic Heart Developments

Category	**Main Observation**
Cardiac Structure	• Heart tube:E8.5 [474] • Primitive atrium and ventricle: E9.5 [352, 475] • Atrium, ventricles and atrioventricular cushions: E10.5 [476] • Four chambered structure:E13.5 [462], E14.5 and E17.5 [476] • Ventricular septation: E13.5 [477] • Ventricular trabeculae:E13.5 [462] • Endocardial cushion: E13.5 [462] • Aorta and pulmonary trunks: E14.5 and E17.5 [476]
Developmental Event	• Heart Looping:E8.5 [478]
Dynamic Process	• One cardiac cycle: E8.5, E9.5, E10.5 [352, 476, 478, 479] • Blood cell circulation, phase delay between beating atrium and ventricle, progression of pule wave in outflow tract wall [352] • Angiograms and cardiac blood flows:E8.5-E10.5 [352, 452, 476, 480-483] • Pulsatile flow: E8.5 [481] • Retrograde flow: E9.0 [452] • Yolk sac vasculature: E8.5 [484], E9.5 [485]
Cardiac Defects	• Heart looping defects [478] • Undeveloped left atriums and ventricles, missing interventricular septum (IVS):E12.5, E13.5 [477]

8.6 Optical Clearing to Facilitate Microscopic Imaging of Mouse Embryos

All high-resolution optical imaging modalities, i.e. confocal microscopy, multi-photon microscopy, OPT and OCT, utilize visible light or near-infrared red light to achieve high-lateral-resolution imaging. However, due to inherent heterogeneity of biological tissues, light transmission inside the tissue is strongly limited to 1-2

millimeters [486]. As is mentioned, the mouse embryonic heart would grow larger and embed deeper underneath the surface, preventing the these optical imaging modalities from resolving the whole heart structure. Tissue optical clearing technologies, a fast growing field, have been developed to effectively improve imaging depth in highly scattering biological tissues to enable high-resolution imaging of whole organs or whole bodies of small animals [486, 487].

In principle, the key steps of optical clearing are fixation, permeabilization, decolorizing and refractive index (RI) matching [487]. First, fixation can preserve the tissue for a long time. Part of the blood inside the tissue would be removed by repeated washing by PBS. Next step, permeabilization, helps to modify the environment of tissue to either hydropholic or hydrophilic environment. Generally, the tissue is immersed in the solvents with gradual increased concentration of chemicals to replace the water inside the tissue with cell-permeable molecules, driven by osmotic pressure. Lipid, another source of high scattering inside the tissue as well as the main components of membranes to inhibit the diffusion of molecules, would be removed in this step, which is called delipidation. After the water is replaced and lipid is removed to improve the molecular permeability, the tissue is decolorized by removing the pigments inside the tissue. These pigments, involving heme, riboflavin, melanin and lipofuscin, would absorption lights and reduce light penetration [488]. The last step is to immerse the tissue in a new media with relative higher RI to match the refractive index of the tissue to reduce light scattering, enabling deep light penetration inside the tissue.

Various tissue optical clearing techniques have been applied together with different optical imaging modalities to image whole organs or whole bodies of small animals. Successful practices involve combining optical clearing with light sheet microscopy (LSFM or SPIM) [489, 490], confocal microscopy [491, 492], MPM [491-493], epifluorescence imaging [494] and OPT [449, 495]. Optical clearing has been demonstrated to work with OCT to enhance the penetration in skin [496, 497] and sclera [498]. In early trial, glycerol has been employed to enhance the OCT imaging depth in mouse embryos [499]. However, only signal enhancement between 200 – 500 μm was reported, which was not sufficient for whole organ imaging. In another study, the whole HH-28 chick embryonic heart, optical-cleared with methyl benzoate, was visualized by OCT [500]. Recently, a novel approach combining perfusion with contrast agent and complete optical clearing has been demonstrated to visualize the microvasculature of embryonic quail organs, including heart and brain [459]. **Table 8.6** shows a list of advanced optical clearing techniques, summarized by Tainaka et

al. and Liu et al. [486, 487]. The key components used in the optical clearing protocols are listed. Based on the sample size and time, we can determine which protocol best suits our needs. Since Table 8.6 is intended to use in combination with OCT, compatibility of fluorescent and immunostaining dyes after fixation is not listed.

Table 8. 6 Tissue Optical Clearing Techniques

Protocol	**Key components**	**Time**	**Sample size**	**Final RI**	**References**
BABB FluoClearBABB	EtOH *tert*-butanol	Days	Medium	1.56	Dodt et al.[489], Schwarz et al.[501]
3DISCO iDISCO iDISCO+	THF, DBE	Hours-Days	Medium	1.56	Becker et al[502], Erturk et al[503], Renier et al.[504], Renier et al.[505]
uDISCO	*tert*-butanol, BABB, DPE, α-tocopherol	Hours-Days	Large	1.56	Pan et al.[506]
TDE	TDE	Days-weeks	Small	1.42	Aoyagi et al.[507], Costantini et al.[508]
Clear^{T} Clear^{T2}	Formamide	Hours - Days	Small	1.44	Kuwajima et al.[494]
Sca*l*e Sca*l*eS	Urea	Weeks-month; Days	Medium; Small	1.38 1.44	Hama et al[491], Hama et al.[509]
CUBIC CUBIC-cancer CB-Perfusion	Urea	Days Days-weeks	Medium Large	1.45	Susaki et al.[510], Kubota et al[511], Tainaka et al[512], Susaki et al.[513]
ClearSee	Urea	Days-weeks	Medium	1.41	Kurihara et al.[514]
FRUIT	Urea Fructose	Days	Small	1.48	Hou et al.[515]
SeeDB SeeDB2	Fructose; Saponin, Histodenz	Days	Small	1.50 1.52	Ke et al.[492], Ke et al.[516]
CLARITY EDC-CLARITY Bone-CLARITY PEA-CLARITY Passive CLARITY (PACT) ePACT mPACT simplified CLARITY (SCM) FASTClear PARS ACT-PRESTO SWITCH Stochastic Electrotransport	Hydrogel embedding; ETC-based or passive clearing; SDS	Days-weeks	Medium Large	1.42-1.48	Chung et al.[493], Sylwestrak et al.[517], Greenbaum et al.[518], Palmer et al.[519], Yang et al.[520], Treweek et al[521], Woo et al[522], Sung et al[523], Liu et al.[524], Yang et al.[520], Lee et al.[525], Murray et al.[526], Kim et al.[527]

* Sample Size: Small: small sample, neonatal samples and embryos, i.e. spinal cord, tumor spheroid, mouse embryo; Medium: Intact and adult samples, i.e. whole adult brain, heart, lung, kidney; Large: whole body of animal sample, i.e. mouse.

8.7 OCT plus optical clearing for mouse embryonic heart imaging

Previous OCT studies on mouse embryonic heart development focused on early stage mouse embryonic hearts from E7.5 – E10.5. Although some studies showed the OCT imaging of the mouse embryonic hearts in E13.5[462], E14.5 and E17.5 [476], only part of the embryonic heart is visible due to limited light penetration, providing limited information of mouse embryonic cardiac developmental events occurred in later stages.

In this chapter, we will use OCT, the non-destructive, high resolution 3D imaging tool, to characterize mouse embryonic hearts in different stages ex vivo to show the full development of embryonic hearts. With the aid of tissue optical clearing technology, we are able to resolve the whole mouse embryonic hearts from E10.5 to E16.5 with significant enhanced light penetration. Morphological changes and developmental events, including formation of four-chamber structure, septation of atria and ventricles, atrio-ventricular septation and progression of cardiac valves, remodeling of common outflow track and formation of mature cardiovascular system, were observed in these images. Combining with other literature, we can generate the OCT atlas of developing mouse heart that are comparable with the histology findings[436]. Furthermore, we imaged a E16.5 mouse embryonic heart with congenital heart defects with OCT. Given its 3D capability and non-destructive imaging advantage, OCT can be a feasible candidate for phenotyping CHDs in mutant mice.

8.8 Sample Preparation for the OCT Imaging of Mouse Embryos

In this study, embryonic days 9.5, 10.5, 11.5, 12.5, 13.5, 16.5 mouse embryos were investigated under OCT. These embryos were obtained from our collaborators, which were fixed in methanol or PFA beforehand and stored in 1.5 mL centrifuge tubes. For 13.5 and 16.5 mouse embryonic hearts, due to its size and location of the hearts, we dissect the heart out to obtain the OCT images.

8.9 Optical clearing protocol for mouse embryo imaging

Based on the information of optical clearing protocols listed in **Table 8.6**, we finally choosed the protocol 3DISCO based on its simplicity and its speed. First, we sorted out the tissue optical clearing protocols which can finish in one day with an overnight immersion step. Only three protocols satisfied our requirement: 3DISCO series, SeeDB series and Clear^{T} series. However, the extremely high viscosity of the saturated

fructose solution, especially 100% concentration version, made it complicated to prepare and handle the solution [487]. Furthermore, Maillard reaction occurred during the long-time immersion in fructose solution [487], yielding the browning of the tissue sample and compromised clearing effects for OCT imaging. The performances of 3DISCO series and Clear^{T} series optical clearing techniques on tissues were not actually compared in the lab. However, based on the fact that medium-size tissue samples could also be optical-cleared by 3DISCO series and overall clearing performance of 3DISCO series was rated higher than Clear^{T} and SeeDB series [487], 3DISCO protocol was finally chosen over Clear^{T}.

Prior to the 3DISCO clearing process, the mouse embryos were fixed in formaldehyde or PFA for >1 days. Then, 3DISCO protocol was conducted [503]. Based on the size of mouse embryos, we use the short-duration version of the 3DISCO protocol. **Table 8.7** summarizes the detailed steps of 3DISCO protocol to clear mouse embryos. The duration of each clearing step was listed in the table.

Table 8. 7 3DISCO Protocol for Optical Clearing of Mouse Embryos (Hearts)

PFA	50% THF	70%THF	80%THF	100%THF	100%THF	100%THF/DCM	DBE
>24 hr	1 hr	1 hr	1 hr	1 hr	overnight	1 hr	0.5-3 hr

8.10 Configuration of OCT system for Mouse Embryo Imaging

We use the same 1310 nm SD-OCT system for mouse embryo imaging (See Chapter 2). A f = 75 mm lens was used as the 1st relay lens in the sample arm, yielding slightly improved lateral resolution. Measured axial resolution was 8.26 µm in air, and 5.29 µm in dibenzyl ether (DBE). Using a 5× objective for imaging, the best lateral resolution of this system was measured to be 6.20 µm. The sensitivity of OCT system was measured to be 102 dB with 47 kHz A-scan rate.

During OCT imaging, Each OCT data consisted of 800 (A-scan) × 800 (B-scan) × 1024 pixels, covering a volume of 3.0 × 3.0 × 2.2 mm^3. Camera rate was set to 47 kHz, 28 kHz and 20 kHz, according to the image quality during the acquisition process. Due to fast refractive index matching process of the optical clearing, OCT imaging was best conducted in the first 30 min of immersion in the final medium of DBE. Total acquisition time for a single OCT dataset was 30 seconds to 1 minute, including the saving time. A glass plate was used at the bottom to hold the mouse embryonic heart. The embryonic heart was then immersed with DBE in a drop. A tilted cover glass was placed on top to maintain the immersion state and reduce the

surface reflection. For large samples (E13.5 and E16.5), the size of the embryonic heart was larger than ~3 mm in diameter, which was too big for SD-OCT with a total imaging depth of ~2.2 mm to image the entire structure. In such case, we would first image upper half of the embryonic heart with a single OCT acquisition. Then moved both the reference and sample arms to show the other half of the heart and take a second OCT dataset. These two OCT datasets would be stitched together to present the entire heart structure. For E16.5 dissected heart, the size of the heart was ~ 5 × 5 × 3 mm^3, which was larger than the FOV of the OCT system. Thus, 8 datasets in a 2 × 2 × 2 manner would be acquired sequentially to cover different parts of the embryonic heart for final stitching.

8.11 OCT Atlas of Developing Mouse Embryonic Hearts

Figure 8.1 showed the OCT atlas of developing mouse embryonic hearts. Different stages of embryonic hearts were captured, starting from early stage of E9.5 to late stage of E16.5. Since mouse embryos or dissected mouse embryonic hearts in E13.5 and E16.5 were optical cleared by 3DISCO, near-infrared light can penetrate sufficiently inside the mouse embryo. In all six stages, we could clearly resolve the entire 3D structures of the mouse embryonic hearts in OCT images. As a comparison, E11.5 and E13.5 mouse embryonic hearts, although visible, couldn't be fully resolved by OCT without optical clearing technology [449].

In **Figure 8.1**, sagittal, coronal and transverse views of developing mouse embryonic hearts were shown, arranged in different rows. Atria and ventricles in different stages and different orientations were labeled in yellow letters. In E9.5 image, primitive atrium and ventricle were distinguished in sagittal view. Coronal and transverse views showed the ongoing process of cardiac looping of the mouse embryonic heart in this stage. By comparing orientation of the mouse embryonic hearts in the coronal and transverse views of E9.5, E10.5 and E11.5 images, we could conclude that the cardiac looping was done at E10.5 stage since the orientation of the mouse embryonic heart maintained the same from E10.5 to E11.5. From E10.5 to E12.5, atrium and ventricles were connected but not fully separated. The primitive four-chambered structure appeared at E10.5 as the atrial chamber further ballooned and formed a relative symmetric structure in the transverse view of E10.5 image (**Figure 8.1N**). Continued development of the four-chamber structure was clearly visible in

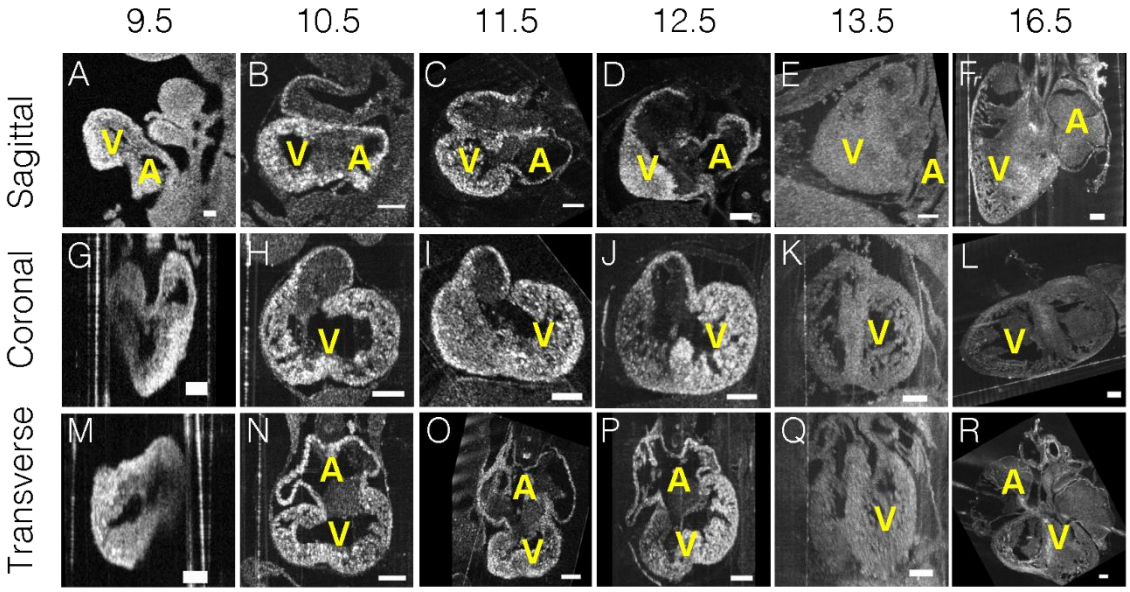

Figure 8. 1 : OCT atlas of developing mouse embryonic hearts. Rows of the Figure 8.1 A-R showed the OCT images of mouse embryonic hearts in sagittal (first row), coronal (second row) and transverse (third row) views. Columns of the Figure 8.1 A-R indicated the mouse embryonic heart images at different developmental stages, including E9.5, E10.5, E11.5, E12.5, E13.5 and E16.5, respectively. A: Atria, V: Ventricles. Scale Bar: 200 µm.

transverse views of E10.5 – E12.5 images (**Figure 8.1 N-P**). In E16.5 image, fully septated four-chamber structure was observed in transverse view (**Figure 8.1 R**).

Starting from E10.5, trabeculae were clearly visible in the ventricles, shown as rippled structure inside the ventricular wall (**Figure 8.1 N**). The increasing trend of thickness of ventricular myocardial walls were distinguable from E11.5 to E13.5 stages in both coronal and transverse views.

Using maximum intensity projection (MIP), 3D rendering of mouse embryo hearts could be reconstructed. **Figure 8.2** presented a 3D MIP rendering of E10.5 mouse embryo hearts. The primitive four chambered structure was clearly visible in this stage, as well as the outflow tract in front.

8.12 Critical Events of Mouse Embryo Heart Development

Based on OCT atlas of mouse embryonic heart development, various critical morphological changes and developmental events could be identified. In the last section, we showed that cardiac looping, the most critical development events in early stage, was done by ~E10.5. In the following section, we would summarize the observation of critical morphological features and developmental events in mouse embryonic hearts between E9.5 to E16.5.

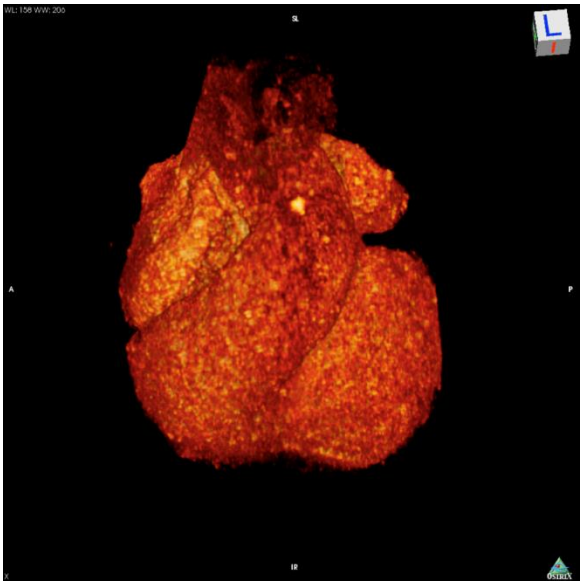

Figure 8. 2 3D MIP rendering of the E10.5 mouse embryonic heart.

8.12.1 Atrioventricular Septation

Figure 8.3 showed the progression of atrioventricular septation visualized by OCT. Atrioventricular cushion (AVC) was apparent in transverse and sagittal views of E10.5, E11.5 and E12.5 mouse embryonic hearts, indicated by yellow arrows. Due to the similar scattering property and insufficient resolution, we couldn't

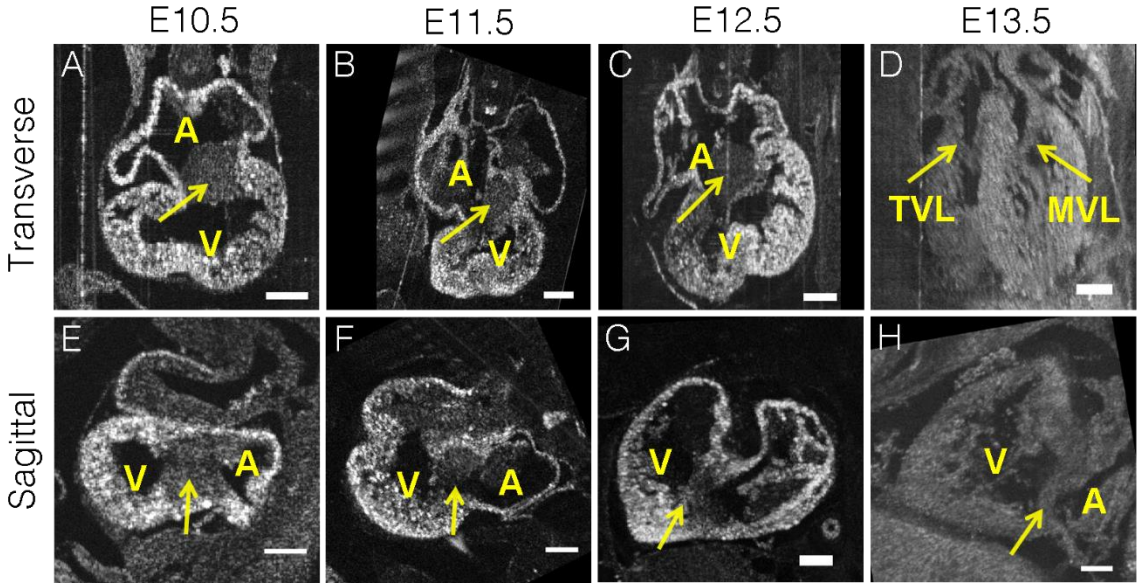

Figure 8. 3 Atrioventricular septation in transverse and sagittal views of (A,E) E10.5, (B, F) E11.5, (C, G) E12.5 and (D, H) E13.5 OCT images of mouse embryonic hearts. Arrows: atrioventricular cushion; TVL: tricuspid valve leaflet; MVL: mitral valve leaflet; A: Atrium; V: Ventricle. Scale bar: 200µm.

further distinguish the inferior, superior, right lateral and left lateral atrioventricular cushions in OCT images. Starting from E12.5, AVC underwent significant structural remodeling. Results of remodeling were presented in transverse view of E13.5 image (**Figure 8.3 D**), showing formation of mitral valve leaflets (MVL, between left atrium and left ventricles) and tricuspid valve leaflet (TVL, between right atrium and right ventricles). Formation of these two valve leaflets marked a complete septation between atria and ventricles.

8.12.2 Atrial and Ventricular Septations

Figure 8.4 showed the results of visualization of progressions of atrial and ventricular septations during E10.5 - E13.5 stages in OCT images. Starting from E10.5, a thin layer of cells called interventricular septum (IVS) started to form from the bottom of the ventricular chamber (Orange arrows in both transverse and coronal views in Figure 8.4). As the mouse embryonic heart further developed, IVS extended and thickened (**Figure 8.4G**). In E12.5 image, IVS moved closer to AVC. In E13.5 image, complete closure of IVS in ventricular chamber was observed, indicating complete ventricular septation. In **Figure 8.4 A-C**, septum

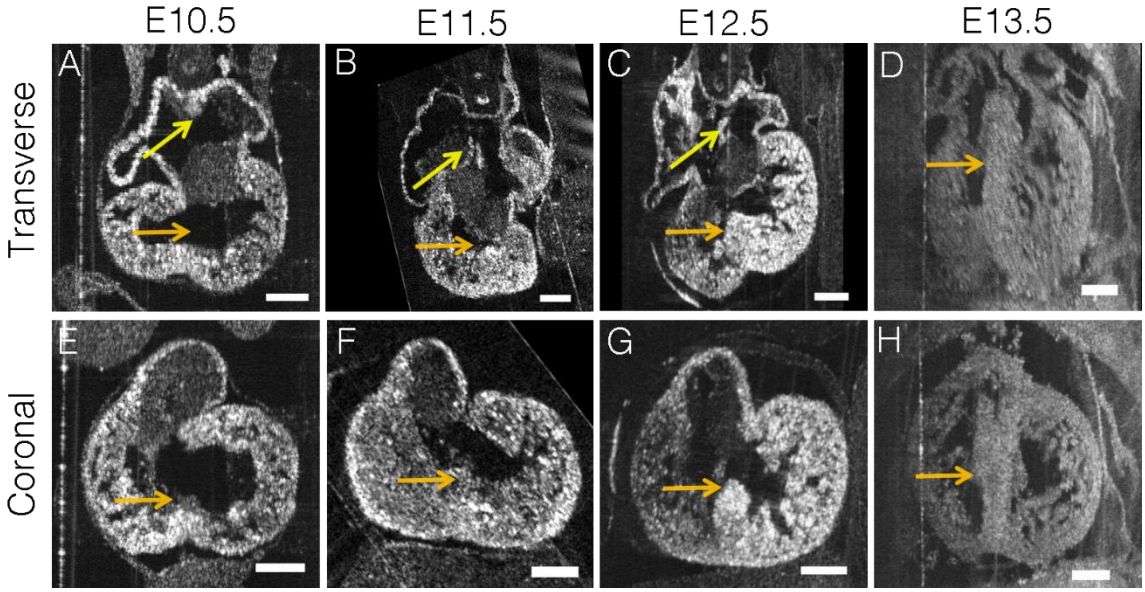

Figure 8. 4 Atrial septation (Yellow arrows) and ventricular septation (Orange arrows) in transverse and coronal views of (A, E) E10.5, (B, F) E11.5, (C, G) E12.5 and (D, H) E13.5 OCT images of mouse embryonic hearts. Orange arrows: interventricular septum (IVS); Yellow arrows: Septum primum (SP). Scale bar: 200µm

primum (SP) was observed to grow from top and move downward, indicated by yellow arrows, marking the progression of atrial septation.

8.12.3 Pharyngeal Arch Arteries

One key feature of vascular development in embryonic mice is pharyngeal arch arteries (PAAs), which undergo a series of transformations between E8.5 – E13 [528]. With micron-scale resolution, we could distinguish pairs of pharyngeal arch arteries of early-stage mouse embryos in OCT images. **Figure 8.5** showed the results of OCT images of PAAs in E9.5 and E10.5 mouse embryos in oblique views. In E9.5, the second and the third pairs of PAAs were recognized and labeled (**Figure 8.5 A**), which were thickest during this stage. The size of the second pair of PAA was ~40 µm by measuring the width of the labeled vessel cavity (black tube) in Figure 8.5A In E10.5, the 3rd, 4th pairs of PAAs were clearly observed arising from aortic sac (AS) region (**Figure 8.5 B**, labeled). The 3rd pair of PAAs had a vessel size of ~60 µm and the 4rd pair had a size of ~90 µm, characterized by measuring the size of black holes in the image. The 6th pair of

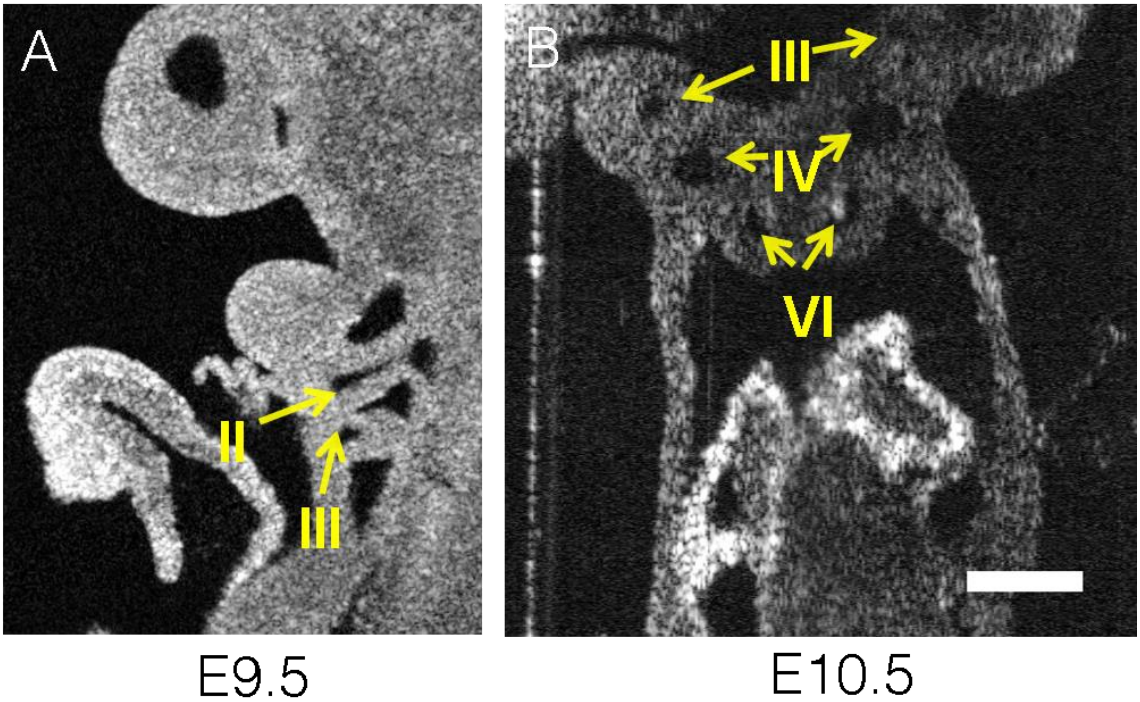

Figure 8. 5 OCT images of pharyngeal arch arteries (PAAs) in E9.5 and E10.5 mouse embryos. (A) OCT image of E9.5 mouse embryo, showing 2nd and 3rd pairs of pharyngeal arch arteries. (B) OCT images of E10.5 mouse embryo, showing 3rd, 4th and 6th pairs of pharyngeal arch arteries. Scale bar: 200µm.

PAAs were formed under the 3rd and 4th pairs, which were distinguished in OCT images (**Figure 8.5B**, labeled) with a size of 50 - 60 µm. The sizes of these vessels were comparable to the literature finding [528].

8.12.4 Outflow Tract Transformation

The other feature of developing mouse embryonic heart in later stages is the remodeling of common outflow track (OFT), which included aortic sac, truncus and conus and contributed to the formation of outlets, valves and aortic and pulmonary trunks by E13.5 [436]. **Figure 8.6** showed OCT images of the development of common OFT from E10.5 to E13.5. In E10.5, common outflow track was revealed as a tube structure in

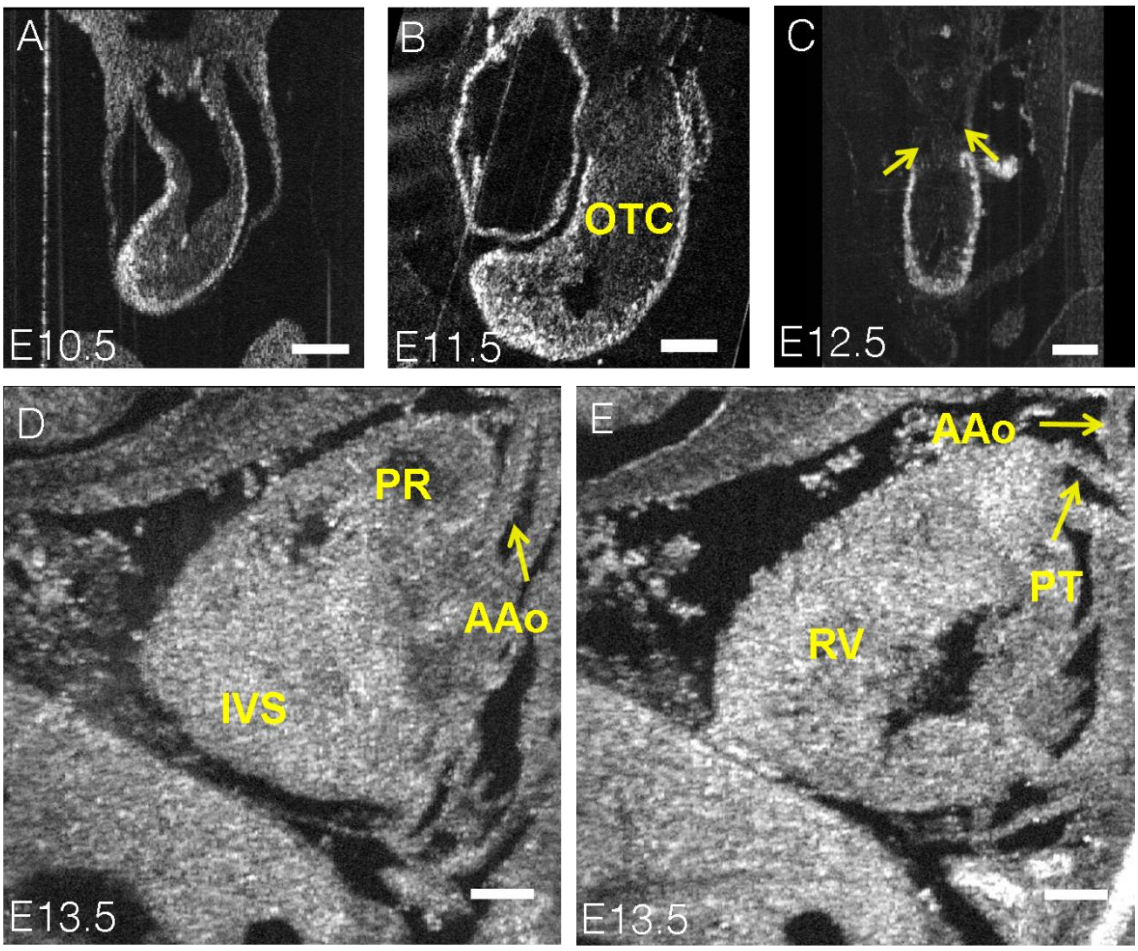

Figure 8. 6 Progression of common outflow tract (OFT) in OCT images. (A) Outflow tract in E10.5 mouse embryo hearts, which includes aortic sac, truncus and conus. (B) The filling of outflow-tract cushion tissue in E11.5 mouse embryo hearts (C) Septation of aortic and pulmonary channel in outflow tract in E12.5 mouse embryo hearts. (D, E) showed the remodeling of outflow tract in E13.5 mouse embryo hearts. It is merged into heart walls and connected to ascending aorta and pulmonary trunk. OTC: outflow tract cushion tissue. PR: pulmonary root, IVS: interventricular septum. RV: right ventricle, PT: pulmonary artery. AAo: ascending aorta. Scale bar: 200 µm

Figure 8.6 A. Note that common OFT was also clearly visible in the sagittal view of E10.5 mouse embryonic heart in Figure 8.2 B, right above the atrium and ventricle. In the distal end of OFT (top region), protruding front of septation complex started to move downward to divide the OFT in two separate channels. In E11.5, the lumen of common outflow tract was filled with outflow tract cushion tissue (OTC), growing from the outflow tract wall (**Figure 8.6 B**). In E12.5, pulmonary and aortic channels, which were shown as two black holes at the distal end of OFT, could be observed in **Figure 8.6 C** and indicated by yellow arrows. They would later form pulmonary and aortic roots (PR, AoR) and connect to ascending aorta (AAo) and pulmonary artery (PT). **Figure 8.6 D-E** showed OCT images of the significant remodeled OFT In E13.5. The truncus and cones merged into vertricular walls. The distal end of OFT was completely divided into ascending aorta (AAo) and pulmonary trunk (PT) orienting in different directions, marking the complete septation of common OFT.

8.13 Phenotyping Congenital Heart Defects in Mutant Mouse Embryos with OCT

We demonstrated that OCT and optical clearing technology could work together to characterize congenital heart defects (CHDs) in mutant mouse embryo models. **Figure 8.7** showed an example of phenotyping CHDs in E16.5 mutant mouse embryos with OCT. In **Figure 8.7 A**, E16.5 wild type (WT) mouse embryonic heart

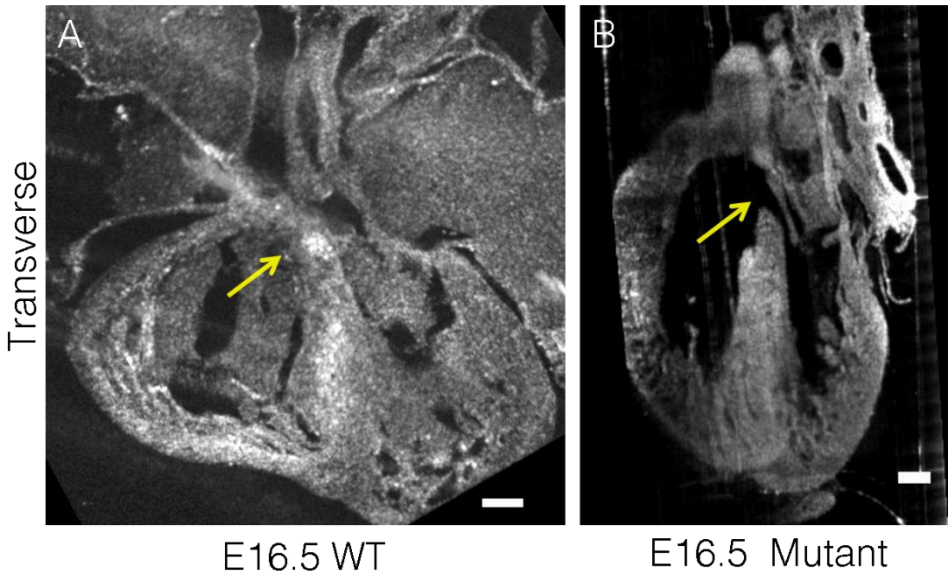

Figure 8. 7 OCT images of ventricular septal defect (VSD) in E16.5 mutant mouse embryonic heart. (A) E16.5 wild type (WT) mouse embryonic heart showing normal interventricular septum (IVS). (B) E16.5 mutant mouse embryonic heart showing the defected IVS that failed to septate the ventricles.

showed a well-developed interventricular septum (IVS) that completely septated the ventricles. As a comparison, **Figure 8.7 B** showed the E16.5 mutant mouse embryonic heart with ventricular septal defect (VSD), one of the most common CHDs found in mutant mouse embryos (See Appendix 8.1). A defect in the IVS was found (indicated by yellow arrow), yielding the failure of ventricular septation.

8.14 Discussions

8.14.1 Comparison between OCT plus optical clearing technique with micro-CT

In this chapter, we have presented the protocol using OCT in combination with optical clearing technique to generate atlases of developing mouse embryonic hearts. 3D, high-resolution OCT images of mouse embryonic hearts from E9.5 to E16.5 were presented, demonstrating its potential in phenotyping CHDs in mutant mouse models. In the following section, we would compare this protocol with other working protocols with different imaging modalities.

Table 8. 8 Comparison of OCT and Micro-CT Protocols to Characterize Mouse Embrynoic Hearts

	OCT protocol	**Micro-CT protocol**
Handling	E13.5 & E16.5. Dissected Heart	No
Staining	No	0.1N Lugol solution Before E15.5: Overnight; E18.5: 3-5 days. Postnatal: 7-10 days Or 0.025N Lugol solution for 48hr.
Optical clearing	3DISCO: ~18 hr (E10.5 or later stages)	(Optional) CLARITY for hydrogel stabilization: 3 days (E15.5 or later stages). Note: This step can shorten the iodine staining from 2 weeks to 3-5 days for E18.5 mouse embryo
Resolution	~5 µm × ~6 µm	Resolution is determined by voxel size: E9.5: 3 µm; E12.5: 5 µm; E15.5 or later: 11 µm
Imaging time	seconds for 3 × 3 × 2.2 mm^3, sufficient to cover E12.5 heart in a dataset	50 min for E9.5 75 min for E12.5 and E15.5 150 min for E18.5
in vivo capability	Yes (Prior to E10.5 stage)	Yes (only for bones). Soft tissues:Not applicable.
Sample Shrinkage	Yes	Yes
System Cost (Commercial)	~$50,000 - 70,000	~$200,000-450,000

Micro-CT is one popular option to characterize small animals as well as embryos. With the revised protocol of iodine staining, micro-CT can provide 3D high-resolution and high contrast data in soft tissue, enabling the characterization of cardiovascular structure in mouse embryos [448]. Up to now, several groups

have shown the capability of micro-CT with iodine staining to characterize different stages of mouse embryos from E9.5 to postnatal day 3 (P3), showing a complete development of mouse embryonic hearts [448, 529, 530].

Table 8.8 shows a comparison between our OCT protocol with the micro-CT protocols to characterize mouse embryonic heart. The major advantage of OCT protocol is the short image acquisition time. A 3D dataset of $3 \times 3 \times 2.2$ mm^3 could be captured in ~30 seconds with a voxel size of ~$4 \times 4 \times 5$ µm^3, as compared to 50 min for E9.5 mouse embryo with micro-CT. For larger samples, OCT requires stitching of the datasets while micro-CT requires larger number of scans. In both cases, the total imaging time grows proportionally. However, as compared to long preparation time for both protocols, the significance of OCT imaging advantage is reduced. For early-stage mouse embryos (before E10.5), OCT can characterize them without optical clearing, yielding the advantage of OCT in *in vivo*, real-time characterization of mouse embryonic heart. Also, dynamic process of embryonic heart could also be monitored[452], which is not applicable for micro-CT. Between E10.5 – E15.5, OCT protocol requires the optical clearing of the sample for ~18 hr, while micro-CT protocol requires the incubation of sample in iodine solution (Lugol solution) for overnight to 48 hr. The time for the preparation step is comparable for both protocols. After E15.5, the additional step of hydrogel embedding and longer incubation of iodine solution significantly lengthen the overall time for micro-CT characterization of mouse embryos.

Regarding the resolution, image quality for both modalities can be comparable. Since micro-CT has longer imaging time and the image reconstruction is based on rotated scans from different angles with the sample rotating during the scan, micro-CT suffers more from the motion artifacts during the reconstruction, as compared to the point-scanning scheme of OCT. The hydrogel-embedding technique by CLARITY can stabilize the sample with minimal tissue distortion during the rotation, at a cost of 3 day incubation [529].

Both OCT and micro-CT systems are commercially available in the market. However, the cost of a commercial micro-CT system can be several times higher than a standard OCT system [531]. For a budget limit option to characterize mouse embryos, OCT would be a better choice.

8.14.2 Comparison between OCT and OPT Protocols

Singh et al. has conducted a study to compare the performance of OCT and OPT imaging of mouse embryos from E9.5 to E13.5 [449]. He concluded that OCT is better suited for live imaging of early stage mouse embryos while OPT has better contrast and image quality. He also pointed out that the optical clearing would induce the shrinkage of embryonic organs and labeled as the drawback of OPT technology. However, if optical clearing is performed prior to both OCT and OPT imaging, the situation becomes the same. In such case, the comparison between OCT and OPT is similar to the question: whether we should use microscope in transmission or reflection mode.

Table 8.9 summarizes a comparison between OCT and OPT. The information of OPT is gathered from Singh et al. [449] and Watson et al. [532]. It would be fairer to compare the OPT with the visible light OCT [23] since the central wavelength of the light source is comparable. If both system uses the same wavelength and the same low-magnification objective lens, the lateral resolution, penetration depth and the depth of focus

Table 8. 9 A comparison between OCT and OPT

	Optical Coherence Tomography (OCT)	**Optical Projection Tomography (OPT)**
λ	800 nm, 1060 nm, 1300 nm, **560 nm**	Visible light (i.e. 482nm)
NA	Low magnification	Low magnification
Contrast	Scattering	Transmission Autofluorescence
SNR from sample [449]	26 dB (E13.5)	51 dB (E13.5)
Resolution	Comparable	
Penetration Depth	Comparable	
DOF	Comparable	
Imaging time	50–250 fps (standard SD-OCT) 200-1000 fps (SS-OCT)	0.5 – 2 fps
Motion Artifact	Mild	Severe
Commerical Availability	Yes.	No.

(DOF) would be exactly the same since they follow the same optical principles. With the back-projection, the lateral resolution of the OPT system might be affected. Currently, the OCT has faster image acquisition time. A volume data can be captured by OCT in seconds, while OPT obtains a volume data in minutes. With the extended exposure time, the SNR of OPT is better than OCT. However, the SNR difference can be purely attributed to the exposure time difference. If we take the average of 100 frames to get a frame of OCT image,

the SNR would increase by 20 dB, making the SNR of OCT comparable with SNR of OPT. In another aspect, OCT suffers less from motion artifacts with short scanning time while OPT suffers more from motion artifacts. Furthermore, the motorized rotation stage would induce a higher chance of sample motion. At last, OCT is a mature technology and is commercially available. If both OCT and OPT are custom built, the price comparison will fall on the choice of the light source and the camera.

8.14.3 Potential of Dual-modality with OCT and Light-sheet Microscopy

Wu et al. has conducted a study comparing the performance of OCT and light-sheet microscopy on the mouse embryo imaging [533]. OCT showed the overall structure of the mouse embryo while light sheet microscopy highlighted specfic regions or organs labeled by fluorescent dyes. Their results pointed out a promising aspect of combining these two modalities to provie more comprehensive characterization of mouse embryos. In the case of optical cleared mouse embryos, the dual-modality is still promising. However, the choices of the fluorescent dyes would be significantly limited since lots of fluorescent signals would be quenched or bleached after fixation, dehydration and decoloring steps. See the review paper of Liu et al. [486] and Tainaka et al. [487] for a list of fluorescent dyes that are compatible with different optical clearing protocols.

Note that OPT and light sheet microscopy have been integrated together to examine the E12.5 mouse embryonic head, demonstrating the combined advantages of fluorescent and nonfluorescent contrast in embryonic studies [534].

8.15 Summary

In this chapter, we have demonstrated OCT atlas of mouse embryonic hearts from E9.5 to E16.5, showing the progression of embryonic heart development. Development of four-chambered cardiac structure was identified in the OCT atlas. Critical morphological changes during later stages of heart development, such as atrial and ventricular septations, atrio-ventricular septation was revealed. Vascular development such as forming of pharyngeal arch arteries and remodeling of common outflow tract was clearly observed. Moreover, we have demonstrated that OCT is capable to detect congenital heart defects (CHDs) in mutant mouse embryos. We have shown that optical-clearing method has significantly enhanced the penetration depth of OCT, making imaging of whole embryo heart possible beyond E10.5 stages. Given its advantages

of fast imaging speed, resolution and low system cost, OCT combining with optical clearing techniques would be a promising protocol for embryonic researches as well as phenotyping CHDs in mutant mouse models.

Appendix 8.1 List of Common Abnormalies Occurred in Transgenic Embryonic Mouse Hearts

Table 8. 10 List of Common Abnormalies Occurred in Transgenic Embryonic Mouse Hearts [436]

Main Categories	**Subcategories**
Abnormal *Heart Septum* Morphology	• Abnormal ventricular septum morphology: *Ventricular Septal Defects (VSD)* • Abnormal atrial septum morphology: *Atrial Septal Defects (ASD)*
Abnormal *Outflow Tract* Development	• Abnormal OFT septation: *Persistent Truncus Arteriosus (PTA)* • Malalignment of the great vessels: *Double Outlet Right Ventricle (DORV)*
Abnormal *Cardiac Valve* Morphology	• Abnormal atrioventricular valve morphology: *Atresia of Mitral or Tricuspid Valve* • Abnormal semilunar valve morphology • Heart valve hyperplasia
Abnormal *Myocardial Trabeculae* Morphology	• Poorly developed ventricular trabeculae • Absent myocardial traveculae
Abnormal *Aortic Arch/Aorta* Morphology	• Abnormal patterning of the aortic arch • Interrupted aortic arch • Right aortic arch • Retroesophageal right subclavian artery • Overriding aorta • Double aortic arch • Coarctation of aorta • Cervical aortic arch
Abnormal *Looping*	• Abnormal direction of looping • Failure of looping
Thin *Myocardial Wall*	
Abnormal *Endocardial Cushion*	• Absent endocardial cushion • Decreased endocardial cushion size: *Complete atrioventricular canal defect (CAVC)* • Failure of endocardial cushion closure • Increased endocardial cushion size
Abnormal *Heart Tube* Morphology	
Abnormal *Atrioventricular Canal*	
Dextrocardia	
Abnormal *Pulmonary Trunk* Morphology	
Mesocardia	
Abnormal *Sinus Venosus*	

The corresponding embryonic heart regions in the main categories are labeled in italic. The most common abnormalies in the subcategories are labeled in italic.

Chapter 9: Summary and Outlook

Optical coherence tomography (OCT) is an established optical imaging modality which can obtain label-free, non-destructive 3D images of samples with micron-scale resolution and millimeter penetration. Serving as "optical biopsy", OCT can be utilized to characterize the internal structures of both biological and non-biological samples *in situ*, up to 1-2 mm below the sample surface. In addition, high-speed OCT can be used to perform time-lapse (or longitudinal) imaging of samples to monitor their dynamic changes over time.

In the first part of my dissertation, I focused on discussing the technical development of high-speed OCT technologies. In the first chapter (Chapter 1), I briefly introduced the OCT technology, with the focus on the principles, key performance metrics and literature reviews of OCT technology in various biomedical applications. Next, I presented a detailed tutorial on how to build a custom spectral domain OCT (SD-OCT) in Chapter 2, including the descriptions of system configuration, a detailed procedure of system alignment and a detailed protocol of performance characterization of the system. In the next chapter, I moved to the space-division-multiplexing OCT (SDM-OCT) technology, a parallel imaging OCT technology with a more complex and intricate system setup. In the chapter, I covered the principles of SDM-OCT, step-by-step procedures to build a first generation fiber-based SDM-OCT and a first generation chip-based SDM-OCT, and characterization of their performance. I have demonstrated the feasibility of both fiber-based and chip-based SDM-OCT to perform *in vivo*, high-speed imaging of human fingers. In Chapter 4, I presented my work on improving the performance of SDM-OCT with the implementation of the galvo-based phase-modulation full-range technique, which can facilitate the SDM-OCT acquisition of multi-channel images with reduced hardware requirements. Various approaches to realize complex reconstruction of interference signals was first reviewed, following with detailed descriptions of theoretical foundations, experimental designs and post-processing procedures of the galvo-based phase-modulation full-range technique. The feasibilty of the full-range SDM-OCT (FR-SDM-OCT) has been demonstrated by characterizing its performance in mirror and tape images and acquiring the images from human fingers *in vivo*. We should note that, full-range technique can also expand the potential of SDM-OCT technology to render more channels

simultaneously within a doubled imaging range, as compared to the total imaging range of the standard SDM-OCT system with the same experimental setup and imaging protocol.

In the second part of my dissertation, I presented the unique observations using high-speed OCT systems to characterize dynamic processes in biological and non-biological samples. **Figure 9.1** showed a timeline indicating the duration (or time window) for different dynamic processes in biological and non-biological samples. By choosing the interval for different time-lapse acquisition protocols, we can utilize OCT to monitor both fast dynamics and slow dynamics in samples. In Chapter 5, I presented a functional OCT, OCT

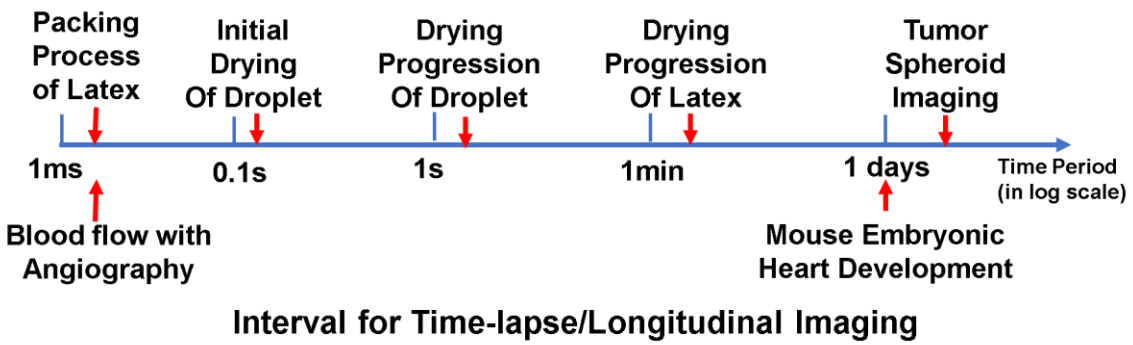

Figure 9. 1 A timeline showing the duration (time window) for different dynamic processes in biological and non-biological samples.

angiography (OCTA), to visualize the vascular network in the human skin. Specifically, I demonstrated the feasibility of SDM-OCT to visualize the capillary network in the human finger nail, showing the advantages of SDM-OCT technology with a parallel imaging scheme to further improve the imaging speed and the field of view (FOV) with reduce motion artifacts. In Chapter 6, I covered my research work of characterization of drying process of droplets and latex systems. With a short time window from a few milliseconds to ~1 second, high-speed OCT systems can capture the fast fluid flows in the drying droplets and the fast packing process in drying latex system. With a multi-modal imaging platform including OCT, gravimetry and video measurements, we successfully characterized progressions of global and local drying phenomena in polystyrene latex system (~500 min). In Chapter 7, I presented my work on establishing an OCT-based, 3D high-throughput imaging (HTI) platform to perform screening of tumor spheroid assays in 96-well plate. I showed my work on developing a program for quantification of tumor spheroid morphology (i.e. diameter, height, volume) to track growth kinetics. I also developed a strategy to label the 3D distribution of dead-cell regions within the tumor spheroid for viability characterization, based on intrinsic optical attenuation

contrast. With the established platform, I performed the OCT screening of tumor spheroid invasion assays to characterize 3D cell invasion and evaluate inhibition effects of drugs. In Chapter 8, I described my research work on utilizing OCT to image mouse embryonic hearts at different developmental stages, with the implementation of optical clearing methods to enhance the light penetration in mouse embryos. A representation result of using OCT to phenotype congenital heart defects (CHDs) in mutant mouse embryo models was shown.

At the end of Chapter 5-8, I have shown the potential OCT applications in different research fields and discussed how advances in OCT technology can benefit various OCT applications. Overall, two trends of future OCT research work can be envisioned. First, OCT with a MHz A-scan rate (or higher) will potentially enable the video-rate volumetric imaging, bringing in new applications with 4D imaging capability [352]. Second, with a broad dissemination of OCT technology, OCT can go beyond biomedical application and have more significant impacts in non-destructive evaluation and testing (NDE/T) of samples in both fundamental science and industrial applications [62].

Publications

1. **Huang, Y.**, Jerwick, J., Liu, G., Zhou, C., Full-range space-division multiplexing optical coherence tomography angiography, 2019 (in preparation).
2. **Huang, Y.,** Huang, H., Jiang, Z., Ou-yang, H.D., Zhou, C., Non-destructive characterization of drying dynamics in droplets and colloidal systems using optical coherence tomography, in *Optical Coherence Tomography and Its Non-medical Applications*, ed. Wong, M. (in preparation)
3. **Huang, Y.**, Degenhardt, K.R., Astrof, S., Zhou, C., "Imaging of murine embryonic cardiovascular development using optical coherence tomography", (in preparation)
4. Shi, W., Reid, L., **Huang, Y.**, Uhl, C., He, R., Zhou, C., Liu, Y., Bi-layer blood vessel mimicking microfluidic platform for tumor drug screening based on co-culturing 3D tumor spheroids and endothelial layers (submitted)
5. **Huang, Y.**, Zou, J., Badar, M., Liu, J., Shi, W., Wang, S., Guo, Q., Wang, X., Kessel, S., Chan, L. L., Li, P., Liu, Y., Qiu, J., Zhou, C., Longitudinal morphological and physiological monitoring of three-dimensional tumor spheroids using optical coherence tomography, *Journal of Visualized Experiments*, (144), e59020 (2019).
6. Huang, H.[+], **Huang, Y.**[+], Lau, W. Ou-Yang, H.D., Zhou, C., El-Aasser, M.S., Integrating optical coherence tomography with gravimetric and video analysis (OCT-Gravimetry-Video method) for studying the drying process of polystyrene latex system, *Scientific Reports*, 8, 12962 (2018).
7. Shi, W., Kwon, J., **Huang, Y.**, Tan, J., Uhl, C., He, R., Zhou, C., Liu, Y., Facile tumor spheroids formation in large quantity with controllable size and high uniformity, *Scientific Reports*, 8; 6837 (2018)
8. **Huang, Y.**, Wang, S., Guo, Q., Kessel, S., Rubinoff, I., Chan, L.L.Y, Li, P., Liu, Y., Qiu, J., Zhou, C., Optical coherence tomography detects necrotic regions and volumetrically quantifies multicellular tumor spheroids. *Cancer Research*, 77(21), 6011 (2017).
9. **Huang, Y**., Badar, M., Nitkowski, A., Weinroth, A., Tansu, N., Zhou, C., Wide-field high-speed space-division multiplexing optical coherence tomography using an integrated photonic device, *Biomedical Optics Express*, 8(8), 3856 (2017).

10. Davidson, Z. S., **Huang, Y.**, Gross, A., Martinez, A., Still, T., Zhou, C., Collings, P. J., Kamien, R. D., Yodh, A. G., Deposition and drying dynamics of liquid crystal droplets. *Nature Communications*, 30(8),15642 (2017).

11. Men, J.[+], **Huang, Y.**[+], Solanki, J., Zeng, X., Alex, A., Jerwick, J., Zhang, Z., Tanzi, R.E., Li, A., Zhou, C., Optical coherence tomography for brain imaging and developmental biology. *IEEE Journal of Selected Topics in Quantum Electronics*, 22(4), 6803213 (2016).

References

1. D. Huang, E. A. Swanson, C. P. Lin, J. S. Schuman, W. G. Stinson, W. Chang, M. R. Hee, T. Flotte, K. Gregory, C. A. Puliafito, and a. et, "Optical coherence tomography," Science **254**, 1178 (1991).
2. J. Fujimoto and E. Swanson, "The Development, Commercialization, and Impact of Optical Coherence Tomography," Investigative Ophthalmology & Visual Science **57**, OCT1-OCT13 (2016).
3. T. Klein and R. Huber, "High-speed OCT light sources and systems [Invited]," Biomed. Opt. Express **8**, 828-859 (2017).
4. J. F. de Boer, R. Leitgeb, and M. Wojtkowski, "Twenty-five years of optical coherence tomography: the paradigm shift in sensitivity and speed provided by Fourier domain OCT [Invited]," Biomed. Opt. Express **8**, 3248-3280 (2017).
5. E. A. Swanson, J. A. Izatt, M. R. Hee, D. Huang, C. P. Lin, J. S. Schuman, C. A. Puliafito, and J. G. Fujimoto, "In vivo retinal imaging by optical coherence tomography," Opt. Lett. **18**, 1864-1866 (1993).
6. A. F. Fercher, C. K. Hitzenberger, G. Kamp, and S. Y. El-Zaiat, "Measurement of intraocular distances by backscattering spectral interferometry," Optics Communications **117**, 43-48 (1995).
7. S. R. Chinn, E. A. Swanson, and J. G. Fujimoto, "Optical coherence tomography using a frequency-tunable optical source," Opt. Lett. **22**, 340-342 (1997).
8. G. Haeusler and M. W. Lindner, *"Coherence radar" and "Spectral radar"- new tools for dermatological diagnosis* (SPIE, 1998), Vol. 3, pp. 21-31, 11.
9. A. M. Rollins, M. D. Kulkarni, S. Yazdanfar, R. Ung-arunyawee, and J. A. Izatt, "In vivo video rate optical coherence tomography," Opt. Express **3**, 219-229 (1998).
10. R. Leitgeb, C. Hitzenberger, and A. Fercher, "Performance of fourier domain vs. time domain optical coherence tomography," Opt. Express **11**, 889-894 (2003).
11. J. F. de Boer, B. Cense, B. H. Park, M. C. Pierce, G. J. Tearney, and B. E. Bouma, "Improved signal-to-noise ratio in spectral-domain compared with time-domain optical coherence tomography," Opt. Lett. **28**, 2067-2069 (2003).

12. M. Choma, M. Sarunic, C. Yang, and J. Izatt, "Sensitivity advantage of swept source and Fourier domain optical coherence tomography," Optics Express **11**, 2183-2189 (2003).

13. M. Wojtkowski, T. Bajraszewski, P. Targowski, and A. Kowalczyk, "Real-time in vivo imaging by high-speed spectral optical coherence tomography," Opt. Lett. **28**, 1745-1747 (2003).

14. B. Potsaid, I. Gorczynska, V. J. Srinivasan, Y. Chen, J. Jiang, A. Cable, and J. G. Fujimoto, "Ultrahigh speed Spectral / Fourier domain OCT ophthalmic imaging at 70,000 to 312,500 axial scans per second," Opt. Express **16**, 15149-15169 (2008).

15. W. Wieser, B. R. Biedermann, T. Klein, C. M. Eigenwillig, and R. Huber, "Multi-Megahertz OCT: High quality 3D imaging at 20 million A-scans and 4.5 GVoxels per second," Opt. Express **18**, 14685-14704 (2010).

16. J. Kang, P. Feng, X. Wei, E. Y. Lam, K. K. Tsia, and K. K. Y. Wong, "102-nm, 44.5-MHz inertial-free swept source by mode-locked fiber laser and time stretch technique for optical coherence tomography," Opt. Express **26**, 4370-4381 (2018).

17. J. S. Schuman, M. R. Hee, A. V. Arya, T. Pedut-Kloizman, C. A. Puliafito, J. G. Fujimoto, and E. A. Swanson, "Optical coherence tomography: a new tool for glaucoma diagnosis," Curr Opin Ophthalmol **6**, 89-95 (1995).

18. M. R. Hee, C. A. Puliafito, C. Wong, J. S. Duker, E. Reichel, B. Rutledge, J. S. Schuman, E. A. Swanson, and J. G. Fujimoto, "Quantitative Assessment of Macular Edema With Optical Coherence Tomography," Archives of Ophthalmology **113**, 1019-1029 (1995).

19. C. A. Puliafito, M. R. Hee, C. P. Lin, E. Reichel, J. S. Schuman, J. S. Duker, J. A. Izatt, E. A. Swanson, and J. G. Fujimoto, "Imaging of Macular Diseases with Optical Coherence Tomography," Ophthalmology **102**, 217-229 (1995).

20. M. R. Hee, C. R. Baumal, C. A. Puliafito, J. S. Duker, E. Reichel, J. R. Wilkins, J. G. Coker, J. S. Schuman, E. A. Swanson, and J. G. Fujimoto, "Optical Coherence Tomography of Age-related Macular Degeneration and Choroidal Neovascularization," Ophthalmology **103**, 1260-1270 (1996).

21. E. A. Swanson and J. G. Fujimoto, "The ecosystem that powered the translation of OCT from fundamental research to clinical and commercial impact [Invited]," Biomed. Opt. Express **8**, 1638-1664 (2017).

22. M. Wojtkowski, "High-speed optical coherence tomography: basics and applications," Applied Optics **49**, D30 (2010).

23. X. Shu, L. J. Beckmann, and H. F. Zhang, *Visible-light optical coherence tomography: a review* (SPIE, 2017), Vol. 22, pp. 1-14, 14.

24. J. Yi, W. Liu, S. Chen, V. Backman, N. Sheibani, C. M. Sorenson, A. A. Fawzi, R. A. Linsenmeier, and H. F. Zhang, "Visible light optical coherence tomography measures retinal oxygen metabolic response to systemic oxygenation," Light: Science &Amp; Applications **4**, e334 (2015).

25. J. Yi, Q. Wei, W. Liu, V. Backman, and H. F. Zhang, "Visible-light optical coherence tomography for retinal oximetry," Optics Letters **38**, 1796-1798 (2013).

26. J. Yi, S. Chen, X. Shu, A. A. Fawzi, and H. F. Zhang, "Human retinal imaging using visible-light optical coherence tomography guided by scanning laser ophthalmoscopy," Biomedical Optics Express **6**, 3701-3713 (2015).

27. N. Nishizawa, H. Kawagoe, M. Yamanaka, M. Matsushima, K. Mori, and T. Kawabe, "Wavelength Dependence of Ultrahigh-Resolution Optical Coherence Tomography Using Supercontinuum for Biomedical Imaging," IEEE Journal of Selected Topics in Quantum Electronics **25**, 1-15 (2019).

28. S. P. Chong, C. W. Merkle, D. F. Cooke, T. Zhang, H. Radhakrishnan, L. Krubitzer, and V. J. Srinivasan, "Noninvasive, in vivo imaging of subcortical mouse brain regions with 1.7 μm optical coherence tomography," Optics letters **40**, 4911-4914 (2015).

29. A. C. Akcay, J. P. Rolland, and J. M. Eichenholz, "Spectral shaping to improve the point spread function in optical coherence tomography," Optics Letters **28**, 1921-1923 (2003).

30. R. Tripathi, N. Nassif, J. S. Nelson, B. H. Park, and J. F. de Boer, "Spectral shaping for non-Gaussian source spectra in optical coherence tomography," Optics Letters **27**, 406-408 (2002).

31. D. L. Marks, P. S. Carney, and S. A. Boppart, *Adaptive spectral apodization for sidelobe reduction in optical coherence tomography images* (SPIE, 2004), Vol. 9, pp. 1281-1287, 1287.

32. R. A. Leitgeb, W. Drexler, A. Unterhuber, B. Hermann, T. Bajraszewski, T. Le, A. Stingl, and A. F. Fercher, "Ultrahigh resolution Fourier domain optical coherence tomography," Opt. Express **12**, 2156-2165 (2004).

33. W. Drexler, M. Liu, A. Kumar, T. Kamali, A. Unterhuber, and R. A. Leitgeb, *Optical coherence tomography today: speed, contrast, and multimodality* (SPIE, 2014), Vol. 19, p. 34.

34. M. A. X. Born and E. Wolf, *Principles of Optics (Sixth Edition)* (Pergamon, 1980).

35. T. Still, P. J. Yunker, and A. G. Yodh, "Surfactant Induced Marangoni Eddies Alter the Coffee-Rings of Evaporating Colloidal Drops," Langmuir **28**, 4984-4988 (2012).

36. W. Drexler and J. G. Fujimoto, *Optical Coherence Tomography: Technology and Applications*, 2 ed. (Springer International Publishing, 2015), pp. XXX,2571.

37. M. Wojtkowski, B. Kaluzny, and R. J. Zawadzki, "New Directions in Ophthalmic Optical Coherence Tomography," Optom. Vis. Sci. **89**, 524-542 (2012).

38. W. Drexler and J. G. Fujimoto, "State-of-the-art retinal optical coherence tomography," Prog. Retin. Eye Res. **27**, 45-88 (2008).

39. Z. A. Ali, K. K. Galougahi, A. Maehara, R. A. Shlofmitz, O. Ben-Yehuda, G. S. Mintz, and G. W. Stone, "Intracoronary Optical Coherence Tomography 2018," Jacc-Cardiovascular Interventions **10**, 2473-2487 (2017).

40. T. Yonetsu, B. E. Bouma, K. Kato, J. G. Fujimoto, and I. K. Jang, "Optical Coherence Tomography - 15 Years in Cardiology," Circ. J. **77**, 1933-1940 (2013).

41. T. Kume and S. Uemura, "Current clinical applications of coronary optical coherence tomography," Cardiovasc. Interv. Ther. **33**, 1-10 (2018).

42. G. J. Tearney, "Intravascular optical coherence tomography," European Heart Journal **39**, 3685-3686 (2018).

43. J. Olsen, J. Holmes, and G. B. E. Jemec, *Advances in optical coherence tomography in dermatology—a review* (SPIE, 2018), Vol. 23, pp. 1-10, 10.

44. M. Liu and W. Drexler, "Optical coherence tomography angiography and photoacoustic imaging in dermatology," Photochemical & Photobiological Sciences (2019).

45. A. J. Deegan and R. Wang, "Microvascular imaging of the skin," Physics in Medicine and Biology (2019).

46. C. L. Leggett, D. K. Chan, and K. K. Wang, "Optical Coherence Tomography: Clinical Applications in Gastrointestinal Endoscopy," in *Endoscopic Imaging Techniques and Tools*, V. J. A. Konda and I. Waxman, eds. (Springer International Publishing, Cham, 2016), pp. 115-128.

47. T.-H. Tsai, C. L. Leggett, A. J. Trindade, A. Sethi, A.-F. Swager, V. Joshi, J. J. Bergman, H. Mashimo, N. S. Nishioka, and E. Namati, *Optical coherence tomography in gastroenterology: a review and future outlook* (SPIE, 2017), Vol. 22, pp. 1-17, 17.

48. J. Wang, Y. Xu, and S. A. Boppart, *Review of optical coherence tomography in oncology* (SPIE, 2017), Vol. 22, pp. 1-23, 23.

49. B. Baumann, "Optical Coherence Tomography for Brain Imaging," in *Advanced Optical Methods for Brain Imaging*, F.-J. Kao, G. Keiser, and A. Gogoi, eds. (Springer Singapore, Singapore, 2019), pp. 49-68.

50. J. Men, Y. Huang, J. Solanki, X. Zeng, A. Alex, J. Jerwick, Z. Zhang, R. E. Tanzi, A. Li, and C. Zhou, "Optical Coherence Tomography for Brain Imaging and Developmental Biology," IEEE Journal of Selected Topics in Quantum Electronics **22**, 120-132 (2016).

51. *Optical Coherence Tomography in Neurologic Diseases* (Cambridge University Press, Cambridge, 2015).

52. T. Shaipanich, H. Pahlevaninezhad, and S. Lam, "Optical Coherence Tomography: A Review," in *Interventions in Pulmonary Medicine*, J. P. Díaz-Jimenez and A. N. Rodriguez, eds. (Springer International Publishing, Cham, 2018), pp. 267-279.

53. M. Y. Kirillin, T. Motovilova, and N. M. Shakhova, *Optical coherence tomography in gynecology: a narrative review* (SPIE, 2017), Vol. 22, pp. 1-9, 9.

54. T. Wang, M. Brewer, and Q. Zhu, "An overview of optical coherence tomography for ovarian tissue imaging and characterization," Wiley Interdisciplinary Reviews: Nanomedicine and Nanobiotechnology **7**, 1-16 (2015).

55. M. Machoy, J. Seeliger, L. Szyszka-Sommerfeld, R. Koprowski, T. Gedrange, and K. Wozniak, "The Use of Optical Coherence Tomography in Dental Diagnostics: A State-of-the-Art Review," J. Healthc. Eng., 31 (2017).

56. Y.-S. Hsieh, Y.-C. Ho, S.-Y. Lee, C.-C. Chuang, J.-c. Tsai, K.-F. Lin, and C.-W. Sun, "Dental Optical Coherence Tomography," Sensors **13**, 8928 (2013).

57. J. E. Freund, M. Buijs, C. D. Savci-Heijink, D. M. de Bruin, J. J. M. C. H. de la Rosette, T. G. van Leeuwen, and M. P. Laguna, "Optical Coherence Tomography in Urologic Oncology: a Comprehensive Review," SN Comprehensive Clinical Medicine **1**, 67-84 (2019).

58. M. J. Hawkshaw, J. B. Sataloff, and R. T. Sataloff, "New Concepts in Vocal Fold Imaging: A Review," Journal of Voice **27**, 738-743 (2013).

59. M. T. El-Haddad and Y. K. Tao, "Advances in intraoperative optical coherence tomography for surgical guidance," Current Opinion in Biomedical Engineering **3**, 37-48 (2017).

60. O. M. Carrasco-Zevallos, C. Viehland, B. Keller, M. Draelos, A. N. Kuo, C. A. Toth, and J. A. Izatt, "Review of intraoperative optical coherence tomography: technology and applications Invited," Biomed. Opt. Express **8**, 1607-1637 (2017).

61. R. Raghunathan, M. Singh, M. E. Dickinson, and K. V. Larin, *Optical coherence tomography for embryonic imaging: a review* (SPIE, 2016), Vol. 21, pp. 1-22, 22.

62. J. Golde, L. Kirsten, C. Schnabel, J. Walther, and E. Koch, "Optical Coherence Tomography for NDE," in *Handbook of Advanced Non-Destructive Evaluation*, N. Ida and N. Meyendorf, eds. (Springer International Publishing, Cham, 2018), pp. 1-44.

63. M. Iwanicka, M. Sylwestrzak, and P. Targowski, "Optical Coherence Tomography (OCT) for Examination of Artworks," in *Advanced Characterization Techniques, Diagnostic Tools and Evaluation Methods in Heritage Science*, D. M. Bastidas and E. Cano, eds. (Springer International Publishing, Cham, 2018), pp. 49-59.

64. P. Targowski and M. Iwanicka, "Optical Coherence Tomography: its role in the non-invasive structural examination and conservation of cultural heritage objects-a review," Appl. Phys. A-Mater. Sci. Process. **106**, 265-277 (2012).

65. R. A. Leitgeb and B. Baumann, "Multimodal Optical Medical Imaging Concepts Based on Optical Coherence Tomography," Front. Physics **6**, 17 (2018).

66. M. J. Gora, M. J. Suter, G. J. Tearney, and X. Li, "Endoscopic optical coherence tomography: technologies and clinical applications [Invited]," Biomed. Opt. Express **8**, 2405-2444 (2017).

67. G. L. Monroy, J. Won, D. R. Spillman, R. Dsouza, and S. A. Boppart, "Clinical translation of handheld optical coherence tomography: practical considerations and recent advancements," J. Biomed. Opt. **22**, 30 (2017).

68. B. N. Anoop, G. N. Girish, P. V. Sudeep, and R. Jeny, "Despeckling Algorithms for Optical Coherence Tomography Images: A Review," in *Advanced Classification Techniques for Healthcare Analysis*, C. Chinmay, ed. (IGI Global, Hershey, PA, USA, 2019), pp. 286-310.

69. D. S. W. Ting, L. R. Pasquale, L. Peng, J. P. Campbell, A. Y. Lee, R. Raman, G. S. W. Tan, L. Schmetterer, P. A. Keane, and T. Y. Wong, "Artificial intelligence and deep learning in ophthalmology," British Journal of Ophthalmology **103**, 167 (2019).

70. P. S. Grewal, F. Oloumi, U. Rubin, and M. T. S. Tennant, "Deep learning in ophthalmology: a review," Canadian Journal of Ophthalmology **53**, 309-313 (2018).

71. O. Thouvenin, C. Apelian, A. Nahas, M. Fink, and C. Boccara, "Full-Field Optical Coherence Tomography as a Diagnosis Tool: Recent Progress with Multimodal Imaging," Appl. Sci.-Basel **7**, 28 (2017).

72. O. Thouvenin, K. Grieve, P. Xiao, C. Apelian, and A. C. Boccara, "En face coherence microscopy [Invited]," Biomed. Opt. Express **8**, 622-639 (2017).

73. R. F. Spaide, J. G. Fujimoto, N. K. Waheed, S. R. Sadda, and G. Staurenghi, "Optical coherence tomography angiography," Prog. Retin. Eye Res. **64**, 1-55 (2018).

74. C.-L. Chen and R. K. Wang, "Optical coherence tomography based angiography [Invited]," Biomed. Opt. Express **8**, 1056-1082 (2017).

75. A. Q. Zhang, Q. Q. Zhang, C. L. Chen, and R. K. K. Wang, "Methods and algorithms for optical coherence tomography-based angiography: a review and comparison," J. Biomed. Opt. **20**, 13 (2015).

76. B. Baumann, "Polarization Sensitive Optical Coherence Tomography: A Review of Technology and Applications," Applied Sciences **7**, 474 (2017).

77. J. F. de Boer, C. K. Hitzenberger, and Y. Yasuno, "Polarization sensitive optical coherence tomography - a review Invited," Biomed. Opt. Express **8**, 1838-1873 (2017).

78. K. V. Larin and D. D. Sampson, "Optical coherence elastography - OCT at network in tissue biomechanics invited," Biomed. Opt. Express **8**, 1172-1202 (2017).

79. S. Wang and K. V. Larin, "Optical coherence elastography for tissue characterization: a review," Journal of Biophotonics **8**, 279-302 (2015).

80. R. S. Jonnal, O. P. Kocaoglu, R. J. Zawadzki, Z. L. Liu, D. T. Miller, and J. S. Werner, "A Review of Adaptive Optics Optical Coherence Tomography: Technical Advances, Scientific Applications, and the Future," Investigative Ophthalmology & Visual Science **57**, OCT51-OCT68 (2016).

81. X. Shu, L. Beckmann, and H. F. Zhang, "Visible-light optical coherence tomography: a review," J. Biomed. Opt. **22**, 14 (2017).

82. J. Kim, W. Brown, J. R. Maher, H. Levinson, and A. Wax, "Functional optical coherence tomography: principles and progress," Physics in Medicine and Biology **60**, R211-R237 (2015).

83. B. J. Vakoc, R. M. Lanning, J. A. Tyrrell, T. P. Padera, L. A. Bartlett, T. Stylianopoulos, L. L. Munn, G. J. Tearney, D. Fukumura, R. K. Jain, and B. E. Bouma, "Three-dimensional microscopy of the tumor microenvironment in vivo using optical frequency domain imaging," Nature Medicine **15**, 1219-U1151 (2009).

84. Wikipedia, "Near-infrared window in biological tissue", retrieved 03/11/2019, 2019, https://en.wikipedia.org/wiki/Near-infrared_window_in_biological_tissue#cite_note-10.

85. K. F. Palmer and D. Williams, "Optical properties of water in the near infrared*," J. Opt. Soc. Am. **64**, 1107-1110 (1974).

86. D. D. John, B. Lee, B. Potsaid, A. C. Kennedy, M. E. Robertson, C. B. Burgner, A. E. Cable, J. G. Fujimoto, and V. Jayaraman, "Single-Mode and High-Speed 850nm MEMS-VCSEL," in *Lasers Congress 2016 (ASSL, LSC, LAC)*, OSA Technical Digest (online) (Optical Society of America, 2016), ATh5A.2.

87. E. G. Loewen and E. Popov, *Diffraction Gratings and Applications* (CRC Press, 1997).

88. M. Wojtkowski, V. J. Srinivasan, T. H. Ko, J. G. Fujimoto, A. Kowalczyk, and J. S. Duker, "Ultrahigh-resolution, high-speed, Fourier domain optical coherence tomography and methods for dispersion compensation," Opt. Express **12**, 2404-2422 (2004).

89. S. Song, J. Xu, and R. K. Wang, "Long-range and wide field of view optical coherence tomography for in vivo 3D imaging of large volume object based on akinetic programmable swept source," Biomed. Opt. Express **7**, 4734-4748 (2016).

90. Wikipedia, "1951 USAF resolution test chart", retrieved 03/14/2019, 2019, https://en.wikipedia.org/wiki/1951_USAF_resolution_test_chart.

91. T.-H. Tsai, B. Potsaid, Y. K. Tao, V. Jayaraman, J. Jiang, P. J. S. Heim, M. F. Kraus, C. Zhou, J. Hornegger, H. Mashimo, A. E. Cable, and J. G. Fujimoto, "Ultrahigh speed endoscopic optical coherence tomography using micromotor imaging catheter and VCSEL technology," Biomed. Opt. Express **4**, 1119 (2013).

92. T. Wang, T. Pfeiffer, E. Regar, W. Wieser, H. van Beusekom, C. T. Lancee, G. Springeling, I. Krabbendam, A. F. W. van der Steen, R. Huber, and G. van Soest, "Heartbeat OCT: in vivo intravascular megahertz-optical coherence tomography," Biomed. Opt. Express **6**, 5021-5032 (2015).

93. B. Baumann, B. Potsaid, M. F. Kraus, J. J. Liu, D. Huang, J. Hornegger, A. E. Cable, J. S. Duker, and J. G. Fujimoto, "Total retinal blood flow measurement with ultrahigh speed swept source/Fourier domain OCT," Biomed. Opt. Express **2**, 1539-1552 (2011).

94. U. Baran, W. Wei, J. Xu, X. Qi, W. O. Davis, and R. K. Wang, "Video-rate volumetric optical coherence tomography-based microangiography," Opt. Eng **55**, 040503-040503 (2016).

95. M. Zaitsev, J. Maclaren, and M. Herbst, "Motion artifacts in MRI: A complex problem with many partial solutions," Journal of magnetic resonance imaging : JMRI **42**, 887-901 (2015).

96. M. Wojtkowski, "High-speed optical coherence tomography: basics and applications," Applied Optics **49**, D30-D61 (2010).

97. S. H. Yun, G. Tearney, J. de Boer, and B. Bouma, "Pulsed-source and swept-source spectral-domain optical coherence tomography with reduced motion artifacts," Opt. Express **12**, 5614-5624 (2004).

98. A. M. Rollins and J. A. Izatt, "Optimal interferometer designs for optical coherence tomography," Opt. Lett. **24**, 1484-1486 (1999).

99. A. G. Podoleanu, "Unbalanced versus balanced operation in an optical coherence tomography system," Appl. Opt. **39**, 173-182 (2000).

100. S. H. Yun, G. J. Tearney, J. F. de Boer, N. Iftimia, and B. E. Bouma, "High-speed optical frequency-domain imaging," Opt. Express **11**, 2953-2963 (2003).

101. S. Zotter, M. Pircher, T. Torzicky, M. Bonesi, E. Goetzinger, R. A. Leitgeb, and C. K. Hitzenberger, "Visualization of microvasculature by dual-beam phase-resolved Doppler optical coherence tomography," Optics Express **19**, 1217-1227 (2011).

102. C. Blatter, S. Coquoz, B. Grajciar, A. S. G. Singh, M. Bonesi, R. M. Werkmeister, L. Schmetterer, and R. A. Leitgeb, "Dove prism based rotating dual beam bidirectional Doppler OCT," Biomedical Optics Express **4**, 1188-1203 (2013).

103. W. Trasischker, R. M. Werkmeister, S. Zotter, B. Baumann, T. Torzicky, M. Pircher, and C. K. Hitzenberger, "In vitro and in vivo three-dimensional velocity vector measurement by three-beam spectral-domain Doppler optical coherence tomography," Journal of Biomedical Optics **18**(2013).

104. A. Wartak, M. Augustin, R. Haindl, F. Beer, M. Salas, M. Laslandes, B. Baumann, M. Pircher, and C. K. Hitzenberger, "Multi-directional optical coherence tomography for retinal imaging," Biomed. Opt. Express **8**, 5560-5578 (2017).

105. P. Eugui, A. Lichtenegger, M. Augustin, D. J. Harper, M. Muck, T. Roetzer, A. Wartak, T. Konegger, G. Widhalm, C. K. Hitzenberger, A. Woehrer, and B. Baumann, "Beyond backscattering: optical neuroimaging by BRAD," Biomed. Opt. Express **9**, 2476-2494 (2018).

106. M. K. K. Leung, A. Mariampillai, B. A. Standish, K. K. C. Lee, N. R. Munce, I. A. Vitkin, and V. X. D. Yang, "High-power wavelength-swept laser in Littman telescope-less polygon filter and dual-amplifier configuration for multichannel optical coherence tomography," Opt. Lett. **34**, 2814-2816 (2009).

107. B. Potsaid, B. Baumann, D. Huang, S. Barry, A. E. Cable, J. S. Schuman, J. S. Duker, and J. G. Fujimoto, "Ultrahigh speed 1050nm swept source / Fourier domain OCT retinal and anterior segment imaging at 100,000 to 400,000 axial scans per second," Opt. Express **18**, 20029-20048 (2010).

108. D. Choi, H. Hiro-Oka, H. Furukawa, R. Yoshimura, M. Nakanishi, K. Shimizu, and K. Ohbayashi, "Fourier domain optical coherence tomography using optical demultiplexers imaging at 60,000,000 lines/s," Opt. Lett. **33**, 1318-1320 (2008).

109. O. P. Kocaoglu, T. L. Turner, Z. Liu, and D. T. Miller, "Adaptive optics optical coherence tomography at 1 MHz," Biomed. Opt. Express **5**, 4186-4200 (2014).

110. W. Wieser, W. Draxinger, T. Klein, S. Karpf, T. Pfeiffer, and R. Huber, "High definition live 3D-OCT in vivo: design and evaluation of a 4D OCT engine with 1 GVoxel/s," Biomed. Opt. Express **5**, 2963-2977 (2014).

111. H. Y. Lee, H. Sudkamp, T. Marvdashti, and A. K. Ellerbee, "Interleaved optical coherence tomography," Opt. Express **21**, 26542-26556 (2013).

112. H. Y. Lee, T. Marvdashti, L. Duan, S. A. Khan, and A. K. Ellerbee, "Scalable multiplexing for parallel imaging with interleaved optical coherence tomography," Biomed. Opt. Express **5**, 3192-3203 (2014).

113. D. Nankivil, A.-H. Dhalla, N. Gahm, K. Shia, S. Farsiu, and J. A. Izatt, "Coherence revival multiplexed, buffered swept source optical coherence tomography: 400kHz imaging with a 100kHz source," Opt. Lett. **39**, 3740-3743 (2014).

114. C. Zhou, A. Alex, J. Rasakanthan, and Y. Ma, "Space-division multiplexing optical coherence tomography," Opt. Express **21**, 19219-19227 (2013).

115. Y. Huang, M. Badar, A. Nitkowski, A. Weinroth, N. Tansu, and C. Zhou, "Wide-field high-speed space-division multiplexing optical coherence tomography using an integrated photonic device," Biomed. Opt. Express **8**, 3856-3867 (2017).

116. S. Song, J. Xu, and R. K. Wang, "Flexible wide-field optical micro-angiography based on Fourier-domain multiplexed dual-beam swept source optical coherence tomography," Journal of Biophotonics **11**, e201700203 (2018).

117. N. Iftimia, B. E. Bouma, and G. J. Tearney, *Speckle reduction in optical coherence tomography by "path length encoded" angular compounding* (SPIE, 2003), Vol. 8, pp. 260-263, 264.

118. B. Wang, B. Yin, J. Dwelle, H. G. Rylander, M. K. Markey, and T. E. Milner, "Path-length-multiplexed scattering-angle-diverse optical coherence tomography for retinal imaging," Opt. Lett. **38**, 4374-4377 (2013).

119. D. Cui, E. Bo, Y. Luo, X. Liu, X. Wang, S. Chen, X. Yu, S. Chen, P. Shum, and L. Liu, "Multifiber angular compounding optical coherence tomography for speckle reduction," Opt. Lett. **42**, 125-128 (2017).

120. K. S. I. LLP, "Photonic Integrated Circuit (PIC) Market - Forecasts from 2017 to 2022" (2017), retrieved 05/01, 2019, https://www.researchandmarkets.com/reports/4435912/photonic-integrated-circuit-pic-market.

121. Z. Wang, B. Potsaid, L. Chen, C. Doerr, H.-C. Lee, T. Nielson, V. Jayaraman, A. E. Cable, E. Swanson, and J. G. Fujimoto, "Cubic meter volume optical coherence tomography," Optica **3**, 1496-1503 (2016).

122. T. Pfeiffer, W. Draxinger, W. Wieser, T. Klein, M. Petermann, and R. Huber, "Analysis of FDML lasers with meter range coherence," in *SPIE BiOS*, (SPIE, 100531T.

123. C. Zhou, "Apparatus and Method for Space-Division Multiplexing Optical Coherence Tomography," US 2014/0160488 A1, WO 2014/088650 A1 (2014).

124. Wikipedia, "PCI Express", retrieved 05/01, 2019, https://en.wikipedia.org/wiki/PCI_Express.

125. M. Wojtkowski, A. Kowalczyk, R. Leitgeb, and A. F. Fercher, "Full range complex spectral optical coherence tomography technique in eye imaging," Opt. Lett. **27**, 1415-1417 (2002).

126. M. Wojtkowski, R. Leitgeb, A. Kowalczyk, T. Bajraszewski, and A. F. Fercher, "In vivo human retinal imaging by Fourier domain optical coherence tomography," Journal of Biomedical Optics **7**, 457-463 (2002).

127. R. A. Leitgeb, C. K. Hitzenberger, A. F. Fercher, and T. Bajraszewski, "Phase-shifting algorithm to achieve high-speed long-depth-range probing by frequency-domain optical coherence tomography," Opt. Lett. **28**, 2201-2203 (2003).

128. Y. Yasuno, S. Makita, T. Endo, G. Aoki, H. Sumimura, M. Itoh, and T. Yatagai, "One-shot-phase-shifting Fourier domain optical coherence tomography by reference wavefront tilting," Opt. Express **12**, 6184-6191 (2004).

129. D. J. Fechtig, B. Grajciar, T. Schmoll, C. Blatter, R. M. Werkmeister, W. Drexler, and R. A. Leitgeb, "Line-field parallel swept source MHz OCT for structural and functional retinal imaging," Biomed. Opt. Express **6**, 716-735 (2015).

130. D. Hillmann, H. Spahr, H. Sudkamp, C. Hain, L. Hinkel, G. Franke, and G. Hüttmann, "Off-axis reference beam for full-field swept-source OCT and holoscopy," Opt. Express **25**, 27770-27784 (2017).

131. S. H. Yun, G. J. Tearney, J. F. de Boer, and B. E. Bouma, "Removing the depth-degeneracy in optical frequency domain imaging with frequency shifting," Opt. Express **12**, 4822-4828 (2004).

132. J. Zhang, J. S. Nelson, and Z. Chen, "Removal of a mirror image and enhancement of the signal-to-noise ratio in Fourier-domain optical coherence tomography using an electro-optic phase modulator," Opt. Lett. **30**, 147-149 (2005).

133. A. Maheshwari, M. A. Choma, and J. A. Izatt, *Heterodyne swept-source optical coherence tomography for complete complex conjugate ambiguity removal* (SPIE, 2005), Vol. 10, pp. 1-6, 6.

134. E. Götzinger, M. Pircher, R. A. Leitgeb, and C. K. Hitzenberger, "High speed full range complex spectral domain optical coherence tomography," Opt. Express **13**, 583-594 (2005).

135. A. H. Bachmann, R. A. Leitgeb, and T. Lasser, "Heterodyne Fourier domain optical coherence tomography for full range probing with high axial resolution," Opt. Express **14**, 1487-1496 (2006).

136. K.-S. Lee, P. Meemon, W. Dallas, K. Hsu, and J. P. Rolland, "Dual detection full range frequency domain optical coherence tomography," Opt. Lett. **35**, 1058-1060 (2010).

137. Z. Wang, H.-C. Lee, D. Vermeulen, L. Chen, T. Nielsen, S. Y. Park, A. Ghaemi, E. Swanson, C. Doerr, and J. Fujimoto, "Silicon photonic integrated circuit swept-source optical coherence tomography receiver with dual polarization, dual balanced, in-phase and quadrature detection," Biomed. Opt. Express **6**, 2562-2574 (2015).

138. M. A. Choma, C. Yang, and J. A. Izatt, "Instantaneous quadrature low-coherence interferometry with 3×3 fiber-optic couplers," Opt. Lett. **28**, 2162-2164 (2003).

139. M. V. Sarunic, M. A. Choma, C. Yang, and J. A. Izatt, "Instantaneous complex conjugate resolved spectral domain and swept-source OCT using 3×3 fiber couplers," Opt. Express **13**, 957-967 (2005).

140. E. Bo, S. Chen, D. Cui, S. Chen, X. Yu, Y. Luo, and L. Liu, "Single-camera full-range high-resolution spectral domain optical coherence tomography," Appl. Opt. **56**, 470-475 (2017).

141. B. J. Vakoc, S. H. Yun, G. J. Tearney, and B. E. Bouma, "Elimination of depth degeneracy in optical frequency-domain imaging through polarization-based optical demodulation," Opt. Lett. **31**, 362-364 (2006).

142. M. Siddiqui, S. Tozburun, E. Z. Zhang, and B. J. Vakoc, "Compensation of spectral and RF errors in swept-source OCT for high extinction complex demodulation," Opt. Express **23**, 5508-5520 (2015).

143. B. Hofer, B. Považay, B. Hermann, A. Unterhuber, G. Matz, and W. Drexler, "Dispersion encoded full range frequency domain optical coherence tomography," Opt. Express **17**, 7-24 (2009).

144. L. Wang, B. Hofer, J. A. Guggenheim, and B. Považay, *Graphics processing unit-based dispersion encoded full-range frequency-domain optical coherence tomography* (SPIE, 2012), Vol. 17, pp. 1-8, 8.

145. F. Köttig, P. Cimalla, M. Gärtner, and E. Koch, "An advanced algorithm for dispersion encoded full range frequency domain optical coherence tomography," Opt. Express **20**, 24925-24948 (2012).

146. A.-H. Dhalla, D. Nankivil, and J. A. Izatt, "Complex conjugate resolved heterodyne swept source optical coherence tomography using coherence revival," Biomed. Opt. Express **3**, 633-649 (2012).

147. Y. Yasuno, S. Makita, T. Endo, G. Aoki, M. Itoh, and T. Yatagai, "Simultaneous B-M-mode scanning method for real-time full-range Fourier domain optical coherence tomography," Appl. Opt. **45**, 1861-1865 (2006).

148. R. K. Wang, "In vivo full range complex Fourier domain optical coherence tomography," Applied Physics Letters **90**, 054103 (2007).

149. S. Makita, T. Fabritius, and Y. Yasuno, "Full-range, high-speed, high-resolution 1-μm spectral-domain optical coherence tomography using BM-scan for volumetric imaging of the human posterior eye," Opt. Express **16**, 8406-8420 (2008).

150. M. Yamanari, S. Makita, Y. Lim, and Y. Yasuno, "Full-range polarization-sensitive swept-source optical coherence tomography by simultaneous transversal and spectral modulation," Opt. Express **18**, 13964-13980 (2010).

151. B. Baumann, M. Pircher, E. Götzinger, and C. K. Hitzenberger, "Full range complex spectral domain optical coherence tomography without additional phase shifters," Opt. Express **15**, 13375-13387 (2007).

152. R. A. Leitgeb, R. Michaely, T. Lasser, and S. C. Sekhar, "Complex ambiguity-free Fourier domain optical coherence tomography through transverse scanning," Opt. Lett. **32**, 3453-3455 (2007).

153. L. An and R. K. Wang, "Use of a scanner to modulate spatial interferograms for in vivo full-range Fourier-domain optical coherence tomography," Opt. Lett. **32**, 3423-3425 (2007).

154. H. Kawagoe, M. Yamanaka, S. Makita, Y. Yasuno, and N. Nishizawa, "Full-range ultrahigh-resolution spectral-domain optical coherence tomography in 1.7 μm wavelength region for deep-penetration and high-resolution imaging of turbid tissues," Applied Physics Express **9**, 127002 (2016).

155. Q. Li, K. Karnowski, M. Villiger, and D. D. Sampson, *Local birefringence of the anterior segment of the human eye in a single capture with a full range polarisation-sensitive optical coherence tomography*, International Conference on Biophotonics V (SPIE, 2017), Vol. 10340, p. 1.

156. W. Choi, K. J. Mohler, B. Potsaid, C. D. Lu, J. J. Liu, V. Jayaraman, A. E. Cable, J. S. Duker, R. Huber, and J. G. Fujimoto, "Choriocapillaris and Choroidal Microvasculature Imaging with Ultrahigh Speed OCT Angiography," Plos One **8**(2013).

157. H. C. Hendargo, R. P. McNabb, A.-H. Dhalla, N. Shepherd, and J. A. Izatt, "Doppler velocity detection limitations in spectrometer-based versus swept-source optical coherence tomography," Biomedical Optics Express **2**, 2175-2188 (2011).

158. S. Moon and Z. Chen, "Phase-stability optimization of swept-source optical coherence tomography," Biomed. Opt. Express **9**, 5280-5295 (2018).

159. C. Underwood, "Fluorescein Angiography" (2016), retrieved 04/30, 2019, https://www.healthline.com/health/fluorescein-angiography#risks.

160. J. Xia and L. V. Wang, "Small-Animal Whole-Body Photoacoustic Tomography: A Review," IEEE Transactions on Biomedical Engineering **61**, 1380-1389 (2014).

161. P. Beard, "Biomedical photoacoustic imaging," Interface Focus **1**, 602-631 (2011).

162. J. J. Yao and L. H. V. Wang, "Photoacoustic microscopy," Laser Photon. Rev. **7**, 758-778 (2013).

163. E. M. Strohm, M. J. Moore, and M. C. Kolios, "Single Cell Photoacoustic Microscopy: A Review," Ieee Journal of Selected Topics in Quantum Electronics **22**, 15 (2016).

164. R. F. Spaide, J. Klancnik, and M. J. Cooney, "Retinal Vascular Layers Imaged by Fluorescein Angiography and Optical Coherence Tomography Angiography," JAMA Ophthalmol. **133**, 45-50 (2015).

165. Y. L. Jia, S. T. Bailey, D. J. Wilson, O. Tan, M. L. Klein, C. J. Flaxel, B. Potsaid, J. J. Liu, C. D. Lu, M. F. Kraus, J. G. Fujimoto, and D. Huang, "Quantitative Optical Coherence Tomography Angiography of Choroidal Neovascularization in Age-Related Macular Degeneration," Ophthalmology **121**, 1435-1444 (2014).

166. T. E. de Carlo, M. A. Bonini, A. T. Chin, M. Adhi, D. Ferrara, C. R. Baumal, A. J. Witkin, E. Reichel, J. S. Duker, and N. K. Waheed, "Spectral-Domain Optical Coherence Tomography Angiography of Choroidal Neovascularization," Ophthalmology **122**, 1228-1238 (2015).

167. V. J. Srinivasan, S. Sakadzic, I. Gorczynska, S. Ruvinskaya, W. C. Wu, J. G. Fujimoto, and D. A. Boas, "Quantitative cerebral blood flow with Optical Coherence Tomography," Opt. Express **18**, 2477-2494 (2010).

168. R. K. Wang and L. An, "Doppler optical micro-angiography for volumetric imaging of vascular perfusion in vivo," Opt. Express **17**, 8926-8940 (2009).

169. R. K. K. Wang, "Optical Microangiography: A Label-Free 3-D Imaging Technology to Visualize and Quantify Blood Circulations Within Tissue Beds In Vivo," Ieee Journal of Selected Topics in Quantum Electronics **16**, 545-554 (2010).

170. Y. D. Li, U. Baran, and R. K. K. Wang, "Application of Thinned-Skull Cranial Window to Mouse Cerebral Blood Flow Imaging Using Optical Microangiography," Plos One **9**(2014).

171. Z. P. Chen, T. E. Milner, S. Srinivas, X. J. Wang, A. Malekafzali, M. J. C. vanGemert, and J. S. Nelson, "Noninvasive imaging of in vivo blood flow velocity using optical Doppler tomography," Optics Letters **22**, 1119-1121 (1997).

172. M. A. Choma, A. K. Ellerbee, S. Yazdanfar, and J. A. Izatt, *Doppler flow imaging of cytoplasmic streaming using spectral domain phase microscopy* (SPIE, 2006), Vol. 11, pp. 1-8, 8.

173. J. Fingler, D. Schwartz, C. Yang, and S. E. Fraser, "Mobility and transverse flow visualization using phase variance contrast with spectral domain optical coherence tomography," Optics Express **15**, 12636-12653 (2007).

174. J. Fingler, C. Readhead, D. M. Schwartz, and S. E. Fraser, "Phase-Contrast OCT Imaging of Transverse Flows in the Mouse Retina and Choroid," Investigative Ophthalmology & Visual Science **49**, 5055-5059 (2008).

175. D. A. Boas and A. K. Dunn, "Laser speckle contrast imaging in biomedical optics," Journal of Biomedical Optics **15**(2010).

176. A. Mariampillai, B. A. Standish, E. H. Moriyama, M. Khurana, N. R. Munce, M. K. K. Leung, J. Jiang, A. Cable, B. C. Wilson, I. A. Vitkin, and V. X. D. Yang, "Speckle variance detection of microvasculature using swept-source optical coherence tomography," Optics Letters **33**, 1530-1532 (2008).

177. A. Mariampillai, M. K. K. Leung, M. Jarvi, B. A. Standish, K. Lee, B. C. Wilson, A. Vitkin, and V. X. D. Yang, "Optimized speckle variance OCT imaging of microvasculature," Optics Letters **35**, 1257-1259 (2010).

178. R. Motaghiannezam and S. Fraser, "Logarithmic intensity and speckle-based motion contrast methods for human retinal vasculature visualization using swept source optical coherence tomography," Biomedical Optics Express **3**, 503-521 (2012).

179. J. Enfield, E. Jonathan, and M. Leahy, "In vivo imaging of the microcirculation of the volar forearm using correlation mapping optical coherence tomography (cmOCT)," Biomedical Optics Express **2**, 1184-1193 (2011).

180. E. Jonathan, J. Enfield, and M. J. Leahy, "Correlation mapping method for generating microcirculation morphology from optical coherence tomography (OCT) intensity images," Journal of Biophotonics **4**, 583-587 (2011).

181. Y. Jia, O. Tan, J. Tokayer, B. Potsaid, Y. Wang, J. J. Liu, M. F. Kraus, H. Subhash, J. G. Fujimoto, J. Hornegger, and D. Huang, "Split-spectrum amplitude-decorrelation angiography with optical coherence tomography," Optics Express **20**, 4710-4725 (2012).

182. Y. Jia, J. C. Morrison, J. Tokayer, O. Tan, L. Lombardi, B. Baumann, C. D. Lu, W. Choi, J. G. Fujimoto, and D. Huang, "Quantitative OCT angiography of optic nerve head blood flow," Biomedical Optics Express **3**(2012).

183. R. K. Wang, S. L. Jacques, Z. Ma, S. Hurst, S. R. Hanson, and A. Gruber, "Three dimensional optical angiography," Optics Express **15**, 4083-4097 (2007).

184. J. Xu, S. Song, Y. Li, and R. K. Wang, "Complex-based OCT angiography algorithm recovers microvascular information better than amplitude- or phase-based algorithms in phase-stable systems," Physics in Medicine & Biology **63**, 015023 (2017).

185. Y. H. Zhao, Z. P. Chen, C. Saxer, Q. M. Shen, S. H. Xiang, J. F. de Boer, and J. S. Nelson, "Doppler standard deviation imaging for clinical monitoring of in vivo human skin blood flow," Optics Letters **25**, 1358-1360 (2000).

186. L. Wang, Y. Wang, S. Guo, J. Zhang, M. Bachman, G. P. Li, and Z. Chen, "Frequency domain phase-resolved optical Doppler and Doppler variance tomography," Optics Communications **242**, 345-350 (2004).

187. A. S. Nam, I. Chico-Calero, and B. J. Vakoc, "Complex differential variance algorithm for optical coherence tomography angiography," Biomedical Optics Express **5**, 3822-3832 (2014).

188. B. Braaf, S. Donner, A. S. Nam, B. E. Bouma, and B. J. Vakoc, "Complex differential variance angiography with noise-bias correction for optical coherence tomography of the retina," Biomedical Optics Express **9**, 486-506 (2018).

189. C. Chen, W. Shi, and W. Gao, "Imaginary part-based correlation mapping optical coherence tomography for imaging of blood vessels in vivo," Journal of Biomedical Optics **20**(2015).

190. M. Guizar-Sicairos, S. T. Thurman, and J. R. Fienup, "Efficient subpixel image registration algorithms," Optics letters **33**, 156-158 (2008).

191. R. F. Spaide, J. G. Fujimoto, and N. K. Waheed, "IMAGE ARTIFACTS IN OPTICAL COHERENCE TOMOGRAPHY ANGIOGRAPHY," Retina-the Journal of Retinal and Vitreous Diseases **35**, 2163-2180 (2015).

192. S. Sangiorgi, A. Manelli, T. Congiu, A. Bini, G. Pilato, M. Reguzzoni, and M. Raspanti, "Microvascularization of the human digit as studied by corrosion casting," Journal of Anatomy **204**, 123-131 (2004).

193. U. Baran, L. Shi, and R. K. Wang, "Capillary blood flow imaging within human finger cuticle using optical microangiography," Journal of Biophotonics **8**, 46-51 (2015).

194. B. H. Park, M. C. Pierce, B. Cense, S. H. Yun, M. Mujat, G. J. Tearney, B. E. Bouma, and J. F. de Boer, "Real-time fiber-based multi-functional spectral-domain optical coherence tomography at 1.3 mu m," Optics Express **13**, 3931-3944 (2005).

195. M. A. Choma, A. K. Ellerbee, C. Yang, T. L. Creazzo, and J. A. Izatt, "Spectral-domain phase microscopy," Opt. Lett. **30**, 1162-1164 (2005).

196. B. J. Vakoc, S. H. Yun, J. F. d. Boer, G. J. Tearney, and B. E. Bouma, "Phase-resolved optical frequency domain imaging," Opt. Express **13**, 5483-5493 (2005).

197. S. Song, J. Xu, S. Men, T. T. Shen, and R. K. Wang, "Robust numerical phase stabilization for long-range swept-source optical coherence tomography," Journal of biophotonics **10**, 1398-1410 (2017).

198. A. Zhang, Q. Zhang, and R. K. Wang, "Minimizing projection artifacts for accurate presentation of choroidal neovascularization in OCT micro-angiography," Biomedical Optics Express **6**, 4130-4143 (2015).

199. L. Liu, S. S. Gao, S. T. Bailey, D. Huang, D. Li, and Y. Jia, "Automated choroidal neovascularization detection algorithm for optical coherence tomography angiography," Biomedical Optics Express **6**, 3564-3575 (2015).

200. M. Zhang, T. S. Hwang, J. P. Campbell, S. T. Bailey, D. J. Wilson, D. Huang, and Y. Jia, "Projection-resolved optical coherence tomographic angiography," Biomedical Optics Express **7**, 816-828 (2016).

201. A. Li, J. You, C. Du, and Y. Pan, "Automated segmentation and quantification of OCT angiography for tracking angiogenesis progression," Biomedical Optics Express **8**, 5604-5616 (2017).

202. P. Li, Z. Huang, S. Yang, X. Liu, Q. Ren, and P. Li, "Adaptive classifier allows enhanced flow contrast in OCT angiography using a histogram-based motion threshold and 3D Hessian analysis-based shape filtering," Optics Letters **42**, 4816-4819 (2017).

203. S. Yousefi, T. Liu, and R. K. Wang, "Segmentation and quantification of blood vessels for OCT-based micro-angiograms using hybrid shape/intensity compounding," Microvascular research **97**, 37-46 (2015).

204. J. Lee, J. Y. Jiang, W. Wu, F. Lesage, and D. A. Boas, "Statistical intensity variation analysis for rapid volumetric imaging of capillary network flux," Biomedical Optics Express **5**, 1160-1172 (2014).

205. A. Nemeth, "Optical Coherence Tomography – Applications in Non- Destructive Testing and Evaluation," G. n. Hannesschläger, ed. (IntechOpen, Rijeka, 2013), pp. Ch. 9-Ch. 9.

206. A. Nemeth, R. Gahleitner, G. Hannesschlager, G. Pfandler, and M. Leitner, "Ambiguity-free spectral-domain optical coherence tomography for determining the layer thicknesses in fluttering foils in real time," Optics and Lasers in Engineering **50**, 1372-1376 (2012).

207. S. C. Zhong, Y. C. Shen, L. Ho, R. K. May, J. A. Zeitler, M. Evans, P. F. Taday, M. Pepper, T. Rades, K. C. Gordon, R. Muller, and P. Kleinebudde, "Non-destructive quantification of pharmaceutical tablet coatings using terahertz pulsed imaging and optical coherence tomography," Optics and Lasers in Engineering **49**, 361-365 (2011).

208. D. M. Koller, G. Hannesschlager, M. Leitner, and J. G. Khinast, "Non-destructive analysis of tablet coatings with optical coherence tomography," European Journal of Pharmaceutical Sciences **44**, 142-148 (2011).

209. H. Y. Lin, Y. Dong, D. Markl, Z. J. Zhang, Y. C. Shen, and J. A. Zeitler, "Pharmaceutical Film Coating Catalog for Spectral Domain Optical Coherence Tomography," Journal of Pharmaceutical Sciences **106**, 3171-3176 (2017).

210. M. Wiesner, J. Ihlemann, H. H. Muller, E. Lankenau, and G. Huttmann, "Optical coherence tomography for process control of laser micromachining," Review of Scientific Instruments **81**(2010).

211. L. Thrane, T. M. Jorgensen, M. Jorgensen, and F. C. Krebs, "Application of optical coherence tomography (OCT) as a 3-dimensional imaging technique for roll-to-roll coated polymer solar cells," Solar Energy Materials and Solar Cells **97**, 181-185 (2012).

212. M. T. Tsai, F. Y. Chang, Y. C. Yao, J. Mei, and Y. J. Lee, "Optical inspection of solar cells using phase-sensitive optical coherence tomography," Solar Energy Materials and Solar Cells **136**, 193-199 (2015).

213. T. Prykari, J. Czajkowski, E. Alarousu, and R. Myllyla, "Optical coherence tomography as an accurate inspection and quality evaluation technique in paper industry," Optical Review **17**, 218-222 (2010).

214. E. Alarousu, L. Krehut, T. Prykari, and R. Myllyla, "Study on the use of optical coherence tomography in measurements of paper properties," Measurement Science and Technology **16**, 1131-1137 (2005).

215. X. Shao, X. Chen, X. Yu, Y. Hu, L. Liu, F. Shi, W. Shao, and J. Mo, "Nondestructive Measurement of Conformal Coating Thickness on Printed Circuit Board With Ultra-High Resolution Optical Coherence Tomography," IEEE Access **7**, 18138-18145 (2019).

216. K. A. Serrels, M. K. Renner, and D. T. Reid, "Optical coherence tomography for non-destructive investigation of silicon integrated-circuits," Microelectronic Engineering **87**, 1785-1791 (2010).

217. T. Anna, C. Shakher, and D. S. Mehta, "Simultaneous tomography and topography of silicon integrated circuits using full-field swept-source optical coherence tomography," Journal of Optics a-Pure and Applied Optics **11**(2009).

218. I. V. Meglinski, C. Buranachai, and L. A. Terry, "Plant photonics: application of optical coherence tomography to monitor defects and rots in onion," Laser Physics Letters **7**, 307-310 (2010).

219. J. Goclawski, J. Sekulska-Nalewajko, E. Korzeniewska, and A. Piekarska, "The use of optical coherence tomography for the evaluation of textural changes of grapes exposed to pulsed electric field," Computers and Electronics in Agriculture **142**, 29-40 (2017).

220. P. Verboven, A. Nemeth, M. K. Abera, E. Bongaers, D. Daelemans, P. Estrade, E. Herremans, M. Hertog, W. Saeys, E. Vanstreels, B. Verlinden, M. Leitner, and B. Nicolai, "Optical coherence tomography visualizes microstructure of apple peel," Postharvest Biology and Technology **78**, 123-132 (2013).

221. J. H. Lee, J. G. Shin, H. Y. Kim, and B. H. Lee, "Quantitative discrimination of pearls using polarization-sensitive optical coherence tomography," Applied Optics **57**, 2197-2201 (2018).

222. Y. Zhou, T. B. Liu, Y. Shi, Z. W. Chen, J. W. Mao, and W. J. Zhou, "Automated Internal Classification of Beadless Chinese ZhuJi Fleshwater Pearls based on Optical Coherence Tomography Images," Scientific Reports **6**, 1-7 (2016).

223. M. L. Yang, C. W. Lu, I. J. Hsu, and C. C. Yang, "The use of Optical Coherence Tomography for monitoring the subsurface morphologies of archaic jades," Archaeometry **46**, 171-182 (2004).

224. S. D. Chang, Y. X. Mao, G. M. Chang, and C. Flueraru, "Jade detection and analysis based on optical coherence tomography images," Optical Engineering **49**(2010).

225. C. S. Cheung, J. M. O. Daniel, M. Tokurakawa, W. A. Clarkson, and H. Liang, "Optical coherence tomography in the 2-mu m wavelength regime for paint and other high opacity materials," Optics Letters **39**, 6509-6512 (2014).

226. C. S. Cheung, M. Spring, and H. Liang, "Ultra-high resolution Fourier domain optical coherence tomography for old master paintings," Optics Express **23**, 10145-10157 (2015).

227. P. Targowski, M. Iwanicka, L. Tyminska-Widmer, M. Sylwestrzak, and E. A. Kwiatkowska, "Structural Examination of Easel Paintings with Optical Coherence Tomography," Accounts of Chemical Research **43**, 826-836 (2010).

228. B. R. Davidson and J. K. Barton, "Application of optical coherence tomography to automated contact lens metrology," Journal of Biomedical Optics **15**(2010).

229. B. J. Coldrick, C. Richards, K. Sugden, J. S. Wolffsohn, and T. E. Drew, "Developments in contact lens measurement: A comparative study of industry standard geometric inspection and optical coherence tomography," Contact Lens & Anterior Eye **39**, 270-276 (2016).

230. R. Su, M. Kirillin, E. W. Chang, E. Sergeeva, S. H. Yun, and L. Mattsson, "Perspectives of mid-infrared optical coherence tomography for inspection and micrometrology of industrial ceramics," Optics Express **22**, 15804-15819 (2014).

231. R. Su, M. Kirillin, P. Ekberg, A. Roos, E. Sergeeva, and L. Mattsson, "Optical coherence tomography for quality assessment of embedded microchannels in alumina ceramic," Optics Express **20**, 4603-4618 (2012).

232. A. Haussmann, L. Kirsten, S. Schmidt, P. Cimalla, L. Wehmeier, E. Koch, and L. M. Eng, "Three-Dimensional, Time-Resolved Profiling of Ferroelectric Domain Wall Dynamics by Spectral-Domain Optical Coherence Tomography," Annalen Der Physik **529**(2017).

233. M. Lenz, C. Mazzon, C. Dillmann, N. C. Gerhardt, H. Welp, M. Prange, and M. R. Hofmann, "Spectral Domain Optical Coherence Tomography for Non-Destructive Testing of Protection Coatings on Metal Substrates," Applied Sciences-Basel **7**(2017).

234. J. Veilleux, C. Moreau, D. Levesque, M. Dufour, and M. Boulos, "Optical coherence tomography for the inspection of plasma-sprayed ceramic coatings," Journal of Thermal Spray Technology **16**, 435-443 (2007).

235. N. Zhang, C. M. Wang, Z. W. Sun, H. C. Mei, W. Huang, L. Xu, L. C. Xie, J. J. Guo, Y. W. Yan, Z. H. Li, X. J. Xu, P. Xue, and N. N. Liu, "Characterization of automotive paint by optical coherence tomography," Forensic Science International **266**, 239-244 (2016).

236. Y. Dong, S. Lawman, Y. L. Zheng, D. Williams, J. K. Zhang, and Y. C. Shen, "Nondestructive analysis of automotive paints with spectral domain optical coherence tomography," Applied Optics **55**, 3695-3700 (2016).

237. J. K. Zhang, B. M. Williams, S. Lawman, D. Atkinson, Z. J. Zhang, Y. C. Shen, and Y. L. Zheng, "Non-destructive analysis of flake properties in automotive paints with full-field optical coherence tomography and 3D segmentation," Optics Express **25**, 18614-18628 (2017).

238. Z. Y. Chen, C. Zhao, Y. Shen, P. Li, X. P. Wang, and Z. H. Ding, "Ultrawide-field parallel spectral domain optical coherence tomography for nondestructive inspection of glass," Optics Communications **341**, 122-130 (2015).

239. Z. Y. Chen, Y. Shen, W. Bao, P. Li, X. P. Wang, and Z. H. Ding, "Identification of surface defects on glass by parallel spectral domain optical coherence tomography," Optics Express **23**, 23634-23646 (2015).

240. J. Kunicki-Goldfinger, P. Targowski, M. Gora, P. Karaszkiewicz, and P. Dzierzanowski, "Characterization of Glass Surface Morphology by Optical Coherence Tomography," Studies in Conservation **54**, 117-128 (2009).

241. C. W. Xi, D. Marks, S. Schlachter, W. Luo, and S. A. Boppart, "High-resolution three-dimensional imaging of biofilm development using optical coherence tomography," Journal of Biomedical Optics **11**(2006).

242. C. Dreszer, A. D. Wexler, S. Drusova, T. Overdijk, A. Zwijnenburg, H. C. Flemming, J. C. Kruithof, and J. S. Vrouwenvelder, "In-situ biofilm characterization in membrane systems using Optical Coherence Tomography: Formation, structure, detachment and impact of flux change," Water Research **67**, 243-254 (2014).

243. F. Blauert, H. Horn, and M. Wagner, "Time-resolved biofilm deformation measurements using optical coherence tomography," Biotechnology and Bioengineering **112**, 1893-1905 (2015).

244. M. Wagner and H. Horn, "Optical coherence tomography in biofilm research: A comprehensive review," Biotechnology and Bioengineering **114**, 1386-1402 (2017).

245. H. D. Ford and R. P. Tatam, "Spatially-resolved volume monitoring of adhesive cure using correlated-image optical coherence tomography," International Journal of Adhesion and Adhesives **42**, 21-29 (2013).

246. P. Makishi, Y. Shimada, A. Sadr, J. Tagami, and Y. Sumi, "Non-destructive 3D imaging of composite restorations using optical coherence tomography: Marginal adaptation of self-etch adhesives," Journal of Dentistry **39**, 316-325 (2011).

247. B. Bista, A. Sadr, A. Nazari, Y. Shimada, Y. Sumi, and J. Tagami, "Nondestructive assessment of current one-step self-etch dental adhesives using optical coherence tomography," Journal of Biomedical Optics **18**(2013).

248. J. P. Dunkers, F. R. Phelan, D. P. Sanders, M. J. Everett, W. H. Green, D. L. Hunston, and R. S. Parnas, "The application of optical coherence tomography to problems in polymer matrix composites," Optics and Lasers in Engineering **35**, 135-147 (2001).

249. D. Stifter, K. Wiesauer, M. Wurm, E. Schlotthauer, J. Kastner, M. Pircher, E. Gotzinger, and C. K. Hitzenberger, "Investigation of polymer and polymer/fibre composite materials with optical coherence tomography," Measurement Science and Technology **19**(2008).

250. P. Liu, R. M. Groves, and R. Benedictus, "Optical Coherence Tomography for the Study of Polymer and Polymer Matrix Composites," Strain **50**, 436-443 (2014).

251. M. F. Shirazi, M. Jeon, and J. Kim, "Structural Analysis of Polymer Composites Using Spectral Domain Optical Coherence Tomography," Sensors **17**(2017).

252. S. Tarafdar, Y. Y. Tarasevich, M. Dutta Choudhury, T. Dutta, and D. Zang, "Droplet Drying Patterns on Solid Substrates: From Hydrophilic to Superhydrophobic Contact to Levitating Drops," Advances in Condensed Matter Physics **2018**, 24 (2018).

253. H. B. Eral, D. M. Augustine, M. H. G. Duits, and F. Mugele, "Suppressing the coffee stain effect: how to control colloidal self-assembly in evaporating drops using electrowetting," Soft Matter **7**, 4954-4958 (2011).

254. Z. S. Davidson, Y. Huang, A. Gross, A. Martinez, T. Still, C. Zhou, P. J. Collings, R. D. Kamien, and A. G. Yodh, "Deposition and drying dynamics of liquid crystal droplets," Nature Communications **8**, 15642 (2017).

255. J. Jeong, Z. S. Davidson, P. J. Collings, T. C. Lubensky, and A. G. Yodh, "Chiral symmetry breaking and surface faceting in chromonic liquid crystal droplets with giant elastic anisotropy," PNAS **111**, 1742-1747 (2014).

256. C. Sadek, P. Schuck, Y. Fallourd, N. Pradeau, C. Le Floch-Fouéré, and R. Jeantet, "Drying of a single droplet to investigate process–structure–function relationships: a review," Dairy Science & Technology **95**, 771-794 (2015).

257. R. D. Deegan, "Pattern formation in drying drops," Physical Review E **61**, 475-485 (2000).

258. Y. Shimokawa, T. Kajiya, K. Sakai, and M. Doi, "Measurement of the skin layer in the drying process of a polymer solution," Physical Review E **84**(2011).

259. M. Anyfantakis, Z. Geng, M. Morel, S. Rudiuk, and D. Baigl, "Modulation of the Coffee-Ring Effect in Particle/Surfactant Mixtures: the Importance of Particle-Interface Interactions," Langmuir **31**, 4113-4120 (2015).

260. T. Kajiya, D. Kaneko, and M. Doi, "Dynamical Visualization of "Coffee Stain Phenomenon" in Droplets of Polymer Solution via Fluorescent Microscopy," Langmuir **24**, 12369-12374 (2008).

261. S. J. Gokhale, J. L. Plawsky, and P. C. Wayner, "Spreading, evaporation, and contact line dynamics of surfactant-laden microdrops," Langmuir **21**, 8188-8197 (2005).

262. H. Kim, F. Boulogne, E. Um, I. Jacobi, E. Button, and H. A. Stone, "Controlled Uniform Coating from the Interplay of Marangoni Flows and Surface-Adsorbed Macromolecules," Physical Review Letters **116**(2016).

263. D. Kaya, V. A. Belyi, and M. Muthukumar, "Pattern formation in drying droplets of polyelectrolyte and salt," Journal of Chemical Physics **133**(2010).

264. N. M. Kovalchuk, A. Trybala, and V. M. Starov, "Evaporation of sessile droplets," Current Opinion in Colloid & Interface Science **19**, 336-342 (2014).

265. K. Sefiane, "Patterns from drying drops," Advances in Colloid and Interface Science **206**, 372-381 (2014).

266. J. Z. Wang, Z. H. Zheng, H. W. Li, W. T. S. Huck, and H. Sirringhaus, "Dewetting of conducting polymer inkjet droplets on patterned surfaces," Nature Materials **3**, 171-176 (2004).

267. V. Dugas, J. Broutin, and E. Souteyrand, "Droplet evaporation study applied to DNA chip manufacturing," Langmuir **21**, 9130-9136 (2005).

268. J. R. Trantum, M. L. Baglia, Z. E. Eagleton, R. L. Mernaugh, and F. R. Haselton, "Biosensor design based on Marangoni flow in an evaporating drop," Lab on a Chip **14**, 315-324 (2014).

269. C. P. Gulka, J. D. Swartz, J. R. Trantum, K. M. Davis, C. M. Peak, A. J. Denton, F. R. Haselton, and D. W. Wright, "Coffee Rings as Low-Resource Diagnostics: Detection of the Malaria Biomarker Plasmodium falciparum Histidine-Rich Protein-II Using a Surface-Coupled Ring of Ni(II)NTA Gold-Plated Polystyrene Particles," Acs Applied Materials & Interfaces **6**, 6257-6263 (2014).

270. T. A. Yakhno and V. G. Yakhno, "Structural Evolution of Drying Drops of Biological Fluids," Technical Physics **54**, 1219-1227 (2009).

271. T. A. Yakhno, V. V. Kazakov, O. A. Sanina, A. G. Sanin, and V. G. Yakhno, "Drops of biological fluids drying on a hard substrate: Variation of the morphology, weight, temperature, and mechanical properties," Technical Physics **55**, 929-935 (2010).

272. E. Rapis, "A change in the physical state of a nonequilibrium blood plasma protein film in patients with carcinoma," Technical Physics **47**, 510-512 (2002).

273. L. Bahmani, M. Neysari, and M. Maleki, "The study of drying and pattern formation of whole human blood drops and the effect of thalassaemia and neonatal jaundice on the patterns," Colloids and Surfaces a-Physicochemical and Engineering Aspects **513**, 66-75 (2017).

274. M. O. Kokornaczyk, G. Dinelli, I. Marotti, S. Benedettelli, D. Nani, and L. Betti, "Self-Organized Crystallization Patterns from Evaporating Droplets of Common Wheat Grain Leakages as a Potential Tool for Quality Analysis," Thescientificworldjournal **11**, 1712-1725 (2011).

275. N. R. Devlin, K. Loehr, and M. T. Harris, "The separation of two different sized particles in an evaporating droplet," Aiche Journal **61**, 3547-3556 (2015).

276. H. M. Abdel-Mageed, S. A. Fouad, M. H. Teaima, A. M. Abdel-Aty, A. S. Fahmy, D. S. Shaker, and S. A. Mohamed, "Optimization of nano spray drying parameters for production of α-amylase nanopowder for biotheraputic applications using factorial design," Drying Technology, 1-9 (2019).

277. C. Arpagaus, "A Novel Laboratory-Scale Spray Dryer to Produce Nanoparticles," Drying Technology **30**, 1113-1121 (2012).

278. J. R. Trantum, Z. E. Eagleton, C. A. Patil, J. M. Tucker-Schwartz, M. L. Baglia, M. C. Skala, and F. R. Haselton, "Cross-Sectional Tracking of Particle Motion in Evaporating Drops: Flow Fields and Interfacial Accumulation," Langmuir **29**, 6221-6231 (2013).

279. P. A. Lovell and M. S. El-Aasser, "Emulsion Polymerization and Emulsion Polymers," (1997).

280. R. D. Deegan, O. Bakajin, T. F. Dupont, G. Huber, S. R. Nagel, and T. A. Witten, "Capillary flow as the cause of ring stains from dried liquid drops," Nature **389**, 827-829 (1997).

281. A. M. J. Edwards, P. S. Atkinson, C. S. Cheung, H. Liang, D. J. Fairhurst, and F. F. Ouali, "Density-Driven Flows in Evaporating Binary Liquid Droplets," Physical Review Letters **121**, 184501 (2018).

282. Z. S. Davidson, Y. Huang, A. Gross, A. Martinez, T. Still, C. Zhou, P. J. Collings, R. D. Kamien, and A. G. Yodh, "Deposition and drying dynamics of liquid crystal droplets," Nature Communications **8**(2017).

283. S. Manukyan, H. M. Sauer, I. V. Roisman, K. A. Baldwin, D. J. Fairhurst, H. Liang, J. Venzmer, and C. Tropea, "Imaging internal flows in a drying sessile polymer dispersion drop using Spectral Radar Optical Coherence Tomography (SR-OCT)," Journal of Colloid and Interface Science **395**, 287-293 (2013).

284. A. F. Routh, "Drying of thin colloidal films," Reports on Progress in Physics **76**(2013).

285. J. Keddie and A. F. Routh, "Fundamentals of Latex Film Formation: Processes and Properties," Springer Laboratory (2010).

286. H. Huang, Y. Y. Huang, W. Lau, H. D. Ou-Yang, C. Zhou, and M. S. El-Aasser, "Integrating optical coherence tomography with gravimetric and video analysis (OCT-Gravimetry-Video method) for studying the drying process of polystyrene latex system," Scientific Reports **8**(2018).

287. M. Schulz and J. L. Keddie, "A critical and quantitative review of the stratification of particles during the drying of colloidal films," Soft Matter **14**, 6181-6197 (2018).

288. H. M. van der Kooij and J. Sprakel, "Watching paint dry; more exciting than it seems," Soft Matter **11**, 6353-6359 (2015).

289. R. Jovanovic and M. A. Dube, "Emulsion-based pressure-sensitive adhesives: A review," Journal of Macromolecular Science-Polymer Reviews **C44**, 1-51 (2004).

290. M. Elgammal, R. Schneider, and M. Gradzielski, "Preparation of latex nanoparticles using nanoemulsions obtained by the phase inversion composition (PIC) method and their application in textile printing," Colloids and Surfaces a-Physicochemical and Engineering Aspects **470**, 70-79 (2015).

291. Y. Guan, B. Tawiah, L. P. Zhang, C. S. Du, and S. H. Fu, "Preparation of UV-cured pigment/latex dispersion for textile inkjet printing," Colloids and Surfaces a-Physicochemical and Engineering Aspects **462**, 90-98 (2014).

292. H. P. Borase, C. D. Patil, R. K. Suryawanshi, and S. V. Patil, "Ficus carica Latex-Mediated Synthesis of Silver Nanoparticles and Its Application as a Chemophotoprotective Agent," Appl. Biochem. Biotechnol. **171**, 676-688 (2013).

293. S. M. H. Najafi, M. Tajvidi, and D. W. Bousfield, "Production and mechanical characterization of free-standing pigmented paper coating layers with latex and starch as binder," Progress in Organic Coatings **123**, 138-145 (2018).

294. Y. M. Wu, H. D. Duan, Y. Q. Yu, and C. G. Zhang, "Preparation and performance in paper coating of silicone-modified styrene-butyl acrylate copolymer latex," Journal of Applied Polymer Science **79**, 333-336 (2001).

295. H. Nakagami, T. Keshikawa, M. Matsumura, and H. Tsukamoto, "APPLICATION OF AQUEOUS SUSPENSIONS AND LATEX DISPERSIONS OF WATER-INSOLUBLE POLYMERS FOR TABLET AND GRANULE COATINGS," Chem. Pharm. Bull. **39**, 1837-1842 (1991).

296. M. Ladika, T. H. Kalantar, H. Shao, S. L. Dean, J. K. Harris, P. J. Sheskey, K. Coppens, K. M. Balwinski, and D. L. Holbrook, "Polyampholyte Acrylic Latexes for Tablet Coating Applications," Journal of Applied Polymer Science **131**, 12 (2014).

297. R. P. Brentin, "LATEX COATING SYSTEMS FOR CARPET BACKING," Journal of Coated Fabrics **12**, 82-91 (1982).

298. M. Schulz, H. Romermann, K. Pohl, C. Chindawong, and D. Johannsmann, "Latex Films with In-Plane Composition Gradients Caused by Lateral Drying," Soft Mater. **13**, 138-143 (2015).

299. K. S. Kolegov, "Simulation of Patterned Glass Film Formation in the Evaporating Colloidal Liquid under IR Heating," Microgravity Sci. Technol. **30**, 113-120 (2018).

300. A. Georgiadis, F. N. Muhamad, A. Utgenannt, and J. L. Keddie, "Aesthetically textured, hard latex coatings by fast IR-assisted evaporative lithography," Progress in Organic Coatings **76**, 1786-1791 (2013).

301. R. D. Deegan, O. Bakajin, T. F. Dupont, G. Huber, S. R. Nagel, and T. A. Witten, "Capillary flow as the cause of ring stains from dried liquid drops," Nature **389**, 827-829 (1997).

302. A. F. Routh and W. B. Russel, "Horizontal drying fronts during solvent evaporation from latex films," Aiche Journal **44**, 2088-2098 (1998).

303. V. Divry, A. Gromer, M. Nassar, C. Lambour, D. Collin, and Y. Holl, "Drying Mechanisms in Plasticized Latex Films: Role of Horizontal Drying Fronts," Journal of Physical Chemistry B **120**, 6791-6802 (2016).

304. A. F. Routh and W. B. Zimmerman, "Distribution of particles during solvent evaporation from films," Chemical Engineering Science **59**, 2961-2968 (2004).

305. T. Narita, P. Hebraud, and F. Lequeux, "Effects of the rate of evaporation and film thickness on nonuniform drying of film-forming concentrated colloidal suspensions," European Physical Journal E **17**, 69-76 (2005).

306. A. M. Koenig, T. G. Weerakkody, J. L. Keddie, and D. Johannsmann, "Heterogeneous drying of colloidal polymer films: Dependence on added salt," Langmuir **24**, 7580-7589 (2008).

307. F. T. Carter, R. M. Kowalczyk, I. Millichamp, M. Chainey, and J. L. Keddie, "Correlating Particle Deformation with Water Concentration Profiles during Latex Film Formation: Reasons That Softer Latex Films Take Longer to Dry," Langmuir **30**, 9672-9681 (2014).

308. M. S. Tirumkudulu and W. B. Russel, "Cracking in drying latex films," Langmuir **21**, 4938-4948 (2005).

309. M. S. Tirumkudulu and W. B. Russel, "Role of capillary stresses in film formation," Langmuir **20**, 2947-2961 (2004).

310. N. Birk-Braun, K. Yunus, E. J. Rees, W. Schabel, and A. F. Routh, "Generation of strength in a drying film: How fracture toughness depends on dispersion properties," Physical Review E **95**(2017).

311. L. F. Francis, A. V. McCormick, D. M. Vaessen, and J. A. Payne, "Development and measurement of stress in polymer coatings," Journal of Materials Science **37**, 4717-4731 (2002).

312. A. Brun, H. Dihang, and L. Brunel, "Film formation of coatings studied by diffusing-wave spectroscopy," Progress in Organic Coatings **61**, 181-191 (2008).

313. H. M. van der Kooij, R. Fokkink, J. van der Gucht, and J. Sprakel, "Quantitative imaging of heterogeneous dynamics in drying and aging paints," Scientific Reports **6**(2016).

314. B. M. Weon and J. H. Je, "Capillary force repels coffee-ring effect," Physical Review E **82**(2010).

315. H. Luo, L. E. Scriven, and L. F. Francis, "Cryo-SEM studies of latex/ceramic nanoparticle coating microstructure development," Journal of Colloid and Interface Science **316**, 500-509 (2007).

316. Y. Ma, H. T. Davis, and L. E. Scriven, "Microstructure development in drying latex coatings," Progress in Organic Coatings **52**, 46-62 (2005).

317. H. Luo, C. M. Cardinal, L. E. Scriven, and L. F. Francis, "Ceramic nanoparticle/monodisperse latex coatings," Langmuir **24**, 5552-5561 (2008).

318. J. L. Keddie, P. Meredith, R. A. L. Jones, and A. M. Donald, "KINETICS OF FILM FORMATION IN ACRYLIC LATICES STUDIED WITH MULTIPLE-ANGLE-OF-INCIDENCE ELLIPSOMETRY AND ENVIRONMENTAL SEM," Macromolecules **28**, 2673-2682 (1995).

319. K. I. Dragnevski, A. F. Routh, M. W. Murray, and A. M. Donald, "Cracking of Drying Latex Films: An ESEM Experiment," Langmuir **26**, 7747-7751 (2010).

320. A. M. Donald, "The use of environmental scanning electron microscopy for imaging wet and insulating materials," Nature Materials **2**, 511-516 (2003).

321. Y. Wang, D. Juhue, M. A. Winnik, O. M. Leung, and M. C. Goh, "ATOMIC FORCE MICROSCOPY STUDY OF LATEX FILM FORMATION," Langmuir **8**, 760-762 (1992).

322. L. Goehring, W. J. Clegg, and A. F. Routh, "Plasticity and Fracture in Drying Colloidal Films," Physical Review Letters **110**(2013).

323. J. Mallegol, O. Dupont, and J. L. Keddie, "Morphology and elasticity of waterborne acrylic pressure-sensitive adhesives investigated, with atomic force microscopy," Journal of Adhesion Science and Technology **17**, 243-259 (2003).

324. J. M. Salamanca, E. Ciampi, D. A. Faux, P. M. Glover, P. J. McDonald, A. F. Routh, A. Peters, R. Satguru, and J. L. Keddie, "Lateral drying in thick films of waterborne colloidal particles," Langmuir **17**, 3202-3207 (2001).

325. M. D. Mantle and A. J. Sederman, "Dynamic MRI in chemical process and reaction engineering," Progress in Nuclear Magnetic Resonance Spectroscopy **43**, 3-60 (2003).

326. J. Mallegol, G. Bennett, P. J. McDonald, J. L. Keddie, and O. Dupont, "Skin development during the film formation of waterborne acrylic pressure-sensitive adhesives containing tackifying resin," Journal of Adhesion **82**, 217-238 (2006).

327. E. R. Dufresne, D. J. Stark, N. A. Greenblatt, J. X. Cheng, J. W. Hutchinson, L. Mahadevan, and D. A. Weitz, "Dynamics of fracture in drying suspensions," Langmuir **22**, 7144-7147 (2006).

328. E. R. Dufresne, E. I. Corwin, N. A. Greenblatt, J. Ashmore, D. Y. Wang, A. D. Dinsmore, J. X. Cheng, X. S. Xie, J. W. Hutchinson, and D. A. Weitz, "Flow and fracture in drying nanoparticle suspensions," Physical Review Letters **91**(2003).

329. I. Ludwig, W. Schabel, M. Kind, J. C. Castaing, and P. Ferlin, "Drying and film formation of industrial waterborne latices," Aiche Journal **53**, 549-560 (2007).

330. I. Ludwig, W. Schabel, P. Ferlin, J. C. Castaing, and M. Kind, "Drying, film formation and open time of aqueous polymer dispersions," European Physical Journal-Special Topics **166**, 39-43 (2009).

331. H. N. Yow, M. Goikoetxea, L. Goehring, and A. F. Routh, "Effect of film thickness and particle size on cracking stresses in drying latex films," Journal of Colloid and Interface Science **352**, 542-548 (2010).

332. K. von der Ehe and D. Johannsmann, "Maps of the stress distributions in drying latex films," Review of Scientific Instruments **78**(2007).

333. A. M. Koenig, E. Bourgeat-Lami, V. Mellon, K. von der Ehe, A. F. Routh, and D. Johannsmann, "Dilational Lateral Stress in Drying Latex Films," Langmuir **26**, 3815-3820 (2010).

334. Y. Xu, W. C. Engl, E. R. Jerison, K. J. Wallenstein, C. Hyland, L. A. Wilen, and E. R. Dufresne, "Imaging in-plane and normal stresses near an interface crack using traction force microscopy," Proceedings of the National Academy of Sciences of the United States of America **107**, 14964-14967 (2010).

335. E. R. Jerison, Y. Xu, L. A. Wilen, and E. R. Dufresne, "Deformation of an Elastic Substrate by a Three-Phase Contact Line," Physical Review Letters **106**(2011).

336. S. M. Rossnagel, P. Gilstrap, and R. Rujkorakarn, "STRESS MEASUREMENT IN THIN-FILMS BY GEOMETRICAL-OPTICS," Journal of Vacuum Science & Technology **21**, 1045-1046 (1982).

337. V. R. Gundabala and A. F. Routh, "Thinning of drying latex films due to surfactant," Journal of Colloid and Interface Science **303**, 306-314 (2006).

338. C. J. Martinez and J. A. Lewis, "Shape evolution and stress development during latex-silica film formation," Langmuir **18**, 4689-4698 (2002).

339. D. M. Holmes, R. V. Kumar, and W. J. Clegg, "Cracking during lateral drying of alumina suspensions," Journal of the American Ceramic Society **89**, 1908-1913 (2006).

340. J. Li, B. Cabane, M. Sztucki, J. Gummel, and L. Goehring, "Drying Dip-Coated Colloidal Films," Langmuir **28**, 200-208 (2012).

341. J. Rieger, E. Hadicke, G. Ley, and P. Lindner, "CRYSTALS MADE OF CLOSE-PACKED POLYMERIC SPHERES - A NEUTRON-SCATTERING STUDY ON LATEX FILMS," Physical Review Letters **68**, 2782-2785 (1992).

342. J. Mallegol, J. P. Gorce, O. Dupont, C. Jeynes, P. J. McDonald, and J. L. Keddie, "Origins and effects of a surfactant excess near the surface of waterborne acrylic pressure-sensitive adhesives," Langmuir **18**, 4478-4487 (2002).

343. V. R. Gundabala, W. B. Zimmerman, and A. F. Routh, "A model for surfactant distribution in latex coatings," Langmuir **20**, 8721-8727 (2004).

344. J. P. Kunkel and M. W. Urban, "SURFACE AND INTERFACIAL FT-IR SPECTROSCOPIC STUDIES OF LATEXES .8. THE EFFECT OF PARTICLE AND COPOLYMER COMPOSITION ON SURFACTANT EXUDATION IN STYRENE-N-BUTYL ACRYLATE COPOLYMER LATEX FILMS," Journal of Applied Polymer Science **50**, 1217-1223 (1993).

345. C. L. Zhao, F. Dobler, T. Pith, Y. Holl, and M. Lambla, "SURFACE-COMPOSITION OF COALESCED ACRYLIC LATEX FILMS STUDIED BY XPS AND SIMS," Journal of Colloid and Interface Science **128**, 437-469 (1989).

346. P. Zakharov and F. Scheffold, "Monitoring Spatially Heterogeneous Dynamics in a Drying Colloidal Thin Film," Soft Mater. **8**, 102-113 (2010).

347. R. Balamurugan and G. Rajarajan, "Study of drying process of paint by dynamic speckle with B/D pixel counting technique," Optics and Lasers in Engineering **98**, 62-68 (2017).

348. H. Huang, "Drying inhomogeneity during film formation of waterborne latex systems: A mechanistic study on skin layer formation," (Lehigh University, 2018).

349. P. Ekanayake, P. J. McDonald, and J. L. Keddie, "An experimental test of the scaling prediction for the spatial distribution of water during the drying of colloidal films," European Physical Journal-Special Topics **166**, 21-27 (2009).

350. B. Yang, J. S. Sharp, and M. I. Smith, "Shear Banding in Drying Films of Colloidal Nanoparticles," Acs Nano **9**, 4077-4084 (2015).

351. P.-C. Kiatkirakajorn and L. Goehring, "Formation of Shear Bands in Drying Colloidal Dispersions," Physical Review Letters **115**(2015).

352. S. Wang, M. Singh, A. L. Lopez, C. Wu, R. Raghunathan, A. Schill, J. Li, K. V. Larin, and I. V. Larina, "Direct four-dimensional structural and functional imaging of cardiovascular dynamics in mouse embryos with 1.5 MHz optical coherence tomography," Opt. Lett. **40**, 4791-4794 (2015).

353. R. Dsouza, J. Won, G. L. Monroy, D. R. Spillman, and S. A. Boppart, *Economical and compact briefcase spectral-domain optical coherence tomography system for primary care and point-of-care applications* (SPIE, 2018), Vol. 23, pp. 1-11, 11.

354. S. Kim, M. Crose, W. J. Eldridge, B. Cox, W. J. Brown, and A. Wax, "Design and implementation of a low-cost, portable OCT system," Biomed. Opt. Express **9**, 1232-1243 (2018).

355. WHO, "Cancer" (World Health Organization, 2018), retrieved http://www.who.int/cancer/en/.

356. I. Kola and J. Landis, "Can the pharmaceutical industry reduce attrition rates?," Nature Reviews Drug Discovery **3**, 711-716 (2004).

357. S. Breslin and L. O'Driscoll, "Three-dimensional cell culture: the missing link in drug discovery," Drug Discovery Today **18**, 240-249 (2013).

358. J. A. Hickman, R. Graeser, R. de Hoogt, S. Vidic, C. Brito, M. Gutekunst, H. van der Kuip, and I. P. consortium, "Three ‐ dimensional models of cancer for pharmacology and cancer cell biology: Capturing tumor complexity in vitro/ex vivo," Biotechnology Journal **9**, 1115-1128 (2014).

359. J. Friedrich, C. Seidel, R. Ebner, and L. A. Kunz-Schughart, "Spheroid-based drug screen: considerations and practical approach," Nature Protocols **4**, 309-324 (2009).

360. M. Vinci, S. Gowan, F. Boxall, L. Patterson, M. Zimmermann, W. Court, C. Lomas, M. Mendiola, D. Hardisson, and S. A. Eccles, "Advances in establishment and analysis of three-dimensional tumor spheroid-based functional assays for target validation and drug evaluation," BMC biology **10**, 29 (2012).

361. F. Pampaloni, N. Ansari, and E. H. K. Stelzer, "High-resolution deep imaging of live cellular spheroids with light-sheet-based fluorescence microscopy," Cell and Tissue Research **352**, 161-177 (2013).

362. Y. Huang, S. Wang, Q. Guo, S. Kessel, I. Rubinoff, L. L.-Y. Chan, P. Li, Y. Liu, J. Qiu, and C. Zhou, "Optical coherence tomography detects necrotic regions and volumetrically quantifies multicellular tumor spheroids," canres.0821.2017.

363. Y. Huang, J. Zou, M. Badar, J. Liu, W. Shi, S. Wang, Q. Guo, X. Wang, S. Kessel, L. L.-Y. Chan, P. Li, Y. Liu, J. Qiu, and C. Zhou, "Longitudinal Morphological and Physiological Monitoring of Three-dimensional Tumor Spheroids Using Optical Coherence Tomography," JoVE, e59020 (2019).

364. M. Sharma, Y. Verma, K. D. Rao, R. Nair, and P. K. Gupta, "Imaging growth dynamics of tumour spheroids using optical coherence tomography," Biotechnology Letters **29**, 273-278 (2006).

365. W. E. Thorell, M. M. Chow, R. A. Prayson, M. A. Shure, S. W. Jeon, D. Huang, E. Zeynalov, H. H. Woo, P. A. Rasmussen, A. M. Rollins, and T. J. Masaryk, "Optical coherence tomography: a new method to assess aneurysm healing," Journal of Neurosurgery **102**, 348-354 (2005).

366. C. L. Evans, I. Rizvi, T. Hasan, and J. F. d. Boer, "In vitro ovarian tumor growth and treatment response dynamics visualized with time-lapse OCT imaging," Opt. Express **17**, 8892-8906 (2009).

367. W. T. Shi, J. Kwon, Y. Y. Huang, J. F. Tan, C. G. Uhl, R. He, C. Zhou, and Y. L. Liu, "Facile Tumor Spheroids Formation in Large Quantity with Controllable Size and High Uniformity," Scientific Reports **8**(2018).

368. D. M. Kingsley, C. L. Roberge, A. Rudkouskaya, D. E. Faulkner, M. Barroso, X. Intes, and D. T. Corr, "Laser-based 3D bioprinting for spatial and size control of tumor spheroids and embryoid bodies," Acta Biomaterialia (2019).

369. J. P. Celli, B. Q. Spring, I. Rizvi, C. L. Evans, K. S. Samkoe, S. Verma, B. W. Pogue, and T. Hasan, "Imaging and Photodynamic Therapy: Mechanisms, Monitoring, and Optimization," Chemical Reviews **110**, 2795-2838 (2010).

370. C. L. Evans, A. O. Abu-Yousif, Y. J. Park, O. J. Klein, J. P. Celli, I. Rizvi, X. Zheng, and T. Hasan, "Killing Hypoxic Cell Populations in a 3D Tumor Model with EtNBS-PDT," PLoS ONE **6**, e23434 (2011).

371. Y. Jung, A. J. Nichols, O. J. Klein, E. Roussakis, and C. L. Evans, "Label-free, longitudinal visualization of PDT response in vitro with optical coherence tomography," Isr. J. Chem. **52**, 728-744 (2012).

372. O. J. Klein, Y. K. Jung, and C. L. Evans, "Longitudinal, quantitative monitoring of therapeutic response in 3D in vitro tumor models with OCT for high-content therapeutic screening," Methods **66**, 299-311 (2014).

373. Y. Jung, O. J. Klein, H. Wang, and C. L. Evans, "Longitudinal, label-free, quantitative tracking of cell death and viability in a 3D tumor model with OCT," Sci. Rep. **6**, 27017 (2016).

374. P. Yu, M. Mustata, J. J. Turek, P. M. W. French, M. R. Melloch, and D. D. Nolte, "Holographic optical coherence imaging of tumor spheroids," Applied Physics Letters **83**, 575-577 (2003).

375. P. Yu, M. Mustata, L. Peng, J. J. Turek, M. R. Melloch, P. M. W. French, and D. D. Nolte, "Holographic optical coherence imaging of rat osteogenic sarcoma tumor spheroids," Appl. Opt. **43**, 4862-4873 (2004).

376. D. D. Nolte, R. An, J. Turek, and K. Jeong, "Tissue Dynamics Spectroscopy for Three-Dimensional Tissue-Based Drug Screening," JALA: Journal of the Association for Laboratory Automation **16**, 431-442 (2011).

377. D. D. Nolte, R. An, J. Turek, and K. Jeong, "Tissue dynamics spectroscopy for phenotypic profiling of drug effects in three-dimensional culture," Biomedical Optics Express **3**, 2825-2841 (2012).

378. Y. Jian, K. Wong, and M. V. Sarunic, "GPU accelerated OCT processing at megahertz axial scan rate and high resolution video rate volumetric rendering," in *Optical Coherence Tomography and Coherence Domain Optical Methods in Biomedicine XVII*, (International Society for Optics and Photonics, 2013), 85710Z.

379. J. Canny, "A computational approach to edge detection," IEEE Transactions on pattern analysis and machine intelligence, 679-698 (1986).

380. K. A. Vermeer, J. Mo, J. J. A. Weda, H. G. Lemij, and J. F. de Boer, "Depth-resolved model-based reconstruction of attenuation coefficients in optical coherence tomography," Biomed. Opt. Express **5**, 322-337 (2014).

381. S. Kessel, S. Cribbes, O. Dery, D. Kuksin, E. Sincoff, J. Qiu, and L. L. Y. Chan, "High-Throughput 3D Tumor Spheroid Screening Method for Cancer Drug Discovery Using Celigo Image Cytometry," Journal of Laboratory Automation, 2211068216652846 (2016).

382. S. Kessel, S. Cribbes, O. Dery, D. Kuksin, E. Sincoff, J. Qiu, and L. L. Y. Chan, "High-Throughput 3D Tumor Spheroid Screening Method for Cancer Drug Discovery Using Celigo Image Cytometry.," Journal of Laboratory Automation, 2211068216652846 (2016).

383. C. L. Chaffer and R. A. Weinberg, "A Perspective on Cancer Cell Metastasis," Science **331**, 1559-1564 (2011).

384. D. Hanahan and R. A. Weinberg, "Hallmarks of Cancer: The Next Generation," Cell **144**, 646-674 (2011).

385. S. Valastyan and R. A. Weinberg, "Tumor Metastasis: Molecular Insights and Evolving Paradigms," Cell **147**, 275-292 (2011).

386. K. F. Lei, H.-P. Tseng, C.-Y. Lee, and N.-M. Tsang, "Quantitative Study of Cell Invasion Process under Extracellular Stimulation of Cytokine in a Microfluidic Device," Scientific Reports **6**, 25557 (2016).

387. A. W. Lambert, D. R. Pattabiraman, and R. A. Weinberg, "Emerging Biological Principles of Metastasis," Cell **168**, 670-691 (2017).

388. T. Brabletz, R. Kalluri, M. A. Nieto, and R. A. Weinberg, "EMT in cancer," Nature Reviews Cancer **18**, 128-+ (2018).

389. I. J. Fidler, "Timeline - The pathogenesis of cancer metastasis: the 'seed and soil' hypothesis revisited," Nature Reviews Cancer **3**, 453-458 (2003).

390. J. E. Talmadge and I. J. Fidler, "AACR Centennial Series: The Biology of Cancer Metastasis: Historical Perspective," Cancer Research **70**, 5649-5669 (2010).

391. N. A. Evensen, J. Li, J. Yang, X. J. Yu, N. S. Sampson, S. Zucker, and J. Cao, "Development of a High-Throughput Three-Dimensional Invasion Assay for Anti-Cancer Drug Discovery," Plos One **8**, 11 (2013).

392. M. Vinci, C. Box, and S. A. Eccles, "Three-Dimensional (3D) Tumor Spheroid Invasion Assay," Jove-Journal of Visualized Experiments (2015).

393. S. Boyden, "THE CHEMOTACTIC EFFECT OF MIXTURES OF ANTIBODY AND ANTIGEN ON POLYMORPHONUCLEAR LEUCOCYTES," The Journal of Experimental Medicine **115**, 453 (1962).

394. C. R. Justus, N. Leffler, M. Ruiz-Echevarria, and L. V. Yang, "In vitro Cell Migration and Invasion Assays," JoVE, e51046 (2014).

395. J. Marshall, "Transwell® Invasion Assays," in *Cell Migration*, W. C. and P. M., eds. (Humana Press, 2011).

396. E. B. Berens, J. M. Holy, A. T. Riegel, and A. Wellstein, "A Cancer Cell Spheroid Assay to Assess Invasion in a 3D Setting," Jove-Journal of Visualized Experiments, 6 (2015).

397. L. R. C. Castillo, A. D. Oancea, C. Stullein, and A. Regnier-Vigouroux, "A Novel Computer-Assisted Approach to evaluate Multicellular Tumor Spheroid Invasion Assay," Scientific Reports **6**(2016).

398. M. Vinci, C. Box, M. Zimmermann, and S. A. Eccles, "Tumor Spheroid-Based Migration Assays for Evaluation of Therapeutic Agents," in *Target Identification and Validation in Drug Discovery*, M. J. and C. R., eds. (Humana Press, 2013).

399. F. Lefranc, J. Brotchi, and R. Kiss, "Possible future issues in the treatment of glioblastomas: Special emphasis on cell migration and the resistance of migrating glioblastoma cells to apoptosis," J. Clin. Oncol. **23**, 2411-2422 (2005).

400. M. Vinci, S. Gowan, F. Boxall, L. Patterson, M. Zimmermann, W. Court, C. Lomas, M. Mendiola, D. Hardisson, and S. A. Eccles, "Advances in establishment and analysis of three-dimensional tumor spheroid-based functional assays for target validation and drug evaluation," Bmc Biology **10**(2012).

401. I. A. Khawar, J. K. Park, E. S. Jung, M. A. Lee, S. Chang, and H. J. Kuh, "Three Dimensional Mixed-Cell Spheroids Mimic Stroma-Mediated Chemoresistance and Invasive Migration in hepatocellular carcinoma," Neoplasia **20**, 800-812 (2018).

402. M. Vinci, A. Burford, V. Molinari, K. Kessler, S. Popov, M. Clarke, K. R. Taylor, H. N. Pemberton, C. J. Lord, A. Gutteridge, T. Forshew, D. Carvalho, L. V. Marshall, E. Y. Qin, W. J. Ingram, A. S. Moore, H. K. Ng, S. Trabelsi, D. Hmida-Ben Brahim, N. Entz-Werle, S. Zacharoulis, S. Vaidya, H. C. Mandeville, L. R. Bridges, A. J. Martin, S. Al-Sarraj, C. Chandler, M. Sunol, J. Mora, C. de

Torres, O. Cruz, A. M. Carcaboso, M. Monje, A. Mackay, and C. Jones, "Functional diversity and cooperativity between subclonal populations of pediatric glioblastoma and diffuse intrinsic pontine glioma cells," Nature Medicine **24**, 1204-+ (2018).

403. S. Cribbes, S. Kessel, S. McMenemy, J. Qiu, and L. L. Y. Chan, "A Novel Multiparametric Drug-Scoring Method for High-Throughput Screening of 3D Multicellular Tumor Spheroids Using the Celigo Image Cytometer," Slas Discovery **22**, 547-557 (2017).

404. T. J. Puls, X. H. Tan, M. Husain, C. F. Whittington, M. L. Fishel, and S. L. Voytik-Harbin, "Development of a Novel 3D Tumor-tissue Invasion Model for High-throughput, High-content Phenotypic Drug Screening," Scientific Reports **8**(2018).

405. T. Eisemann, B. Costa, J. Strelau, M. Mittelbronn, P. Angel, and H. Peterziel, "An advanced glioma cell invasion assay based on organotypic brain slice cultures," Bmc Cancer **18**, 10 (2018).

406. M. E. Boutin, T. C. Voss, S. A. Titus, K. Cruz-Gutierrez, S. Michael, and M. Ferrer, "A high-throughput imaging and nuclear segmentation analysis protocol for cleared 3D culture models," Scientific Reports **8**, 11135 (2018).

407. Y.-C. Tung, A. Y. Hsiao, S. G. Allen, Y.-s. Torisawa, M. Ho, and S. Takayama, "High-throughput 3D spheroid culture and drug testing using a 384 hanging drop array," The Analyst **136**, 473-478 (2011).

408. N. J. Martinez, S. A. Titus, A. K. Wagner, and A. Simeonov, "High-throughput fluorescence imaging approaches for drug discovery using in vitroand in vivothree-dimensional models," Expert Opinion on Drug Discovery **10**, 1347-1361 (2015).

409. T. Klein, W. Wieser, L. Reznicek, A. Neubauer, A. Kampik, and R. Huber, "Multi-MHz retinal OCT," Biomed. Opt. Express **4**, 1890-1908 (2013).

410. C. Zhou, A. Alex, J. Rasakanthan, and Y. Ma, "Space-division multiplexing optical coherence tomography.," Opt. Express **21**, 19219-19227 (2013).

411. N. J. Martucci, K. Morgan, G. W. Anderson, P. C. Hayes, J. N. Plevris, L. J. Nelson, and P. O. Bagnaninchi, "Nondestructive Optical Toxicity Assays of 3D Liver Spheroids with Optical Coherence Tomography," Advanced Biosystems **2**, 1700212 (2018).

412. R. K. Chhetri, Z. F. Phillips, M. A. Troester, and A. L. Oldenburg, "Longitudinal Study of Mammary Epithelial and Fibroblast Co-Cultures Using Optical Coherence Tomography Reveals Morphological Hallmarks of Pre-Malignancy," Plos One **7**(2012).

413. A. L. Oldenburg, X. Yu, T. Gilliss, O. Alabi, R. M. Taylor, and M. A. Troester, "Inverse-power-law behavior of cellular motility reveals stromal-epithelial cell interactions in 3D co-culture by OCT fluctuation spectroscopy," Optica **2**, 877-885 (2015).

414. W.-C. Yan, P. Davoodi, S. Vijayavenkataraman, Y. Tian, W. C. Ng, J. Y. H. Fuh, K. S. Robinson, and C.-H. Wang, "3D bioprinting of skin tissue: From pre-processing to final product evaluation," Adv. Drug Deliv. Rev. **132**, 270-295 (2018).

415. A. Zein-Sabatto, J. S. Lee, M. Kuhn, I. Aponte, B. Felalaga, J. Sevetson, B. Ip, D. Hoffman-Kim, J. Morgan, and J. Lee, *Label-free cellular viability imaging in 3D tissue spheroids with dynamic optical coherence tomography (Conference Presentation)*, SPIE BiOS (SPIE, 2019), Vol. 10883.

416. J. Scholler, V. Mazlin, O. Thouvenin, K. Groux, P. Xiao, J.-A. Sahel, M. Fink, C. Boccara, and K. Grieve, "Probing dynamic processes in the eye at multiple spatial and temporal scales with multimodal full field OCT," Biomed. Opt. Express **10**, 731-746 (2019).

417. E. E. Capowski, K. Samimi, S. J. Mayerl, M. J. Phillips, I. Pinilla, S. E. Howden, J. Saha, A. D. Jansen, K. L. Edwards, L. D. Jager, K. Barlow, R. Valiauga, Z. Erlichman, A. Hagstrom, D. Sinha, V. M. Sluch, X. Chamling, D. J. Zack, M. C. Skala, and D. M. Gamm, "Reproducibility and staging of 3D human retinal organoids across multiple pluripotent stem cell lines," Development **146**, dev171686 (2019).

418. A. W. Browne, C. Arnesano, N. Harutyunyan, T. Khuu, J. C. Martinez, H. A. Pollack, D. S. Koos, T. C. Lee, S. E. Fraser, R. A. Moats, J. G. Aparicio, and D. Cobrinik, "Structural and Functional Characterization of Human Stem-Cell-Derived Retinal Organoids by Live Imaging," Investigative Ophthalmology & Visual Science **58**, 3311-3318 (2017).

419. F. Li, T. Xu, D.-H. T. Nguyen, X. Huang, C. S. Chen, and C. Zhou, "Label-free evaluation of angiogenic sprouting in microengineered devices using ultrahigh-resolution optical coherence microscopy," Journal of Biomedical Optics **19**, 016006 (2014).

420. H. Takahashi, K. Kato, K. Ueyama, M. Kobayashi, G. Baik, Y. Yukawa, J. Suehiro, and Y. T. Matsunaga, "Visualizing dynamics of angiogenic sprouting from a three-dimensional microvasculature model using stage-top optical coherence tomography," Scientific Reports **7**(2017).

421. E. Lee, H. Takahashi, J. Pauty, M. Kobayashi, K. Kato, M. Kabara, J. Kawabe, and Y. T. Matsunaga, "A 3D in vitro pericyte-supported microvessel model: visualisation and quantitative characterisation of multistep angiogenesis," Journal of Materials Chemistry B **6**, 1085-1094 (2018).

422. A. T. Yeh, B. S. Kao, W. G. Jung, Z. P. Chen, J. S. Nelson, and B. J. Tromberg, "Imaging wound healing using optical coherence tomography and multiphoton microscopy in an in vitro skin-equivalent tissue model," Journal of Biomedical Optics **9**, 248-253 (2004).

423. F. Spoler, M. Forst, Y. Marquardt, D. Hoeller, H. Kurz, H. Merk, and F. Abuzahra, "High-resolution optical coherence tomography as a non-destructive monitoring tool for the engineering of skin equivalents," Skin Research and Technology **12**, 261-267 (2006).

424. Y. Hara, Y. Ogura, T. Yamashita, D. Furukawa, and S. Saeki, "Visualization of viscoelastic behavior in skin equivalent using optical coherence tomography-based straingraphy," Skin Research and Technology **24**, 334-339 (2018).

425. W. W. Burggren, "Cardiovascular Development and Angiogenesis in the Early Vertebrate Embryo," Cardiovascular Engineering and Technology **4**, 234-245 (2013).

426. A. Santhanakrishnan and L. A. Miller, "Fluid Dynamics of Heart Development," Cell Biochemistry and Biophysics **61**, 1-22 (2011).

427. W. J. Kowalski, K. Pekkan, J. P. Tinney, and B. B. Keller, "Investigating developmental cardiovascular biomechanics and the origins of congenital heart defects," Front Physiol **5**, 408 (2014).

428. S. M. Gilboa, O. J. Devine, J. E. Kucik, M. E. Oster, T. Riehle-Colarusso, W. N. Nembhard, P. Xu, A. Correa, K. Jenkins, and A. J. Marelli, "Congenital Heart Defects in the United States Estimating the Magnitude of the Affected Population in 2010," Circulation **134**, 101-+ (2016).

429. M. Fink, C. Callol-Massot, A. Chu, P. Ruiz-Lozano, J. C. Izpisua Belmonte, W. Giles, R. Bodmer, and K. Ocorr, "A new method for detection and quatification of heartbeat parameters in Drosophila, zebrafish and embryonic mouse hearts," Biotechniques **46(2)**, 101-113 (2009).

430. E. Pierpont Mary, T. Basson Craig, D. W. Benson, D. Gelb Bruce, M. Giglia Therese, E. Goldmuntz, G. McGee, A. Sable Craig, D. Srivastava, and L. Webb Catherine, "Genetic Basis for Congenital Heart Defects: Current Knowledge," Circulation **115**, 3015-3038 (2007).

431. M. C. Digilio and B. Marino, "What Is New in Genetics of Congenital Heart Defects?," Frontiers in pediatrics **4**, 120-120 (2016).

432. A. Sifrim, M.-P. Hitz, A. Wilsdon, J. Breckpot, S. H. A. Turki, B. Thienpont, J. McRae, T. W. Fitzgerald, T. Singh, G. J. Swaminathan, E. Prigmore, D. Rajan, H. Abdul-Khaliq, S. Banka, U. M. M. Bauer, J. Bentham, F. Berger, S. Bhattacharya, F. Bu'Lock, N. Canham, I.-G. Colgiu, C. Cosgrove, H. Cox, I. Daehnert, A. Daly, J. Danesh, A. Fryer, M. Gewillig, E. Hobson, K. Hoff, T. Homfray, I. S. the, A.-K. Kahlert, A. Ketley, H.-H. Kramer, K. Lachlan, A. K. Lampe, J. J. Louw, A. K. Manickara, D. Manase, K. P. McCarthy, K. Metcalfe, C. Moore, R. Newbury-Ecob, S. O. Omer, W. H. Ouwehand, S.-M. Park, M. J. Parker, T. Pickardt, M. O. Pollard, L. Robert, D. J. Roberts, J. Sambrook, K. Setchfield, B. Stiller, C. Thornborough, O. Toka, H. Watkins, D. Williams, M. Wright, S. Mital, P. E. F. Daubeney, B. Keavney, J. Goodship, U. K. K. C. the, R. M. Abu-Sulaiman, S. Klaassen, C. F. Wright, H. V. Firth, J. C. Barrett, K. Devriendt, D. R. FitzPatrick, J. D. Brook, S. the Deciphering Developmental Disorders, and M. E. Hurles, "Distinct genetic architectures for syndromic and nonsyndromic congenital heart defects identified by exome sequencing," Nature Genetics **48**, 1060 (2016).

433. J. Jenkins Kathy, A. Correa, A. Feinstein Jeffrey, L. Botto, E. Britt Amy, R. Daniels Stephen, M. Elixson, A. Warnes Carole, and L. Webb Catherine, "Noninherited Risk Factors and Congenital Cardiovascular Defects: Current Knowledge," Circulation **115**, 2995-3014 (2007).

434. S. S. Patel and T. L. Burns, "Nongenetic Risk Factors and Congenital Heart Defects," Pediatric Cardiology **34**, 1535-1555 (2013).

435. K. Tobita, X. Liu, and C. W. Lo, "Imaging modalities to assess structural birth defects in mutant mouse models," Birth Defects Research Part C: Embryo Today: Reviews **90**, 176-184 (2010).

436. S. M. Savolainen, J. F. Foley, and S. A. Elmore, "Histology Atlas of the Developing Mouse Heart with Emphasis on E11.5 to E18.5," Toxicologic Pathology **37**, 395-414 (2009).

437. X. Liu, A. J. Kim, W. Reynolds, Y. Wu, and C. W. Lo, "Phenotyping cardiac and structural birth defects in fetal and newborn mice," Birth Defects Research **109**, 778-790 (2017).

438. W. J. Kowalski, K. Pekkan, J. P. Tinney, and B. B. Keller, "Investigating developmental cardiovascular biomechanics and the origins of congenital heart defects," Frontiers in Physiology **5**, 408 (2014).

439. S. R. Schultz, C. S. Copeland, A. J. Foust, P. Quicke, and R. Schuck, "Advances in two photon scanning and scanless microscopy technologies for functional neural circuit imaging," Proceedings of the IEEE. Institute of Electrical and Electronics Engineers **105**, 139-157 (2017).

440. S. Srinivasan, H. S. Baldwin, O. Aristizabal, L. Kwee, M. Labow, M. Artman, and D. H. Turnbull, "Noninvasive, In Utero Imaging of Mouse Embryonic Heart Development With 40-MHz Echocardiography," Circulation **98**, 912-918 (1998).

441. C. K. L. Phoon, "Imaging Tools for the Developmental Biologist: Ultrasound Biomicroscopy of Mouse Embryonic Development," Pediatric Research **60**, 14 (2006).

442. Q. Huang and Z. Zeng, "A Review on Real-Time 3D Ultrasound Imaging Technology," BioMed Research International **2017**, 20 (2017).

443. D. Dawson, C. A. Lygate, J. Saunders, J. E. Schneider, X. Ye, K. Hulbert, J. A. Noble, and S. Neubauer, "Quantitative 3-Dimensional Echocardiography for Accurate and Rapid Cardiac Phenotype Characterization in Mice," Circulation **110**, 1632-1637 (2004).

444. X. Qin, S. Wang, M. Shen, X. Zhang, S. Lerakis, M. B. Wagner, and B. Fei, *3D in vivo imaging of rat hearts by high frequency ultrasound and its application in myofiber orientation wrapping*, SPIE Medical Imaging (SPIE, 2015), Vol. 9419.

445. J. Laufer, F. C. Norris, J. O. Cleary, E. Z. Zhang, B. E. Treeby, B. T. Cox, S. P. Johnson, P. Scambler, M. F. Lythgoe, and P. C. Beard, *In vivo photoacoustic imaging of mouse embryos* (SPIE, 2012), Vol. 17, pp. 1-8, 8.

446. C.-M. Chen, A. M. A. Miranda, G. Bub, and S. Srinivas, "Detecting cardiac contractile activity in the early mouse embryo using multiple modalities," Frontiers in physiology **5**, 508-508 (2015).

447. K. Ivanovitch, S. Temiño, and M. Torres, "Live imaging of heart tube development in mouse reveals alternating phases of cardiac differentiation and morphogenesis," eLife **6**, e30668 (2017).

448. K. Degenhardt, C. Wright Alexander, D. Horng, A. Padmanabhan, and A. Epstein Jonathan, "Rapid 3D Phenotyping of Cardiovascular Development in Mouse Embryos by Micro-CT With Iodine Staining," Circulation: Cardiovascular Imaging **3**, 314-322 (2010).

449. M. Singh, R. Raghunathan, V. Piazza, A. M. Davis-Loiacono, A. Cable, T. J. Vedakkan, T. Janecek, M. V. Frazier, A. Nair, C. Wu, I. V. Larina, M. E. Dickinson, and K. V. Larin, "Applicability, usability, and limitations of murine embryonic imaging with optical coherence tomography and optical projection tomography," Biomed. Opt. Express **7**, 2295-2310 (2016).

450. A. Bassi, L. Fieramonti, C. D'Andrea, G. Valentini, and M. Mione, *In vivo label-free three-dimensional imaging of zebrafish vasculature with optical projection tomography* (SPIE, 2011), Vol. 16, pp. 1-4, 4.

451. J.-F. Colas and J. Sharpe, "Live optical projection tomography," Organogenesis **5**, 211-216 (2009).

452. S. Wang, D. S. Lakomy, M. D. Garcia, A. L. Lopez III, K. V. Larin, and I. V. Larina, "Four-dimensional live imaging of hemodynamics in mammalian embryonic heart with Doppler optical coherence tomography," Journal of Biophotonics **9**, 837-847 (2016).

453. S. A. Boppart, G. J. Tearney, B. E. Bouma, J. F. Southern, M. E. Brezinski, and J. G. Fujimoto, "Noninvasive assessment of the developing xenopus cardiovascular system using optical coherence tomography," Proc. Natl. Acad. Sci. U.S.A. **94**, 4256-4261 (1997).

454. V. X. D. Yang, M. Gordon, E. Seng-Yue, S. Lo, B. Qi, J. Pekar, A. Mok, B. Wilson, and I. Vitkin, "High speed, wide velocity dynamic range Doppler optical coherence tomography (Part II): Imaging in vivo cardiac dynamics of Xenopus laevis," Opt. Express **11**, 1650-1658 (2003).

455. L. Kagemann, H. Ishikawa, J. Zou, P. Charukamnoetkanok, G. Wollstein, K. A. Townsend, M. L. Gabriele, N. Bahary, X. Wei, J. G. Fujimoto, and J. S. Schuman, "Repeated, noninvasive, high resolution spectral domain optical coherence tomography imaging of zebrafish embryos," Molecular Vision **14**, 2157-2170 (2008).

456. N. V. Iftimia, D. X. Hammer, R. D. Ferguson, M. Mujat, D. Vu, and A. A. Ferrante, "Dual-beam Fourier domain optical Doppler tomography of zebrafish," Opt. Express **16**, 13624-13636 (2008).

457. G. H. Karunamuni, S. Gu, M. R. Ford, L. M. Peterson, P. Ma, T. Wang, A. M. Rollins, M. W. Jenkins, and M. Watanabe, "Capturing structure and function in an embryonic heart with biophotonic tools," Frontiers in Physio. **5**, 1-21 (2014).

458. G. Karunamuni, S. Gu, Y. Q. Doughman, A. I. Noonan, A. M. Rollins, M. W. Jenkins, and M. Watanabe, "Using optical coherence tomography to rapidly phenotype and quantify congenital heart defects associated with prenatal alcohol exposure," Dev. Dyn. **244**, 607-618 (2015).

459. Y. Liu, M. C. G. Broberg, M. Watanabe, A. M. Rollins, and M. W. Jenkins, "SLIME: robust, high-speed 3D microvascular mapping," Scientific Reports **9**, 893 (2019).

460. M. W. Jenkins, D. C. Adler, M. Gargesha, R. Huber, F. Rothenberg, J. Belding, M. Watanabe, D. L. Wilson, J. G. Fujimoto, and A. M. Rollins, "Ultrahigh-speed optical coherence tomography imaging and visualization of the embryonic avian heart using a buffered Fourier Domain Mode Locked laser," Opt. Express **15**, 6251-6267 (2007).

461. M. W. Jenkins, O. Q. Chughtai, A. N. Basavanhally, M. Watanabe, and A. M. Rollins, *In vivo gated 4D imaging of the embryonic heart using optical coherence tomography* (SPIE, 2007), Vol. 12, pp. 1-3, 3.

462. M. W. Jenkins, F. Rothenberg, D. Roy, V. P. Nikolski, Z. Hu, M. Watanabe, D. L. Wilson, I. R. Efimov, and A. M. Rollins, "4D embryonic cardiography using gated optical coherence tomography," Opt. Express **14**, 736-748 (2006).

463. M. W. Jenkins, L. Peterson, S. Gu, M. Gargesha, D. L. Wilson, M. Watanabe, and A. M. Rollins, "Measuring hemodynamics in the developing heart tube with four-dimensional gated Doppler optical coherence tomography," J. Biomed. Opt **15**, 066022 (2010).

464. P. Ma, Y. T. Wang, S. Gu, M. Watanabe, M. W. Jenkins, and A. M. Rollins, "Three-dimensional correction of conduction velocity in the embryonic heart using integrated optical mapping and optical coherence tomography," J. Biomed. Opt **19**, 076004-076004 (2014).

465. P. Li, A. Liu, L. Shi, X. Yin, S. Rugonyi, and R. K. Wang, "Assessment of strain and strain rate in embryonic chick heart in vivo using tissue Doppler optical coherence tomography," Phys Med Biol **56**, 7081-7092 (2011).

466. S. Gu, Y. T. Wang, P. Ma, A. A. Werdich, A. M. Rollins, and M. W. Jenkins, "Mapping conduction velocity of early embryonic hearts with a robust fitting algorithm," Biomed. Opt. Express **6**, 2138-2157 (2015).

467. A. Li, C. Zhou, J. Moore, P. Zhang, T. H. Tsai, H. C. Lee, D. M. Romano, M. L. McKee, D. A. Schoenfeld, and M. J. Serra, "Changes in the expression of the Alzheimer's disease-associated presenilin gene in drosophila heart leads to cardiac dysfunction," Current Alzheimer Research **8**, 313 (2011).

468. A. Alex, A. Li, X. Zeng, R. E. Tate, M. L. McKee, D. E. Capen, Z. Zhang, R. E. Tanzi, and C. Zhou, "A circadian clock gene, cry , affects heart morphogenesis and function in drosophila as revealed by optical coherence microscopy," PLoS ONE **10**, e0137236 (2015).

469. A. F. Pena, J. Devine, A. Doronin, and I. Meglinski, "Imaging of the interaction of low-frequency electric fields with biological tissues by optical coherence tomography," Optics Letters **38**, 2629-2631 (2013).

470. M. A. Choma, S. D. Izatt, R. J. Wessells, R. Bodmer, and J. A. Izatt, "In vivo imaging of the adult Drosophila melanogaster heart with real-time optical coherence tomography," Circulation **114**, e35-e36 (2006).

471. M. J. Wolf, H. Amrein, J. A. Izatt, M. A. Choma, M. C. Reedy, and H. A. Rockman, "Drosophila as a model for the identification of genes causing adult human heart disease," Proceedings of the National Academy of Sciences **103**, 1394-1399 (2006).

472. M. T. Tsai, C. K. Lee, F. Y. Chang, J. T. Wu, C. P. Wu, T. T. Chi, and C. C. Yang, "Noninvasive imaging of heart chamber in Drosophila with dual‐beam optical coherence tomography," J. Biophoton. **6**, 708-717 (2013).

473. M. A. Choma, M. J. Suter, B. J. Vakoc, B. E. Bouma, and G. J. Tearney, "Physiological homology between Drosophila melanogaster and vertebrate cardiovascular systems," Disease models & mechanisms **4**, 411-420 (2011).

474. K. V. Larin, I. V. Larina, M. Liebling, and M. E. Dickinson, "Live imaging of early developmental processes in mammalian embryos with optical coherence tomography," J Innov Opt Health Sci **02**, 253-259 (2009).

475. S. Bhat, I. V. Larina, K. V. Larin, M. E. Dickinson, and M. Liebling, "4D reconstruction of the beating embryonic heart from two orthogonal sets of parallel optical coherence tomography slice-sequences," Medical Imaging, IEEE Transactions on **32**, 578-588 (2013).

476. W. Luo, D. L. Marks, T. S. Ralston, and S. A. Boppart, "Three-dimensional optical coherence tomography of the embryonic murine cardiovascular system," J. Biomed. Opt **11**, 021014-021014-021018 (2006).

477. M. W. Jenkins, P. Patel, H. Deng, M. M. Montano, M. Watanabe, and A. M. Rollins, "Phenotyping transgenic embryonic murine hearts using optical coherence tomography," Applied Optics **46**, 1776-1781 (2007).

478. A. L. Lopez, S. Wang, K. V. Larin, P. A. Overbeek, and I. V. Larina, "Live four-dimensional optical coherence tomography reveals embryonic cardiac phenotype in mouse mutant," J. Biomed. Opt **20**, 090501 (2015).

479. A. L. Lopez, S. Wang, M. Garcia, C. Valladolid, K. V. Larin, and I. V. Larina, "Live dynamic imaging and analysis of developmental cardiac defects in mouse models with optical coherence tomography," SPIE BiOS **9334**, 93340S-93340S-93345 (2015).

480. M. D. Garcia, A. L. Lopez, K. V. Larin, and I. V. Larina, "Imaging of cardiovascular development in Mammalian embryos using optical coherence tomography," Methods Mol. Biol. **1214**, 151-161 (2015).

481. I. V. Larina, S. Ivers, S. Syed, M. E. Dickinson, and K. V. Larin, "Hemodynamic measurements from individual blood cells in early mammalian embryos with Doppler swept source OCT," Optics Letters **34**, 986-988 (2009).

482. I. V. Larina, N. Sudheendran, M. Ghosn, J. Jiang, A. Cable, K. V. Larin, and M. E. Dickinson, "Live imaging of blood flow in mammalian embryos using doppler swept-source optical coherence tomography," J. Biomed. Opt **13**, 060506-060506-060503 (2008).

483. O. A. Grishina, S. Wang, and I. V. Larina, "Speckle variance optical coherence tomography of blood flow in the beating mouse embryonic heart," J. Biophoton. **10**, 735-743 (2017).

484. S. H. Syed, A. J. Coughlin, M. D. Garcia, S. Wang, J. L. West, K. V. Larin, and I. V. Larina, *Optical coherence tomography guided microinjections in live mouse embryos: high-resolution targeted manipulation for mouse embryonic research* (SPIE, 2015), Vol. 20, pp. 1-7, 7.

485. N. Sudheendran, S. H. Syed, M. E. Dickinson, I. V. Larina, and K. V. Larin, "Speckle variance OCT imaging of the vasculature in live mammalian embryos," Laser Physics Letters **8**, 247-252 (2011).

486. T. Yu, Y. Qi, H. Gong, Q. Luo, and D. Zhu, "Optical clearing for multiscale biological tissues," Journal of Biophotonics **11**, e201700187 (2018).

487. K. Tainaka, A. Kuno, S. I. Kubota, T. Murakami, and H. R. Ueda, "Chemical Principles in Tissue Clearing and Staining Protocols for Whole-Body Cell Profiling," Annual Review of Cell and Developmental Biology **32**, 713-741 (2016).

488. V. V. Tuchin, "Tissue Optics and Photonics: Light-Tissue Interaction," 2015 **1**, 37 (2015).

489. H. U. Dodt, U. Leischner, A. Schierloh, N. Jahrling, C. P. Mauch, K. Deininger, J. M. Deussing, M. Eder, W. Zieglgänsberger, and K. Becker, "Ultramicroscopy: three-dimensional visualization of neuronal networks in the whole mouse brain," Nature methods **4**, 331-336 (2007).

490. A. Erturk, C. P. Mauch, F. Hellal, F. Forstner, T. Keck, K. Becker, N. Jahrling, H. Steffens, M. Richter, M. Hubener, E. Kramer, F. Kirchhoff, H. U. Dodt, and F. Bradke, "Three-dimensional imaging of the unsectioned adult spinal cord to assess axon regeneration and glial responses after injury," Nature Medicine **18**, 166-171 (2012).

491. H. Hama, H. Kurokawa, H. Kawano, R. Ando, T. Shimogori, H. Noda, K. Fukami, A. Sakaue-Sawano, and A. Miyawaki, "Scale: a chemical approach for fluorescence imaging and reconstruction of transparent mouse brain," Nature Neuroscience **14**, 1481-U1166 (2011).

492. M.-T. Ke, S. Fujimoto, and T. Imai, "SeeDB: a simple and morphology-preserving optical clearing agent for neuronal circuit reconstruction," Nature Neuroscience **16**, 1154-U1246 (2013).

493. K. Chung, J. Wallace, S.-Y. Kim, S. Kalyanasundaram, A. S. Andalman, T. J. Davidson, J. J. Mirzabekov, K. A. Zalocusky, J. Mattis, A. K. Denisin, S. Pak, H. Bernstein, C. Ramakrishnan, L.

Grosenick, V. Gradinaru, and K. Deisseroth, "Structural and molecular interrogation of intact biological systems," Nature **497**, 332-+ (2013).

494. T. Kuwajima, A. A. Sitko, P. Bhansali, C. Jurgens, W. Guido, and C. Mason, "ClearT: a detergent- and solvent-free clearing method for neuronal and non-neuronal tissue," Development (Cambridge, England) **140**, 1364-1368 (2013).

495. M. D. Wong, M. C. van Eede, S. Spring, S. Jevtic, J. C. Boughner, J. P. Lerch, and R. M. Henkelman, "4D atlas of the mouse embryo for precise morphological staging," Development (Cambridge, England) **142**, 3583-3591 (2015).

496. X. Wen, S. L. Jacques, V. V. Tuchin, and D. Zhu, "Enhanced optical clearing of skin in vivo and optical coherence tomography in-depth imaging," J. Biomed. Opt **17**, 066022 (2012).

497. N. Sudheendran, M. Mohamed, M. G. Ghosn, V. V. Tuchin, and K. V. Larin, "Assessment of tissue optical clearing as a function of glucose concentration using optical coherence tomography," J Innov Opt Health Sci **03**, 169-176 (2010).

498. M. G. Ghosn, V. V. Tuchin, and K. V. Larin, "Depth-resolved monitoring of glucose diffusion in tissues by using optical coherence tomography," Optics Letters **31**, 2314-2316 (2006).

499. I. V. Larina, E. F. Carbajal, V. V. Tuchin, M. E. Dickinson, and K. V. Larin, "Enhanced OCT imaging of embryonic tissue with optical clearing," Laser Physics Letters **5**, 476-479 (2008).

500. L. Thrane, T. M. Jørgensen, and J. Männer, *Optical tissue clearing improves usability of optical coherence tomography (OCT) for high-throughput analysis of the internal structure and 3D morphology of small biological objects such as vertebrate embryos*, SPIE BiOS (SPIE, 2014), Vol. 8953.

501. M. K. Schwarz, A. Scherbarth, R. Sprengel, J. Engelhardt, P. Theer, and G. Giese, "Fluorescent-Protein Stabilization and HighResolution Imaging of Cleared, Intact Mouse Brains," Plos One **10**(2015).

502. K. Becker, N. Jaehrling, S. Saghafi, R. Weiler, and H.-U. Dodt, "Chemical Clearing and Dehydration of GFP Expressing Mouse Brains," Plos One **7**(2012).

503. A. Ertuerk, K. Becker, N. Jaehrling, C. P. Mauch, C. D. Hojer, J. G. Egen, F. Hellal, F. Bradke, M. Sheng, and H.-U. Dodt, "Three-dimensional imaging of solvent-cleared organs using 3DISCO," Nature Protocols **7**, 1983-1995 (2012).

504. N. Renier, Z. Wu, D. J. Simon, J. Yang, P. Ariel, and M. Tessier-Lavigne, "iDISCO: A Simple, RapidMethod to Immunolabel Large Tissue Samples for Volume Imaging," Cell **159**, 896-910 (2014).

505. N. Renier, E. L. Adams, C. Kirst, Z. Wu, R. Azevedo, J. Kohl, A. E. Autry, L. Kadiri, K. U. Venkataraju, Y. Zhou, V. X. Wang, C. Y. Tang, O. Olsen, C. Dulac, P. Osten, and M. Tessier-Lavigne, "Mapping of Brain Activity by Automated Volume Analysis of Immediate Early Genes," Cell **165**, 1789-1802 (2016).

506. C. Pan, R. Cai, F. P. Quacquarelli, A. Ghasemigharagoz, A. Lourbopoulos, P. Matryba, N. Plesnila, M. Dichgans, F. Hellal, and A. Ertuerk, "Shrinkage-mediated imaging of entire organs and organisms using uDISCO," Nature Methods **13**, 859-+ (2016).

507. Y. Aoyagi, R. Kawakami, H. Osanai, T. Hibi, and T. Nemoto, "A Rapid Optical Clearing Protocol Using 2,2'-Thiodiethanol for Microscopic Observation of Fixed Mouse Brain," Plos One **10**(2015).

508. I. Costantini, J.-P. Ghobril, A. P. Di Giovanna, A. L. A. Mascaro, L. Silvestri, M. C. Muellenbroich, L. Onofri, V. Conti, F. Vanzi, L. Sacconi, R. Guerrini, H. Markram, G. Iannello, and F. S. Pavone, "A versatile clearing agent for multi-modal brain imaging," Scientific Reports **5**(2015).

509. H. Hama, H. Hioki, K. Namiki, T. Hoshida, H. Kurokawa, F. Ishidate, T. Kaneko, T. Akagi, T. Saito, T. Saido, and A. Miyawaki, "Sca/eS: an optical clearing palette for biological imaging," Nature Neuroscience **18**, 1518-+ (2015).

510. E. A. Susaki, K. Tainaka, D. Perrin, F. Kishino, T. Tawara, T. M. Watanabe, C. Yokoyama, H. Onoe, M. Eguchi, S. Yamaguchi, T. Abe, H. Kiyonari, Y. Shimizu, A. Miyawaki, H. Yokota, and H. R. Ueda, "Whole-Brain Imaging with Single-Cell Resolution Using Chemical Cocktails and Computational Analysis," Cell **157**, 726-739 (2014).

511. S. I. Kubota, K. Takahashi, J. Nishida, Y. Morishita, S. Ehata, K. Tainaka, K. Miyazono, and H. R. Ueda, "Whole-Body Profiling of Cancer Metastasis with Single-Cell Resolution," Cell Reports **20**, 236-250 (2017).

512. K. Tainaka, S. I. Kubota, T. Q. Suyama, E. A. Susaki, D. Perrin, M. Ukai-Tadenuma, H. Ukai, and H. R. Ueda, "Whole-Body Imaging with Single-Cell Resolution by Tissue Decolorization," Cell **159**, 911-924 (2014).

513. E. A. Susaki, K. Tainaka, D. Perrin, H. Yukinaga, A. Kuno, and H. R. Ueda, "Advanced CUBIC protocols for whole-brain and whole-body clearing and imaging," Nature Protocols **10**, 1709-1727 (2015).

514. D. Kurihara, Y. Mizuta, Y. Sato, and T. Higashiyama, "ClearSee: a rapid optical clearing reagent for whole-plant fluorescence imaging," Development **142**, 4168-4179 (2015).

515. B. Hou, D. Zhang, S. Zhao, M. Wei, Z. Yang, S. Wang, J. Wang, X. Zhang, B. Liu, L. Fan, Y. Li, Z. Qiu, C. Zhang, and T. Jiang, "Scalable and Dil-compatible optical clearance of the mammalian brain," Frontiers in Neuroanatomy **9**(2015).

516. M.-T. Ke, Y. Nakai, S. Fujimoto, R. Takayama, S. Yoshida, T. S. Kitajima, M. Sato, and T. Imai, "Super-Resolution Mapping of Neuronal Circuitry With an Index-Optimized Clearing Agent," Cell Reports **14**, 2718-2732 (2016).

517. E. L. Sylwestrak, P. Rajasethupathy, M. A. Wright, A. Jaffe, and K. Deisseroth, "Multiplexed Intact-Tissue Transcriptional Analysis at Cellular Resolution," Cell **164**, 792-804 (2016).

518. A. Greenbaum, K. Y. Chan, T. Dobreva, D. Brown, D. H. Balani, R. Boyce, H. M. Kronenberg, H. J. McBride, and V. Gradinaru, "Bone CLARITY: Clearing, imaging, and computational analysis of osteoprogenitors within intact bone marrow," Science Translational Medicine **9**(2017).

519. W. M. Palmer, A. P. Martin, J. R. Flynn, S. L. Reed, R. G. White, R. T. Furbank, and C. P. L. Grof, "PEA-CLARITY: 3D molecular imaging of whole plant organs," Scientific Reports **5**(2015).

520. B. Yang, J. B. Treweek, R. P. Kulkarni, B. E. Deverman, C.-K. Chen, E. Lubeck, S. Shah, L. Cai, and V. Gradinaru, "Single-Cell Phenotyping within Transparent Intact Tissue through Whole-Body Clearing," Cell **158**, 945-958 (2014).

521. J. B. Treweek, K. Y. Chan, N. C. Flytzanis, B. Yang, B. E. Deverman, A. Greenbaum, A. Lignell, C. Xiao, L. Cai, M. S. Ladinsky, P. J. Bjorkman, C. C. Fowlkes, and V. Gradinaru, "Whole-body tissue stabilization and selective extractions via tissue-hydrogel hybrids for high-resolution intact circuit mapping and phenotyping," Nature Protocols **10**, 1860-1896 (2015).

522. J. Woo, M. Lee, J. M. Seo, H. S. Park, and Y. E. Cho, "Optimization of the optical transparency of rodent tissues by modified PACT-based passive clearing," Experimental and Molecular Medicine **48**(2016).

523. K. Sung, Y. Ding, J. Ma, H. Chen, V. Huang, M. Cheng, C. F. Yang, J. T. Kim, D. Eguchi, D. Di Carlo, T. K. Hsiai, A. Nakano, and R. P. Kulkarni, "Simplified three-dimensional tissue clearing and incorporation of colorimetric phenotyping," Scientific Reports **6**(2016).

524. A. K. L. Liu, H. M. Lai, R. C. C. Chang, and S. M. Gentleman, "Free of acrylamide sodium dodecyl sulphate (SDS)-based tissue clearing (FASTClear): a novel protocol of tissue clearing for three-dimensional visualization of human brain tissues," Neuropathology and Applied Neurobiology **43**, 346-351 (2017).

525. E. Lee, J. Choi, Y. Jo, J. Y. Kim, Y. J. Jang, H. M. Lee, S. Y. Kim, H.-J. Lee, K. Cho, N. Jung, E. M. Hur, S. J. Jeong, C. Moon, Y. Choe, I. J. Rhyu, H. Kim, and W. Sun, "ACT-PRESTO: Rapid and consistent tissue clearing and labeling method for 3-dimensional (3D) imaging," Scientific Reports **6**(2016).

526. E. Murray, J. H. Cho, D. Goodwin, T. Ku, J. Swaney, S.-Y. Kim, H. Choi, Y.-G. Park, J.-Y. Park, A. Hubbert, M. McCue, S. Vassallo, N. Bakh, M. P. Frosch, V. J. Wedeen, H. S. Seung, and K. Chung, "Simple, Scalable Proteomic Imaging for High-Dimensional Profiling of Intact Systems," Cell **163**, 1500-1514 (2015).

527. S.-Y. Kim, J. H. Cho, E. Murray, N. Bakh, H. Choi, K. Ohn, L. Ruelas, A. Hubbert, M. McCue, S. L. Vassallo, P. J. Keller, and K. Chung, "Stochastic electrotransport selectively enhances the transport of highly electromobile molecules," Proceedings of the National Academy of Sciences of the United States of America **112**, E6274-E6283 (2015).

528. T. Hiruma, Y. Nakajima, and H. Nakamura, "Development of pharyngeal arch arteries in early mouse embryo," Journal of anatomy **201**, 15-29 (2002).

529. M. D. Wong, S. Spring, and R. M. Henkelman, "Structural Stabilization of Tissue for Embryo Phenotyping Using Micro-CT with Iodine Staining," PLOS ONE **8**, e84321 (2014).

530. C.-W. Hsu, L. Wong, T. L. Rasmussen, S. Kalaga, M. L. McElwee, L. C. Keith, R. Bohat, J. R. Seavitt, A. L. Beaudet, and M. E. Dickinson, "Three-dimensional microCT imaging of mouse

development from early post-implantation to early postnatal stages," Developmental Biology **419**, 229-236 (2016).

531. V. B. Sampson, J. M. David, I. Puig, P. U. Patil, A. Garcia de Herreros, G. V. Thomas, and A. K. Rajasekaran, "Wilms' Tumor Protein Induces an Epithelial-Mesenchymal Hybrid Differentiation State in Clear Cell Renal Cell Carcinoma," Plos One **9**(2014).

532. T. Watson, N. Andrews, S. Davis, L. Bugeon, M. D. Dallman, and J. McGinty, "OPTiM: Optical projection tomography integrated microscope using open-source hardware and software," PLOS ONE **12**, e0180309 (2017).

533. C. Wu, H. Le, S. Ran, M. Singh, I. V. Larina, D. Mayerich, M. E. Dickinson, and K. V. Larin, "Comparison and combination of rotational imaging optical coherence tomography and selective plane illumination microscopy for embryonic study," Biomed. Opt. Express **8**, 4629-4639 (2017).

534. J. Mayer, A. Robert-Moreno, R. Danuser, J. V. Stein, J. Sharpe, and J. Swoger, "OPTiSPIM: integrating optical projection tomography in light sheet microscopy extends specimen characterization to nonfluorescent contrasts," Opt. Lett. **39**, 1053-1056 (2014).

Vita

Yongyang Huang joined Lehigh University in 2013 as a graduate research assistant in Zlab, supervised by Prof. Chao Zhou. Before Lehigh, Yongyang Huang got a Bachelor's degree in Physics from Peking University, Beijing, China. Yongyang's research work focuses on developing optical coherence tomography (OCT) systems, a 3D biomedical imaging modality with high resolution and speed. Yongyang has taken the lead in the project to establish an OCT imaging platform for high-throughput imaging of tumor spheroid assays, which involved developing a custom OCT system, preparing 3D cell cultures, optimizing OCT imaging protocols and performing data analyses with various software toolkits. With the established platform, Yongyang has lead a team to conduct OCT screens of tumor spheroid assays to characterize their morphology, 3D dead-cell distribution, 3D cell invasion and invasion-inhibition effects under drug treatment. With his experience in SDM-OCT technology, Yongyang has developed several SDM-OCT systems with various optimization approaches, including the integration of a photonic chip, implementation of full-range technique, and improved strategy for phase stabilization for OCT angiography. Additionally, Yongyang has explored the potential OCT applications in non-destructive characterization of various samples, including the liquid crystal droplet, polystyrene latex, mouse embryos and skin equivalents, in collaborations with investigators from different academic institutions and companies. Yongyang has been nominated as Rossin Doctoral Fellow of Lehigh University since 2016.